Edited by Sabu Thomas, Kuruvilla Joseph,
S. K. Malhotra, Koichi Goda, M. S. Sreekala

WILEY-VCH

Polymer Composites

Volume 2: Nanocomposites

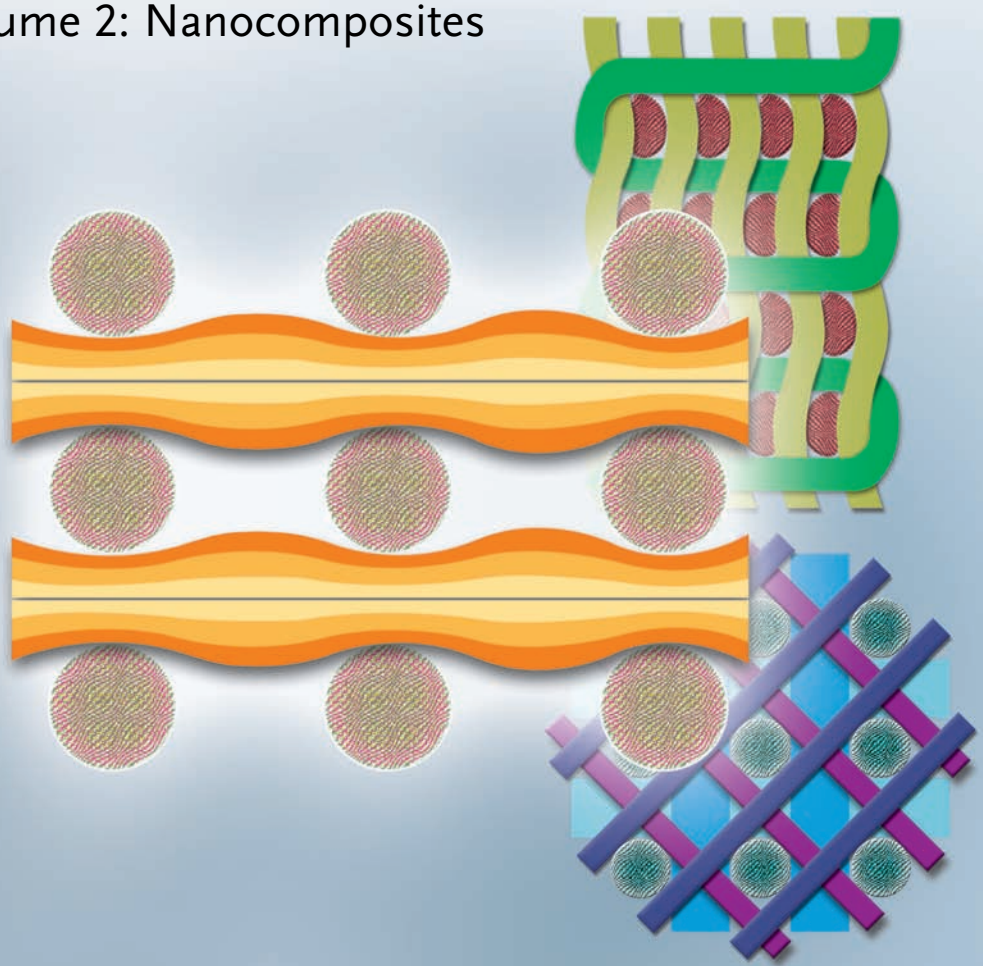

Edited by
Sabu Thomas, Kuruvilla Joseph,
Sant Kumar Malhotra, Koichi Goda,
and Meyyarappallil Sadasivan Sreekala

Polymer Composites

Related Titles

Thomas, S., Joseph, K., Malhotra, S. K., Goda, K., Sreekala, M. S. (eds.)

Polymer Composites

Series: Polymer Composites

Volume 1
2012
ISBN: 978-3-527-32624-2

Volume 3
2014
ISBN: 978-3-527-32980-9

3 Volume Set
2014
ISBN: 978-3-527-32985-4

Thomas, S., Durand, D., Chassenieux, C., Jyotishkumar, P. (eds.)

Handbook of Biopolymer-Based Materials

From Blends and Composites to Gels and Complex Networks

2 Volumes
2013
ISBN: 978-3-527-32884-0

Decher, G., Schlenoff, J. (eds.)

Multilayer Thin Films

Sequential Assembly of Nanocomposite Materials
Second, completely revised and enlarged edition

2012
ISBN: 978-3-527-31648-9

Kumar, C. S. S. R. (ed.)

Nanocomposites

Series: Nanomaterials for the Life Sciences (Volume 8)

2010
ISBN: 978-3-527-32168-1

Thomas, S., Stephen, R.

Rubber Nanocomposites

Preparation, Properties and Applications

2010
ISBN: 978-0-470-82345-3

Mittal, V. (ed.)

Optimization of Polymer Nanocomposite Properties

2010
ISBN: 978-3-527-32521-4

Mittal, V. (ed.)

In-situ Synthesis of Polymer Nanocomposites

Series: Polymer Nano-, Micro- and Macrocomposites (Volume 2)

2011
ISBN: 978-3-527-32879-6

Mittal, V. (ed.)

Characterization Techniques for Polymer Nanocomposites

Series: Polymer Nano-, Micro- and Macrocomposites (Volume 3)

2012
ISBN: 978-3-527-33148-2

Mittal, V. (ed.)

Modeling and Prediction of Polymer Nanocomposite Properties

Series: Polymer Nano-, Micro- and Macrocomposites (Volume 4)

2013
ISBN: 978-3-527-33150-5

Edited by Sabu Thomas, Kuruvilla Joseph, Sant Kumar Malhotra, Koichi Goda, and Meyyarappallil Sadasivan Sreekala

Polymer Composites

Volume 2

WILEY-VCH Verlag GmbH & Co. KGaA

The Editors

Prof. Dr. Sabu Thomas
Mahatma Gandhi University
Centre for Nanosc.a. Nanotech.
Priyadarshini Hills P.O.
Kottayam, Kerala 686560
India

Prof. Dr. Kuruvilla Joseph
Peringattu House
Thellakom P.O.
Kottayam, Kerala 686016
India

Dr. Sant Kumar Malhotra
Flat-YA, Kings Mead
Srinagar Colony
14/3, South Mada Street
Saidafet, Chennai 60015
India

Prof. Dr. Koichi Goda
Yamaguchi University
Faculty of Engineering
Tokiwadai 2-16-1
Ube, Yamaguchi 755-8611
Japan

Dr. Meyyarappallil Sadasivan Sreekala
Sree Sankara College
Grad. Dept. of Chemistry
Sankar Nagar, Mattoor
Ernakulam, Kerala 683574
India

Library of Congress Card No.: applied for

British Library Cataloguing-in-Publication Data
A catalogue record for this book is available from the British Library.

Bibliographic information published by the Deutsche Nationalbibliothek
The Deutsche Nationalbibliothek lists this publication in the Deutsche Nationalbibliografie; detailed bibliographic data are available on the Internet at <http://dnb.d-nb.de>.

Print ISBN: 978-3-527-32979-3
ePDF ISBN: 978-3-527-65240-2
ePub ISBN: 978-3-527-65239-6
mobi ISBN: 978-3-527-65238-9
oBook ISBN: 978-3-527-65237-2

Composition Thomson Digital, Noida, India
Printing and Binding Markono Print Media Pte Ltd, Singapore
Cover Design Adam Design, Weinheim

Printed in Singapore
Printed on acid-free paper

Contents

The Editors

Sabu Thomas is a Professor of Polymer Science and Engineering at Mahatma Gandhi University (India). He is a Fellow of the Royal Society of Chemistry and a Fellow of the New York Academy of Sciences. Thomas has published over 430 papers in peer reviewed journals on polymer composites, membrane separation, polymer blend and alloy, and polymer recycling research and has edited 17 books. He has supervised 60 doctoral students.

Kuruvilla Joseph is a Professor of Chemistry at Indian Institute of Space Science and Technology (India). He has held a number of visiting research fellowships and has published over 50 papers on polymer composites and blends.

S. K. Malhotra is Chief Design Engineer and Head of the Composites Technology Centre at the Indian Institute of Technology, Madras. He has published over 100 journal and proceedings papers on polymer and alumina-zirconia composites.

Koichi Goda is a Professor of Mechanical Engineering at Yamaguchi University. His major scientific fields of interest are reliability and engineering analysis of composite materials and development and evaluation of environmentally friendly and other advanced composite materials.

M. S. Sreekala is an Assistant Professor of Chemistry at Post Graduate Department of Chemistry, SreeSankara College, Kalady (India). She has published over 40 paperson polymer composites (including biodegradable and green composites) in peer reviewed journals and has held a number of Scientific Positions and Research Fellowships including those from the Humboldt Foundation, Germany and Japan Society for Promotion of Science, Japan.

List of Contributors

Marcelo Antunes
Universitat Politècnica de Catalunya (UPC)
Departament de Ciència dels Materials i Enginyeria Metallúrgica
Centre Català del Plàstic
C. Jordi Girona, 31
08034 Barcelona
Spain

David Arencón
Universitat Politècnica de Catalunya (UPC)
Departament de Ciència dels Materials i Enginyeria Metallúrgica
Centre Català del Plàstic
C. Jordi Girona, 31
08034 Barcelona
Spain

Lucilene Betega de Paiva
Institute for Technological Research (IPT)
Laboratory of Chemical Process and Particle Technology
Group for Bionanomanufacturing
Avenida Professor Almeida Prado, 532, Butantã
05508-901, São Paulo, SP
Brazil

Valerio Causin
Università degli Studi di Padova
Dipartimento di Scienze Chimiche
Via Marzolo, 1
35131 Padova
Italy

Carola Esposito Corcione
Università del Salento
Dipartimento di Ingegneria dell'Innovazione
Complesso Ecotekne – edificio "Corpo O"
Via per Monteroni
73100 Lecce
Italy

Mariaenrica Frigione
Università del Salento
Dipartimento di Ingegneria dell'Innovazione
Complesso Ecotekne – edificio "Corpo O"
Via per Monteroni
73100 Lecce
Italy

Koichi Goda
Yamaguchi University
Faculty of Engineering
Tokiwadai 2–16-1
Ube, Yamaguchi 755–8611
Japan

Antonio Greco
Università del Salento
Dipartimento di Ingegneria dell'Innovazione
Complesso Ecotekne – edificio "Corpo O"
Via per Monteroni
73100 Lecce
Italy

Ruoyu Hong
Soochow University
College of Chemistry, Chemical Engineering and Materials Science
Key Laboratory of Organic Synthesis of Jiangsu Province
Suzhou Industrial Park
Suzhou 215123
Jiangsu
China

and

Kailuan Energy Chemical Co., Ltd.
Coal Chemical R&D Center
Seaport Economic Development Zone
Tangshan 063611
Hebei
China

Kuruvilla Joseph
Peringattu House
Thellakom
Kottayam 686016
Kerala
India

and

Indian Institute of Space Science and Technology
Department of Space
Government of India Valiyamala P. O.
Nedumangadu
Thiruvananthapuram
Kerala
India

Iren E. Kuznetsova
Institute of Radio Engineering and Electronics of RAS
Saratov Branch
Zelyonaya str., 38
Saratov 410019
Russia

Jianhua Li
Kailuan Energy Chemical Co., Ltd.
Coal Chemical R&D Center
Seaport Economic Development Zone
Tangshan 063611
Hebei
China

Hongzhong Li
Chinese Academy of Sciences
Institute of Process Engineering
State Key Laboratory of Multiphase Complex Systems
Beijing 100080
China

Alfonso Maffezzoli
Università del Salento
Dipartimento di Ingegneria dell'Innovazione
Complesso Ecotekne – edificio "Corpo O"
Via per Monteroni
73100 Lecce
Italy

Sant Kumar Malhotra
Flat-YA, Kings Mead
Srinagar Colony
14/3, South Mada Street
Saidafet, Chennai 60015
Tamil Nadu
India

Ana Rita Morales
School of Chemical Engineering
Department of Materials Engineering and Bioprocess
State University of Campinas - UNICAMP
P.O. Box 6066
Avenida Albert Einstein, 500
13083-852, Campinas, SP
Brazil

Thien Phap Nguyen
Université de Nantes
CNRS
Institut des Matériaux Jean Rouxel
2 rue de la Houssinière
44322 Nantes Cedex 3
France

Kostas Papagelis
University of Patras
Department of Materials Science
26504 Rio Patras
Greece

Vera Realinho
Universitat Politècnica de Catalunya (UPC)
Departament de Ciència dels Materials i Enginyeria Metallúrgica
Centre Català del Plàstic
C. Jordi Girona, 31
08034 Barcelona
Spain

Lucas Reijnders
University of Amsterdam
IBED
Science Park 904
1090 GE Amsterdam
The Netherlands

Amrita Saritha
Amrita Vishwavidyapeetham
University
Amritapuri
Kollam 690525
Kerala
India

Alexander M. Shikhabudinov
Institute of Radio Engineering and Electronics of RAS
Saratov Branch
Zelyonaya str., 38
Saratov 410019
Russia

Meyyarappallil Sadasivan Sreekala
Sree Sankara College
Graduate Department of Chemistry
Sankar Nagar
Mattoor, Ernakulam 683574
Kerala
India

Dimitrios Tasis
University of Patras
Department of Materials Science
26504 Rio Patras
Greece

Sabu Thomas
Mahatma Gandhi University
Centre for Nanoscience and Nanotechnology
Priyadarshini Hills
Kottayam 686560
Kerala
India

José I. Velasco
Universitat Politècnica de Catalunya (UPC)
Departament de Ciència dels Materials i Enginyeria Metallúrgica
Centre Català del Plàstic
C. Jordi Girona, 31
08034 Barcelona
Spain

Liaosha Wang
Soochow University
College of Chemistry, Chemical Engineering and Materials Science
Key Laboratory of Organic Synthesis of Jiangsu Province
Suzhou Industrial Park
Suzhou 215123
Jiangsu
China

Aibing Yu
The University of New South Wales
School of Materials Science and Engineering
Sydney
NSW 2052
Australia

Boris D. Zaitsev
Institute of Radio Engineering and Electronics of RAS
Saratov Branch
Zelyonaya str., 38
Saratov 410019
Russia

Qinghua Zeng
University of Western Sydney
School of Engineering
Penrith South DC
NSW 1797
Australia

1
State of the Art – Nanomechanics

Amrita Saritha, Sant Kumar Malhotra, Sabu Thomas, Kuruvilla Joseph, Koichi Goda, and Meyyarappallil Sadasivan Sreekala

1.1
Introduction

Nanomechanics, a branch of *nanoscience*, focuses on the fundamental *mechanical* properties of physical systems at the nanometer scale. It has emerged on the crossroads of classical mechanics, solid-state physics, statistical mechanics, materials science, and quantum chemistry. Moreover, it provides a scientific foundation for *nanotechnology*. Often, it is looked upon as a *branch* of nanotechnology, that is, an applied area with a focus on the mechanical properties of *engineered* nanostructures and nanosystems that include nanoparticles, nanopowders, nanowires, nanorods, nanoribbons, nanotubes, including carbon nanotubes (CNTs) and boron nitride nanotubes (BNNTs), nanoshells, nanomembranes, nanocoatings, nanocomposites, and so on.

Nanotechnology can be broadly defined as "The creation, processing, characterization, and utilization of materials, devices, and systems with dimensions on the order of 0.1–100 nm, exhibiting novel and significantly enhanced physical, chemical, and biological properties, functions, phenomena, and processes due to their nanoscale size" [1]. Nanobiotechnology, nanosystems, nanoelectronics, and nanostructured materials, especially nanocomposites, are of current interest in nanotechnology. Polymer nanocomposites have gained attention as a means of improving polymer properties and extending their utility by using molecular or nanoscale reinforcements rather than conventional particulate fillers. The transition from microparticles to nanoparticles yields dramatic changes in physical properties.

Recently, the advances in synthesis techniques and the ability to characterize materials on atomic scale have led to a growing interest in nanosized materials. The invention of nylon 6/clay nanocomposites by the Toyota Research Group of Japan heralded a new chapter in the field of polymer composites. Polymer nanocomposites combine these two concepts, that is, composites and nanosized materials. Polymer nanocomposites are materials containing inorganic components that have dimensions in nanometers. In this chapter, the discussion is restricted to polymer

Polymer Composites: Volume 2, First Edition. Edited by Sabu Thomas, Kuruvilla Joseph, Sant Kumar Malhotra, Koichi Goda, and Meyyarappallil Sadasivan Sreekala.

nanocomposites made by dispersing two-dimensional layered nanoclays as well as nanoparticles into polymer matrices. In contrast to the traditional fillers, nanofillers are found to be effective even at as low as 5 wt% loading. Nanosized clays have dramatically higher surface area compared to their macrosized counterparts such as china clay or talc. This allows them to interact effectively with the polymer matrix even at lower concentrations. As a result, polymer–nanoclay composites show significantly higher modulus, thermal stability, and barrier properties without much increase in the specific gravity and sometimes retaining the optical clarity to a great extent. As a result, the composites made by mixing layered nanoclays in polymer matrices are attracting increasing attention commercially. Thus, the understanding of the links between the microstructure, the flow properties of the melt, and the solid-state properties is critical for the successful development of polymer–nanoclay composite products.

Nevertheless, these promising materials exhibit behavior different from conventional composite materials with microscale structure due to the small size of the structural unit and high surface area/volume ratio. Nanoscale science and technology research is progressing with the use of a combination of atomic scale characterization and detailed modeling [2]. In the early 1990s, Toyota Central Research Laboratories in Japan reported work on a nylon 6 nanocomposite [3], for which a very small amount of nanofiller loading resulted in a pronounced improvement in thermal and mechanical properties. Common particle geometries and their respective surface area/volume ratios are shown in Figure 1.1. For the fiber and the layered material, the surface area/volume ratio is dominated, especially for nanomaterials, by the first term in the equation. The second term ($2/l$ and $4/l$) has a very small influence (and is often omitted) compared to the first term. Therefore, logically, a change in particle diameter, layer thickness, or fibrous material diameter from the micrometer to nanometer range will affect the surface area/volume ratio by three orders of magnitude [4]. Typical nanomaterials currently under investigation include

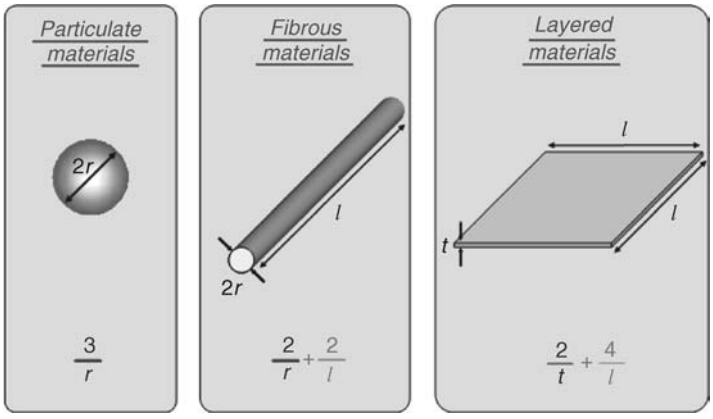

Figure 1.1 Common particle reinforcements and their respective surface area/volume ratios [4].

nanoparticles, nanotubes, nanofibers, fullerenes, and nanowires. In general, these materials are classified by their geometries; broadly, the three classes are particle, layered, and fibrous materials [4,5]. Carbon black, silica nanoparticles, and polyhedral oligomeric silsesquioxanes (POSS) can be classified as nanoparticle reinforcing agents while nanofibers and carbon nanotubes are examples of fibrous materials [5]. When the filler has a nanometer thickness and a high aspect ratio (30–1000) plate-like structure, it is classified as a layered nanomaterial (such as an organosilicate) [6]. The change of length scales from meters (finished woven composite parts), micrometers (fiber diameter), and submicrometers (fiber/matrix interphase) to nanometers (nanotube diameter) presents tremendous opportunities for innovative approaches in the processing, characterization, and analysis/modeling of this new generation of composite materials. As scientists and engineers seek to make practical materials and devices from nanostructures, a thorough understanding of the material behavior across length scales from the atomistic to macroscopic levels is required. Knowledge of how the nanoscale structure influences the bulk properties will enable design of the nanostructure to create multifunctional composites.

Wang *et al*. synthesized poly(styrene–maleic anhydride) (PSMA)/TiO_2 nanocomposites via the hydrolysis and condensation reactions of multicomponent sol since the PSMA has functional groups that can anchor TiO_2 and prevent it from aggregating [7]. Polystyrene or polycarbonate rutile nanocomposites have been synthesized by Nussbaumer *et al*. [8]. Singh *et al*. [9] studied the variation in fracture toughness of polyester resin due to the addition of aluminum particles of 20, 3.5, and 100 nm diameter. Results indicate an initial enhancement in fracture toughness followed by decrease at higher particle volume fraction. This phenomenon is attributed to the agglomeration of nanoparticles at higher particle volume content. Lopez *et al*. [10] examined the elastic modulus and strength of vinyl ester composites after the addition of 1, 2, and 3 wt% of alumina particles of 40 nm, 1 μm, and 3 μm size. For all particle sizes, the composite modulus increases monotonically with particle weight fraction. However, the strengths of composites are all below the strength of neat resin due to nonuniform particle size distribution and particle aggregation. The mechanical behavior of alumina-reinforced poly(methyl methacrylate) (PMMA) composites was studied by Ash *et al*. [11].

1.2 Nanoplatelet-Reinforced Composites

In the case of layered silicates, the filler is present in the form of sheets one to a few nanometer thick and hundreds to thousands nanometer long. In general, the organically modified silicate nanolayers are referred to as "nanoclays" or "organosilicates" [12]. It is important to know that the physical mixture of a polymer and layered silicate may not form nanocomposites [13]. Pristine-layered silicates usually contain hydrated Na^+ or K^+ ions [13]. To render layered silicates miscible with other polymer matrices, it is required to convert the normally hydrophilic silicate surface into an organophilic one, which can be carried out by ion-exchange reactions with

cationic surfactants [13]. Sodium montmorillonite (Na-MMT, $Na_x(Al_{2-x}Mg_x)(Si_4O_{10})(OH)_2 \cdot mH_2O$)-type layered silicate clays are available as micron-sized tactoids, which consist of several hundred individual plate-like structures with dimensions of 1 μm × 1 μm × 1 nm. These are held together by electrostatic forces (the gap in between two adjacent particles is 0.3 nm). The MMT particles, which are not separated, are often referred to as tactoids. The most difficult task is to break down the tactoids to the scale of individual particles in the dispersion process to form true nanocomposites, which has been a critical issue in current research [14,15–24]. Natural flake graphite (NFG) is also composed of layered nanosheets [25], where carbon atoms positioned on the NFG layer are tightened by covalent bonds, while those positioned in adjacent planes are bound by much weaker van der Waals forces. The weak interplanar forces allow for certain atoms, molecules, and ions to intercalate into the interplanar spaces of the graphite. The interplanar spacing is thus increased [25]. As it does not bear any net charge, intercalation of graphite cannot be carried out by ion-exchange reactions in the galleries like layered silicates [25]. The original graphite flakes with a thickness of 0.4–60 mm may expand up to 2–20 000 mm in length [26]. These sheets/layers get separated down to 1 nm thickness, forming high aspect ratio (200–1500) and high modulus (~1 TPa) graphite nanosheets. Furthermore, when dispersed in the matrix, the nanosheet exposes an enormous interface surface area (2630 m^2/g) and plays a key role in the improvement of both the physical and mechanical properties of the resultant nanocomposite [27]. The various preparative techniques for this type of nanocomposites are discussed below.

1.3 Exfoliation–Adsorption

This technique is based on a solvent system in which the polymer or prepolymer is soluble and the silicate layers are swellable. The layered silicates, owing to the weak forces that stack the layers together, can be easily dispersed in an adequate solvent such as water, acetone, chloroform, or toluene. When the polymer and the layered silicate are mixed, the polymer chains intercalate and displace the solvent within the interlayer of the silicate. The solvent is evaporated and the intercalated structure remains. For the overall process, in which polymer is exchanged with the previously intercalated solvent in the gallery, a negative variation in Gibbs free energy is required. The driving force for polymer intercalation into layered silicate from solution is the entropy gained by desorption of solvent molecules, which compensates for the decreased entropy of the intercalated chains. This method is good for the intercalation of polymers with little or no polarity into layered structures and facilitates production of thin films with polymer-oriented clay intercalated layers. The major disadvantage of this technique is the nonavailability of compatible polymer–clay systems. Moreover, this method involves the copious use of organic solvents, which is environmentally unfriendly and economically prohibitive. Biomedical poly(urethane–urea) (PUU)/MMT (MMT modified with

dimethyl ditallow ammonium cation) nanocomposites were prepared by adding OMLS (organically modified layered silicate) suspended in toluene dropwise to the solution of PUU in *N*,*N*-dimethylacetamide (DMAC). The mixture was then stirred overnight at room temperature, the solution was degassed, and the films were cast on round glass Petri dishes. The films were air dried for 24 h, and subsequently dried under vacuum at 50 °C for 24 h. Wide-angle X-ray diffraction (WAXD) analysis indicated the formation of intercalated nanocomposites [28]. The effects of heat and pressure on microstructures of isobutylene–isoprene rubber/clay nanocomposites prepared by solution intercalation (S-IIRCNs) were investigated [29]. A comparison of the WAXD patterns of untreated S-IIRCN and nanocomposites prepared by melt intercalation (M-IIRCN) reveals that the basal spacing of the intercalated structures in untreated M-IIRCN (i.e., 5.87 nm) is much larger than that in S-IIRCN (i.e., 3.50 nm), which is likely a result of the different methods of preparation. Tolle and Anderson [30] investigated the sensitivity of exfoliation for processing. They found that both lower temperatures for isothermal curing and higher heating rates for nonisothermal curing cause an inhibition of exfoliated morphology. There are several reports regarding the preparation of nanocomposites using the solvents [31–36]. Kornmann *et al*. [37] investigated the effect of three different curing agents upon the organoclay exfoliation in the diglycidyl ether of bisphenol A (DGEBA)-based system. In their work, exfoliation of organoclay occurred in cycloaliphatic diamine-cured DGEBA nanocomposites only at higher temperatures. Messermith and Giannelis [38] prepared exfoliated layered silicate epoxy nanocomposites from DGEBA and a nadic methyl anhydride curing agent and found that the dynamic storage modulus improved. The Toyota Research Group has been the first to use this method to produce polyimide (PI) nanocomposites [39,40]. Du *et al*. [41] prepared expandable polyaniline/graphite nanocomposites by chemical and physical treatments, especially by microwave irradiation. Instead of the usual HNO_3–H_2SO_4 route, they prepared the nanocomposites through the H_2O_2–H_2SO_4 route to avoid the evolution of poisonous NO_x. Shioyama [42] reported improved exfoliation at weight fractions of graphite below 1 wt% through polymerization with vaporized monomers such as styrene and isoprene. Fukushima and Drazal [43] used O_2 plasma-treated graphite nanoplatelets in an acrylamide/benzene solution. Improved mechanical and electrical properties were achieved using this technique. In the case of graphite, the term "complete exfoliation" has no exact meaning. It does not mean a single layer sheet as in the case of polymer–clay nanocomposites; it may mean a separated graphite flake that is completely delaminated layer by layer.

1.4 *In Situ* Intercalative Polymerization Method

In this method, the layered silicate is swollen within the liquid monomer or a monomer solution, so the formation cannot occur between the intercalated sheets. Polymerization can be initiated by heat or radiation, by the diffusion of a suitable initiator, or by an organic initiator or catalyst fixed through cation exchange inside

the interlayer before the swelling step. Yao *et al.* [44] reported the preparation of a novel kind of PU/MMT nanocomposite using a mixture of modified 4,4′-diphenylmethane diisocyanate (MMDI), modified polyether polyol (MPP), and Na-MMT. In a typical synthetic route, a known amount of Na-MMT was first mixed with 100 ml of MPP and then stirred at 50 °C for 72 h. Then, the mixture of MPP and Na-MMT was blended with a known amount of MMDI and stirred for 30 s at 20 °C, and finally cured at 78 °C for 168 h. Wang and Pinnavaia [45] reported the preparation of polyurethane–MMT nanocomposites using this technique. It can be seen that the extent of gallery expansion is mainly determined by the chain length of the gallery onium ions and is independent of the functionality or molecular weight of the polyols and the charge density of the clay. These nanocomposites exhibit an improvement in elasticity, as well as in modulus. In another study, Pinnavaia and Lan [46] reported the preparation of nanocomposites with a rubber/epoxy matrix obtained from DGEBA derivatives cured with a diamine so as to reach subambient glass transition temperatures. It has been shown that depending on the alkyl chain length of modified MMT, an intercalated and partially exfoliated or a totally exfoliated nanocomposite can be obtained.

1.5
Melt Intercalation

Recently, the melt intercalation technique has become the standard for the preparation of polymer nanocomposites. During polymer intercalation from solution, a relatively large number of solvent molecules have to be desorbed from the host to accommodate the incoming polymer chains. The desorbed solvent molecules gain one translational degree of freedom, and the resulting entropic gain compensates for the decrease in conformational entropy of the confined polymer chains. There are many advantages to direct melt intercalation over solution intercalation. Direct melt intercalation is highly specific for the polymer, leading to new hybrids that were previously inaccessible. In addition, the absence of solvent makes the process economically favorable method for industries from a waste perspective. On the other hand, during this process only a slow penetration (transport) of polymer takes place within the confined gallery. Polyamide 66/SEBS-*g*-MA alloys and their nanocomposites were prepared by melt compounding using a twin-screw extruder. Morphological investigations with different methods show pseudo-one-phase-type morphology for these prepared alloys at all percentages of rubber. Impact and tensile test results showed that rubber-toughened samples exhibit significantly more impact strength and elongation at break compared to virgin polyamide. Samples with 20% of rubber show impact strength about 15 times and elongation at yield several times more than those of virgin polyamide. So, these rubber-modified polyamides can be considered as supertoughened rubber. A general type organoclay at 4 and 8% has been used with rubber-toughened samples to tolerate their modulus and tensile strength. Obtained results show that nanoclay could significantly increase modulus and tensile strength of rubber-modified

polyamide 66 without considerable effects on impact strength. WAXD and scanning electron microscopy (SEM) results show that the polyamide 66 nanocomposites are better exfoliated in the presence of SEBS-*g*-MA. The reduced modulus and strength of alloys with functional rubber addition were counteracted by incorporation of organoclay without significant negative effects on the impact strength. Comparison of mechanical properties of these rubber-toughened polyamides with virgin polyamides shows an increase of about 1200 and 240% for impact strength and elongation at break, respectively, which is a very interesting result and shows excellent toughening of polyamide 66 with SEBS-*g*-MA rubber [47].

1.6 Nanofiber-Reinforced Composites

Vapor-grown carbon nanofibers (CNFs) have been used to reinforce a variety of polymers, including polypropylene (PP), polycarbonate, nylon, poly(ether sulfone), poly(ethylene terephthalate), poly(phenylene sulfide), acrylonitrile–butadiene–styrene (ABS), and epoxy. Carbon nanofibers are known to have wide-ranging morphologies, including structures with a disordered bamboo-like structure [48]. Finegan *et al.* [49,50] have investigated the processing and properties of carbon nanofiber/PP nanocomposites. In their work, they used a variety of as-grown nanofibers. Carbon nanofibers that were produced with longer gas-phase feedstock residence times were less graphitic but adhered better to the PP matrix, with composites showing improved tensile strength and Young's modulus. Oxidation of the carbon nanofiber was found to increase adhesion to the matrix and increase composite tensile strength, but extended oxidation deteriorated the properties of the fibers and their composites. In their investigation on the nanofiber composite damping properties, Finegan *et al.* [50] concluded that the trend of stiffness variation with fiber volume content is opposite to the trend of loss factor and damping in the composite is matrix dominated. Ma *et al.* [51] have spun polymer fibers with carbon nanofibers as reinforcement.

1.7 Characterization of Polymer Nanocomposites

Characterization tools are crucial to comprehend the basic physical and chemical properties of polymer nanocomposites. The commonly used powerful techniques are WAXD, small-angle X-ray scattering (SAXS), SEM, and transmission electron microscopy (TEM). The SEM provides images of surface features associated with a sample. However, there are two other techniques, scanning probe microscopy (SPM) and scanning tunneling microscopy (STM), that are indispensable in nanotube research. The SPM uses the interaction between a sharp tip and a surface to obtain an image. In STM, a sharp conducting tip is held sufficiently close to a surface (typically about 0.5 nm) such that electrons can "tunnel" across the gap. This method provides surface structural and electronic information at atomic level. The

invention of the STM inspired the development of other "scanning probe" microscopes, such as the atomic force microscope (AFM).

Due to its simplicity and availability, WAXD is most commonly used to probe the nanocomposite structure [52–58] and occasionally to study the kinetics of the polymer melt intercalation [59]. By monitoring the position, shape, and intensity of the basal reflections from the distributed silicate layers, the nanocomposite structure (intercalated or exfoliated) may be identified. For example, in an exfoliated nanocomposite, the extensive layer separation associated with the delamination of the original silicate layers in the polymer matrix results in the eventual disappearance of any coherent X-ray diffraction from the distributed silicate layers. On the other hand, for intercalated nanocomposites, the finite layer expansion associated with the polymer intercalation results in the appearance of a new basal reflection corresponding to the larger gallery height. Although WAXD offers a convenient method to determine the interlayer spacing of the silicate layers in the original layered silicates and in the intercalated nanocomposites (within 1–4 nm), little can be said about the spatial distribution of the silicate layers or any structural nonhomogeneities in nanocomposites. On the other hand, TEM allows a qualitative understanding of the internal structure, spatial distribution of the various phases, and views of the defect structure through direct visualization. However, special care must be exercised to guarantee a representative cross section of the sample. However, TEM is time intensive and gives only qualitative information on the sample as a whole, while low-angle peaks in WAXD allow quantification of changes in layer spacing.

1.8 Recent Advances in Polymer Nanocomposites

The effects of the coating amount of surfactant and the particle concentration on the impact strength of PP/$CaCO_3$ nanocomposites were investigated [60]. The morphological features and the free volume properties of an acrylic resin/laponite nanocomposite are investigated using X-ray diffraction and positron annihilation lifetime spectroscopy [61]. Structure and rheological properties of hybrids with polymer matrix and layered silicates as filler were studied. The peculiarity of this study is that the matrix depending on temperature can form different phase states including liquid crystalline (LC). So, a possibility of coexistence and superposition of different ordered structures can be realized at different temperatures. Three different fillers were used, natural Na-MMT and organoclays obtained by treating MMT with surfactants varying in polarity of their molecules. Depending on the type of clay, materials with different morphologies can be obtained. X-ray data showed that polyethylene glycol (PEG) intercalates all types of clay used whereas penetration of hydroxypropyl cellulose (HPC) macromolecules into clay galleries during mixing does not occur. Clay modified with more polar surfactants should be treated as the most convenient material to be intercalated by PEG [62]. With the incorporation of less than 9 wt% nanoclay, the dynamic storage modulus above the glass transition region of such a blend increases from 2 to 54 MPa. This tremendous reinforcing as well as the compatibilization effect of the nanoclay was understood by

thermodynamically driven preferential framework-like accumulation of exfoliated nanoclay platelets in the phase border of CR and EPDM, as observed, that is, from TEM [63]. A modified method for interconnecting multiwalled carbon nanotubes (MWCNTs) was put forward. Interconnected MWCNTs were obtained by reaction of acyl chloride and amino groups. SEM shows that heterojunctions of MWCNTs with different morphologies were formed. Then specimens of pristine MWCNTs, chemically functionalized MWCNTs, and interconnected MWCNT-reinforced epoxy resin composites were fabricated by cast molding. Tensile properties and fracture surfaces of the specimens were investigated [64]. A model to simulate the conductivity of carbon nanotube/polymer nanocomposites is presented. The proposed model is based on hopping between the fillers. A parameter related to the influence of the matrix in the overall composite conductivity is defined. It is demonstrated that increasing the aspect ratio of the fillers will increase the conductivity. Finally, it is demonstrated that the alignment of the filler rods parallel to the Measurement direction results in higher conductivity values, in agreement with results from recent experimental work done by Silva and coworkers. [65]. Polybutadiene (PB)/allylisobutyl polyhedral oligomeric silsesquioxane (A-POSS) nanocomposites have been prepared by using A-POSS and butadiene (Bd) as comonomers, *n*-BuLi as initiator, cyclohexane as solvent, and ethyl tetrahydrofurfuryl ether as structure modifier through the anionic polymerization technique. The reaction conditions, the type and content of the modifier and POSS, and so on affecting the copolymerization process and the microstructure of the nanocomposites were also investigated. The results showed that POSS incorporation obviously decreased the rate of polymerization and the molecular weight of the copolymers and increased polydispersity index of the copolymers. The reaction conditions (the reaction time and reaction temperature) had little effect on copolymerization [66].

1.9 Future Outlook

Biodegradable polymer-based nanocomposites have a great deal of future promise for potential applications as high-performance biodegradable materials. Scientists must continue to investigate strategies to optimize the fabrication of nanotube-enabled materials to achieve both improved mechanical and transport properties. The nanoscale of the reinforcement also presents additional challenges in mechanics research since we now must account for interactions at the atomic scale. Ultimately, a basic understanding of the structure–property relations will enable the nanoscale design of multifunctional materials for engineering applications ranging from structural and functional materials to biomaterials and beyond.

References

1 American Ceramic Society Bulletin (2004) **83** (10), 6.

2 Meyyappan, M. (2005) Introduction to Nanotechnology. In Nanotechnology

Aerospace Applications (pp. I-1 – I-2). Educational Notes RTO-EN-AVT-129.

3 Usuki, A., Kawasumi, M., Kojima, Y., Okada, A., Kurauchi, T., and Kamigaito, O.J. (1993) Swelling behavior of montmorillonite cation exchanged for ω-amino acids by ε-caprolactam. *Materials Research*, **8** (5), 1174–1175.

4 Thostenson, E., Li, C., and Chou, T. (2005) Review. Nanocomposites in context. *Journal of Composites Science & Technology*, **65**, 491–516.

5 Schmidt, D., Shah, D., and Giannelis, E.P. (2002) New advances in polymer/layered silicate nanocomposites. *Current Opinion in Solid State and Materials Science*, **6** (3), 205–212.

6 Alexandre, M. and Dubois, P. (2000) Polymer-layered silicate nanocomposites: preparation, properties and uses of a new class of materials. *Materials Science & Engineering Reports*, **28**, 1–63.

7 Wang, S.X., Wang, M., and Zhang, L.D. (1999) Anchor effect of poly (strene maleic anhydride)/TiO_2 nanocomposites. *Journal of Materials Science Letters*, **18**, 2009.

8 Nussbaumer, R.J., Caseri, W.R., Tervoort, T., and Smith, P. (2002) Synthesis and Characterization of Surface-modified Rutile Nanoparticles And\Transparent Polymer Composites Thereof. *Journal of Nanoparticle Research*, **4**, 319.

9 Singh, R.P., Zhang, M., and Chan, D. (2002) Toughening of a brittle thermosetting polymer: effects of reinforcement particle size and volume fraction. *Journal of Materials Science*, **37** (4), 781–788.

10 Lopez, L., Song, B.M.K., and Hahn, H.T. (2003) The effect of particle size in alumina nanocomposites. *Proceedings of the 14th International Conference on Composite Materials (ICCM-14), San Diego, CA*, Paper No. 138a.

11 Ash, B.J., Siegel, R.W., and Schadler, L.S. (2004) Mechanical behavior of alumina/poly(methyl methacrylate) nanocomposites. *Macromolecules*, **37** (4), 1358–1369.

12 Schmidt, D., Shah, D., and Giannelis, E.P. (2002) New advances in polymer/layered silicate nanocomposites. *Current Opinion in Solid State and Materials Science*, **6** (3), 205–212.

13 Ray, S.S. and Okamoto, M. (2003) Polymer/layered silicate nanocomposite: a review from preparation to processing. *Progress in Polymer Science*, **28**, 1539–1641.

14 Usuki, A., Kawasumi, M., Kojima, Y., Okada, A., Kurauchi, T., and Kamigaito, O.J. (1993) Swelling behavior of montmorillonite cation exchanged for ω-amino acids by ε-caprolactam. *Materials Research*, **8** (5), 1174.

15 Kornmann, X., Linderberg, H., and Bergund, L.A. (2001) Synthesis of epoxy–clay nanocomposites: influence of the nature of the clay on structure. *Polymer*, **42**, 1303–1310.

16 Kornmann, X., Linderberg, H., and Bergund, L.A. (2001) Synthesis of epoxy–clay nanocomposites: influence of the nature of the curing agent on structure. *Polymer*, **42**, 4493–4499.

17 Becker, O., Cheng, Y.B., Varley, R.J., and Simon, G.P. (2003) Layered silicate nanocomposites, based on various high-functionality epoxy resins: the influence of cure temperature on morphology, mechanical properties, and free volume. *Macromolecules*, **36**, 1616–1625.

18 Dennis, H.R., Hunter, D., Chang, D., Kim, S., and Paul, D.R. (2001) Effect of melt processing condition on the extent of exfoliation in organoclay-based nanocomposites. *Polymer*, **42**, 9513–9522.

19 Okada, A. and Usuki, A. (1995) The chemistry of polymer–clay hybrids. *Materials Science and Engineering*, **C3**, 109–115.

20 Lan, T., Kaviratna, P.D., and Pinnavaia, T.J. (1995) Mechanism of clay tactoid exfoliation in epoxy–clay nanocomposites. *Chemistry of Materials*, **7** (11), 2144–2150.

21 Lan, T. and Pinnavaia, T.J. (1994) On the nature of polyimide–clay hybrid nanocomposites. *Chemistry of Materials*, **6** (5), 573–575.

22 Lan, T. and Pinnavaia, T.J. (1994) Clay reinforced epoxy nanocomposites. *Chemistry of Materials*, **6** (12), 2216–2219.

23 Vaia, R.A., Jant, K.D., Kramer, E.J., and Giannelis, E.P. (1996) Microstructural evaluation of melt-intercalated polymer–organically modified layered silicate nanocomposites. *Chemistry of Materials*, **8**, 2628–2635.

24 Vaia, R.A., Ishii, H., and Giannelis, E.P. (1993) Synthesis and properties of two-dimensional nanostructures by direct intercalation of polymer melts in layered

silicates. *Chemistry of Materials*, **5**, 1694–1696.

25 Pan, Y.X., Yu, Z., Ou, Y., and Hu, G. (2000) A new process of fabricating electrically conducting nylon 6/graphite nanocomposites via intercalation polymerization. *Journal of Polymer Science Part B: Polymer Physics*, **38**, 1626–1633.

26 Findeissen, B. and Thomasius, M. (1981) East Germany Patent DD 150739.

27 Yasmin, A., Luo, J., and Daniel, I.M. (2006) Processing of expanded graphite reinforced polymer nanocomposites. *Composites Science and Technology*, **66** (9), 1182–1189.

28 Laus, M., Francescangeli, O., and Sandrolini, F. (1997) New hybrid nanocomposites based on an organophilic clay and poly(styrene-*b*-butadiene) copolymers. *Materials Research*, **12**, 3134.

29 Fakhru'l-Razi, A., Atieh, M.A., Girun, N., Chuah, T.G., El-Sadig, M., and Biak, D.R.A. (2006) Effect of multi-wall carbon nanotubes on the mechanical properties of natural rubber. *Composite Structures*, **75** (1–4), 496.

30 Tolle, T.B. and Anderson, D.P. (2002) Morphology development in layered silicate thermoset nanocomposites. *Composites Science and Technology*, **62**, 1033–1041.

31 Shen, Z., Simon, G.P., and Cheng, Y.B. (2002) Comparison of solution intercalation and melt intercalation of polymer–clay nanocomposites. *Polymer*, **43** (15), 4251–4260.

32 Liang, Y., Wang, Y., Wu, Y., Lu, Y., Zhang, H., and Zhang, L. (2004) Preparation and properties of isobutylene–isoprene rubber (IIR)/clay nanocomposites. *Polymer Testing*, **24** (1), 12–17.

33 Strawhecker, K. and Manias, E. (2000) Polypropylene/Montmorillonite Nanocomposites. Review of the Synthetic Routes and Materials Properties. *Chemistry of Materials*, **12** (10), 2943–2949.

34 Plummer, CJG., Garamszegi, L., Leterrier, Y., Rodlert, M., and Manson, J.E. (2002) Hyperbranched Polymer Layered Silicate Nanocomposites. *Chemistry of Materials*, **14** (2), 486–488.

35 Sur, G.S., Sun, H.L., Lyu, S.G., and Mark, J.E. (2001) Synthesis, structure, mechanical properties, and thermal stability of some polysulfone/organoclay nanocomposites. *Polymer*, **42** (24), 9783–9789.

36 Malwitz, MM., Lin-Gibson, S., Hobbie, EK., Butler, PD., and Schmidt, G. (2003) Orientation of platelets in multilayered nanocomposite polymer films. *Journal of Polymer Science Part B: Polymer Physics*, **41** (24), 3237–3248.

37 Kornmann, X., Linderberg, H., and Bergund, L.A. (2001) Synthesis of epoxy–clay nanocomposites: influence of the nature of the curing agent on structure. *Polymer*, **42**, 4493–4499.

38 Messermith, P.B. and Giannelis, E.P. (1994) Synthesis and characterization of layered silicate epoxy nanocomposites. *Chemistry of Materials*, **6**, 1719–1725.

39 Alexandre, M. and Dubois, P. (2000) Polymer-layered silicate nanocomposites: preparation, properties and uses of a new class of materials. *Materials Science & Engineering Reports*, **28**, 1–63.

40 Yano, K. and Usuki, A. (1993) Synthesis and properties of polyimide–clay hybrid. *Journal of Polymer Science Part A: Polymer Chemistry*, **31**, 2493–2498.

41 Du, X.S., Xiao, M., and Meng, Y.Z. (2004) Synthesis and characterization of polyaniline/graphite conducting nanocomposites. *Journal of Polymer Science Part B: Polymer Physics*, **42**, 1972–1978.

42 Shioyama, H. (1997) Polymerization of isoprene and styrene in the interlayer spacing of graphite. *Carbon*, **35**, 1664.

43 Fukushima, H. and Drazal, L.T. (2003) Graphite nanocomposites: structural & electrical properties. *Proceedings of the 14th International Conference on Composite Materials (ICCM-14), San Diego, CA*.

44 Yao, K.J., Song, M., Hourston, D.J., and Luo, D.Z. (2002) Polymer/layered clay nanocomposites: 2 polyurethane nanocomposites. *Polymer*, **43**, 1017.

45 Wang, Z. and Pinnavaia, T.J. (1998) Nanolayer Reinforcement of Elastomeric Polyurethane. *Chemistry of Materials*, **10**, 3769.

46 Lan, T. and Pinnavaia, T.J. (1994) Clay-Reinforced Epoxy Nanocomposites. *Chemistry of Materials*, **6**, 2216.

47 Farahani, R.D. and Ahmad Ramazani, S.A. (2007) *Macromolecular Materials and Engineering*, **1**, 9.

48 Merkulov, V.I., Lowndes, D.H., Wei, Y.Y., Eres, G., and Voelkl, E. (2000) Patterned growth of individual and multiple vertically

aligned carbon nanofibers. *Applied Physics Letters*, **76** (24), 3555–3557.

49 Finegan, I.C., Tibbetts, G.G., and Glasgow, D.G. (2003) Surface treatments for improving the mechanical properties of carbon nanofiber/thermoplastic composites. *Journal of Materials Science*, **38** (16), 3485–3490.

50 Finegan, I.C., Tibbetts, G.G., and Gibson, R.F. (2003) Modeling and characterization of damping in carbon nanofiber/polypropylene composites. *Composites Science and Technology*, **63** (11), 1629–1635.

51 Ma, H.M., Zeng, J.J., Realff, M.L., Kumar, S., and Schiraldi, D.A. (2003) Processing, structure, and properties of fibers from polyester/carbon nanofiber composites. *Composites Science and Technology*, **63** (11), 1617–1628.

52 Ganter, M., Gronski, W., Reichert, P., and Muhlhaupt, R. (2001). Rubber Nanocomposites: Morphology and Mechanical Properties of BR and SBR Vulcanizates Reinforced by Organophilic Layered Silicate. *Rubber Chemistry and Technology*, **74**, 221.

53 Wang, Y., Zhang, L., Tang, C., and Yu, D. (2000) Preparation and characterization of rubber–clay nanocomposites. *Journal of Applied Polymer Science*, **78**, 1879.

54 Ma, J., Xiang, P., Mai, Y.-W., and Zhang, L.-Q. (2004) A Novel Approach to High Performance Elastomer by Using Clay. *Macromolecular Rapid Communications*, **25**, 1692.

55 Ma, H., Xu, Z., Tong, L., Gu, A., and Fang, Z. (2006) Studies of ABS-graft-maleic anhydride/clay nanocomposites: Morphologies, thermal stability and flammability properties. *Polymer Degradation and Stability*, **91**, 2951–2959.

56 Vaia, R.A., Jant, K.D., Kramer, E.J., and Giannelis, E.P. (1996) Microstructural evaluation of melt-intercalated polymer-organically modified layered silicate nanocomposites. *Chemistry of Materials*, **8**, 2628.

57 Reichert, P., Kressler, J., Thomann, R., Mulhaupt, R., and Stoppelmann, G. (1998) Nanocomposites based on a synthetic layer silicate and polyamide-12. *Acta Polymer*, **49** (2–3), 116–123.

58 Yano, K. and Usuki, A. (1993) Synthesis and properties of polyimide–clay hybrid. *Journal of Polymer Science Part A: Polymer Chemistry*, **31**, 2493–2498.

59 Yano, K., Usuki, A., Okada, A., and Kurauchi, T. (1991) Synthesis and properties of polyimide–clay hybrid. *Polymer Preparation (Japan)* **32** (1), 65.

60 Lin, Y., Chen, H., Chan, C.-M., and Wu, J. (2011) Effects of coating amount and particle concentration on the impact toughness of polypropylene/CaCO3 nanocomposites. *European Polymer Journal*, **47** (3), 294.

61 Choudalakis, G., Gotsis, A.D., Schut, H., and Picken, S.J. (2011) The free volume in acrylic resin/laponite nanocomposite coatings. *European Polymer Journal*, **47** (3), 264.

62 Vasilyev, G.B., Makarova, V.V., Rebrov, A. V., Picken, S.J., Smirnova, N.M., Malkin, A. Y.A., and Kulichikhin, V.G. (2011) Morphology and rheology of composites based on anisotropic polymer matrix and different clays. *Journal of Applied Polymer Science*, **120** (6), 3642.

63 Das, A., Mahaling, R.N., Stöckelhuber, K.W., and Heinrich, G. (2011) Reinforcement and migration of nanoclay in polychloroprene/ethylene–propylene–diene-monomer rubber blends. *Composites Science and Technology*, **71** (3), **276**, 7.

64 Zhang, J. and Jiang, D. (2011) Interconnected multi-walled carbon nanotubes reinforced polymer-matrix composites. *Composites Science and Technology*, **71** (4), 28 466.

65 Silva, J., Ribeiro, S., Lanceros-Mendez, S., and Simões, R. (2011) The influence of matrix mediated hopping conductivity, filler concentration, aspect ratio and orientation on the electrical response of carbon nanotube/polymer nanocomposite. *Composite Science and Technology*, **643**,

66 Liao, M., Zhang, X., Fan, C., Wang, L., and Jin, M. (2011) Preparation and characterization of polybutadiene/allylisobutyl polyhedral oligomeric silsesquioxane nanocomposites by anionic polymerization, **120** (5), 2800.

2
Synthesis, Surface Modification, and Characterization of Nanoparticles

Liaosha Wang, Jianhua Li, Ruoyu Hong, and Hongzhong Li

2.1
Introduction

Nanocomposites are made from two or more solid-phase materials, with at least one dimension in nanometers (1–100 nm). The solid phase can be amorphous, semi-crystalline, grain, or a combination. The solid phase can also be organic, inorganic, or a combination. According to the size of the solid phase, nanocomposites generally include the following three types: nanoparticles and nanoparticle compounds (0–0 composites), nanoparticles and conventional bulk composites (0–3 composites), and composite nanofilms (0–2 composites). In addition, the nanolayered structure material is referred to as nanomaterial, and the multilayer nanocomposite made of different materials is also known as nanocomposite.

Composite materials exhibit excellent performance, which can be widely used in aerospace, defense, transportation, sports, and other fields. Nanocomposites are one of the most attractive parts of the composite materials. Due to the fast development in recent years, nanocomposites are widely used by the developed countries for manufacturing new materials. The research on nanocomposites includes organic–inorganic composites, nanopolymer matrix composites, and inorganic–inorganic composites. In this chapter, combined with our research experience, we mainly introduce the nanopolymer matrix composites to the readers. The synthesis and modification of nanoparticles and preparation, characterization, and applications of nanopolymer matrix composites are mainly discussed.

2.2
Synthesis and Modification of Nanoparticles

2.2.1
Synthesis of Nanoparticles

Nanomaterials are solid particles at the intermediate state, that is, between atoms/molecules and macroscopic objects. Owing to small size effect, large surface effect,

Polymer Composites: Volume 2, First Edition. Edited by Sabu Thomas, Kuruvilla Joseph, Sant Kumar Malhotra, Koichi Goda, and Meyyarappallil Sadasivan Sreekala.

and quantum tunneling effect, the nanomaterials demonstrate special physical properties and can be widely used in high-density magnetic recording, radar signal absorbing, magnetic fluids, radio wave shielding, precision polishing, optical devices, microchip and wiring substrate thermal conducting, electronic packaging, optoelectronics, high-performance batteries, solar cells, catalysts, fire retardants, sensitive components, high-toughness ceramics, body repairing, cancer therapy, and so on. The preparation of nanomaterials is an important branch of materials science and engineering. The study of nanomaterials is related to various scientific fields, for example, chemistry, physics, optics, electronics, magnetism, and mechanism of materials. Some nanomaterials have entered practical stage. In order to meet the nanotechnology and nanomaterials development in the next century, it is necessary to review the preparation techniques of nanomaterials.

Methods for the preparation of nanomaterials can be divided into physical and chemical methods based on whether there exist chemical reactions. On the other hand, these methods can be classified into gas-phase, liquid-phase, and solid-phase methods based on the state of the reaction system. Gas-phase methods include gas-phase evaporation method (resistance heating, high-frequency induction heating, plasma heating, electron beam heating, laser heating, electric heating evaporation method, vacuum deposition on the surface of flowing oil, and exploding wire method), chemical vapor reaction (heat pipe gas reaction, laser-induced chemical vapor reaction, and plasma-enhanced chemical vapor reaction), chemical vapor condensation, and sputtering method. Liquid-phase methods for synthesizing nanoparticles mainly include precipitation, hydrolysis, spray, solvent thermal method (high temperature and high pressure), solvent evaporation, pyrolysis, oxidation–reduction (room pressure), emulsion, radiation chemical synthesis, and sol–gel method. Solid-phase methods include thermal decomposition, solid-state reaction, spark discharge, stripping, and milling method.

We have synthesized several nanoparticles in our laboratory, such as TiO_2, Fe_3O_4, ZnO, SiO_2, and YIG nanoparticles.

2.2.2
Synthesis of Titania Nanoparticles

Using titanium tetrachloride ($TiCl_4$) as a precursor [1], titania nanoparticles were synthesized in the diffusion flame (DF) of air and liquid petroleum gas (LPG) (Figure 2.1). The effects of air and LPG flow rates and flow ratio, flame temperature, and flame shape on the synthesized TiO_2 nanoparticles were investigated. Experimental investigation showed that the mean particle size of TiO_2 increased with increasing airflow rate, and not with that of LPG, the mean particle size at optimal experimental condition was less than 20 nm, the rutile fraction in the synthesized powder increased with increasing flame temperature, and the particle size was affected by the flame height. A particle dynamic model, describing the nucleation and coagulation of titania monomers/nanoparticles, was used to account for the experimental results based on the isothermal assumption. Generally speaking, the

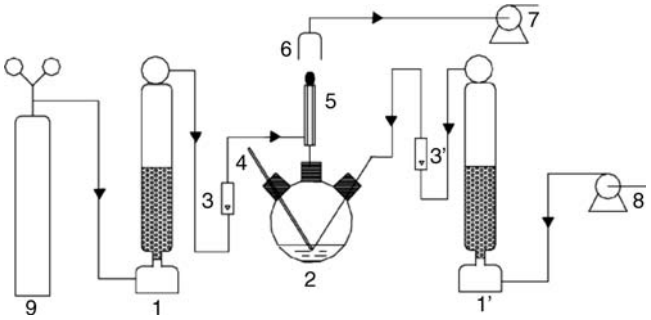

Figure 2.1 Experimental flow diagram for synthesizing TiO_2 nanoparticles using LPG/air flame (1 and 1′: dryer; 2: $TiCl_4$ evaporator; 3 and 3′: rotameters; 4: thermometer; 5: combustor; 6: filter; 7: circulating water vacuum pump; 8: air compressor; 9: LPG cylinder) [1].

calculated particle sizes from the particle dynamics were consistent with the experimental measurements, especially when the feed concentration of $TiCl_4$ was low.

2.2.3
Microwave Synthesis of Magnetic Fe_3O_4 Nanoparticles

Fe_3O_4 magnetic nanoparticles were prepared by the coprecipitation of Fe^{3+} and Fe^{2+}, $NH_3{\cdot}H_2O$ [2,3] was used as the precipitating agent to adjust the pH of the suspension, and the aging of Fe_3O_4 magnetic nanoparticles was accelerated by microwave (MW) irradiation [2]. The obtained Fe_3O_4 magnetic nanoparticles were characterized by Fourier transform infrared (FT-IR) spectroscopy, transmission electron microscopy (TEM), X-ray diffraction (XRD), and vibrating sample magnetometer (VSM). The average size of Fe_3O_4 crystallites was found to be around 8–9 nm. Aged under MW irradiation, Fe_3O_4 nanoparticles have more complete crystalline structure than those aged for 7 days at room temperature. The obtained nanoparticles are well indexed to the inverse cubic spinel phase of Fe_3O_4. In addition, Fe_3O_4 nanoparticles aged under MW irradiation have a higher saturation magnetization than those aged for 7 days at room temperature (Figure 2.2), which is due to the good crystallinity of Fe_3O_4 nanoparticles. Compared to Fe_3O_4 nanoparticles aged for 7 days, the coercivity of samples aged under MW irradiation increased, which could be ascribed to the reduction of particle size of Fe_3O_4.

2.2.4
Magnetic Field Synthesis of Fe_3O_4 Nanoparticles

Fe_3O_4 nanoparticles were prepared by coprecipitation, and the aging of nanoparticles was improved by applied magnetic field [4]. The obtained nanoparticles were characterized by FT-IR, scanning electron microscopy (SEM), XRD, and VSM.

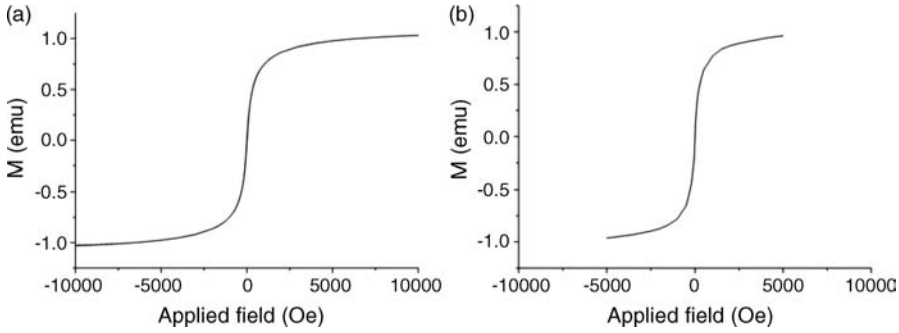

Figure 2.2 Magnetic hysteresis curves of Fe_3O_4 nanoparticles: sample A was aged under MW irradiation (a) and sample B was aged for 7 days at room temperature (b) [2].

The results show that under applied magnetic field, the aging time could be greatly reduced and the magnetic properties of Fe_3O_4 nanoparticles could be improved.

2.2.5
Synthesis of Fe_3O_4 Nanoparticles without Inert Gas Protection

Fe_3O_4 nanoparticles were hydrothermally synthesized under continuous MW irradiation from $FeCl_3{\cdot}6H_2O$ and $FeSO_4{\cdot}7H_2O$ aqueous solutions, using NH_4OH as a precipitating reagent and $N_2H_4{\cdot}H_2O$ as an oxidation-resistant reagent [5]. The results of XRD, FT-IR spectroscopy, and SEM measurements showed that the synthesized magnetite (Fe_3O_4) nanoparticles had an average diameter of 10 nm. The magnetic properties of the Fe_3O_4 nanoparticles were measured using a VSM, indicating that the nanoparticles possessed high saturation magnetization at room temperature. The Fe_3O_4 nanoparticles synthesized at the optimal ratio of Fe^{3+}/Fe^{2+} of about 1.75 : 1 exhibit a maximal saturation magnetization of 84.83 emu/g (Figure 2.3). Hydrazine plays a dual role both as the precursor of precipitator and as the oxidation-resistant reagent in the reaction system. The saturation magnetization of Fe_3O_4 nanoparticles synthesized with hydrazine was greatly improved.

2.2.6
Synthesis of ZnO Nanoparticles by Two Different Methods

The ZnO precursor was synthesized by direct precipitation from zinc acetate and ammonium carbonate [6,7]. ZnO nanoparticles were synthesized by calcination of the precursor at 450 °C for 3 h and calcination after the heterogeneous azeotropic distillation of the precursor. The synthesized ZnO nanoparticles were characterized by FT-IR, XRD, and TEM. It is concluded that the heterogeneous azeotropic distillation of the precursor effectively reduced the formation of hard agglomerates. The photocatalytic activity of the synthesized ZnO nanoparticles is high.

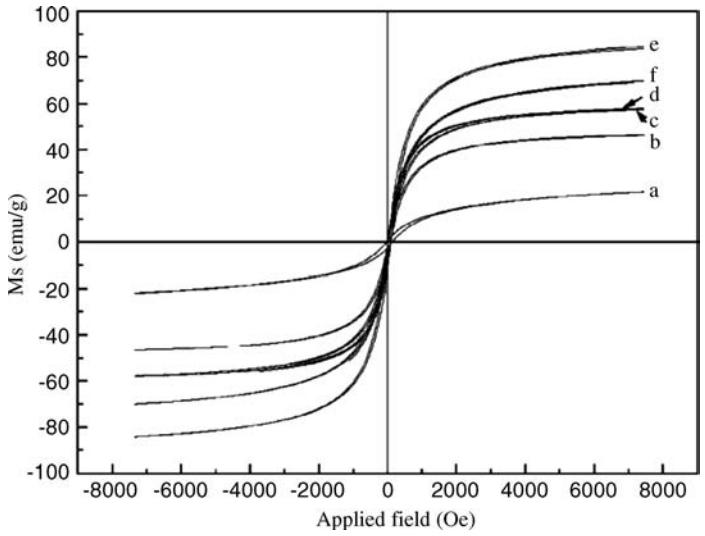

Figure 2.3 (a) Hysteresis regression curve of Fe_3O_4 nanoparticles synthesized using NaOH as precipitator at the ratio (Fe^{3+}/Fe^{2+}) of 1.75 : 1 without hydrazine. (b, f, e, and d) Hysteresis regression curve of Fe_3O_4 nanoparticles synthesized using NH_4OH as precipitator at the ratio (Fe^{3+}/Fe^{2+}) of 1.25 : 1, 1.5 : 1, 1.75 : 1, and 2.0 : 1, respectively, with hydrazine. (c) Hysteresis regression curve of Fe_3O_4 nanoparticles synthesized using NH_4OH as precipitator at the ratio (Fe^{3+}/Fe^{2+}) of 1.5 : 1 without hydrazine [5].

2.2.7
Synthesis of Silica Powders by Pressured Carbonation

A method was proposed for the preparation of silica powders using inexpensive materials such as sodium silicate (Na_2SiO_3) and carbon dioxide (CO_2) by pressured carbonation, in which carbon dioxide acted as a precipitating reagent (Figure 2.4) [8].

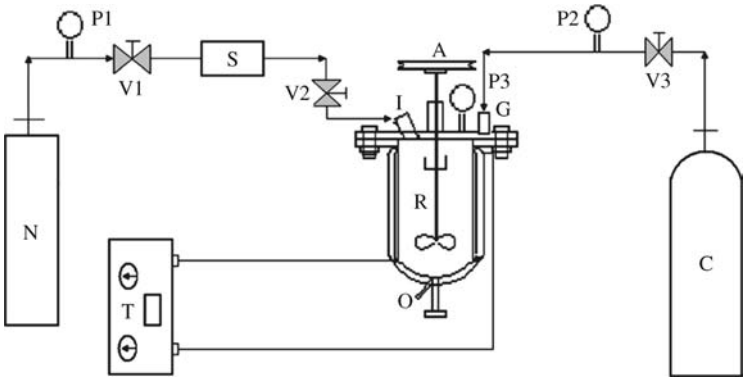

Figure 2.4 Apparatus for the formation of ultrafine silica powders using carbon dioxide (R: high-pressure reactor; C: carbon dioxide cylinders; T: temperature controller; I: solution inlet; O: production outlet; G: gas inlet; A: agitator; P1, P2, and P3: pressure gauges; V1, V2, and V3: control values; S: solution injection device) [8].

Table 2.1 Effect of temperature, content of Na_2SiO_3 and PEG, and reaction time on the yield and average size of the products [8].

No.	Temperature (°C)	Na_2SiO_3 (mol/l)	PEG (%)	Reaction time (h)	Average size (nm)	Yield (%)
1	80	1.0	5.0	3	54	86.4
2	70	1.0	10	2	52	84.5
3	60	1.0	15	1	46	75.2
4	80	0.50	15	2	36	84.7
5	70	0.50	5.0	1	33	82.3
6	60	0.50	10	3	36	88.6
7	80	0.25	10	1	19	85.3
8	70	0.25	15	3	17	86.3
9	60	0.25	5.0	2	15	86.8

Microstructure and size analyses of the precipitated silica powders were carried out using TEM and dynamic light scattering. The average particle size, size distribution, and yield of silica powders were affected by reaction time, temperature, and concentrations of surfactant and sodium silicate solutions (Table 2.1). The particle size of silica powders increased with reaction temperature and concentration of sodium silicate, and the yield of silica powders increased with increasing reaction time. The size distribution of silica powders was affected by concentration of surfactant PEG. The optimal preparation conditions were experimentally determined for obtaining the silica powders with nanometer size, narrow size distribution, spherical shape, and high purity without sodium carbonate and surfactant.

2.2.8
MW-Assisted Synthesis of Bisubstituted Yttrium Garnet Nanoparticles

Bisubstituted yttrium garnet (Bi-YIG, $Bi_{1.8}Y_{1.2}Fe_5O_{12}$) nanoparticles were prepared by MW-assisted coprecipitation as well as conventional coprecipitation using ammonia aqueous solution as precipitant [9,10]. The nanoparticles were characterized by thermogravimetric (TG) analysis, differential thermal analysis, XRD, TEM, dynamic light scattering, VSM, and Faraday rotation meter. Results demonstrate that the Bi-YIG nanoparticles prepared by MW-assisted coprecipitation show smaller particle size and higher Faraday rotation than those prepared by the conventional coprecipitation (Figure 2.5).

2.2.9
Molten Salt Synthesis of Bisubstituted Yttrium Garnet Nanoparticles

Compared to the MW-assisted method [11], Bi-YIG nanoparticles were successfully synthesized by the molten salt method in NaCl–KCl flux at 650 °C. XRD, SEM, dynamic light scattering, VSM, and Faraday rotation meter were used to characterize the phase, morphology, size distribution, magnetic properties, and Faraday rotation

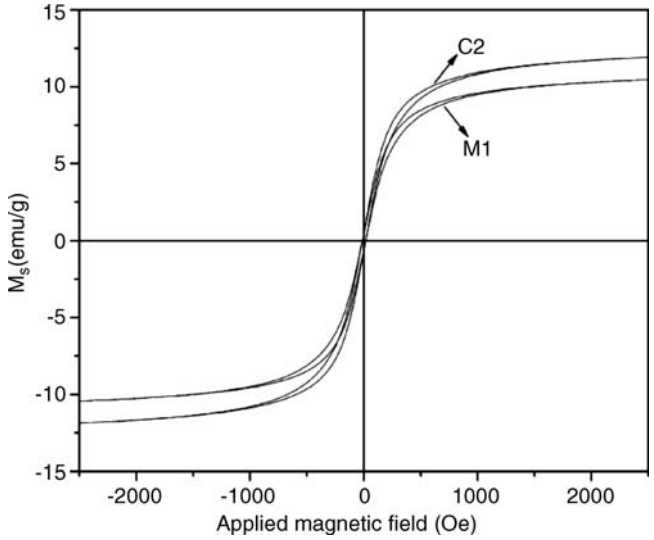

Figure 2.5 Magnetic hysteresis of Bi-YIG particles: (M1) prepared by MW coprecipitation and (C2) prepared by conventional coprecipitation [9].

of the as-prepared Bi-YIG nanoparticles, respectively. Results show that the average size of Bi-YIG nanoparticles synthesized by the molten salt method is about 50 nm. The formation of Bi-YIG nanoparticles in the molten salt process was associated with the type of the raw material used. One can obtain pure Bi-YIG nanoparticles using oxide mixture, but not using Bi-YIG precursors. The formation of Bi-YIG nanoparticles starts at 600 °C and is complete at 650 °C, and one can obtain pure Bi-YIG phase at 650–800 °C using the molten salt method.

2.3 Modification of Nanoparticles

To improve or change the dispersion of nanoparticles, enhance the surface activity of nanoparticles, generate new physical, chemical, and mechanical properties and new features on the surface of the particles, and improve the compatibility between the nanoparticles and other materials, physical or chemical methods are needed to alter the structure and the surface state of nanoparticles.

In order to control the surface of nanoparticles and to apply those nanoparticles in industry and biomedicine, an in-depth understanding of the basic properties of the nanoparticles is indispensable.

According to the principles of surface modification, the surface modification of nanoparticles can be divided into partial chemical modification, mechanical and chemical modification, external membrane modification (i.e., capsule), high-energy surface modification, and surface modification using precipitation, esterification, coupling, and grafting reactions. Surface modification in general through physical

adsorption, coating, or grafting depends on the properties of the particle surface. The use of ultraviolet rays for the plasma surface modification of particles belongs to the physical modification. By the chemical reactions between the nanoparticle surface and modifier, the surface structure and state of nanoparticles are changed. Surface chemical modification of nanoparticles plays a very important role in reducing the agglomeration. Due to modifier adsorption or bonding at the particle surface, which reduces the surface force of hydroxyl groups, the hydrogen bonds between particles are eliminated to prevent the formation of oxygen bridge bonds when nanoparticles are drying, thereby preventing the agglomeration.

2.3.1 Surface Modification of ZnO Nanoparticles

ZnO nanoparticles were synthesized by homogeneous precipitation. To reduce the aggregation among ZnO nanoparticles, an effective surface modification method was proposed by grafting poly(methyl methacrylate) (PMMA) onto the ZnO particles [12]. That is, the surface of ZnO nanoparticles was first treated with a γ-methacryloxypropyltrimethoxysilane (KH570) coupling agent, which introduces functional double bonds onto the surface of ZnO nanoparticles, followed by radical grafting polymerization in nonaqueous medium. The obtained nanocomposite was characterized by FT-IR, TG, sedimentation test, SEM, and XRD. Results of FT-IR and TG showed that the desired polymer chains have been covalently bonded to the surface of ZnO nanoparticles. It was found that the increasing monomer concentration could increase the grafting percentage and hence promote the dispersibility.

To reduce the aggregation among nanoparticles and to improve the compatibility between nanoparticles and the organic matter, polystyrene (PS) was grafted onto the ZnO nanoparticles in a nonaqueous suspension. The test shows that bare ZnO nanoparticles have high photocatalytic activity, while PS-grafted ZnO composites have almost no photocatalytic activity. Surface modification by grafting polymerization can reduce the aggregation of nanoparticles and help to form a stable suspension in organic solvents.

2.3.2 Surface Modification of Fe_3O_4 Nanoparticles

In order to prepare a stable magnetic fluid, the surface of Fe_3O_4 nanoparticles was modified with different surfactants in our research [13], as that did for silica nanoparticles [14].

Using two kinds of surfactants, a stable water-based magnetic fluid was prepared. The surface of Fe_3O_4 nanoparticles was coated with oleate sodium as the primary layer and polyethylene glycol 4000 (PEG-4000) as the secondary layer to improve the stability of the water-based magnetic fluid (Figure 2.6) [15]. The dosages of oleate sodium and PEG-4000 were found to have an important effect on increasing the solid content. Gouy magnetic balance showed that the saturation magnetization could be as high as 1.44×10^5 A/m.

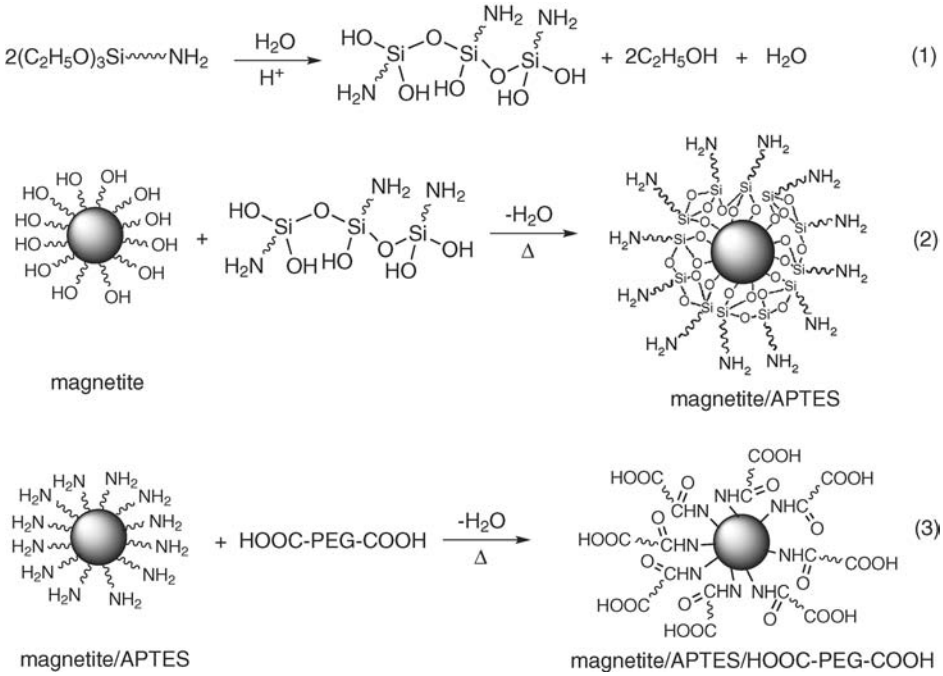

Figure 2.6 Synthesis route for the PEG diacid-coated magnetite nanoparticles: (1) simplified reaction of hydrolysis and condensation with production of silane polymer; (2) scheme of the simplified silanization reaction of APTES on the magnetite surface; (3) simplified reaction of HOOC–PEG–COOH on the magnetite surface after treatment by APTES [17].

To prepare a biocompatible water-based magnetic fluid, the Fe_3O_4 nanoparticles were modified by dextran through a two-step method [16]. The Fe_3O_4 nanoparticles were first surface modified with aminosilane and then coated with dextran. The effects of the molecular weight of dextran on the size, morphology, coating efficiency, and magnetic property of the magnetite/dextran nanocomposite were investigated. The magnetite/dextran nanocomposite was dispersed in water to form a magnetic fluid by ball milling. The molecular weight of dextran plays an important role in the size, morphology, coating efficiency, and magnetic property of the magnetite/dextran nanocomposite. The surface modification of Fe_3O_4 nanoparticles with dextran is propitious to the stability of the magnetic fluid. The viscosity of the magnetic fluid increases with the increasing molecular weight of dextran. An external magnetic field can enhance the interaction in the magnetic fluid; therefore, the viscosity of the magnetic fluid increases under the external magnetic field. The magnetic field could also rearrange the Fe_3O_4 nanoparticles, leading to the formation of orderly microstructures. When there is no magnetic field, the viscosity of the magnetic fluid increases linearly with the solid content. If an external magnetic field is applied, the viscosity increases quadratically with the solid content. Then, the dextran-stabilized magnetic fluid was used to perform the MRI experiments on the living rabbits with VX2 malignant tumor; the results

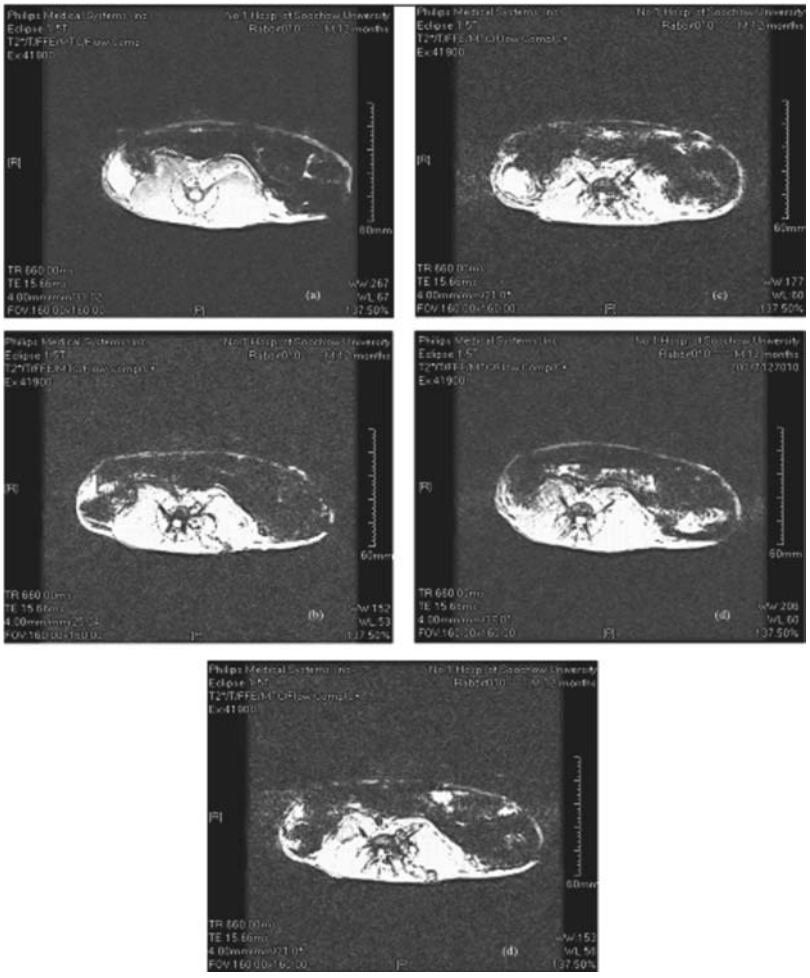

Figure 2.7 T2-weighted MR images acquired before (a) and at different times after the injection of magnetic fluid (b: 30 min; c: 60 min; d: 90 min; e: 120 min) [17].

showed that these nanoparticles appear to be a promising vehicle for MR imaging (Figure 2.7) [17].

In addition, we prepared kerosene-based magnetic fluid via a simple one-step phase-transfer method [18]. The Fe_3O_4 nanoparticles formed in the aqueous phase were first modified by oleic acid and then migrated to the organic phase of kerosene to form a magnetic fluid. The size of Fe_3O_4 nanoparticles was found to be around 10 nm by TEM. The magnetic fluid demonstrated good stability and had a susceptibility of 7.78×10^{-4} and a saturation magnetization of 27.3 emu/g. The rheological property [19] of the prepared magnetic fluid was investigated using a rotating rheometer attached to a custom-built solenoid coil (Figure 2.8). It was found that the viscosity of the magnetic fluid increased with the increasing intensity of the

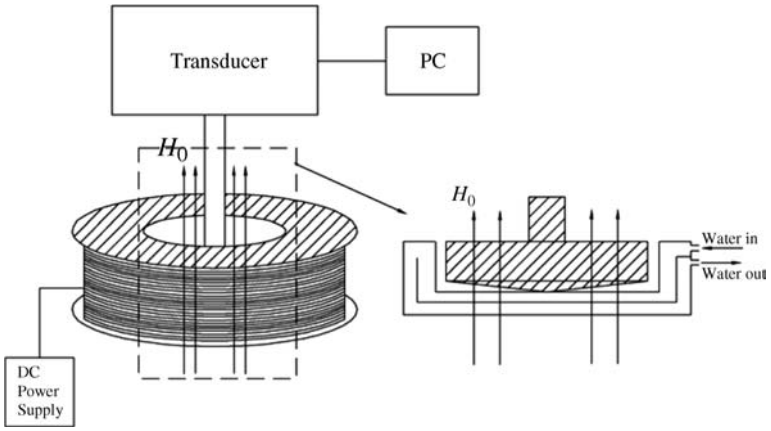

Figure 2.8 A rotating rheometer for measuring viscosity under applied magnetic field [18].

magnetic field, and the magnetic fluid demonstrated shear thinning behavior and could be described by the Herschel–Bulkley model.

2.3.3
Surface Modification of Silica Nanoparticles

To prepare excellent silica-reinforced PMMA [14,20], we first modified the silica with a silane coupling agent (KH570), followed by solution polymerization. The modified silica nanoparticles were characterized by FT-IR, TEM, and TG. Sedimentation tests and lipophilic degree (LD) measurements were also performed to observe the compatibility between the modified silica nanoparticles and organic solvents. The resultant polymers were characterized by UV–Vis, sclerometer, and differential scanning calorimetry (DSC). The mechanical properties of the hybrid materials were measured. The results showed that the glass transition temperature, surface hardness, flexural strength, and impact strength of the silica nanoparticle-reinforced PMMA slices were improved. Moreover, the tensile properties of PMMA films doped with silica nanoparticles via solution blending were improved (Figure 2.9).

2.4
Preparation and Characterization of Polymer–Inorganic Nanocomposites

2.4.1
Nanopolymer Matrix Composites

Since the 1960s, P.J. Flory began to study the chain structure of polymers in solution. He thought that the polymer structure can be divided into three levels. One is chain structure, such as polyethylene; the second one is conformation structure, such as

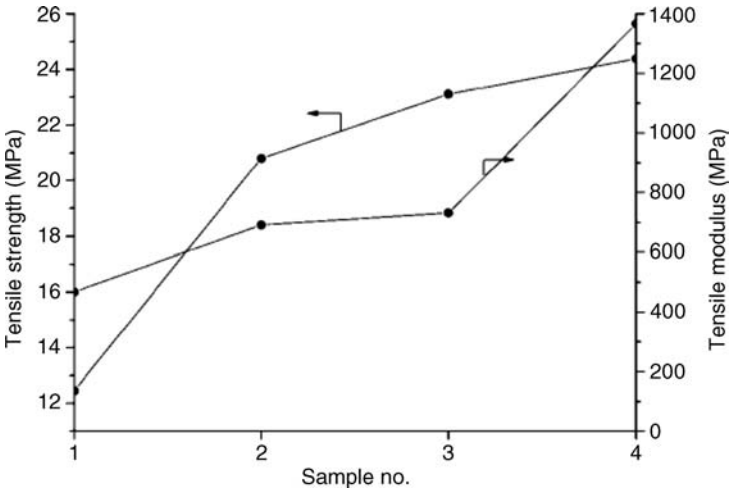

Figure 2.9 Effects of silica nanoparticles on the properties of PMMA films (1: neat PMMA; 2: unmodified silica + PMMA; 3: KH570-grafted silica + PMMA; 4: PMMA-grafted silica + PMMA) [20].

isotactic polypropylene and syndiotactic polypropylene; and the last one is condensed state, such as liquid crystalline polycarbonate, semicrystalline polyether ether ketone, and so on. Researchers have proposed several models for the polymers possessing secondary or tertiary structure, as shown in Figure 2.10.

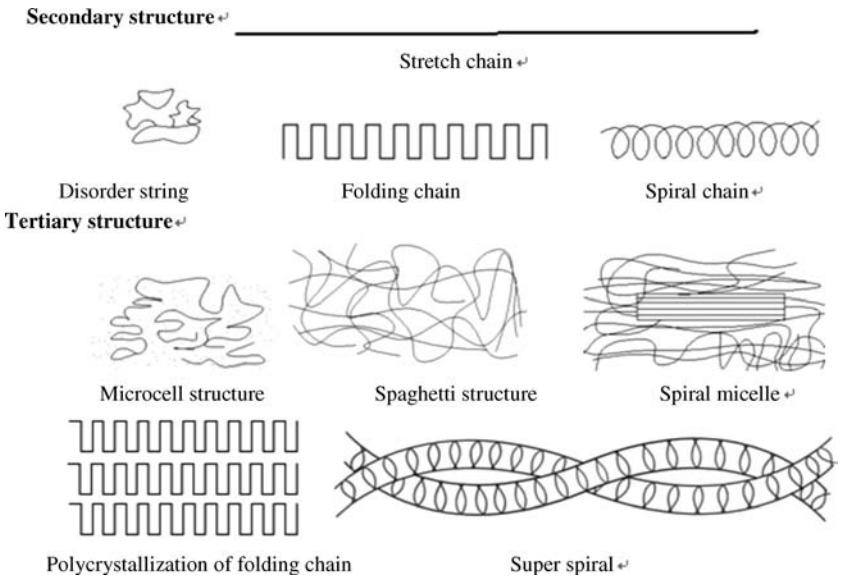

Figure 2.10 Several models for the polymers possessing secondary or tertiary structure.

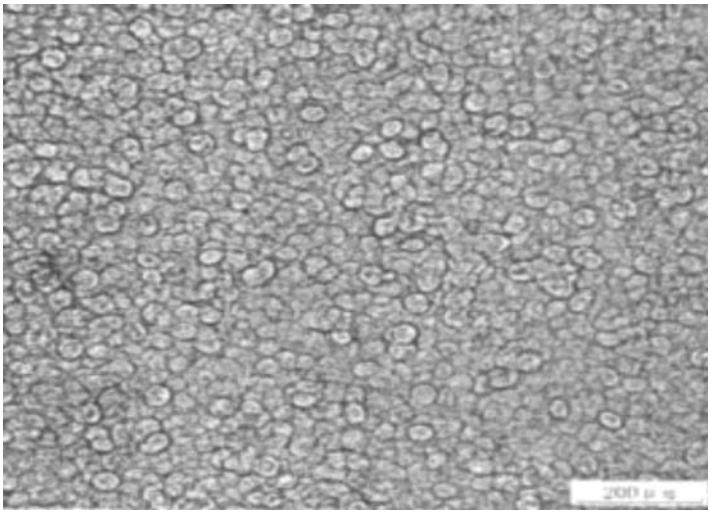

Figure 2.11 Crystalline spherulite form of polypropylene under polarizing microscope [21].

Polymers possess condensed state mainly referred to as crystalline state, and the crystalline spherulite form is shown in Figure 2.11. The condensed state can be divided into four phases, namely, no fixed shape, the transition state, liquid crystalline state, and crystalline state. Due to the complex formation process and peculiar phenomenon, transition state and liquid crystalline state have attracted much attention. The crystalline state is interesting mainly due to its multicrystalline form.

A nanocomposite material is the combination of the nanosized ultrafine powders and the polymer matrix. In such materials, organic polymer generally is a continuous phase and the nanoparticles form the dispersed phase, such as BiI_3–nylon 11 nanocomposites and nylon–montmorillonite nanocomposites. In this century, nanocomposite materials have become one of the most advanced composite materials.

When the nanoparticles are introduced into the organic polymer matrix, the polymorphic crystalline form would be induced, giving the nanopolymer matrix composites many excellent properties. Advantages of the nanopolymer matrix composites mainly include the following: (1) the improved properties of polymers, such as higher heat distortion temperature, rapid crystallization, improved mechanical properties, and so on; (2) a resource-saving compound, using only the common raw materials and no other new materials; and (3) the original process route: the nanocomposite uses the original route of polymer processing. These features make the industrial production of the nanocomposites easier, once a breakthrough is obtained. In other words, nanopolymer matrix composites can provide an epoch-making performance by adjusting the complex dispersion of the original materials.

Polymer–inorganic nanocomposites exhibit the machinability of organic materials and the functional and structural properties of inorganic materials, becoming the hot spot of today's science and technology. In the nanocomposites, a large part of

the nanomaterials is functional. For example, BiI_3–nylon 11 nanocomposites show X-ray-induced conductivity, the nanoparticles in the PS–clay nanocomposites display liquid crystal inducing behavior, α-FeOOH is used as a nuclear assembly agent in polymer LB films, and so on. In addition, nanomaterials provide directional characteristics, and their direction-related features, including the coupling characteristics, can be used in the design process. Due to the presence of anisotropy and coupling characteristics, the direction and sequence can be designed and tailored, according to the mechanical characteristics and function. Due to the presence of a dual nature, nanomaterials can be more evenly dispersed in the matrix by adjusting the interaction of the interface of the two roles. The use of nanowhiskers, nanorods, nanowires, and nanobeams offers the possibility of enhanced orientation and maintains the processing facilities of the filled nanoparticles. In the polymer–inorganic nanocomposites, different interfaces also create synergies. To maximize the beneficial effects and synergies of different interfaces of the nanocomposites, the surface modification or treatment is generally appropriated, which forms a link with the substrates (e.g., covalent, hydrogen bond, intermolecular force, etc.), maximizing the dispersion and the appropriate combination.

Generally, the inorganic materials used to prepare the nanocomposites mainly include layered silicate clay, layered compounds, metal powder, and a variety of inorganic oxides. In our research works, nanosized zinc oxide, iron oxide, silica, and YIG particles were synthesized and used to prepare a variety of polymer nanocomposites, giving the composite materials many new features. This chapter based on our research discusses the methods of preparation and characterization of the polymer–inorganic nanocomposites.

2.5
Preparation of Polymer–Inorganic Nanocomposites

Many methods could be applied to prepare polymer–inorganic nanocomposites, such as sol–gel processing, *in situ* polymerization, particle *in situ* formation, blending, radiation synthesis, and so on.

2.5.1
Sol–Gel Processing

Sol–gel processing is the method for converting the metal alkoxide or inorganic salt, through solution, sol, gel, curing, and then heat treatment, to solid oxide or other compounds. Organic/inorganic nanocomposites are usually prepared in the solvent containing precursors and organic polymers by using the sol–gel technique. The most direct way involves hydrolysis and condensation of precursors in the presence of polymer in the solvent systems. If the conditions are under control, the polymer would not occur in isolation during the formation and drying process, through which we can obtain optically transparent composite materials. Materials prepared by sol–gel processing have uniformity, high purity, and low sintering temperature compared to those prepared by conventional solid-state reactions. The biggest

problem of sol–gel processing is that the gel process would lead to a considerable contraction of the internal stress, which could result in contraction of brittle materials, due to the evaporation of solvents, small molecules, and water. Moreover, this method requires polymers in the sol–gel system to be dissolved in the condensate. In addition, the precursors are expensive and sometimes toxic, preventing further improvement and application.

2.5.2 *In Situ* Polymerization

This is the simplest and most representative method for the preparation of composite materials. Generally, the inorganic precursor and organic monomer were first mixed together, and then water and catalyst were added for condensation of inorganic precursors. Subsequently, oxidant was added for *in situ* polymerization, and the obtained materials were dried, through which organic/inorganic nanocomposites were prepared. We prepared PMMA/silica nanocomposites by *in situ* bulk polymerization of a silicic acid sol and MMA mixture [14]. Silicic acid was prepared by hydrolysis and condensation of sodium silicate in the presence of 3.6 M HCl. Silicic acid sol was obtained by tetrahydrofuran (THF) extraction of silicic acid from water. Each set of PMMA/silica composites was subjected to thermal and mechanical studies. With increase in silica content, the PMMA/silica nanocomposites filled with silica particles showed improved thermal and mechanical properties, whereas a decrease in thermal stability.

2.5.3 Particle *In Situ* Formation

Polymers and inorganic hybrid precursors were dissolved in a suitable solvent, and the molecules of polymer and precursors were combined together. Via a reaction, such as metal alkoxide hydrolysis, oxidation and reduction reactions, and so on, inorganic nanoparticles were *in situ* formed in the polymer. Using the adsorption and complexation of metal ions of polymer-specific functional groups or the space constraints between polymer and reactant, nanocomposites were prepared *in situ*. The nanoparticles can be generated by radiation, heat, light, gas reactions, and so on. In this way, the obtained inorganic particles were usually of nanometer size and uniformly dispersed in polymer. Therefore, the compounds exhibit a transparent stable structure. Moreover, the polymer plays a role in controlling the size and preventing aggregation of inorganic nanoparticles. In our research, ultrasmall magnetite nanoparticles were prepared by using chitosan–poly(acrylic acid) (CS–PAA) nanospheres as a template (Figure 2.12) [22]. The CS–PAA hollow nanospheres could be prepared by polymerization of acrylic acid monomers in the presence of chitosan. The Fe_3O_4 loading was done by dissolving $FeCl_3{\cdot}6H_2O$ and $FeSO_4{\cdot}7H_2O$ into CS–PAA nanosphere solution followed by the addition of NH_4OH. Finally, the CS–PAA template could be removed by adjusting with HCl to pH <1. The obtained particles were characterized by dynamic light scattering (DLS) in aqueous solution and observed by TEM, FT-IR, and X-ray. The results

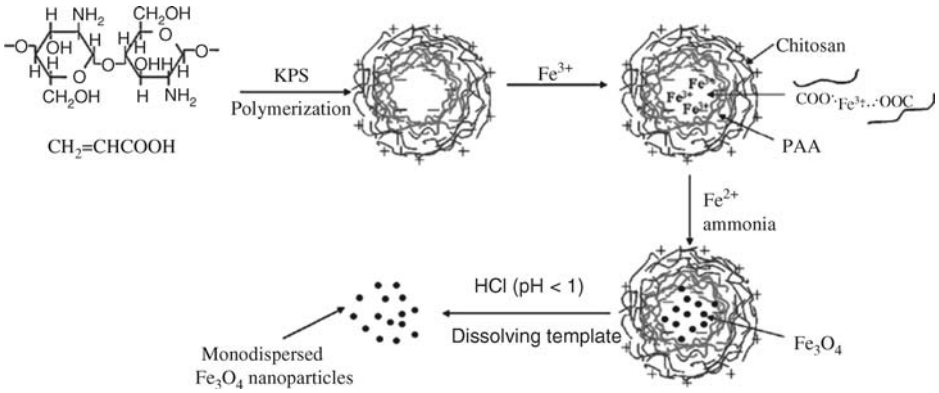

Figure 2.12 The procedure for monodisperse magnetite nanoparticles via chitosan–poly(acrylic acid) template [22].

revealed that the Fe_3O_4 nanoparticles were 3–5 nm in size with excellent dispersibility. The particles exhibited superparamagnetic property with a saturation magnetization of 40.7 emu/g (Figure 2.13).

2.5.4 Blending

Blending is the simplest way to prepare nanocomposites and is suitable for all kinds of nanoparticles. Depending on the conditions, blending usually can be divided into solution blending, emulsion or suspension blending, and melt blending.

2.5.4.1 Solution Blending

First, the nanoparticles were added after the base resin was dissolved in solvent. The obtained mixture was agitated to prepare a uniform mixture. The nanocomposites were prepared by removing the solvent or by polymerization of the monomer. In our research, polyurethane-based coatings reinforced by ZnO nanoparticles (about

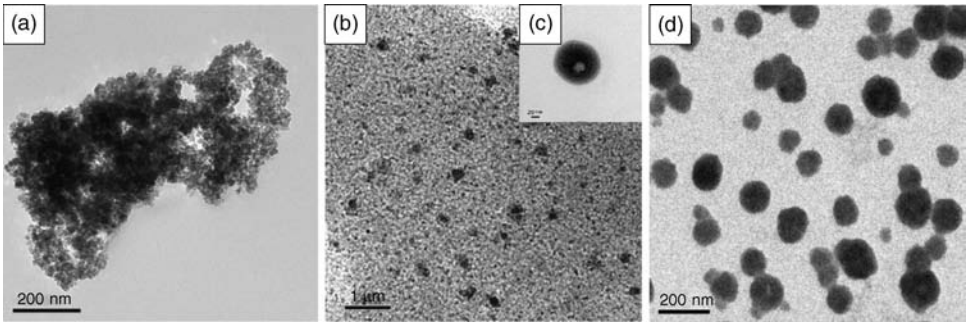

Figure 2.13 TEM images of (a) bare Fe_3O_4 nanoparticles; (b) CS–PAA particles; (c) magnified CS–PAA particles; and (d) Fe_3O_4 nanoparticles synthesized by CS–PAA template [22].

27 nm) were prepared via solution blending. The ZnO/PU films and coatings were fabricated by a simple method of solution casting and evaporation. The mechanical properties of the films were investigated by a universal material test, and the abrasion resistance of the prepared coatings was evaluated by a pencil-abrasion-resistance tester. A significant improvement in Young's modulus and tensile strength was achieved for the PU films by incorporating up to 2.0 wt% ZnO nanoparticles, and the abrasion resistance of the PU coatings was greatly enhanced due to the addition of ZnO nanoparticles (Figure 2.14). Moreover, the antibacterial property test was carried out via the agar dilution method and the results indicated that PU films doped with ZnO nanoparticles showed excellent antibacterial activity, especially for *Escherichia coli* (Table 2.2).

Besides, the $Bi_xY_{3-x}Fe_5O_{12}$ ($x = 0$, 1, and 1.8)-doped PMMA nanocomposites were prepared by *in situ* bulk polymerization. Some $Bi_xY_{3-x}Fe_5O_{12}$ nanoparticles (0.05 wt%) were dispersed in the MMA monomer, and the obtained suspension was mixed in a high-performance ball mill operating at 40 rpm for 4 h. Some AIBN (0.1 wt% of monomer) as initiator was added. The prepolymerization was performed at $80 \pm 2\,^{\circ}C$ under mechanical stirring for about 20 min until the conversion of MMA was about 12–15%. Then, the suspension was poured into a stainless steel mold, which was coated with a thin film of Garry Mould Release Agent (non-paintable). The aperture at the top of the mold was wrapped with a plastic foil. Thereafter, the mold containing the prepolymer and $Bi_xY_{3-x}Fe_5O_{12}$ nanoparticles was kept at 40 °C for 24 h, and solidification took place. Then, the temperature was adjusted to 100 °C and kept for 1 h to increase the molecular weight of PMMA. Finally, $Bi_xY_{3-x}Fe_5O_{12}$ ($x = 0$, 1, and 1.8)-doped PMMA nanocomposites were obtained after disassembling the molds. The PMMA slice doped with Bi-YIG

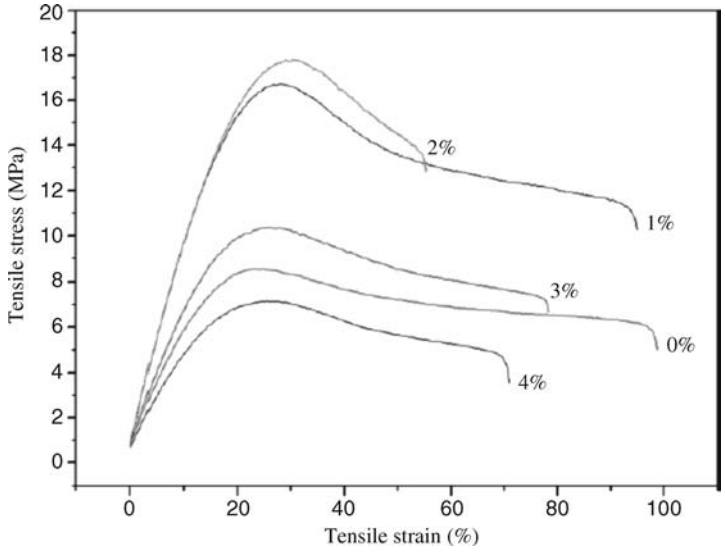

Figure 2.14 Tensile stress–strain curves of different PU films [23].

Table 2.2 Antibacterial rates of PU films containing different amounts of ZnO nanoparticles [23].

	Antibacterial rate	
ZnO (wt%)	***Escherichia* (CPU)**	***Bacillus subtilis* (CPU)**
0	0	0
1.0	20	0
2.0	26	18
3.0	71	61
4.0	90	84

nanoparticles is a new promising material for magneto-optical devices. The Faraday rotation test showed that the angle of Faraday rotation increased with increasing Bi content in PMMA composites, and the maximum value of the figure of merit was 1.46°, which was comparable to the value of a sputtered film.

2.5.4.2 Emulsion or Suspension Blending

Similar to solution blending, emulsion or suspension solution was used instead of solution [23]. The method is mainly applicable to polymers that are difficult to dissolve. Superparamagnetic magnetite/polystyrene composite particles were prepared by inverse emulsion polymerization with water-based ferrofluid as a dispersing phase and organic solvent and styrene as a continuous phase (Figure 2.15). The resulting brownish Fe_3O_4/PS emulsion showed magnetism in an applied magnetic field. The obtained magnetic Fe_3O_4/PS microspheres were characterized by FT-IR, TEM, SEM, XRD, and TG. The magnetic Fe_3O_4/PS microspheres with a diameter of 200 nm were observed. The results showed that magnetite particles were well encapsulated in PS and the composite particles have high magnetite content, which was more than 15%.

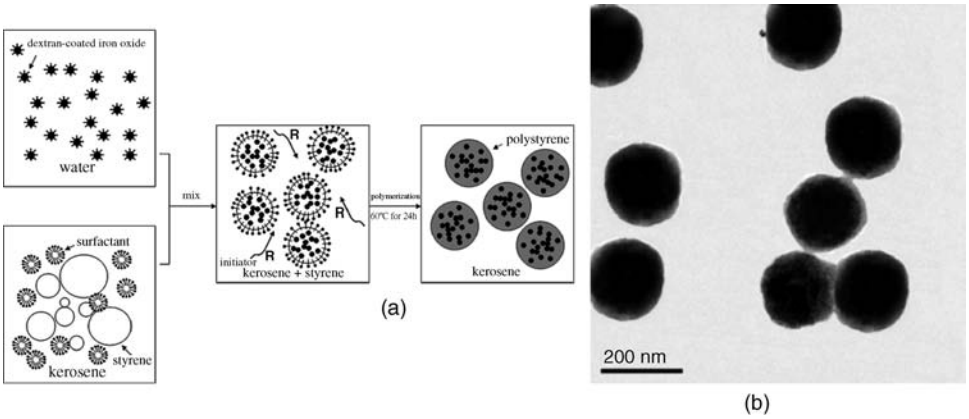

Figure 2.15 (a) The procedure for preparation of Fe_3O_4/PS composite particles by inverse emulsion polymerization. (b) TEM images of Fe_3O_4/PS composite microspheres [24].

2.5.4.3 Melt Blending

To prevent aggregation, the surface of the nanoparticles was first modified with a suitable agent, and then the nanoparticles were added to the polymer in the molten state uniformly. The advantage of the method is similar to ordinary polymer modification, and it is easy to industrialize. LDPE/EGP electrical conducting composites were prepared by using low-density polyethylene (LDPE) and expanded graphite (EGP) via melt blending [25]. The effects of EGP on the electrical and mechanical properties and PTC of the prepared composites were investigated. Results showed that the tensile strength of the composites decreased with the increasing content of EGP, and the EGP content should be lower than 40%. The PTC strength of the composites first increases and then decreases with the increasing EGP content and achieved the maximum value of about 5.85 at 33% of filling content. Moreover, it was found that the PTC strength of the composites was affected by the heat treatment and blending time (Figure 2.16).

2.5.4.4 Mechanical Grinding/Blending

Using mechanical grinding/blending, many kinds of magnetic fluids could be prepared. First, the polymer and some surfactants were dissolved in a solvent. Then, some magnetic nanoparticles were added and mixed together. The mixture was ball milled at 40 rpm for 3 h at room temperature using a high-performance ball mill under airtight conditions. The pots and balls were made of agate. After ball milling for a suitable time, magnetic fluids were prepared.

2.5.5 Others

Recently, there are many reports on the use of special methods for preparing polymer/inorganic nanocomposites, such as MD and LB membrane methods and radiation synthesis. In the LB membrane method, single or multilayer film is first preformed with metal ions, and then reacted to form sulfide nanoparticles. The MD membrane method is used to prepare single or multi-ordered membrane, using

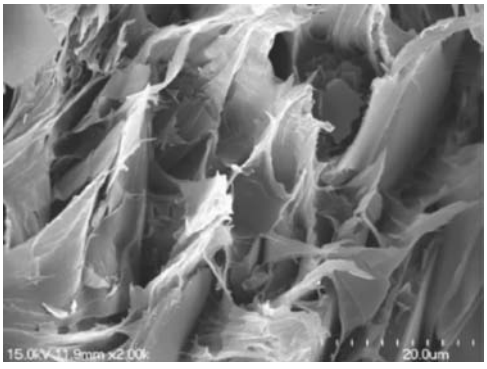

Figure 2.16 SEM of the fracture of EGP/LEDP composites (35% EGP, no phase separation) [25].

electrostatic interaction between cation and anion. Radiation synthesis is a recently developed method for the preparation of nanocomposites. First, polymer monomer and metal salt are mixed together at the molecular level, and then reacted under irradiation. The preparation method can be divided into two categories depending on the system: the water system and the non-water system.

2.6 Characterization of Polymer–Inorganic Nanocomposites

Nanomaterials possess the following characteristics: small size and large specific surface area, high surface energy, and a large proportion of surface atoms. As a result, one must have special "eye" and "hand" to characterize the nanoscale structure and properties of materials and to effectively control their size, morphology, crystalline phase, composition, and structure.

2.6.1 X-Ray Diffraction

From the XRD data, one can obtain the material composition, structure (three-dimensional coordinates of atoms, chemical bonding, molecular conformation and three-dimensional conformation, electron density, etc.), and the information on the interaction between molecules. XRD is a common means of measuring nanoparticles. It can determine not only the sample phase and the phase content, but also the particle size. When the grain size is less than 100 nm, diffraction line broadening will occur. The diffraction lines of the half-peak width of degree β and crystal grain size (D) obey the following relationship:

$$\beta = 0.89\lambda / D\cos\theta.$$

Accordingly, the strongest diffraction peaks can be calculated according to the particle size of the prepared nanomaterials.

From X-ray photoelectron spectroscopy, one can obtain the following information: (1) One can qualitatively analyze various elements, except H and He, from the fingerprint of the E_b (the binding energy of atoms in a particular orbit) spectrum. (2) One can obtain the chemical valence state, chemical structure, and physical state from the displacement of peak and the shape. (3) One can obtain different elements and semiquantitative analysis of chemical states from the relative intensity ratio of peak. (4) Different elements, chemical state depth distribution, and film thickness can be obtained from the peak and the change in the background intensity. In general, the higher the E_b, the lesser the electron density corresponding to the element.

In our research, it was found that the magnetism of Fe_3O_4 nanoparticles disappeared at 550 °C when exposed in the atmosphere for 2 h [26]. To find the reason for the disappearance of magnetism of pure Fe_3O_4 nanoparticles, XRD was performed using Cu Kα radiation. The XRD patterns of pure Fe_3O_4 nanoparticles calcined at different temperatures are shown in Figure 2.17. From Figure 2.17, one can find that there is

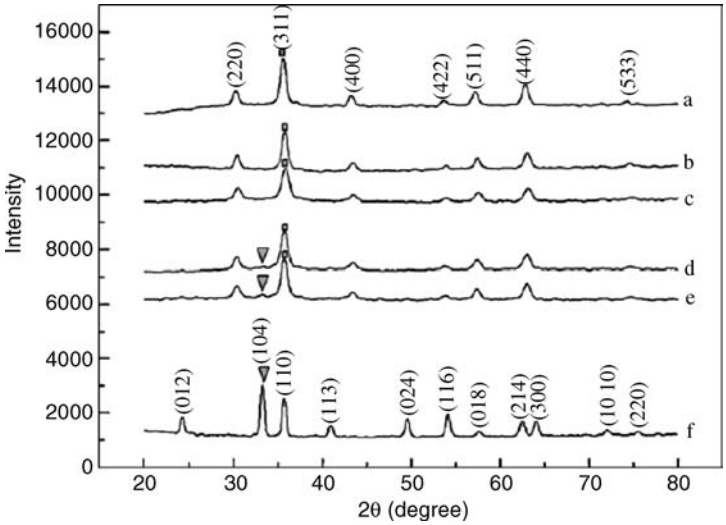

Figure 2.17 XRD patterns of pure Fe_3O_4 nanoparticles at room temperature (a) and calcined at 150 °C (b), 250 °C (c), 350 °C (d), 450 °C (e), and 550 °C (f) for 2 h in the atmosphere [26].

almost no difference among the diffraction peaks of the particles calcined at 150 and 250 °C, except the weakening in intensity of magnetite, especially for the (311) peak. From 350 to 550 °C, the (311) peak keeps reducing, while the (104) peak of hematite develops and becomes stronger and stronger. The magnetite (Fe_3O_4) transforms to hematite (α-Fe_2O_3) completely at 550 °C, and the magnetism of the nanoparticles disappears.

2.6.2 Infrared Spectroscopy

From the IR spectrum, one can observe the absorption and emission due to the molecular vibration and rotation in the electromagnetic wave infrared region (15 000–10 cm^{-1}). It reveals the unknown composition qualitatively according to the band characteristic frequency and determines the component content of the sample (quantification) according to band intensity. It can also reveal the molecular structure (such as functional group and bond), identify isomer, and determine structures of compounds. The interaction among molecules can also be understood by anatomizing the band change. This method can be used to measure samples in the state of gas, liquid, and solid. There are also extremely sensitive changes in molecular structure called "fingerprint zone" (1300–400 cm^{-1}), which help us to analyze unknown composition and structure.

Figure 2.17 shows that no change of XRD patterns can be observed for pure Fe_3O_4 nanoparticles after being calcined at 150 and 250 °C. To reveal the difference, IR spectra (as shown in Figure 2.18) of magnetite samples calcined at different temperatures were obtained using FT-IR. From Figure 2.18, one can find the absorption peak of Fe—O in Fe_3O_4 at 571.1 cm^{-1}. After calcination at 150 °C for

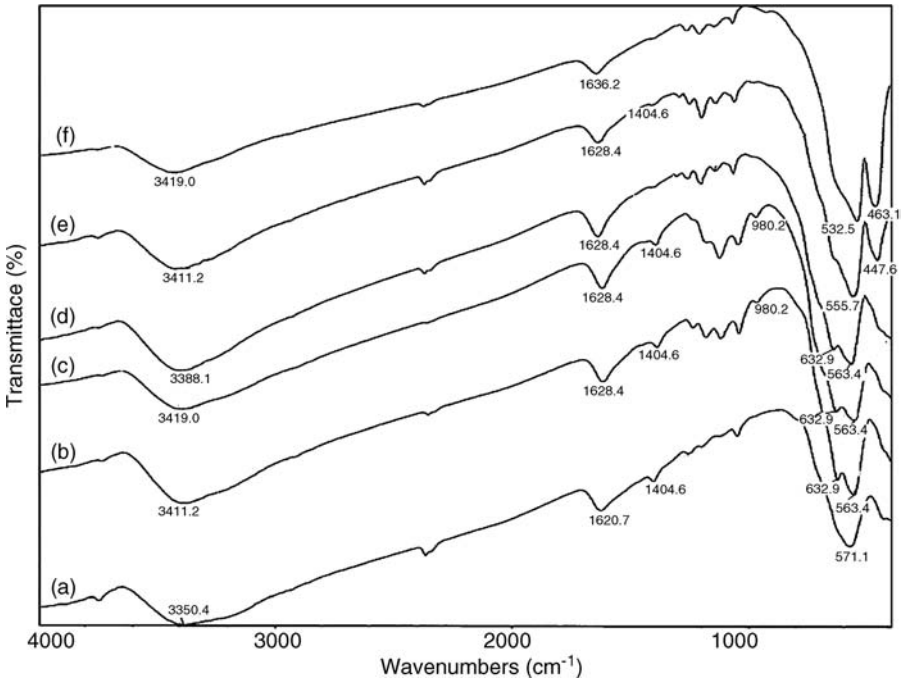

Figure 2.18 IR spectra of pure Fe_3O_4 nanoparticles at room temperature (a) and calcined at 150 °C (b), 250 °C (c), 350 °C (d), 450 °C (e), and 550 °C (f) for 2 h in the atmosphere [26].

2 h, the peak at 571.1 cm^{-1} splits into two peaks at 632.9 and 563.4 cm^{-1}, respectively. The newly formed absorption peaks at 632.9 and 563.4 cm^{-1}, which are associated with the Fe—O bond, are the characteristic peaks of γ-Fe_2O_3. XRD is not sensitive enough to differentiate between Fe_3O_4 and γ-Fe_2O_3, due to extreme similarity in the crystal structure of the two phases. Provided that there is an intergradation, Fe_3O_4 and γ-Fe_2O_3 coexist at a certain proportion that exhibits the maximal magnetism. The intergradation appears when the pure Fe_3O_4 nanoparticles are calcined at 250 °C for 2 h in air, leading to the maximal magnetism. Afterward, the peak at 632.9 cm^{-1} becomes increasingly weaker, and disappears at 550 °C. Another new peak at 447.6 cm^{-1} appears at 450 °C and becomes stronger and shifts to 463.1 cm^{-1} at 550 °C. According to Nasrazadani and Raman, the two absorption peaks at 532.5 and 463.1 cm^{-1} can be assigned to the Fe—O absorption in hematite (α-Fe_2O_3). Therefore, one can conclude that 550 °C is the minimal temperature for the complete transformation from magnetite (Fe_3O_4) to hematite (α-Fe_2O_3), consistent with the results of XRD and magnetic properties analysis.

2.6.3 Mechanical Property Test

The mechanical property of the prepared films can be measured using a universal material testing machine (WDT-0.2, KQL Testing Instruments Inc., China). The

Table 2.3 Mechanical properties of the PU films filled with different ZnO content [27].

ZnO (wt%)	Young's modulus (MPa)	Tensile strength (MPa)	Elongation ratio at rupture (%)
0.0	517.42	8.58	98.37
1.0	660.34	16.74	94.35
2.0	710.48	17.83	54.79
3.0	557.70	10.42	77.96
4.0	512.76	7.24	70.69

force transducer with a precision of ±0.02‰ was made by Transcell Technology, Inc., USA. The crosshead speed was 5 mm/min during the tests. The films were cut into dumbbell shape and the mechanical property measurement was performed according to our previous article [23].

The mechanical property of pure PU films and ZnO-doped PU films prepared using PU coatings was measured [27]. Figure 2.14 shows the tensile stress–strain curves of the PU films and the mechanical parameters are listed in Table 2.3. It can be seen that the Young's modulus and tensile strength first increase and then decrease with the increasing ZnO content and the optimal ZnO content for the Young's modulus and tensile strength is 2.0 wt%. However, the elongation at rupture is inversely related to the Young's modulus and tensile strength. Repeated tests show that the filled ZnO nanoparticles can enhance the strength but not the flexibility of the composite films. The increase in Young's modulus and tensile strength of the composite films may be due to the limit of moving scale of chain segments of the PU matrix with the addition of ZnO. Moreover, when ZnO nanoparticles are filled into the interstices of PU chains, an interactive force against the PU chains may be generated. Therefore, when an external force is applied onto the two ends of the dumbbell-shaped PU film, the film ruptures easily due to the strong interaction force generated between ZnO nanoparticles and PU chains. Besides, the percolation effect could cause the aggregation of ZnO nanoparticles in the dry film, leading to the deterioration of mechanical property.

2.6.4 Abrasion Resistance Test

The neat PU coatings and 2.0 wt% ZnO nanoparticle-filled PU coatings were sprayed onto the ABS substrate with a 1 mm × 1 mm grounding area. The obtained wet coating was roasted for curing under infrared radiation at 60 °C for 30 min. The abrasion resistance of the selected coating was tested using a pencil-abrasion-resistance tester. In the testing process, a sample area, which was free of blemishes and painting imperfection, was selected. The eraser was kept in close contact with the surface of the sample at 90°. The moving distance was limited to 2.54 cm, and the frequency was maintained at 25 rpm. The test was performed by moving the free

Table 2.4 The abrasion resistance of the composite coatings with various thicknesses ranging from 10 to 18 μm [23].

	Neat PU coating		Composite coating (2.0 wt% ZnO)	
Thickness (μm)	**Dry coating**	**Wetted with alcohol**	**Dry coating**	**Wetted with alcohol**
10	148	60	361	86
12	155	77	410	97
14	162	91	437	113
16	187	101	497	133
18	206	110	560	156

end of the pencil until the grounding area, which was a useful indicator when some cracks were made, was revealed. The number of times the eraser moves back and forth indicates the abrasion resistance of the coating.

Table 2.4 shows the abrasion resistance of the dry and alcohol-wetted PU composite coatings. It demonstrates that the abrasion resistance of the composite coatings is improved when ZnO nanoparticles were filled into the PU matrix. The improvement of abrasion resistance for the samples with ZnO nanoparticles may be attributed to the polymer bond formed around the hard nanoparticles. Compared to the dry coatings, the wet coatings demonstrate poor abrasion resistance, indicating poor endurance against organic solvent, such as alcohol. Besides, one can also see that the abrasion resistance of the dry and wet coatings is proportional to the thickness, and the slopes are 0.9664 (dry, neat), 0.9906 (wet, neat), 0.9910 (dry, composite), and 0.9937 (wet, composite), respectively. Moreover, the PU composite coatings possessing the same abrasion resistance are much thinner than the pure PU coatings, which reveals that the addition of ZnO nanoparticles is favorable for reducing manufacturing cost and displays an outstanding prospect in applications.

2.6.5 Impact Strength

To obtain the impact strength of nanocomposites, an Izod impact machine tester with digital display (JBL-22, Shenzhen KQL Testing Instruments Co., Ltd) was used according to GB/T 1843–1996. Unnotched specimens with rectangular dimensions of $80 \times 10 \times 4\,mm^3$ were fractured by an impact energy of 5.5 J with an impact speed of 3.5 m/s at room temperature. The distance between the impact point and fixed point was set to be 22 mm.

The impact strength of PMMA nanocomposites is shown in Figure 2.19. For sample A, the filling of silica particles obviously improves the impact strength of PMMA nanocomposites. The impact strength of PMMA nanocomposites increases with the increasing silica content, which can be ascribed to the more reinforcement sites formed among the polymer chains. It suggests the importance of incorporating

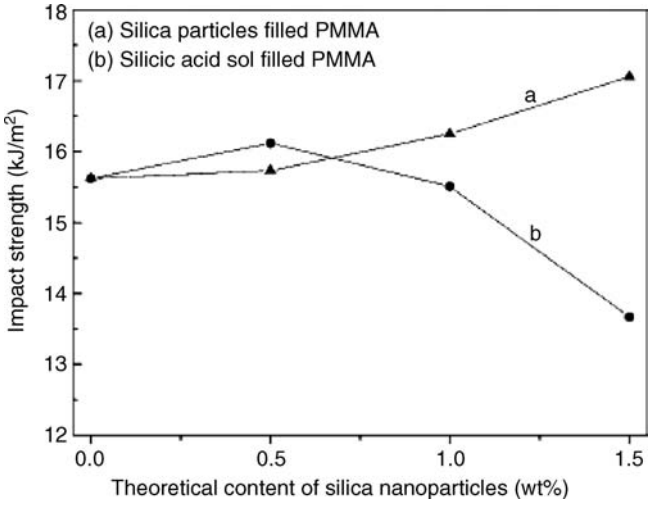

Figure 2.19 Impact strength of different PMMA nanocomposites [14].

the silica particles to improve the mechanical properties of PMMA nanocomposites. Considering the strong increase in impact strength of PMMA nanocomposites, it is obvious that some energy is eliminated by the filled silica particles during the breaking down process. For sample B, the impact strength increases at low silica content ($x = 0.5$) and then decreases at high content ($x = 1$ or 1.5). With the increasing silica content, more THF remains in the polymer composites and thereafter induces the formation of small pinholes in PMMA during the heat treatment at 100 °C. During the test of impact strength, such pinholes become the weak points and the PMMA nanocomposites can easily be broken under an abrupt impact and the impact strength decreases.

2.6.6
Flexural Test

Flexural test could be performed according to GB/T 9341–200026 using a universal testing machine (WDT20, Shenzhen KQL Testing Instruments Co., Ltd) in a three-point bending configuration at room temperature. A PC was connected to the testing machine, and the crosshead speed was set to be 2 mm/min. The force transducer with a precision of ±0.02% was made by Transcell Technology, Inc., USA.

The effect of particulate fillers on the stress–strain behavior of polymeric materials is different due to the interaction between the particles and the polymer. The flexural strength measured for different PMMA nanocomposites is shown in Figure 2.20. It can be concluded that as the silica content increases, the flexural strength of PMMA nanocomposites filled either by silica particles or by silicic acid sol increases. The reinforcement mechanism of polymer by silica can be explained as follows: as the active surface of silica particles connected with some long polymer chains and

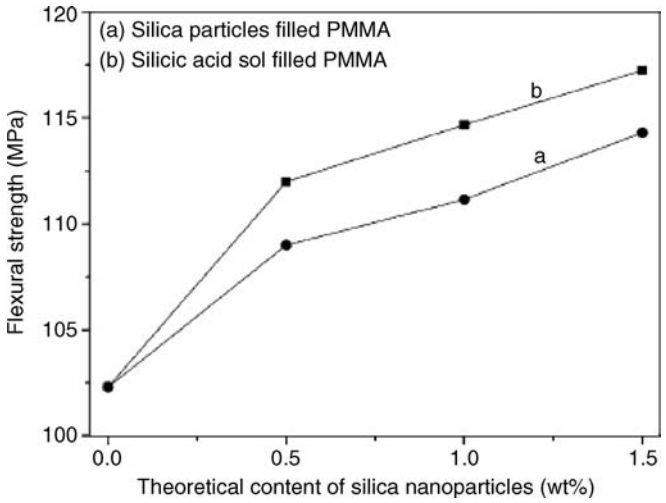

Figure 2.20 Flexural strength of different PMMA nanocomposites [14].

the physical bonding between silica and polymer chains are formed, the flexural stress could be transferred through the inorganic linking point to the other polymer chains. When one chain ruptures under external stresses, the others can still support the polymer structure. So the whole specimen is not threatened by the stresses, and the flexural strength increases. For sample A, as the content of silica particles increases, the number of coupling points between PMMA and silica particles also increases; therefore, the flexural strength is improved. For sample B, contrary to the impact strength, the flexural strength increases with the addition of more silicic acid sol, though there may be small pinholes existing in the composites. Two factors influence the flexural strength of PMMA nanocomposites: the addition of silica and the existence of pinholes in the structure. During the test, stress was imposed slowly on the samples, though the pinholes might lower the flexural strength; however, such influence was negligible. On the contrary, the silica well dispersed in PMMA nanocomposites leads to an obvious increase in the flexural strength. As a result of the two opposite effects, the flexural strength of silicic acid sol-filled PMMA nanocomposites is improved.

2.6.7
Others

Scanning tunneling microscopy (STM) is a technique based on the principles of electron tunneling. Between two very close conductors (typically only a few Å apart), electrons can pass through the barrier between two conductors and flow under external electric field, which is called the tunneling effect. These electrons produce measurable current; this value and the distance between the conductors have an exponential relationship: $I \propto V\exp[-C(\varphi S)^{1/2}]$, where I is the tunneling current, V is

the added voltage between conductors, φ is the effective tunneling barrier (eV), C is a constant, and S is the conductor spacing (Å). STM is precise enough to control the positioning of individual atoms on the probe and can scan atoms one by one in an atomic array, which provides atomic resolution of surface analysis.

The main feature of atomic force microscopy (AFM) is that it does not require the surface conductivity, because it measures the scanning probe and the interaction between the tip of AFM and the sample surface. The interaction includes electrostatic, van der Waals, friction, surface tension (capillary), and the magnetic forces, which overcomes the inadequacy of the STM. Unlike the STM, a force map can be obtained from the AFM probe. This map can be interpreted as a reflection of the surface structure and a geometric topology map of magnetic and electrostatic forces.

In addition to the above spectroscopic methods, there are still a variety of other methods, such as Mössbauer spectroscopy and various other surface analysis methods and dynamic structure spectroscopy. As is well known, there are more than 100 types of surface analysis and surface characterization methods. This shows the difficulty of surface characterization. When one characterizes the surface and its structure, it is necessary to integrate different analysis and characterization methods to complement each other and confirm each other.

2.7
Applications of Polymer–Inorganic Nanocomposites

2.7.1
Applications of Bi-YIG Films and Bi-YIG Nanoparticle-Doped PMMA

Bi-YIG films and Bi-YIG nanoparticle-doped PMMA nanocomposites are the functional materials with magneto-optical effects from the ultraviolet to the infrared region. With profound investigation of Faraday rotation and gradual recognition of the importance of the effect, researchers began to take advantage of this effect in practical applications. Various magneto-optical devices prepared using the magneto-optical materials have been widely used in the field of optical communication and optical storage. Magneto-optical modulator, magneto-optical switch, magneto-optical isolator, magneto-optical circulator, magneto-optical rotator, and magneto-optical phase shifter have been invented since 1966.

With the development of optical fiber communication and integrated optics, the integrated magneto-optical waveguide-type device was invented in 1972. The first-generation magneto-optical disk was launched in 1988, which has many distinct advantages, such as high-density recording (10^7–10^{10} bits/cm^2), erasable writing, rewritable, and so on. In addition, the materials with magneto-optical effect are also widely used in the field of magnetic field measurement, high-voltage transmission lines and current measurement sensors, and magneto-optical storage. As the core material of the magneto-optical devices, magneto-optical materials determined the merits of the performance of devices directly. Magneto-optical devices have high

sensitivity, strong anti-interference, high insulation, low cost, small size, light weight, and so on. These materials are also widely used in the fields of space, guidance, and satellite monitoring and controlling. Due to the independence of the magnetic rotation direction from the incident light direction, the materials can be used for making a single-pass optical gate and modulator. The magneto-optical glass with high Verdet constant (also known as *Vd* values) can be used for the measurement of high current to prevent accidents caused by lightning and short-circuit of electrical devices.

Magnetic nanoparticles with magneto-optical effect have important applications. PMMA doped with these nanoparticles demonstrates magneto-optical effect and can be used to prepare a variety of devices. Some of the mature applications are discussed below.

2.7.1.1 **Magneto-Optical Isolator**

In the optical fiber communication, optical information processing, and some measurement systems, a stable light source is usually needed. The junctions of different devices tend to reflect part of the light. Once the reflected light enters the laser cavity, the output instability of the laser occurs, and the whole system will be affected. The magneto-optical isolator is a non-reciprocal device designed to solve this problem. It enables the forward transmitted light to go through without being blocked, and no light will be reflected back from the optical fiber joint, thus effectively eliminating the noise of the laser source. With the development of near-infrared optical fiber technology, practical optical fiber that is operated at wavelengths of 1.3 and 1.55 μm is considered to be a low-loss and low-dispersion material, and is widely used in the fiber optic technology. To make the semiconductor laser (as the light source) stable, we must use magneto-optical isolators. Magneto-optical isolators are the optical devices that block unwanted reflected light and are indispensable for stable operation of semiconductor lasers. A commercially available magneto-optical isolator is composed of a Faraday rotator and linear polarizers, as shown in Figure 2.21.

The working principle is as follows: after the linearly polarized light from the polarizer goes through the 45° Faraday rotator, the optical vibration plane rotates

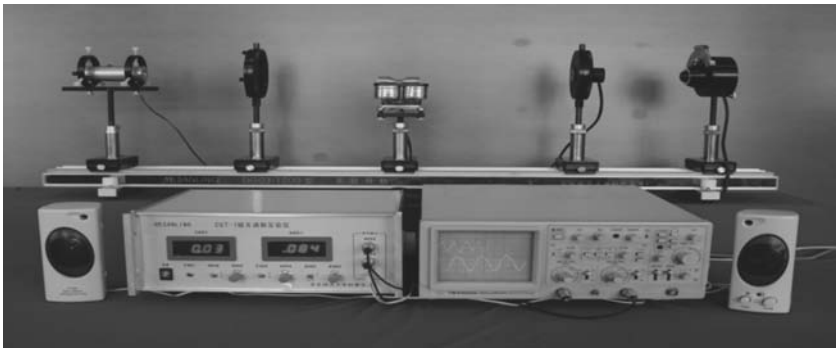

Figure 2.21 The setup of a commercially available magneto-optical isolator.

by 45°. The vibration plane is parallel to the analyzer's optical axis, so the linearly polarized light propagates through analyzer. If the light reflects during propagation, the reflected light goes through the Faraday rotator and rotates 45° again. Vibration plane rotates around 45°, which is perpendicular to the polarizer's optical axis. The reflected light is blocked to avoid entering the laser and the stability of the light source is not affected.

The performance of the magneto-optical isolator is determined by the Faraday rotator. As the core component of magneto-optical isolator, the quality of magneto-optical materials has a direct influence on the performance of the device. Fundamentally, the materials should have a large Faraday rotation angle, high transparency, and low light absorption in the near-infrared wavelength. In the beginning, researchers used YIG as the material for the magnetic rotator, but its performance is still unsatisfactory. Subsequently, researchers found that for the rare earth-substituted garnet crystal, especially by bismuth, the Faraday rotation increased dramatically. So the bismuth-substituted YIG naturally became the most widely used magneto-optical material.

2.7.1.2 **Magneto-Optical Sensor**

Magneto-optic sensor is a device that takes advantage of magneto-optical effects to detect the changes in magnetic field or current strength. It combines laser, optical fiber, and optical techniques in one. It is widely used in high-voltage network testing, monitoring, precision measurement, remote control, telemetry, and automated control systems.

The typical structure of a current sensor using optical fiber is shown in Figure 2.22. The working principle is as follows: the light sent off by a laser through the polarizer becomes linearly polarized light, and then the linearly polarized light is transmitted through the optical fiber wound around the electrical wire. As a result of the Faraday rotation, the polarization angle of linearly polarized light deflects. Owing to the changes in light intensity, the analyzer detects the change in the linearly polarized light intensity caused by the Faraday deflection, so the actual current can be measured. Traditionally, high-voltage measurement and monitoring were done using the oil-filled magnetic flux current transformer (OFMFCT). The transformer

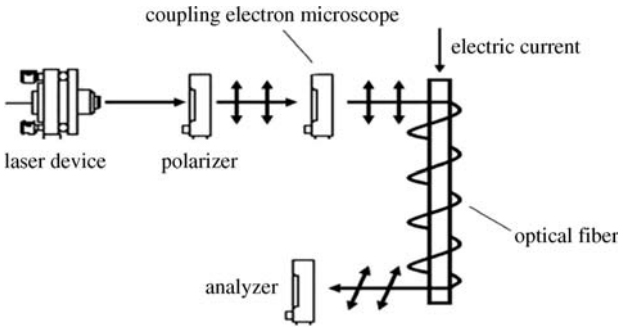

Figure 2.22 The structure of a current sensor using optical fiber.

was made of copper wire, insulation materials, and machining parts. Compared to OFMFCT, the magneto-optical sensor has some benefits, such as a simple structure, small size, and low cost. It is considered to be the most promising high-voltage and high-current measuring device.

2.7.1.3 **Tuned Filter**

A YIG-tuned filter is a device used for filtering. A YIG small ball, as the oscillator, selects input signal through the resonant frequency generated by coupling. It works in the frequency range 3–40 GHz, and 3 dB bandwidth can be adjusted between 5 and 70 MHz. Since YIG has a very wide frequency tuning range (up to several octaves), it is widely used in broadband MW, millimeter-wave receiver for tracking and preselecting RF signals.

In the MW frequency, the YIG molecules have a magnetic moment. Normally, the moment is randomly arranged. When a static magnetic field is applied, the magnetic moment arranges toward a certain direction. If an alternating magnetic field is applied, the moment changes back and forth. The oscillation frequency is the function of the properties of YIG materials (e.g., magnetic properties, crystal shape and size) and the intensity of magnetic field. The maximum amplitude that appears in alternating magnetic fields is exactly equal to the oscillation frequency of YIG crystals. Therefore, we can take advantage of this resonance phenomenon to create filters, as shown in Figure 2.23.

A typical YIG resonator consists of a highly polished YIG sphere with a diameter of 0.25–0.5 mm. A small ball is put in the static magnetic field with a field strength of H. When a signal enters the input side, the ball produces a circular polarized magnetic moment around the small ball if the signal frequency is equal to the resonant frequency of resonator. When the magnetic field couples with the output coil, energy is generated from the output coil. Otherwise, the small ball is not inspired and no energy is generated.

2.7.1.4 **Magneto-Optical Recorder**

The principle of magneto-optical recording was proposed early in the 1950s, but its specific application was developed in recent years. Magneto-optical recording is the most advanced information storage technology, which combines the advantages of both magnetic disk and CD-ROM. Magnetic disks are widely used in many applications that

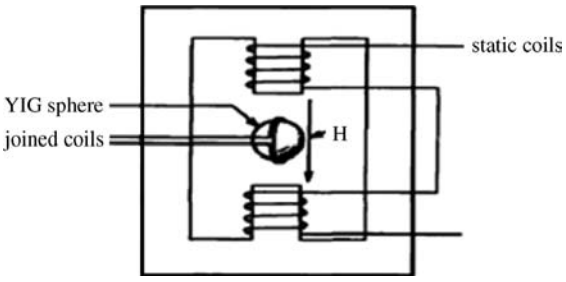

Figure 2.23 The use of resonance phenomenon to create filters.

require large-scale real-time data collection, recording, storage, and analysis. The magneto-optical storage systems will replace the traditional storage methods.

Magneto-optical recording technology records information by heating the small magnetic area to change the orientation of magnetization vector, and then reads out the information using magneto-optical effects. In practical applications, the thin and amorphous film placed in reverse magnetic field was heated by a laser, resulting in magnetization perpendicular to the membrane surface. Information can be written onto the magnetic domain and read out by magneto-optic Kerr effect. The most important characteristic of the magneto-optical recording material is that magnetic recording medium should be perpendicular to the membrane surface and can maintain the stable structure of the small magnetic domain. The magneto-optical Kerr rotation angle of the materials must be large, and reflectivity must be high to achieve high sensitivity, high signal to noise ratio, and low noise. Moreover, the chemical structure must be stable, and the large film can easily be produced.

A practical magneto-optical recording medium must have the following features: the magnetic anisotropy perpendicular to the membrane surface and $K_\alpha > 2\pi M_2 s$; a rectangular hysteresis loop ($M_r/M_s = 1$) and high coercivity at room temperature; high magneto-optical recording sensitivity (lower laser recording power); large magneto-optical effect (a large Kerr angle θ_k or a large Faraday angle θ_F); low disk writing noise (no big grain); high enough reading and writing cycles; good oxidation resistance, corrosion resistance, and long-term stability; Curie temperature between 400 and 600 K and a compensation temperature of 25 °C. In the past two decades, a new magneto-optical material, magneto-optical disk, has been introduced to the market, which has replaced the rare earth transition metal (RE-TM) materials. However, owing to its weak magneto-optical effect, chemical instability, high price, and poor magneto-optical effects near the ultraviolet region, researchers began to explore the next-generation materials. (Bi, Ga)-substituted yttrium iron garnet magneto-optical materials have been researched and developed as a new generation of magneto-optical materials.

2.7.1.5 **Magneto-Optic Modulator**

A magneto-optic modulator modulates light beam by rotating the polarization plane of the incident light through the magneto-optical medium. The modulator has a wide range of applications, for example, infrared detector chopper, infrared radiation pyrometer, TV signal transmission and distance measuring devices, and optical detection and transmission system.

The structure and working principle of a magneto-optical modulator are illustrated in Figure 2.24. There is no external magnetic field in the absence of modulated signals. When a beam of intensity I_0 goes through the polarizer, the output intensity is as follows, according to the Malus law:

$$I = I_0 \cos 2\alpha,$$

where α is the angle between the optical axis of polarizer and the analyzer. When the two optical axes are parallel ($\alpha = 0$), the light intensity I is maximum. When the two polarizers are perpendicular to the beam ($\alpha = \pi/2$), the light intensity I is zero (the

Figure 2.24 The structure and working principle of a magneto-optical modulator.

output is extinct). When the alternating signal is applied on the electrical coils of magneto-optical materials, an alternating magnetic field is generated and the polarization plane of light is rotated. The output light intensity is as follows:

$$I = I_0 \cos 2(\alpha \pm \theta).$$

When α is constant, the output light intensity changes only with θ. Due to the Faraday rotation effect, the signal current modulates the rotation signal of polarized light into intensity signal. Modulation information was carried by the output light in the form of intensity change.

For the production of magneto-optic modulators, the magneto-optical materials should have high transparency and large Faraday rotation (Faraday rotation angle per unit length). The magneto-optical glass was previously used. At present, the YIG is used, which has high transparency and high Faraday rotation angle in the 1.1–5.5 μm wavelength. As the single-crystal epitaxial thin film magneto-optical material, the Bi-doped YIG is more suitable for preparing the optical modulator. The Faraday rotation angle of the device is as high as 10^3–10^4 rad/cm, while the transparency to visible light is still high.

2.7.1.6 Magneto-Optic Switch

By using the Faraday rotation effect to change the polarization plane of incident light in the magnetic field, the magneto-optic modulator switches the light route by varying the magnetic field intensity. Compared to the traditional mechanical optical switches, it has high switching speed and high stability. Compared to other nonmechanical optical switches, it has the advantage of low driving voltage and little crosstalk. It can be expected that the magneto-optical switch would be highly competitive in the near future.

2.8 Application of Magnetic Fe_3O_4-Based Nanocomposites

With increasing industrial activities, wastewater from many industries such as tannery, chemical manufacturing, mining, battery manufacturing industries, and so

on contains toxic heavy metals, which are not biodegradable and tend to accumulate in living organisms, causing various diseases and disorders. Chromium (Cr), copper (Cu), cadmium (Cd), and nickel (Ni) are listed among the 11 hazardous priority substances of pollutants [28]. For instances, chromium is present in effluent waters from several different industries. It affects human physiology, accumulates in the food chain, and causes many ailments. Chromium can result in severe health problems ranging from simple skin irritation to lung carcinoma [29]. Strong exposure to Cr(VI) could cause cancer in the digestive tract and lungs, epigastric pain, and nausea. Hence, it is necessary to clear Cr(VI) from effluent to meet the industrial effluent standard before its discharge into the environment [30]. Copper is the most important and frequently used metal in industries such as plating, mining, and petroleum refining. The industries mentioned above produce a great amount of wastewater and sludge containing a high concentration of copper cations, which have negative effects on the water environment [31]. Cadmium and solutions of its compounds are toxic and serious toxicity problems have been found from long-term exposure and work with cadmium plating baths. Finally, nickel sulfide fume and dust is recognized as having carcinogenic potential. At the same time, the market for Ni–Cd batteries has been growing significantly in recent years. It means that there is enhanced potential for an increasing content of Ni and/or Cd in water. Hence, it is utmost important to purify water before its use, as it is one of the basic needs for the existence of mankind. The effective disposal of heavy metals has been arousing worldwide concern in the past few decades.

Today, various treatment techniques and processes have been used to remove the metallic ions from the wastewater, including precipitation, evaporation, solvent extraction, ion exchange, reverse osmosis, membrane separation, and so on. Most of these methods suffer from some drawbacks such as high capital and operational costs for the treatment and disposal of the residual metal sludge [32–34]. Therefore, efforts are made to develop low-cost materials to remove contaminants from aqueous solutions. Fortunately, recent development of nanotechnique has shed a light on this field. Nanoparticles, often characterized by a significant amount of surfaces, have been attracting much interest because of their unique properties and potential applications.

For instance, magnetic Fe_3O_4 nanoparticles have attracted much attention not only in the field of magnetic recording but also in the areas of medical care and magnetic sensing in the recent decades [35–37]. It is believed that magnetic nanoparticles exhibit the finite-size effect or high surface area/volume ratio, resulting in a higher adsorption capacity for metal removal. In addition, the easy separation of metal-loaded magnetic adsorbent from solution can be achieved using an external magnetic field. Thus, an efficient, economic, scalable, and nontoxic synthesis of Fe_3O_4 nanoparticles is highly preferred for potential applications and fundamental research [38–40].

Several recent studies sought to adsorb heavy metals onto magnetic nanoparticles. For example, the removal and recovery of Cr(VI) has been achieved by synthesized maghemite (γ-Fe_2O_3) nanoparticles, and it is proved that Cr(VI) adsorption capacity of nanoscale maghemite compared favorably with other

adsorbents such as activated carbon and clay [41,42]. Very interestingly, a further study from the same group suggests that the Cr(VI) adsorption onto the δ-FeOOH-coated γ-Fe_2O_3 is mainly controlled by the outer sphere complexation [43]. They also proved that the Cr(VI) can be effectively removed from synthetic wastewater using surface-modified jacobsite nanoparticles, in which the adsorption process followed by magnetic separation leads to the rapid, effective, and inexpensive removal of toxic ions [44]. The results from another group have shown that magnetic nanostructured particles (γ-Fe_3O_4) can be successfully applied to adsorb metal ions, in which the combined technique of biosorption and magnetic separation holds the advantages of flexibility, eco-friendly characteristics, and low operational cost [45]. A successful removal of Cr(VI) has been achieved by electrocoagulation with Fe electrodes [46].

2.9
Applications of ZnO-Based Nanocomposites

Nanosized ZnO has great potentiality for being used in preparing solar cells, gas sensors, chemical absorbent varistors, electrical and optical devices, electrostatic dissipative coatings, catalysts for liquid-phase hydrogenation, and catalysts for photocatalytic degradation instead of titania nanoparticles. Hence, investigations on the synthesis and modification of nanosized ZnO have attracted tremendous attention.

2.9.1
Gas Sensing Materials

ZnO is a multifunctional material. Because of its high chemical stability, low dielectric constant, large electromechanical coupling coefficient, and high luminous transmittance, ZnO materials have been widely used as dielectric ceramic, pigment, catalyst, and sensing material [47]. As a gas sensing material [48], it is one of the earliest discovered and the most widely applied oxide gas sensing material. It is sensitive to many gases and has satisfactory stability. Its gas selectivity can be improved by doping additives and catalysts. But its working temperature is rather high, normally 400–500 °C, and its gas selectivity is poor. In recent years, the studies on ZnO gas sensing materials, which can improve its preparation method and decrease its working temperature, are one of its major research topics [49].

2.9.2
Photocatalyst for Degradation of Organic Dye

The use of semiconductor colloids as photocatalyst for a variety of chemical reactions, due to their peculiar optoelectronic photocatalytic properties, is well stated in the recent literatures [50–52]. The effectiveness of the photodegradation processes has already been tested for different types of matrices and results have been encouraging, as the literature reports on a large number of successes in the

degrading of organic dyes in wastewater [53]. Under photoexcitation, semiconductors undergo charge separation and initiate oxidation of the organic compounds at the interface. Nanostructured semiconductors are a potential candidate to photodegradation of organic compounds because of the size dependence of their bandgap [54], when the semiconductor nanocrystal size is comparable to or smaller than the bulk exciton diameter. Therefore, photocatalytic electron and hole redox potentials of size-quantized semiconductor nanocrystals can be tuned to achieve increased catalytic effect for selective photochemical reaction. Moreover, as photocatalytic reaction occurs on the surface of nanoparticles, high surface area/volume ratio of nanosized semiconductors will contribute to increase the decomposition rate.

Colloidal chemistry synthetic routes provide the possibility of separating nucleation from growth, avoiding inter-particle aggregation and controlling their growth. In this work, nanostructured TiO_2 and ZnO were prepared by using new nonhydrolytic methods [55,56]. These preparative approaches are based on the rapid thermal decomposition of molecular precursors in the presence of strong coordinating agents to produce highly crystalline, redispersible, nanosized semiconductor particles, with controllable size and size distribution. The reactions occur at high temperatures in anhydrous organic solvents, providing oxide nanoparticles with no surface hydroxyl groups, which are known to significantly influence surface oxidation power as well as decrease interfacial electron-transfer rates with respect to their dehydroxylated counterparts. After optical and structural characterization, the obtained nanoparticles were immobilized onto transparent support in order to exploit them in a photocatalytic process devoted to the photodegradation of methyl red, an organic dye. Then a comparison between the efficiency of nanocatalysts and their equivalent commercial oxides was made. The obtained results showed a good efficiency of nanostructured materials.

2.9.3
Benard Convection Resin Lacquer Coating

The motion of the liquid can be visualized using fine powder particles as trace. Benard convection often occurs in paint coatings [57], and it is easily observed by movement of pigment. Benard convection is a troublesome phenomenon in paint coatings, giving rise to flocculent patterns as a trace of the cell structure, and is only applied to "hammer finish," a technique to hide rough surfaces. Hansen and Pierce [58] reviewed the theoretical background of Benard convection in polymer coatings and showed practical remedies for suppressing undesirable effects such as pigment flocculation, pigment segregation, and loss of gloss.

Particles that consist of four needle crystals united at a common juncture are formed in ZnO smoke and are called fourlings [59] or tetrapod-like particles. Kitano *et al.* [60] have developed a new method by which tetrapod-like ZnO particles are produced with four legs, several tens or hundreds of micrometers in length. The ZnO particles grow by heavy surface oxidation of ZnO powder in water and subsequent thermal oxidation of ZnO/Zn particles with some catalysis. The ZnO particles have high electroconductivity.

2.10 Applications of Magnetic Fluid

Magnetic fluids, which are colloidal suspensions of magnetic nanoparticles stabilized by coating surfactants, have attracted much interest recently. Magnetic fluids have been widely used in dynamic loudspeakers, computer hardware, dynamic sealing, electronic packing, mechanical engineering, aerospace, bioengineering, biological and medical diagnosis and therapy, pharmacy, and biosensors.

Sealing techniques of magnetic fluid take advantage of response of magnetic fluids. When a magnetic fluid is placed into a gap between the surfaces of rotating and stationary elements in the presence of magnetic fluid, it assumes the shape of a "liquid O-ring" to completely fill the gap.

The magnetic fluid vacuum rotary feedthrough is a device that transmits rotary motion into a vacuum chamber. The basic components are permanent magnet, two pole pieces, a magnetically permeable shaft, and magnetic fluid. The shaft (of pole pieces) contains a multistage structure, completed by the pole pieces and the shaft, concentrating magnetic flux in the radial gap under each stage. In the ideal situation, all flux lines are confined under each stage, and none are in the increase region. The magnetic fluid is trapped and held in each stage, forming a series of "liquid O-ring" with intervening regions that are filled with air. Each stage can typically sustain a pressure difference of 0.15–0.2 atm. All stages act in series to provide a total pressure capability for the seal. For vacuum applications, magnetic fluid seals are normally designed to sustain a pressure difference of >2 atm, thus allowing a safety margin.

In our research works, biocompatible magnetic fluids based on dextran-coated Fe_3O_4 magnetic nanoparticles were prepared through a one-step method [61]. In contrast to the conventional coprecipitation method, hydrazine hydrate was added as reducing agent and precipitator in the present investigation. The prepared biocompatible magnetic fluids were intravenously injected into rabbits, the iron contents in blood and organs at different times were measured by atomic absorption spectrometer, and the biodistribution and the biotransportation of magnetic fluids in organs were examined (Table 2.5). Then, the magnetic resonance (MR) images of liver, marrow, and lymph (shown in Figure 2.25) were acquired by MRI experiments

Table 2.5 The Fe contents in some organs of rabbits at different times [61].

t (h)	Blood (mg/g)	Lymph (mg/g)	Liver (mg/g)	Spleen (mg/g)	Lung (mg/g)	Heart (mg/g)
0	0.048	0.010	0.079	0.297	0.038	0.042
0.5	0.255	0.019	0.08	0.316	0.056	0.047
1	0.275	0.02	0.23	0.931	0.093	0.056
2	0.256	0.053	0.188	1.028	0.137	0.095
3	0.14	0.154	0.169	0.656	0.152	0.091
6	0.105	0.206	0.14	0.652	0.097	0.072
9	0.081	0.073	0.113	0.598	0.061	0.071
12	0.050	0.07	0.106	0.594	0.042	0.063

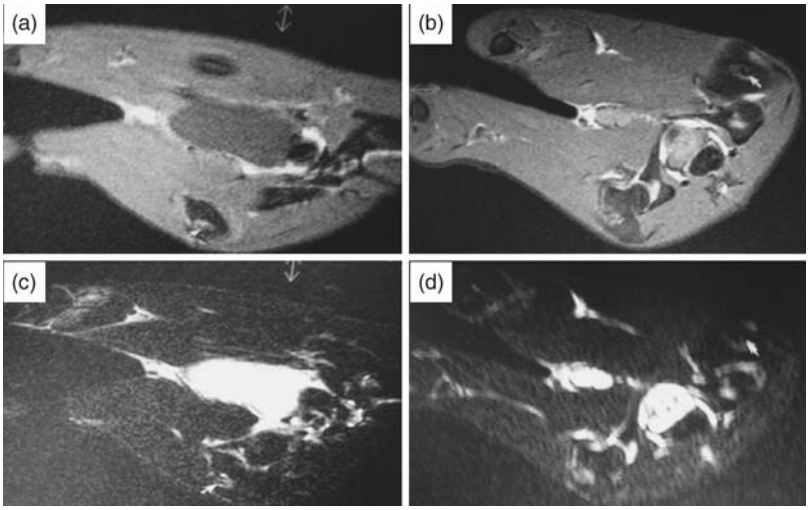

Figure 2.25 MR signal intensity of lymph of rabbit in T1-weighted sequences (a and b) and T2-weighted sequences (c and d). Images were acquired before (a and c) and 6 h after intravenous injection of Fe_3O_4 MNPs (b and d) [61].

before and after intravenous injection of magnetic fluids. Image analysis revealed that the MR signal intensity of these organs notably decreased after being intensified by magnetic fluids. However, when there exist tumors in organs, the signal intensity of tumor did not change after injection. From that the tumor can easily be identified, which indicated a potential application of the as-prepared magnetic fluids in functional molecular imaging for biomedical research and clinical diagnosis.

Acknowledgments

The project was supported by the National Natural Science Foundation of China (NSFC, Nos. 20876100 and 21246002), the National Basic Research Program of China (973 Program, No. 2009CB219904), Technology Innovation Foundation of MOST (No. 11C26223204581), Priority Academic Program Development of Jiangsu Higher Education Institution, National Postdoctoral Science Foundation (20090451176), the Key Laboratory of Environmental Materials and Environmental Engineering of Jiangsu Province of Yangzhou University (No. K11025), the Natural Science Foundation of Jiangsu Province (No. BK2011328), and the Minjiang Scholarship of Fujian Province.

References

1 Hong, R.Y., Ren, Z.Q., Ding, J.M., and Li, H.Z. (2005) *Chemical Engineering Journal*, **108**, 203–212.

2 Hong, R.Y., Pan, T.T., and Li, H.Z. (2006) *Journal of Magnetism and Magnetic Materials*, **303**, 60–68.

3 Hong, R.Y., Li, J.H., Wang, J., and Li, H.Z. (2007) *China Particuology*, **5**, 186–191.
4 Hong, R.Y., Pan, T.T., Han, Y.P., Li, H.Z., Ding, J., and Han, S.J. (2007) *Journal of Magnetism and Magnetic Materials*, **310**, 37–47.
5 Hong, R.Y., Li, J.H., Li, H.Z., Ding, J., Zheng, Y., and Wei, D.G. (2008) *Journal of Magnetism and Magnetic Materials*, **320**, 1605–1614.
6 Hong, R.Y., Pan, T.T., Qian, J.Z., and Li, H.Z. (2006) *Chemical Engineering Journal*, **119**, 71–81.
7 Hong, R.Y., Li, J.H., Chen, L.L., Liu, D.Q., Li, H.Z., Zheng, Y., and Ding, J. (2009) *Powder Technology*, **189**, 426–432.
8 Cai, X., Hong, R.Y., Wang, L.S., Wang, X.Y., Li, H.Z., Zheng, Y., and Wei, D.G. (2009) *Chemical Engineering Journal*, **151**, 380–386.
9 Hong, R.Y., Wu, Y.J., Feng, B., Di, G.Q., Li, H.Z., Xu, B., Zheng, Y., and Wei, D.G. (2009) *Journal of Magnetism and Magnetic Materials*, **321**, 1106–1110.
10 Fu, H.P., Hong, R.Y., Wu, Y.J., Di, G.Q., Xu, B., Zheng, Y., and Wei, D.G. (2008) *Journal of Magnetism and Magnetic Materials*, **320**, 2584–2590.
11 Wu, Y.J., Hong, R.Y., Wang, L.S., Di, G.Q., Li, H.Z., Xu, B., Zheng, Y., and Wei, D.G. (2009) *Journal of Alloys and Compounds*, **481**, 96–99.
12 Hong, R.Y., Qian, J.Z., and Cao, J.X. (2006) *Powder Technology*, **163**, 160–168.
13 Hong, R.Y., Pan, T.T., Han, Y.P., Zhang, S.Z., Li, H.Z., and Ding, J. (2007) *Journal of Applied Polymer Science*, **106**, 1439–1447.
14 Fu, H.P., Hong, R.Y., Zhang, Y.J., Li, H.Z., Xu, B., Zheng, Y., and Wei, D.G. (2008) *Polymers for Advanced Technologies*, **19**, 1–8.
15 Hong, R.Y., Zhang, S.Z., Han, Y.P., Li, H.Z., Ding, J., and Zheng, Y. (2006) *Powder Technology*, **170**, 1–11.
16 Hong, R.Y., Li, J.H., Qu, J.M., Chen, L.L., and Li, H.Z. (2009) *Chemical Engineering Journal*, **150**, 572–580.
17 Feng, B., Hong, R.Y., Wang, L.S., Guo, L., Li, H.Z., Ding, J., Zheng, Y., and Wei, D.G. (2008) *Colloids and Surfaces A: Physicochemical and Engineering Aspects*, **328**, 52–59.
18 Hong, R.Y., Feng, B., Ren, Z.Q., Xu, B., Li, H.Z., Zheng, Y., and Wei, D.G. (2008) *Chemical Engineering Journal*, **144**, 329–335.
19 Hong, R.Y., Ren, Z.Q., Han, Y.P., Li, H.Z., Zheng, Y., and Ding, J. (2007) *Chemical Engineering Science*, **62**, 5912–5924.
20 Hong, R.Y., Fu, H.P., Zhang, Y.J., Liu, L., Wang, J., Li, H.Z., and Zheng, Y. (2007) *Journal of Applied Polymer Science*, **105**, 2176–2184.
21 Zhu, T., Wu, Y.J., Zhou, F., Zhu, J.P., and Chen, Z.S. (2008) *Journal of Guizhou University of Technology (Natural Science Edition)*, **37**, 17–23.
22 Feng, B., Hong, R.Y., Wu, Y.J., Liu, G.H., Zhong, L.H., Zheng, Y., Ding, J.M., and Wei, D.G. (2009) *Journal of Alloys and Compounds*, **473**, 356–362.
23 Li, J.H., Hong, R.Y., Li, M.Y., Li, H.Z., Zheng, Y., and Ding, J. (2009) *Progress in Organic Coatings*, **64**, 504–509.
24 Hong, R.Y., Feng, B., Liu, G., Wang, S., Li, H.Z., Ding, J.M., Zheng, Y., and Wei, D.G. (2009) *Journal of Alloys and Compounds*, **476**, 612–618.
25 Li, J.H., Hong, R.Y., Chen, Z.X., and Li, H.Z. (2009) *New Chemical Materials*, **37**, 31–33.
26 Li, J.H., Hong, R.Y., Li, H.Z., Zheng, Y., Ding, J., and Wei, D.G. (2009) *Materials Chemistry and Physics*, **113**, 140–144.
27 Hu, J.Q., Li, J.H., and Hong, R.Y. (2007) *Shanghai Coatings*, **46**, 8–12.
28 Rozada, F., Otero, M., Morán, A., and García, A.I. (2008) *Bioresource Technology*, **99**, 6332–6338.
29 Jha, M.K., Kumar, V., Bagchi, D., Singh, R. J., and Lee, J.C. (2007) *Journal of Hazardous Materials*, **145**, 221–226.
30 Gupta, V.K., Shrivastava, A.K., and Neeraj, J. (2001) *Water Research*, **35**, 4079–4085.
31 Chen, J.P. and Wang, W. (2000) *Separation Technology*, **19**, 157–167.
32 Jha, M.K., Kumar, V., Maharaj, L., and Singh, R. (2004) *Journal of Industrial & Engineering Chemistry Research*, **43**, 1284–1295.
33 Kentish, S.E. and Stevens, G.W. (2001) *Journal of Chemical Engineering*, **84**, 149–159.
34 Jha, M.K., Upadhyay, R.R., Lee, J.C., and Kumar, V. (2008) *Desalination*, **228**, 97–107.
35 Sun, S.H., Murray, C.B., Weller, D., Folks, L., and Moser, A. (2000) *Science*, **287**, 1989–1992.

36 Xie, J., Xu, C., Kohler, N., Hou, Y., and Sun, S.H. (2007) *Advanced Materials*, **19**, 3163–3166.

37 Pankhurst, Q.A., Connolly, J., Jones, S.K., and Dobson, J. (2003) *Journal of Physics D: Applied Physics*, **36**, R167–R181.

38 Sun, S.H. and Zeng, H. (2002) *Journal of the American Chemical Society*, **124**, 8204–8205.

39 Si, S., Kotal, A., Mandal, T.K., Giri, S., Nakamura, H., and Kohara, T. (2004) *Chemistry of Materials*, **16**, 3489–3496.

40 Wan, S.R., Huang, J.S., Yan, H.S., and Liu, K.L. (2006) *Journal of Materials Chemistry*, **16**, 298–303.

41 Hu, J., Chen, G.H., and Lo-Irene, M.C. (2005) *Water Research*, **39**, 4528–4536.

42 Hu, J., Lo-Irene, M.C., and Chen, G.H. (2007) *Separation and Purification Technology*, **56**, 249–256.

43 Hu, J., Lo-Irene, M.C., and Chen, G.H. (2007) *Separation and Purification Technology*, **58**, 76–82.

44 Hu, J., Lo-Irene, M.C., and Chen, G.H. (2005) *Langmuir*, **21**, 11173–11179.

45 Li, H.D., Li, Z., Liu, T., Xiao, X., Peng, Z.H., and Deng, L. (2008) *Bioresource Technology*, **99**, 6271–6279.

46 Heidmann, I. and Calmano, W. (2007) *Separation and Purification Technology*, **61**, 15–21.

47 Lou, X. (1991) *Journal of Sensor and Transducer Technology*, **3**, 1–5.

48 Seiyama, T. and Kato, A. (1962) *Analytical Chemistry*, **34**, 1502–1503.

49 Pan, S. and Mei, S. (1993) *Journal of Sensor and Transducer Technology*, **3**, 18–20.

50 Vinogdopal, K. and Kamat, P.V. (1995) *Environmental Science & Technology*, **29**, 841–845.

51 Muneer, M., Philip, R., and Das, S. (1997) *Research on Chemical Intermediates*, **23**, 233–237.

52 Tang, W.Z., Zhang, Z., An, H., Quintana, M.O., and Torres, D.F. (1997) *Environmental Technology*, **18**, 112–117.

53 Zang, L., Liu, C.Y., and Ren, X.M. (1995) *Journal of the Chemical Society, Faraday Transactions*, **91** (5), 917–922.

54 Al_Ekabi, H., Serpone, N., Pelizzetti, E., Minero, C., Fox, M.A., and Draper, R.B. (1989) *Langmuir*, **5**, 250–257.

55 Hagfeldt, A. and Gratzel, M. (1995) *Chemical Reviews*, **95**, 49–56.

56 Trentler, T., Denler, T., Bertone, J., Agrawal, A., and Colvin, V. (1999) *Journal of the American Chemical Society*, **121**, 1613–1621.

57 Barrel, F.E. and Van Loo, M. (1925) *Industrial & Engineering Chemistry*, **17**, 1051–1058.

58 Hansen, C.M. and Pierce, P.E. (1973) *Industrial & Engineering Chemistry Product Research and Development*, **12**, 67–74.

59 Fuller, M.L. (1944) *Journal of Applied Physics*, **15**, 164–172.

60 Kitano, M., Hamabe., T., Maeda, S., and Okabe, T. (1990) *Journal of Crystal Growth*, **102**, 965–973.

61 Hong, R.Y., Feng, B., Chen, L.L., Liu, G.H., Li, H.Z., Zheng, Y., and Wei, D.G. (2008) *Biochemical Engineering Journal*, **42**, 290–300.

3
Theory and Simulation in Nanocomposites

Qinghua Zeng and Aibing Yu

3.1
Introduction

During the past two decades, nanocomposites have emerged as a new class of materials that received considerable interest in scientific development and engineering applications [1]. Nanostructure generated by introducing discrete nanoparticles into a continuous solid matrix represents a radical alternative to the structure of conventional particle-reinforced composites. In nanocomposites, particle–matrix interface is dramatically increased due to the high specific surface area of nanoparticles. More importantly, their interactions can be controlled at the molecular level because of the equivalent magnitude of nanoparticles and polymer chain. Such structural features lead to many new phenomena, exceptional properties, and promising applications. However, further development in nanocomposites is hindered because of the poor understanding of some key fundamental issues.

3.1.1
Dispersion of Nanoparticles

The promise of the improved and novel properties of nanocomposites depends largely on the degree of nanoparticle dispersion. Given a uniform dispersion, the large specific surface area of nanoparticles will produce a large interfacial area per unit volume between nanoparticle and matrix, which fundamentally differentiates nanocomposites from conventional composites. Recently, various approaches have been used to improve the dispersion of nanoparticles in matrix, for example, the modification of nanoparticle surface, *in situ* synthesis of nanoparticles, and functionalization of polymer chains. However, it is very difficult to achieve an optimal dispersion of nanoparticles because (i) nanoparticles have large active surface atoms and tend to form agglomerates (e.g., nanoparticle aggregate, carbon nanotube bundle, and stack of clay platelets), (ii) nanoparticles may possess chemical dissimilarity (e.g., hydrophilic versus hydrophobic) with the matrix, and (iii) nanoparticles exhibit a large amount of defects and uncertainty of properties.

Polymer Composites: Volume 2, First Edition. Edited by Sabu Thomas, Kuruvilla Joseph, Sant Kumar Malhotra, Koichi Goda, and Meyyarappallil Sadasivan Sreekala.

3.1.2 Interface

Interfaces are important for many properties and applications of multiphase materials. This is particularly true for the particle-reinforced polymer composites, where the interfacial characteristics between particle and polymer play a crucial role in load transfer and mechanical properties. The adhesion strength between polymer matrix and particle is a major factor in determining the mechanical properties of composites, since it determines the effectiveness of the interface in transferring an applied load from matrix to nanoparticle phase. With the decrease in particle size from micrometer to nanometer range, the volume fraction of interfacial region significantly increases, which largely determines many mechanical properties of polymer nanocomposites. Thus, it is of importance in quantifying the properties of interfacial region and its contributions to the overall properties of polymer nanocomposites. Understanding the characteristics of the interfacial region and estimating the structure–processing–property relationships are the current research frontiers in nanocomposites.

3.1.3 Crystallization

It is well known that the behavior of polymer chains around the particle surface is different from that of bulk polymer chains. Depending on the nanoparticle–polymer interactions, polymer in the vicinity of the nanoparticle may be developed into crystallized, amorphized, or heterogeneously nucleated structures. The crystallization of polymer will dramatically affect the overall properties of polymer nanocomposites. As a result, when predicting nanocomposite properties, the morphological features and properties of the interfacial polymer must be taken into account in addition to the properties of individual nanoparticles and bulk polymer.

3.1.4 Property Prediction

The efficient design of new materials with specific properties and applications requires the property prediction of candidate materials and the use of these predictions to evaluate, screen, and guide the material synthesis. To meet this challenge, we need to extend the existing theoretical methods and develop new prediction approaches for nanocomposites. Such prediction requires some important information such as the properties of individual components (i.e., nanoparticle and polymer), processing methods and conditions, structure and morphology of the nanocomposites, and, more importantly, the nature of the interfacial region.

Various methods are available at different levels of complexity and time- and length scales [2]. These methods can also be divided into two general classes: analytical model and numerical simulation. Analytical models have the advantage of greater simplicity and require very little computational resources. However, this

simplicity and ease of application compromise the level of detail that can be taken into account and the limited accuracy of the predictions. In contrast, numerical simulations can provide more accurate predictions as their models are based on the more realistic physics and detailed morphology of the system of interest. With the increasing need for understanding and prediction of nanocomposite properties, numerical simulations of more sophistication will play an important role as they are developed further and integrated more seamlessly with each other.

In the following sections, we will discuss briefly some analytical and numerical techniques, followed by their applications to the property prediction of nanocomposites with a focus on nanoparticle-reinforced polymer nanocomposites.

3.2
Analytical and Numerical Techniques

3.2.1
Analytical Models

Analytical models are mathematical models that have a closed form solution to the equations used for describing changes in a system. Some analytical models are developed for highly specific applications, whereas others for general applications. In material science, micromechanical models are developed to analyze the composite or heterogeneous materials on the level of individual constituents. They can predict the properties of the composite materials and account for interfaces between constituents, discontinuities, and coupled mechanical and nonmechanical properties.

Micromechanical models have been widely used to estimate the mechanical and transport properties of composite materials. For nanocomposites, such analytical models are still preferred due to their predictive power, low computational cost, and reasonable accuracy for some simplified structures. Recently, these analytical models have been extended to estimate the mechanical and physical properties of nanocomposites. Among them, the rule of mixtures is the simplest and most intuitive approach to estimate approximately the properties of composite materials. The Halpin–Tsai model is a well-known analytical model for predicting the stiffness of unidirectional composites as a function of filler aspect ratio. The Mori–Tanaka model is based on the principles of the Eshelby's inclusion model for predicting the elastic stress field in and around the ellipsoidal filler in an infinite matrix.

The direct use of micromechanical models for nanocomposites is however doubtful due to the significant scale difference between nanoparticles and macroparticles. As such, two methods have recently been proposed for modeling the mechanical behavior of polymer nanocomposites: equivalent continuum approach and self-similar approach. In equivalent continuum approach, molecular dynamics (MD) simulation is first used to model the molecular interaction between nanoparticle and polymer. Then, a homogeneous equivalent continuum reinforcing element (i.e., an effective nanoparticle) is constructed. Finally, micromechanical models are used to determine the effective bulk properties of a

nanoparticle–polymer system with the equivalent continuum reinforcing elements embedded in a continuous polymer. Self-similar approach consists of three major steps. For example, in the case of carbon nanotube–polymer composites, a helical array of single-walled carbon nanotubes is first assembled. Such array is termed as nanotube nanoarray where 91 nanotubes make up the cross section of the helical nanoarray. Then, the nanotube nanoarrays are surrounded by a polymer matrix and assembled into a second twisted array, termed as nanotube nanowire. Finally, the nanotube nanowires are further impregnated with a polymer matrix and assembled into the final helical array–nanotube microfiber. The self-similar geometries described in the nanoarray, nanowire, and microfiber allow using same mathematical and geometric model for all three geometries.

3.2.2 Numerical Methods

Numerical methods with different time- and length scales are employed and developed to investigate material properties and behaviors. Among them, molecular modeling can predict the molecular behaviors and correlate macroscopic properties of a material with various variables. The most popular techniques include molecular mechanics (MM), MD, and Monte Carlo (MC) simulation. These techniques are now routinely used to investigate the structure, dynamics, and thermodynamics of inorganic, biological, and polymer systems. They have recently been used to predict the thermodynamic and kinetic properties of nanoparticle–matrix mixtures, interfacial molecular structure and interactions, molecular dynamic properties, and mechanical properties.

Microscale modeling aims to avoid the shortcomings of molecular methods and continuum methods and bridge both methods. Specifically, in nanoparticle–polymer systems, the study of structural evolution (i.e., dynamics of phase separation) involves the description of bulk flow (i.e., hydrodynamic behavior) and the interactions between nanoparticle and polymer components. Note that hydrodynamic behavior is relatively straightforward when handled by continuum methods, but it is very difficult and expensive when treated by atomistic methods. In contrast, the interactions between components can be examined at an atomistic level, but they are usually not straightforward when incorporated at the continuum level. Therefore, various microscale models and simulation methods have been evaluated and extended to study the microscopic structure and phase separation of polymer nanocomposites, including Brownian dynamics (BD), dissipative particle dynamics (DPD), lattice Boltzmann (LB), time-dependent Ginzburg–Landau theory (TDGLT), and dynamic density functional theory (DFT).

Despite the importance of understanding the molecular structure and nature of materials, their behavior can be homogenized with respect to different aspects and at different scales. Typically, the observed macroscopic behavior is usually explained by ignoring the discrete atomic and molecular structures and assuming that the material is continuously distributed throughout its volume. The continuum material is thus assumed to have an average density and can be subjected to body forces such

as gravity and surface forces. Generally speaking, continuum methods at macroscale obey the fundamental laws of continuity, equilibrium, moment of momentum principle, conservation of energy, and entropy. Common continuum methods include finite element method (FEM) and boundary element method (BEM).

3.2.3 Multiscale Modeling

One main goal of computational materials science is to rapidly and accurately predict the behaviors and properties of a material, which is very challenging with traditional analytical and numerical techniques of single time- and length scales under the current computer power. Therefore, it is expected to use the multiscale modeling strategies to bridge the models and simulation techniques across a broad range of time- and length scales to address the macroscopic or mesoscopic behaviors of materials from a detailed molecular description. The challenge for multiscale modeling is to move, as seamlessly as possible, from one scale to another so that the calculated parameters, properties, and numerical information can be efficiently transferred across scales.

In polymer nanocomposites, the challenge is to accurately predict their hierarchical structures and behaviors and to capture the phenomena on length scales that typically span five–six orders of magnitude and timescales that can span a dozen orders of magnitude (Figure 3.1). Some efforts have recently been made to develop

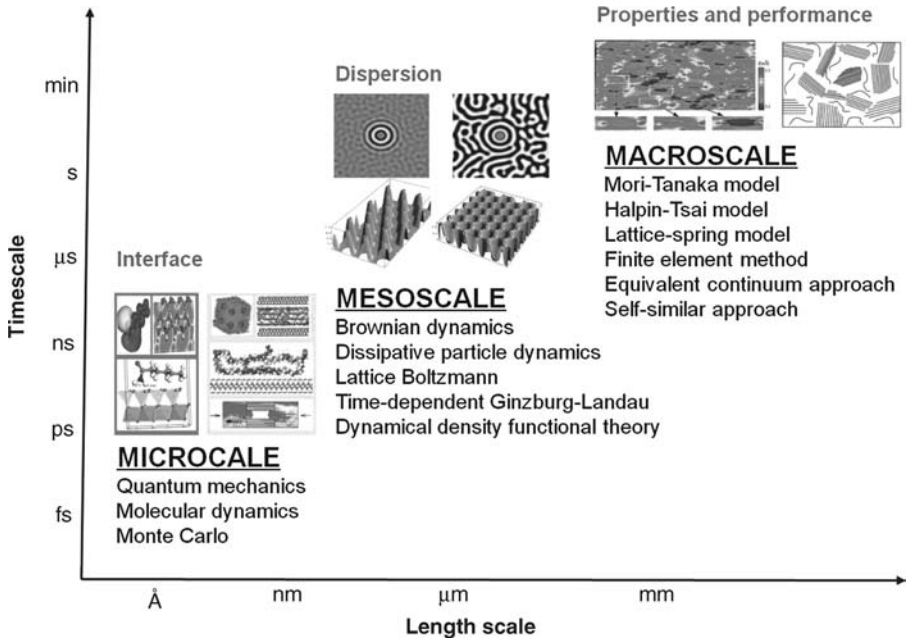

Figure 3.1 Multiscale modeling and simulation techniques for polymer nanocomposites.

multiscale models spanning from molecular to macroscopic levels that, in general, can be divided into sequential and concurrent approaches. In sequential approaches, a series of hierarchical computational methods are linked in such a way that the calculated quantities from a computational simulation at one scale are used to define the parameters of the model operative on the adjoining larger scale. Such parameter-passing sequential approaches have proven effective, especially when material behavior can be parsed into several scales, each with its own distinct characteristics. In concurrent approaches, several computational methods are linked together in a combined model in which different scales of material behavior are considered concurrently and communicate using some sort of handshaking procedure. Such approaches resemble the multigrid techniques used for partial differential equations or the general renormalization group idea of statistical physics.

3.3
Formation of Nanocomposites

3.3.1
Thermodynamics of Nanocomposite Formation

The formation of nanocomposites is a result of mixing of nanoparticles, matrix, and other constituents. To achieve a stable nanostructure, such mixing must meet the thermodynamic requirement, which is related to the intrinsic properties of the constituents (e.g., structure and polarity), their pretreatment (e.g., surface modification and grafting), interaction strength, and processing conditions (e.g., mass ratio). Experimentally, it is very difficult to investigate at the nanoscale the effects of these factors on the final structure of the mixture. This issue can be overcome by using different analytical and numerical methods at atomic or particle scale, including mean field model, self-consistent field (SCF), DFT, and MD.

The mean field model provides a simple and quick method to evaluate the possibility of nanocomposite formation upon mixing the nanoparticles and matrix. Such mixing process is usually associated with the rearrangement of different constituents and thus with the change of the free energy of the systems. The energy change can be attributed to the entropy and enthalpy changes. The former is associated with the intermolecular interactions between the different constituents and thus depends on their relative position or distribution within the system. The latter is related to the configuration changes of the individual constituents, for example, the confined polymer chains between nanoparticles or on the surface of nanoparticles. When applied to clay–polymer systems, this method can predict three kinds of equilibrium structures: conventional immiscible microstructure, intercalated nanostructure, and exfoliated–delaminated nanostructure. The advantage of mean field model is its capability of exploring the effects of polymer and nanoparticle on morphologies of their mixture. However, the method decouples the configurational terms and intermolecular interactions.

To overcome some of the limitations, other methods have been developed to examine how the different factors affect the final structures of the mixture of clay and polymer. For example, by using SCF, it is predicted that increasing clay–polymer interaction can lead to the change of mixing free energy from positive to negative, indicating a final structural change from immiscible to intercalated and exfoliated. By integrating DFT with the SCF model, it is predicted that adding polymers with one reactive end group to a melt of chemically identical nonfunctionalized polymers can lead to the formation of exfoliated nanostructures, while adding polymers with two reactive end groups can promote the formation of thermodynamically stable intercalated nanostructures [3,4].

MD simulations can be first used to calculate the binding energy between polymer and nanoparticle and then to predict the dispersion of nanoparticle within polymer matrix and the equilibrium structure. For example, in the mixture of clay and nylon, it is predicted that (i) increasing surfactant volume would increase clay–polymer binding energy, but decrease polymer–surfactant and surfactant–clay binding energies; (ii) using surfactants with polar groups (i.e., –OH and –COOH) generally results in a stronger polymer–surfactant interaction. In the mixture of nanosphere and polymer, coarse-grained MD simulation [5] showed that a relatively weak interaction between polymer and nanosphere promotes nanosphere aggregation, while increased attractive interaction can lead to strong adsorption of the polymer chains on nanosphere surface and thus promote dispersion of nanospheres.

3.3.2 Kinetics of Nanocomposite Formation

Kinetics is another important factor in determining if a mixture of nanoparticles and polymer can form a nanocomposite. The extent of nanoparticle dispersion (e.g., exfoliation of the stacks of clay platelets, debonding of nanotube bundles, and deagglomeration of nanosphere agglomerates) in a polymer matrix is affected critically by the kinetic barriers. Such kinetic barriers often inhibit the formation of thermodynamically favorable structure.

The kinetics of nanocomposite formation is much less understood. In clay–polymer mixtures, it is still unclear how the surfactant or polymer get into clay gallery and form the intercalated or exfoliated structure since the gallery is initially separated by less than 1 nm and thus hinders the infusion of external species. Thus, some important issues must be addressed: (i) How do the galleries open for the accommodation of intercalating surfactant or polymer? (ii) By what mechanisms do the chains enter the galleries? (iii) What factors may affect the penetration of polymers into the galleries? (iv) How does the diffusivity of the intercalated chains compare to that of bulk chains? Some theoretical efforts have recently been made toward such kinetics issues of nanocomposite formation.

Coarse-grained MD simulations have been employed to study the kinetics of polymer flow into the slit – a process similar to the intercalation of polymer into clay gallery. It is showed that a moderate clay–polymer affinity is needed to achieve the spontaneous intercalation of polymer and swelling of clay [6]. A relatively higher

clay–polymer affinity would slow down the intercalation process of polymer. In addition, the flow of a symmetric diblock copolymer from a bulk melt into a surfactant-grafted slit can produce morphology unattainable by the intercalation of homopolymer.

The shear flow is commonly used to promote greater intermixing of nanoparticle and polymer. Balazs *et al.* [7,8] developed a multiscale model that combines a coarse-grained description of binary fluids with a discrete model for particles. It is predicted that the addition of solid particles significantly changes the speed and morphology of phase separation. If the particles are preferentially wet by one of the fluids, the phase separation is captured in the later stage. The domain size depends strongly on the particle concentration and diffusion constant. If the binary fluid–particle mixture is under shear, the domains initially grow in an isotropic manner and then grow faster along the shear direction and ultimately grow extremely slowly in the perpendicular direction. If particle density is sufficiently high, the shear-induced anisotropic growth is destroyed by the randomly moving coated particles, and thus isotropic morphology can be observed even at large shear strains.

Although nanoparticles are usually regarded as rigid particles, some of them may show a certain level of flexibility (e.g., the bending of nanotubes or clay platelets). When the bending of clay platelets and external shear are considered, the intercalation process can take place by soliton-like excitations (i.e., kinks). If the initial opening of clay galleries and the kinetic features of the process are considered, it is found that the activation of intercalation process by the external force is sufficient for further propagation of the kink with finite velocity.

3.3.3
Morphology of Polymer Nanocomposites

The mixing of nanoparticles and polymers (e.g., homopolymer and copolymer) provides an efficient self-assembly route to create highly ordered nanophase structures. However, the final structures are very complex and usually consist of a multiscale structure and different phases (Figure 3.2). It is thus very important to identify the different possible phases and the phase diagram. Theoretically, it is a great challenge to properly predict the morphology of such systems because the

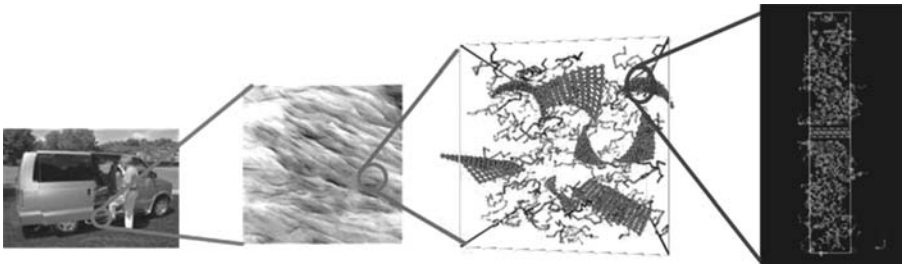

Figure 3.2 Multiscale structures in clay–polymer nanocomposites.

theories must be able to capture features of the mesophase formation of polymers and the interactions among the various components and correlate the morphologies with the composition and architecture of polymers, size and shape of nanoparticles, volume fraction of nanoparticles, mobility of nanoparticles, and chemical modification of nanoparticle surface. In the past, some numerical methods have been developed and used to predict the morphology of nanoparticle–polymer mixtures, including the combined SCF–DFT method, polymer reference interaction site model (PRISM), DPD, dynamic DFT, CDM, and MC.

The mixtures of nanoparticle and homopolymer are promising systems for advanced nanostructures. By using the integrated SCF–DFT method [9–12], it has been identified that there are several different phases in polymer–rigid disk mixtures, including isotropic, nematic, smectic, crystal, columnar phase, and house-of-cards plastic solid. Such phase diagram is closely related to the polymer chain length, particle shape, particle–particle interaction, particle–polymer interaction, particle volume fraction, and functionalization of polymer. In the case of nanosphere polymer, the PRISM study shows that the ratio of particle diameter to monomer diameter is a key geometric variable in the final phase diagram that may include four kinds of polymer-mediated organizations (i.e., contact aggregation, segment-level tight particle bridging, steric stabilization, and telebridging) and two distinct phase separation behaviors. In carbon nanotube–polymer mixtures, DPD study shows that unfunctionalized nanotubes are immiscible with polymethyl methacrylate matrix. However, when functionalized with 30% of acrylate groups, the nanotubes are dispersed well into the matrix [13]. The mixtures of nanoparticle and copolymer represent another class of promising systems for ordered nanostructures. A hybrid CDM has been used to correlate microphase separation of the mixture of A–B diblock copolymers and spherical nanoparticles with the interaction strength, particle number density, and particle mobility [14]. It is predicted that mobile particles can destroy the bicontinuous structure observed typically for symmetric diblocks. In particular, if the interactions between A block and particle are weak, the A blocks form the continuous phase and the B blocks form isolated domains. In contrast, if the interactions are strong, the B phase is continuous and the A blocks self-assemble into distinct islands.

In another study [15], MC simulation is integrated with a scaling theory to consider the multiple length scales (i.e., monomer size, particle size, and the gyration radius of the polymer chain) in the mixtures of diblock copolymers and spherical nanoparticles. It was found that phase diagram strongly depends on particle size. When particle size is comparable to the gyration radius of the minority A block and the particles have a strong preferential attraction to this A block, a new microphase ordering takes place in a narrow range of particle volume fractions and diblock compositions. Thompson *et al.* [16] employed a combined SCF–DFT approach to examine the contributions of enthalphic and entropic energies to the observed morphologies and the role of copolymer architecture (e.g., triblocks, multiblocks, combs, and stars), particle shape, and composition of the mixture. They predicted a variety of one-, two-, and three-dimensional morphologies for particles.

In addition to monosized nanoparticle, the morphology of binary nanoparticles filled in microphase separating AB diblock copolymers has also been studied. For chemically identical spherical particles, large particles are concentrated in the preferred, compatible phase and small particles spread out in the interfacial regions and in the incompatible phase of the diblock copolymer [17]. Theoretical efforts have also been made toward the morphology of copolymer filled with anisotropic particles (e.g., rod-like particles, plate-like particles, or the mixtures of particles of different shapes). It is found that the distribution of particles within the copolymers depends not only on the relative interaction energies between nanoparticles and different blocks but also on the aspect ratio of the rod-like nanoparticles.

3.4 Mechanical Properties

Fillers added to polymer matrix can change the mechanical properties of the matrix in several ways. They can impart additional strength and toughness, inhibit failure by blocking the propagation of cracks, and alter mechanical properties through the structural changes of polymer layer near the filler surface. With particle size reduced from micrometer to nanometer, a dramatic improvement in mechanical behavior of the polymer composites can be achieved. Understanding the exceptional mechanical properties exhibited in polymer nanocomposites is important for the design and development of nanocomposites for engineering applications.

Mechanical properties of polymer nanocomposites can be predicted by using analytical models and numerical simulations at a wide range of time- and length scales, for example, from molecular scale (e.g., MD) to microscale (e.g., Halpin–Tsai), to macroscale (e.g., FEM), and their combinations. MD simulations can study the local load transfers, interface properties, or failure modes at the nanoscale. Micromechanical models and continuum models may provide a simple and rapid way to predict the global mechanical properties of nanocomposites and correlate them with the key factors (e.g., particle volume fraction, particle geometry and orientation, and property ratio between particle and matrix). Recently, some of these models have been applied to polymer nanocomposites to predict their thermal–mechanical properties, Young's modulus, and reinforcement efficiency and to examine the effects of the nature of individual nanoparticles (e.g., aspect ratio, shape, orientation, clustering, and the modulus ratio of nanoparticle to polymer matrix).

3.4.1 Stiffness and Strength

Stiffness is often a critical property of a material that determines how much a component will deform in response to force (e.g., stretching, compression, or bending). Molecular modeling has been used to predict the stiffness and strength of polymer nanocomposites with different types of nanoparticles, for example, carbon

nanotubes, clay nanoplatelets, nanospheres, and fullerene buckyballs. In carbon nanotube–polymer composites, it is found that (i) the stiffness enhancement depends on the length of carbon nanotubes and the direction of applied loading, (ii) the polymer configuration (e.g., crystalline and amorphous) plays an important role in the tensile response and fracture, and (iii) the modulus can be effectively improved by deliberately adding chemical cross-linking. In nanocomposites containing spherical and platelet nanoparticles, the toughness improvement could be attributed to the equivalent timescale of motion of nanospheres and polymer chains. The elastic properties of nanocomposites with fullerene buckyballs are significantly enhanced upon the reduction of fullerene size.

Micromechanical models have been widely used to predict the mechanical properties of conventional polymer composites. Recently, these models (e.g., Mori–Tanaka, Halpin–Tsai, Cox, and Guth) have been revised and extended to predict the mechanical properties of polymer nanocomposites containing nanotubes, nanoclay, or other nanoparticles. For example, Lee and Paul [18] combined the Eshelby's equivalent tensor with the Mori–Tanaka model and predicted the mechanical properties of composites containing ellipsoids. The model predicted that the longitudinal Young's modulus increases with the primary and secondary aspect ratios, whereas the transverse Young's modulus and shear modulus decrease as the secondary aspect ratio increases. Luo and Daniel [19] applied the Mori–Tanaka model to predict the modulus of polymer nanocomposites containing either intercalated or partially exfoliated clay platelets. It was found that (i) a higher degree of clay platelet dispersion leads to a higher modulus; (ii) a large intercalation basal spacing is preferred, but its effect on the modulus is marginal unless it is accompanied by a high cluster aspect ratio; and (iii) the exfoliation ratio and aspect ratio of clay platelet have a distinct effect on the stiffness enhancement.

Continuum mechanics, in particular, FEM, has also been widely used to predict the mechanical properties of polymer nanocomposites. In most cases, FEM is integrated with other methods such as micromechanical model, constitutive model, or MD simulation. Comparison has been made with the predictive capability of micromechanical models and FEM. For example, Hbaieb *et al.* [20] assessed the accuracy of the Mori–Tanaka model against FEM in predicting the stiffness of clay–polymer nanocomposites. They found that two-dimensional FEM models do not predict an accurate elastic modulus as that of three-dimensional FEM models. The Mori–Tanaka model accurately predicts the stiffness of intercalated clay–polymer nanocomposites with clay volume fraction up to about 5%, but underestimates the stiffness at higher volume fractions and overestimates the stiffness of exfoliated clay–polymer nanocomposites. Odegard *et al.* [21] applied both equivalent continuum model and self-similar approach to predict the elastic properties of single-walled nanotube polymer composites. The predicted Young's moduli are consistent for a single-walled nanotube polymer composite. Recently, we have used such equivalent continuum approach to determine the effective particle size of clay platelets in polymer nanocomposites and their effective mechanical properties (Figure 3.3). This information will be used to predict the mechanical properties of the overall polymer nanocomposites.

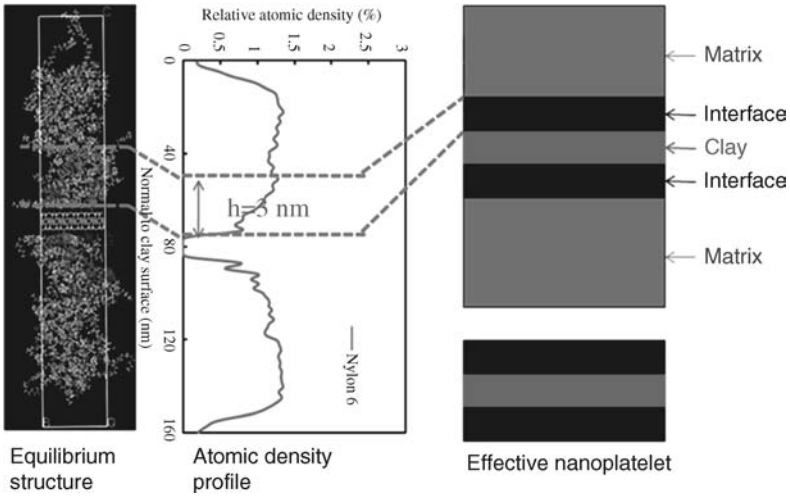

Figure 3.3 Effective size of clay nanoplatelet determined by molecular simulation.

3.4.2
Stress Transfer

The mechanism and magnitude of load transfer between polymer matrix and nanoparticles remain unclear and research in this area is still in the preliminary stage. Recently, some theoretical efforts have been made to predict stress–load transfer across the nanoparticle–polymer interface using molecular modeling, combined molecular mechanics and continuum models (e.g., FEM and shear lag), and micromechanical models. It is predicted that (i) the load transfer of nanotube–polymer composites can be effectively enhanced by deliberately adding chemical cross-linking; (ii) the interfacial shear stress is about one order of magnitude higher than that of the microfiber-reinforced composites; (iii) the surface tension and the intertube corrugation contribute to load transfer in the parallel bundle, and the twisting of nanotubes in the bundle significantly enhances the load transfer; and (iv) the interfacial shear strength between the nanotube and epoxy resin is up to 75 MPa. Results from a shear lag model show that the well-dispersed clay platelets can significantly enhance load transfer efficiency, whereas clay tactoids (i.e., stacks or clusters of clay platelets) lead to much lower enhancement of load transfer. Using micromechanical models, Sheng *et al.* [22] predicted that particle interaction has negative effects on load transfer: High aspect ratio shields the matrix from straining and thus reduces the efficiency of load transfer to neighboring particles.

3.4.3
Mechanical Reinforcement

The molecular origins of mechanical reinforcement of polymer nanocomposites have been studied by various analytical and numerical methods, which led to two different opinions: one attributes exclusively the reinforcement to nanoparticle

aggregation or clustering, while the other attributes it to the formation of the interphase between nanoparticle and bulk polymer. MD study on amorphous polymers filled with solid nanoparticles shows that the mechanical reinforcement results from either the particle agglomeration or a polymer-based network. Their relative contribution depends strongly on the particle–polymer interaction energy, the particle volume fraction, and the state of particle dispersion.

Micromechanical and continuum models can provide a rapid assessment of the reinforcement of nanoparticles and the effects of various parameters. Composite theory study suggests that the superior reinforcement in exfoliated nylon 6 nanocomposites is attributed to the high modulus and high aspect ratio of clay platelets and their ability to reinforce in two directions. In the single-walled carbon nanotube–epoxy composites, the mechanical reinforcement is closely correlated with the covalent nanotube–polymer bonding, matrix crystallinity, tensile properties of reinforcement and matrix, and bundle curvature and alignment. Study from lattice spring model shows that polymers filled with platelets experience the most significant increase in reinforcement efficiency, while those with spheres have the lowest reinforcement efficiency. In nanoparticle diblock copolymer composites, study from the coupling CHC–BD–LSM models indicates that the confinement of nanoparticles within a given domain of a bicontinuous diblock mesophase causes the nanoparticles to percolate and form essentially a rigid backbone throughout the material.

3.4.4
Interfacial Bonding

The strength of interfacial bonding will determine the formation and nature of nanoparticle–polymer interface, stress transfer, and reinforcement. Thus, quantifying the interfacial interactions and strength will provide further understanding of the issues already discussed. The interfacial bonding is mainly studied by using MD simulation. In nanotube–polymer composites, it is found that polymer conformation, nanotube chirality, and diameter play a very important role in determining the interfacial strength. In clay–polymer nanocomposites, polymer grafting and clay surface modification are critical in tuning the interaction energies. It is found that interaction energy is more negative for the functionalized polypropylenes than for the pure polypropylene, which indicates an improved interaction between the polymer and the inorganic surface in the presence of functional groups (i.e., maleic anhydride).

3.5
Mechanical Failure

3.5.1
Buckling

Buckling is a structural instability failure mode and a major concern for structural design. Some theoretical and numerical efforts have been made to predict the

buckling in polymer nanocomposites. Guz [23] proposed a compressive failure theory for laminated and fibrous polymer nanocomposites with different microstructures. Their study shows that the helical (torsional) buckling modes occur in a single CNT but not in nanocomposites. Another MD study [24] shows that the interwall shear coupling has a strong influence on load transfer and compressive load-carrying capacity of multiwall carbon nanotubes. Moreover, the multiwall carbon nanotubes can be engineered through the control of interwall coupling to increase the load transfer, buckling strength, and energy dissipation by nanotube pullout for good performance of nanocomposites.

3.5.2 Fatigue

Fatigue is one of the primary reasons for failure in structural materials. Nanoparticles are believed to improve the fatigue behavior without sacrificing stiffness of polymer composites. The mechanisms for the enhanced fatigue resistance may include crack pinning, crack tip deflection, and particle debonding. Reference [25] shows that the addition of carbon nanotubes results in an order of magnitude reduction in fatigue crack propagation rate for epoxy systems. In addition, the fatigue crack growth rates can be significantly reduced by reducing the nanotube diameter and length and improving their dispersion. Such reduction can be explained by a fracture mechanics model based on crack bridging and pullout of the nanotubes.

3.5.3 Fracture

The fracture mechanisms of polymer nanocomposites have not been systematically investigated. Boo *et al.* [26] have reviewed the research efforts on the fracture behavior of polymer nanocomposites, including the various toughening and fracture mechanisms and the effects of nanoparticle aspect ratio and dispersion. The interfacial interactions and the difference of relaxation time between clay and polymer chains have significant influences on the fracture strength of polymers. The failure strength of carbon nanotube systems under biaxial tensile–torsional loads is significantly different from what occurs under uniaxial tensile loading. In Al–Si nanocomposites, the failure occurs by void damage accumulation, culminating in crack formation, which is different from the failure of crack initiation at triple junctions and grain boundaries in single-phase all-Al polycrystals.

3.5.4 Wear

Wear is the erosion of material from a solid surface induced by the action of repeated rubbing. Many wear mechanisms have been proposed such as abrasion, adhesion, surface fatigue, corrosion, erosion, and delamination. Friedrich and Schlarb [27]

have given a full description of polymer nanocomposites and coatings as well as their tribological behavior (e.g., friction, wear, scratch, and lubrication) and potential tribological applications. Mai and coworkers [28] gave a comprehensive review on the recent progress in understanding wear and scratch damage in polymer nanocomposites containing different nanoparticles (e.g., TiO_2, Si_3N_4, ZnO, carbon nanotube, and nanoclay). They concluded that nanoparticles do not always improve the wear–scratch properties and that material properties (e.g., modulus, hardness, fracture toughness, extent of wear rate, and scratch penetration depth) are not the sole indicators to assess the candidate materials.

3.5.5
Creep

Creep is a time-dependent plastic deformation (i.e., strain increase) caused by the action of a constant applied load. Many studies showed that the addition of nanoparticles to neat polymers can significantly improve the creep resistance of the polymers. However, a few studies have been reported on the prediction of creep behavior of nanoparticle–polymer composites. Yang *et al.* [29] investigated the tensile creep resistance of polyamide 66 nanocomposites reinforced with either TiO_2 or clay nanoparticles by using the constitutive Burgers creep model and the empirical Findley power law. Ohji [30] reported the delayed fracture behavior (i.e., the creep and creep rupture behavior) under tensile loading at elevated temperatures for three engineering ceramics. The results show that the dispersion of silicon carbide nanoparticles into an alumina matrix improves dramatically creep resistance as compared with that of alumina with an equivalent grain size, which is attributed to the impeded grain boundary sliding induced by intergranular silicon carbide nanoparticles.

3.6
Thermal Properties

3.6.1
Thermal Conductivity

In conventional composites, the models of thermal conduction are based on the Fourier heat conduction theory. However, these models are not valid at the nanoscale due to the ballistic phonon transport and interfacial scattering. Chen *et al.* [31] have reviewed the status and progress of theoretical and experimental studies of thermal transport phenomena in nanostructures. We discuss here some theoretical and numerical efforts toward the prediction of thermal conductivity of nanoparticle–polymer nanocomposites.

One significant progress is the use of phonon Boltzmann equation and MC simulation to study the thermal conductivity of nanocomposites with different nanoparticles (e.g., nanowires and nanoparticles). The effects of various factors have

been examined, including the nature of nanoparticles (e.g., shape and size), volume fraction, thermal conductivity ratio, and the spatial arrangement of nanoparticles (e.g., regularly aligned and randomly dispersed). The nanocomposites consisting of silicon (solid nanowires, tubular nanowires, or nanoparticles) and germanium (e.g., nanowires, nanoparticles, or continuous matrix) have received particular interest because of their potential for thermoelectric materials.

MD simulation and analytical thermal modeling have also been used to predict the interfacial thermal transport between carbon nanotubes. The interfacial thermal resistance is found to reduce by four orders of magnitude as the nanotubes are brought into intimate contact. Clancy and Gates [32] presented a multiscale modeling approach in which MD simulation is used to calculate the interfacial thermal resistance values of nanotube–polymer composites. Then, these values are used in an analytical model to predict the bulk thermal conductivity of the composites. They found that the interfacial thermal resistance values are strongly influenced by the grafting density and chain length of linear hydrocarbon chains covalently bonded to the nanotube surface. The thermal conductivity depends strongly on nanotube length, volume fraction, thermal conductivity, and interfacial thermal resistance.

Effective medium theory (EMT) is commonly used to describe the microstructure–property relationships in heterogeneous materials and predict the effective physical properties. It has recently been revised to predict the thermal conduction of nanocomposites. For nanocomposites with nanoparticles on the order of or smaller than the phonon mean free path, the interface density of nanoparticles is a primary factor in determining the thermal conductivity. In graphite nanosheet polymer composites, the interfacial thermal resistance still plays a role in the overall thermal transport. However, the thermal conductivity depends strongly on the aspect ratio and on the orientation of graphite nanosheets.

3.6.2 Thermal Expansion

In nanoparticle–polymer composites, thermal stability is one of the most important property enhancements. Recently, some theoretical efforts have been made to predict the thermal stability of such composites. For example, FEM and the theory of Chow have been used to predict the thermal expansion of clay–polymer nanocomposites. The results indicate that it is possible to considerably reduce and eventually match the thermal expansion of metal and polymer parts by dispersing a small amount of exfoliated muscovite mica platelets into a polymer matrix. Moreover, reduction is controlled by the product of aspect ratio and volume fraction of the platelets.

Lee *et al.* [33] predicted the coefficient of thermal expansion of composites with aligned isotropic fiber- and disk-like fillers and its dependence on the aspect ratio of fillers. They found that the longitudinal coefficients of thermal expansion decrease and approach that of fillers. However, the transverse coefficients may increase or decrease with the aspect ratios. They also developed a new model, based on

Eshelby's method, to predict the coefficients of thermal expansion of composites containing either aligned axisymmetric or nonaxisymmetric ellipsoidal particles. For composites consisting of axisymmetric particles (e.g., spheres, fibers, and disks) and epoxy resin, they predicted that (i) the coefficients of thermal expansion for spherical inclusions are the same in all directions and decrease modestly as the volume fraction of particles increases and (ii) with the increase in aspect ratio, the thermal expansion becomes anisotropic. For composites consisting of three-dimensional nonaxisymmetric ellipsoidal particles (i.e., clay platelets) and nylon 6, they predicted that (i) the coefficient of thermal expansion in the longitudinal direction decreases as the primary and secondary aspect ratios increase and (ii) the value in the transverse direction decreases as the primary aspect ratio increases but decrease with the secondary aspect ratio.

3.7 Barrier Properties

The barrier property refers to the physical resistance of a polymer material to the passage of any molecule or compound through the material. Polymer nanocomposites, particularly those reinforced with exfoliated clay platelets, have demonstrated significantly improved barrier properties to oxygen, moisture, carbon dioxide, nitrogen, and liquid water, which makes them the ideal materials for regular food packing and coating applications, special gases and liquid storage, and fuel cell applications. Although Darcy's law can successfully describe the permeability of gas–liquid molecules through a homogeneous medium, it could not explain the superior barrier properties observed in such polymer nanocomposites.

So far, most fundamental studies on the barrier properties of polymer nanocomposites are based on the tortuous pathway concept. This concept was initially developed by Nielsen [34] to predict the barrier properties of polymer composites containing oriented and regularly arrayed fillers. This has been widely accepted and fits well with some experimental observations. Recently, some new models have been developed to account for the effects of aspect ratio, orientation, volume fraction of nanoparticles, nanoparticle–matrix interaction, and polymer structure on the barrier properties of polymer nanocomposites. These include Cussler model, Fredrickson–Bicerano model, Gusev–Lusti model, multipole-accelerated BEM, Bharadwaj model, renormalization group model, and geometric model. It should be noted that Nielsen model and Cussler model are actually 2D models, but can be viewed as 3D models if the fillers are considered to be ribbons with infinite length. The Gusev–Lusti model and the Fredrickson–Bicerano model are 3D models in which the disks are assumed to be perfectly parallel to the membrane surface, that is, normal to the penetrant flow direction. The Bharadwaj model is developed based on the 2D Nielsen model, although it can be viewed as a 3D model.

Xu *et al.* [35] used the relative permeability theory in combination with the tortuous pathway model to examine the barrier properties of polymer nanocomposites containing impermeable and oriented clay layers. It was found that

intercalated and/or partially exfoliated structures can effectively enhance the barrier properties of the materials. Liu and De Kee [36] modeled the non-Fickian diffusion process of a simple fluid through a complex polymer–clay nanocomposite membrane that describes well the diffusion process quantitatively. Sridhar *et al.* [37] developed a model based on the resistance-in-series and resistance-in-parallel approaches to predict the diffusivities of nanoflake-filled polymer nanocomposites and correlated the diffusivity reduction with the filler loading level and filler geometry.

MC simulation has been used to predict the diffusion of gas molecules across membranes containing impermeable flakes or oriented platelets and to evaluate the Aris model. It is found that Airs model can correlate well with a 2D MC simulation, but overestimate the barrier effect of platelets by 50% to the 3D MC simulation. Goodyer and Bunge [38] used a 3D FEM to examine the steady-state permeation through membranes filled with impermeable ribbon- and square-shaped flakes and evaluated the geometry-based equations. For 2D flakes, the BEM results agree well with their FEM results, while the MC results are generally about two thirds of the FEM results. For regularly arranged 3D square flakes, the FEM results are compared only with the available MC results, which differed by a factor of 2 or 3.

3.8 Rheological Properties

The addition of fillers into polymer matrix can alter the rheological properties of the polymer and its processing performance. The rheological properties are affected by the nature of nanoparticles and polymer (e.g., molecular weight and polarity) and nanoparticle–polymer interactions. Meanwhile, the applications of polymer nanocomposites depend on their viscoelastic properties that determine their processibility and mechanical integrity. Although some theoretical work has recently been done, our understanding of the viscoelastic properties of polymer nanocomposites and the influence of nanoparticle–polymer interactions is quite immature.

DPD simulation has been applied to predict the rheological and viscoelastic behaviors of nanoparticle–polymer nanocomposites and to examine the effects of particle shape, particle–particle interaction, and particle dispersion states of such behaviors. It was found that particle–particle interaction has a distinct effect on the dynamic shear modulus. Havet and Isayev [39,40] proposed a rheological model to predict the dependence of dynamic properties of highly interactive filler–polymer mixtures on strain and the dependence of shear stress on shear rate.

MD simulation can gain insight into the viscoelastic behavior of nanoparticle–polymer composites. The shear stress relaxation modulus can be calculated using the time autocorrelation function of the stress tensor, while the viscosity is calculated based on the Einstein relations. Compared to conventional composites, the viscoelastic properties are strongly perturbed by the nanoparticles and depend upon the nature of nanoparticle–polymer interactions. The viscosity and dynamic shear modulus can be dramatically increased for composites with attractive

nanoparticle–polymer interactions, less dramatically increased with neutral interactions, and reduced with repulsive interactions.

Sarvestani and Picu [41] used a theoretical network model to investigate the viscoelastic behavior of polymer nanocomposites. Their results demonstrated that the overall material viscoelasticity can be controlled by the lifetime of filler–polymer junctions. Besides, the model exhibited the transition to rubber-like behavior at low frequencies, constant viscosity at low strain rates, and shear thinning response in fast flows. Pyrz [42] proposed a new atomic strain concept that allows calculation of the continuum quantities directly within a discrete molecular system. The obtained atomic strain tensor is applied to investigate interfacial stress distribution of nanotube–polymer nanocomposites. Wang *et al.* [43] developed a nanostructurally based model for carbon nanofiber–polystyrene composites. When applied to shear flows, the model can predict the steady-state viscosities and normal stress differences of the composites as a function of shear rate, polymer matrix properties, fiber length, and mass concentration. Chabert *et al.* [44] proposed a combined self-consistent scheme and discrete model to predict the viscoelasticity of nanocomposites and examined the effect of nanoparticle loading and nanoparticle–nanoparticle interaction. They found that the interaction becomes important for reinforcement above the percolation threshold. Liu and Brinson [45] developed a hybrid numerical–analytical modeling method to predict the viscoelastic response of polymer nanocomposites with nanotubes and nanoplatelets, respectively. The predicted pattern is in agreement with the experimental observation. However, quantitative comparison between the prediction and experimental results is not possible due to the uncertain properties and the limitation of 2D description in the model.

3.9 Conclusions

The development of polymer nanocomposites needs a comprehensive understanding of the phenomena and an accurate prediction of the material properties and behaviors at different time- and length scales. In the past, this need has significantly stimulated the theoretical and simulation efforts in nanoparticle–polymer nanocomposites. In this connection, many analytical and numerical techniques are employed to predict nanocomposite properties.

The analytical and numerical methods developed thus far have different strengths and weaknesses, depending on the need of research. Molecular modeling has been applied to investigate the molecular interactions and structures on the nanoscale (e.g., 0.1–10 nm), which is very useful in understanding the interaction strength at nanoparticle–polymer interfaces and the molecular origin of mechanical improvement. However, it is computationally very demanding and cannot be applied to predict mesoscopic structure and properties defined on the microscale (e.g., 0.1–10 μm) such as the dispersion of nanoparticles in polymer matrix and the morphology of polymer nanocomposites. To explore the morphology on these scales, mesoscopic simulations are more effective. On the other hand, the macroscopic

properties of materials can often be estimated by using meso- or macroscale techniques. However, they may have limitations when applied to polymer nanocomposites because of the difficulty to deal with the interfacial interaction between nanoparticle and polymer and the nature of the interface, which are crucial to the accurate prediction of nanocomposite properties.

There are still a number of challenges and a long way to go toward the prediction of nanocomposite properties. One challenge comes from the complicated multiscale morphology and dynamics. The second challenge comes from the polydispersion of nanoparticles in polymer matrix as a result of the unique nature of nanoparticles and the uncertainty of surface defects. Therefore, it is essential to develop new and improved analytical and numerical techniques, in particular the integration of methods at different time- and length scales and the formulation of an efficient multiscale method. Developing such a multiscale method is very challenging, but indeed represents the future of our theoretical efforts not only in polymer nanocomposites but also in other fields. New concepts, theories, and computational tools should be developed in the future to make truly seamless multiscale modeling a reality. Such development is crucial in order to achieve the long-standing goal of designing nanocomposites with predictable properties.

Acknowledgment

The authors would like to thank Australian Research Council (ARC) for the financial support.

References

1 Zeng, Q.H. *et al.* (2005) Clay-based polymer nanocomposites: research and commercial development. *Journal of Nanoscience and Nanotechnology*, **5** (10), 1574–1592.

2 Zeng, Q.H., Yu, A.B., and Lu, G.Q. (2008) Multiscale modeling and simulation of polymer nanocomposites. *Progress in Polymer Science*, **33** (2), 191–269.

3 Balazs, A.C., Singh, C., and Zhulina, E. (1998) Modeling the interactions between polymers and clay surfaces through self-consistent field theory. *Macromolecules*, **31** (23), 8370–8381.

4 Zhulina, E., Singh, C., and Balazs, A.C. (1999) Attraction between surfaces in a polymer melt containing telechelic chains: guidelines for controlling the surface separation in intercalated polymer–clay composites. *Langmuir*, **15** (11), 3935–3943.

5 Smith, J.S., Bedrov, D., and Smith, G.D. (2003) A molecular dynamics simulation study of nanoparticle interactions in a model polymer–nanoparticle composite. *Composites Science and Technology*, **63** (11), 1599–1605.

6 Lee, J.Y., Baljon, A.R.C., and Loring, R.F. (1999) Spontaneous swelling of layered nanostructures by a polymer melt. *Journal of Chemical Physics*, **111** (21), 9754–9760.

7 Ginzburg, V.V. *et al.* (1999) Kinetic model of phase separation in binary mixtures with hard mobile impurities. *Physical Review E*, **60** (4), 4352–4359.

8 Balazs, A.C. *et al.* (2000) Multi-scale model for binary mixtures containing nanoscopic particles. *Journal of Physical Chemistry B*, **104** (15), 3411–3422.

9 Lyatskaya, Y. and Balazs, A.C. (1998) Modeling the phase behavior of polymer–

clay composites. *Macromolecules*, **31** (19), 6676–6680.
10 Ginzburg, V.V. and Balazs, A.C. (1999) Calculating phase diagrams of polymer–platelet mixtures using density functional theory: implications for polymer/clay composites. *Macromolecules*, **32**, 5681–5688.
11 Ginzburg, V.V., Singh, C., and Balazs, A.C. (2000) Theoretical phase diagrams of polymer/clay composites: the role of grafted organic modifiers. *Macromolecules*, **33** (3), 1089–1099.
12 Ginzburg, V.V. and Balazs, A.C. (2000) Calculating phase diagrams for nanocomposites: the effect of adding end-functionalized chains to polymer/clay mixtures. *Advanced Materials*, **12** (23), 1805–1809.
13 Maiti, A., Wescott, J., and Kung, P. (2005) Nanotube–polymer composites: insights from Flory–Huggins theory and mesoscale simulations. *Molecular Simulation*, **31** (2–3), 143–149.
14 Ginzburg, V.V. *et al.* (2000) Modeling the dynamic behavior of diblock copolymer/particle composites. *Macromolecules*, **33** (16), 6140–6147.
15 Huh, J., Ginzburg, V.V., and Balazs, A.C. (2000) Thermodynamic behavior of particle/diblock copolymer mixtures: simulation and theory. *Macromolecules*, **33** (21), 8085–8096.
16 Thompson, R.B. *et al.* (2002) Block copolymer-directed assembly of nanoparticles: forming mesoscopically ordered hybrid materials. *Macromolecules*, **35** (3), 1060–1071.
17 Lee, J.Y. *et al.* (2002) Entropically driven formation of hierarchically ordered nanocomposites. *Physical Review Letters*, **89** (15), 155503.
18 Lee, K.Y. and Paul, D.R. (2005) A model for composites containing three-dimensional ellipsoidal inclusions. *Polymer*, **46** (21), 9064–9080.
19 Luo, J.J. and Daniel, I.M. (2003) Characterization and modeling of mechanical behavior of polymer/clay nanocomposites. *Composites Science and Technology*, **63** (11), 1607–1616.
20 Hbaieb, K. *et al.* (2007) Modelling stiffness of polymer/clay nanocomposites. *Polymer*, **48** (3), 901–909.
21 Odegard, G.M., Pipes, R.B., and Hubert, P. (2004) Comparison of two models of SWCN polymer composites. *Composites Science and Technology*, **64** (7–8), 1011–1020.
22 Sheng, N. *et al.* (2004) Multiscale micromechanical modeling of polymer/clay nanocomposites and the effective clay particle. *Polymer*, **45** (2), 487–506.
23 Guz, A.N. (2006) Three-dimensional theory of stability of a carbon nanotube in a matrix. *International Applied Mechanics*, **42** (1), 19–31.
24 Xia, Z.H., Guduru, P.R., and Curtin, W.A. (2007) Enhancing mechanical properties of multiwall carbon nanotubes via sp^3 interwall bridging. *Physical Review Letters*, **98** (24), 245501.
25 Zhang, W., Picu, R.C., and Koratkar, N. (2007) Suppression of fatigue crack growth in carbon nanotube composites. *Applied Physics Letters*, **91** (19), 193109
26 Boo, W.J., Liu, J., and Sue, H.J. (2006) Fracture behaviour of nanoplatelet reinforced polymer nanocomposites. *Materials Science and Technology*, **22** (7), 829–834.
27 Friedrich, K. and Schlarb, A.K. (2008) *Tribology of Polymeric Nanocomposites: Friction and Wear of Bulk Materials and Coatings*, Tribology and Interface Engineering Series, vol. 55, 1st edn, Elsevier, Oxford, xvi and 551 pp.
28 Dasari, A., Yu, Z.-Z., and Mai, Y.-W. (2009) Fundamental aspects and recent progress on wear/scratch damage in polymer nanocomposites. *Materials Science and Engineering: R: Reports*, **63** (2), 31–80.
29 Yang, J.L. *et al.* (2006) On the characterization of tensile creep resistance of polyamide 66 nanocomposites. Part II: modeling and prediction of long-term performance. *Polymer*, **47** (19), 6745–6758.
30 Ohji, T. (2003) Delayed fracture behavior of ceramics under tensile loading at elevated temperatures. *Journal of the Ceramic Society of Japan*, **111** (11), 793–799.
31 Chen, G., Borca-Tasciuc, D.A., and Yang, R. (2004) Nanoscale heat transfer, in *Encyclopedia of Nanoscience and Nanotechnology* (ed. H.S. Nalwa), American Scientific Publishers, pp. 429–459.

32 Clancy, T.C. and Gates, T.S. (2006) Modeling of interfacial modification effects on thermal conductivity of carbon nanotube composites. *Polymer*, **47** (16), 5990–5996.

33 Lee, K.Y. *et al.* (2007) Study on the coefficient of thermal expansion for composites containing 2-dimensional ellipsoidal inclusions. *Polymer (Korea)*, **31** (2), 160–167.

34 Nielsen, L.E. (1967) Models for the permeability of filled polymer systems. *Journal of Macromolecular Science Part A: Pure and Applied Chemistry*, **1** (5), 929–942.

35 Xu, B. *et al.* (2006) Calculating barrier properties of polymer/clay nanocomposites: effects of clay layers. *Polymer*, **47** (8), 2904–2910.

36 Liu, Q. and De Kee, D. (2005) Modeling of diffusion through nanocomposite membranes. *Journal of Non-Newtonian Fluid Mechanics*, **131** (1–3), 32–43.

37 Sridhar, L.N., Gupta, R.K., and Bhardwaj, M. (2006) Barrier properties of polymer nanocomposites. *Industrial & Engineering Chemistry Research*, **45** (25), 8282–8289.

38 Goodyer, C.E. and Bunge, A.L. (2009) Comparison of numerical simulations of barrier membranes with impermeable flakes. *Journal of Membrane Science*, **329** (1–2), 209–218.

39 Havet, G. and Isayev, A.I. (2001) A thermodynamic approach to the rheology of highly interactive filler–polymer mixtures. Part I: theory. *Rheologica Acta*, **40** (6), 570–581.

40 Havet, G. and Isayev, A.I. (2003) A thermodynamic approach to the rheology of highly interactive filler–polymer mixtures. Part II: comparison with polystyrene/nanosilica mixtures. *Rheologica Acta*, **42** (1–2), 47–55.

41 Sarvestani, A.S. and Picu, C.R. (2004) Network model for the viscoelastic behavior of polymer nanocomposites. *Polymer*, **45** (22), 7779–7790.

42 Pyrz, R. (2006) Atomistic/continuum transition: the concept of atomic strain tensor, in *Fracture of Materials: Moving Forwards* (eds H.Y. Liu, X.Z. Hu, and M. Hoffman), Trans Tech Publications, Switzerland, pp. 193–198.

43 Wang, Y.R. *et al.* (2006) Melt shear rheology of carbon nanofiber/polystyrene composites. *Rheologica Acta*, **45** (6), 919–941.

44 Chabert, E. *et al.* (2004) Prediction of the elastic response of polymer based nanocomposites: a mean field approach and a discrete simulation. *Composites Science and Technology*, **64** (2), 309–316.

45 Liu, H. and Brinson, L.C. (2006) A hybrid numerical–analytical method for modeling the viscoelastic properties of polymer nanocomposites. *Journal of Applied Mechanics*, **73** (5), 758–768.

4
Characterization of Nanocomposites by Scattering Methods

Valerio Causin

4.1
Introduction

Polymer-based nanocomposites stem from the formidable intuition that if the size of fillers were decreased in the nanometer range, then a dramatic increase in interfacial area, with a concurrent attainment of novel and better properties, could be achieved with very low filler content. Owing to their economic viability, polymer-layered silica nanocomposites (PLSNs) are the most promising polymer-based nanocomposite materials, and they are rapidly transitioning from academic research to industrial development. A number of other nanosized particles were proposed as possible nanofillers, such as silica nanoparticles, polyhedral oligomeric silsesquioxane (POSS), carbon nanotubes, carbon nanofibers, graphite, and graphene. Although in some cases this resulted in commercial applications, a number of open issues still exist, especially, in the opinion of the author, in the field of their characterization. The improvement of properties of the nanocomposites due to nanofillers is derived from a subtle interplay between the reinforcing action that the nanoparticles exert *per se* and the influence of the filler on the semicrystalline framework and on the structure and morphology of the polymer matrix. In other words, attention should be paid not only to the dispersion of the filler in the matrix but also to the extent of modification of the polymer due to the presence of the filler. This calls for characterization procedures that help in optimizing the picture of filler dispersion and that can shed light on the hierarchical features of the morphology of the polymer matrix, from the scale of crystalline cells up to the domain of spherulites. Scattering studies can be extremely useful in achieving this. Neutron scattering, in general, is sensitive to fluctuations in the density of nuclei in the sample. X-ray scattering is sensitive to inhomogeneities in electron densities, whereas light scattering is sensitive to fluctuations in polarizability. By changing the characteristics of the light/particle beam, different scale lengths and morphological features can be probed and a complete picture of the morphology of the material can be obtained.

An interesting advantage of scattering methods is that, in contrast to microscopy techniques, they sample the whole bulk of the specimen, thus giving a more

Polymer Composites: Volume 2, First Edition. Edited by Sabu Thomas, Kuruvilla Joseph, Sant Kumar Malhotra, Koichi Goda, and Meyyarappallil Sadasivan Sreekala.

generalized picture of its morphology. Being able to exploit this peculiarity at its full extent offers an invaluable tool for a complete characterization of polymer-based nanocomposite materials. Microscopy has the advantage that data are acquired in direct (real) space, whereas scattering methods (such as small-angle neutron scattering, SANS) measure in reciprocal space, and are thus much more demanding in terms of data interpretation. When all these methods are used complementarily, a rich amount of information can be obtained, and a really complete picture of the several levels of morphological organization in nanocomposite systems can be drawn.

4.2
X-Ray Diffraction and Scattering

4.2.1
Wide-Angle X-Ray Diffraction

X-rays are the light source that found more extensive application in scattering techniques in the polymer science field.

When X-rays propagate in space, they are accompanied by a periodically changing electric field. If X-rays impinge on a sample, the electrons of the atoms that constitute that sample will be excited to periodic vibrations by this changing field, and will become themselves sources of electromagnetic waves of the same frequency and wavelength. New spherical waves are originated then from the electrons of the atoms, which are said to scatter the original beam. The scattered X-ray waves from the atoms can interfere constructively or destructively along certain directions of space, provided that certain geometrical conditions are met. Diffraction is observed when the scattered waves, along a certain direction, have a difference in phase equal to an integer number of wavelengths. When this condition does not hold, destructive interference occurs, and scattered radiation is canceled along that direction. Liquids or glasses, that is, amorphous materials, produce diffuse X-ray patterns, whereas when a crystalline order exists in the sample, sharp and neat signals appear because of diffraction.

A crystal is a regular arrangement of atoms, produced by the periodic repetition of a unit cell, which can also be considered as a family of planes composed of the atoms of the lattice, defined by three integer numbers (the Miller indices, *hkl*). Incident X-ray waves are assumed to be reflected by these planes, if the Bragg condition is met:

$$n\lambda = 2d_{hkl}\sin\theta. \tag{4.1}$$

The *hkl* family of planes, equally spaced by a d_{hkl} distance, impinged by an incident beam of wavelength λ, will give a diffraction signal of order n only at a precise angular value θ given by Bragg law. Along the other directions, destructive interference will occur and no reflections will be observed.

In wide-angle X-ray diffraction (WAXD), diffracted intensities at angles wider than about 2° 2θ are detected, allowing to study features of characteristic size of

about 30–40 Å or less. In other words, WAXD is useful to study the dispersion of layered fillers and the crystalline cell of semicrystalline polymers or of crystalline fillers.

4.2.2
Wide-Angle X-Ray Diffraction in the Characterization of Polymer-Based Nanocomposites

The most extensive use of WAXD in the field of nanocomposites was done with clay–polymer nanocomposites. Such fillers are composed of inorganic layers stacked one above another. The layers are characterized by a high aspect ratio since they have thicknesses of about 1 nm and diameters ranging from 30 to over 500 nm. Weak van der Waals forces keep together hundreds or thousands of these layers, stacked in structures called tactoids. The performance of clay-based nanocomposites is strongly dependent on the breaking-up of clay particles in the polymer matrix. In general, authors consider three possible systems, which occur as a function of the degree of interaction between the polymer and the filler:

- Clay sheets may remain stacked in tactoids, as in the original mineral. In some cases, clay layers can also collapse, with a sort of "reverse intercalation" [1,2]. Gatos *et al*. proposed a terminology in which "confinement" covers the collapse of layers up to the pristine basal spacing of the organoclay[1)] in the nanocomposite and deintercalation, on the other hand, is the further collapse due to extraction of the initial intercalant [3].
- When polymer chains penetrate into interlayer spacing, an intercalated system is obtained, where clay layers are more separated than in the pristine mineral.
- An exfoliated structure appears when the single clay sheets are delaminated and dispersed in the matrix. Some authors proposed to consider exfoliated also those systems where the layers are intercalated but with a large interlayer of more than 5–10 nm [4–7].

The exfoliated system is almost always quoted as the most desirable, since nanometric dispersion of clay platelets maximizes the interfacial region between the filler and the polymer matrix, thus allowing to exploit the excellent mechanical properties of the individual clay layers. Moreover, when exfoliation is attained, the number of reinforcing components is dramatically increased, since each clay particle contains a very large number of clay sheets. To further complicate matters, often a mixed dispersion is observed for clay with different populations of tactoids or with partial exfoliation of single layers. Transmission electron microscopy (TEM) and WAXD are by far the most employed characterization techniques that assess the morphology of PLSN.

1) To favor the interaction between the polymer (usually nonpolar) and the clay layers, which are polar in nature, an organic molecule, often an alkylammonium salt, is intercalated within the clay tactoids to enlarge the distance between the layers and to alleviate the polarity mismatch between the components of the composite.

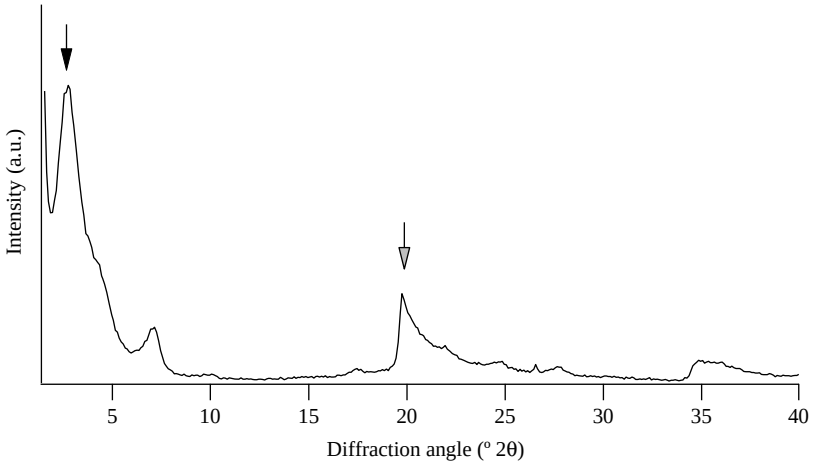

Figure 4.1 Diffraction pattern of an organomodified montmorillonite. The black arrow shows the (001) basal peak, the gray arrow points to a (*hk*0) peak.

The WAXD patterns of clays show two different kinds of signals: symmetrical peaks, usually positioned in the small-angle region of the angular range, and asymmetric reflections, which show a peculiar shape with a very steep side and a gradual decrease on the other side (Figure 4.1). The former are indexed (00*l*) and are defined as basal signals. Their positions are related with the spacing between the silicate platelets, and will hence shift when water, organomodifier, or polymer molecules penetrate between the platelets. On the contrary, the asymmetric reflections, indexed (*hk*0), are due to the internal structure of the platelets and thus remain fixed for a given silicate.

The position of the basal signal (001) of clay in the X-ray diffractogram of a nanocomposite sample is of great help in defining which degree of dispersion of clay layers in the matrix was attained (Figure 4.2). In general, a shift of this reflection toward small angles would be associated to a widening of interlayer space, and thus to intercalation. On the other hand, if the (001) peak shifts to wider angles, it is a sign that the layers are collapsing one onto the other, usually because of the degradation, exchange, or removal of the organomodificant interposed between them.

Although, in principle, WAXD is a powerful and easy technique for defining the dispersion of clay in the matrix, there are issues that should be taken into account when interpreting data.

Table 4.1 shows a collection of spacings of the clay layers, measured by X-ray diffraction, before and after inclusion in a polymer matrix. Owing to the immense literature on the subject, Table 4.1 is intended just as an array of data that may exemplify the various PLSN systems based on different polymer matrices and with different morphologies.

As can be seen, a wide range of interlayer distances has been reported for different systems. It is obvious that the interaction between filler and polymer and the final

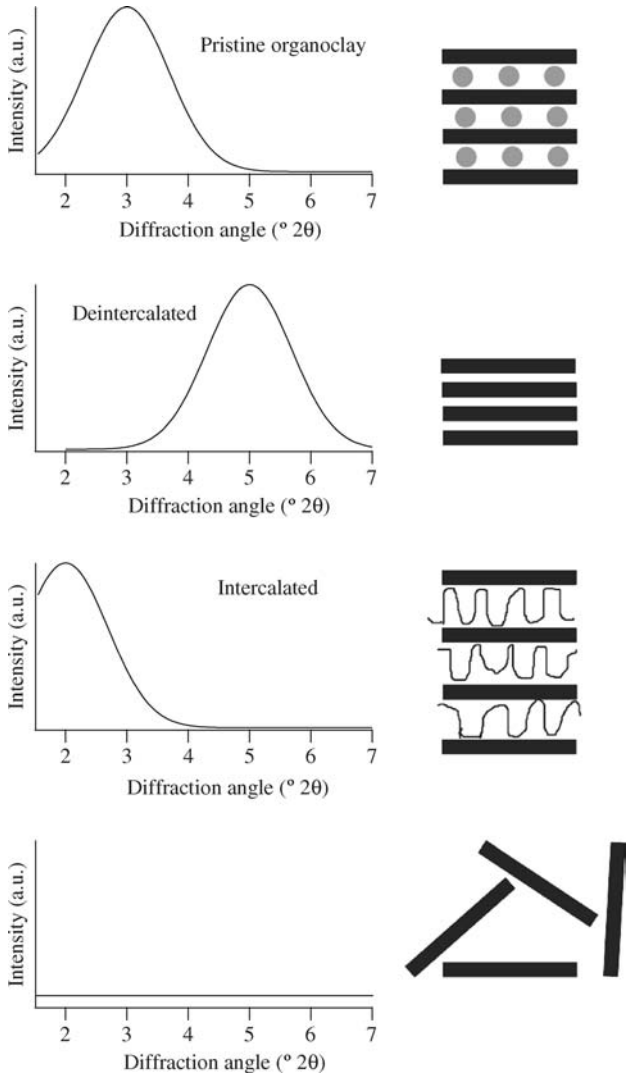

Figure 4.2 Schematic of the WAXD patterns yielded by different filler morphologies.

dispersion of the former in the latter are strongly dependent on the system taken into account and on the processing strategy. What is of interest in this context is that, most often, when an increase in *d*-spacing is observed, it is interpreted as a sign that intercalation has occurred. Quite rarely this conclusion is supported by an assessment of the steric hindrance of polymer chains and by a comparison between the experimental Δd and the one that is expected if polymer chains were inserted between clay layers.

Table 4.1 Characterization data obtained by X-ray diffraction on a variety of different nanocomposite systems.

Matrix	Clay	Pristine *d*-spacing (Å)	Composite *d*-spacing (Å)	Δd (Å)	Interpretation	Reference
PANI	MMT	12.8	13.2/14.1	0.4/1.3	Intercalated	[8]
PEO-PI	Laponite	12.5	18	5.5	Intercalated	[9]
Epoxy	MMT	13/28	>100	>70	Exfoliated	[10]
PP-MA	MMT	14.5	16.0	1.5	Intercalated	[11]
PVDF	Lucentite	17.5	18.4	0.9	Intercalated	[12]
PP	MMT	19	30	11	Intercalated	[13]
PMMA	MMT	18.5	37.1	18.6	Intercalated	[14]
PEO	Laponite	12	18	6	Intercalated	[15]
PA6	MMT	14.2	23.9	9.7	Intercalated	[16]
PET	MMT	28	32.5	4.5	Intercalated	[6]
PU	MMT	12.1	13.9/152	1.8/139.9	Intercalated/ exfoliated	[1]
PHA	MMT	17.7	36–48	18.3–30.3	Intercalated	[17]
Epoxy	MMT	18	35–150	17–132	Intercalated	[18]
PE-MA	MMT	25	28	3	Intercalated	[19]
PDMS	MMT	12.6	15–52.5	2.4–39.9	Intercalated	[20]
PLPVS	MMT	24	33	9.3	Intercalated	[21]
Epoxy	MMT	20.9	35–39	14.1–18.1	Intercalated	[7]
PVDF	MMT	12.1	15.1	3	Intercalated	[22]
PP	MMT	37	48	11	Intercalated	[23]
PEO	MMT	11.5	18	6.5	Intercalated	[24]
PP-MA	MMT	29	34	5	Intercalated	[25]
PLLA	MMT	32	38	6	Intercalated	[26]
PMMA	MMT	35	39	4	Intercalated	[27]
BR	MMT	15.3	40	24.7	Intercalated	[28]
PMMA	MMT	20.9	34.5	13.6	Intercalated	[29]
PTT	MMT	30.6	32	1.4	Nonintercalated	[30]
PTT	MMT	23.4	29.4	6	Intercalated	[30]
PVME	MMT	91	98	7	Nonintercalated	[31]
NR	Rectorite	22	23	1	Nonintercalated	[32]
NBR	MMT	12.5	15	2.5	Nonintercalated	[33]

PANI, polyaniline; MMT, montmorillonite; PEO, poly(ethylene oxide); PI, polyisoprene; PP, polypropylene; MA, maleic anhydride; PVDF, poly(vinylidene fluoride); PA6, nylon 6; PET, poly(ethylene terephthalate); PU, polyurethane; PHA, poly(hydroxyalkanoate); PE, polyethylene; PDMS, poly(dimethylsiloxane); PLPVS, poly(vinylsilsesquioxanes); PLLA, poly(L-lactide); BR, butyl rubber; PTT, poly(trimethylene terephthalate); PVME, poly(vinyl methyl ether); NR, natural rubber; NBR, nitrile rubber.

A number of papers in the literature focused on the study of the conformation of the intercalants within the layers of clays. Theoretical and experimental studies showed that linear monodisperse polymeric chains in the vicinity of flat surfaces tend to orient with their long axes parallel to the surfaces in order to minimize conformational distortions to the chains ([34] and references therein). The height of such an arrangement can be quantified in 4–7 Å [35–41]. On the basis of these data, then, it is reasonable to propose an increase in *d*-spacing of 4 Å as a significant threshold that allows to conclude for intercalation. Smaller expansions in *d*-spacing should be ascribed to a reorganization of the interlayer space or to an alteration of the organomodificant. *d*-Spacings larger than about 7 Å were reported to be coherent with double or triple layers of chains [9,37,42]. In certain conditions, orientation of chains (or chain portions) extended and tilted with respect to the clay layers can be advocated, resulting in a very large increase in *d*-spacing: a C18 chain in an all-*trans* conformation is 2.7 nm long [43,44].

WAXD diffractograms of intercalated or otherwise stacked tactoid structures may show second-order and even third-order reflections, which are associated to very ordered stacking of the intercalated layers [24,26,28,45–48]. On the other hand, the absence of high order (00*l*) peaks in the WAXD patterns of nanocomposites, especially with low amounts of MMT fillers, can be due to different reasons, such as a decrease in the regularity of the stacking layers or a diminution of the size and number of tactoids with highly parallel stacking, and a consequent increase in the proportion of exfoliated silicate layers dispersed in the polymer matrix [27,49].

WAXD can also yield quantitative information on the degree of order and on the dimensions of tactoids. The intensity and breadth of the basal signals are in fact related to the length and order of the repetitive layer structure of clay [17,18,45,50–52]. Among the possible reasons for the decrease in intensity of the basal reflection, there are decrease in the degree of coherent silicate layer stacking and the occurrence of exfoliation and destruction of some intercalated silicates [45]. However, variations in scattering may be due to more complex causes than simply exfoliation and/or orientation, such as polarization, interference effects, and issues linked to sample preparation [53]. In particular, an accurate sample preparation that assures a smooth surface and a control of orientation, concentration, and distribution of particles is fundamental for the correct acquisition and for the subsequent analysis of WAXD data [54]. Other very critical issues for an accurate assessment of the intensity of the (001) signal of clay are also overlooked in the common practice. Most of the times relative intensity data are reported. It is very important that the reference signal be independent of the morphology of the layered filler. A (*hk*0) reflection is ideal for this aim because it is related to the in-plane structure of clay layers, irrespective of whether or not they are stacked in tactoids. Unfortunately, (*hk*0) usually overlap polymer diffraction peaks and are rarely visible. Polymer peaks can be used as reference for the measurement of the intensity of the (001) basal peak just in a very limited number of cases. This is possible only if samples of the same composition are studied, and provided that no alteration of the semicrystalline framework of the matrix occurs. Such conditions are almost never met, so the assessment of the extent of exfoliation on the

basis of the intensity of the WAXD basal peak should be avoided. Much caution should be exercised in interpreting a broadening of the basal peak as a symptom of partial exfoliation because this variation in persistence lengths (which correspond to regions that have a constant value in the *d*-spacing) can result from a number of different reasons: incomplete exchange of the cations present in the pristine clay galleries with the organomodifier, uneven polymer intercalation, single clay layers organized in tactoids with large interlayer spacing and not regularly ordered, variable composition within a tactoid that affects clay surface charge, and small tactoid effects [14,55]. Small-angle X-ray scattering (SAXS) is a more promising technique for the quantification of tactoid size, as discussed later in this chapter.

The disappearance of basal signals from a WAXD pattern is often considered a sign that exfoliation occurred. Considerable attention should be exercised in taking this conclusion, though, because WAXD alone is not sufficient to prove exfoliation [16,17,53,56–58]. Alternative explanations of the absence, or of the dramatic weakening, of a diffraction peak in composite materials could be poor dispersion quality, preferential orientation of the layers, or low clay content, rather than exfoliation. In order to correctly assess the degree of interaction between polymer and clay, WAXD, SAXS, and TEM must be used complementarily. Extensive intercalation could separate clay layers to a distance undetectable by WAXD but that can still be determined by SAXS [1,10,13,56,59–63]. Only the simultaneous disappearance of SAXS signals and TEM observations can confirm that exfoliation has occurred.

The presence of (*hk*0) signals in the diffractograms can be a precious indicator to rule out that the (001) peak disappeared because of the low quantity of clay in the composite. These reflections are due to the in-plane structure of the single-clay sheet, and so they should always be visible, even in exfoliated nanocomposites, provided they do not overlap diffraction signals due to the polymer matrix [64–66].

Comparisons with TEM data showed that the WAXD signal can disappear even if some intercalation or aggregates are present [67–69]. The lack of Bragg scattering can suggest that a wide range of basal layer spacings is present within the tactoids.

Finally, X-ray diffraction experiments in two dimensions help in obtaining more detailed information on the orientation of the structural features within the sample [48,50,70]. An advantage of such a two-dimensional approach is the possibility to quantitatively assess the orientation of the filler or of the polymer crystallites by calculating the Hermans orientation parameter [71].

Another family of fillers that can be characterized by WAXD is POSS. These are three-dimensional, molecularly precise molecules with an inorganic silica-like core surrounded by organic groups, which can be used as nanofillers to be included into polymer matrices, or even inserted into the chains as comonomeric units. POSS molecules have a detrimental tendency to crystallize, inducing a phase separation in the material rather than bonding to the polymer backbones or otherwise dispersing into the polymer matrix [72–74]. The most immediate application of XRD to these systems is in the determination of their crystalline structure. As prepared POSS yield very sharp and intense crystalline reflections, which allow to determine the type and dimensions of the crystalline cell [75]. The presence of signals due to

crystallized POSS can moreover be used as indicators of the aggregation of POSS or of the formation of phase-separated filler domains [73,75–77]. A similar application of WAXD can be devised for every filler that is able to crystallize (e.g., starch nanocrystals [78], organic additives [79], or organometallic complexes [80]), and especially in those cases where crystallization is a signal that an undesired aggregation occurred.

4.2.3
Wide-Angle X-Ray Diffraction in the Characterization of the Structure of the Polymer Matrix

An often-overlooked aspect of nanocomposite characterization is the interrelation between filler dispersion and polymer crystal structure and morphology. How does the filler added in the formulation of nanocomposites alter the morphology of a semicrystalline polymer? The hypothesis that the reasons of mechanical reinforcement partly lie in a modification of the semicrystalline framework was put forth by a number of researchers [26,63,81,82]. Taking PLSN as a representative example, observations of the effect of clay on the polymorphism, degree of crystallinity, secondary morphology, and crystallization behavior supported this assumption [12,13,16,22,25,26,49,65,83–91]. The most common method used to characterize the structure of the polymer matrix is WAXD, which allows to measure the degree of crystallinity and crystal cell dimensions and to assess polymorphism. Polymers that are able to crystallize are called semicrystalline because, owing to entropic constrains, large macromolecular chains are unable to form a crystalline lattice extended to the whole sample. The structure and morphology of polymers is therefore better described as an alternation of crystalline and amorphous domains. The degree of crystallinity represents the fraction (in mass or volume) of sample that is arranged in the crystalline domains, and it is a very important and peculiar parameter on which many of the physical and mechanical properties of the material depend.

Both regions of the semicrystalline framework contribute to the XRD pattern of a polymeric sample: crystalline domains originate sharp reflections, whereas the amorphous zones produce a wide and diffused halo. A fitting procedure for the experimental patterns can be performed, by which the contributions of the crystalline and amorphous domains are deconvoluted [92] (Figure 4.3).

A certain degree of subjectivity exists in such data treatment, especially in the choice of the fitting functions (usually Gaussians or Lorentzians) and of the width and position of the amorphous halo. In order to make the results independent of such choices, it is paramount to use, in the comparison of samples, always the same width and position of the amorphous halo, by changing just its intensity, and the same kind of fitting functions throughout the sample series. Crystallinity can thus be evaluated as the ratio between the area of crystalline peaks over the total area of the diffractograms.

Polymorphism is also a very common feature of polymers, which, depending on crystallization conditions, can order themselves according to different unit cells.

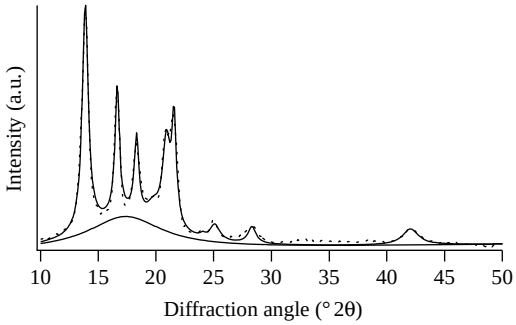

Figure 4.3 Example of the deconvolution procedure applied to calculate the degree of crystallinity from the XRD trace of polypropylene.

Obviously, WAXD is the technique of choice for studying the polymorphism of polymers because different crystalline phases display different diffractometric patterns. When more than one phase coexist in the same material, the intensity of the areas of the characteristic peaks of each of them yields a measure of their relative abundances [93,94]. Further information obtainable by WAXD is the size of crystallites, which can be obtained from the width of the peak applying the Scherrer equation [95], and the characteristic dimensions of the crystalline cell, which can be assessed on the basis of the angular position of the peaks.

All these data, easily available by a straightforward analysis of WAXD patterns, allow assessing how the semicrystalline framework is modified by the addition of filler, therefore yielding precious information in the development of structure–property relationships and for the comprehension of the mechanism of reinforcement due to nanofillers. Under this aspect, it is very important to study the material under a variety of length scales, as better detailed in the rest of this chapter.

4.2.4
Small-Angle X-Ray Scattering

As may be easily assessed by applying Bragg law, the analysis of aggregates of size over the tens of Å requires that the investigation be focused in an angular range between 0 and 2° 2θ.

Shifting to SAXS means concentrating on larger dimensional scales, neglecting the minute details of the crystallographic cell that are the domain of WAXD, and obtaining a wider view of the entire system. SAXS is observed whenever, in the material, regions of different electron density with a size between tens and thousands Å exist. For particles immersed in a medium, the parameter that determines the scattered amplitude, and therefore the scattered intensity, is the difference in electron density between the "solute" and the "solvent": $\Delta\rho$. If the dispersed particles have the same electron density than the matrix, the X-ray beam does not distinguish between the two components and the scattered waves will be

extinguished in any direction. SAXS is not different from WAXD under a physical point of view: when X-rays impinge the sample, its electrons resonate with the frequency of the incident light and emit coherent secondary waves that interfere with each other.

In the case of a single particle, the scattered intensity $I(q)$ (where $q = (4\pi \sin\theta)/\lambda$, θ being half the scattering angle, according to the glancing angle used in crystallography) can be calculated taking into account the distribution function of the electrons $p(r)$, which is obtained by geometrical considerations on the particle shape [96]:

$$I(q) = 4\pi \int_0^\infty p(r) \frac{\sin qr}{qr} \mathrm{d}r. \tag{4.2}$$

$p(r)$ can be obtained by Fourier inversion of the scattering curve [96]:

$$p(r) = \frac{1}{2\pi^2} \int_0^\infty I(q) \cdot qr \sin qr \cdot \mathrm{d}q. \tag{4.3}$$

If these single particles are homogeneously dispersed in a dilute system (so that interference between the particles can be neglected), the total scattered intensity will be given by the sum of the intensities scattered by each individual particle. Under this assumption, all the independent contributions to the diffracted intensity can be treated as coming from one single particle representative of all the others. SAXS data analysis in these cases thus consists in developing adequate models that reproduce the experimental traces as a function of morphological parameters, such as size, shape, or mass of the particles.

Theoretical $I(q)$ and $p(r)$ have been derived for a number of different geometries, so a fitting based on these models helps in obtaining a good picture of the morphology of the system. More complex shapes can be approximated by a collection of primary particles, such as spheres.

What has been said so far applies to dilute systems, but densely packed colloidal particles, such as highly filled nanocomposites, require to take into account the interparticle interference effects. Another assumption that is not always valid is that the particles are homogeneous and monodisperse in size. Particle anisotropy and polydispersity are very common factors that bring about severe deviations of the system from ideality. A distribution of sizes must therefore usually be included in the theoretical models used to reproduce the experimental SAXS patterns.

As said earlier, many intensity functions have been calculated for a number of different shapes, for example, spheres, ellipsoids, parallelepipedons, and cylinders, which are all similar in the central range. A universal approximation exists for the central part of SAXS traces. Guinier [97] proposed an exponential function only dependent on the radius of gyration R:

$$I(q) = (\Delta\rho)^2 V^2 \exp\left(-\frac{q^2 R^2}{3}\right), \tag{4.4}$$

where V is the scattering volume. R is the root mean square of the distances of all electrons from their center of gravity and is related to the physical dimensions of the particles by geometrical relationships. The Guinier formula holds surprisingly well for a wide variety of cases, failing only for anisometric particles.

V can be obtained directly from the diffraction pattern by

$$V = \frac{2\pi^2 I(0)}{\int_0^\infty q^2 I(q)\,\mathrm{d}q}, \tag{4.5}$$

where $I(0)$ is the scattered intensity at zero angle, and the integral at the denominator is the invariant Q, which is directly related to the mean square fluctuation of electron density, irrespective of special features of the structure. In other words, alterations or deformations of the structure of part of the system would alter the shape of the diffraction pattern, but the invariant would not change.

Another model-independent parameter can be found in the final slope of the SAXS pattern. In this region, which depends mainly on the fine structure of the particle and not on the mutual arrangement of particles, the intensity $I(q)$ can be approximated by the so-called Porod's law [98,99], $I(q) \underset{q\to\infty}{\to} ((\Delta\rho)^2 2\pi S)/q^4$, where S is the surface area of the particle. This dependence on q^{-4} holds very well for single particles, densely packed systems, and nonparticulate structures, as long as a defined internal surface exists. Deviations from this law can be due to factors such as a surface fractal structure of the filler particles [100,101], the existence of a layer of bound polymer at the surface of the filler [102], or an internally inhomogeneous structure of the filler [103]. The practical application of this relationship requires the measurements of absolute intensity, but introducing the invariant, this problem can be avoided and the specific surface can be determined from the diffraction pattern alone, without any additional data:

$$\frac{S}{V} = \frac{\pi \lim_{q\to\infty} I(q)q^4}{Q}. \tag{4.6}$$

Three main approaches can be individuated for the treatment of SAXS data.

1) Qualitative inspection of the pattern.
2) Application of the Guinier approximation for the determination of the size of dispersed particles.
3) Fitting methods based on functions, dependent on morphological features, which reproduce the experimental intensity.

A simple inspection of the SAXS patterns can by itself yield interesting preliminary information on the morphology of the samples. The appearance of a peak in the SAXS spectrum is indicative of a strong spatial correlation between the scattering particles embedded in the polymeric matrix, yielding a repetitive and regular pattern of electron density [104]. Differences in electron density that originate these kinds of patterns are caused by the presence of scattering domains, which can be crystalline polymer lamellae alternated to amorphous polymer, or inorganic filler particles

within a polymeric matrix. A SAXS signal thus can be used to assess the degree of dispersion of fillers or clay [17,105–108]. Measuring the position of the peak and applying the Bragg relationship (Eq. (4.1)), it is possible to determine the average distance between the scattering domains that originate these differences in electron density. In the case of lamellar geometries, for example, those of polymeric lamellar stacks or of lamellar fillers such as clay or graphite, this distance is the identity period or periodicity of the lamellae. When the microdomains are cylinders or spheres, it is related to their nearest neighbor distance. The width of the peak is informative as well, since broader peaks are consistent with a less homogeneous and consistent correlation length [109].

As introduced earlier, the Guinier approximation helps to calculate the dimension of dispersed particles [109–111], in the hypothesis that they are homogeneous in size and that the system is dilute, that is, the distance between the particles is much larger than particle size. Under these assumptions, Eq. (4.4) is valid. Equation (4.4) is easily linearized, allowing to obtain the radius of gyration of the particles R from the slope of a ln $I(q)$ versus q^2 plot:

$$\ln I(q) = \ln K_0 - \frac{q^2 R^2}{3}, \tag{4.7}$$

where K_0 is a constant. This is the most straightforward approach for characterizing the dimensions of spherical particles such as silica, TiO_2, or other compounds because there is an easy relationship that allows to calculate the radius r of such spheres from the radius of gyration R: $R = (3/5)^{1/2} r$. Many other relationships between the radius of gyration and the size of objects of different shapes have been calculated and proposed [96]. Probably one of the most useful is that for elliptic cylinders with semiaxes a and b and of height h [96], which approximates well clay layers:

$$R^2 = \frac{a^2 + b^2}{4} + \frac{h^2}{12}. \tag{4.8}$$

Caution should be used in applying this approach. Interparticle interference may influence the initial part of the scattering curve, but this problem can be eliminated by measuring samples with different concentrations and extrapolating to infinite dilution [112]. Possible aggregation of particles may also lead to distortion of the scattering curve [112]. It is advisable to restrict the range of q-values to $q^{-1} \leq 2\pi/r$ when performing the fitting according to the Guinier equation [112].

In inhomogeneous systems, made of particles with a polydisperse distribution of sizes, the ln $I(q)$ versus q^2 is no longer linear, but becomes concave, and the radius of gyration so obtained is skewed toward the size of the largest objects. The size and distribution of the particles can be obtained by extracting sequential tangents, as described by Wang *et al.* [28], or using some more sophisticated approaches based on the fitting of the experimental patterns.

A versatile approach for reproducing SAXS patterns is by deconvoluting the intensity $I(q)$ into two factors, a form factor and a structure factor [43,44,62,112–118]:

$$I(q) = AP(q)S(q), \tag{4.9}$$

where A consists of both instrument- and sample-dependent terms and can be treated as a scaling factor. $P(q)$ is a function that describes the interference effects between X-rays scattered by different parts of the same scattering body (microdomain) and is dependent on both the size and shape of the scattering body [119]. $S(q)$ is a function that describes the interference effects between X-rays scattered by different scattering bodies in the sample and depends on their relative positions [119].

A particularly recurrent shape for filler particles is the spherical one. The particle form factor $P(q)$ for a spherical particle of radius r_0 and contrast $\Delta\rho$ can be written as [112,120]

$$P(q) = \Delta\rho^2 v_p^2 \left\{ \frac{3[\sin(qr_0) - qr_0\cos(qr_0)]}{(qr_0)^3} \right\}^2, \tag{4.10}$$

where $v_p = (4/3)\pi r_0^3$ is the volume of a single particle.

Another often-encountered shape is flat particles of thickness $2H$, which yield a small-angle scattered intensity of [96]

$$P(q) = \frac{4B(\Delta\rho)^2 H^2}{q^2} \left(\frac{\sin qH}{qH} \right)^2, \tag{4.11}$$

where B is a constant dependent on the surface of the flat particle. Form factors for a wide variety of particle shapes have been calculated [96].

If, such as in the real case, the size of the scattering particles is not monodisperse, the scattered intensity derives from the sum of the contributions of each population of particles, each with its particular shape and size, and may be accounted for by multiplying $P(q)$ by an appropriate distribution function [62,120,121].

The formalization of the structure factor is less prone to generalizations and must be carried out according to models that describe as closely as possible the expected morphology of the samples. Usually it derives from the modification, by introduction of a distribution function, of a regular arrangement of the scattering particles. An example of such approach can be cited, regarding lamellar fillers. The short-range interference between clay layers (that becomes important as the clay loading increases) can be represented as a one-dimensional lattice [43,114,115]. In the ideal case of a perfectly periodic system, all the clay layers would be equidistant and the structure factor would be a series of equidistant peaks, which become infinitely sharp in the limit of infinitely large stacks [43]. In the more realistic case of a disordered system, the distances between the layers in the one-dimensional lattice vary according to some kind of distribution, which can be thought as the probability of displacement from the ideal periodicity [114].

When the dispersed particles are spherical, a "hard-sphere" fluid can be assumed, for which the interparticle interactions exclude particles from approaching within a center–center distance r equal to the collision diameter for the interaction, that is, $\sigma_c = 2r_c$. For distances r greater than σ_c the interparticle interactions are assumed to be negligible [120]. An informative example of the difficulties encountered in choosing and optimizing the structure and form factors of a particular system can be found in a work from Justice *et al.* [122].

Sometimes, the morphology of scattering objects is significantly more complex than a set of similarly sized objects arranged in some kind of quasiordered lattice. Maghemite in magnetoplastics displayed interparticle interactions that produced a complex morphology, with a consequently rich SAXS pattern [123]. Fillers such as silica, carbon black (CB), or carbon nanotubes have been shown to possess a very detailed hierarchical fractal structure, and ultrasmall-angle X-ray scattering (USAXS) measurements proved as a valuable source of information on the study of their aggregates and on their mutual interpenetration [100,102,122,124–131]. A fractal is an object that contains self-similarity over different length scales or, in other words, an object whose structure appears similar at different magnifications within some scale range [132]. CB primary particles display a surface fractal structure and are fused together into spherical aggregate units. These units are further clustered into agglomerates that then form, by organizing on an even superior level, open, multiarmed mass-fractal structures [100,102]. The scattering patterns of such systems are similar to that shown in Figure 4.4, which was acquired on a very large q range, spanning from $q = 0.0001\ \mathrm{nm}^{-1}$ to more than $1\ \mathrm{nm}^{-1}$ thanks to the application of ultrasmall-angle neutron scattering (USANS), USAXS, and SAXS [102].

These profiles yield a rich amount of information. The portions of the pattern that appear as straight lines in Figure 4.4 can be fit with a simple power law $I(q) \propto q^{-D}$: the parameter D can be obtained by the slope of log–log plots of the experimental scattering intensity $I(q)$ as a function of the modulus of the scattering vector, q.

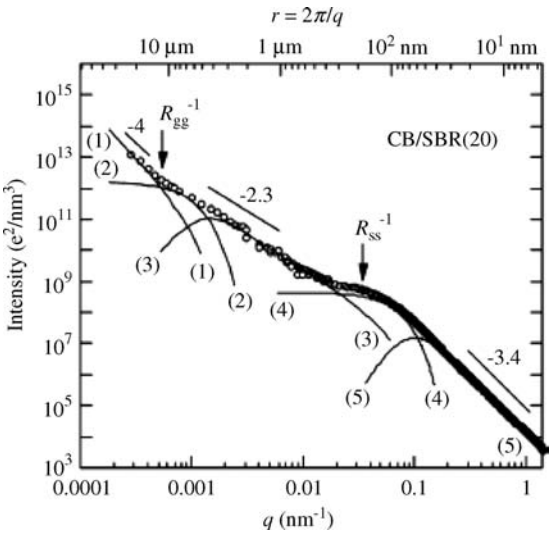

Figure 4.4 Decomposition of the observed SAXS profile for a carbon black/styrene butadiene rubber nanocomposite into each scattering component (solid lines numbered 1–5) from each structural level comprising the hierarchical structure based on the Beaucage unified fit analysis. Reprinted from Ref. [102] with permission from American Chemical Society, Copyright 2008.

Indeed, on the basis of this slope, different kinds of shapes and of fractal structures can be distinguished [111,133,134]. $D = 1$, 2, or 3 are expected for rods, disks, and spheres, respectively [128–132,134]. A slope $D = 4$ represents a smooth surface for the scattering particle, whereas $3 < D < 4$ is due to rough interfaces, characteristic of surface fractals.

Power law regimes alternate with discrete form-factor (Guinier scattering) profiles so that the radius of gyration of the fractal aggregates of that length scale can be determined by applying Guinier's law [96,135]. The reciprocal values of the q coordinate corresponding to the crossovers toward the Guinier and Porod regimes yield approximate estimates of the size of the aggregates and of the primary clusters, respectively.

The Beaucage unified fit model [104,136–138] is particularly useful for the interpretation of patterns similar to those shown in Figure 4.4 because it was ideated to describe scattering functions containing multiple length scales separated by power law regimes. Scattering from a hierarchy of structural levels are fitted considering only the four parameters (G, R_g, K_p, p) required to define the single structural levels, each with its radius of gyration, R_g, and power law exponent $-p$. The actual function used for each level is

$$I(q) = G\exp(-q^2R_g^2/3) + K_p[(\mathrm{erf}(qR_g/6^{1/2})^3/q]^p, \tag{4.12}$$

where G is the Guinier prefactor, K_p is the Porod prefactor, and erf is the error function. This model is effective when it is necessary to extract the parameters associated with each hierarchical level in complex structures that yield many power law regimes. The unified model works best with well-separated length scales, but it shows its limits when different structural regimes overlap [127].

When a peak due to a lamellar morphology appears in the SAXS pattern, a very useful method can be used to reproduce the experimental trace, obtaining a rich amount of data. This fitting method was developed on the basis of a theoretical model [57,139–142], and it is well suited for the description of the lamellar morphology of semicrystalline polymers or of clay tactoids. This is represented by an alternation of high electron density regions (crystalline layers in polymer lamellar stacks or clay layers in smectites) and of low-density matter (amorphous layers in polymer lamellar stacks or polymer and/or compatibilizing agent in clay). This technique refers to the Hosemann model [143], which assumes for electron density a one-dimensional variation along the normal direction to the lamellae, and introduces an independent variation for both the high- and low-density region thicknesses. The reader is referred to the relevant literature for the mathematical details of this approach [57,139,140]. This technique was recently applied to a number of polymers and polymeric composites [86–90,144–150]. For polymer lamellar stacks, this method was proven to accurately determine the thickness of the crystalline and amorphous layers, the long period of the stacks, the crystallinity associated to the lamellar stacks, along with their respective variances, and the average number of lamellae in each stack [56,88–90,140,151]. Similarly, when applied to clay, this technique allows to measure the distance between the

aluminosilicate layers, its variance, and most importantly, it is a quite straightforward method to count the average number of layers in the tactoids [56,57]. Saravanan *et al.* [152] and Bandyopadhyay and Ray [153] proposed an alternative approach, based on the generalized indirect Fourier transformation, to achieve the same aim. These authors were able, by this data analysis procedure, to reconstruct the electron density profile of clay tactoids [152,153]. The importance of such results is evident, if one considers that in order to obtain significant data from TEM pictures, a lot of micrographs of different areas must be taken (TEM allows to observe only tiny areas of the specimen), with a considerable expense in terms of time and money. SAXS, on the other hand, helps in obtaining the same quantitative information, on the whole sample volume, and without sample preparation. On the other hand, the main advantage of TEM, that of providing useful data, regardless of the level of order of the system, calls for a complementary use of X-ray techniques and TEM for a thorough representation of the morphology of nanocomposites.

The real advantage of SAXS is that one can probe the scale length of the tens of nanometers, which is not easily accessible by other techniques, but which is particularly important because it comprehends the characteristic size of most nanofillers and of polymer lamellae. In particular, the polymer lamellar morphology is particularly worth attention, and should be quantitatively assessed by established methods of treatment of SAXS data, such as fitting methods derived from the Hosemann's model or the correlation function [140,154]. An accurate determination of the polymer lamellar morphology is necessary because a number of reports highlighted the fact that nanofillers may exert a minor role in shaping the structure at a crystalline cell level, but at the same time, they have their most significant effects on polymer lamellae [82,85,144,145,147,155,156]. In these cases, SAXS was able to detect differences in the lamellar morphology due to the addition of the filler, whereas the degree of crystallinity measured by WAXD or DSC did not show appreciable differences. Evidences exist that the orientation of polymer lamellae is also influenced by the orientation of clay layers [83,157–159].

Information from SAXS can be derived from the scattering curve, such as in the cases reported earlier, or after Fourier transformation, that is, from the correlation function. This approach is particularly useful for the assessment of the morphology of the polymeric lamellar stacks. Strobl and Schneider showed that a simple graphical extrapolation procedure can directly yield the following structural parameters: the specific inner surface, the crystallinity, the average lamellar thickness, and the long spacing [154]. If the intensity is measured in absolute units, the electron density difference between the crystalline and amorphous regions can be measured. Figure 4.5 schematizes a practical example of this construction, showing most of the features that may be obtained [160].

The correlation function is widely employed in the analysis of the polymeric lamellar morphology [151,161–164] and can therefore be used to obtain a quantitative assessment of the effect of the addition of nanofillers on such a feature of semicrystalline matrices.

It is very surprising that this function was not applied at a comparable extent to the study of lamellar nanofillers in polymer-based nanocomposites. To the knowledge of

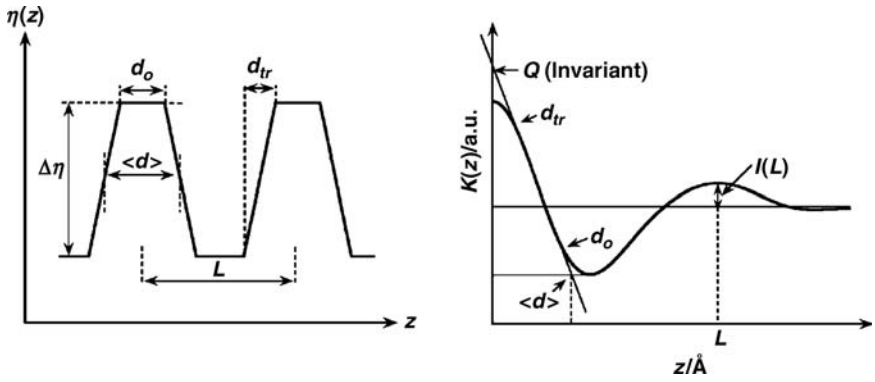

Figure 4.5 Model of the one-dimensional electron density distribution in a lamellar system and the corresponding electron density correlation function $K(z)$. Q is the invariant; d_{tr} is the thickness of the transition zone between the crystalline lamella and the amorphous part; d_0 is the thickness of the crystalline lamella; $\langle d \rangle$ is the average lamellae thickness; L is the long period; and $I(L)$ is the electron density. Reprinted with permission from Ref. [160].

the author, just one contribution exists on this topic, focused on the application of the correlation function to clay-based nanocomposites. Abdul Rasheed *et al.* [165] recently demonstrated the validity of an integrated correlation function that readily provides information on the extent of organoclay exfoliation and on the morphological parameters of various grades of polypropylene–organoclay nanocomposites.

An advantage of microscopy analysis is immediate information on the spatial distribution and orientation of clay layers in the nanocomposite, but these data are attainable from multiple methods of X-ray diffraction data acquisition and analysis. A very cheap and straightforward method for obtaining such information can be simply mounting the sample along different directions and following the modification of the signal [166]. More sophisticated techniques involve the use of two-dimensional detectors for data collection and usually the Hermans orientation parameter [71] for data treatment. These methods are particularly useful for the study of the anisotropy in the distribution of the filler in the matrix [167–170], to follow the anisotropic changes to the structure and morphology during mechanical deformation [171–175], or other self-assembly processes [176–178]. Iconic examples of such studies are those regarding strain-induced crystallization of rubber and rubber-based composites [167,179–186]. Time-resolved SAXS can moreover be applied for studying crystallization [187–191], allowing also to quantify the crystallization kinetics, by following the trend of the invariant as a function of time.

The issue of self-assembly is particularly important in polyurethanes [50,192–196] and especially in block [197–204] or grafted [205–207] copolymers that are remarkably fit for SAXS characterization. When the blocks in such copolymers are not mutually soluble, the system has a natural tendency toward phase segregation. The presence of covalent bonds between the chemically different parts of the molecules, though, prevents a macroscopic phase separation similar to that seen in polymer–

polymer heterogeneous mixtures. This drives self-organization into highly regular dispersion of glassy and rubbery domains that make them similar, as far as performance is concerned, to composites [208,209]. Typical SAXS patterns of these kind of copolymers consist of an intense principal peak followed by several higher order reflections. In the case of a lamellar morphology, the higher order signals appear at positions that are integer multiples of the first-order reflection. The principal peak is indexed as (001), while the higher order ones as (002), (003), ... The positions of the secondary maxima in hexagonally packed cylinders, relative to the principal peak, follow the scaling $1, 3^{1/2}, 4^{1/2}, 7^{1/2}, \ldots$ [210,211]. The most intense peak is indexed as a (100) hexagonal peak, and the additional peaks are assigned the (110), (200), and (210) indices [210]. The characteristic sequence of a body-centered cubic (bcc) packing of spherical microdomains is according to the ratios $2^{1/2} : 3^{1/2} : 4^{1/2} : 6^{1/2} : 10^{1/2} : 12^{1/2} : 14^{1/2}$ with respect to the first-order peak [210]. The most intense peak is indexed as a (110) peak and the additional peaks are assigned (200), (211), (220), (310), (222), and (321) indexes. Temperature-dependent SAXS experiments are very useful for the determination of the phase diagram of these materials.

4.3 Neutron Scattering

Scattering by neutrons can be exploited for obtaining precious structural and morphological information on polymeric materials. An excellent textbook covering all the aspects of neutron scattering, from instrumentation to theory to data interpretation, has recently been written by Hammouda, and is freely available on the World Wide Web [212].

Neutrons are very advantageous as probes for condensed matter because they are very penetrating and they allow a nondestructive investigation of the samples. Moreover, their wavelengths are comparable to atomic sizes and interdistance spacings. The instrumentation for small-angle neutron scattering is very demanding and expensive. Neutrons are generated in nuclear reactors; then they are monochromatized and collimated. Detection of the neutrons scattered by the sample, which can be investigated in various physical forms, is usually obtained by two-dimensional area detectors.

Neutron scattering is a very flexible technique, which allows to probe structures with sizes from the near atomic to the near micrometer scale. This made SANS a method of choice when the hierarchical structure of complex materials must be elucidated, especially in conjunction with other techniques such as WAXD, SAXS, or light scattering [213–222].

The scattering objects can be either polymer chains, or dispersed particles, such as fillers for example.

Analogous to other scattering methods, SANS yields a picture of the sample in the reciprocal space. SANS data must therefore be interpreted basically with one of the following four approaches, which are very similar to those enumerated for SAXS [212]:

1) Qualitative inspection of the SANS pattern. Similar to SAXS, many SANS spectra show a broad peak, whose position is related to the characteristic distance between the scattering inhomogeneities.
2) Application of the Guinier equation to obtain a radius of gyration.
3) Fitting with a Porod-like power law. The obtained exponents vary between 1 (for rod-shaped objects) and 4 (objects with a smooth surface). The interpretation is analogous to that described in the previous paragraph on SAXS.
4) Nonlinear least squares fitting to appropriate models. Many models have been developed, both for macromolecular scattering and for particulate scattering. Most of them are based on the formalization of appropriate structure and form factors.

The advantage of SANS over other small-angle scattering methods (such as SAXS) is that scattering contrast depends on electron density for X-rays, and on neutron scattering length density for neutrons. This allows use of both techniques as very complementary methods to obtain a really detailed picture of complex samples. For example, Yamauchi *et al*. studied the structure of a blend of natural rubber (NR) and high-density polyethylene (HDPE) [223]. The X-ray contrast factors for polyethylene–NR and amorphous–crystalline polyethylene pairs are of the same order of magnitude. Therefore, both phase-separated structures and crystalline lamellar structures contributed to the SAXS intensity [223]. On the opposite, the neutron contrast factor for amorphous–crystalline polyethylene pair is negligibly small compared with that for the polyethylene–NR pair. In other words, SANS is sensitive just to the phase-separated structure and is not influenced by the crystalline structure of HDPE in unfilled samples [223]. The two contributors to the morphology of the sample can be thus decoupled and studied separately, obtaining a very accurate picture of the composite.

Full exploitation of this advantage can be obtained by the deuteration method. Scattering lengths for hydrogen and deuterium are widely different, so introduction of deuterium labels into the analyte will greatly increase the contrast. In order to perform the same contrast enhancement with X-rays, heavy atoms must be introduced, with the risk of unacceptable modifications of the sample morphology. Deuterium labeling is much less invasive under this point of view. SANS is capable of measuring density fluctuations and composition (or concentration) fluctuations, whereas SAXS is only sensitive to density fluctuation.

In the case of complex systems composed by p components (e.g., clay, polymer, and solvent), the scattering intensity, $I(q)$, can be split into a number of partial scattering functions. Some of them are self-terms (e.g., $S_{cc}(q)$ and $S_{pp}(q)$ for the scattering of clay and polymer), which describe the scattering due to the arrangement and the morphology of scatterers of the same kind. Others are cross-terms, for example, between clay and polymer (e.g., $S_{cp}(q)$), which directly relate to the interaction between the two components [224,225]. Figure 4.6 schematizes the information contained within each of these terms.

Each of these terms is multiplied by the relevant difference in scattering length density. Contrast variation-SANS (CV-SANS) is a powerful technique that allows to

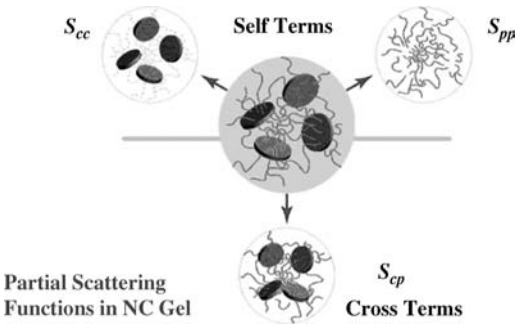

Figure 4.6 The CV-SANS leads to obtain the partial scattering functions of each component quantitatively. Self-terms yield information on the morphology and spatial arrangement of like scatterers; the cross-terms describe the interaction between filler and polymer. Reprinted with permission from Ref. [226].

efficiently investigate such cross-terms. An informative description of CV-SANS is given in the work of Endo *et al.* [226,227]. In this technique, different SANS measurements are performed, each time changing the composition of the solution, normally a H_2O–D_2O mixture. This modifies the density of the medium surrounding the scatterers. When the scattering length density of the solvent matches that of a particular binary system (e.g., of the clay–polymer couple), the corresponding contribution to the total scattering intensity will be depressed, at the same time enhancing the scattering term due to the scatterers with a density farthest from that of the medium [224,228,229]. This allows a very detailed description of the morphology and of the behavior also of quite complex systems, such as polyelectrolyte–protein adducts [230].

The potential of SANS for probing the various morphological details of the samples and the high flux apparatus recently made available allowed to perform several time-resolved experiments, in which the structure and morphology development in response to external stimuli could be followed. The most interesting examples of this approach regard *in situ* deformation studies, which are very useful to investigate the behavior under stress and strain of materials, and therefore useful to understand their failure mechanisms and to devise reinforcement strategies [231–233].

When the energy and momentum of the impinging neutrons are the same as those of scattered neutrons, the observed phenomenon is elastic scattering, which is most useful when studying the structure of the samples. If the dynamics of the system is of interest, quasielastic or inelastic neutron scattering is exploited. Inelastic scattering is encountered whenever there is a transfer of both momentum and energy. Quasielastic scattering is a form of inelastic scattering where the energy transfer peak is located around $E = 0$ [212]. Although they require special instrumentation and nonstraightforward data-interpretation methods, quasielastic and inelastic SANS have been proven to be very precious techniques that may complement thermal analysis and dielectric spectroscopy for obtaining a thorough characterization of molecular dynamics of nanocomposite systems [234–237].

4.4 Light Scattering

In addition to X-rays or neutrons, visible light can also be used as the incoming radiation in scattering experiments. Such experiments are performed on solutions or on colloidal dispersions. When the dispersed or dissolved particles are very small compared to the wavelength of the light, the intensity of the scattered light is uniform in all directions (Rayleigh scattering), whereas when the size of particles increases (above ~250 nm in diameter), the intensity is angle dependent (Mie scattering).

If on one hand, as described in the rest of this paragraph, light scattering allows to gather interesting information on the morphology of polymeric composite materials, on the other hand it suffers the limitation of the need to work with solutions or dispersions. It is nevertheless a very useful technique because it allows a thorough characterization of the separate components of the composites, such as the polymer matrix or the filler. Many different systems, some of them quite complex, have been characterized by light scattering, among them clay [238], core–shell particles [239–241], cross-linked networks embedding nanofillers [242–244], raspberry-like composites [245], polymer-bound carbon black [246].

Under a methodological point of view, in order to obtain significant data, utmost care must be taken in getting rid of any contaminant, such as dust or impurities.

Static light scattering, in which the scattered intensity is measured as a function of the angle around the sample, is a mainstream technique for the determination of the molecular weight of polymers. By acquiring the scattered intensity at several angles on solutions at different concentrations, a Zimm plot can be drawn, from which the molecular mass and the radius of gyration of the polymer can be obtained [247,248].

Methods similar to those illustrated for X-ray or neutron scattering can be applied to light scattering, such as the Guinier relationship [249] or the fitting by appropriate theoretical models developed formalizing a shape and structure factors [250].

Dynamic light scattering focuses on the observation of time-dependent fluctuations in scattered intensity, by using coherent and monochromatic light from a laser source and an appropriate photon counting device. Dynamic light scattering (also known as quasielastic light scattering and photon correlation spectroscopy) is particularly suited to determine small changes in mean diameter such as those due to adsorbed layers on the particle surface or slight variations in manufacturing processes. The detailed theoretical background to this technique is covered in several specialized monographs [251,252].

When particles are small enough to undergo Brownian motion, there is a continuous variation in the distance between the particles. As a consequence of this motion, constructive and destructive interference of the light scattered by neighboring particles yields intensity fluctuations. Following the intensity fluctuations as a function of time, the diffusion coefficient of the particles can be measured, and consequently, via the Stokes–Einstein equation, if the viscosity of the medium is known, the hydrodynamic radius or diameter of the particles can be calculated. Dynamic light scattering is therefore a very efficient method to determine the

dispersion of filler [253–260] and the dynamics of morphological changes [261–266] in nanocomposites.

Intensity fluctuations are usually analyzed by determining the intensity autocorrelation function, which can be described as the ensemble average of the product of the signals (i.e., the number of photons in a given sampling interval) at time t and at time $t + \tau$, where τ is the delay time, as a function of the delay time itself, over a delay range 100 ns to several seconds depending on the particle size and viscosity of the medium.

At short time delays, the correlation is high because the particles do not have a chance to move very far away from their initial state. The two signals are thus essentially unchanged when compared after only a very short time interval. As the time delays become longer, the correlation tends to exponentially decay to zero because after a long time, the initial and final states are very different and uncorrelated.

A truly monodisperse sample would give rise to a single exponential decay, which is quite easy to fit with a particle size distribution. In the case of polydisperse samples or when multiple dynamic processes coexist, the pattern can be more complex. For example, Aoki *et al.* studied the formation of a network of bridged polysilsesquioxanes and found that cooperative diffusion of entangled chains and the translational diffusion of cross-linked clusters coexisted, giving rise to step-like features in the light scattering autocorrelation functions [267]. Obviously, the fitting of these complex patterns requires more sophisticated theoretical models.

The range of particle sizes detectable by this technique depends on the refractive index of the chosen solvent system, on the characteristics (intensity and wavelength) of the incident light and on the instrumental conditions, and it is usually in the submicrometer–micrometer range.

Iconic examples of how an appropriate treatment of dynamic light scattering can bring about remarkable results can be found in reports on carbon nanotubes and carbon nanofibers. By fitting the intensity autocorrelation functions of such materials (an example of such functions is shown in Figure 4.7), it was possible to measure the length and the aspect ratio of these important and promising fillers for innovative nanocomposites [268–270]. This technique is thus a valid alternative for the measure of the nanofiber or nanotube length, with the advantage that light scattering data are a result of sampling over the whole specimen. This provides a better estimate of the average length, rather than the few hundred fibers that can be randomly sampled using image analysis in a reasonable timescale.

Other examples of works that fully exploit the potential of the various light scattering techniques can be found in studies of cellulose nanowhiskers [250,271,272]

One of the limitations of dynamic light scattering is that it works best when the scatterers in the systems are completely mobile. Conventional light scattering systems often fail to accurately describe samples with an inherent structure, such as polymer gels, in which static inhomogeneities are inevitably memorized in the network and are not free to move within the system. A solution to this problem has been proposed with the scanning microscopic light scattering (SMILS) system,

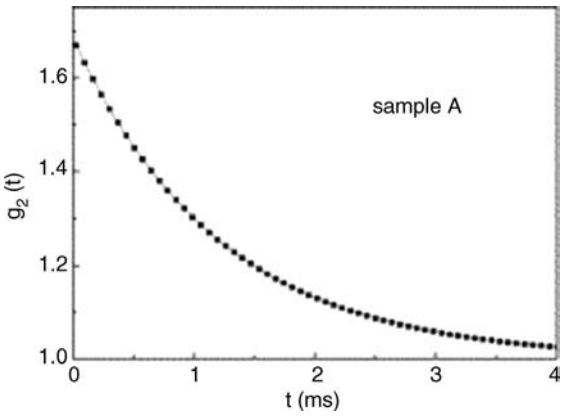

Figure 4.7 Autocorrelation function of a carbon nanotube sample. Reprinted with permission from Ref. [270].

which allows to scan and measure at many different positions in an inhomogeneous gel [273–276]. By this technique, time- and space-averaged autocorrelation functions of the fluctuating mesh size in the gel can be determined. Analysis of the ensemble-averaged functions makes it possible to quantitatively characterize the mesh size distribution of the network structure in inhomogeneous gels.

Time-resolved light scattering can also be employed to follow the crystallization kinetics of polymers [81,277]. Coupling a light scattering apparatus with a hot stage, the scattering intensity can be measured. Similar to what can be done with SAXS [187], the trend of the invariant, that is, the integrated scattering intensity, as a function of time helps in determining the induction time and the rate of crystallization [277].

Gupta and coworkers [249,278] and Yalcin and Cakmak [279] reported interesting sets of experiments in which real-time light scattering measurements were performed during tensile deformation. In particular, Gupta and coworkers [249] showed how, fitting the light scattering data with the Guinier expression, it is possible to quantify the deformation as the ratio of the radius of gyration of optical inhomogeneities along the direction of elongation and in the direction orthogonal to it.

Small-angle light scattering (SALS) is a suitable technique for determining the spherulitic radius, from four-lobe patterns [22,279–282] such as those shown in Figure 4.8. Equations such as the following can be used [280]

$$R = \frac{1.025\lambda_0}{n\pi \sin(\theta'_m/2)}, \tag{4.13}$$

where R is the average spherulitic radius, λ_0 is the wavelength of the light in the air, and θ'_m is the corrected scattering angle for maximum intensity, which is related to the actual scattering angle, θ_m, as $\sin\theta'_m = \sin(\theta_m)/n$, where n is the refractive index of the sample. A very interesting feature of such technique is that one can

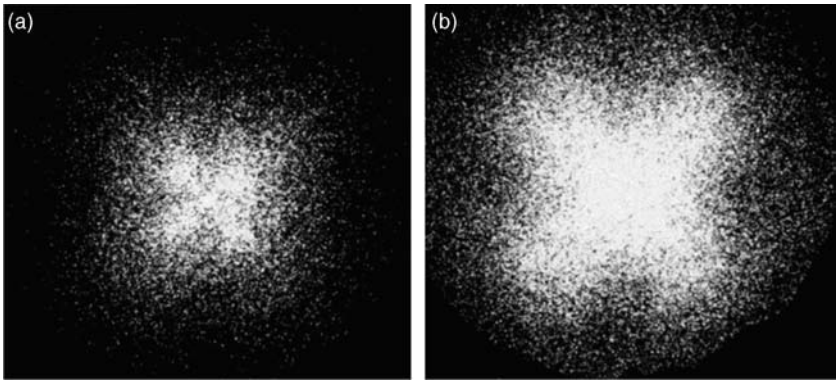

Figure 4.8 Photographs of small-angle light scattering (SALS) patterns of PVDF composites containing ammonium clay (a) and phosphonium clay (b), crystallized at 156 °C. Reprinted with permission from Ref. [22].

apply light scattering to solid samples. Measurements can not only be performed during crystallization [22,279,280] but also during melting [283]. Akpalu and coworkers also showed how SALS data can be interpreted to deconvolute the contribution to the signal due to the semicrystalline framework of the polymeric matrix (in that case polyethylene) and to the arrangement of the inorganic filler particles (in that case TiO_2) [284]. The results of this group's research show the potential of SALS for obtaining structure–property relationships, and how it moreover correlates well with other complementary characterization techniques, such as electron microscopy [285].

References

1 Ayres, E. and Orefice, R.L. (2007) Nanocomposites derived from polyurethane aqueous dispersion and clay: influence of the clay on the morphology and mechanical properties. *Polimeros-Ciencia E Tecnologia*, **17**, 339–345.

2 Ellis, T.S. (2003) Reverse exfoliation in a polymer nanocomposite by blending with a miscible polymer. *Polymer*, **44**, 6443–6448.

3 Gatos, K.G., Százdi, L., Pukánszky, B., and Karger-Kocsis, J. (2005) Controlling the deintercalation in hydrogenated nitrile rubber (HNBR)/organo-montmorillonite nanocomposites by curing with peroxide. *Macromolecular Rapid Communications*, **26**, 915–919.

4 Strawhecker, K.E. and Manias, E. (2000) Structure and properties of poly(vinyl alcohol)/Na^+ montmorillonite nanocomposites. *Chemistry of Materials*, **12**, 2943–2949.

5 Benson Tolle, T. and Anderson, D.P. (2004) The role of preconditioning on morphology development in layered silicate thermoset nanocomposites. *Journal of Applied Polymer Science*, **91**, 89–100.

6 Todorov, L.V. and Viana, J.C. (2007) Characterization of PET nanocomposites produced by different melt-based production methods. *Journal of Applied Polymer Science*, **106**, 1659–1669.

7 Montserrat, S., Roman, F., Hutchinson, J.M., and Campos, L. (2008) Analysis of the cure of epoxy based layered silicate nanocomposites: reaction kinetics and nanostructure development. *Journal of Applied Polymer Science*, **108**, 923–938.

8 Do Nascimento, G.M., Constantino, V.R.L., Landers, R., and Temperini, M.L.A. (2004) Aniline polymerization into montmorillonite clay: a spectroscopic investigation of the intercalated conducting polymer. *Macromolecules*, **37**, 9373–9385.

9 Gournis, D. and Floudas, G. (2004) "Hairy" plates: poly(ethylene oxide)-*b*-polyisoprene copolymers in the presence of Laponite clay. *Chemistry of Materials*, **16**, 1686–1692.

10 Chen, C. and Curliss, D. (2003) Preparation, characterization, and nanostructural evolution of epoxy nanocomposites. *Journal of Applied Polymer Science*, **90**, 2276–2287.

11 Dudkina, M.M., Tenkovtsev, A.V., Pospiech, D., Jehnichen, D., Haüßler, L., and Leuteritz, A. (2005) Nanocomposites of NLO chromophore-modified layered silicates and polypropylene. *Journal of Polymer Science Part B: Polymer Physics*, **43**, 2493–2502.

12 Buckley, J., Cebe, P., Cherdack, D., Crawford, J., Ince, B.S., Jenkins, M. *et al.* (2006) Nanocomposites of poly(vinylidene fluoride) with organically modified silicate. *Polymer*, **47**, 2411–2422.

13 Bertini, F., Canetti, M., Audisio, G., Costa, G., and Falqui, L. (2006) Characterization and thermal degradation of polypropylene–montmorillonite nanocomposites. *Polymer Degradation and Stability*, **91**, 600–605.

14 Yun, S.I., Attard, D., Lo, V., Davis, J., Li, H., Latella, B. *et al.* (2008) Spray-dried microspheres as a route to clay/polymer nanocomposites. *Journal of Applied Polymer Science*, **108**, 1550–1556.

15 Stefanescu, E.A., Stefanescu, C., Donose, B.C., Garno, J.C., Daly, W.H., Schmidt, G. *et al.* (2008) Polymer/clay nanocomposites: influence of ionic strength on the structure and adhesion characteristics in multilayered films. *Macromolecular Materials and Engineering*, **293**, 771–780.

16 Li, T.C., Ma, J., Wang, M., Tjiu, W.C., Liu, T., and Huang, W. (2007) Effect of clay addition on the morphology and thermal behavior of polyamide 6. *Journal of Applied Polymer Science*, **103**, 1191–1199.

17 Bordes, P., Pollet, E., Bourbigot, S., and Averous, L. (2008) Structure and properties of PHA/clay nano-biocomposites prepared by melt intercalation. *Macromolecular Chemistry and Physics*, **209**, 1473–1484.

18 Chen, C. and Anderson, D.P. (2007) E-beam-cured layered-silicate and spherical silica epoxy nanocomposites. *Journal of Applied Polymer Science*, **106**, 2132–2139.

19 Filippi, S., Marazzato, C., Magagnini, P., Famulari, A., Arosio, P., and Meille, S.V. (2008) Structure and morphology of HDPE-*g*-MA/organoclay nanocomposites: effects of the preparation procedures. *European Polymer Journal*, **44**, 987–1002.

20 Kaneko, M.L.Q.A., Torriani, I.L., and Yoshida, I.V.P. (2007) Morphological evaluation of silicone/clay slurries by small-angle/wide-angle X-ray scattering. *Journal of the Brazilian Chemical Society*, **18**, 765–773.

21 Liu, L., Song, L., Hu, Y., and Chen, H. (2006) Synthesis and characterization of intercalated ladder-like poly (vinylsilsesquioxanes)/organically modified montmorillonite nanocomposites. *Polymer Composites*, **27**, 660–664.

22 Patro, T.U., Mhalgi, M.V., Khakhar, D.V., and Misra, A. (2008) Studies on poly (vinylidene fluoride)–clay nanocomposites: effect of different clay modifiers. *Polymer*, **49**, 3486–3499.

23 Pospiech, D., Kretzschmar, B., Willeke, M., Leuteritz, A., Jehnichen, D., Janke, A. *et al.* (2007) Exfoliation behavior of montmorillonite modified by poly (oxyalkylene)s in polypropylene and the properties of the resulting nanocomposites. *Polymer Engineering and Science*, **47**, 1262–1271.

24 Loyens, W., Jannasch, P., and Maurer, F.H.J. (2005) Effect of clay modifier and matrix molar mass on the structure and properties of poly(ethylene oxide)/Cloisite

nanocomposites via melt-compounding. *Polymer*, **46**, 903–914.

25 Maiti, P., Nam, P.H., Okamoto, M., Kotaka, T., Hasegawa, N., and Usuki, A. (2002) The effect of crystallization on the structure and morphology of polypropylene/clay nanocomposites. *Polymer Engineering and Science*, **42**, 1864–1871.

26 Nam, P.H., Ninomiya, N., Fujimori, A., and Masuko, T. (2006) Less-ordered lamellar structure of intercalated poly(L-lactide)/organo-modified montmorillonite hybrids. *Polymer Engineering and Science*, **46**, 703–711.

27 Si, M., Goldman, M., Rudomen, G., Geifer, M.Y., Sokolov, J.C., and Rafailovich, M.H. (2006) Effect of clay type on structure and properties of poly (methyl methacrylate)/clay nanocomposites. *Macromolecular Materials and Engineering*, **291**, 602–611.

28 Wang, S., Zhang, Y., Ren, W., Zhang, Y., and Lin, H. (2005) Morphology, mechanical and optical properties of transparent BR/clay nanocomposites. *Polymer Testing*, **24**, 766–774.

29 Wang, H.M., Mei, M.H., Jiang, J.C., Li, Q. S., Zhang, X.H., and Wu, S.K. (2001) A study on the preparation of polymer/montmorillonite nano-composite materials by photo-polymerization. *Polymer International*, **51**, 7–11.

30 Hu, X.B. and Lesser, A.J. (2003) Effect of a silicate filler on the crystal morphology of poly(trimethylene terephthalate)/clay nanocomposites. *Journal of Polymer Science Part B: Polymer Physics*, **41**, 2275–2289.

31 Kurian, M., Dasgupta, A., Galvin, M.E., Ziegler, C.R., and Beyer, F.L. (2006) A novel route to inducing disorder in model polymer-layered silicate nanocomposites. *Macromolecules*, **39**, 1864–1871.

32 Wang, Y., Zhang, H., Wu, Y., Yang, J., and Zhang, L. (2005) Preparation and properties of natural rubber/rectorite nanocomposites. *European Polymer Journal*, **41**, 2776–2783.

33 Wu, Y.P., Wang, Y.Q., Zhang, H.F., Wang, Y.Z., Yu, D.S., Zhang, L.Q. *et al.* (2005) Rubber–pristine clay nanocomposites prepared by co-coagulating rubber latex and clay aqueous suspension. *Composites Science and Technology*, **65**, 1195–1202.

34 Ozmusul, M.S., Picu, C.R., Sternstein, S.S., and Kumar, S.K. (2005) Lattice Monte Carlo simulations of chain conformations in polymer nanocomposites. *Macromolecules*, **38**, 4495–4500.

35 Wen, X., He, H., Zhu, J., Jun, Y., Ye, C., and Deng, F. (2006) Arrangement, conformation, and mobility of surfactant molecules intercalated in montmorillonite prepared at different pillaring reagent concentrations as studied by solid-state NMR spectroscopy. *Journal of Colloid and Interface Science*, **299**, 754–760.

36 Zidelkheir, B. and Abdel-Goad, M. (2008) Effect of surfactant agent upon the structure of montmorillonite – X-ray diffraction and thermal analysis. *Journal of Thermal Analysis and Calorimetry*, **94**, 181–187.

37 Yang, G., Hou, W., Feng, X., Xu, L., Liu, Y., Wang, G. *et al.* (2007) Nanocomposites of polyaniline and a layered inorganic acid host: polymerization of aniline in the layers, conformation, and electrochemical studies. *Advanced Functional Materials*, **17**, 401–412.

38 Ferreira, M., Zucolotto, V., Huguenin, F., Torresi, R.M., and Oliveira, O.N.J. (2002) Layer-by-layer nanostructured hybrid films of polyaniline and vanadium oxide. *Journal of Nanoscience and Nanotechnology*, **2**, 29–32.

39 Deng, Y., Dixon, J.B., and White, G.N. (2006) Bonding mechanisms and conformation of poly(ethylene oxide)-based surfactants in interlayer of smectite. *Colloid and Polymer Science*, **284**, 347–356.

40 Lee, T.W., Park, O.O., Hong, J.M., Kim, D.Y., and Kim, Y.C. (2001) Carrier mobilities of polymer/organo-clay nanocomposite electroluminescent devices. *Thin Solid Films*, **393**, 347–351.

41 Lin, J.J., Chen, I.J., and Chou, C.C. (2003) Critical conformational change of poly(oxypropylene)diamines in layered aluminosilicate confinement. *Macromolecular Rapid Communications*, **24**, 492–495.

42 Greesh, N., Hartmann, P.C., Cloete, V., and Sanderson, R.D. (2008) Adsorption of

2-acrylamido-2-methyl-1-propanesulfonic acid (AMPS) and related compounds onto montmorillonite clay. *Journal of Colloid and Interface Science*, **319**, 2–11.

43 Gelfer, M., Burger, C., Fadeev, A., Sics, I., Chu, B., Hsiao, B.S. *et al.* (2004) Thermally induced phase transitions and morphological changes in organoclays. *Langmuir*, **20**, 3746–3758.

44 Connolly, J., van Duijneveldt, J.S., Klein, S., Pizzey, C., and Richardson, R.M. (2006) Effect of surfactant and solvent properties on the stacking behavior of non-aqueous suspensions of organically modified clays. *Langmuir*, **22**, 6531–6538.

45 Lu, Y.L., Liang, Y.R., Wu, Y.P., and Zhang, L.Q. (2006) Effects of heat and pressure on microstructures of isobutylene-isoprene rubber (IIR)/clay nanocomposites. *Macromolecular Materials and Engineering*, **291**, 27–36.

46 Ma, Y., Li, Q.F., Zhang, L.Q., and Wu, Y.P. (2007) Role of stearic acid in preparing EPDM/clay nanocomposites by melt compounding. *Polymer Journal*, **39**, 48–54.

47 Vaia, R.A. and Giannelis, E.P. (1997) Lattice model of polymer melt intercalation in organically-modified layered silicates. *Macromolecules*, **30**, 7990–7999.

48 Ogata, N., Kawakage, S., and Ogihara, T. (1997) Structure and thermal/mechanical properties of poly(ethylene oxide)–clay mineral blends. *Polymer*, **38**, 5115–5118.

49 Hikosaka, M.Y., Pulcinelli, S.H., Santilli, C.V., Dahmouche, K., and Craievich, A.F. (2006) Montmorillonite (MMT) effect on the structure of poly(oxyethylene) (PEO)–MMT nanocomposites and silica–PEO–MMT hybrid materials. *Journal of Non-Crystalline Solids*, **352**, 3705–3710.

50 Finnigan, B., Jack, K., Campbell, K., Halley, P., Truss, R., Casey, P. *et al.* (2005) Segmented polyurethane nanocomposites: impact of controlled particle size nanofillers on the morphological response to uniaxial deformation. *Macromolecules*, **38**, 7386–7396.

51 Varlot, K., Reynaud, E., Kloppfer, M.H., Vigier, G., and Varlet, J. (2001) Clay-reinforced polyamide: preferential orientation of the montmorillonite sheets and the polyamide crystalline lamellae. *Journal of Polymer Science Part B: Polymer Physics*, **39**, 1360–1370.

52 Lertwilmolnun, W. and Vergnes, B. (2005) Influence of compatibilizer and processing conditions on the dispersion of nanoclay in a polypropylene matrix. *Polymer*, **46**, 3462–3471.

53 Vaia, R.A. and Liu, W. (2002) X-ray powder diffraction of polymer/layered silicate nanocomposites: model and practice. *Journal of Polymer Science Part B: Polymer Physics*, **40**, 1590–1600.

54 Fornes, T.D., Hunter, D.L., and Paul, D.R. (2004) Effect of sodium montmorillonite source on nylon 6/clay nanocomposites. *Polymer*, **45**, 2321–2331.

55 Yoonessi, M., Toghiani, H., Daulton, T.L., Lin, J.S., and Pittman, C.U.Jr. (2005) Clay delamination in clay/poly (dicyclopentadiene) nanocomposites quantified by small angle neutron scattering and high-resolution transmission electron microscopy. *Macromolecules*, **38**, 818–831.

56 Benetti, E.M., Causin, V., Marega, C., Marigo, A., Ferrara, G., Ferraro, A. *et al.* (2005) Morphological and structural characterization of polypropylene based nanocomposites. *Polymer*, **46**, 8275–8285.

57 Causin, V., Marega, C., Marigo, A., and Ferrara, G. (2005) Assessing organo-clay dispersion in polymer layered silicate nanocomposites: a SAXS approach. *Polymer*, **46**, 9533–9537.

58 Costa, F.R., Abdel-Goad, M., Wagenknecht, U., and Heinrich, G. (2005) Nanocomposites based on polyethylene and Mg–Al layered double hydroxide. I. Synthesis and characterization. *Polymer*, **46**, 4447–4453.

59 Chen, C., Khobaib, M., and Curliss, D. (2003) Epoxy layered-silicate nanocomposites. *Progress in Organic Coatings*, **47**, 376–383.

60 Jeon, H.S., Rameshwaram, J.K., Kim, G., and Weinkauf, D.H. (2003) Characterization of polyisoprene–clay nanocomposites prepared by solution blending. *Polymer*, **44**, 5749–5758.

61 Kim, S.H., Park, S.H., and Kim, S.C. (2005) Novel clay treatment and preparation of poly(ethylene

terephthalate)/clay nanocomposite by *in-situ* polymerization. *Polymer Bulletin*, **53**, 285–292.

62 Hernandez, M., Sixou, B., Duchet, J., and Sautereau, H. (2007) The effect of dispersion state on PMMA-epoxy-clay ternary blends: *in situ* study and final morphologies. *Polymer*, **48**, 4075–4086.

63 Masenelli-Varlot, K., Vigier, G., Vermogen, A., Gauthier, C., and Cavaille, J.Y. (2007) Quantitative structural characterization of polymer–clay nanocomposites and discussion of an "ideal" microstructure, leading to the highest mechanical reinforcement. *Journal of Polymer Science Part B: Polymer Physics*, **45**, 1243–1251.

64 Chen, T., Zhu, J., Li, B., Guo, S., Yuan, Z., Sun, P. *et al.* (2005) Exfoliation of organo-clay in telechelic liquid polybutadiene rubber. *Macromolecules*, **38**, 4030–4033.

65 Ristolainen, N., Vainio, U., Paavola, S., Torkkeli, M., Serimaa, R., and Seppälä, J. (2005) Polypropylene/organoclay nanocomposites compatibilized with hydroxyl-functional polypropylenes. *Journal of Polymer Science Part B: Polymer Physics*, **43**, 1892–1903.

66 Miyagawa, H., Drzal, L.T., Miyagawa, H., and Carsello, J.A. (2006) Intercalation and exfoliation of clay nanoplatelets in epoxy-based nanocomposites: TEM and XRD observations. *Polymer Engineering and Science*, **46**, 452–463.

67 Landry, V., Riedl, B., and Blanchet, P. (2008) Nanoclay dispersion effects on UV coatings curing. *Progress in Organic Coatings*, **62**, 400–408.

68 Lee, S.H., Cho, E.R., and Youn, J.R. (2007) Rheological behavior of polypropylene/layered silicate nanocomposites prepared by melt compounding in shear and elongational flows. *Journal of Applied Polymer Science*, **103**, 3506–3515.

69 Schaefer, D.W. and Justice, R.S. (2007) How nano are nanocomposites? *Macromolecules*, **40**, 8501–8517.

70 Bafna, A., Beaucage, G., Mirabella, F., Skillas, G., and Sukumaran, S. (2001) Optical properties and orientation in polyethylene blown films. *Journal of Polymer Science Part B: Polymer Physics*, **39**, 2923.

71 Yoonessi, M., Toghiani, H., and Pittman, C.U.Jr. (2006) Orientation of montmorillonite clay in dicyclopentadiene/organically modified clay dispersions and nanocomposites. *Journal of Applied Polymer Science*, **102**, 2743–2751.

72 Zhang, Y., Lee, S., Yoonessi, M., Liang, K., and Pittman, C.U. (2006) Phenolic resin–trisilanolphenyl polyhedral oligomeric silsesquioxane (POSS) hybrid nanocomposites: structure and properties. *Polymer*, **47**, 2984–2996.

73 Zheng, L., Waddon, A.J., Farris, R.J., and Coughlin, E.B. (2002) X-ray characterizations of polyethylene polyhedral oligomeric silsesquioxane copolymers. *Macromolecules*, **35**, 2375–2379.

74 Strachota, A., Kroutilová, I., Kovářová, J., and Matějka, L. (2004) Epoxy networks reinforced with polyhedral oligomeric silsesquioxanes (POSS). *Thermomechanical Properties Macromolecules*, **37**, 9457.

75 Fu, B.X., Hsiao, B.S., Pagola, S., Stephens, P., White, H., Rafailovich, M. *et al.* (2001) Structural development during deformation of polyurethane containing polyhedral oligomeric silsesquioxanes (POSS) molecules. *Polymer*, **42**, 599–611.

76 Liu, L., Tian, M., Zhang, W., Zhang, L., and Mark, J.E. (2007) Crystallization and morphology study of polyhedral oligomeric silsesquioxane (POSS)/polysiloxane elastomer composites prepared by melt blending. *Polymer*, **48**, 3201–3212.

77 Zheng, L., Hong, S., Cardoen, G., Burgaz, E., Gido, S.P., and Coughlin, E.B. (2004) Polymer nanocomposites through controlled self-assembly of cubic silsesquioxane scaffolds. *Macromolecules*, **37**, 8606–8611.

78 Angellier, H., Molina-Boisseau, S., Lebrun, L., and Dufresne, A. (2005) Processing and structural properties of waxy maize starch nanocrystals reinforced natural rubber. *Macromolecules*, **38**, 3783–3792.

79 Wan, Y., Xiong, C., Yu, J., and Wen, D. (2005) Effect of processing parameters on electrical resistivity and thermo-sensitive properties of carbon-black/styrene–butadiene–rubber composite membranes. *Composites Science and Technology*, **65**, 1769–1779.

80 Liu, L., Zhang, W., Li, X., Wu, X.F., Yang, C., Liu, Y.D. *et al.* (2007) Preparation and luminescence properties of $Sm(TTA)_3phen$/NBR composites. *Composites Science and Technology*, **67**, 2199–2207.

81 Somwangthanaroj, A., Lee, E.C., and Solomon, M.J. (2003) Early stage quiescent and flow-induced crystallization of intercalated polypropylene nanocomposites by time-resolved light scattering. *Macromolecules*, **36**, 2333–2342.

82 Lincoln, D.M., Vaia, R.A., Wang, Z.G., and Hsiao, B.S. (2001) Secondary structure and elevated temperature crystallite morphology of nylon-6. *Polymer*, **42**, 1621–1631.

83 Weon, J.I., Xia, Z.Y., and Sue, H.J. (2005) Morphological characterization of nylon-6 nanocomposite following a large-scale simple shear process. *Journal of Polymer Science Part B: Polymer Physics*, **43**, 3555–3566.

84 Yalcin, B., Valladares, D., and Cakmak, M. (2003) Amplification effect of platelet type nanoparticles on the orientation behavior of injection molded nylon 6 composites. *Polymer*, **44**, 6913–6925.

85 Homminga, D., Goderis, B., Dolbnya, I., Reynaers, H., and Groeninckx, G. (2005) Crystallization behavior of polymer/montmorillonite nanocomposites. Part I. Intercalated poly(ethylene oxide). *Polymer*, **46**, 11359–11365.

86 Marega, C., Causin, V., Marigo, A., Ferrara, G., and Tonnaer, H. (2009) Perkalite as an Innovative filler for isotactic polypropylene-based nanocomposites. *Journal of Nanoscience and Nanotechnology*, **9**, 2704–2714.

87 Causin, V., Carraro, M.L., Marega, C., Saini, R., Campestrini, S., and Marigo, A. (2008) Structure and morphology of solution blended poly(vinylidene fluoride)/montmorillonite nanocomposites. *Journal of Applied Polymer Science*, **109**, 2354–2361.

88 Causin, V., Marega, C., Marigo, A., Ferrara, G., Ferraro, A., and Selleri, R. (2008) Structure–property relationships in isotactic poly(propylene)/ethylene propylene rubber/montmorillonite nanocomposites. *Journal of Nanoscience and Nanotechnology*, **8**, 1823–1834.

89 Causin, V., Marega, C., Saini, R., Marigo, A., and Ferrara, G. (2007) Crystallization behavior of isotactic polypropylene based nanocomposites. *Journal of Thermal Analysis and Calorimetry*, **90**, 849–857.

90 Causin, V., Marega, C., Marigo, A., Ferrara, G., Idiyatullina, G., and Fantinel, F. (2006) Morphology, structure and properties of a poly(1-butene)/montmorillonite nanocomposite. *Polymer*, **47**, 4773–4780.

91 Yuan, M., Song, Q., and Turng, L.S. (2007) Spatial orientation of nanoclay and crystallite in microcellular injection molded polyamide-6 nanocomposites. *Polymer Engineering and Science*, **47**, 765–779.

92 Hindeleh, A.M. and Johnson, D.J. (1971) The resolution of multipeak data in fiber science. *Journal of Physics D: Applied Physics*, **4**, 259–263.

93 Turner Jones, A., Aizlewood, J.M., and Beckett, D.R. (1964) Crystalline forms of isotactic polypropylene. *Die Makromolekulare Chemie*, **75**, 134–158.

94 Turner Jones, A. (1971) Development of the γ-crystal form in random copolymers of propylene and their analysis by DSC and X-ray methods. *Polymer*, **12**, 487–508.

95 Klug, H.P. and Alexander, L.E. (1974) *X-Ray Diffraction Procedures*, John Wiley & Sons, Inc., New York.

96 Glatter, O. and Kratky, O. (1982) *Small Angle X-Ray Scattering*, Academic Press, London.

97 Guinier, A. (1939) La diffraction des rayons X aux trés petits angles: application à l'étude de phénomènes ultramicroscopiques. *Annales de Physique*, **12**, 161–237.

98 Porod, G. (1951) The X-ray small angle scattering of close packed colloid systems Part I. *Kolloid Zeitschrift*, **124**, 83–114.

99 Debye, P., Anderson, H.R.J., and Brumberger, H. (1957) Scattering by an inhomogeneous solid. II. The correlation function and its application. *Journal of Applied Physics*, **28**, 679–683.

100 Rieker, T.P., Hindermann-Bischoff, M., and Ehrburger-Dolle, F. (2000) Small-angle X-ray scattering study of the morphology of carbon black mass fractal aggregates in polymeric composites. *Langmuir*, **16**, 5588–5592.

101 Schmidt, P.W. (1991) Small-angle scattering studies of disordered, porous and fractal systems. *Journal of Applied Crystallography*, **24**, 414–435.

102 Koga, T., Hashimoto, T., Takenaka, M., Aizawa, K., Amino, N., Nakamura, M. *et al.* (2008) New insight into hierarchical structures of carbon black dispersed in polymer matrices: a combined small-angle scattering study. *Macromolecules*, **41**, 453–464.

103 Schaefer, D.W., Rieker, T., Agamalian, M., Lin, J.S., Fischer, D., Sukunaran, S. *et al.* (2000) Multilevel structure of reinforcing silica and carbon. *Journal of Applied Crystallography*, **33**, 587–591.

104 Santilli, C.V., Sarmento, V.H.V., Dahmouche, K., Pulcinelli, S.H., and Craievich, A.F. (2009) Effects of synthesis conditions on the nanostructure of hybrid sols produced by the hydrolytic condensation of (3-methacryloxypropyl) trimethoxysilane. *Journal of Physical Chemistry C*, **113**, 14708–14714.

105 Karesoia, M., Jokinen, H., Karalainen, E., Pulkkinen, P., Torkkeli, M., Soininen, A. *et al.* (2009) Grafting of montmorillonite nano-clay with butyl acrylate and methyl methacrylate by atom transfer radical polymerization: blends with poly(BuA-*co*-MMA). *Journal of Polymer Science Part A: Polymer Chemistry*, **47**, 3086–3097.

106 Ali, Z., Le, H.H., Ilisch, S., Busse, K., and Radusch, H. (2009) Nanoclay exfoliation in rubber compounds characterized by online measurements of electrical conductance. *Journal of Applied Polymer Science*, **113**, 667–677.

107 Discacciati, J.A.C. and Orefice, R.L. (2007) Structural analysis on photopolymerized dental resins containing nanocomponents. *Journal of Materials Science*, **42**, 3883–3893.

108 Yun, S.I., Attard, D., Lo, V., Davis, J., Li, H., Latella, B. *et al.* (2008) Spray-dried microspheres as a route to clay/polymer nanocomposites. *Journal of Applied Polymer Science*, **108**, 1550–1556.

109 Paranhos, C.M., Dahmouche, K., Zaioncz, S., Soares, B.G., and Pessan, L.A. (2008) Relationships between nanostructure and thermomechanical properties in poly(vinyl alcohol)/montmorillonite nanocomposite with an entrapped polyelectrolyte. *Journal of Polymer Science Part B: Polymer Physics*, **46**, 2618–2629.

110 Yurkov, G.Y., Astaf'ev, D.A., Nikitin, L.N., Koksharov, Y.A., Kataeva, N.A., Shtykova, E.V. *et al.* (2006) Fe-containing nanoparticles in siloxane rubber matrices. *Inorganic Materials*, **42**, 496–502.

111 Sedlakova, Z., Plestil, J., Baldrian, J., Slouf, M., and Holub, P. (2009) Polymer–clay nanocomposites prepared via *in situ* emulsion polymerization. *Polymer Bulletin*, **63**, 365–384.

112 Peterlik, H. and Fratzl, P. (2006) Small-angle X-ray scattering to characterize nanostructures in inorganic and hybrid materials chemistry. *Monatshefte Fur Chemie*, **137**, 529–543.

113 Varlot, K., Reynaud, E., Vigier, G., and Varlet, J. (2002) Mechanical properties of clay-reinforced polyamide. *Journal of Polymer Science Part B: Polymer Physics*, **40**, 272–283.

114 Vaia, R.A., Liu, W., and Koerner, H. (2003) Analysis of small-angle scattering of suspensions of organically modified montmorillonite: implications to phase behavior of polymer nanocomposites. *Journal of Polymer Science Part B: Polymer Physics*, **41**, 3214–3236.

115 Ruland, W. and Smarsly, B. (2004) SAXS of self-assembled oriented lamellar nanocomposite films: an advanced method of evaluation. *Journal of Applied Crystallography*, **37**, 575–584.

116 Gelfer, M.Y., Burger, C., Chu, B., Hsiao, B.S., Drozdov, A.D., Si, M. *et al.* (2005) Relationships between structure and rheology in model nanocomposites of ethylene-vinyl-based copolymers and

organoclays. *Macromolecules*, **38**, 3765–3775.

117 Diaconu, G., Paulis, M., and Leiza, J.R. (2008) Towards the synthesis of high solids content waterborne poly(methyl methacrylate-*co*-butyl acrylate). *Polymer*, **49**, 2444–2454.

118 Pizzey, C., Klein, S., Leach, E., van Duijneveldt, J.S., and Richardson, R.M. (2004) Suspensions of colloidal plates in a nematic liquid crystal: a small-angle X-ray scattering study. *Journal of Physics: Condensed Matter*, **16**, 2479–2495.

119 King, S.M. (1999) *Modern Techniques for Polymer Characterisation* (eds R.A. Pethrick and J.V. Dawkins), John Wiley & Sons, Inc., New York.

120 Terrill, N.J., Crowley, T., Gill, M., and Armes, S.P. (1993) Small-angle X-ray scattering studies on colloidal dispersions of polyaniline–silica nanocomposites. *Langmuir*, **9**, 2093–2096.

121 Vermogen, A., Masenelli-Varlot, K., Vigier, G., Sixou, B., Thollet, G., and Duchet-Rumeau, J. (2007) Clay dispersion and aspect ratios in polymer–clay nanocomposites. *Journal of Nanoscience and Nanotechnology*, **7**, 3160–3171.

122 Justice, R.S., Wang, D.H., Tan, L.S., and Schaefer, D.W. (2007) Simplified tube form factor for analysis of small-angle scattering data from carbon nanotube filled systems. *Journal of Applied Crystallography*, **40**, s88–s92

123 Millan, A., Urtizberea, A., Silva, N.J.D.O., Boesecke, P., Natividad, E., Palacio, F. *et al.* (2007) Multiple-length-scale small-angle X-ray scattering analysis on maghemite nanocomposites. *Journal of Applied Crystallography*, **40** (Suppl.), s696–s700.

124 Chaker, J.A., Dahmouche, K., Santilli, C.V., Pulcinelli, S.H., and Craievich, A. (2003) Gelation and drying of weakly bonded silica–PPO nanocomposites. *Journal of Applied Crystallography*, **36**, 689–693.

125 Mélé, P., Marceau, S., Brown, D., De Puydt, Y., and Albérola, N.D. (2002) Reinforcement effects in fractal-structure-filled rubber. *Polymer*, **43**, 5577–5586.

126 Matejka, L., Dukh, O., and Kolařik, J. (2000) Reinforcement of crosslinked rubbery epoxies by *in-situ* formed silica. *Polymer*, **41**, 1449–1459.

127 Suryawanshi, C.N., Pakdel, P., and Schaefer, D.W. (2003) Effect of drying on the structure and dispersion of precipitated silica. *Journal of Applied Crystallography*, **36**, 573–577.

128 Schaefer, D.W., Zhao, J., Brown, J.M., Anderson, D.P., and Tomlin, D.W. (2003) Morphology of dispersed carbon single-walled nanotubes. *Chemical Physics Letters*, **375**, 369–375.

129 Zhou, W., Islam, M.F., Wang, H., Ho, D.L., Yodh, A.G., Winey, K.I. *et al.* (2004) Small angle neutron scattering from single-wall carbon nanotube suspensions: evidence for isolated rigid rods and rod networks. *Chemical Physics Letters*, **384**, 185–189.

130 Hernández, J.J., Garcia-Gutiérrez, M.C., Nogales, A., Rueda, D.R., and Ezquerra, T.A. (2006) Small-angle X-ray scattering of single-wall carbon nanotubes dispersed in molten poly(ethylene terephthalate). *Composites Science and Technology*, **66**, 2629–2632.

131 Bauer, B.J., Hobbie, E.K., and Becker, M.L. (2006) Small-angle neutron scattering from labeled single-wall carbon nanotubes. *Macromolecules*, **39**, 2637–2642.

132 Mandelbrot, B.B. (1982) *The Fractal Geometry of Nature*, W. H. Freeman and Company, San Francisco.

133 Tian, D., Blacher, S., and Jerome, R. (1999) Biodegradable and biocompatible inorganic–organic hybrid materials: 4. Effect of acid content and water content on the incorporation of aliphatic polyesters into silica by the sol–gel process. *Polymer*, **40**, 951–957.

134 Martin, J.E. and Hurd, A.J. (1987) Scattering from fractals. *Journal of Applied Crystallography*, **20**, 61–78.

135 Guinier, A. (1963) *X-Ray Diffraction*, W. H. Freeman and Company, San Francisco.

136 Beaucage, G. and Schaefer, D.W. (1994) Structural studies of complex systems using small-angle scattering: a unified Guinier/power-law approach. *Journal of Non-Crystalline Solids*, **172**, 797–805.

137 Beaucage, G. (1995) Approximations leading to a unified exponential/power-

law approach to small-angle scattering. *Journal of Applied Crystallography*, **28**, 717–728.

138 Beaucage, G. (1996) Small-angle scattering from polymeric mass fractals of arbitrary mass-fractal dimension. *Journal of Applied Crystallography*, **29**, 134–146.

139 Blundell, D. (1978) Models for small-angle X-ray scattering from highly dispersed lamellae. *Polymer*, **19**, 1258–1266.

140 Marega, C., Marigo, A., Cingano, G., Zannetti, R., and Paganetto, G. (1996) Small-angle X-ray scattering from high-density polyethylene: lamellar thickness distributions. *Polymer*, **37**, 5549–5557.

141 Marigo, A., Marega, C., Zannetti, R., and Sgarzi, P. (1998) A study of the lamellar thickness distribution in 1-butene. 4-methyl-1-pentene and 1-hexene LLDPE by small and wide angle X-ray scattering and transmission electron microscopy. *European Polymer Journal*, **34**, 597–603.

142 Marega, C., Marigo, A., and Causin, V. (2003) Small-angle X-ray scattering from polyethylene: distorted lamellar structures. *Journal of Applied Polymer Science*, **90**, 2400–2407.

143 Hosemann, R. and Bagchi, S.N. (1962) *Direct Analysis of Diffraction by Matter*, North Holland, Amsterdam.

144 Neppalli, N., Marega, C., Marigo, A., Bajgai, M.P., Kim, H.Y., and Causin, V. (2010) Poly(epsilon-caprolactone) filled with electrospun nylon fibres: a model for a facile composite fabrication. *European Polymer Journal*, **46**, 968–976.

145 Causin, V., Yang, B.X., Marega, C., Goh, S.H., and Marigo, A. (2009) Nucleation, structure and lamellar morphology of isotactic polypropylene filled with polypropylene-grafted multiwalled carbon nanotubes. *European Polymer Journal*, **45**, 2155–2163.

146 Marega, C., Causin, V., Marigo, A., and Ferrara, G. (2009) Reduction in tactoid size as a means for reinforcing high density polyethylene/montmorillonite nanocomposites. *Journal of Applied Polymer Science*, **113**, 3920–3928.

147 Causin, V., Yang, B.X., Marega, C., Goh, S.H., and Marigo, A. (2008) Structure–property relationship in polyethylene reinforced by polyethylene-grafted multiwalled carbon nanotubes. *Journal of Nanoscience and Nanotechnology*, **8**, 1790–1796.

148 Causin, V., Marega, C., Marigo, A., Ferrara, G., and Ferraro, A. (2006) Morphological and structural characterization of polypropylene/conductive graphite nanocomposites. *European Polymer Journal*, **42**, 3153–3161.

149 Preschilla, N., Sivalingam, G., Rasheed, A.S.A., Tyagi, S., Biswas, A., and Bellare, J.R. (2008) Quantification of organoclay dispersion and lamellar morphology in poly(propylene)–clay nanocomposites with small angle X-ray scattering. *Polymer*, **49**, 4285–4297.

150 Marega, C., Causin, C., Marigo, A., Saini, R., and Ferrara, G. (2010) Crystallization of a (1-butene)–ethylene copolymer in Phase I directly from the melt in nanocomposites with montmorillonite. *Journal of Nanoscience and Nanotechnology*, **10**, 3078–3084.

151 Marega, C., Causin, V., and Marigo, A. (2008) A SAXS–WAXD study on the mesomorphic-α transition of isotactic polypropylene. *Journal of Applied Polymer Science*, **109**, 32–37.

152 Saravanan, P., Premkumar, M., Singh, A.K., Gopalan, R., and Chandrasekaran, V. (2009) Study on morphology and magnetic behavior of SMCo5 and SMCo5/Fe nanoparticles synthesized by surfactant-assisted ball milling. *Journal of Alloys and Compounds*, **480**, 645–649.

153 Bandyopadhyay, J. and Ray, S.S. (2010) The quantitative analysis of nano-clay dispersion in polymer nanocomposites by small angle X-ray scattering combined with electron microscopy. *Polymer*, **51**, 1437–1449.

154 Strobl, G.R. and Schneider, M. (1980) Direct evaluation of the electron density correlation function of partially crystalline polymers. *Journal of Polymer Science Part B: Polymer Physics*, **18**, 1343–1359.

155 Lincoln, D.M., Vaia, R.A., Wang, Z.G., Hsiao, B.S., and Krishnamoorti, R. (2001) Temperature dependence of polymer crystalline morphology in nylon 6. *Polymer*, **42**, 9975–9985.

156 Lincoln, D.M., Vaia, R.A., and Krishnamoorti, R. (2004) Isothermal crystallization of nylon-6. *Macromolecules*, **37**, 4554–4561.

157 Bafna, A., Beaucage, G., Mirabella, F., and Mehta, S. (2003) 3D hierarchical orientation in polymer–clay nanocomposite films. *Polymer*, **44**, 1103–1115.

158 Jimenez, G., Ogata, N., Kawai, H., and Ogihara, T. (1997) Structure and thermal/mechanical properties of poly (ε-caprolactone)–clay blend. *Journal of Applied Polymer Science*, **64**, 2211–2220.

159 Kiersnowski, A., Gutmann, J.S., and Pigtowski, J. (2007) Influence of organic modifiers on morphology and crystallization of poly(epsilon-caprolactone)/synthetic clay intercalated nanocomposites. *Journal of Polymer Science Part B: Polymer Physics*, **45**, 2350–2367.

160 Reddy, K.R., Tashiro, K., Sakurai, T., Yamaguchi, N., Sasaki, S., Masunaga, H. *et al.* (2009) Isothermal crystallization behavior of isotactic polypropylene H/D blends as viewed from time-resolved FTIR and synchrotron SAXS/WAXD measurements. *Macromolecules*, **42**, 4191–4199.

161 Hsiao, M., Zheng, J.X., Horn, R.M.V., Quirk, R.P., Thomas, E.L., Chen, H. *et al.* (2009) Poly(ethylene oxide) crystal orientation change under 1D nanoscale confinement using polystyrene-block-poly (ethylene oxide) copolymers: confined dimension and reduced tethering, density effects. *Macromolecules*, **42**, 8343–8352.

162 Hu, J., Huang, L., Lang, L., Liu, Y., Zhuang, X., Chen, X. *et al.* (2009) The study of electroactive block copolymer containing aniline pentamer isolated from different solvents. *Journal of Polymer Science Part A: Polymer Chemistry*, **47**, 1298–1307.

163 Kim, G.S., Son, J.M., Lee, J.K., and Lee, K.H. (2010) Morphology development and crystallization behavior of poly(ethylene terephthalate)/poly(trimethylene terephthalate) blends. *European Polymer Journal*, **46**, 1696–1704.

164 Lee, S.S. and Phillips, P.J. (2007) Melt crystallized polyamide 6.6 and its copolymers, Part I. Melting point – lamellar thickness relations in the homopolymer. *European Polymer Journal*, **43**, 1933–1951.

165 Abdul Rasheed, A.S., Preschilla, N., Sivalingam, G., Tyagi, S., Biswas, A., and Bellare, J.R. (2009) SAXS analysis of polypropylene-layered silicate nanocomposites: an integrated correlations functions approach using an exfoliation factor. *Journal of Nanoscience and Nanotechnology*, **9**, 4948–4960.

166 Herrmann, W., Uhl, C., Heinrich, G., and Jehnichen, D. (2006) Analysis of HNBR–montmorillonite nanocomposites: morphology, orientation and macroscopic properties. *Polymer Bulletin*, **57**, 395–405.

167 Ehrburger-Dolle, F., Hindermann-Bischoff, M., Livet, F., Bley, F., Rochas, C., and Geissler, E. (2001) Anisotropic ultra-small-angle X-ray scattering in carbon black filled polymers. *Langmuir*, **17**, 329–334.

168 Chen, X., Burger, C., Fang, D., Sics, I., Wang, X., He, W. *et al.* (2006) *In-situ* X-ray deformation study of fluorinated multiwalled carbon nanotube and fluorinated ethylene–propylene nanocomposite fibers. *Macromolecules*, **39**, 5427–5437.

169 Ha, Y.H. and Thomas, E.L. (2002) Deformation behavior of a roll-cast layered-silicate/lamellar triblock copolymer nanocomposite. *Macromolecules*, **35**, 4419–4428.

170 Lee, J.Y., Park, M.S., Yang, H.C., Cho, K., and Kim, J.K. (2003) Alignment and orientational proliferation of HEX cylinders in a polystyrene-block-polyisoprene-block-polystyrene copolymer in the presence of clay. *Polymer*, **44**, 1705–1710.

171 Wang, W., Murthy, N.S., Chae, H.G., and Kumar, S. (2009) Small-angle X-ray scattering investigation of carbon nanotube-reinforced polyacrylonitrile fibers during deformation. *Journal of Polymer Science Part B: Polymer Physics*, **47**, 2394–2409.

172 Li, X., Schneider, K., Kretzschmar, B., and Stamm, M. (2008) Deformation behavior of PP and PP/ZnO nanocomposites as

studied by SAXS and WAXS. *Macromolecules*, **41**, 4371–4379.

173 Dencheva, N., Denchev, Z., Oliveira, M.J., Nunes, T.G., and Funari, S.S. (2008) Relationship between the crystalline structure and mechanical behavior in isotropic and oriented polyamide 12. *Journal of Applied Polymer Science*, **109**, 288–302.

174 Kawakami, D., Burger, C., Ran, S., Avila-Orta, C., Sics, I., Chu, B. *et al.* (2008) New insights into lamellar structure development and SAXS/WAXD sequence appearance during uniaxial stretching of amorphous poly(ethylene terephthalate) above glass transition temperature. *Macromolecules*, **41**, 2859–2867.

175 He, C., Liu, T., Tjiu, W.C., Sue, H., and Yee, A.F. (2008) Microdeformation and fracture mechanisms in polyamide-6/organoclay nanocomposites. *Macromolecules*, **41**, 193–202.

176 Zhao, Y., Saijo, K., Takenaka, M., Koizumi, S., and Hashimoto, T. (2009) Time-resolved SAXS studies of self-assembling process of palladium nanoparticles in templates of polystyrene-block-polyisoprene melt: effects of reaction fields on the self-assembly. *Polymer*, **50**, 2696–2705.

177 Tanaka, H., Koizumi, S., Hashimoto, T., Itoh, H., Satoh, M., Naka, K. *et al.* (2007) Combined *in situ* and time-resolved SANS and SAXS studies of chemical reactions at specific sites and self-assembling processes of reaction products: reduction of palladium ions in self-assembled polyamidoamine dendrimers as a template. *Macromolecules*, **40**, 4327–4337.

178 Zucchi, I.A., Hoppe, C.E., Galante, M.J., Williams, R.J.J., Lopez-Quintela, M.A., Matejka, L. *et al.* (2008) Self-assembly of gold nanoparticles as colloidal crystals induced by polymerization of amphiphilic monomers. *Macromolecules*, **41**, 4895–4903.

179 Ikeda, Y., Yasuda, Y., Yamamoto, S., and Morita, Y. (2007) Study on two-dimensional small-angle X-ray scattering of *in situ* silica filled nanocomposite elastomer during deformation. *Journal of Applied Crystallography*, **40** (Suppl.), s549–s552.

180 Morfin, I., Ehrburger-Dolle, F., Grillo, I., Livet, F., and Bley, F. (2006) ASAXS, SAXS and SANS investigations of vulcanized elastomers filled with carbon black. *Journal of Synchrotron Radiation*, **13**, 445–452.

181 Shinohara, Y., Kishimoto, H., Inoue, K., Suzuki, Y., Takeuchi, A., Uesugi, K. *et al.* (2007) Characterization of two-dimensional ultra-small-angle X-ray scattering apparatus for application to rubber filled with spherical silica under elongation. *Journal of Applied Crystallography*, **40**, s397–s401

182 Toki, S., Sics, I., Hsiao, B.S., Tosaka, M., Poompradub, S., Ikeda, Y. *et al.* (2005) Probing the nature of strain-induced crystallization in polyisoprene rubber by combined thermomechanical and *in situ* X-ray diffraction techniques. *Macromolecules*, **38**, 7064–7073.

183 Tosaka, M., Senoo, K., Kohjiya, S., and Ikeda, Y. (2007) Crystallization of stretched network chains in cross-linked natural rubber. *Journal of Applied Physics*, **101**, 084909.

184 Trabelsi, S., Albouy, P.-A., and Rault, J. (2003) Crystallization and melting processes in vulcanized stretched natural rubber. *Macromolecules*, **36**, 7624–7639.

185 Poompradub, S., Tosaka, M., Kohjiya, S., Ikeda, Y., Toki, S., Sics, I. *et al.* (2005) Mechanism of strain-induced crystallization in filled and unfilled natural rubber vulcanizates. *Journal of Applied Physics*, **97**, 103529.

186 Trabelsi, S., Albouy, P.-A., and Rault, J. (2003) Effective local deformation in stretched filled rubber. *Macromolecules*, **36**, 9093–9099.

187 Gesti, S., Zanetti, M., Lazzari, M., Franco, L., and Puiggali, J. (2009) Degradable polyoctamethylene suberate/clay nanocomposites. Crystallization studies by DSC and simultaneous SAXS/WAXD synchrotron radiation. *European Polymer Journal*, **45**, 398–409.

188 Su, C.H., Jeng, U., Chen, S.H., Cheng, C.-Y., Lee, J.-J., Lee, Y.-H. *et al.* (2009) Thermodynamic characterization of polymorphs in bulk-crystallized syndiotactic polystyrene via small/wide-angle X-ray scattering and differential

scanning calorimetry. *Macromolecules*, **42**, 4200–4207.

189 Garcia-Gutierrez, M.C., Hernandez, J.J., Nogales, A., Pantine, P., Rueda, D.R., and Ezquerra, T.A. (2008) Influence of shear on the templated crystallization of poly (butylene terephthalate)/single wall carbon nanotube nanocomposites. *Macromolecules*, **41**, 844–851.

190 Shin, Y.H., Lee, W.D., and Im, S.S. (2007) Effect of A-zeolite on the crystallization behavior of *in-situ* polymerized poly (ethylene terephthalate) (PET) nanocomposites. *Macromolecular Research*, **15**, 662–670.

191 Patil, N., Balzano, L., Portale, G., and Rastogi, S. (2009) Influence of nanoparticles on the rheological behaviour and initial stages of crystal growth in linear polyethylene. *Macromolecular Chemistry and Physics*, **210**, 2174–2187.

192 Chang, S.L., Yu, T.L., Huang, C.C., Chen, W.C., Linliu, K., and Lin, T.L. (1998) Effect of polyester side-chains on the phase segregation of polyurethanes using small-angle X-ray scattering. *Polymer*, **39**, 3479–3489.

193 Yu, H., Natansohn, A., Singh, M.A., and Plivelic, T. (1999) A comparative study using small-angle X-ray scattering and solid-state NMR of microdomain structures in poly (styrene−butadiene−styrene) triblock copolymers. *Macromolecules*, **32**, 7562–7571.

194 Tonelli, C., Ajroldi, G., Marigo, A., Marega, C., and Turturro, A. (2001) Synthesis methods of fluorinated polyurethanes. 2. Effects on morphology and microstructure. *Polymer*, **42**, 9705–9711.

195 Laity, P.R., Taylor, J.E., Wong, S.S., Khunkamchoo, P., Norris, K., Cable, M. *et al.* (2004) A review of small-angle scattering models for random segmented poly(ether-urethane) copolymers. *Polymer*, **45**, 5215–5232.

196 Song, M., Xia, H.S., Yao, K.J., and Hourston, D.J. (2005) A study on phase morphology and surface properties of polyurethane/organoclay nanocomposite. *European Polymer Journal*, **41**, 259–266.

197 Stefik, M., Mahajan, S., Sai, H., Epps, T., Bates, F.S., Gruner, S.M. *et al.* (2009) Ordered three- and five-ply nanocomposites from ABC block terpolymer microphase separation with niobia and aluminosilicate sols. *Chemistry of Materials*, **21**, 5466–5473.

198 Stefik, M., Sai, H., Sauer, K., Gruner, S.M., DiSalvo, F.J., and Wiesner, U. (2009) Three-component porous–carbon–titania nanocomposites through self-assembly of ABCBA block terpolymers with titania sols. *Macromolecules*, **42**, 6682–6687.

199 Hu, Y., Yusufoglu, Y., Kanapathipillai, M., Yang, C., Wu, Y., Thiyagarajan, P. *et al.* (2009) Self-assembled calcium phosphate nanocomposites using block copolypeptide templates. *Soft Matter*, **5**, 4311–4320.

200 Liu, Y.R. (2009) One-pot route to synthesize ordered mesoporous polymer/silica and carbon/silica nanocomposites using poly (dimethylsiloxane)–poly(ethylene oxide) (PDMS–PEO) as co-template. *Microporous and Mesoporous Materials*, **124**, 190–196.

201 Li, Y. and Shimizu, H. (2009) Toward a stretchable, elastic, and electrically conductive nanocomposite: morphology and properties of poly[styrene-*b*-(ethylene-*co*-butylene)-*b*-styrene]/multiwalled carbon nanotube composites fabricated by high-shear processing. *Macromolecules*, **42**, 2587–2593.

202 Ganguly, A., Bhowmick, A.K., and Li, Y. (2008) Insights into montmorillonite nanoclay based *ex situ* nanocomposites from SEBS and modified SEBS by small-angle X-ray scattering and modulated DSC studies. *Macromolecules*, **41**, 6246–6253.

203 Zhang, K., Gao, L., and Chen, Y. (2007) Organic–inorganic hybrid materials by self-gelation of block copolymer assembly and nanoobjects with controlled shapes thereof. *Macromolecules*, **40**, 5916–5922.

204 Costanzo, P.J. and Beyer, F.L. (2007) Thermally driven assembly of nanoparticles in polymer matrices. *Macromolecules*, **40**, 3996–4001.

205 Samanta, S., Chatterjee, D.P., Manna, S., Mandal, A., Garai, A., and Nandi, A.K. (2009) Multifunctional hydrophilic

poly(vinylidene fluoride) graft copolymer with supertoughness and supergluing properties. *Macromolecules*, **42**, 3112–3120.

206 Choi, A.K., Kim, Y.W., Koh, J.H., Kim, J.H., and Mayes, A.M. (2007) Synthesis and characterization of nanocomposite films consisting of vanadium oxide and microphase-separated graft copolymer. *Macromolecular Research*, **15**, 553–559.

207 Kim, Y.W., Lee, D.K., Lee, K.J., Min, B.R., and Kim, J.H. (2007) *In situ* formation of silver nanoparticles within an amphiphilic graft copolymer film. *Journal of Polymer Science Part B: Polymer Physics*, **45**, 1283–1290.

208 Arridge, R.G.C. and Folkes, M.J. (1972) The mechanical properties of a 'single crystal' of SBS copolymer – a novel composite material. *Journal of Physics D: Applied Physics*, **5**, 344–360.

209 Folkes, M.J., Keller, A., and Scalisi, F.P. (1973) An extrusion technique for the preparation of "single-crystals" of block copolymers. *Colloid and Polymer Science*, **251**, 1–4.

210 Lee, C.H., Kim, H.B., Lim, S.T., Kim, H. S., Kwon, Y.K., and Choi, H.J. (2006) Ordering behavior of layered silicate nanocomposites with a cylindrical triblock copolymer. *Macromolecular Chemistry and Physics*, **207**, 444–445.

211 Hamley, I.W. (1998) *The Physics of Block Copolymers*, Oxford University Press, Oxford.

212 Hammouda, B. (2009) *Probing nanoscale structures – the SANS toolbox*, http:www.ncnr.nist.gov/staff/hammouda/the_sans_toolbox.pdf (accessed March 10th, 2013).

213 Sena, D., Khan, A., Bahadur, J., Mazumder, S., and Sapra, B.K. (2010) Use of small-angle neutron scattering to investigate modifications of internal structure in self-assembled grains of nanoparticles synthesized by spray drying. *Journal of Colloid and Interface Science*, **347**, 25–30.

214 Bahadur, J., Sen, D., Mazumder, S., Parkash, J., Sathiyamoorthy, D., and Venugopalan, R. (2010) Decoration of carbon nanotubes with metal nanoparticles by wet chemical method: a small-angle neutron scattering study. *Journal of Nanoscience and Nanotechnology*, **10**, 2963–2971.

215 Zhao, J., Shi, D.L., and Lian, J. (2009) Small angle light scattering study of improved dispersion of carbon nanofibers in water by plasma treatment. *Carbon*, **47**, 2329–2336.

216 Lazzara, G., Milioto, S., Gradzielski, M., and Prevost, S. (2009) Small angle neutron scattering, X-ray diffraction, differential scanning calorimetry, and thermogravimetry studies to characterize the properties of clay nanocomposites. *Journal of Physical Chemistry C*, **113**, 12213–12219.

217 Singh, P.S. and Aswal, V.K. (2008) Probing polymer nanocomposite morphology by small angle neutron scattering. *Pramana: Journal of Physics*, **71**, 947–952.

218 Yoonessi, M., Toghiani, H., Daulton, T.L., Lin, J.S., and Pittman, C.U. (2005) Clay delamination in clay/poly (dicyclopentadiene) nanocomposites quantified by small angle neutron scattering and high-resolution transmission electron microscopy. *Macromolecules*, **38**, 818–831.

219 Yoonessi, M., Toghiani, H., Wheeler, R., Porcar, L., Kline, S., and Pittman, C.U. (2008) Neutron scattering, electron microscopy and dynamic mechanical studies of carbon nanofiber/phenolic resin composites. *Carbon*, **46**, 577–588.

220 Wilson, K.S., Allen, A.J., Washburn, N.R., and Antonucci, J.M. (2007) Interphase effects in dental nanocomposites investigated by small-angle neutron scattering. *Journal of Biomedical Materials Research Part A*, **81A**, 113–123.

221 Stefanescu, E.A., Dundigalla, A., Ferreiro, V., Loizou, E., Porcar, L., Negulescu, I. *et al.* (2006) Supramolecular structures in nanocomposite multilayered films. *Physical Chemistry Chemical Physics*, **8**, 1739–1746.

222 Tanaka, H., Hashimoto, T., Koizumi, S., Itoh, H., Naka, K., and Chujo, Y. (2008) Control of self-assembling processes of polyamidoamine dendrimers and Pd nanoparticles. *Macromolecules*, **41**, 1815–1824.

223 Yamauchi, K., Akasaka, S., Hasegawa, H., Koizumi, S., Deeprasertkul, C., Laokijcharoen, P. *et al.* (2005) Structural study of natural rubber thermoplastic elastomers and their composites with carbon black by small-angle neutron scattering and transmission electron microscopy. *Composites Part A: Applied Science and Manufacturing*, **36**, 423–429.

224 Matsunaga, T., Endo, H., Takeda, M., and Shibayama, M. (2010) Microscopic structure analysis of clay–poly(ethylene oxide) mixed solution in a flow field by contrast-variation small-angle neutron scattering. *Macromolecules*, **43**, 5075–5082.

225 Osaka, N., Endo, H., Nishida, T., Suzuki, T., Li, H., Haraguchi, K. *et al.* (2009) Microphase separation in nanocomposite gels. *Physical Review E*, **79**, 060801.

226 Endo, H., Miyazaki, S., Haraguchi, K., and Shibayama, M. (2008) Structure of nanocomposite hydrogel investigated by means of contrast variation small-angle neutron scattering. *Macromolecules*, **41**, 5406–5411.

227 Endo, H., Schwahn, D., and Cölfen, J. (2004) On the role of block copolymer additives for calcium carbonate crystallization: small angle neutron scattering investigation by applying contrast variation. *Journal of Chemical Physics*, **120**, 9410–9423.

228 Doe, C., Jang, H.S., Kline, S.R., and Choi, S.M. (2010) SANS investigation of selectively distributed single-walled carbon nanotubes in a polymeric lamellar phase. *Macromolecules*, **43**, 5411–5416.

229 Loizou, E., Porcar, L., Schexnailder, P., Schmidt, G., and Butler, P. (2010) Shear-induced nanometer and micrometer structural responses in nanocomposite hydrogels. *Macromolecules*, **43**, 1041–1049.

230 Boue, F., Cousin, F., Gummel, J., Oberdisse, J., Carrot, G., and El Harrak, A. (2007) Small angle scattering from soft matter – application to complex mixed systems. *Comptes Rendus Physique*, **8**, 821–844.

231 Shibayama, M., Karino, T., Miyazaki, S., Okabe, S., Takehisa, T., and Haraguchi, K. (2005) Small-angle neutron scattering study on uniaxially stretched poly(*N*-isopropylacrylamide)–clay nanocomposite gels. *Macromolecules*, **38**, 10772–10781.

232 Saric, M., Dietsch, H., and Schurtenberger, P. (2006) *In situ* polymerisation as a route towards transparent nanocomposites: time-resolved light and neutron scattering experiments. *Colloids and Surfaces A: Physicochemical and Engineering Aspects*, **291**, 110–116.

233 Tanaka, H., Koizumi, S., Hashimoto, T., Itoh, H., Satoh, M., Naka, K. *et al.* (2007) Combined *in situ* and time-resolved SANS and SAXS studies of chemical reactions at specific sites and self-assembling processes of reaction products: reduction of palladium ions in self-assembled polyamidoamine dendrimers as a template. *Macromolecules*, **40**, 4327–4337.

234 Fullerton-Shirey, S.K. and Maranas, J.K. (2010) Structure and mobility of $PEO/LiClO_4$ solid polymer electrolytes filled with Al_2O_3 nanoparticles. *Journal of Physical Chemistry C*, **114**, 9196–9206.

235 Wong, H.C., Sanz, A., Douglas, J.F., and Cabral, J.T. (2010) Glass formation and stability of polystyrene–fullerene nanocomposites. *Journal of Molecular Liquids*, **153**, 79–87.

236 Anastasiadis, S.H., Chrissopoulou, K., and Frick, B. (2008) Structure and dynamics in polymer/layered silicate nanocomposites. *Materials Science and Engineering B: Advanced Functional Solid-State Materials*, **152**, 33–39.

237 Sanz, A., Ruppel, M., Douglas, J.F., and Cabral, J.T. (2008) Plasticization effect of C-60 on the fast dynamics of polystyrene and related polymers: an incoherent neutron scattering study. *Journal of Physics: Condensed Matter*, **20** (10), 104209.

238 Botana, A., Mollo, M., Eisenberg, P., and Torres Sanchez, R.M. (2010) Effect of modified montmorillonite on biodegradable PHB nanocomposites. *Applied Clay Science*, **47**, 263–270.

239 Liu, G., Wang, H., Yang, X., and Li, L. (2009) Synthesis of tri-layer hybrid microspheres with magnetic core and functional polymer shell. *European Polymer Journal*, **45**, 2023–2032.

240 Wei, Q., Ji, J., and Shen, J. (2008) Synthesis of near-infrared responsive gold

nanorod/PNIPAAm core/shell nanohybrids via surface initiated ATRP for smart drug delivery. *Macromolecular Rapid Communications*, **29**, 645–650.

241 Li, P. and Huang, J. (2008) Preparation of poly (ethylene oxide)-graft-poly(acrylic acid) copolymer stabilized iron oxide nanoparticles via an *in situ* templated process. *Journal of Applied Polymer Science*, **109**, 501–507.

242 Sawada, H., Furukuwa, R., Sasazawa, K., Mugisawa, M., and Ohnishi, K. (2007) Preparation of novel cross-linked fluoroalkyl end-capped adamantane cooligomer/copper nanocomposites. *European Polymer Journal*, **43**, 3258–3263.

243 Kim, J.K., Yoon, K.H., Bang, D.S., Park, Y., Kim, H., and Bang, Y. (2008) Morphology and rheological behaviors of poly(ethylene terephthalate) nanocomposites containing polyhedral oligomeric silsesquioxanes. *Journal of Applied Polymer Science*, **107**, 272–279.

244 Liu, W.F., Guo, Z.X., and Yu, J. (2005) Preparation of crosslinked composite nanoparticles. *Journal of Applied Polymer Science*, **97**, 1538–1544.

245 Zhang, H., Su, Z., Liu, P., and Zhang, F. (2007) Preparation and property of raspberry-like AS/SiO_2 nanocomposite particles. *Journal of Applied Polymer Science*, **104**, 415–421.

246 Liu, T.Q., Jia, S.J., Kowalewski, T., Matyjaszewski, K., Casado-Portilla, R., and Belmont, J. (2006) Water-dispersible carbon black nanocomposites prepared by surface-initiated atom transfer radical polymerization in protic media. *Macromolecules*, **39**, 548–556.

247 Huglin, M.B. (1972) *Light Scattering from Polymer Solutions*, Academic Press, London.

248 Cowie, J.M.G. and Arrighi, V. (2007) *Polymers: Chemistry and Physics of Modern Materials*, 3rd edn, CRC Press, Boca Raton, FL.

249 Prasad, R., Gupta, R.K., Cser, F., and Bhattacharya, S.N. (2009) Investigation of melt extensional deformation of ethylene–vinyl acetate nanocomposites using small-angle light scattering. *Polymer Engineering and Science*, **49**, 984–992.

250 Braun, B., Dorgan, J.R., and Chandler, J.P. (2008) Cellulosic nanowhiskers. Theory and application of light scattering from polydisperse spheroids in the Rayleigh–Gans–Debye regime. *Biomacromolecules*, **9**, 1255–1263.

251 Berne, B.J. and Pecora, R. (2000) *Dynamic Light Scattering with Applications to Chemistry, Biology and Physics*, Dover Publications, Mineola, NY.

252 Brown, W. (ed.) (1993) *Dynamic Light Scattering, the Methods and Applications*, Clarendon Press, Oxford.

253 Ben Elmabrouk, A., Wim, T., Dufresne, A., and Boufi, S. (2009) Preparation of poly(styrene-*co*-hexylacrylate)/cellulose whiskers nanocomposites via miniemulsion polymerization. *Journal of Applied Polymer Science*, **114**, 2946–2955.

254 Chemtob, A., Croutxe-Barghorn, C., Soppera, O., and Rigolet, S. (2009) Cationic photopolymerization in presence of functionalized silica nanoparticles. *Macromolecular Chemistry and Physics*, **210**, 1127–1137.

255 Mueller, W., Koynov, K., Fischer, K., Hartmann, S., Pierrat, S., Basche, T. *et al.* (2009) Hydrophobic shell loading of PB-*b*-PEO vesicles. *Macromolecules*, **42**, 357–361.

256 Sawada, H., Sasaki, A., Sasazawa, K., Toriba, K., Kakehi, H., Miura, M. *et al.* (2008) Preparation of colloidal stable fluoroalkyl end-capped oligomer/silver nanocomposites – application to the surface modification of traditional organic polymers with these nanocomposites. *Polymers for Advanced Technologies*, **19**, 419–424.

257 Chai, S.L. and Tan, H.M. (2008) Structure and property characterization of nanograde core-shell polyurethane/polyacrylate composite emulsion. *Journal of Applied Polymer Science*, **107**, 3499–3504.

258 Zong, Z.G., Soucek, M.D., and Xue, C.C. (2005) Unusual inorganic phase formation in ultraviolet-curable organic–inorganic hybrid films. *Journal of Polymer Science Part A: Polymer Chemistry*, **43**, 1607–1623.

259 Moraes, R.P., Valera, T.S., Demarquette, N.R., Oliveira, P.C., da Silva, M.L.C.P.,

and Santos, A.M. (2009) Influence of granulometry and organic treatment of a Brazilian montmorillonite on the properties of poly(styrene-*co*-*n*-butyl acrylate)/layered silicate nanocomposites prepared by miniemulsion polymerization. *Journal of Applied Polymer Science*, **112**, 1949–1958.

260 Vale, J.M., Justice, R.S., Schaefer, D.W., and Mark, J.E. (2005) Calcium alginate barrier films modified by montmorillonite clay. *Journal of Macromolecular Science: Physics*, **B44**, 821–831.

261 Nie, J.J., Du, B.Y., and Oppermann, W. (2005) Swelling, elasticity, and spatial inhomogeneity of poly(*N*-isopropylacrylamide)/clay nanocomposite hydrogels. *Macromolecules*, **38**, 5729–5736.

262 Kalinina, N.A., Silinskaya, I.G., Kipper, A.I., Valueva, S.V., Kopeikin, V.V., and Filippov, A.P. (2004) Structuring in aqueous solutions of anionic polyelectrolyte nanocomposites with zero-valence selenium nanoparticles: a polarized light scattering study. *Polymer Science Series A*, **46**, 857–862.

263 Shibayama, M., Suda, J., Karino, T., Okabe, S., Takehisa, T., and Haraguchi, K. (2004) Structure and dynamics of poly(*N*-isopropylacrylamide)–clay nanocomposite gel. *Macromolecules*, **37**, 9606–9612.

264 Negrete-Herrera, N., Putaux, J., David, L., and Bourgeat-Lami, E. (2006) Polymer/laponite composite colloids through emulsion polymerization: influence of the clay modification level on particle morphology. *Macromolecules*, **39**, 9177–9184.

265 Okay, O. and Oppermann, W. (2007) Polyacrylamide–clay nanocomposite hydrogels: rheological and light scattering characterization. *Macromolecules*, **40**, 3378–3387.

266 Peng, M., Li, D., Chen, Y., and Zheng, Q. (2007) Effect of an organoclay on the reaction-induced phase-separation kinetics and morphology of a poly(ether imide)/epoxy mixture. *Journal of Applied Polymer Science*, **104**, 1205–1214.

267 Aoki, Y., Norisuye, T., Tran-Cong-Miyata, Q., Nomura, S., and Sugimoto, T. (2003) Dynamic light scattering studies on network formation of bridged polysilsesquioxanes catalyzed by polyoxometalates. *Macromolecules*, **36**, 9935–9942.

268 Badaire, S., Poulin, P., Maugey, M., and Zakri, C. (2004) *In situ* measurements of nanotube dimensions in suspensions by depolarized dynamic light scattering. *Langmuir*, **20**, 10367–10370.

269 Foster, R.J., Hine, P.J., and Ward, I.M. (2009) Characterisation and modelling of polypropylene/carbon nanofibre nanocomposites. *Polymer*, **50**, 4018–4027.

270 Branca, C., Magazù, V., and Mangione, A. (2005) Determination of MWNTs length-to-diameter ratio by static and dynamic light scattering. *Diamonds and Related Materials*, **14**, 846–849.

271 Lima, M.M.D. and Borsali, R. (2004) Rodlike cellulose microcrystals: structure, properties, and applications. *Macromolecular Rapid Communications*, **25**, 771–787.

272 Braun, B. and Dorgan, J.R. (2009) Single-step method for the isolation and surface functionalization of cellulosic nanowhiskers. *Biomacromolecules*, **10**, 334–341.

273 Naga, N., Kihara, Y., Miyanaga, T., and Furukawa, H. (2009) Synthesis of organic–inorganic hybrid gels from siloxane or silsesquioxane and alpha, omega-nonconjugated dienes by means of a photo hydrosilylation reaction. *Macromolecules*, **42**, 3454–3462.

274 Naga, N., Oda, E., Toyota, A., and Furukawa, H. (2007) Mesh size control of organic–inorganic hybrid gels by means of a hydrosilylation co-gelation of siloxane or silsesquioxane and alpha, omega-non-conjugated dienes. *Macromolecular Chemistry and Physics*, **208**, 2331–2338.

275 Naga, N., Oda, E., Toyota, A., Horie, K., and Furukawa, H. (2006) Tailored synthesis and fundamental characterization of organic–inorganic hybrid gels by means of a hydrosilylation reaction. *Macromolecular Chemistry and Physics*, **207**, 627–635.

276 Furukawa, H., Horie, K., Nozaki, R., and Okada, M. (2003) Swelling-induced modulation of static and dynamic fluctuations in polyacrylamide gels observed by scanning microscopic light scattering. *Physical Review E*, **68**, 031406.

277 Katoh, Y. and Okamoto, M. (2009) Crystallization controlled by layered silicates in nylon 6–clay nano-composite. *Polymer*, **50**, 4718–4726.

278 Prasad, R., Pasanovic-Zujo, V., Gupta, R. K., Cser, F., and Bhattacharya, S.N. (2004) Morphology of EVA based nanocomposites under shear and extensional flow. *Polymer Engineering and Science*, **44**, 1220–1230.

279 Yalcin, B. and Cakmak, M. (2004) Superstructural hierarchy developed in coupled high shear/high thermal gradient conditions of injection molding in nylon 6 nanocomposites. *Polymer*, **45**, 2691–2710.

280 Misra, A. and Garg, S.N. (1986) Block copolymers of poly(ethylene terephthalate)–poly(butylene terephthalate). II. Small-angle light-scattering studies. *Journal of Polymer Science Part B: Polymer Physics*, **24**, 999–1008.

281 Lin, Y., Zhong, W., Shen, L., Xu, P., and Du, Q. (2005) Study on the relationship between crystalline structures and physical properties of polyamide-6. *Journal of Macromolecular Science: Physics*, **B44**, 161–175.

282 Li, J., Fang, Z., Zhu, Y., Tong, L., Gu, A., and Uu, F. (2007) Isothermal crystallization kinetics and melting behavior of multiwalled carbon nanotubes/polyamide-6 composites. *Journal of Applied Polymer Science*, **105**, 3531–3542.

283 Li, Y. and Akpalu, Y.A. (2004) Probing the melting behavior of a homogeneous ethylene/1-hexene copolymer by small-angle light scattering. *Macromolecules*, **37**, 7265–7277.

284 Xiao, Z.C., Li, Y., Ma, D.L., Schadler, L.S., and Akpalu, Y.A. (2006) Probing the use of small-angle light scattering for characterizing structure of titanium dioxide/low-density polyethylene nanocomposites. *Journal of Polymer Science Part B: Polymer Physics*, **44**, 1084–1095.

285 Xiao, Z., Li, Y., and Akpalu, Y.A. (2009) Enabling controlled dispersion in polyethylene nanocomposites using small-angle scattering. *Polymer Composites*, **30**, 559–568.

5
Mechanical–Viscoelastic Characterization in Nanocomposites

Vera Realinho, Marcelo Antunes, David Arencón, and José I. Velasco

5.1
Introduction

Since the first studies of polymer–clay nanocomposites, carried out by the research team at Toyota Automotive Corporation, much research has been performed on the incorporation of low and high aspect ratio nanofillers in polymers, and these have already demonstrated their capability to improve mechanical properties and other important properties such as wear resistance and electrical resistivity [1–4]. However, high material costs, complex processes, and limitations in production technology hamper the production and application of these nanocomposites on a large industrial scale.

Specifically, there are still difficulties in distributing individual nanoparticles homogeneously in the matrix, and thus clay nanoparticles need modification to enable intercalated structures (polymer molecules enter into the clay host galleries and the clay remains a regular gallery structure, although the basal spacing rises) or exfoliated structures (individual layers are dispersed in the matrix and segregated from one another, and the gallery structures are completely destroyed). These structures are usually studied by wide-angle X-ray diffraction (WAXD), dynamic mechanical thermal analysis (DMTA), and transmission electron microscopy (TEM). DMTA analysis is also a useful tool to reveal interactions between the matrix and the nanoparticles.

Nonetheless, these materials often sustain low fracture toughness restricting their widespread usage. This is because clay nanolayers restrict the mobility of the surrounding matrix chains and limit the plastic deformation of the polymer matrix. In general, to increase the fracture toughness, it is necessary to initiate several effective energy dissipation processes in the front of the crack tip such as crazing and shear yielding so that the total amount of plastic energy absorbed during fracture is high. The more brittle polymer nanocomposites can be characterized by the plane strain fracture toughness K_{Ic} obtained from the well-established linear elastic fracture mechanics (LEFM); however, even here due attention is not always given to obtaining valid K_{Ic} values, especially with respect to the specimen size,

Polymer Composites: Volume 2, First Edition. Edited by Sabu Thomas, Kuruvilla Joseph, Sant Kumar Malhotra, Koichi Goda, and Meyyarappallil Sadasivan Sreekala.

which is often minimized because nanocomposites are usually produced in rather small volumes. However, provided the standard test methods are strictly followed, there is no real difficulty in obtaining valid plane strain fracture toughness values. The more ductile polymer nanocomposites are characterized by the values of *J* integral, although later the essential work of fracture (EWF) gained acceptance. Fracture toughness characterization is also performed by using either analogical or instrumented impact tests (Izod, Charpy, falling weight), when a value of energy absorbed during rupture is given.

All these aspects have been overviewed in the following sections, preceded by a summary of the main factors affecting the mechanical behavior of nanocomposites and some modeling approaches that have been proposed.

5.2
Factors Affecting the Mechanical Behavior of Nanocomposites

Compared to the better known microcomposites, where mechanical enhancement is usually reached at the expense of other properties (e.g., stiffness and tensile strength improvement are conventionally attained in detriment of fracture toughness), nanosized fillers have been proven to allow, due to a high specific area interaction, a highly synergistic effect with the polymer chains, enabling the improvement of a wider combination of mechanical properties. Their extremely small size and high specific area do not create large stress concentrations as in the case of conventional microcomposites, thus limiting fracture toughness loss, in some cases even improving it [5–7].

Compared to microcomposites, where the mechanical behavior is mainly a function of the characteristics of filler and matrix and their respective concentrations, generally speaking, two major characteristics define the mechanical performance of polymer nanocomposites [8]: the nanoscale size and geometry of the fillers (aspect ratio) and their dispersion into the polymer matrix, and the interaction between the polymer chains and said nanofillers (interphase). This section highlights the influence of these two factors on the mechanical behavior of polymer nanocomposites.

5.2.1
Influence of the Filler's Aspect Ratio and Dispersion

Although nanofillers may be considered as a good strategy for mechanical enhancement due to their high aspect ratio and thus theoretically high interaction with the polymer chains (Figure 5.1), their efficiency depends on their good dispersion into the matrix. Depending on the type of filler, different strategies have been used, always with the objective of reaching a high effective filler concentration. Due to their extremely small sizes, nanofillers may be used in low amounts, conventionally between 1 and 5 wt%, allowing a high improvement of the specific mechanical properties of the composite [9–12].

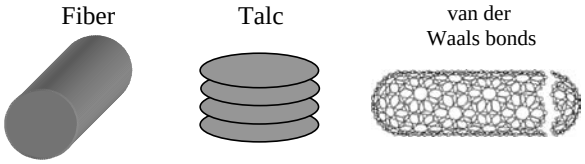

Particle size	10 μm	1 μm	10 nm
Volume content	30%	30%	3%
Number of particles	around 10^6	around 10^{10}	around 10^{15}
Interface	around 0.1 m^2	around 1 m^2	around 100 m^2
Aspect ratio	around 20	around 100	around 1000

Figure 5.1 Influence of particle size on the aspect ratio. Adapted from Ref. [13].

Together with their extremely small sizes (at least one of their dimensions is in the nanometer range, that is, 10^{-6} mm), nanofillers can be found in different shapes, from spherical, such as nanosilica, to plate-like such as layered silicates or fibrillar [carbon nanotubes (CNTs) and nanofibers], defining the anisotropy degree of the nanofiller, commonly known as aspect ratio. A higher aspect ratio has been found to generally increase the elastic modulus of the nanocomposites, although dependent on other characteristics such as filler–polymer interphase or filler orientation during processing [8]. That is why it is expected that fibrillar-like nanofillers such as CNTs, with aspect ratios around 1000 (length $\approx$ 10 μm and diameter $\approx$ 10 nm), may result in high mechanical enhancement even at very low concentrations [13]. For some nanocomposites, it has been proven that at similar filler volume fractions, the stiffness and tensile strength increase as the aspect ratio of the filler increases [14–20].

On the other hand, many works have dealt with parameters affecting the nanofiller dispersion into polymers, mainly the preparation method and processing parameters, as well as nanofiller modification, the use of compatibilizers, and other characteristics of the matrix such as its molecular weight [8]. Different preparation methods have been used, from *in situ* polymerization to solution blending and melt compounding [21–24]. Particularly, melt compounding has attracted great attention due to the fact that conventional polymer processing methods such as extrusion or injection molding may be used [25].

In the case of well-known silicate clays that display an initial structure resembling that of a stack of nanometric-sized plate-like silicate layers with cations in the interlayer gallery (Figure 5.2), it has been shown that optimized mechanical improvement (elastic modulus and tensile strength) at low amounts is reached with a partial or complete exfoliation of the clay into individual ~1 nm thick platelets (Figure 5.3).

Although polymer nanocomposites display a stiffness enhancement that as with more conventional composites tends to be linear with increasing filler volume fraction, this may not be fully linear and may also more conventionally exhibit a critical volume fraction, beyond which stiffness starts to decrease due to nanofiller accumulation and thus efficiency loss [26].

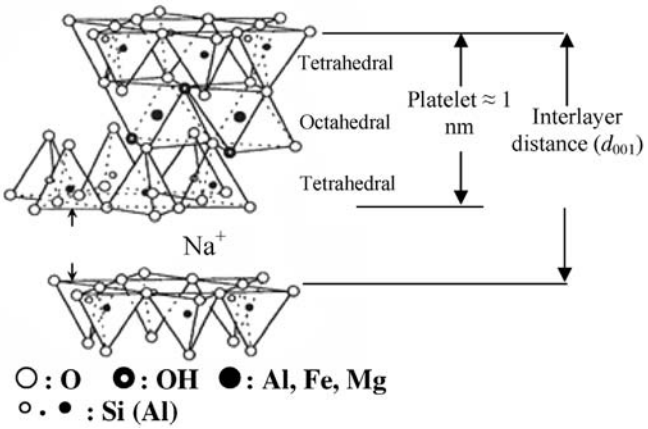

Figure 5.2 Schematic of a cationic clay, $[M_{+\gamma}(Al_{2-\gamma}\,Mg_{\gamma})(Si_4)\,O_{10}(OH)_2 \times nH_2O]$.

5.2.2
Influence of the Filler–Matrix Interphase

It is quite accepted that the mechanical properties of polymer nanocomposites strongly depend on the interphase between the nanofiller and the polymer matrix, mainly due to the high specific contact area between both [27]. This interphase can be seen as a transition region where there is a high interaction between the polymer chains and the surface of the filler, strongly affecting the bulk properties of the nanocomposite. Its particular microstructure (chain mobility, chain conformation, and, in the case of semicrystalline polymers, degree of crystallinity, among others) and thus different properties compared to that of both polymer matrix and filler are

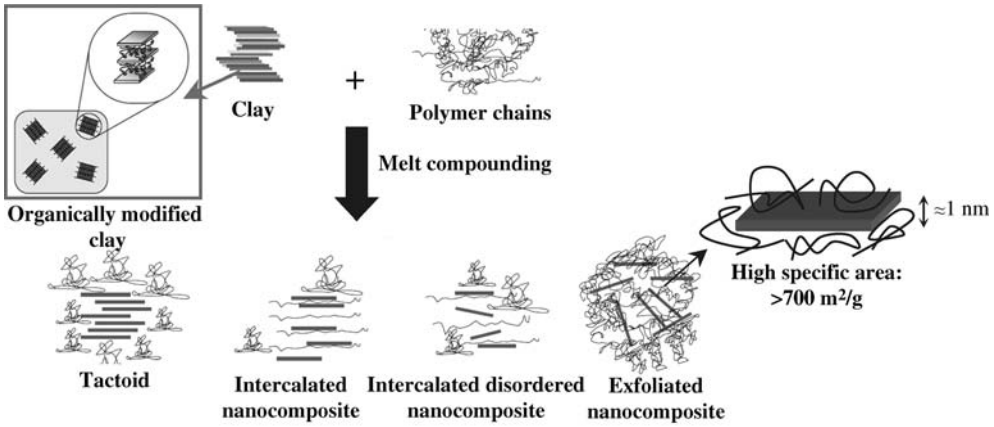

Figure 5.3 Schematic of the microstructures that can be developed in clay-filled polymer nanocomposites.

important to the overall mechanical response of the nanocomposite, as it controls the load transfer between both components. Unlike microcomposites, where continuum mechanics can be used to depict effects of microscale interphase on the stress transfer in the composites considering the system as a three-phase material in which the bulk properties can be characterized taking into account the proportion and average properties of the phases, that is, matrix, filler, and interphase, at nanoscale the discrete nature of the matter has to be considered [28,29].

Despite classical composite theories predicting that an improved bonding between polymer matrix and filler leads to improved mechanical properties, mechanical characterization of nanocomposites has shown mixed results, in some cases inconsistent for similar systems. For instance, Boutaleb *et al.* [30] investigated the influence of the interphase on the mechanical behavior of nanosilica-filled polymer composites by both analytical and finite element models. They considered the interphase as a third phase around the nanosilica particles and proved that this interphase is dominant in controlling the overall nanocomposite behavior, mainly related to a polymer chain immobilization reinforcing mechanism. Ciprari *et al.* [31] studied the effect of the interphase on the mechanical properties of poly(methyl methacrylate) (PMMA) and polystyrene (PS) nanocomposites reinforced with alumina and magnetite. A decrease in elastic modulus was observed for every system incorporating the nanoparticles, and a limited interphase interaction between the nanofillers and polymer matrices was attained. The influence of the interphase in polymer nanocomposite systems reinforced with other nanosized fillers such as nanotubes or silicate-layered clays has also been addressed [32,33]. It has been proven that although nanotubes generally result in higher mechanical enhancements for aligned orientations and nanoplatelets allow better reinforcing for random orientations, nanotubes often generate a larger amount of interphase, leading to higher stiffness.

In the case of semicrystalline polymers, chain conformation and developed crystallinity are sensitive to surface interactions. That is why in the case of polymer nanocomposites, where there is a high surface interaction between the polymer chains and surface of the nanoparticles, a transcrystalline region is commonly observed in the polymer–filler interphase, directly affecting the overall mechanical properties of the material. Nanofillers tend to change the crystallinity degree and rate of crystallization because of a heterogeneous nucleation effect [34], leading to materials with improved mechanical response, particularly stiffness and strength, due to a combined reinforcing effect promoted by the inherently more rigid fillers and enhanced crystallinity [35–42].

5.3
Micromechanical Models for Nanocomposites

The attempt to predict the behavior of nanocomposites from a mechanical or physical point of view has led to the development of various models [43–46]. However, further development of such nanomaterials depends on the fundamental understanding of their hierarchical structures and behaviors, which requires multiscale modeling and

simulation strategies [47,48]. Recently, mechanical properties of polymer nanocomposites are predicted by using computer modeling and simulation methods at a wide range of time- and length scales, for example, from molecular scale, using molecular dynamics (MD) simulations, microscale to macroscale applying continuum models based on micromechanics [e.g., the Halpin–Tsai or Mori–Tanaka model and finite element method (FEM), respectively] and their combination or the so-called multiscale methods [48]. In this chapter, micromechanics-based models are summarized, and the use of this kind of models in the recent advances in polymer nanocomposites reinforced by using nanofillers with different geometric shapes (e.g., spherical nanoparticles, nanotubes, and clay platelets) is reviewed.

5.3.1 Basic Assumptions and Preliminary Concepts

When applied to particle-reinforced polymer composites, micromechanics models usually follow certain basic assumptions: linear elasticity of fillers and polymer matrix; the fillers are axisymmetric, identical in shape and size, and can be characterized by parameters such as aspect ratio; well-bonded filler–polymer interface, so no interfacial slip is considered; filler–matrix debonding; and matrix microcracking. Further details of some important preliminary concepts such as linear elasticity, average stress and strain, composites average properties, and the strain concentration and stress concentration tensors can be found in preview literature [48–50].

5.3.1.1 Continuum Models

The Halpin–Tsai equations and the Mori–Tanaka model are the most used to predict mechanical properties of composites. The Halpin–Tsai equations predict stiffness of the unidirectional composites as a function of aspect ratio. In this model, the longitudinal stiffness and transverse engineering moduli are expressed in the following general form:

$$\frac{E}{E_m} = \frac{1 + \xi\eta\phi_f}{1 - \eta\phi_f} \tag{5.1}$$

where E and E_m are the Young's moduli of the composite and matrix, respectively; ϕ_f is the volume fraction of filler, and η is given by

$$\eta = \frac{E/E_m - 1}{E_f/E_m + \xi_f} \tag{5.2}$$

where E_f is the Young's modulus of the filler and ξ_f is the shape parameter depending on the filler geometry and loading direction. When calculating longitudinal modulus E_{11}, ξ_f is equal to l/t, and when calculating transverse modulus E_{22}, ξ_f is equal to w/t. Here, the parameters l, w, and t are the length, width, and thickness of the dispersed fillers, respectively [48]. If $\xi_f \to 0$, the Halpin–Tsai theory converges to the inverse rule of mixture (lower bound).

$$\frac{1}{E} = \frac{\phi_f}{E_f} + \frac{1 - \phi_f}{E_m} \tag{5.3}$$

Conversely, if $\xi_f \to \infty$, the theory reduces to the rule of mixtures (upper bound):

$$E = \phi_f E_f + (1 - \phi_f) E_m. \tag{5.4}$$

The Mori–Tanaka model is derived based on the principles of Eshelby's inclusion model for predicting an elastic stress field in and around ellipsoidal filler in an infinite matrix. The complete analytical solutions for longitudinal (E_{11}) and transverse (E_{22}) elastic moduli of an isotropic matrix filled with aligned spherical inclusions are [51]

$$\frac{E_{11}}{E_m} = \frac{A_0}{A_0 + \nu_f(A_1 + 2\nu_0 A_2)}, \tag{5.5}$$

$$\frac{E_{11}}{E_m} = \frac{2A_0}{2A_0 + \nu_f(-2A_3 + (1 - \nu_0)A_4 + (1 + \nu_0)A_5 A_0)}, \tag{5.6}$$

where E_m is the matrix Young's modulus, ν_f is the filler volume fraction, ν_0 is the matrix Poisson's ratio, parameters A_0, A_1, . . . , A_5 are functions of the Eshelby's tensor and properties of the filler and the matrix (Young's modulus, Poisson's ratio, and filler concentration and filler aspect ratio) [52].

5.3.1.2 Equivalent Continuum Model and Self-Similar Model

Due to the structure filler hierarchical morphology and surrounding polymer matrix at nanometer length scale, the well-defined concepts in conventional two-phase composites should not be directly applied to polymer nanocomposites. Polymer molecules and nanofillers have equivalent size and the polymer–filler interactions are highly dependent on the local molecular structure and bonding at the interface. Therefore, nanofillers and polymer chains structures cannot be considered as continuous phase at these length scales, and the bulk mechanical properties cannot be determined, for that reason, using traditional continuum-based micromechanical approaches [47,48].

Molecular models (MMs) are used to model the specific polymer–filler interactions (effective filler) and used by several authors to provide a consistent and rigorous scheme to determine continuum properties for the polymer nanocomposites by incorporating this MM into the traditional continuum models [47,53]. A scheme of a MM used to predict the effective interface of silica nanoparticles [48] is displayed in Figure 5.4.

The equivalent continuum approach developed by Odegard *et al.* [54] consists of four major steps: establishing representative volume elements (RVEs) for the molecular and equivalent continuum models, deriving and equating potential energies of deformation for both models subjected to identical boundary conditions, establishing a constitutive relationship for the equivalent continuum model, and using traditional micromechanics techniques to determine larger scale properties of the composite.

5.3.1.3 Finite Element Modeling

FEM is a powerful numerical analysis tool used to predict mechanical properties of composite materials. Zeng *et al.* [48] resumed the necessary steps to implement FEM

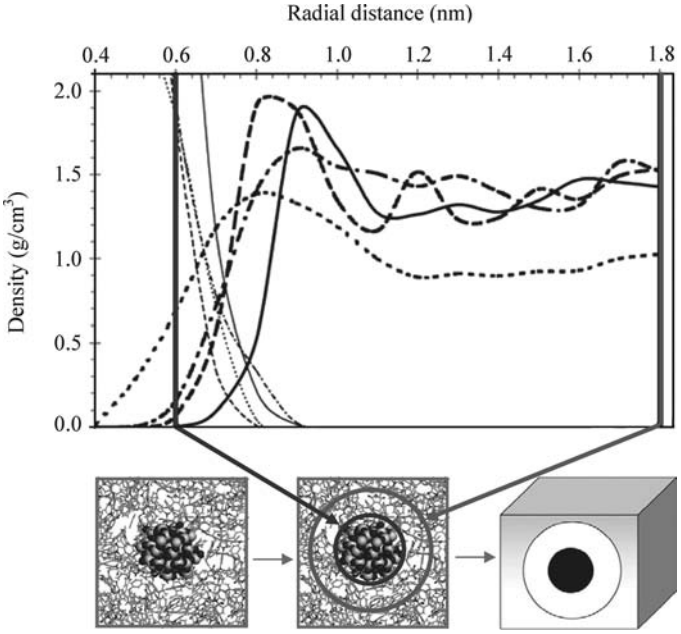

Figure 5.4 Schematic of the process used to determine the effective interface and effective particle. Adapted from Ref. [48].

to predict the mechanical properties of polymer nanocomposites. The mechanical behavior of nanocomposites can be effectively studied using a RVE in FEM modeling [55,56]. It is assumed that both the CNTs and the matrix in a RVE are continua of linearly elastic, isotropic, and homogenous materials, with the given Young's moduli and Poisson's ratios. In simplified systems, it is also assumed that the CNTs and matrix are perfectly bonded at the interface in the RVE to be studied.

Mainly, three types of RVEs can be found in the literature [57]: (a) cylindrical, (b) square, and (c) hexagonal (Figure 5.5). Square and hexagonal RVEs are believed to yield the best results because of their ability to fill the space compared to the cylindrical RVE. It is also shown in the literature that cylindrical RVEs tend to overestimate the elastic modulus of the composites compared to the numerical results obtained from a square RVE [57,58]. However, several studies have been carried out using cylindrical RVEs due to the availability of analytical solutions and

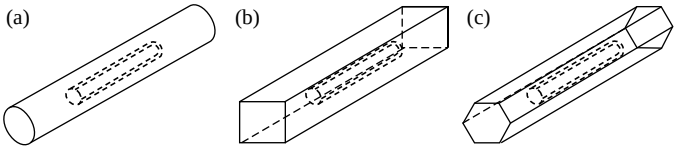

Figure 5.5 Nanoscale representative volume elements (RVE) for modeling CNT-based nanocomposites. (a) Cylindrical. (b) Rectangular. (c) Hexagonal. Adapted from Ref. [57].

2D axisymmetric FEM models that can reduce computational time [59]. The multiscale RVE integrates nanomechanics and continuum mechanics, bridging the length scales from nanoscale to mesoscale.

5.3.2 Micromechanical Nanocomposites Modeling

Over several decades, theoretical frameworks have been developed for predicting properties of composite materials based on the properties of pure components and the morphology of the composite. An assumption inherent in all these theories is that each component of the composite acts independently of the other. Such continuum micromechanical models generally assumed simplified geometries for each component and perfect load transfer by neglecting interfacial phenomena between them. Nevertheless, they provide a rapid assessment of the key factors (e.g., particle volume fraction, particle geometry and orientation, and the property ratios of particle and matrix) in controlling the reinforcement and mechanical properties [47]. In recent years, some of these models (e.g., Halpin–Tsai, Mori–Tanaka, and FEM) have been applied to estimate the thermal–mechanical properties [60], Young's modulus [61,62], and reinforcement efficiency [63] of polymer nanocomposites and the dependence of materials modulus on the individual factor of fillers (e.g., aspect ratio, shape, and orientation) and the modulus ratio of filler to polymer matrix.

Tucker *et al.* [50] prepared an application review of different classes of micromechanical models. The authors remarked that Halpin–Tsai equations [46] are the most widely used, but the Mori–Tanaka type models [45] give the best results for large aspect ratio fillers.

The direct use of these models for nanoreinforced composites is questionable due to the significant scale difference. The development of nanoscale continuum theories that integrate continuum mechanics theories with the nanoscale molecular structure has aroused a greater interest. These modeling techniques are referred to as "nanoscale mechanics" or "molecular structural mechanics" in the literature, and they link the interatomic potentials of atomic structure to the continuum level of materials [64].

Based on the Halpin–Tsai model, Brune and Bicerano [47] developed analytical solutions for elastic equations by including a new concept of effective particle and addressed some important aspects of micromechanics of clay-based polymer nanocomposites. Sheng *et al.* [65] calculated the clay nanocomposite stiffness by considering multiscale micromechanical models accounting for the hierarchical morphology of the nanocomposite. They compared the results from their FEM model with that from the Halpin–Tsai empirical method and Mori–Tanaka method. The strong dependence of clay's modulus on the polymer modulus has been a significant conclusion drawn by their study. In addition, they compared FEM, Mori–Tanaka, and Halpin–Tsai results with that of experimental ones and concluded that the Halpin–Tsai model predicts the nanocomposite to be stiff, while the FEM and Mori–Tanaka models agree well with experiments.

Odegard *et al.* [66] proposed two methods, equivalent continuum model and self-similar model, for modeling the mechanical properties of polymer nanotube-reinforced composites in which the molecular structure and interactions were incorporated into continuum mechanics-based models. Fisher *et al.* [67] developed a FEM model with a continuum micromechanical method (Mori–Tanaka model) to predict the mechanical properties of a polymer reinforced with a distribution of wavy nanotubes. Liu and Chen [57] proposed a multiscale modeling approach to study the compressive behavior of CNT polymer nanocomposites. They modeled the nanotube at the atomistic scale and analyzed the matrix deformation using the continuum FEM. Shi *et al.* [68] numerically predicted the waviness of nanofibers and incorporated this into the Mori–Tanaka micromechanical method. This theoretical model for predicting stiffness of nanocomposites assumes perfect bonding and consequently yielded an upper bound of the composite properties. The true value of the performance parameters can be considerably lower than those predicted by these models. Therefore, it is important to account for the degree of adhesion of the reinforcement to the matrix theoretically to improve the accuracy of a micromechanics model. Shi *et al.* [69] have modified their approach for stiffness prediction of nanocomposites [68] to include the effect of the interface. They considered the interface as a third phase (an inclusion with different modulus than that of the nanotube) and used the Mori–Tanaka micromechanical method to estimate the composite stiffness. Models using FEM can also be used to estimate the mechanical properties of polymer nanocomposites reinforced with other nanoparticles.

For example, the effective elastic properties of silica nanoparticles-reinforced polymer nanocomposites were predicted by means of various FEM-based computational models [70], including an interphase layer around particles as a third constituent material in the prediction of the mechanical properties. Boutaleb *et al.* [30] studied the influence of structural characteristics on the overall behavior of silica spherical nanoparticles–polymer nanocomposites by means of analytical method and FEM. They assumed that the interphase between silica particle and polymer matrix presents a graded modulus, ranging from that of the silica to that of the polymer matrix, for example, a gradual transition from the properties of the silica to the properties of the polymer matrix (Figure 5.6). The change in elastic modulus in the interphase was described by a power law introducing a parameter linked to interfacial features.

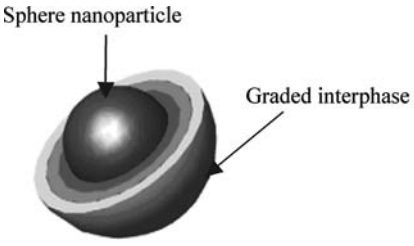

Figure 5.6 Spherical nanoparticle coated with a graded interphase. Adapted from Ref. [30].

5.4
Mechanical Characterization of Nanocomposites under Static Loading

Mechanical characterization under static loading of polymer-based nanocomposites has been widely studied in order to evaluate the influence of nanofiller content, dispersion, geometry, orientation, interfacial adhesion quality, and others on their mechanical performance. Layered silicates and CNTs are the most studied reinforcing agents in polymers due to their large aspect ratio and mechanical properties, but in the past decade particulate nanofillers such as silica or functionalized graphene (FG) have received special interest.

5.4.1
Polymer-Layered Silicate Nanocomposites

Polymer-layered silicate (PLS) nanocomposites represent one of the alternatives to conventionally filled polymers. Because of their nanometer-size dispersion, the nanocomposites exhibit markedly improved mechanical properties compared with the pure polymers or conventional composites.

Some reviews about PLS nanocomposites have been presented in the past 10 years [1,2,39,71–73]. Alexandre and Dubois [72] reviewed the developments of syntheses and PLS-relating properties with the nanocomposites structure. These authors commented that dispersed silicate layers increase the Young's modulus of the polymer and that the main factor responsible for that stiffness improvement is the exfoliation degree of clay particles. Such reinforced nanocomposites that used epoxy resins [74–77] and thermoplastic polymers as the matrix materials have been the topic of several studies. It was noted in the nylon 6-based nanocomposites synthesized by *in situ* intercalative polymerization of ε-caprolactam using Na–montmorillonite that the nature of the acid added to catalyze the polymerization influences the degree of exfoliation [78]. For nylon 6-based nanocomposites prepared by melt compounding, a nanoclay threshold of 10 wt% in nylon 6-based nanocomposites was noted. Above this value of nanoclay content, the Young's modulus seemed to level off. This change was attributed to the passage from a totally exfoliated structure (below 10 wt%) to a partially exfoliated partially intercalated structure (for 10 wt% and above) supported by the XRS and TEM analyses [79].

The increase of stress at break in thermoplastic-based nanocomposites is usually related to the nature of the interactions between the matrix and the filler. Table 5.1 shows the tensile stress values for different matrix clay nanocomposites. Nanocomposites such as exfoliated nylon 6-based nanocomposites [78] or intercalated PMMA-based nanocomposites [80] exhibit an increase in the stress at break. This increase is usually due to the polar (PMMA) and even ionic interactions (nylon 6 grafted onto the layers) between the polymer and silicate layers. In polypropylene (PP) and PS nanocomposites, the interactions between polymer matrix and clay interface are weak, so no enhancements in tensile stress were observed.

Table 5.1 Elastic modulus and tensile yield stress of several clay–thermoplastic nanocomposites.

Matrix	Clay content (wt%)	Elastic modulus (GPa)	Tensile yield stress (MPa)
PP	0	1.4	33.6
	0.5	1.5	33.5
	1.0	1.6	34.1
	3.0	1.9	33.9
	5.0	1.9	32.8
PS	0	1.2	28.7
	5	1.3	21.7
	10	1.6	23.4
	20	2.6	16.6
	30	1.8	16.0
PA 6	0	2.7	69.7
	1.5	3.5	84.0
	2.9	4.2	85.2
	4.6	4.7	90.7
	6.6	5.2	69.7
PA 11	0	1.3	41.3
	1.8	1.6	44.3
	3.1	1.9	47.1
	4.0	2.0	49.9
	5.7	2.3	51.4
PA 12	0	1.5	40.9
	1.7	1.8	44.9
	2.9	2.0	46.7
	4.4	2.3	48.4
	6.5	2.7	50.5
PMMA	0	3.1	53.9
	10	4.6	62.0
	20	4.9	62.0

Data adapted from Refs [80–83] and [182].

Tarapow *et al.* [83] studied the influence of clay surface chemistry and the processing conditions on the structure and mechanical properties of PP–clay nanocomposites prepared by a melt mixing process. They observed that although the Young's modulus improved with unmodified clay incorporation, the tensile strength and the impact toughness values decreased. These results were attributed to a poor interfacial adhesion between PP matrix and unmodified clay.

Enhancements in impact toughness with the incorporation of the most hydrophobic, organically modified clay were noted. This behavior was attributed to the presence of intercalated or exfoliated clay layers that were able to hinder the crack path caused by impact. Impact strength also increased because the stress could be dispersed by those layers having higher stiffness and strength than the matrix. The processing conditions showed no important influence on the degree of dispersion or mechanical properties. Another factor that influences the mechanical properties of

semicrystalline polymers is the degree of crystallinity because a higher fraction of crystals leads to an increase in the strength and stiffness of the material. No important influence in PP crystallinity was noted in these nanocomposites.

Fornes *et al.* [84] studied the effect of matrix molecular weight in the mechanical properties of clay nanocomposites. These authors showed that high molecular grade of nylon 6 leads to better exfoliation of clay platelets, and that the level of clay platelet exfoliation affects polyamide crystalline morphology, which in turn influences nanocomposite's physical and mechanical properties. These studies showed that crystallization kinetics of the nanocomposites is dramatically increased at very low filler concentrations relative to extruded polyamide matrices; however, higher clay loadings retard the crystallization process. In general, crystallization rates are enhanced more for nanocomposites formed from high molecular weight polyamides, most likely due to better platelet exfoliation, which provides more filler surface for crystal nucleation [85].

5.4.2
Polymer–CNT Nanocomposites

Since the discovery of CNTs (hereafter called "nanotubes") by Iijima [86], the number of researches related to nanotubes and their correlated composite materials has dramatically increased [87]. The combination of the exceptional mechanical properties of CNT (with Young's modulus and tensile strength of 1.2 TPa and of 50–200 GPa, respectively) along with low density, high aspect ratio, and high surface area makes CNT an ideal candidate for reinforcement in composite materials [88], as showed in Table 5.2.

Table 5.2 Enhancement of elastic modulus in CNT nanocomposites with several polymeric matrices.

Matrix	Carbon nanotube content (wt %)	Elastic modulus (GPa)
PP	0.0	0.9
	0.8	1.2
HDPE	0.0	1.0
	1.0	1.4
PS	0.0	1.2
	1.0	1.7
PMMA	0.0	0.7
	17.0	1.6
PC	0.0	0.8
	15.0	1.1
PA 6	0.0	2.6
	12.5	4.2
PVA	0.0	6.3
	60.0	12.6
Bisphenol A thermoset resin	0.0	1.2
	1.0	2.4

The applications of CNTs as reinforcing agents of polymer matrix composites are widespread due to the deeply strong dependence of nanocomposites mechanical properties on the dispersion state of these nanofillers promoted by the employed process conditions. It is fundamental to disperse the nanotubes homogeneously throughout the matrix without destroying their integrity and get a good interfacial bonding to achieve load transfer across the CNT–matrix interface. Qian *et al.* [89] reported a 35–42% increase in the elastic modulus and a 25% increase in strength just by adding only 1 wt% CNT to a polyester resin. Similar encouraging results have also been reported [90], but other reports demonstrated only modest improvements in modulus and strength. For example, the mechanical properties of CNT–epoxy nanocomposites are reinforced by two types of multiwalled carbon nanotubes (MWCNTs) with different aspect ratios, and it was found that the impact resistance and fracture toughness were significantly improved only for those containing CNTs of a higher aspect ratio [91]. However, the corresponding tensile modulus and strength showed very limited improvements below 5%, probably due to weak bonds between the CNTs and polymer matrix and CNTs agglomeration [88].

Many reports [87,92,93] showed that there is a critical CNT content in the matrix below which the strengthening effect of CNT–polymer composites increases with increasing CNT content. Above this critical CNT content, however, the mechanical properties of CNT–polymer composites decrease, and in some cases, they decrease below those of the neat matrix material. These observations can be attributed to (i) the difficulties associated with uniform dispersion of CNTs at high CNT contents and (ii) the lack of polymerization reactions that are adversely affected by the high CNT content. The latter effect becomes more pronounced when functionalized CNTs are employed to produce CNT–polymer nanocomposites [88].

5.4.3
Particulate Polymer Nanocomposites

During the last decade, there has been a great interest in PP-based nanocomposite blends that contain finely dispersed nanosilica [94–96]. Owing to the nonpolar character of the PP, functionalization of the polymer matrix and/or treatment of the nanoparticles are needed to achieve a good dispersion of the rigid nanoparticles and satisfactory mechanical properties. Bailly and Kontopoulou [97] studied the effect of adding three different types of silica nanoparticles in the mechanical properties of a silane-grafted PP toughened with an elastomeric ethylene–octene copolymer (POE). These authors found that the tensile and flexural properties of the composites were improved upon addition of the rigid nanofillers, whereas the impact strength was maintained when the nanosilica was treated with octylsilane. The maximum values were obtained at 5 wt% silica content in tensile tests and at 7 wt% in flexural tests. These improvements in properties are attributed to a combination of the localization of finely dispersed fillers in the PP matrix and the presence of covalent bonding due to a hydrolysis reaction between the silanol groups present on the surface of the silica and the silane grafts in the polymer. The most substantial losses in ductility were noted

beyond 5 wt% octylsilane–SiO_2 content. This can be explained by the presence of a percolation threshold at contents above 5 wt%. Higher silica contents lead to the formation of agglomerates, which act as stress concentrators.

FG has recently been under the spotlight due to its interesting electrical, mechanical, and thermal properties [98]. FG is the generic name for graphene oxide and graphene with other functionalities. Graphene is one of the strongest materials ever measured. The intrinsic strength and Young's modulus of graphene reach 130 GPa and 1 TPa, respectively. However, the interface is central to the mechanical enhancement of polymer nanocomposites rather than to the intrinsic strength of nanofillers themselves [99]. The functionalities present on the graphene surface can enhance the dispersion of graphene in polymeric matrices and the interfacial interaction between graphene and polymeric matrices by the formation of chemical bonding. In a silicone system, it was expected that hydroxyl groups on the FG could bond to the SiH-containing component during curing of the silicone elastomer. The modulus of the silicone foam with 0.25 wt% FG increased by over 200% in comparison to that of pure silicone foam [100]. Xu *et al.* [101] disclosed the excellent reinforcing effect of FG for PVA, justifying this effect on the formation of hydrogen bonds between FG and PVA.

5.5
Characterization by Dynamic Mechanical Thermal Analysis

In DMTA, when a polymer, after undergoing a sinusoidal deformation, reaches the temperature or frequency range at which a chain movement occurs, the energy dissipated increases up to a maximum. As the stress wave is delayed with respect to the strain one, its decomposition leads to a component in phase and another one out of phase, related with two parts of the complex modulus (shear, bending, compression, or tensile modulus, depending on the geometry of the sample clamping) and named storage (E') and loss modulus (E''), respectively. The ratio of loss modulus to storage modulus is the loss tangent (tan δ), connected with the mechanical damping. Glass transition temperature (T_g) can be determined from the loss tangent peak of a certain chain relaxation. Thus, dynamic mechanical analysis (DMA) allows us to study the variations of these parameters, linked to macromolecular motions, not only the main one, the glass transition but also the local movements not detected by other techniques.

It has been found that the interaction of intercalated and/or exfoliated nanoparticles may restrict the mobility of the matrix polymer chains, which lead to an increase of T_g values, as observed in nanocomposites of polyamide-12–layered silicates [102], nitrile rubber–organophilic montmorillonite [103], natural rubber–montmorillonite [104], and EVA–clay [105]. A slight increase with the organosurface treatment in T_g values was noticed in poly(vinyl chloride)–clay [106,107], poly(vinyl chloride)–CNTs [108], polyurethane–montmorillonite [109–111], LLDPE–layered tetrasilisic fluoromica [112], PP–montmorillonite [113–115], PP–silica [116], and styrene–butadiene rubber [117].

The increased interaction between polymer and nanoparticles can also be extracted from the enhanced values of the storage modulus, as observed in PP–carbon nanofibers (Table 5.3) [118], PS–montmorillonite [119], PLA–montmorillonite [120,121], PA6–montmorillonite [122], LDPE–ethylene-octene–montmorillonite [123], HDPE–montmorillonite [124], PP–montmorillonite [125], and PBT–montmorillonite [126].

Nevertheless, in other cases, a plasticizing effect of the nanoparticles has been reported, which leads to a decrease in both the values of T_g and the storage modulus. Artzi *et al*. [127] reported in EVOH–montmorillonite nanocomposites a decrease of T_g values from 5 wt% of clay. The same authors predict two opposing effects on the transition: the confined chain mobility owing to interaction buildup, and an increased mobility due to reduction in the crystallinity degree as a consequence of polymer–clay interaction [128]. The addition of a compatibilizer, either maleic anhydride-grafted ethylene–vinyl acetate (EVA-*g*-MA) or maleic anhydride-grafted linear low-density polyethylene (LLDPE-*g*-MA), led to a decrease in the T_g values [129]. This 5 wt% clay content maximum is also described by McAdam *et al*. in PA6–clay nanocomposites [130].

A small content (4 *phr*) of organomodified montmorillonite led to a decrease of T_g values in PA6–PP–montmorillonite nanocomposites [131,132], although the addition of PP-*g*-MA increased T_g values, due to a restricted molecular mobility. This plasticizing effect at low nanofiller contents was also reported by Wang *et al*. in PP–montmorillonite systems [133] with organomodified clays. The organic-based surface treatment of layered double hydroxides (LDHs) led to similar results in EVA–LDH nanocomposites [134] and PA6–PU–montmorillonite [135]. A slight plasticizing effect was found by Realinho *et al*. [136] in PMMA–montmorillonite nanocomposites (Table 5.3).

Table 5.3 Storage modulus and glass transition temperature of several PP and PMMA nanocomposites.

Matrix	Clay	Storage modulus (GPa)	T_g (°C)
PP	None	1.9	5.4
	Montmorillonite (5 wt%)	2.0	6.0
	Carbon nanofiber (5 wt%)	1.8	5.2
	Carbon nanofiber (10 wt%)	2.3	7.3
	Carbon nanofiber (20 wt%)	2.7	7.5
PMMA	None	3.0	131
	Montmorillonite (2.5 wt%)	2.9	128
	Montmorillonite (5 wt%)	3.0	128
	Montmorillonite (20 wt%)	3.9	131

Data adapted from Refs [118,136].

5.6
Mechanical Characterization by Means of Indentation Techniques

Nanoindentation is nowadays one of the most used methods to measure the mechanical properties of polymers, attracting great attention as a technique to mechanically characterize polymer nanocomposites [137–142]. This technique uses the same principle as microindentation, but with much smaller probe areas and very low loads (on the order of nanonewtons), so as to produce indentations from less than a hundred nanometers to a few micrometers in size and depth [143]. Although it has been vastly used to characterize the mechanical properties, particularly hardness, elastic modulus, yield stress, and fracture toughness, of several polymers [144–152] and shown to be mainly influenced by the testing procedure, penetration depths, and holding time, limited work has been dedicated to the characterization of the mechanical behavior of polymer nanocomposites using this technique.

Conventionally, the compliance method proposed by Oliver and Pharr [153] has been used to determine the hardness (H) and elastic modulus (E) by means of nanoindentation from the analysis of the load–displacement curve. In this method, the unloading segment of the curve is fitted to a power law function to obtain the contact depth and thus the contact area (A) at the peak load (P_{max}) required to determine H ($H = P_{max}/A$). A typical load–unload displacement curve for a viscoelastic–plastic material is shown in Figure 5.7. As can be seen, and as the indenter penetrates the sample, there is a rise in the load value until a maximum is reached (P_{max}), followed by unloading. In the case of a perfectly elastic material, loading and unloading curves are expected to be identical and thus h_{max} gives the maximum displacement of the indenter, while h_f represents the residual displacement due to plastic deformation. The value of h_c, determined as the intercept of the tangent line to the first part of the unloading curve, is considered as the real value of the displacement during the nanoindentation test since it takes into account the plastic deformation of the material.

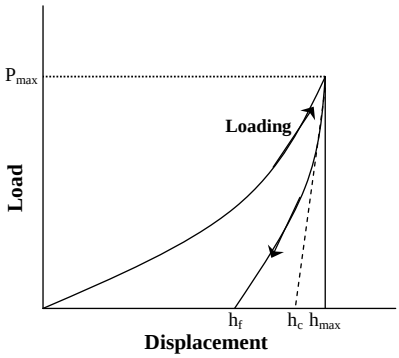

Figure 5.7 Schematic of nanoindentation load–unload versus displacement for a viscoelastic–plastic material. Adapted from Ref. [154].

Nonetheless, this method assumes that the unloading is purely elastic, even though the contact may be elastoplastic, such as in polymer-based systems. Likewise, the so-called indentation size effect (ISE), related to the fact that the hardness measured at small depths is higher than at large depths, especially for depths higher than 10 μm [155], tends to result in an overestimation of the values given by the Oliver–Pharr compliance method. Several mechanisms have been suggested to explain this effect, the most important being the friction between the tip of the indenter and the sample [156].

Other nanoindentation-based techniques have been developed in recent years that, instead of applying a static load and determining material stiffness from the unloading curve, employ an oscillating force [157]. Such is the case of the continuous stiffness module (CSM), which enables us to determine the contact stiffness throughout the whole experiment during loading, and thus has proved to be a useful technique in the study of polymer's plastic and elastic properties [158].

Due to the particularities of the nanoindentation test and complexity of a viscoelastic–plastic system such as in polymer nanocomposites, the elastic moduli determined using this technique, although qualitatively comparable to the ones obtained from conventional mechanical testing such as tensile or DMA, are quantitatively different. In the case of the first, this has been related to direction-dependent loading application and a scale factor and size effect between nanoindentation and tensile testing [155]; while in the case of the latter, this has been related to the frequency used during testing, as it is known that higher moduli are obtained with increasing frequency (typical frequency in DMA testing is around 1 Hz, while in nanoindentation a value of 35–45 Hz is conventionally used).

Other critical factors affecting nanoindentation results are the local properties of the material, such as crystallinity or cross-linking, due to the extremely small probe areas. In the particular case of polymer nanocomposites, it has been shown that nanofiller presence tends to restrain chain mobility and, in the case of semicrystalline polymers, induces a higher crystallinity due to a heterogeneous nucleation effect. These phenomena are expected to have a great effect on the local properties of the material and thus on the values given by nanoindentation. Sikdar *et al.* [159,160] have demonstrated that higher crystallinity induces lower amounts of polymer chain entanglements and thus lower interphase interactions, decreasing the value of the elastic modulus of the nanocomposites.

Most of the work dedicated to the mechanical characterization of polymer nanocomposites using nanoindentation has been done on polymers filled with silicate-layered clays [157,161–166], although CNTs and nanosilica have recently been considered [167–169]. Generally speaking, with increasing filler concentration with respect to indentation depth, the hardness and elastic modulus of the nanocomposites have been shown to gradually increase [163,168]. Nonetheless, this mechanical enhancement is marginal at low filler concentrations in the case of nanoclays [170], and in some cases the improvement in elastic modulus is not even 20% for a 5 wt% clay content [163]. In the case of what are already considered as highly filled nanocomposites (>5 wt% clay content), this has been related to difficulties in obtaining a partially exfoliated clay morphology and thus a more

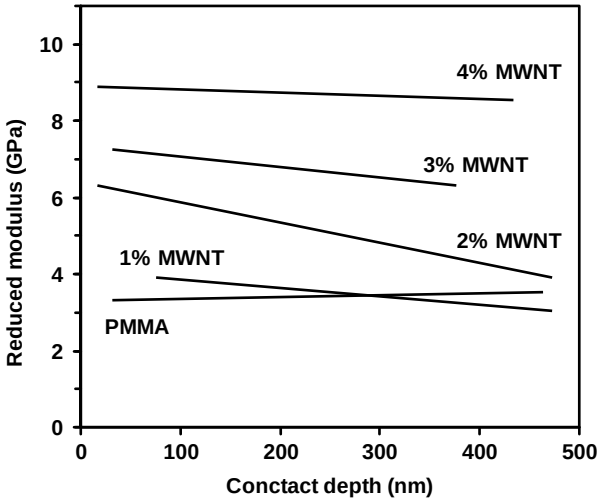

Figure 5.8 Evolution of reduced modulus of several MWNT–PMMA nanocomposites. Adapted from Ref. [171].

heterogeneous nanocomposite structure, increasing possible inaccuracies during the nanoindentation measurements, especially in the case of sharpened tip geometries such as Berkovitch. In a similar manner, it has been shown that flattened conical tip geometry gives a better accuracy between measurements for polymer nanocomposites filled with silicate-layered clays.

Likewise, it has been demonstrated that the elastic modulus and hardness of CNT-reinforced polymer nanocomposites measured by nanoindentation are not improved or only slightly improved by the addition of the CNTs, related to an inhomogeneous dispersion of the nanotubes (aggregate formation), weak bonding between the polymer and the filler, and to the intrinsic elastic properties of CNTs that tend to bend and show a curved morphology [171]. Possible mechanical enhancement strategies have included improving the bending strength of CNTs by using a silica-coated shell and demonstrated it to be effective in increasing the hardness and elastic modulus of MWCNT–polymer composites by increasing the concentration of MWCNT in the matrix, with enhancements in the order of two to three times for a 4 wt% MWCNT content (Figure 5.8) [171].

5.7
Fracture Toughness Characterization of Nanocomposites

Several experimental procedures are employed in order to give an estimation of the fracture toughness of nanocomposites, which makes it sometimes difficult to assess this feature. The simplest ones are those that employ either analogical or instrumented impact tests (Charpy, Izod, and falling weight), and the impact strength is

evaluated in terms of energy per unit area, as the energy that better defines the impact resistance is that absorbed by the sample during its deformation and rupture.

More specific values of the fracture toughness are obtained by the application of the experimental procedures derived from the fracture mechanics theories. In the case of no plastic deformation in front of the crack tip, the LEFM is employed, obtaining the values of the stress critical intensity factor (K_c) or critical stress energy release rate (G_c). On the other hand, when there is plasticity in front of the crack tip, we must use the principles of the elastoplastic fracture mechanics; in this sense, two experimental procedures are widely employed: the J-integral analysis and the EWF.

Kanny *et al.* [172] report that the stress intensity factor and strain energy release of PP increased with the addition of commercial montmorillonite, exhibiting a maximum improvement for a clay content of 5 wt%. This improvement is attributed to the presence of intercalated nanoclay structures in the PP nanocomposite structure that acted as both the load-bearing agents and crack-stopping agents. The intercalated microstructure seems to be more beneficial than the exfoliated one to stop the decrease in the fracture toughness [173,174]. Realinho *et al.* found a dramatic increase in the fracture toughness values of SAN with 5% of organo-modified hydrotalcite with a intercalated microstructure [175] and also an increase in K_{Ic} and G_{Ic} values [176]. The effect of a good nanoplatelet dispersion affects positively the values of the fracture toughness [177], as well as the clay orientation and aspect ratio [178].

Chen *et al.* [179,180] report a dramatic increase in J_{Ic} from 4 kJ/m^2 for the unfilled MAPP to about 17 kJ/m^2 for 2.5 wt% of montmorillonite surface-treated with octadecylamine, although they report a moderate increase in the tearing modulus, as indicated by Cotterell *et al.* [7], and these values should be taken with caution. Higher clay contents cause particle agglomerates and thus a reduction in the fracture toughness is observed. Kim *et al.* showed a decreasing trend of the Izod impact with the montmorillonite content [181], also noticed in nanocomposites of nylon 6, 11, and 12 [182], PP [183], PMMA [184], and polyvinyl chloride [185], but an improvement of the impact strength values in the case of epoxy-based nanocomposites [186–188]. The K_{Ic} and G_{Ic} values of PA66–organoclay nanocomposites decreased with increasing clay content [189], which was a direct result of reduced plastic zone at the crack tip region, as clay particles produced sparse micrometer- and submicrometer-size voids around the clay platelets, promoting void coalescence and thereby slashing fracture toughness (Figure 5.9).

A maximum value of notched Charpy impact strength was found at 2 wt% of CNTs within the range of 0–5 wt%[190]. An optimum of J_c values at 5 wt% of $CaCO_3$ nanoparticles was reported by Khosh *et al.* [191], two times higher than those of neat PP. Wang *et al.* [192] reported an optimum value of notched Charpy impact strength at 10 wt% of $CaCO_3$, and then the impact strength of the nanocomposites decreased with increasing filler loading; however, at 20 wt% of $CaCO_3$, it still reached a value five times that of neat PP.

Zhao *et al.* [193] found in composites with Al_2O_3 nanoparticles that at quasi-static loading rate the fracture toughness was found nearly unvaried with the filler content. Under impact loading rate, the notched Izod impact strength and the impact

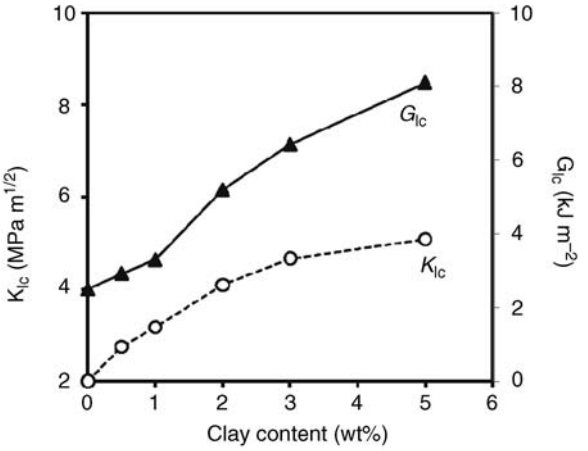

Figure 5.9 Influence of montmorillonite content on K_{Ic} and G_{Ic} values of PP nanocomposites. Adapted from Ref. [172].

fracture toughness indicate that the impact fracture toughness increases initially with the addition of 1.5 wt% of Al_2O_3 nanoparticles to the PP matrix. However, with the further addition of up to 3.0–5.0 wt% of Al_2O_3 nanoparticles, both notched Izod impact strength and impact G_c decreased slightly. Crazing and microcracking with dilatational feature were found to be the main fracture mechanisms for the virgin PP and the Al_2O_3–PP nanocomposites.

The surface treatment of montmorillonite with sodium salt of alkylammonium within the range 1–3 wt% [194] resulted in notched Izod impact strength of 11–12 kJ/m^2, higher than that showed by unfilled PP, about 4 kJ/m^2. PP containing 4 wt% montmorillonite clay surface-modified with dimethyldialkylammonium improved the Izod impact behavior in the temperature range 0–70 °C, observing differences in the fracture surfaces [195]. The fracture initiation and propagation of neat PP were characterized by crazing and vein-type features, whereas the reinforcement of PP with nanoclay alters the primary mechanism of plastic deformation from crazing and vein-type to microvoid coalescence process. Silane functionalization of CNTs improved the K_{Ic} values of epoxy–CNT composites [196], as well as acidic surface treatment on epoxy–red mud nanocomposites [197]. Silane-treated silica nanoparticles were blended by using *in situ* cross-linking method [198] leading to an enhanced filler–matrix interaction, and thus the volume fraction of interphase was increased, leading to an improvement of the Charpy impact strength. Zhang *et al.* [199] studied the fracture toughness of nanocomposites of $CaCO_3$ through the reflective optical caustics method, a way to evaluate the stress singularities at the crack tip because of its simple optical patterns, which can establish the relation between the stress field parameters and the maximum transverse diameter of caustic curve. They found nanocomposites of $CaCO_3$ with a nonionic modifier, polyoxyethylene, increasing the values of the stress intensity factor. The absence of the nonionic modifier gave smaller values. The addition of POE-*g*-MA in PP–$CaCO_3$

Table 5.4 EWF parameters of PP nanocomposites with differences in the interfacial adhesion between phases.

Matrix	Clay	MAPP	w_e (kJ/m^2)	βw_p (MJ/m^3)
PP			14.9	0.38
PP	2% Cloisite 15A		3.8	1.29
PP	2% Cloisite 15A	4% Epolene E43	7.0	1.63
PP	2% Cloisite 15A	4% Polybond 3150	6.8	1.59
PP	2% Cloisite 15A	4% Polybond 3150	15.9	0.65
PP	2% Cloisite 30B	4% Polybond 3150	12.9	1.19

Adapted from Ref. [147].

nanocomposites [192] increased the impact strength, but reports that the addition of PP-*g*-MA or EVA-*g*-MA was detrimental to the impact strength. A positive effect of the surface treatment of $CaCO_3$ nanoparticles with stearic acid on the notched Izod impact strength is reported [200].

Bureau *et al*. modified the interfacial adhesion between PP and clay through the addition of surface-treated montmorillonite and maleic anhydride-grafted PP [201] and studied the fracture behavior by the EWF methodology (Table 5.4). Clay particles were found to act as void nucleation sites within the PP matrix, which led to higher void nucleation, reduced void growth, and rapid void coalescence, accompanied by extensive fibrillation, causing not only an important reduction in fracture toughness with respect to PP but also an important increase in plastic work dissipation. The presence of grafted PP increased notably the fracture toughness. It has also been reported that the molecular weight of MAPP had an effect on the quality of clay particle dispersion [202] – the lower molecular weight, the higher the values of specific work of fracture, w_e, provided by the dispersion. Saminathan *et al*. [203] also studied a PP–MAPP–montmorillonite system through the EWF methodology, with clay content 5 wt%, and found an increase in the values of w_e from 23.3 kJ/m^2 for pure PP to 29.3 kJ/m^2 for the nanocomposite. The EWF methodology has proven to be successful in the evaluation of the fracture toughness of multiwalled CNT–PET nanocomposites [204] and multiwalled CNT–polycarbonate [205].

Lim *et al*. modified the interfacial interaction between nylon 6 and montmorillonite with maleic anhydride-grafted polyoxyethylene [206] and found that the internal cavitation of POE-*g*-MA particles led to effective relief of crack tip triaxial stress along with craze-like damage features consisting of line arrays of expanded voids, and subsequently a large-scale yielding of nylon 6 matrix was observed. This improvement in the fracture toughness due to an enhanced interfacial adhesion promoted by a functionalized elastomer was also observed in PA6–PP–organoclay nanocomposites modified with SEBS-*g*-MA [207] and PA6–montmorillonite nanocomposites [208].

Maspoch *et al*. [209] added organomodified montmorillonite to poly(ethylene–vinyl alcohol) (EVOH), studying the fracture behavior of 400 μm thick cast films. The presence of the montmorillonite particles promoted an increase in

Table 5.5 EWF parameters of EVOH–montmorillonite nanocomposites.

Material composition	Orientation	w_e (kJ/m^2)	βw_p (MJ/m^3)	w_p (MJ/m^3)
EVOH (100)	MD	29	9.6	45
	TD	37	9.3	45
EVOH/clay (99/1)	MD	43	10.5	35
	TD	78	4.6	31
EVOH/clay (97.5/2.5)	MD	51	12.0	36
	TD	94	3.4	25

Testing conditions: DDENT specimens cut out from extrusion-calendered films (400 μm thick); crosshead speed = 10 mm/min
Data adapted from Ref. [209].

w_e values in both MD and TD orientations due to the matrix–particle interaction (Table 5.5).

5.8 Conclusions

Compared to conventional microcomposites, the theoretical interactions between nanosized fillers and polymer chains are more effective due to the higher specific area of the nanofillers, allowing a good combination of mechanical properties at lower filler concentrations (usually below 5 wt%). Geometric factors such as the aspect ratio have been found to influence the effectiveness of the reinforcement. Higher filler aspect ratios tend to increase the elastic modulus of polymer nanocomposites, although dependent on other characteristics such as polymer–filler interactions and induced filler orientations during processing.

Many computer modeling and simulation methods have been developed to study polymer nanocomposites with different nanofiller geometries. Resulting information on molecular simulation is very useful to understand the level of interaction at the interphase between polymer matrix and nanofiller. Molecular simulations results have been incorporated by several authors into continuum mechanics-based models in order to predict the mechanical behavior of polymer nanocomposites.

Mechanical properties such as the elastic modulus or tensile strength of polymer nanocomposites may be optimized by achieving a good dispersion of nanofillers into the polymer and by promoting strong interphases between both components. These can be accomplished by previous nanofiller modification, the use of compatibilizers, and/or tailoring other characteristics of the matrix such as its molecular weight. These variables also have a strong influence on the fracture parameters obtained at low and high strain rates using several experimental methodologies such as LEFM, J-integral, and EWF, which are employed depending on the plasticity degree of polymer nanocomposites.

DMTA has shown its sensitivity in determining the plasticizing effect that some nanofillers exert on polymeric matrices. It has also been used to evaluate the

degree of interaction between nanofiller particles and polymer matrix through the analysis of the variation of the glass transition temperature and storage modulus.

Even though it has been shown that the mechanical properties of polymer nanocomposites given by nanoindentation measurements are highly dependent on a variety of aspects such as surface roughness, local crystallinity, geometry of the indenter tip and interaction with the surface of the material, or applied test load, this technique may be used to assess direction-dependent mechanical properties, separating elastic and plastic deformations by applying extremely low loads and small displacements, and to identify the possible differences in the material generated during processing or induced by filler presence.

References

1 Pavlidou, S. and Papaspyrides, C.D. (2008) *Progress in Polymer Science*, **33**, 1119–1198.
2 Utracki, L.A., Sepehr, M., and Boccaleri, E. (2007) *Polymers for Advanced Technologies*, **18**, 1–37.
3 Okada, A. and Usuki, A. (2006) *Macromolecular Materials and Engineering*, **291**, 1449–1476.
4 Ruiz-Perez, L., Royston, G.J., Fairclough, J.P.A., and Ryan, A.J. (2008) *Polymer*, **49**, 4475–4488.
5 Kelnar, I., Kotek, J., Kaprálková, L., and Munteanu, B.S. (2005) *Journal of Applied Polymer Science*, **96**, 288–293.
6 Deshmane, C., Yuan, Q., and Misra, R.D. K. (2007) *Materials Science Engineering A*, **460**, 277–287.
7 Cotterell, B., Chia, J.Y.H., and Hbaieb, K. (2007) *Engineering Fracture Mechanics*, **74**, 1054–1078.
8 Móczó, J. and Pukánszky, B. (2008) *Journal of Industrial and Engineering Chemistry*, **14**, 535–563.
9 Cho, J., Chen, J.Y., and Daniel, I.M. (2007) *Scripta Materialia*, **56**, 685–688.
10 Subramaniyan, A.K. and Sun, C.T. (2006) *Composites Part A: Applied Science and Manufacturing*, **37**, 2257–2268.
11 Wetzel, B., Haupert, F., and Zhang, M.Q. (2003) *Composites Science and Technology*, **63**, 2055–2067.
12 Ou, Y., Yang, F., and Yu, Z.Z. (1998) *Journal of Polymer Science Part B: Polymer Physics*, **36**, 789–795.
13 Bauhofer, W. and Kovacs, J.Z. (2009) *Composites Science and Technology*, **69**, 1486–1498.
14 Adnan, A., Sun, C.T., and Mahfuz, H. (2007) *Composites Science and Technology*, **67**, 348–356.
15 Bondioli, F., Cannillo, V., Fabbri, E., and Messori, M. (2005) *Journal of Applied Polymer Science*, **97**, 2382–2386.
16 Cho, J., Joshi, M.S., and Sun, C.T. (2006) *Composites Science and Technology*, **66**, 1941–1952.
17 Chisolm, N., Mahfuz, H., Rangari, V.K., Adnan, A., and Jeelani, S. (2005) *Composite Structures*, **67**, 115–124.
18 Voros, G. and Pukánszky, B. (2002) *Composites Part A: Applied Science and Manufacturing*, **33**, 1317–1322.
19 Reynaud, E., Jouen, T., Gauthier, C., Vigier, G., and Varlet, J. (2001) *Polymer*, **42**, 8759–8768.
20 Friedrich, K., Fakirov, S., and Zhang, Z. (eds) (2005) *Polymer Composites: From Nano- to Macro-Scale*, Springer, New York.
21 Alexandre, M., Dubois, P., Sun, T., Garcés, J.M., and Jérome, R. (2002) *Polymer*, **43**, 2123–2132.
22 Sun, T. and Garcés, J.M. (2002) *Advanced Materials*, **14**, 128–130.
23 Ray, S.S. and Okamoto, M. (2003) *Progress in Polymer Science*, **28**, 1539–1641.
24 Gopakumar, T.G., Lee, J.A., Kontopoulou, M., and Parent, J.S. (2002) *Polymer*, **43**, 5483–5491.

25 Hussain, F., Hojjati, M., Okamoto, M., and Gorga, R.E. (2006) *Journal of Composite Materials*, **40**, 1511–1576.

26 Kontou, E. and Anthoulis, G. (2007) *Journal of Applied Polymer Science*, **105**, 1723–1731.

27 Ajayan, P.M., Schadler, L.S., and Braun, P.V. (eds) (2003) *Nanocomposite Science and Technology*, Wiley-VCH Verlag GmbH, Weinheim.

28 Jancar, J. (2008) *Journal of Materials Science*, **43**, 6747–6757.

29 Maranganti, R. and Sharma, P. (2007) *Journal of the Mechanics and Physics of Solids*, **55**, 1823–1852.

30 Boutaleb, S., Zairi, F., Mesbah, A., Nait-Abdelaziz, M., Gloaguen, J.M., Boukharouba, T., and Lefebvre, J.M. (2009) *International Journal of Solids and Structures*, **46**, 1716–1726.

31 Ciprari, D., Jacob, K., and Tannenbaum, R. (2006) *Macromolecules*, **39**, 6565–6573.

32 Hernández-Pérez, A. and Avilés, F. (2010) *Computational Materials Science*, **47**, 926–933.

33 Miltner, H.E., Van Assche, G., Pozsgay, A., Pukánszky, B., and Van Mele, B. (2006) *Polymer*, **47**, 826–835.

34 McClurg, R.B. (2004) *Chemical Engineering Science*, **59**, 5779–5786.

35 Uddin, M.F. and Sun, C.T. (2008) *Composites Science and Technology*, **68**, 1637–1643.

36 Tsai, J.L. and Wu, M.D. (2007) *Journal of Composite Materials*, **41**, 2513–2528.

37 Iwahori, Y., Ishiwata, S., Sumizawa, T., and Ishikawa, T. (2005) *Composites Part A: Applied Science and Manufacturing*, **36**, 1430–1439.

38 Giannelis, E.P., Krishnamoorti, R., and Manias, E. (1999) *Advances in Polymer Science*, **138**, 107–147.

39 LeBaron, P.C., Wang, Z., and Pinnavaia, T.J. (1999) *Applied Clay Science*, **15**, 11–29.

40 Vaia, R.A., Price, G., Ruth, P.N., Nguyen, H.T., and Lichtenhan, J. (1999) *Applied Clay Science*, **15**, 67–92.

41 Biswas, M. and Sinha Ray, S. (2001) *Advances in Polymer Science*, **155**, 167–221.

42 Giannelis, E.P. (1998) *Applied Organometallic Chemistry*, **12**, 675–680.

43 Eshelby, J.D. (1957) *Proceedings of the Royal Society of London Series A: Mathematical and Physical Sciences*, **241**, 376–396.

44 Hill, R. (1965) *Journal of the Mechanics and Physics of Solids*, **13**, 213–222.

45 Mori, T. and Tanaka, K. (1973) *Acta Metallurgica*, **21**, 571–574.

46 Halpin, J.C. (1969) *Journal of Composite Materials*, **3**, 732–734.

47 Brune, D.A. and Bicerano, J. (2002) *Polymer*, **43**, 369–387.

48 Zeng, Q.H., Yu, A.B., and Lu, G.Q. (2008) *Progress in Polymer Science*, **33**, 191–269.

49 Hill, R. (1963) *Journal of the Mechanics and Physics of Solids*, **11**, 357–372.

50 Tucker, C.L. and Liang, E. (1999) *Composites Science and Technology*, **59**, 655–671.

51 Fornes, T.D. and Paul, D.R. (2003) *Polymer*, **44**, 4993–5013.

52 Tandon, G.P. and Weng, G.J. (1984) *Polymer Composites*, **5**, 327–333.

53 Odegard, G.M., Clancy, T.C., and Gates, T. S. (2005) *Polymer*, **46**, 553–562.

54 Odegard, G.M., Gates, T.S., Wise, K.E., Park, C., and Siochi, E.J. (2003) *Composites Science and Technology*, **63**, 1671–1687.

55 Li, C.Y. and Chou, T.W. (2006) *Composites Science and Technology*, **66**, 2409–2414.

56 Parameswaran, V. and Shukla, D.K. (2010) *Materials Science and Engineering A*, **527**, 3792–3799.

57 Liu, Y.J. and Chen, X.L. (2003) *Mechanics of Materials*, **35**, 69–81.

58 Chen, X.L. and Liu, Y.J. (2004) *Computational Materials Science*, **29**, 1–11.

59 Kulkarni, M., Carnahan, D., Kulkarni, K., Qian, D., and Abot, J.L. (2005) *Composites Part B: Engineering*, **41**, 414–421.

60 Ozdilek, C., Norder, B., and Picken, S.J. (2008) *Thermochimica Acta*, **472**, 31–37.

61 Yung, K.C., Wang, J., and Yue, T.M. (2006) *Journal of Reinforced Plastics and Composites*, **25**, 847–861.

62 Ji, X.Y., Cao, Y.P., and Feng, X.Q. (2010) *Modelling and Simulation in Materials Science and Engineering*, **18**, 045005.

63 Fornes, T., Yoon, P., Hunter, D., Keskkula, H., and Paul, D. (2002) *Polymer*, **43**, 5915–5933.

64 Shokrieh, M.M. and Rafiee, R. (2010) *Mechanics of Composite Materials*, **46**, 155–172.

65 Sheng, N., Boyce, M., Parks, D., Rutledge, G., Abes, J., and Cohen, R. (2004) *Polymer*, **45**, 487–506.

66 Odegard, G.M., Gates, T.S., Nicholson, L. M., and Wise, K.E. (2002) *Composites Science and Technology*, **62**, 1869–1880.

67 Fisher, F.T., Bradshaw, R.D., and Brinson, L.C. (2003) *Composites Science and Technology*, **63**, 1689–1703.

68 Shi, D.L., Feng, X.Q., Huang, Y.G.Y., Hwang, K.C., and Gao, H.J. (2004) *Journal of Engineering Materials and Technology: Transactions of the ASME*, **126**, 250–257.

69 Shi, D.L., Feng, X.Q., Huang, Y.Y., and Hwang, K.C. (2004) in *Advances in Fracture and Failure Prevention: Parts 1 and 2* (eds K. Kishimoto, M. Kikuchi, T. Shoji, and M. Saka), Trans Tech Publications, Ltd., pp. 261–263 and 1487–1492.

70 Avella, M., Bondioli, F., Cannillo, V., Errico, M.E., Ferrari, A.M., Focher, B., Malinconico, M., Manfredini, T., and Montorsi, M. (2004) *Materials Science and Technology*, **20**, 1340–1344.

71 Tjong, S.C. (2006) *Materials Science and Engineering: R: Reports*, **53**, 73–197.

72 Alexandre, M. and Dubois, P. (2000) *Materials Science and Engineering: R: Reports*, **28**, 1–63.

73 Ray, S. and Easteal, A.J. (2007) *Materials and Manufacturing Processes*, **22**, 741–749.

74 Johnsen, B.B., Kinloch, A.J., Mohammed, R.D., Taylor, A.C., and Sprenger, S. (2007) *Polymer*, **48**, 530–541.

75 Wang, K., Chen, L., Wu, J., Toh, M., He, C., and Yee, A. (2005) *Macromolecules*, **38**, 788–800.

76 Zunjarrao, S.C., Sriraman, R., and Singh, R.P. (2006) *Journal of Materials Science*, **41**, 2219–2228.

77 Zhao, Q. and Hoa, S.V. (2007) *Journal of Composite Materials*, **41**, 201–219.

78 Kojima, Y., Usuki, A., Kawasumi, M., Okada, A., Kurauchi, T., and Kamigaito, O. (1993) *Journal of Polymer Science Part A: Polymer Chemistry*, **31**, 1755–1758.

79 Liu, L.M., Qi, Z.N., and Zhu, X.G. (1999) *Journal of Applied Polymer Science*, **71**, 1133–1138.

80 Lee, D. and Jang, L. (1996) *Journal of Applied Polymer Science*, **61**, 1117–1122.

81 Hasegawa, N., Kawasumi, M., Kato, M., Usuki, A., and Okada, A. (1998) *Journal of Applied Polymer Science*, **67**, 87–92.

82 Noh, M.W. and Lee, D.C. (1999) *Polymer Bulletin*, **42**, 619–626.

83 Tarapow, J.A., Bernal, C.R., and Álvarez, V.A. (2009) *Journal of Applied Polymer Science*, **111**, 768–778.

84 Fornes, T.D., Yoon, P.J., Keskkula, H., and Paul, D.R. (2001) *Polymer*, **42**, 9929–9940.

85 Fornes, T.D. and Paul, D.R. (2003) *Polymer*, **44**, 3945–3961.

86 Iijima, S. (1991) *Nature*, **354**, 56–58.

87 Lau, K.T., Gu, C., and Hui, D. (2006) *Composites Part B: Engineering*, **37**, 425–436.

88 Ma, P.C., Siddiqui, N.A., Marom, G., and Kim, J.K. (2010) *Composites Part A: Applied Science and Manufacturing*, **41**, 1345–1367.

89 Qian, D., Dickey, E.C., Andrews, R., and Rantell, T. (2000) *Applied Physics Letters*, **76**, 2868–2870.

90 Coleman, J.N., Khan, U., Blau, W.J., and Gun'ko, Y.K. (2006) *Carbon*, **44**, 1624–1652.

91 Hernandez-Pérez, A., Avilés, F., May-Pat, A., Valadez-González, A., Herrera-Franco, P.J., and Bartolo-Pérez, P. (2008) *Composites Science and Technology*, **68**, 1422–1431.

92 Kosmidou, T.V., Vatalis, A.S., Delides, C. G., Logakis, E., Pissis, P., and Papanicolaou, G.C. (2008) *Express Polymer Letters*, **2**, 364–372.

93 Gorga, R.E. and Cohen, R.E. (2004) *Journal of Polymer Science Part B: Polymer Physics*, **42**, 2690–2702.

94 Liu, Y.Q. and Kontopoulou, M. (2006) *Polymer*, **47**, 7731–7739.

95 Elias, L., Fenouillot, F., Majeste, J.C., and Cassagnau, P. (2007) *Polymer*, **48**, 6029–6040.

96 Yang, H., Zhang, X.Q., Qu, C., Li, B., Zhang, L.J., Zhang, Q., and Fu, Q. (2007) *Polymer*, **48**, 860–869.

97 Bailly, M. and Kontopoulou, M. (2009) *Polymer*, **50**, 2472–2480.

98 Cai, D.Y. and Song, M. (2010) *Journal of Materials Chemistry*, **20**, 7906–7915.

99 Lee, C., Wei, X.D., Kysar, J.W., and Hone, J. (2008) *Science*, **321**, 385–388.

100 Verdejo, R., Barroso-Bujans, F., Rodríguez-Perez, M.A., de Saja, J.A., and

López-Manchado, M.A. (2008) *Journal of Materials Chemistry*, **18**, 2221–2226.
101 Xu, Y.X., Hong, W.J., Bai, H., Li, C., and Shi, G.Q. (2009) *Carbon*, **47**, 3538–3543.
102 Mc Nally, T., Murphy, W.R., Lew, C.Y., Turner, R.J., and Brennan, G.P. (2003) *Polymer*, **44**, 2761–2772.
103 Kim, J.T., Oh, T.S., and Lee, D.H. (2003) *Polymer International*, **52**, 1058–1063.
104 Teh, P.L., Mohd Ishak, Z.A., Hashim, A. S., Karger-Kocsis, J., and Ishiaku, U.S. (2004) *Journal of Applied Polymer Science*, **94**, 2438–2445.
105 Zhang, W., Chen, Z., Zhao, Q., and Fang, Y. (2003) *Polymer*, **44**, 7953–7961.
106 Wan, C., Qiao, X., Zhang, Y., and Zhang, Y. (2003) *Polymer Testing*, **22**, 453–461.
107 Wang, Q., Zhang, Z., Jin, Y., Gui, H., Dong, W., Lal, J., Liu, Y., Gao, J., Huang, F., Song, Z., and Qiao, J. (2006) *Macromolecular Materials and Engineering*, **291**, 665–660.
108 Sterzynski, T., Tomaszewska, J., Piszczek, K., and Skórczewska, K. (2010) *Composites Science and Technology*, **70**, 966–969.
109 Zhang, X., Xu, R., Wu, Z., and Zhou, C. (2003) *Polymer International*, **52**, 790–794.
110 Finnigan, B., Martin, D., Halley, P., Truss, R., and Campbell, K. (2004) *Polymer*, **45**, 2249–2260.
111 Barick, A.K. and Tripathy, D.K. (2010) *Materials Science and Engineering*, **A527**, 812–823.
112 Lew, C.Y., Murphy, W.R., and McNally, G. M. (2004) *Polymer Engineering and Science*, **44**, 1027–1035.
113 Ding, C., Jia, D., He, H., Guo, B., and Hong, H. (2005) *Polymer Testing*, **24**, 94–100.
114 Wang, Y. and Huan, S.W. (2007) *Polymer-Plastics Technology and Engineering*, **46**, 1039–1047.
115 Lee, S.H., Kim, S.Y., and Youn, J.R. (2009) *Composites: Part A*, **40**, 968–974.
116 Jain, S., Goossens, H., van Duin, M., and Lemstra, P. (2005) *Polymer*, **46**, 8805–8818.
117 Jia, Q.X., Wu, Y.P., Wang, Y.Q., Lu, M., and Zhang, L.Q. (2008) *Composites Science and Technology*, **68**, 1050–1056.
118 Antunes, M., Velasco, J.I., Realinho, V., and Arencón, D. (2010) *Journal of Nanoscience and Nanotechnology*, **10**, 1241–1250.
119 Ding, C., Guo, B., He, H., Jia, D., and Hong, H. (2005) *European Polymer Journal*, **41**, 1781–1786.
120 Pluta, M., Paul, M.A., Alexandre, M., and Dubois, P. (2006) *Journal of Polymer Science Part B: Polymer Physics*, **44**, 299–311.
121 Fukushima, K., Tabuani, D., and Camino, G. (2009) *Materials Science and Engineering*, **C29**, 1433–1441.
122 Wilkinson, A.N., Man, Z., Stanford, J.L., Mankainen, P., Clemens, M.L., Lees, G. C., and Liauw, C.M. (2006) *Macromolecular Materials and Engineering*, **291**, 655–660.
123 Baghaei, B., Jafari, S.Y., Khonakdar, H.A., and Ashabi, L. (2009) *e-Polymers*, **82**, 1–11.
124 Chu, D., Nguyen, Q., and Baird, D.G. (2007) *Polymer Composites*, **28**, 499–511.
125 Dong, Y., Bhattacharyya, D., and Hunter, P.J. (2008) *Composites Science and Technology*, **68**, 2864–2875.
126 Chow, W.S. (2008) *Journal of Applied Polymer Science*, **110**, 1642–1648.
127 Artzi, N., Nir, Y., Narkis, M., and Siegmann, A. (2002) *Journal of Polymer Science Part B: Polymer Physics*, **40**, 1741–1753.
128 Artzi, N., Nir, Y., Wang, D., Narkis, M., and Siegmann, A. (2001) *Polymer Composites*, **22**, 710–720.
129 Artzi, N., Nir, Y., Narkis, M., and Siegmann, A. (2003) *Polymer Composites*, **44**, 1027–1035.
130 McAdam, C.P., Hudson, N.E., Liggat, J.J., and Pethrick, R.A. (2008) *Journal of Applied Polymer Science*, **108**, 2242–2251.
131 Chow, W.S., Mohd Ishak, Z.A., Karger-Kocsis, J., Apostolov, A.A., and Ishiaku, U. S. (2003) *Polymer*, **44**, 7427–7440.
132 Chow, W.S., Abu Bakar, A., Mohd Ishak, Z.A., Karger-Kocsis, J., and Ishiaku, U.S. (2005) *European Polymer Journal*, **41**, 687–696.
133 Wang, K., Liang, S., Deng, J., Yang, H., Zhang, Q., Fu, Q., Dong, X., Wang, D., and Han, C.C. (2006) *Polymer*, **47**, 7131–7144.
134 Zhang, G., Ding, P., Zhang, M., and Qu, B. (2007) *Polymer Degradation and Stability*, **92**, 1715–1720.

135 Stankowski, M., Kropidlowska, A., Gazda, M., and Haponiuk, J.T. (2008) *Journal of Thermal Analysis and Calorimetry*, **94**, 817–823.

136 Realinho, V., Velasco, J.I., Antunes, M., Sánchez-Soto, M., and Maspoch, M.L. (2010) *Journal of Nanoscience and Nanotechnology*, **10**, 1304–1312.

137 Lee, S.H., Wang, S., Pharr, G.M., and Xu, H. (2007) *Composites Part A*, **38**, 1517–1524.

138 Qi, H.J., Teo, K.B.K., Lau, K.K.S., Boyce, M. C., Milne, W.I., Robertson, J., and Gleason, K.K. (2003) *Journal of the Mechanics and Physics of Solids*, **51**, 2213–2237.

139 Li, X. and Bhushan, B. (2002) *Materials Characterization*, **48**, 11–36.

140 Gao, S.L. and Mader, E. (2002) *Composites Part A: Applied Science and Manufacturing*, **33**, 559–576.

141 Downing, T.D., Kumar, R., Cross, W.M., Kjerengtroen, L., and Kellar, J.J. (2000) *Journal of Adhesion Science and Technology*, **14**, 1801–1812.

142 Munz, M., Sturm, H., Schulz, E., and Hinrichsen, G. (1998) *Composites Part A*, **29**, 1251–1259.

143 Hu, H., Onyebueke, L., and Abatan, A. (2010) *Journal of Minerals and Materials Characterization and Engineering*, **9**, 275–319.

144 Briscoe, B.J., Sebastian, K.S., and Adams, M.J. (1994) *Journal of Physics D: Applied Physics*, **27**, 1156–1162.

145 Beake, B.D., Goodes, S.R., Smith, J.F., and Gao, F.J. (2004) *Journal of Materials Research*, **19**, 237–247.

146 Drechsler, D., Karbach, A., and Fuchs, H. (1998) *Applied Physics A: Materials Science and Processing*, **66**, S825–S829.

147 Fang, T.H. and Chang, W.J. (2004) *Microelectronics Journal*, **35**, 595–599.

148 Flores, A. and Calleja, F.J.B. (1998) *Philosophical Magazine A*, **78**, 1283–1297.

149 Hochstetter, G., Jimenez, A., Cano, J.P., and Felder, E. (2003) *Tribology International*, **36**, 973–985.

150 Park, K., Mishra, S., Lewis, G., Losby, J., Fan, Z.F., and Park, J.B. (2004) *Biomaterials*, **25**, 2427–2436.

151 Penumadu, D., Dutta, A., Pharr, G.M., and Files, B. (2003) *Journal of Materials Research*, **18**, 1849–1853.

152 Van Landingham, M.R., Villarrubia, J.S., Guthrie, W.F., and Meyers, G.F. (2001) *Macromolecular Symposia*, **167**, 15–43.

153 Oliver, W.C. and Pharr, G.M. (1992) *Journal of Materials Research*, **7**, 1564–1583.

154 Briscoe, B.J., Fiori, L., and Pelillo, E. (1998) *Journal of Physics D: Applied Physics*, **31**, 2395–2405.

155 Rodríguez, R. and Gutiérrez, I. (2003) *Materials Science and Engineering A*, **361**, 377–384.

156 Li, H., Ghosh, A., Han, Y.H., and Bradt, R. C. (1993) *Journal of Materials Research*, **8**, 1028–1032.

157 Shen, L., Phang, I.Y., Liub, T., and Zeng, K. (2004) *Polymer*, **45**, 8221–8229.

158 Lucas, B.N., Oliver, W.C., and Swindeman, J.E. (1998) *Materials Research Society Symposia Proceedings*, **522**, 3–14.

159 Sikdar, D., Pradhan, S.M., Katti, D.R., Katti, K.S., and Mohanty, B. (2008) *Langmuir*, **24**, 5599–5607.

160 Sikdar, D., Katti, D., Katti, K., and Mohanty, B. (2007) *Journal of Applied Polymer Science*, **105**, 790–802.

161 Palacio, M., Bhushan, B., Ferrell, N., and Hansford, D. (2007) *Sensors and Actuators A*, **135**, 637–650.

162 Beake, B.D., Chen, S., Hull, J.B., and Gao, F. (2002) *Journal of Nanoscience and Nanotechnology*, **2**, 73–79.

163 Shen, L., Phang, I.Y., Chen, L., Liu, T., and Zeng, K. (2004) *Polymer*, **45**, 3341–3349.

164 Phang, I.Y., Liu, T., Mohamed, A., Pramoda, K.P., Chen, L., Shen, L., Chow, S.Y., He, C., Lu, X., and Hu, X. (2005) *Polymer International*, **54**, 456–464.

165 Nai, M.H., Lim, C.T., Zeng, K.Y., and Tan, V.B.C. (2005) *Journal of Metastable and Nanocrystalline Materials*, **23**, 363–366.

166 Dhakal, H.N., Zhang, Z.Y., and Richardson, M.O.W. (2006) *Polymer Testing*, **25**, 846–852.

167 Li, X., Gao, H., Scrivens, W.A., Fei, D., Xu, X., Sutton, M.A., Reynolds, A.P., and Myrick, M.L. (2004) *Nanotechnology*, **15**, 1416–1423.

168 Liu, T.X., Phang, I.Y., Shen, L., Chow, S.Y., and Zhang, W.D. (2004) *Macromolecules*, **37**, 7214–7222.

169 Xu, G.C., Li, A.Y., De Zhang, L., Yu, X.Y., Xie, T., and Wu, G.S. (2004) *Journal of*

Reinforced Plastics and Composites, **23**, 1365–1372.

170 Zaidi, L., Bruzaud, S., Bourmaud, A., Médéric, P., Kaci, M., and Grohens, Y. (2010) *Journal of Applied Polymer Science*, **116**, 1357–1365.

171 Olek, M., Kempa, K., Jurga, S., and Giersig, M. (2005) *Langmuir*, **21**, 3146–3152.

172 Kanny, K., Jawahar, P., and Moodley, V.K. (2008) *Journal of Materials Science*, **43**, 7230–7238.

173 Dasari, A., Yu, Z.Z., and Mai, Y.W. (2007) *Macromolecules*, **40**, 123–130.

174 Kotek, J., Kelnar, I., Baldrian, J., and Slouf, M. (2008) *Journal of Applied Polymer Science*, **110**, 3752–3757.

175 Realinho, V., Antunes, M., Arencón, D., Fernández, A.I., and Velasco, J.I. (2009) *Journal of Applied Polymer Science*, **111**, 2574–2583.

176 Zerda, A.S. and Lesser, A.J. (2001) *Journal of Polymer Science Part B: Polymer Physics*, **39**, 1137–1146.

177 Boo, W.J., Sun, L.Y., Liu, J., Moghbelli, E., Sue, H.J., Pham, H., and Verghese, N. (2007) *Journal of Polymer Science Part B: Polymer Physics*, **45**, 1459–1469.

178 Weon, J.I. and Sue, H.J. (2005) *Polymer*, **46**, 6325–6334.

179 Chen, L., Wong, S.-C., and Pisharath, S. (2003) *Journal of Applied Polymer Science*, **88**, 3298–3305.

180 Chen, L., Wong, S.-C., Liu, T., Lu, X., and He, C. (2004) *Journal of Polymer Science*, **42**, 2759–2768.

181 Kim, D.H., Fasulo, P.D., Rodgers, W.R., and Paul, D.R. (2007) *Polymer*, **48**, 5308–5323.

182 Fornes, T.D. and Paul, D.R. (2004) *Macromolecules*, **37**, 7698–7709.

183 Wang, K., Liang, S., Deng, J., Yang, H., Zhang, Q., Fu, Q., Dong, X., Wang, D., and Han, C.C. (2006) *Polymer*, **47**, 7131–7144.

184 Park, J.H. and Jana, S.C. (2003) *Polymer*, **44**, 2091–2100.

185 Wan, C., Qiao, X.Y., and Zhang, Y. (2003) *Journal of Applied Polymer Science*, **89**, 2184–2191.

186 Basara, G., Yilmazer, U., and Bayram, G. (2005) *Journal of Applied Polymer Science*, **98**, 1081–1086.

187 Isik, I., Yilmazer, U., and Bayram, G. (2003) *Polymer*, **44**, 6371–6377.

188 Wetzel, B., Rosso, P., Haupert, F., and Friedrich, K. (2006) *Engineering Fracture Mechanics*, **73**, 2375–2398.

189 Chen, L., Phang, I.Y., Wong, S.-C., Lu, P.-F., and Liu, T. (2006) *Materials and Manufacturing Processes*, **22**, 153–158.

190 Prashanta, K., Soulestin, J., Lacrampe, M. F., Krawczak, P., Dupin, G., and Claes, M. (2009) *Composites Science and Technology*, **69**, 1756–1763.

191 Khosh, R.L., Bagheri, R., and Zokaei, S. (2008) *Journal of Applied Polymer Science*, **110**, 4040–4048.

192 Wang, Y., Shen, H., Li, G., and Mai, K. (2009) *Journal of Applied Polymer Science*, **113**, 1584–1592.

193 Zhao, H. and Li, R.K.Y. (2005) *Journal of Polymer Science Part B: Polymer Physics*, **43**, 3652–3664.

194 Wu, D.F., Wang, H.L., Zhou, Y.B., and Ren, Q. (2003) *Acta Polymerica Sinica*, **4**, 559–564.

195 Yuan, Q. and Misra, R.D.K. (2006) *Polymer*, **47**, 4421–4433.

196 Ma, P.C., Kim, J.-K., and Tang, B.Z. (2007) *Composites Science and Technology*, **67**, 2965–2972.

197 Park, S.J., Seo, D.I., and Nah, C. (2002) *Journal of Colloid and Interface Science*, **251**, 225–229.

198 Zhou, T.H., Ruan, W.H., Mai, Y.L., Rong, M.Z., and Zhang, M.Q. (2008) *Composites Science and Technology*, **68**, 2858–2863.

199 Zhang, J.L., Bai, S.L., Liu, D.L., Zhang, Q. X., and Yu, Z.Z. (2007) *Composites Science and Technology*, **67**, 238–243.

200 Liu, Y., Chen, H., Chan, C.-M., and Wu, J. (2009) *Macromolecules*, **41**, 9204–9213.

201 Bureau, M.N., Perrin-Sarazin, F., and Ton-That, M.-T. (2004) *Polymer Engineering and Science*, **44**, 1142–1151.

202 Bureau, M.N., Ton-That, M.-T., and Perrin-Sarazin, F. (2006) *Engineering Fracture Mechanics*, **73**, 2360–2374.

203 Saminathan, K., Selvakumar, P., and Bhatnagar, N. (2008) *Polymer*, **27**, 296–307.

204 Kobayashi, H., Shioya, M., Tanaka, T., Irisawa, T., Sakurai, S., and Yamamoto, K. (2007) *Journal of Applied Polymer Science*, **106**, 152–160.

205 Satapathy, B.K., Weidisch, R., Pötschke, P., and Janke, A. (2005) *Macromolecular Rapid Communications*, **26**, 1246–1252.

206 Lim, S.H., Dasari, A., Yu, Z.Z., Mai, Y.W., Liu, S., and Yong, M.S. (2007) *Composites Science and Technology*, **67**, 2914–2923.

207 Kusmono, Mohd Ishak, Z.A., Chow, W.S., Takeichi, T., and Rochmadi (2008) *European Polymer Journal*, **44**, 1023–1039.

208 Tjong, S.C. and Bao, S.P. (2005) *Journal of Polymer Science Part B: Polymer Physics*, **43**, 585–595.

209 Maspoch, M.L., Franco-Urquiza, E., Gámez-Pérez, J., Santana, O.O., and Sánchez-Soto, M. (2009) *Polymer International*, **58**, 648–655.

6
Characterization of Nanocomposites by Optical Analysis

Lucilene Betega de Paiva and Ana Rita Morales

6.1
Introduction

In conventional composites, the reinforcing agents are microsized particles. Because of the size of the particles when the materials are exposed to light in the visible region, scattering of light occurs which results in reduced light transmittance and optical clarity. In other words, almost all composites based on polymer matrix and inorganic fillers are opaque, unless the refractive index (RI) of inorganic filler is approximately the same as that of the transparent polymer matrix [1].

However, when the fillers have nanometric size, that is, the particles have dimensions far below the wavelength of the light, the scattering of the light can be reduced offering a material with improved optical properties [2]. This is the case of organoclays used to prepare polymeric nanocomposites. The individual layer of the clay mineral presents lateral dimensions in micrometers, but their thickness is less than 1 nm. Therefore, for high translucency on compounds, particles are necessary to have average size smaller than the wavelength of visible light, in the range 400–800 nm.

When single layers of clay minerals are dispersed in a polymer matrix to form a nanocomposite, a material optically clear in the visible region can be obtained, but with loss in the UV region ($\lambda < 250$ nm) mostly due to scattering by layers of the clay mineral. The unique behavior of the nanoparticles when interacting with light leads to special applications such as UV and IR absorbers.

Besides nanoclays, zinc oxide (ZnO) is also a notable inorganic material that can offer optical transparency and shielding to ultraviolet light when used in polymer matrix to prepare nanocomposites [2].

Metal nanoparticles can also be cited. The characteristic properties of metal nanoparticles and nanocomposites have been the subject of study because of their unique optical properties. Combining metal and polymer together enhances the optical properties of nanometals. Srivastava *et al.* [3] studied the optical properties of gold nanocomposites by changing the size and fraction of gold nanoparticles. The optical properties of nanocomposite films of various thicknesses with different sizes and volume fraction of gold nanoparticles have been studied using spectroscopic

Polymer Composites: Volume 2, First Edition. Edited by Sabu Thomas, Kuruvilla Joseph, Sant Kumar Malhotra, Koichi Goda, and Meyyarappallil Sadasivan Sreekala.

ellipsometry, and they showed the ability to obtain optical coatings with tunable optical properties. They also found that the behavior of the optical absorption is a function of interfacial morphology.

Dammer *et al*. [4] also worked with metal nanoparticles and showed the importance of preparation procedure on the optical properties of polymer nanocomposites with gold nanoparticles. Similar to other properties, optical properties depend on the dispersion of nanoparticles caused by the processing conditions.

Several other nanoparticles have been studied because physical properties of the nanostructures differ from the bulk materials [5,6]. Metal nanoparticles such as ZnO and titanium dioxide (TiO_2), for example, provide nanocomposites the attractive nonlinear properties that make them ideal candidates for nonlinear optical (NLO) based devices [5]. Porous system-based nanocomposites, including porous materials such as silicon, gallium phosphide, aluminum oxide, and structures based on them, were considered by Golovan *et al.* [6]. The main focus is on the effect of birefringence, which is caused by the anisotropy of pores in the materials.

Transparent materials nanocomposites with high refractive index ($n \sim 1.65$–1.79) and high transparence in visible light region, with transmittance higher than 90%, are potential materials for fabrication of optical fibers, waveguides, lenses, and LED packages [7].

Although there is a substantial expansion in the field of polymer nanocomposites, especially those based on organophilic clay, there has been little focus on transparent optical nanocomposites and also in the characterization based on optical analysis.

Many times, the optical clarity of nanocomposite can be seen by looking through films produced with these materials. But optical properties can be evaluated by different techniques, such as gloss, haze, and color measurements and UV–visible spectrophotometry. Furthermore, optical analysis such as optical microscopy can be applied to verify the dispersion of the particles in a matrix that can be related to transparency of the nanocomposites. All these techniques applied on nanocomposites based on polymeric matrix and different kinds of nanoparticles are discussed and illustrated in this chapter.

6.2
Influence of Nanoparticles on the Visual Aspect of Nanocomposites

As mentioned earlier, optically transparent materials can be obtained by incorporation of a low quantity of inorganic filler with dimensions below the wavelength of light.

But not only the dimensions and the concentration is enough to obtain an optically transparent material. The morphology and the aggregation of inorganic particles can influence the optical properties of nanocomposites. Nanometric-sized particles compared to micron-sized particles have higher surface/volume ratio. When the particle size decreases, the percentage of molecules/atoms present on the surface is increased. For this reason, the interparticle interactions due to forces such as van der

Waals or magnetic attraction become stronger, and some clusters or agglomerates can be formed. The clusters and agglomerates of nanoparticles cannot disperse individually and uniformly in the polymer matrix, consequently resulting in opaque nanocomposites similar to conventional composites. Therefore, the size control of particles alone may not be enough to acquire materials with good optical properties. It must take into account that surface chemical treatment of particles plays a major role, because of the presence of surface sites that can cause surface interactions leading to agglomeration. Proper chemical treatment of nanoparticles is many times necessary to reduce the surface energy and improve the dispersion in polymer matrix [8,9].

One of the simplest ways to evaluate optical transparency is by looking at visual aspects, with the naked eye. Some examples of the influence of concentration and surface treatment of nanoparticles on visual aspect based on several kinds of nanoparticles and polymer matrix from recent literature are discussed in the following sections.

In the work of Chang *et al.* [10], the optical translucency of poly(lactic acid) nanocomposites with organophilic montmorillonite and synthetic mica was evaluated. Films of nanocomposites loaded with 2, 4, 6, and 8 wt% of clay were compared with the pure polymer. The films were off-white in color, but highly translucent, as shown in Figure 6.1. The levels of translucency of the samples loaded up to 6% of clay were not significantly affected compared to the film without clay. However, the films loaded with 8 wt% of organoclays were slightly cloudier. The translucency slightly decreased with increasing organoclay content because of the clay particles agglomeration. The authors mention that the nanocomposites films have phase domains smaller than the wavelengths of the light and for this reason the materials may be translucent even though the content of clay is increased.

Li *et al.* [2] showed that lamps of pure epoxy resin are transparent and nanocomposites of epoxy matrix and 0.07 wt% of ZnO have the same appearance, Figure 6.2, what means that the incorporation of the inorganic filler does not affect the original transparency of the matrix.

The optical properties of nanocomposites prepared with poly(styrene–maleic anhydride) copolymer coated with alumina nanoparticles and polycarbonate as matrix was evaluated by Chandra *et al.* [8]. The transparencies were compared for samples with 2 mm thick polycarbonate neat resin, the samples of nanocomposites containing 1 and 2 wt% of treated alumina, and a sample containing 2 wt% of untreated alumina. The samples were put on top of a pattern, as shown in Figure 6.3. The sample with 1 wt% of treated alumina was the most transparent among the samples containing nanoparticles, even though some haziness could be observed.

Although higher transparency is expected when a good dispersion is achieved, Hernández *et al.* [11] found different behavior in nanocomposites of poly(ethylene terephthalate) and single-wall nanotubes. A comparison of the transparency of nanocomposites loaded with 0.1 wt% of single-wall carbon nanotubes prepared by direct mixing and by *in situ* polymerization was made. The transparencies of two films with approximately the same thickness placed over 1€ coin is shown

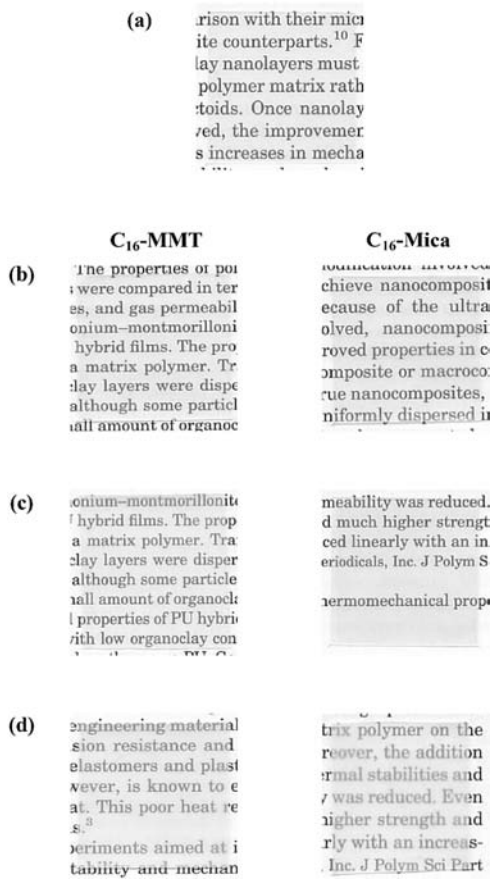

Figure 6.1 Translucency of poly(lactic acid) films containing (a) 0 (pure polymer), (b) 4, (c) 6, and (d) 8 wt% of organoclays. Reproduced from Ref. [10] with permission of Elsevier.

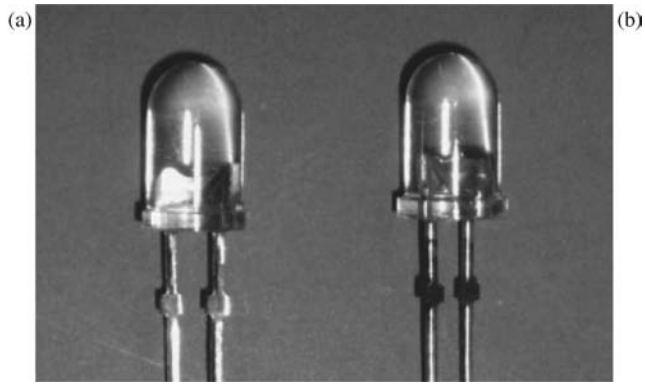

Figure 6.2 UV–WLED lamps encapsulated with (a) pure epoxy resin, and (b) ZnO–T-epoxy nanocomposite with 0.07 wt% ZnO loading. Reproduced from Ref. [2] with permission of Elsevier.

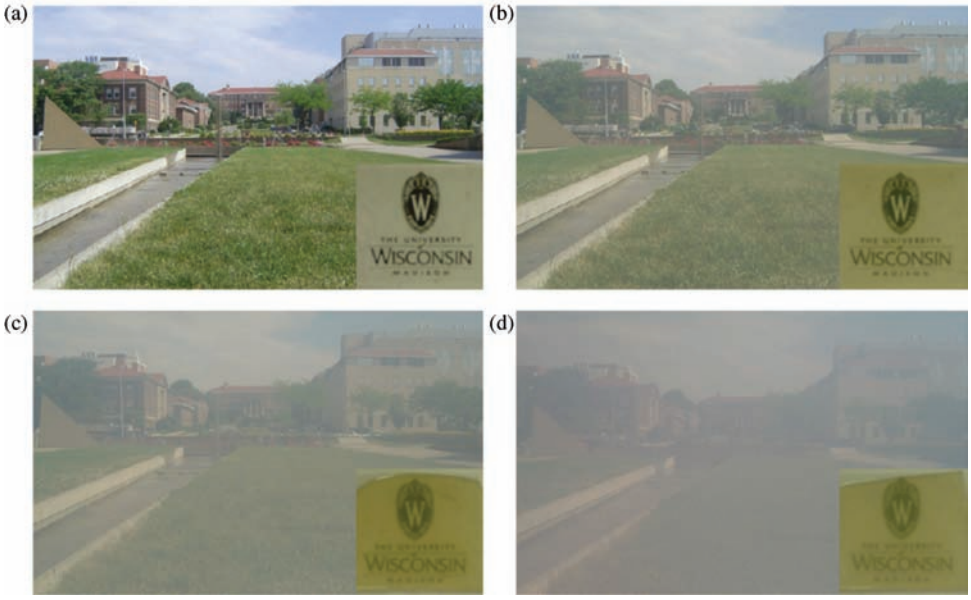

Figure 6.3 Transparencies of the (a) PC neat resin, (b) 1 wt%, and (c) 2 wt% PC/alumina (SMA-coated), and (d) 2 wt% PC/alumina (untreated). Reproduced from Ref. [8] with permission of Elsevier.

in Figure 6.4. While the sample prepared by direct mixing allows seeing the coin behind, the sample prepared by *in situ* polymerization does not. The observed different transmittance for the two investigated samples should be attributed to differences in the dispersion of the carbon nanotubes in polymer matrix that were evaluated by scanning electron microscopy. Nanocomposites prepared by *in situ* polymerization showed the lower transparency because of the better dispersion of nanoadditive compared to the more transparent nanocomposite prepared by direct mixing. The authors proposed that dispersed carbon nanotubes acted as light scatterers, so the better dispersion, the higher number of light scatterers, while the formation of aggregation of the nanoparticles reduced the number of light scatterers, hence favoring the transmittance of the visible light through these materials.

6.3
Characterization of Appearance

Many times, a uniform appearance is an important criterion of quality for products. The human eyes can be a good tool to evaluate appearance, but are insufficient, especially for quality control, because the evaluation conditions are not well defined. Furthermore, different people have different perception, so the perception of appearance is a personal experience.

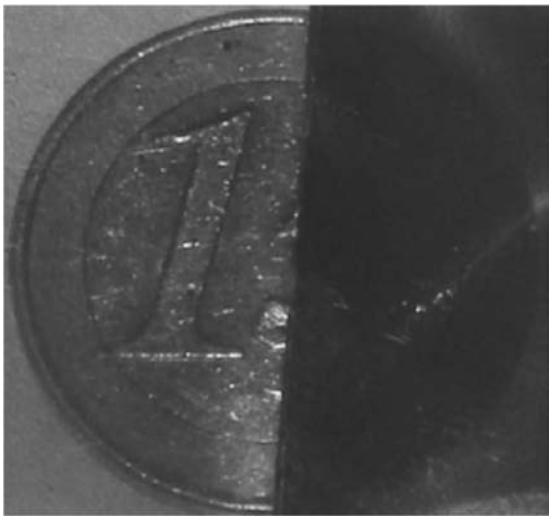

Figure 6.4 Comparison of the transparency of nanocomposites with 0.1 wt% of single-wall carbon nanotubes prepared by direct mixing (left side) and by *in situ* polymerization (right side). Thicknesses of nanocomposites are 270 and 250 μm, respectively. Reproduced from Ref. [11] with permission of Elsevier.

The appearance of materials includes several characteristics, such as gloss, haze, and color. These characteristics are also studied for polymer nanocomposites and are the main objectives of this section.

6.3.1 Gloss

Gloss is characterized as a visual impression resulting from surface evaluation. It depends on the reflection of light over a surface. So, the more direct the reflected light is, the more obvious the impression of gloss will be.

The gloss effects are related to the interaction of light with physical properties of the surface of sample. The properties of the surface include the following:

- *Condition of the surface*: for example, revetment, class of material, plastic, metal.
- *Texture of the surface*: smooth, polished, rough, wavy.

Different surfaces reflect images distinctly. In smooth and highly polished surfaces the incident light is directly reflected on the surface, that is, only in the main direction of the reflection. In this case, the angle of incidence of light is the same to the angle of reflection, resulting in high gloss surface [12].

On the other hand, in rough surfaces the light is diffusely scattered in all directions. In consequence of scattering, a reflected object does not appear brilliant, but blurred, resulting in matte to semigloss surface. The more uniform the light

scattering is, the less intense the reflection in the main direction will be, so the surface will appear dull.

The measure of gloss can be done with a glossmeter. This equipment measures the specular reflection. The light intensity, dependent on the material and the angle of illumination, is registered over a small range of the reflection angle [12].

Measurement results obtained from a glossmeter are associated to the amount of reflected light from a black glass standard with a defined refractive index, but not to the amount of incident light. The measurement value for this technique is defined through a standard scale given in unit gloss, where 100 gloss units is the calibration value. For materials with high refractive index, as some films, the measurement value can be above 100 gloss units. In case of transparent materials, the measurement value can be increased due to multiple reflections in the bulk of the material [12].

Ahmadi *et al.* [13] measured gloss of a nanocomposite based on polyurethane and nano-layered silicates in the concentration of 1, 3, and 5 wt%. The nanocomposite was supposed to be used in on automotive refinish clear coat. The gloss was not changed until 3 wt% of nanofiller, but was slightly reduced with 5 wt% of nanofiller.

6.3.2 Haze

Haze can be defined as a cloudiness of a product that is caused by light scattering. In other words the term haze refers to the visual clarity of a material. The presence of haze can be a positive or a negative factor, it depends on the application.

The haze can be attributed to several factors, such as particles dispersion, particles sizes embedded in film surface or polymer matrix, surface roughness due to large crystallite size, and wide variation in crystallite, presence of voids or pinholes, absorption or trapping of moisture, and so on [14]. There are a large number of defects involved in the structure and surface of materials, for this reason it is sometimes difficult to find the exact cause of haze.

The transmission haze occurs when the light is transmitted through a material, which can be seen as a transparent or slightly translucent material.

The transmission haze is the ratio of the diffuse transmittance (DT) to the total transmittance (TT). Haze measurement documentary standards recommend using an integration sphere to get the summation of transmission light directly, that is, the summation of DT and TT. Since the transmittance depends strongly on the geometry of the incident beam, every documentary standard has a strict definition for the incident beam, such as shape, size, divergent angle, and so on [15].

Currently haze measurement is carried out according to the methods described in several documentary standards such as ASTM D1003 and ISO 13468 among others. In each documentary the apparatus and the measurement precision are different [15].

Many nanocomposites prepared with different polymer matrix can show good low haze. Wang *et al.* [16] elucidated that transparent rubber materials can be prepared if the rubber itself is a transparent material. In case of the *cis*-1,4 polybutadiene

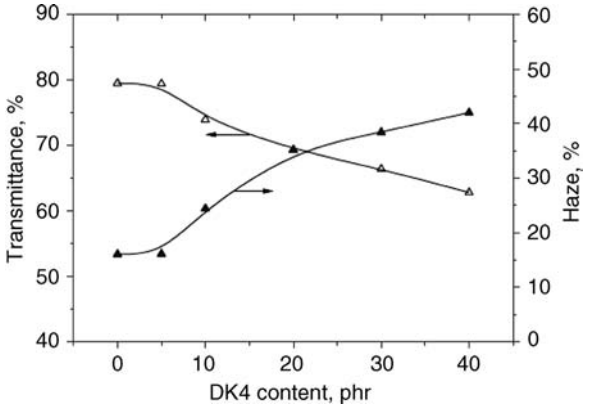

Figure 6.5 Effect of organoclay content (DK4) on optical properties of BR–organoclay nanocomposites. Reproduced from Ref. [16] with permission of Elsevier.

(butadiene rubber, BR) it is possible to prepare transparent BR–clay nanocomposites if the clay is finely dispersed at the nanoscale. This is possible because BR is transparent at room temperature due to its amorphous characteristic, and also because the refractive index of clay (1.53 at 25 °C) is close to that of the BR (1.52 at 20 °C). The authors measured light transmission and haze of the BR nanocomposites loaded with 5, 10, 20, and 30 phr of an organoclay. The analyzed specimens were 1 mm in thickness. It was observed that the transmission and the haze of the matrix were almost unaffected when the organoclay content was lower than 5 phr. However, when the clay content exceeded 5 phr the transmission decreased and the haze increased. The phenomenon was attributed to the aggregation trend of clay particles with high content of organoclay. The effect of the organoclay on optical properties of BR/organoclay is shown in Figure 6.5.

In films of polymer nanocomposites it is expected that there will be reduction in haze with increasing particle dispersion. The haze measurement of nanocomposites with 1 wt% of alumina was also reported by Chandra *et al.* [8]. It indicates that the nanocomposites haziness is 39.5%, which is higher compared to processed polycarbonate, 5.45%, and the virgin polymer, 2.66%. According to the authors the highest haziness is related to light scattering caused by relatively large particles. Besides light scattering, it is also possible that some degree of light adsorption and mismatch of refractive index could further reduce the overall nanocomposite transparency, especially when higher contents of nanoparticles are employed.

6.3.3 Color

The study of color on nanocomposites is not very common on literature. The main concern is related to the yellow shade that the clay can attribute to polymer due to the original color that the natural clay has as some impurities are present.

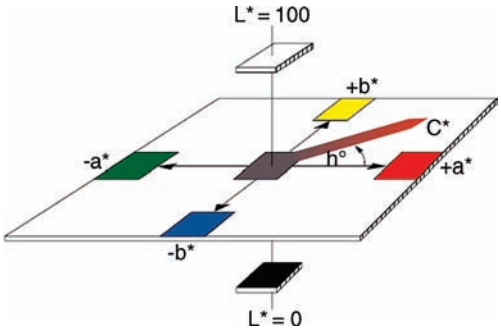

Figure 6.6 Scheme of CIELab system [19].

Modern color instruments measure the amount of light that is reflected by a colored sample. The measurement is done at each wavelength and is called the spectral data. A black object, for example, does not reflect light across the complete spectrum (0% reflection), whereas an ideal white specimen show the opposite behavior, reflects nearly all light (100% reflection). All other colors reflect light in selected parts of the spectrum [17].

The most common methodology to evaluate color is the CIELab system. It is a color scale which intends to provide a standard, approximately uniform color scale which can be used by everyone so that color values can be easily compared.

In a uniform color scale, the differences between points plotted in a color space correspond to visual differences between the colors plotted. The CIELab color space is organized in a cube form. The L^* axis runs from top to bottom. The maximum for L^* is 100, which represents a perfect reflecting diffuser. The minimum for L^* is zero, which represents black. The a^* and b^* axes have no specific numerical limits. Positive a^* is red; negative a^* is green; positive b^* is yellow; negative b^* is blue [18].

Figure 6.6 shows a scheme of the CIELab system. Park and Chang [20] prepared some polyimide nanocomposites films with pristine clay and analyzed the transparency and color change. This is an important aspect since colorless polyimide films have in particular been widely used in electro-optical devices and semiconductor applications. The measurements were obtained for 80 μm thick films by a spectrophotometer and the color coordinates on CIELab system were determined.

The b^* value of the polyimide hybrid with 0.50 wt% of clay is 4.13, and its degree of colorlessness is higher than the pure polyimide, 1.49. The value of b^* was found to increase from 4.13 to 6.89 as the clay content increases from 0.5 to 1.0 wt%, because of the agglomeration of the clay particles. This increase in b^* suggests that the clay particles are better dispersed in the polymer matrix at lower clay loadings. However, the L^* and a^* values remain unchanged.

6.4 Characterization by UV–Visible Spectrophotometry

Spectrophotometry is one of the most widespread analytical techniques employed to characterize the optical properties of polymeric nanocomposites.

The spectrophotometry is a technique based on Lambert–Beer law, which is the math support for measurement of the absorption of radiation by solid, liquid, or gaseous samples. The absorption can occur in the ultraviolet, visible, and infrared regions of the electromagnetic spectrum [21].

For measurements of the absorption of radiation in a determined wavelength the equation (6.1) is used:

$$A = \log(I_0/I) = \varepsilon bc \tag{6.1}$$

where A, absorbancy; I_0, intensity of monochromatic radiation that falls upon the sample; I, intensity of radiation that emerges from the sample; ε, molar absorptivity, is largeness characteristic of the absorbent sample. The magnitude depends on the wavelength of incident radiation. c, concentration of absorbent specimen; b, traveled distance by bundle through the sample.

The results of the analysis are reported as absorbance or transmittance. Some examples of the use of spectrophotometry in the characterization of optical properties of nanocomposites with polymer matrix and different nanoparticles are discussed in the following sections.

Li *et al.* [2] studied the optical properties of the transparent epoxy–ZnO nanocomposites by using a UV–visible spectrophotometer. The analyses were made in the range 250–900 nm. The authors observed that the nanocomposite loaded with only 0.07 wt% of ZnO nanoparticles with an average size of 26.7 nm showed simultaneously high visible light transparency and high ultraviolet light shielding. These are desirable properties for transparent packaging materials and also for engineering applications, as for example, parts for precision optical devices or windows for transportation vehicles.

The UV–visible absorption of nanocomposites of poly(L-lysine) and single walled carbon nanotubes was studied by Kim *et al.* [22]. The carbon nanotubes in water showed an absorption peak at 254 nm, which is typical for this kind of material. For the carbon nanotubes dispersed in the polymer the absorbance occurred at 207 and 266 nm, while the pure poly(L-lysine) showed an absorbance maximum at 219 nm. The peaks of nanocomposite were shifted to shorter wavelengths due to the wrapping of the polymer. The authors suggested that this support the existence of significant van der Waals interactions between the polymer and the nanotubes.

Corcione *et al.* [23] characterized optically nanocomposites based on epoxy matrix and modified boehmite by UV–visible-NIR spectrophotometry. In this work light transmittance in samples of 3 mm thickness of the unfilled epoxy and nanocomposites loaded with 5, 10, and 15% of modified boehmite at wavelength range 200–1500 nm were evaluated. Incorporation of the nanofiller in the epoxy matrix slightly modified the optical transparence of the neat epoxy. The reduction of light transmittance was more pronounced for larger quantities of nanofiller and occurred mainly at relatively shorter wavelengths. The authors explain that both epoxy and

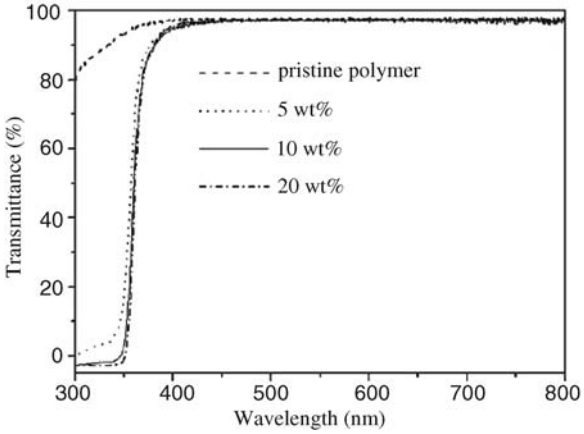

Figure 6.7 UV–visible spectra of pristine polymer and nanocomposites samples containing 5, 10, and 20 wt% of ZnO particles modified with 3-(trimethoxysilyl) propyl methacrylate. Reproduced from Ref. [7] with permission of Elsevier.

boehmite particles do not absorb in the investigated spectral range. For this reason, the reduction in the transparence of the samples can be attributed mainly to the scattering component.

The transmittance of acrylic pure polymer and the nanocomposites samples loaded with 5, 10, and 20 wt% of ZnO particles modified with 3-(trimethoxysilyl) propyl methacrylate was reported by Huang and Hsieh [7]. The transmittance of the nanocomposites samples was not affected by the amounts of filler loading, even with 20 wt% of nanoparticles, when compared to the pure polymer. All samples exhibit high optical transmittances greater than 95% in visible light wavelengths from 400 to 800 nm, as shown in Figure 6.7. The high transparency of the samples was attributed to uniform dispersion of the ZnO nanoparticles in polymer matrix. This is a result of the surface modification of the nanoparticles which acted as both interfacial coupling agent and dispersant of the nanoparticles in acrylic matrix.

Clay layers with sizes less than the wavelength of visible light do not hinder light's passage. However, the clay layers have dimensions in micrometers and only the thickness in nanometer range. Therefore, the large surface of the clay plaques acts to scatter the light transmission and as the content of the plaques increases, the light passage is more hindered. There are many studies which show that when the clay concentration increases, the particle surface per unit volume increases, and the light extinction obtained from scattering at the interface of polymeric matrix and clay particles increase [24].

UV–visible spectrophotometer over wavelengths ranging from 200 to 800 nm on films with thickness of 200 μm was used by Cipriano *et al.* [25] to show that the importance of particle size by doing the fractionation of a montmorillonite before preparing a polystyrene nanocomposite. The objective was to eliminate the microscale aggregates. By confirmation of the absence of large particles by transmission electron microscopy images on the nanocomposite prepared with the fractionated samples, it was clearly evident that the best transparency was reached for the fractionated clay.

6.5
Characterization by Optical Microscopy

The light optical microscopy is a familiar tool to study the morphology of materials. It uses a microscope which have optical and illumination systems as basic elements. In this technique, visible light is transmitted through or reflected from the sample through a single or multiple lenses to allow a magnified view of the sample. The resultant image can be detected directly by the eye, imaged on a photographic plate, or even digitally captured.

For opaque materials to visible light, as metals and some ceramic and polymeric materials, only the surface of the material can be observed. For this reason, the optical microscope should be used in the reflexion mode. The contrasts in produced image result from the differences in the reflectivity of several regions of the microstructure [26].

Optical microscopy is also a technique that can be useful for the characterization of nanocomposites. According to Xie *et al.* [27] transmission electron microscopy has been widely used to estimate clay dispersion and orientation in polymer matrices. Although it can provide direct information on clay layers in the real space, the analysis are focused on a very small volume of the sample and may not be representative. However, optical microscopy can be a complementary technique to substitute for analyze the overall dispersion/distribution of clay particles at a macroscopic level. It can show, for example, the presence of agglomerate particles that can be related to the degree of exfoliation of clay layers in the matrix.

Another important application of the optical microscopy is to evaluate the domain phase in blends filled with nanoparticles as reported by Kelarakis and Yoon [28]. They used optical microscopy to estimate the domain size of the minor phase in systems based on 70 : 30 isotatic polypropylene/poly(ethylene oxide) (PEO) blends filled with 5 wt% of organically modified montmorillonite. Three systems were evaluated, one of the pure blends, one loaded with clay I.30T from Nanocor, and the other loaded with clay Cloisite 30B from Southern Clay Products. The optical micrographs, Figure 6.8, showed that a dramatic modification of the distribution of PEO was induced by incorporation of the clay Cloisite 30B, but only minor changes were obtained for the sample containing the clay I.30T when compared to the pure

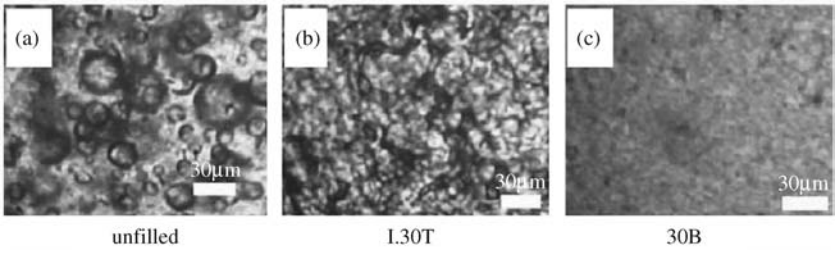

Figure 6.8 Optical micrographs of the (a) unfilled blend and the 5 wt% nanocomposite samples, (b) clay I.30T, and (c) clay Cloisite 30B. Reproduced from Ref. [28] with permission of Elsevier.

blend. The micrographs showed that the clay Cloisite 30B interacted more favorably with PEO compared to I.30T promoting the distribution of PEO droplets with the blend.

Some nonpolar polymers such as polypropylene need functionalized oligomers to have a good level of clay exfoliation. The presence of the compatibilizer may cause a reduction on transparency of the polymer matrix due to the domains and the difference on the refractive index between the polymer and the oligomer. In general

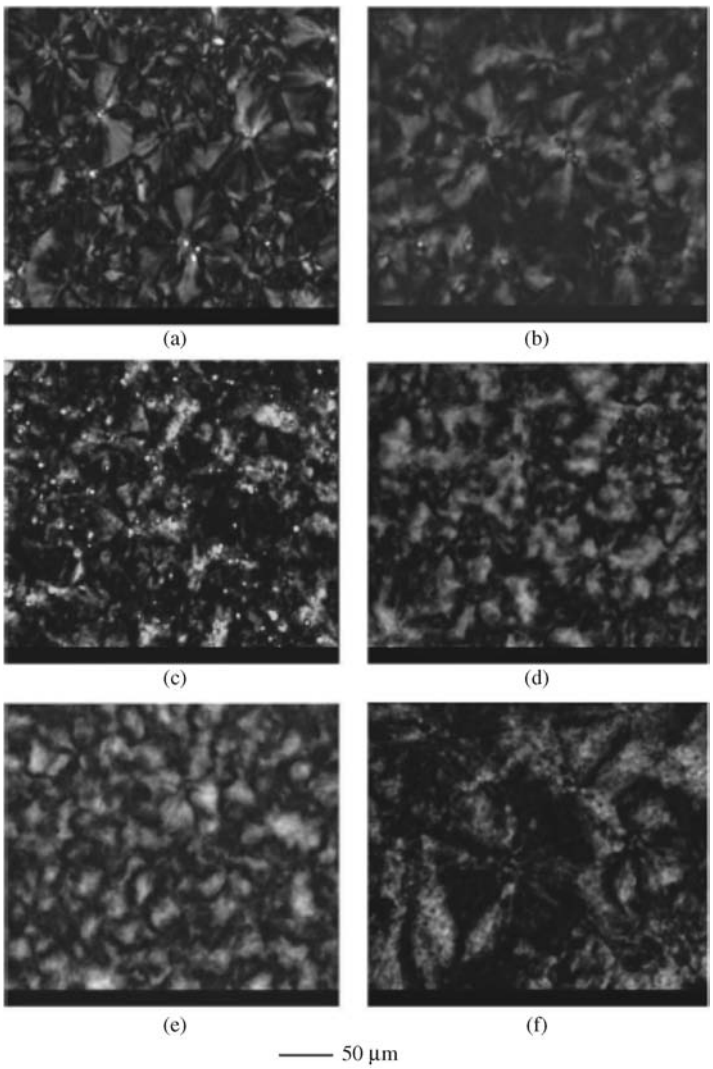

Figure 6.9 Cross-polarized optical microscope images of (a) PP, (b) PP/PP-*g*-MA, (c) PP/POE-*g*-MA, (d) PP/clay (6 phr), (e) PP/PP-*g*-MA/clay (6 phr), and (f) PP/POE-*g*-MA/clay (6 phr). Reproduced from Ref. [29] with permission of Elsevier.

the interfacial refractive index difference between matrix and domains govern the optical properties of polymer composites. In particular, the reduction in dispersed compatibilizer particle size within polypropylene matrix by exploiting added clay was claimed to prevent elastomeric particle coalescence by the clay particles via the barrier mechanism for the polypropylene–clay nanocomposites. This signified the important role of added ingredients to the optical transmittance of prepared nanocomposites [29].

Lai *et al.* [29] discussed this issue for a polypropylene nanocomposite using as compatibilizers polypropylene grafted maleic anhydride (PP-*g*-MA) and polyethylene-octene elastomer grafted maleic anhydride (POE-*g*-MA). Another aspect is related to system crystallinity and its morphology. The optical transmittance for nanocomposite without compatibilizers was generally higher than that of the translucent PP resin.

The evaluation by cross-polarized optical microscope of pure PP, PP with compatibilizers, polypropylene–clay nanocomposites with and without compatibilizers, Figure 6.9, showed that this behavior was mainly due to the reduced spherulite size through the nucleating effect of added nanoclay normally seen in the conventional nucleating agent which was used to prepare the transparent polypropylene.

This indicates that the higher dispersion of clay does not guarantee the higher optical transmittance of the prepared system. The existence of additional compatibilizers could affect the matrix properties. The effects include the induced refractive index difference between the original matrix and the dispersed compatibilizers which offset the positive effect from the increased clay dispersion, leading to the lower optical transmittance of compatibilized nanocomposites sometimes. Apparently, the role of compatibilizer types in the competition between the PP and the clay was rather pertinent to the derived morphology.

References

1 Li, Y.-Q., Yang, Y., and Fu, S.-Y. (2007) *Composites Science and Technology*, **67**, 3465–3471.

2 Li, Y.-Q., Fu, S.-Y., and Mai, Y.-M. (2006) *Polymer*, **47**, 2127–2132.

3 Srivastava, S., Haridas, M., and Basu, J.K. (2008) *Bulletin of Material Science*, **31** (3), 213–217.

4 Dammer, D., Vlˇcková, B., Prochazka, M., Bondarev, D., Vohlídal, J., and Pleger, J. (2009) *Materials Chemistry and Physics*, **115**, 352–360.

5 Iripam, L., Krishnan, B., Nampoori, W.P.N., and Radhakrishnan, P. (2008) *Journal of Colloid and Interface Science*, **324**, 99–104.

6 Golovan, L.A., Timoshenko, V.Y., and Kashkarov, P.K. (2007) *Physics-Uspekhi*, **50** (6), 595–612.

7 Huang, H.-C. and Hsieh, T.-E. (2010) *Ceramics International*, **36**, 1245–1251.

8 Chandra, A., Turng, L.-S., Gopalan, P., Rowell, R.M., and Gong, S. (2008) *Composites Science and Technology*, **68**, 768–776.

9 Pucci, A., Boccia, M., Galembeck, F., Leite, C.A.P., Tirelli, N., and Ruggeri, G. (2008) *Reactive and Functional Polymers*, **68**, 1144–1151.

10 Chang, J.-H., An, Y.U., Cho, D., and Giannelis, E.P. (2003) *Polymer*, **44**, 3715–3720.

11 Hernández, J.J., García-Gutiérrez, M.C., Nogales, A., Rueda, D.R., Kwiatkowska, M., Szumczyk, A., Roslaniec, Z., Conchesco, A., Guinea, I., and Ezquerra, T.A. (2009) *Composites Science and Technology*, **69**, 1867–1872.

12 www.byk.com/instruments/applications/Glossmeter_theory_applications_1_US.php (July 28, 2010).

13 Ahmadi, B., Kassiriha, M., Khodabakhsi, K., and Mafi, E.R. (2007) *Progress in Organic Coatings*, **60**, 99–104.

14 Landry, V., Pierre, B., and Riedl, B. (2010) *Progress in Organic Coatings*, **67**, 381–388.

15 Yu, H.L., Hsiao, C.C., and Liu, W.C. (2006) *Measurement Science and Technology*, **17**, N29–N36.

16 Wang, S., Zhang, Y., Ren, W., Zhang, Y., and Lin, H. (2005) *Polymer Testing*, **24**, 766–774.

17 www.byk.com/instruments/applications/solid_color_2_US.php (July 28, 2010)

18 www.hunterlab.com/appnotes/an07_96a.pdf (July 28, 2010)

19 www.byk.com/instruments/applications/solid_color_3_US.php (July 28, 2010)

20 Park, J.-S. and Chang, J.-H. (2009) *Polymer Engineering and Science*, **49**, 1357–1365.

21 Rocha, F.R.P. and Teixeira, L.S.G. (2004) *Química Nova*, **27**, 807–812.

22 Kim, J.-B., Premkumar, T., Giani, O., Robin, J.-J., Schue, F., and Geckeler, K.E. (2008) *Polymer International*, **57**, 311–315.

23 Corcione, C.E., Manera, M.G., Maffezzoli, A., and Rella, R. (2009) *Materials Science and Engineering C*, **29**, 1798–1802.

24 Kaya, E., Tanoglu, M., and Okur, S. (2008) Layered clay/epoxy nanocomposites: thermomechanical, flame retardancy, and optical properties. *Journal of Applied Polymer Science*, **109**, 834–840.

25 Cipriano, B.H., Kashiwagi, T., Zhang, X., and Raghavan, R.S. (2009) *Applied Materials and Interfaces*, **1** (1), 130–135.

26 Callister, W.D., Jr. (2006) *Fundamentos da Ciência e Engenharia de Materiais: Uma Abordagem Integrada*, LTC – Livros Técnicos e Científicos, Rio de Janeiro.

27 Xie, S., Harkin-Jones, E., Shen, Y., Hornsby, P., Macfee, M., MacNally, T., Patel, R., Benkreira, H., and Coates, P. (2010) *Materials Letters*, **64**, 185–188.

28 Kelarakis, A. and Yoon, K. (2008) *European Polymer Journal*, **44**, 3941–3945.

29 Lai, S.-M., Chen, W.-C., and Zhu, X.S. (2009) *Composites: Part A*, **40**, 754–7765.

7
Characterization of Mechanical and Electrical Properties of Nanocomposites

Iren E. Kuznetsova, Boris D. Zaitsev, and Alexander M. Shikhabudinov

7.1
Introduction

At present, the major focus of the researchers is on the nanocomposite materials based on the nanoparticles of metals and their compounds stabilized within a polymeric dielectric matrix [1–4]. The dielectric and optical properties of these materials have been demonstrated to be highly dependent on the size, structure, and concentration of the nanoparticles, as well as on the type of polymeric matrix [5–8]. These have shown the possibility of the purposeful change of parameters of the nanocomposite materials such as electrical conductivity, complex permittivity, refraction coefficient, and so on. It is believed that these materials would demonstrate low acoustic impedance because they are based on the polymeric matrix [9]. At that, the impedance value should be varied within certain limits by adjusting the parameters of the embedded nanoparticles. All of these would allow one to use these materials for low disturbing substrates in various devices based on the waves in thin piezoelectric plates [10].

As is well known, the important parameter of acoustoelectronic devices is the temperature coefficient of delay, which characterizes the characteristic thermostability of these devices. In Ref. [11], it has been shown that the way of reducing this coefficient in the structure consisting of the piezoelectric plate contacting with liquid. In this case, the permittivity of liquid should decrease in accordance with certain law at an increase in the temperature. Apparently, the production and use of the structures containing the liquid are accompanied by a number of technological difficulties. In this connection, the search of the solid material which in contact with the piezoelectric plate may significantly decrease the temperature coefficient of delay of acoustic wave in such structure at the conservation of the high value of electromechanical coupling coefficient is extremely important. In this case, the permittivity of the sought material should be low and decrease with an increase in temperature.

By now, there are papers devoted to the investigation of the temperature dependencies of the permittivity of the nanocomposite materials based on the low-density polyethylene with nanoparticles of copper oxide [12,13], zinc oxide [14],

Polymer Composites: Volume 2, First Edition. Edited by Sabu Thomas, Kuruvilla Joseph, Sant Kumar Malhotra, Koichi Goda, and Meyyarappallil Sadasivan Sreekala.

and ceric oxide [6] in the wide temperature range from 35 to 110 °C. The molding temperature is about 200 °C. It has been shown that in the temperature range, which is close to the softening point of the polyethylene matrix [15], the temperature dependencies of the permittivity corresponding to the heating and cooling the sample are significantly different. It means that the materials under study do not provide for the stability of the physical parameters in the aforementioned temperature range. Nevertheless, these materials may be used for the development of various radio components operating at the temperatures, which are significantly less than the softening point of the polyethylene matrix. In this connection, the measurement of the temperature dependence of the permittivity of the nanocomposite materials in the aforementioned temperature range has the practical interest.

Besides, the nanocomposite polymeric materials may be used as damping and matching layers for the development of various devices used for bulk acoustic waves.

As is well known, the process of making the nanocomposite materials based on the low-density polyethylene consists of two stages [1]. The first stage is the production of the nanocomposite powder-like material with the given proportion of the nanoparticles and polyethylene. Here, one may use various chemical methods described in Refs. [11–13]. On the second stage, the nanocomposite powder-like material is used for obtaining the nanocomposite sample with the given geometric forms and sizes. It should be noted that the final sample besides polyethylene and nanoparticles may also contain air bubbles; that is, they may be porous. Apparently, the physical properties of such samples are significantly dependent on the degree of the porosity. In one's turn, the degree of the porosity of the nanocomposite sample depends on the conditions of its molding. It should be pointed out that the chemical methods of obtaining the powder-like nanocomposite materials with a given ratio of nanoparticles and polyethylene have been well developed and their advantages and disadvantages have been studied in detail [16–18]. But the molding of samples from the initial powder-like material still needs further investigation. In this connection, this chapter contains the results of the investigation of the molding conditions on the density and degree porosity of the nanocomposite samples based on low-density polyethylene [15]. This chapter also contains the results of the investigation of the influence of the temperature on the permittivity of the nanocomposite samples and results of the study of their density, coefficients of elasticity and viscosity, and acoustic impedance.

7.2
The Influence of the Molding Temperature on the Density of the Nanocomposite Samples Based on the Low-Density Polyethylene

For obtaining the nanocomposite powder-like material, the method developed for the synthesis of cluspol-type materials, which is based on the thermolysis of organometallic compounds in a polymeric melt solution, was used [19,20]. Using this method allowed to obtain powder-like materials containing CdS, Fe, Fe_2O_3, and

MnO nanoparticles with dimensions ranging from 1 to 70 nm. The stabilizing dielectric medium was the modified low-density polyethylene (PEVD 10803-020 grade), which was prepared as follows. The initial granulated polymeric (with a nominal density of 918.5 kg/m^3) was heat treated in a reactor with hot mineral oil, which converted crystalline and amorphous phases of the initial polyethylene into a viscous flow state (polymeric melt solution in oil). Then the polymeric solution melt was cooled and washed from the mineral oil in a Soxhlet apparatus. The resulting powder possessed a highly disperse structure and was capable of molding under the mechanical and heat actions. This pure polyethylene (modified PEVD 10803-020 grade) was used for the synthesis of the nanocomposite powder-like material containing CdS, Fe, Fe_2O_3, and MnO nanoparticles. The density of the initial modified polyethylene measured by the authors was 960 kg/m^3. For the molding of the nanocomposite samples we used the press, the scheme of which is presented in Figure 7.1. The initial powder-like materials of the quantity of 0.4 cm^3 was set in the fluoroplastic cylinder 2 and was pressed by the fluoroplastic piston 4 and spring 3. For obtaining the samples with flat, parallel sides, the lower surfaces of the cylinder 2 and piston 4 were polished together by the special flat polishers. The upper surface of the fluoroplastic Plate 5 was used as the lower side of the cylinder 2. For the prevention of the extrusion of the Plate 5 we used the fixing steel Plate 6. The distinctive peculiarity of the described press is the use of the fluoroplastic cylinder and fluoroplastic piston for the prevention of the adhesion of the nanocomposite

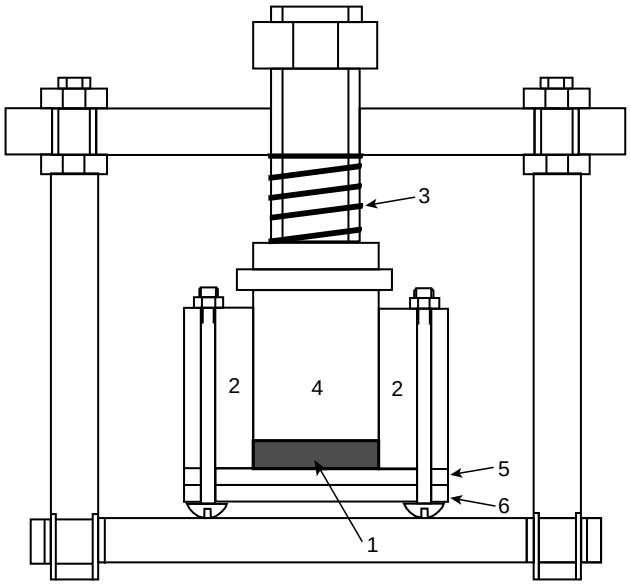

Figure 7.1 The scheme of the press for molding the nanocomposite samples: 1, nanocomposite powder; 2, fluoroplastic cylinder; 3, spring; 4, fluoroplastic piston; 5, fluoroplastic plate; 6, steel plate.

sample to their surfaces. This press together with powder-like material was put in the muffle oven and kept at a given temperature for 1 h.

As is known, the low-density polyethylene molding onset temperature under pressure is about 70 °C [21]. Evidently, this mechanical action also influences the density and porosity of a polymeric sample in the course of the molding. Our experiments were performed using the piston and spring producing a pressure 2.6×10^5 N/m^2. A series of the nanocomposite samples were molded from the same powdered material in the muffle oven at the various temperatures (70, 90, 100, 110, 120, 130, and 150 °C). As a result, we obtained 14 polymeric nanocomposite samples with a 10% concentration of MnO and CdS and 7 pure low-density polyethylene samples molded at the indicated temperatures. A comparison to the pure polyethylene samples revealed the influence of the nanoparticles presence in the polymeric matrix on the density and porosity of obtained nanocomposite materials. Using this technology, it was possible to obtain the flat, parallel disk samples with a thickness of 0.3–1 mm and a diameter of 12–14 mm, which could be readily extracted from the press.

The structure and the surface morphology of the nanocomposite samples were studied using the atomic force microscopy (Solver P-47) and transmission electron microscopy (PEM-100) techniques. Analysis showed that the samples contained the uniformly distributed nanoparticles of used materials with sizes of 10–25 nm. Figure 7.2 presents the typical transmission electron microscope image of a nanocomposite sample containing 5% nanoparticles MnO. As can be seen, MnO particles are situated on the sample surface. These particles are distributed quite uniformly and have dimensions of about 10 nm, but not exceeding 20 nm.

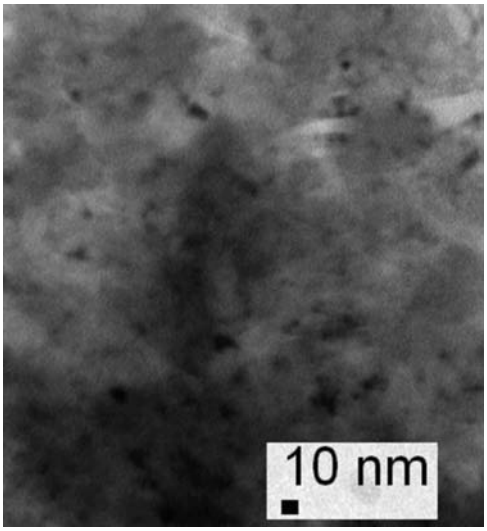

Figure 7.2 The typical TEM image of the surface of the sample based on a low-density polyethylene with MnO nanoparticles of the concentration 5% [15].

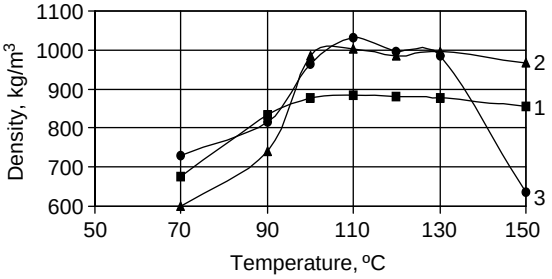

Figure 7.3 The dependence of the density of the nanocomposite samples on the molding temperature for the following materials based on the matrix of a low-density polyethylene: 1, pure modified low-density polyethylene; 2 and 3, nanocomposites containing nanoparticles of 10% concentrations of CdS and MnO, respectively [15].

Then with the help of the precision micrometer, we determined the thicknesses of the obtained samples and their volumes were calculated using the known values of the thickness and diameter. The sample mass was measured by the precision analytical balance. The known sample volume and mass allowed us to find the density of the nanocomposite material. By this way it was possible to determine the dependencies of the material density on the molding temperature. These dependencies are presented in Figure 7.3 for the following samples: pure modified low-density polyethylene (1), and nanocomposite materials based on low-density polyethylene matrix with 10% concentration of nanoparticles CdS (2) and MnO (3).

As can be seen from Figure 7.3, the density of each material depends on the molding temperature, and there is an optimum temperature for which the density is maximum. This behavior indicates that the sample contains in addition to the polymeric and nanoparticles the gas bubbles that make the sample porous. The degree of the porosity depends on the molding temperature.

The degree of the porosity of the sample was determined as the percentage volume content of the air relative to the volume of the nanocomposite material. The porosity was evaluated using the following relations:

$$M_s = V_{pe}\rho_{pe} + V_n\rho_n + V_{air}\rho_{air}, \tag{7.1}$$

$$V_s = V_{pe} + V_n + V_{air}. \tag{7.2}$$

Here M_s is the sample mass; ρ_{pe}, ρ_n, and ρ_{air} are the densities of polyethylene, nanoparticles, and air, respectively; V_{pe}, V_n, V_{air}, and V_s are the volumes of polyethylene, nanoparticles, air, and the entire sample, respectively. Assuming that the sample mass ($V_s\rho_s$), the mass of nanoparticles ($V_n\rho_n$), and the densities of all materials are known, Eqs. (7.1) and (7.2) can be used to determine the volume of air (V_{air}) and its percentage fraction V_{air}/V_s. The calculations were performed for $\rho_{air} = 1.3\,\text{kg/m}^3$, $\rho_{MnO} = 5180\,\text{kg/m}^3$, $\rho_{CdS} = 4820\,\text{kg/m}^3$, $\rho_{pe} = 960\,\text{kg/m}^3$, and it was assumed that $\rho_{air} \ll \rho_{pe}$. The values of porosity (the percentage air fraction) and densities of all samples are listed in Table 7.1. The error was determined primarily by the scatter of sample thicknesses (±4%) and masses (±0.5%) so that the total error of the measurement did not exceed 4.5%.

Table 7.1 The density and porosity of nanocomposite samples based on low-density polyethylene.

	Pure polyethylene		Polyethylene–10% CdS		Polyethylene–10% MnO	
T (°C)	ϱ (kg/m^3)	V_{air}/V_s (%)	ϱ (kg/m^3)	V_{air}/V_s (%)	ϱ (kg/m^3)	V_{air}/V_s (%)
70	674.4	29.75	600.0	42.40	731.10	30.20
90	834.0	13.10	740.0	29.50	814.45	22.05
100	876.0	8.73	986.0	5.10	962.30	8.20
110	885.3	7.80	1002.4	4.00	1032.65	1.36
120	879.0	8.30	984.4	5.73	996.00	4.65
130	879.0	8.30	997.3	4.40	984.00	5.32
150	857.0	10.40	967.4	7.30	887.00	15.02

It is evident that the molding of the polymeric nanocomposite samples from the initial powder-like material is accompanied by the displacement of air from the mixture. An increase in the molding temperature leads to a decrease in the polyethylene viscosity, which makes easier the removal of air and results in growing density of the sample. However, during the molding there is one more process, namely, the emission of air bubbles from polyethylene. This process leading to the decrease in the sample density becomes more intensive at grooving the temperature. The presence of these both mechanisms of the gas evolution and gas displacement determines the existence of the optimal value of the molding temperature for which the air fraction in the sample is minimum. This optimal temperature for all samples under study is in the range 110–120 °C. Figure 7.3 also shows that the aforementioned maximum is not sharply manifested in pure polyethylene, while the presence embedded nanoparticles in the matrix makes the dependence of the sample density on the molding temperature more clearly pronounced. The authors believe that the features of this behavior are determined by the chemical nature of the nanoparticles.

Thus, it was established that the nanocomposite materials based on low-density polyethylene with minimum porosity and maximum density are obtained by molding at temperatures 110–120 °C. The results open the way to controlled modification of the parameters of such samples by varying the molding temperature. Properties, which depend on the material porosity, include the permittivity, refractive index, and elastic modulus.

7.3 Experimental Study of the Temperature Dependence of the Permittivity of the Nanocomposite Materials

It has been discussed earlier that for the development of various acoustoelectronic devices with the thermo-stable parameters, it is possible to use the thermo-stable

acoustic waveguides. In such a waveguide one may use layered structure containing piezoelectric plate and nanocomposite polymeric layer with the specific temperature dependence of the permittivity. In this connection, this chapter is devoted to the results of the experimental study of the temperature dependence of the permittivity of nanocomposite materials with the various content of the iron nanoparticles in the matrix of a low-density polyethylene in the temperature range 0–40 °C [22]. The samples under study had the form of the disk with thickness of about 0.5 mm and diameter of 14 mm.

The dielectric permittivity of the samples was studied using a high-precision LCR meter (Agilent Model 4285A) equipped with a dielectric test fixture (Agilent Model 16451B) for measuring the permittivity of solids. In this test fixture, the sample was placed between the upper and the lower electrodes of a plane capacitor, and a special device with a micrometric driver was used to adjust the interelectrode distance and keep the electrodes parallel to each other. In order to eliminate the influence of the edge parasitic capacitance on the results of the measurements, the upper electrode consisted of two parts, that is, measuring and shielding electrodes with diameters 5 and 10 mm, respectively. The diameter of the lower electrode was 56 mm. The sample permittivity was measured in the contact mode. In the course of the temperature-dependent permittivity measurements, the undesired air gaps between the sample and the electrodes were removed using a spring that slightly pressed the upper electrode against the sample. The measurement procedure consisted in determining the capacitance of the plane capacitor with the sample at a selected temperature, followed by calculating the permittivity of the given material on a computer using special software. The permittivity was calculated using the formula for a plane capacitor with a 5 mm diameter measuring electrode.

The sample temperature was set using a special thermostat that could control the temperature in the interval 0–40 °C. In order to prevent the formation of condensate on the sample and electrodes, the entire test fixture (Agilent Model 16451B) was arranged in a vacuum chamber (Figure 7.4) evacuated by forevacuum pump. The sample temperature was measured by a chromel–alumel thermocouple, one junction of which was fixed with an epoxy glue on the lower electrode, in the immediate vicinity of the sample. The second junction was placed into a water–ice mixture at 0 °C. The thermo emf in the thermocouple was measured by a digital millivoltmeter.

In order to decrease temperature gradients inside the vacuum chamber during the measurements, the temperature was slowly varied so that the temperature dependence of the permittivity of one sample was recorded for about 8 h. Beginning from the initial temperature of 25 °C, the system was slowly (for about 2.5 h) cooled by the thermostat to 0 °C, then slowly (for about 4 h) heated to 40 °C, and finally cooled to 25 °C for 1.5 h. During the entire cycle, the capacitance was determined (and the corresponding value of permittivity was calculated) in 5 °C steps. Therefore, the permittivity at 25 °C was measured three times per cycle, which allowed us to judge the existence of the temperature hysteresis in the system under consideration.

An analysis of the obtained temperature dependencies of the permittivity of the nanocomposite materials based on the low-density polyethylene with various concentrations (2–22%) of iron nanoparticles leads to the following conclusions.

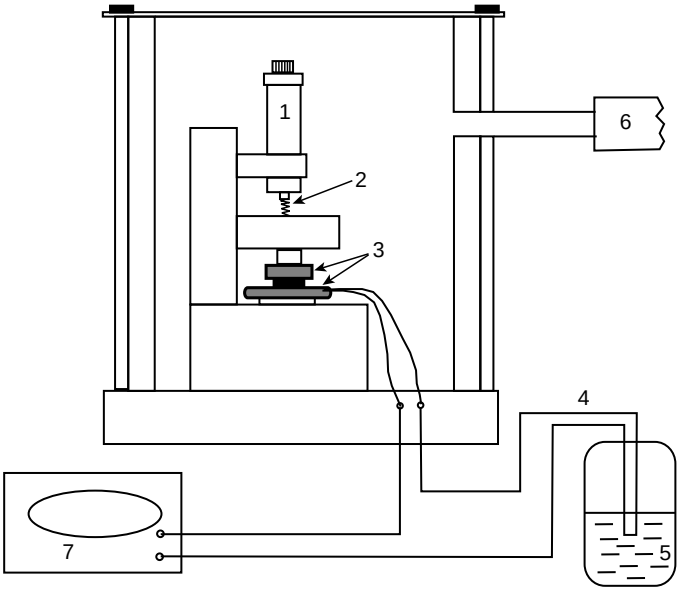

Figure 7.4 Schematic diagram of a vacuum chamber with the dielectric test fixture: 1, micrometric drive; 2, spring; 3, electrodes; 4, thermocouple; 5, water–ice mixture at 0 °C; 6, vacuum pump outlet; 7, millivoltmeter [22].

i) As the temperature increases from 0 to 40 °C, the permittivity decreases for all concentrations of the iron nanoparticles in the range studied.
ii) For the samples with the iron concentrations of 5, 7, 10, and 12%, the temperature hysteresis is nearly absent (i.e., the permittivity at 25 °C remains the same in all stages of the measurement cycle). This fact is illustrated in Figure 7.5 (curve 1), which shows the temperature dependence of the permittivity of a nanocomposite materials containing 5% of the iron nanoparticles [22].
iii) The samples with the iron concentrations 2, 12, 15, 17, and 20% exhibit a slight temperature hysteresis. This is demonstrated in Figure 7.5 (curve 2) for nanocomposite material with 20% of the iron nanoparticles. It should be noted that the hysteresis in all these cases appeared only in the last stage of the temperature variation, in which the sample was cooled from 40 to 25 °C.

The authors believe that the observed hysteresis was related to a small deformation of the sample as a result of the mechanical stresses caused by a change in the temperature. The degree of the deformation could be increased due to the air bubbles presence in the samples. This assumption was confirmed by the small caverns that appeared on the surface of the samples exhibiting hysteresis, which were examined after the termination of the experiment. Indeed, an increase in the temperature must lead to growth in the pressure of an air inside the bubbles and can

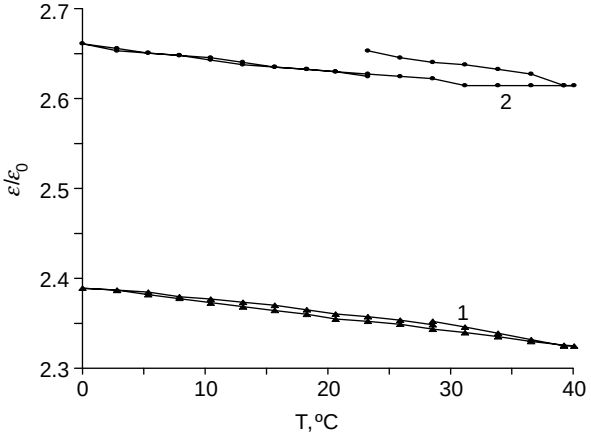

Figure 7.5 The temperature dependence of the relative permittivity for nanocomposite material based on the matrix of a low-density polyethylene with the iron nanoparticles of the concentrations 5 (1) and 20% (2) [22].

result in the escape of air through the sample surface. Then the subsequent decrease in the temperature will lead to a certain deformation of the sample surface.

The results of the permittivity determination at the minimum and maximum temperatures of the interval studied are presented in Table 7.2, where $\varepsilon/\varepsilon_0$ is the ratio of the sample permittivity (ε) to that of vacuum (ε_0). The error of the measurements of the temperature and permittivity amounted to $\pm 2\%$ and was determined entirely by the accuracy of the measuring equipment.

Table 7.2 Values of the relative permittivity measured at the minimum and maximum temperatures in the interval studied for the nanocomposite materials based on low-density polyethylene with various concentrations of the iron nanoparticles.

Fe (%)	$\varepsilon/\varepsilon_0$	
	$T = 0\,^\circ$C	$T = 40\,^\circ$C
0	2.319	2.288
2	2.207	2.157
5	2.389	2.325
7	2.265	2.203
10	2.398	2.345
12	2.331	2.287
15	2.434	2.392
17	3.196	3.168
20	2.661	2.614
22	2.521	2.459

The temperature dependencies of the permittivity of the nanocomposite materials based on low-density polyethylene with iron nanoparticles obtained in our experiments can be used for determining the optimum geometric parameters of acoustic waveguides, the type and operating frequencies of waves in structures of the piezoelectric plate nanocomposite layer, in which the temperature coefficient of delay for acoustic waves can be significantly decreased while the electromechanical coupling coefficient has a fairly high level [10].

7.4 Elastic and Viscous Properties of the Nanocomposite Films Based on the Low-Density Polyethylene Matrix

As it has been discussed earlier, the nanocomposite polymeric materials may be used for the development of various acoustoelectronic devices based on piezoelectric plates and also for the development of the matching devices for launching/receiving acoustic waves in low-impedance media. For the theoretical analysis of such structures, one must know the information about elastic and viscous properties of nanocomposite polymeric materials. In this connection, this section contains the results of the experimental investigation of the elasticity and viscosity coefficients of the nanocomposite materials based on a low-density polyethylene with the embedded Fe and Fe_2O_3 nanoparticles of various concentrations.

7.4.1 Technology of Producing the Nanocomposite Polymeric Films

In our experiments, the nanocomposite materials based on a low-density polyethylene with the Fe and Fe_2O_3 nanoparticles of various concentrations were used as the initial materials. The samples of the aforementioned materials having the shape of the disk with a diameter of 7–8 mm and thickness of 2–3 mm were provided by our colleagues from Laboratory 193 of the Institute of Radio Engineering and Electronics of Russian Academy of Sciences (Moscow). The films under study were made from pointed above disks by the following way [15]. The small piece of the material ($\sim 2 \times 2 \times 2\,mm^3$) was separated from the initial sample and remolded by using the special press. The scheme of the press is presented in Figure 7.6. The aforementioned piece 1 was placed between the optical glasses 2 and compressed by the spring 3. The force of the compressed spring 3 was equal to about 1 kN. For providing the uniform thickness of the needed value of the final sample, we used the foil ring 4 with the inner diameter 20 mm. This press with the nanocomposite sample was placed in the muffle oven. After 1 h prebaking at the temperature 110–120 °C the thickness of the film sample was equal to the thickness of the foil ring. The film thickness was measured after cooling with the help of the precision micrometer. Then by circular knife we cut the film disc with a diameter of 8 mm. This press allowed making the film with uniform thickness in the range 35–60 μm. The film thickness was measured by micrometer after cooling the film and its mass

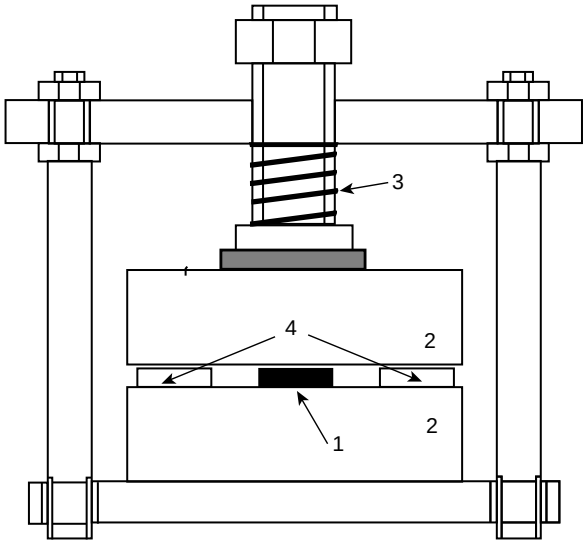

Figure 7.6 The scheme of the press for molding the nanocomposite polymeric films: 1, nanocomposite material; 2, optical glasses; 3, spring; 4, foil disc.

was determined by means of the analytical balance. By using the values of the thickness and diameter of the film sample, we calculated its volume. This data allowed us to find the density of the film. The corresponding values of the density (ρ) of investigated films are presented in Tables 7.3 and 7.4. These tables also contain the values (L) of the film thickness.

7.4.2
Determination of the Coefficients of Elasticity and Viscosity of Nanocomposite Polymeric Films

For measuring the mechanical characteristics of the aforementioned films such as coefficients of elasticity and viscosity, one can use the piezoelectric resonators of bulk acoustic waves [23]. It should be noted that this method may be used when the

Table 7.3 The parameters of the films containing the Fe nanoparticles of various concentrations.

Fe_2O_3 (%)	L (μm)	ϱ (kg/m^3)	C_{11} (10^8 Pa)	η_{11} (Pa s)	C_{66} (10^8 Pa)	η_{66} (Pa s)
0	43	879.5	16	24	1.4	2.9
1	46	893.6	17	8.3	1.5	2.5
10	44	900.0	15	17.8	2.1	0.7
15	56	922.3	20	27.8	2.4	1.7
20	51	1037.0	29.6	17.6	2.5	1.1
35	54	1116.0	29.2	38.7	2.9	1.7

Table 7.4 The parameters of the films containing the Fe_2O_3 nanoparticles of various concentrations.

Fe (%)	L (μm)	ϱ (kg/m^3)	C_{11} (10^8 Pa)	η_{11} (Pa s)	C_{66} (10^8 Pa)	η_{66} (Pa s)
0	43	879.5	16	24	1.4	2.9
2	60	884.1	23.2	24.6	2.6	2.2
5	63	918.6	20.1	6.2	2.8	2.3
7	64	972.6	17.8	4	3.4	2.4
12	55	993.7	15.1	7.6	3.5	1.1
15	60	991.3	14	4	3.4	0.7
17	50	986.6	12.8	11.3	3.0	1.3
20	36	1052.0	10.2	17.6	3.3	1.1

thickness of the film under study is significantly less than the thickness of the resonator. It has been discussed earlier that the values of thickness of the investigated films was equal to 35–60 μm with diameter of 8 mm and the thickness of the resonators lied in the interval 500–800 μm. It was assumed that the investigated materials were isotropic. It is apparent that for measuring the longitudinal coefficients of elasticity $C_{11}^{f} = C_{22}^{f} = C_{33}^{f}$ and viscosity $\eta_{11}^{f} = \eta_{22}^{f} = \eta_{33}^{f}$ one should use the resonators of the longitudinal acoustic wave. Accordingly, for measuring the shear coefficients of elasticity $C_{44}^{f} = C_{55}^{f} = C_{66}^{f}$ and viscosity $\eta_{44}^{f} = \eta_{55}^{f} = \eta_{66}^{f}$ the resonators of the shear acoustic wave are quite suitable. Symbol "f" means the belonging of the variable to the investigated nanocomposite film.

For carrying out the measurements, we used the resonators of the longitudinal and shear waves (Figure 7.7) made of langasite and quartz, respectively. The langasite and quartz resonators had the electrodes with diameters of 7 and 6 mm, respectively. The corresponding values of the thickness were equal to about 0.75 and 0.5 mm. At first, by means the precision LCR meter (Agilent Model 4285A) the frequency dependencies of the real (R) and imaginary (X) parts of the electrical

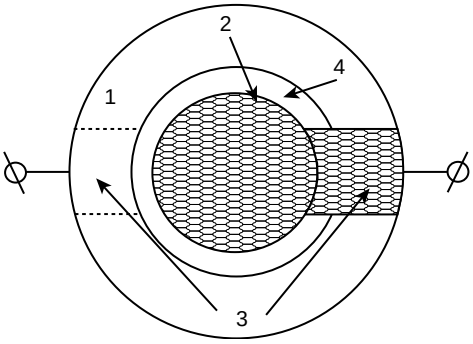

Figure 7.7 The scheme of the measuring resonator: 1, langasite or quartz plate; 2, electrodes; 3, contact area; 4, nanocomposite film.

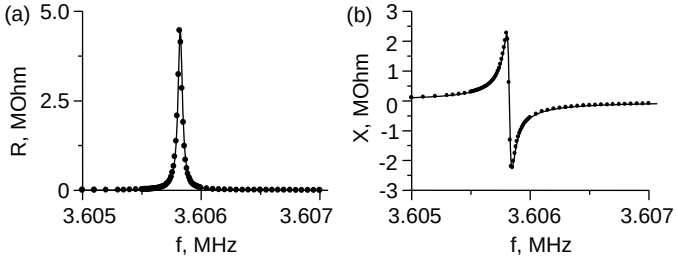

Figure 7.8 The frequency dependencies of the real (a) and imaginary (b) parts of the electrical impedance for the quartz resonator without loading. The circle and solid lines correspond to the experiment and theory, respectively.

impedance of the resonator without the films under study were measured. These dependencies for the quartz resonator are presented by circles in Figure 7.8. The construction of the theoretical frequency dependencies of the impedance of the resonator was based on the analysis of its equivalent circuit, which is presented in Figure 7.9 [24,25]. Here the mechanical impedances z_1 and z_2 have the following form:

$$z_1 = iZ\mathrm{Stg}(kd/2); z_2 = -iZS/\sin(kd), \tag{7.3}$$

where $Z = (C_{jj}\rho)^{1/2}$ is the specific acoustic impedance of the resonator material; C_{jj} and ρ are the elastic constant and density of the resonator material, respectively; $k = \omega/v$ is the wave number; ω and v are the angular frequency and phase velocity of the wave; S and d are the area of the electrode and resonator thickness, respectively, i is the imaginary unit. The equivalent circuit includes the electromechanical transformer, which characterizes the mutual transformation of the electrical and mechanical oscillations [24,25]. The primary winding contacting with the elements C_0 and $-C_0$ is electrical, and the secondary one contacting with impedances z_1 and z_2 is mechanical [24,25]. At that the ratio of "the turns" of this transformer, N is dimensional and equal $N = hC_0$, where $h = e_{1j}/\varepsilon_{11}$ (e_{1j} = piezo constant, ε_{11} = component of the permittivity), $C_0 = \varepsilon_{11}S/d$ is the electrical capacity [24,25]. It was assumed that the main source of the loss is viscosity (η_{jj}) of the resonator material. In this case, the velocity and specific acoustic impedance of the resonator may be written as [25]

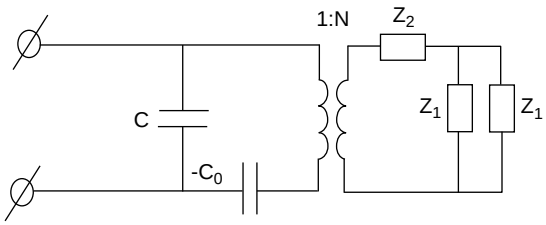

Figure 7.9 The equivalent circuit of unloaded resonator.

$$v = \left\{ \left(C_{jj} + e_{1j}^2/\varepsilon_{11} + i\omega\eta_{jj} \right)/\rho \right\}^{1/2}, \quad Z = \left\{ \left(C_{jj} + e_{1j}^2/\varepsilon_{11} + i\omega\eta_{jj} \right)\rho \right\}^{1/2}. \tag{7.4}$$

Here for the longitudinal waves $j = 1$, and for the shear waves $j = 6$ because in our coordinate system axis x_1 is normal to the resonator surface, and axis x_2 is parallel with the polarization vector of the shear wave. By using the Kirchhoff's equations for the circuit presented in Figure 7.9, we calculated the frequency dependencies of the real and imaginary parts of the electrical impedance for the given values of the material constants of the resonator (C_{jj}, e_{1j}, ε_{11}, η_{jj}) [23]. We varied the material constants in the given limits and exploited the least-squares method to find a set of C_{jj}, e_{1j}, ε_{11}, and η_{jj} that could offer the most close agreement of the theoretical and experimental frequency dependencies of the impedance. Solid lines in Figure 7.8 show the calculated frequency dependencies for the quartz resonator which are most adjusted to the experiment.

As it was discussed earlier, we investigated the nanocomposite films based on a low-density polyethylene with Fe and Fe_2O_3 nanoparticles of the various concentrations.

The reliable acoustic contact between the resonator and the film under study was provided by the thin layer of the castor oil, the parameters of which were considered in the calculations. But it should be noted that the physical parameters of the castor oil strongly depend on the temperature and its chemical composition. These factors have the significant influence on the accuracy of determining the film parameters. In this connection, the coefficients of elasticity and viscosity and density of the used castor oil were determined by the experiment with the environment temperature monitoring. For that, the resonator was immersed in castor oil and the frequency dependencies of the real and imaginary parts of the electrical impedance were measured. Figure 7.10 shows the frequency dependencies of the quartz resonator placed in the castor oil by the circles. The corresponding equivalent circuit of such resonator is presented in Figure 7.11. The aforementioned least-squares method

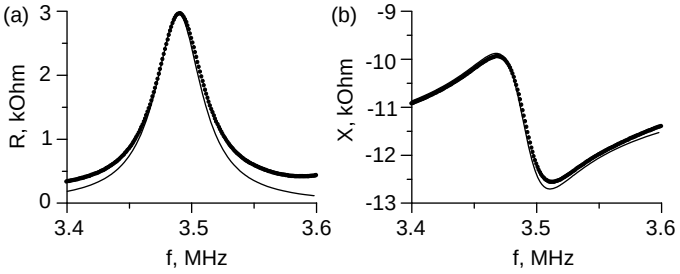

Figure 7.10 The frequency dependencies of the real (a) and imaginary (b) parts of the electrical impedance for the quartz resonator immersed in castor oil. The circle and solid lines correspond to the experiment and theory, respectively.

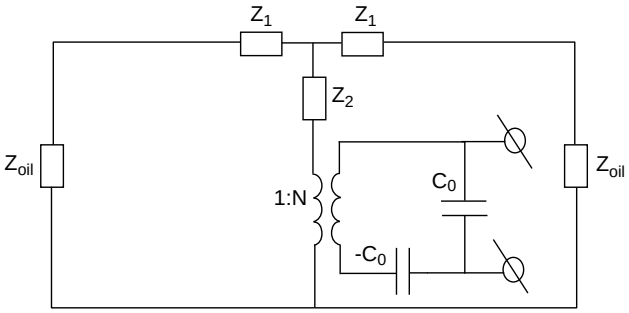

Figure 7.11 The equivalent circuit of the resonator immersed in castor oil.

allowed to find such parameters of the castor oil as coefficients of elasticity and viscosity and density for which the theoretical and experimental frequency dependencies of the real and imaginary parts of the electrical impedance were closest. The theoretical frequency dependencies of the real and imaginary parts of the electrical impedance are shown in Figure 7.10 by the solid lines. Thus while measuring the change in the temperature of the environment, we first measured the oil parameters by using the aforementioned method.

On the next stage of the investigation, we measured the frequency dependencies of the real and imaginary parts of the electrical impedance of the resonator loaded by the nanocomposite film under study through the layer of the castor oil. These dependencies for the quartz resonator with the low-density polyethylene film and nanoparticles of Fe (20%) and Fe_2O_3 (10%) are presented by the circles in Figures 7.12 and 7.13, respectively. For the theoretical analysis of such loaded resonator, we used the equivalent circuit presented in Figure 7.14. Here the mechanical impedances z_3, z_4 and z_5, z_6 corresponding to the film under study and castor oil, respectively, are equal

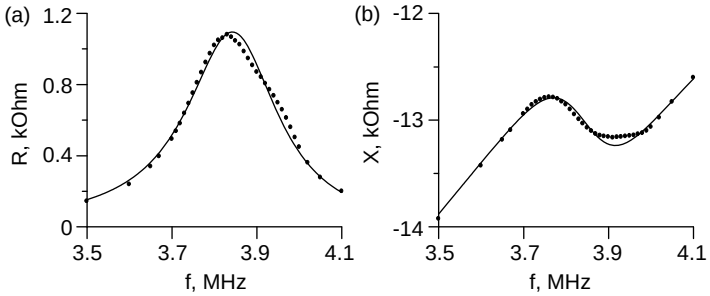

Figure 7.12 The frequency dependencies of the real (a) and imaginary (b) parts of the electrical impedance for the quartz resonator loaded by the nanocomposite film with percentage of Fe 20%. The circle and solid lines correspond to the experiment and theory, respectively.

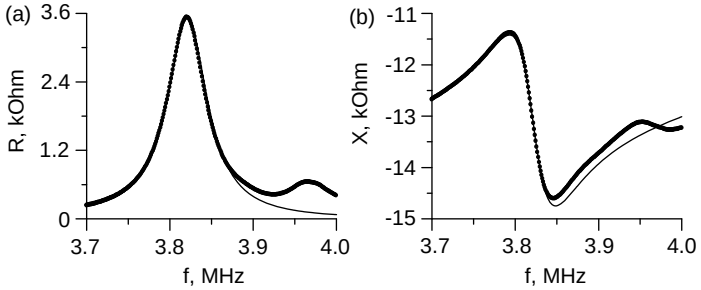

Figure 7.13 The frequency dependencies of the real (a) and imaginary (b) parts of the electrical impedance for the quartz resonator loaded by the nanocomposite film with percentage of Fe_2O_3 10%. The circle and solid lines correspond to the experiment and theory, respectively.

$$z_3 = iZ^{\mathrm{f}}\,\mathrm{Stg}\left(k^{\mathrm{f}}L^{\mathrm{f}}/2\right), \quad z_4 = -iZ^{\mathrm{f}}S/\sin\left(k^{\mathrm{f}}L^{\mathrm{f}}\right), \tag{7.5}$$

$$z_5 = iZ^{\mathrm{o}}\mathrm{Stg}(k^{\mathrm{o}}L^{\mathrm{o}}/2), \quad z_6 = -iZ^{\mathrm{o}}S/\sin(k^{\mathrm{o}}L^{\mathrm{o}}). \tag{7.6}$$

Here $Z^{\mathrm{f,o}} = (C_{jj}^{\mathrm{f,o}}\rho^{\mathrm{f,o}})^{1/2}$ is the specific acoustic impedance; $C_{jj}^{\mathrm{f,o}}$ is the coefficient of elasticity; $\rho^{\mathrm{f,o}}$ is the density; $k^{\mathrm{f,o}} = \omega/v^{\mathrm{f,o}}$ is the wave number; $v^{\mathrm{f,o}}$ is the wave velocity; and $L^{\mathrm{f,o}}$ is the thickness. Indices f and o correspond to the film and oil, respectively. The velocity of the acoustic wave and specific acoustic impedance may be written similarly to Eq. (7.4) as

$$v^{\mathrm{f,o}} = \left\{\left(C_{jj}^{\mathrm{f,o}} + i\omega\eta_{jj}^{\mathrm{f,o}}\right)/\rho^{\mathrm{f,o}}\right\}^{1/2}, \quad Z^{\mathrm{f,o}} = \left\{\left(C_{jj}^{\mathrm{f,o}} + i\omega\eta_{jj}^{\mathrm{f,o}}\right)\rho^{\mathrm{f,o}}\right\}^{1/2}. \tag{7.7}$$

The Kirchhoff's equations for the circuit in Figure 7.14 and the material constants obtained for resonator material and castor oil allowed us to calculate the frequency dependencies of the real and imaginary parts of the electrical impedance of the resonator loaded by the film under study for given values C_{jj}^{f}, η_{jj}^{f}, and L^{o}. Here L^{o} is the thickness of oil layer. Then by changing these parameters with the help of the least-squares method, we found the minimum of the criterion function for which the theoretical and experimental data were closest. Figures 7.12 and 7.13 show by the

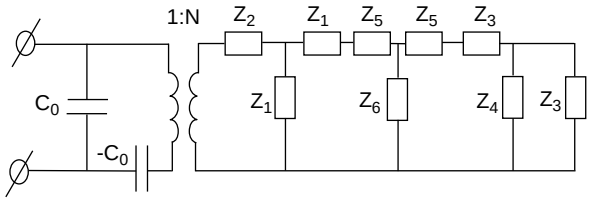

Figure 7.14 The equivalent circuit of the resonator loaded by the film under study.

solid lines the calculated frequency dependencies for the quartz resonator loaded by the film with nanoparticles Fe (20%) and Fe_2O_3 (10%), respectively. Tables 7.3 and 7.4 show the thickness (L), density (ρ), longitudinal and shear coefficients of elasticity (C_{ii}), and viscosity (η_{ii}) of the nanocomposite films based on the low-density polyethylene with various concentrations of nanoparticles of Fe and Fe_2O_3. The first row of these tables demonstrated the parameters for the modified pure low-density polyethylene. The accuracy of the determinations of the material constants is about $\pm$10%.

The analysis of the data presented in Tables 7.3 and 7.4 show that the density of the nanocomposite materials, in practice, monotonically increases at the increase in the concentrations of the nanoparticles of Fe and Fe_2O_3. It is quite natural because the density of Fe and Fe_2O_3 is significantly more than one of the low-density polyethylenes. The changes in the density of the nanocomposite material with an increase in the concentration of the nanoparticles from the minimum value to the maximum one are 16 and 20% for the Fe and Fe_2O_3 nanoparticles, respectively.

As for the elasticity modules, one may draw the following conclusions. The value of C_{66}^{f} increases monotonically with an increase in concentration for both nanoparticle types. As for the longitudinal elasticity modulus, the value of C_{11}^{f} is monotonically decreased for the Fe nanoparticles as their concentration grows. For Fe_2O_3 nanoparticles, the C_{11}^{f} value is reduced with achieving its minimum at a concentration of 15% and then it increases.

The examination of the viscosity coefficient behavior has shown that for Fe nanoparticles, the coefficient η_{11}^{f} is at first reduced passing two local minima and then it increases as their concentration is raised. The coefficient η_{66}^{f} is varied essentially monotonically, and it has only one local slight minimum. In the presence of Fe_2O_3 nanoparticles, coefficient η_{11}^{f} is nonmonotonically increased and has a local maximum and a local minimum. At the same time, a higher particle concentration causes the coefficient to nonmonotonically decrease while having two local minima.

The obtained results are of practical use despite that there is no physical explanation for such a cumbersome behavior of elasticity and viscosity coefficients. They demonstrate the variation of the acoustic impedance of the nanocomposite polymeric materials over 30 and 40% to be possible for the longitudinal and shear acoustic waves, respectively, within the same technological procedure. At that, the longitudinal and shear bulk acoustic wave velocities may be purposefully altered over 40 and 29%, respectively. These results may be useful in the development of the matching and damping layers with the low acoustic impedance for various acoustic devices.

7.5
Effect of the Nanoparticle Material Density on the Acoustic Parameters of Nanocomposites Based on the Low-Density Polyethylene

The results described in Section 7.4 show that the material of the nanoparticles has an influence on the velocity and acoustic impedance of the nanocomposite

polymeric materials. This section demonstrates the results of the detailed analysis of the influence of the density of the nanoparticles material on the acoustic parameters of the nanocomposite polymeric materials. We analyzed the materials based on the matrix of low-density polyethylene with embedded nanoparticles of CdS, Fe_2O_3, and Fe. The choice of these nanoparticles was determined by the differences in their densities.

As it has been shown in Section 7.3, the longitudinal coefficients of elasticity C_{11}^{f} and viscosity η_{11}^{f} and shear viscosity coefficients η_{44}^{f} of the nanocomposite polymeric materials under study almost always decrease with increasing the concentration of nanoparticles. The only exception was for the nanocomposite material with the iron oxide nanoparticles. In this case, the value of C_{11}^{f} decreased with increasing the concentration nanoparticles, passed through a minimum at their concentration of 15%, and increased again. As for the shear elastic coefficient C_{44}^{f}, its value exhibited nonmonotonic variation depending on the concentration of the nanoparticles in all cases.

We demonstrate the results of the investigation of the influence of the nanoparticle material on the longitudinal coefficients of elasticity and viscosity of the nanocomposite films. The values of the mechanical parameters of the nanoparticle materials and nanocomposites with the same percentage content of nanoparticles (10 and 20%) are presented in Table 7.5.

Here superscripts "n" and "f" refer to the nanoparticle material and nanocomposite film, respectively [26].

An analysis of the data in Table 7.5 shows that, as the nanoparticle material density increases, the average of the longitudinal coefficient of elasticity of nanocomposites decrease, while the effective viscosity coefficients remain virtually unchanged.

In order to provide a physical interpretation of the obtained results, the following simple model was proposed for analysis. It was assumed that in the nanocomposite film all nanoparticles have approximately the same sizes (and, hence, masses) and are coupled by the force of the elasticity of the polymeric matrix. In this case, the observed regularities can be analyzed in terms of the model of a linear chain

Table 7.5 The mechanical parameters of the nanoparticle materials and nanocomposite films at values of nanoparticles concentration of 10 and 20%.

Nanoparticle material	ϱ^{n} (kg/m^3)	ϱ^{f} (kg/m^3)	C_{11}^{n}/C_{66}^{n} (10^{11} Pa)	C_{11}^{f} (10^{8} Pa)	η_{11}^{f} (Pa s)	ϱ^{f}/ϱ^{n}
10%						
CdS	4820	1200	0.907/0.15	38.0	19.0	0.249
Fe_2O_3	5250	900	2.21/0.75	22.0	18.0	0.171
Fe	7860	994	2.42/1.12	14.0	19.0	0.126
20%						
CdS	4820	1200	0.907/0.15	32.5	20.0	0.249
Fe_2O_3	5250	1037	2.21/0.75	29.6	18.0	0.198
Fe	7860	994	2.42/1.12	10.2	18.0	0.126

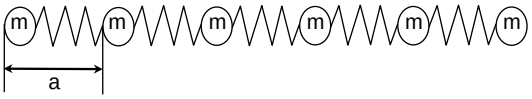

Figure 7.15 The model of the linear chain containing the balls of equal masses m, which are joined by the springs. The distance between the balls is equal to a [26].

comprising alternating the balls of equal masses m linked by the elastic springs with stiffness β (see Figure 7.15). The velocity of an acoustic wave in this chain can be expressed as follows [27]

$$v = \lambda(\beta/m)^{1/2}\sin(\pi a/\lambda)/\pi. \tag{7.8}$$

Here λ is the wavelength, β is the elastic coefficient of the polymeric matrix, a is the distance between the balls, m is the mass of the ball (determined by its size and the material density). Assuming that $a \ll \lambda$, the expression (7.8) may be rewritten as

$$v = \lambda(\beta/m)^{1/2}\pi a/(\lambda\pi) = a(\beta/m)^{1/2}. \tag{7.9}$$

Thus, the wave velocity in the nanocomposite materials with the same concentration of nanoparticles (i.e., distance a is constant) and constant coefficient β must decrease with increasing the nanoparticle mass m.

On the other hand, it is known [25] that the elasticity coefficient of the nanocomposite material C_{ij} determines together with the density ρ the acoustic wave velocity v as

$$v = \left(C_{ij}/\rho\right)^{1/2}. \tag{7.10}$$

Equating the squared right-hand parts of Eqs (7.9) and (7.10) we obtain the following expression

$$a^2\beta/m = C_{ij}/\rho, \tag{7.11}$$

which implies that

$$C_{ij} = \rho a^2\beta/m. \tag{7.12}$$

Using the apparent relation

$$m = \rho^{\mathrm{n}} V^{\mathrm{n}}, \tag{7.13}$$

where V^{n} is the nanoparticle volume, and substituting this into the relation (7.12), we obtain the following formula:

$$C_{ij} = \left(\frac{a^2\beta}{V^{\mathrm{n}}}\right)\frac{\rho^{\mathrm{f}}}{\rho^{\mathrm{n}}}. \tag{7.14}$$

Thus, if the matrix material and the concentration of the nanoparticles remain unchanged, then a and β values can be considered constant. In addition, our investigations of the nanocomposite film structure using the atomic force

microscopy and transmission electron microscopy showed that the averaged size of the dispersed nanoparticles was approximately the same, about 10–20 nm. This means that the value V^n may be considered constant. Then, expression (7.14) shows that as the value ρ^f/ρ^n decreases, the elastic coefficient of the nanocomposite material must decrease as well. The values of this ratio for various nanoparticle materials and concentrations are given in Table 7.5. So, an increase in the nanoparticle material density must lead to a decrease in the elastic coefficient of the nanocomposite material. This conclusion is in agreement with that observed in the experiment. Moreover, expression (7.14) also indicates that as the distance between nanoparticles decreases (i.e., as their concentration increases), the longitudinal elastic coefficient must also decrease. This regularity is also observed in the experiment, except for nanocomposite material with Fe_2O_3 nanoparticles. This discrepancy can be explained by a different degree of the matrix material loosening at the boundaries with various nanoparticles [28].

As for the behavior of viscosity, this parameter not only characterizes the physical viscosity of the film, but also determines the effective viscosity that considers all the other mechanisms of losses (scattering on inhomogeneities of the nanocomposite film, electric losses, contact losses, etc.). The diversity of all these factors hinders the unambiguous interpretation of the behavior of the effective viscosity coefficients in the materials under study.

On the whole, the aforementioned analysis showed that there is a possibility of effectively controlling the acoustic impedance of the nanocomposite materials based on a matrix of a low-density polyethylene with embedded nanoparticles of various densities.

7.6 Conclusions

Thus in the course of the investigations it was shown that for obtaining the nanocomposite samples based on the low-density polyethylene with the minimum porosity or maximum density, one should use the molding temperature which is in the range 110–120 °C. The obtained results also indicate the possibility to change some physical macroscopic parameters (density, permittivity, etc.) by changing the molding temperature.

The obtained temperature dependencies of the permittivity of the nanocomposite materials may be used for searching the geometric parameters of waveguides, types of waves, and operating frequency of the acoustic waves propagating in the structure "piezoelectric plate–nanocomposite film" for which the temperature coefficient of delay may be significantly decreased at the conservation of the high value of the electromechanical coupling coefficient [10].

The longitudinal and shear coefficients of elasticity and viscosity and also density of the nanocomposite materials based on the matrix of a low-density polyethylene with embedded Fe and Fe_2O_3 nanoparticles with various concentrations were experimentally determined. For the measurement we used the quartz and langasite

resonators on the shear and longitudinal acoustic waves, respectively. As a whole, the obtained results show the variation of the acoustic impedance of the nanocomposite polymeric materials over 30 and 40% to be possible for the longitudinal and shear acoustic waves, respectively, within the same technological procedure. At that the longitudinal and shear bulk acoustic wave velocities may be purposefully altered over 40 and 29%, respectively. These results may be useful in the development of the matching and damping layers with the low acoustic impedance for various acoustic devices.

On the whole, the obtained results demonstrate the possibility of purposeful changing of the acoustic impedance of the nanocomposite materials based on the matrix of a low-density polyethylene with embedded nanoparticles of various metals and their compounds with the different concentration and density.

Acknowledgments

This work is supported by the Russian Foundation of Basic Researchers: grant #12-02-01057, grant #12-02-31757, and grant #13-08-00678. Authors thank Gleb Yurkov, Vladimir Kolesov, Alexander Fionov, Nadezhda Petrova, Nikolai Ushakov and Igor Kosobudskii for given samples of nanocomposite materials and useful discussion. Authors also thank Sergey A. Sakharov for the production of the langasite resonators.

References

1 Gubin, S., Yurkov, G., and Kosobudsky, I. (2005) *International Journal of Materials and Product Technology*, **23** (1–2), 2–25.
2 Gubin, S. (2002) *Colloids and Surfaces A: Physicochemical and Engineering Aspects*, **202**, 155–163.
3 Zhang, R., Cao, W., Zhou, Q., Cha, J.-H., Shung, K., and Huang, Y. (2007) *IEEE Transactions on Ultrasonics, Ferroelectrics, and Frequency Control*, **54**, 467–469.
4 Wang, H., Cao, W., Zhou, Q., Shung, K., and Huang, Y. (2004) *Applied Physics Letters*, **85**, 5998–6000.
5 Ushakov, N., Zapsis, K., and Kosobudskii, I. (2003) *Technical Physics Letters*, **29**, 936–937.
6 Ushakov, N., Yurkov, G., Gorobinskii, L., Popkov, O., and Kosobudskii, I. (2008) *Acta Materialia*, **56** (10), 2336–2343.
7 Trakhtenberg, L., Gerasimov, G., Grigoriev, E., Zavjalov, S., Zagorskaja, O., Zufman, V., and Smirnov, V. (2000) *Studies in Surface Science and Catalysis*, **130**, 941–946.
8 Meilikhov, E. (2001) *Physics of the Solid State*, **43** (7), 1225–1228.
9 Hartmann, B. (2001) Elastic properties of polymers, in *Handbook of Elastic Properties of Solids, Liquids, and Gases*, Vol **3** (eds M. Levy, H. Bass, and D. Stern), Academic Press, New York, pp. 51–68.
10 Kuznetsova, I., Zaitsev, B., and Kuznetsova, A. (2008) *Ultrasonics*, **48**, 587–590.
11 Zaitsev, B., Kuznetsova, I., Joshi, S., and Kuznetsova, A. (2001) *IEEE Transactions on Ultrasonics, Ferroelectrics, and Frequency Control*, **48** (1), 322–328.
12 Friedrich, K., Fakirov, S., and Zhang, Z. (2005) *Polymer Composites: From Nano- to Macro-Scale*, Springer, Berlin.
13 Ushakov, N., Ul'zutuev, A., and Kosobudskii, I. (2008) *Technical Physics*, **78** (12), 1597–1600.

14 Ul'zutuev, A. and Ushakov, N. (2008) *Technical Physics Letters*, **34** (10), 851–856.

15 Zaitsev, B., Kuznetsova, I., Shikhabudinov, A., and Razumov, K. (2008) *Technical Physics Letters*, **34** (6), 528–530.

16 Pomogailo, A.D. and Kestelman, V.N. (2005) *Metallopolymer Nanocomposites*, Springer, Berlin.

17 Edelstein, A.S. and Cammarata, R.C. (eds) (1998) *Nanomaterials: Synthesis, Properties and Application*, Institute of Physics Publishing, Bristol.

18 Sugimoto, T. (2001) *Monodispersed Particles*, Elsevier, Amsterdam.

19 Petrakovskii, G., Aplesnin, S., and Piskorskii, V.P. (1985) *Soviet Physics Journal*, **27** (10), 842–862.

20 Kozinkin, A., Vlasenko, V., Gubin, S., Shuvaev, A., and Dubovtsev, I. (1996) *Inorganic Materials*, **32** (4), 376–382.

21 Weast, R.C. (ed.) (2001) *CRC Handbook of Chemistry and Physics*, CRC Press, Boca Raton, FL.

22 Zaitsev, B.D., Shikhabudinov, A.M., and Kuznetsova, I.E. (2009) *Technical Physics Letters*, **35** (7), 30–33.

23 Zaitsev, B., Joshi, S., and Dhuru, V. (1997) *Proceedings of IEEE Ultrasonic Symposium*, **1**, 623–626.

24 Mason, W.P. (1964) Use of piezoelectric crystals and mechanical resonators in filters and oscillators, in *Physical Acoustics*, Vol **1A** (eds W.P. Mason and R.N. Thurston), Academic Press, New York.

25 Dieulesaint, E. and Royer, D. (1980) *Elastic Waves in Solids: Applications to Signal Processing*, John Wiley & Sons, Inc., New York.

26 Kuznetsova, I.E., Zaitsev, B.D., and Shikhabudinov, A.M. (2010) *Technical Physics Letters*, **36** (8), 759–761.

27 Sirotin, Yu.I. and Shaskol'skaya, M.P. (1979) *Fundamentals of Crystallophysics*, Nauka, Moscow (in Russian).

28 Lipatov, Yu.S., Todosiychuk, T.T., Tsarev, P. K., and Sergeeva, L.M. (1984) The estimation of adhesion in filled polymer systems, in *Adhesive Joints: Formation, Characteristics and Testing*, Plenum Press, New York, pp. 433–450.

8
Barrier Properties of Nanocomposites

Amrita Saritha and Kuruvilla Joseph

8.1
Introduction

This chapter presents a short review of the studies on the barrier properties of nanocomposite materials that consist of inorganic fillers in polymeric matrices. It discusses the dominant mechanisms for the transport of molecules in polymers and polymer nanocomposites. We have also tried to emphasize on the various models that have been proposed for the prediction of permeability in polymer–clay nanocomposites. A few applications of these materials as gas barriers are presented. The permeability of small gaseous molecules in a polymer matrix is determined by different factors such as solubility, diffusivity, and morphology of the polymer. Barrier properties in polymers are necessarily associated to their inherent ability to permit the exchange, to a higher or lower extent, of low molecular weight substances through mass transport processes such as permeation. The permeation of low molecular weight chemical species usually takes place through the polymer amorphous phase and is generally envisaged as a combination of two processes, that is, sorption and diffusion. The permeability of gas molecules in polymer nanocomposite is very complex. To determine permeability, one must take into account that nanofillers in polymer matrix affect the solubility and diffusivity of the penetrating molecules, especially in interfacial regions. Nanofillers have high aspect ratio, thus well-dispersed nanofillers increase the tortuous path of penetrating molecules. As consumers demand improved product quality and longer shelf life, there is continuous need for improved barrier properties in packaging for food, cosmetics, beverages, and pharmaceuticals. However, other important properties such as gas barrier properties, which form an absolutely necessary requirement for the use of materials in packaging and storage applications, were relatively neglected. By improving the barrier performance of the materials by incorporation of high aspect ratio nanoplatelets, one can expect to reduce the thickness of the commercial packaging laminates and other materials where thick material is required to be used to provide barrier to various gases. This can thus lead to significant amount of savings in the material costs and can make the polymer materials lighter and also transparent as the nanoscale dispersed filler would not scatter light. This chapter

Polymer Composites: Volume 2, First Edition. Edited by Sabu Thomas, Kuruvilla Joseph, Sant Kumar Malhotra, Koichi Goda, and Meyyarappallil Sadasivan Sreekala.

examines the factors affecting barrier properties enhancement in polar polymer matrices, which are different from the case when nonpolar polymers are involved, thus indicating that the performance has to be quantized on a case-by-case basis. The commonly used conventional models for prediction of permeation reduction are also less representative of the true microstructure of the nanocomposites. Thus, the barrier performance of the polymer nanocomposite materials is also explored, apart from the bulk-based mechanical properties.

8.2
Nanocomposites from Ceramic Oxides

Novel polymer–ceramic nanocomposite membranes were fabricated, characterized, and tested for their barrier performance. Atomic layer deposition (ALD) was used to deposit alumina films on primary, micron-sized (16 and 60 μm) high-density polyethylene (HDPE) particles at a rate of ~0.5 nm/cycle at 77 °C. Well-dispersed polymer–ceramic nanocomposites were obtained by extruding alumina-coated HDPE particles. The dispersion of alumina flakes can be controlled by varying the number of ALD coating cycles and substrate polymer particle size. The diffusion coefficient of fabricated nanocomposite membranes can be reduced to half with the inclusion of 7.29 vol.% alumina flakes. However, a corresponding increase in permeability was also observed due to the voids formed at or near the interface of the polymer and alumina flakes during the extrusion process, as evidenced by electron microscopy [1].

8.3
Nanocomposites from Nanotubes

A fraction (0.1 wt%) of single-walled carbon nanotube (SWNT) and multiwalled carbon nanotube (MWNT) have been dispersed homogeneously throughout polycarbonate (PC) matrix by ultrasonication. The alignment of SWNT and MWNT in PC matrix has been accomplished by applying an external magnetic field of 1200 gauss. These nanocomposites have been studied by FTIR spectroscopy, gas permeation, Raman spectroscopy, and electrical and mechanical measurements. A comparative study of the gas permeation of various gases (H_2, N_2, and CO_2) has been performed on these nanocomposites. H_2 is found to be more selective for SWNT–PC and MWNT–PC nanocomposites in comparison to N_2 and CO_2 [2]. A novel Saran-based (a copolymer of vinylidene chloride and acrylonitrile) polymer nanotube composite, which shows high transparency in the visible region, good barrier properties, and thermal stability was prepared by Jayachandran and coworkers for use as an encapsulant for organic photovoltaic (OPV) devices. Different loadings of Saran and boron nitride nanotubes were taken and the composites were prepared to optimize the composition of the composite. The composites showed excellent transparency in the visible region, good barrier properties, and good thermal stability [3].

8.4
Layered Silicate Nanocomposites

Use of nanosized filler particles to form polymer composites has attracted much attention in recent years because of the potential performance advantages that could create new technological opportunities. The key issue is to obtain an effective dispersion and exfoliation of the platelets into the polymer matrix to yield well-aligned, high aspect ratio particles for mechanical reinforcement or a tortuous diffusion pathway for improved barrier properties. Indeed, the literature contains numerous reports on increased modulus and dimensional stability [4–11], increased strength and heat resistance [5–7], and decreased gas permeability [12–23] caused by addition of layered silicates to various polymer matrices. Much of the literature is devoted to nanocomposites made by addition of organoclays, formed from montmorillonite, to thermoplastics using melt-processing techniques. While it is clear that the property benefits of adding plate-like fillers to polymers will increase as both the volume fraction, f, and the aspect ratio, a, of the platelets increase, there are natural limits on both f and a inherent to this approach imposed by the effect such particles have on melt rheology [1,2,23–25]. Goldberg, Feeney, and coworkers have described a water-based approach for forming elastomeric nanocomposites coatings with high loadings of high aspect ratio platelets specifically designed for gas barrier applications [26–28]. The purpose of this chapter is to explore the permeation characteristics of a series of gases in these materials using experimental techniques developed at the University of Texas at Austin that are readily adaptable for such coatings [29,30]. These coatings are based on butyl rubber, which is well known among elastomers for its superior gas barrier characteristics. The filler is vermiculite, which is a layered silicate that can be dispersed in water similar to montmorillonite but its platelets are believed to have a much higher aspect ratio [9,26]. The butyl rubber is formed into latex that is mixed with an aqueous dispersion of vermiculite in the desired ratio. This water-based formation can then be sprayed onto a substrate where the water eventually evaporates to form a continuous coating. High concentrations of the vermiculite platelets should force them into good alignment, which is essential for good barrier performance.

The role of the aspect ratio of the layered silicate platelets on the mechanical and oxygen permeation properties of hydrogenated nitrile rubber (HNBR) and organophilic layered silicate nanocomposites was investigated. Montmorillonite (MMT) and fluorohectorite (FHT) bearing the same type of intercalant (i.e., octadecylamine, ODA), however, showing different aspect ratio was involved in this study. The dispersion of the layered silicates was assessed by X-ray diffraction (XRD) and transmission electron microscopy (TEM), respectively. Increasing aspect ratio (MMT $<$ FHT) resulted in higher stiffness under uniaxial tensile loading. The dispersion state ("secondary structure") of the organophilic layered silicates reduced dramatically the oxygen permeability of the rubber matrix based on the labyrinth principle. The lowest oxygen permeability was measured for the HNBR/FHT–ODA films in which the layered silicates had the highest aspect ratio. By varying the FHT–ODA volume fraction in the latter compound, the mechanical and permeation

properties were measured and modeled. It was found that the modified Guth's and Nielsen's equations predicted accurately the mechanical and permeation responses, respectively [31].

Using the relative permeability theory in combination with the detour theory, they obtained new relative permeability expressions that allow us to investigate the relative permeability R_p as a function of lateral separation b, layer thickness w, gallery height H, layer length L, and layer volume fraction Φ_s. It was found that intercalated and/or incomplete exfoliated structures and dispersed tactoids with several layers can effectively enhance the barrier properties of the materials. Furthermore, we developed the chain-segment immobility factor to briefly discuss the chain confinement from clay layers. The results showed that the chain confinement enhanced the barrier properties of the intercalated nanocomposites. This model is better consistent with the experiments when $\Phi_s > 0.01$. The findings provide guidelines for tailoring clay layer length, volume fraction, and dispersion for fabricating polymer–clay nanocomposite with the unique barrier properties [32].

Polyurethane–clay nanocomposites were fabricated in solution and tested as gas barrier membranes. Natural montmorillonite was modified with various alkylammonium surfactants and incorporated into a polyurethane matrix. Permeation properties of the nanocomposites were studied as a function of processing methodology. Preprocessing clay samples with sonication instead of plain stirring led to significantly better barrier properties, suggesting that dispersion of the clay particles is a critical factor. Fitting the experimental permeabilities with phenomenological models, which predict the effective permeability of polymer systems filled with barrier flakes as a function of flake concentration, led to unrealistically low values of calculated aspect ratios of the clay layers as shown in Figure 8.1 [33]. Polyurethane/clay nanocomposites were fabricated in solution and tested as gas barrier membranes. Natural montmorillonite was modified with various alkylammonium surfactants and incorporated into a polyurethane matrix. Permeation properties of the

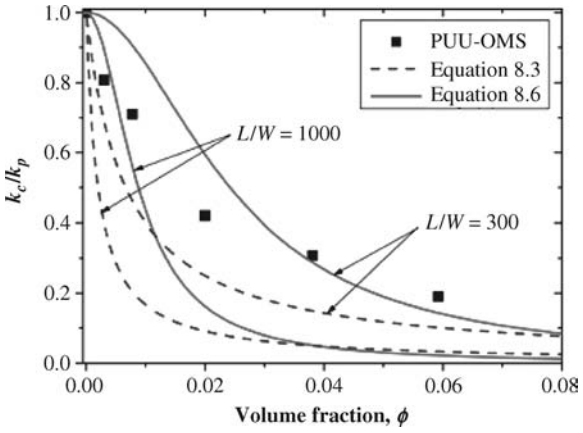

Figure 8.1 Relative water permeability in poly(urethane urea) organically modified layered silicates (PUU–OMS) nanocomposites [33].

nanocomposites were studied as a function of processing methodology. Pre-processing clay samples with sonication instead of plain stirring led to significantly better barrier properties, suggesting that dispersion of the clay particles is a critical factor. Fitting the experimental permeabilities with phenomenological models, which predict the effective permeability of polymer systems filled with barrier flakes as a function of flake concentration, led to unrealistically low values of calculated aspect ratios of the clay layers [34].

Nylon 6–clay nanocomposites of various clay minerals with different cation exchange capacity (CEC) were prepared by *in situ* polymerization method, and properties such as mechanical, thermal, and gas permeability were compared with respect to pure nylon 6 (N6) polymer by Tsai *et al.* [35]. It is shown that the nature of the permeation of carbon dioxide gas depends on the exfoliation or intercalation of clay platelets. It is seen that the exfoliated clay platelets offer effective low permeability than the intercalated platelets as seen in Figure 8.2.

Natural rubber (NR)–rectorite nanocomposite was prepared by co-coagulating NR latex and rectorite aqueous suspension. The TEM and XRD were employed to characterize the microstructure of the nanocomposite. The results showed that the nanocomposite exhibited a higher glass transition temperature, lower tan δ peak value, and slightly broader glass transition region compared with pure NR. The gas barrier properties of the NR–rectorite nanocomposites were remarkably improved by the introduction of nanoscale rectorite because of the increased tortuosity of the diffusive path for a penetrant molecule. The nanocomposites have a unique stress–strain behavior due to the reinforcement and the hindrance of rectorite layers to the tensile crystallization of NR [36].

The polyarylate : poly(tetramethyl bisphenol A-iso/terephthalate) that exhibits high permeability and moderate selectivity was chosen for making nanocomposites with two organically modified clays (Cloisite 6A and 10A) by solution intercalation method. The nanocomposite formation of various clay loadings (3, 5, and 7% w/w)

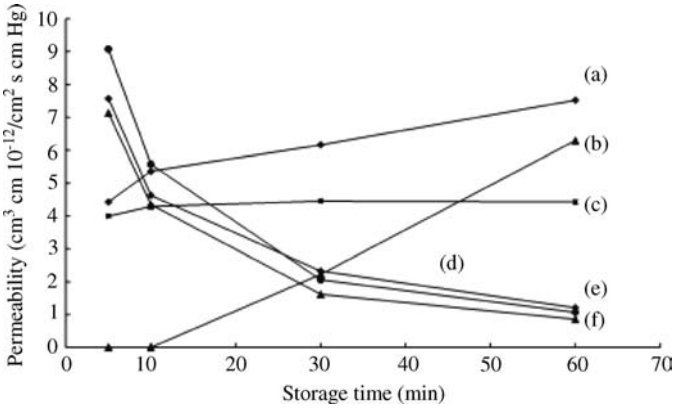

Figure 8.2 Permeability as a function of storage time for (a) N6, (b) N6/CL-42, (c) N6/CL-114, (d) N6/CL-112, (e) N6/CL-120, and (f) N6/CL-88 [35].

in polyarylate was ascertained by change in physical properties (XRD, DMA, and TEM). Behavior of solution viscosity and nanocomposite density indicated existence of polymer–clay layer interactions. As anticipated, though the gas permeability of pure gases, for example, He, N_2, CH_4, and CO_2 exhibited decrease, it was not monotonous. This decrease was more for larger gases (N_2, CH_4, and CO_2) in comparison to the decrease for smaller gas (He) permeability. This led to a decrease in CO_2/N_2 and CO_2/CH_4 selectivities and increase in He/CO_2 selectivity, while He/CH_4 selectivity was increased substantially at 7% clay loading. This variation indicated feasibility of nanocomposites formation as a tool for improving selectivity of certain gas pairs [37]. Barrier membranes of poly(*n*-butyl acrylate) were produced by the *in situ* polymerization of *n*-butyl acrylate in the presence of surface-modified natural montmorillonite. This two-stage process allowed control over the extent of intercalation, most likely leading to exfoliated nanostructures [38]. The first stage of the process consisted of the organic modification of montmorillonite via ion exchange reactions with (acryloyloxy) ethyl alkylammonium cations. This process anchored chemically reactive species on the surface of natural clay and improved the mixing between the clay and the monomer. The second stage of the process comprised the *in situ* polymerization of *n*-butyl methacrylate and the unsaturated acryloxy ethyl groups anchored on the surface of the clay. Resulting membranes were characterized in terms of their microstructure and diffraction (XRD), their thermal properties (TGA and DSC), and gas permeation properties. The resulting exfoliated morphology led to a decrease in gas permeability. Gas barrier properties of the nanocomposites were compared to those predicted by phenomenological models such as those of Cussler and Nielsen. Poly(*n*-butyl methacrylate)–clay and poly(*n*-butyl methacrylate-*co*-methyl methacrylate)–clay nanocomposites were synthesized via emulsion polymerization to act as barrier membranes. Cloisite® Na^+ was modified via ion exchange to tether acryloxy reactive groups on the surface of the silicate platelet in order to promote polymerization and exfoliation of the stacked platelets. The addition of organically modified clays in the matrix improved the thermal and barrier properties of the nanocomposite. Results indicate that the polymer particle size in the emulsion dictated the dispersion of the montmorillonite clay platelets in the polymer matrix and the subsequent barrier properties of the membranes. Membranes fabricated utilizing emulsions with polymer particle sizes down to 120 nm gave rise to the highest barrier properties. The presence of 5 wt% clays decreased [39]. Series of nylon 6–clay (NYC) nanocomposite–poly(vinyl alcohol) (PVA) blends films were prepared via melt compounding and pressing. The good compatibility between NYC and PVA was approved by DMA and FTIR measurements. The macroscopic barrier properties of NYC–PVA blends films were inspected in detail, based on a microscopic free volume point of view. The gasoline permeation properties and the characterized parameters of free volume were adjusted through varying the PVA content. A similarity was found between barrier properties versus PVA content and free volume parameters versus PVA content. The relation between free volume fraction and permeability coefficient could be described exactly as an exponent function, implied that microscopic free volume plays an important role in determining macroscopic barrier properties [40].

8.5
Composite Models of Permeation

Various models for composite permeability as they relate to nanocomposites have been reviewed and different models have been proposed [41–44]. The simplest way to model any composite property is to use a rule of mixtures approach. Polymer nanocomposite properties, however, do not generally follow this rule. Instead, fillers with high aspect ratio particles will influence the permeability of gases through the matrix more than filler particles with lower aspect ratios. Alignment/orientation of the filler particles (with respect to the axis of gas permeation) also plays a significant role in bulk permeability. Five models are briefly described in Sections 8.5.1–8.5.5. Predictions from these models are later compared to experimental mass loss rates.

8.5.1
Nielsen Model

This model describes the maximum decrease in permeability that can be expected for the addition of a filler material to a polymer based on tortuosity arguments alone. There are a few key assumptions in this model. The particles in his model are assumed to be impermeable, which results in the diffusing molecules having to go around the filler particles. Conceptually, the molecules have a longer, more tortuous path to travel, thus resulting in a longer time required for diffusion across the membrane. The filler is assumed to be of the same size uniformly and completely dispersed in the composite matrix parallel to the surface of the composite. Finally, the matrix properties are not affected by the presence of the filler. Incomplete dispersion voids and nonparallel alignment of particles would result in higher permeabilities than predicted by this model. The relative permeability is given as

$$\frac{P}{P_0} = \frac{(1-\Phi)}{1} + \frac{\Phi\alpha}{2}, \tag{8.1}$$

where P is the permeability of the composite, P_0 is the permeability of the neat polymer, Φ is the volume fraction of the filler, and α is the aspect ratio of the filler particles given by Eq. (8.2).

$$\alpha = \frac{w}{t}. \tag{8.2}$$

Here, w is the intermediate dimension of the particle and t is the smallest dimension of the particle [41].

8.5.2
Bharadwaj Model

Similar to the Nielsen model, the Bharadwaj model is based strictly on tortuosity arguments. The main difference is the consideration of the orientation and

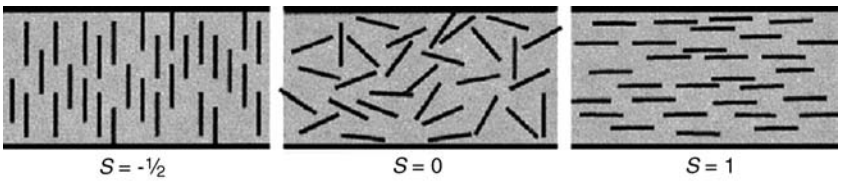

Figure 8.3 Orientation of particles corresponding to orientation factor, *S* [45].

alignment of the particles. Where the Nielsen model assumed that the particles were perfectly aligned perpendicular to the gas flow, the Bharadwaj model makes no such assumption. The Bharadwaj model for the relative permeability of a composite is given by Eq. (8.3)

$$\frac{P}{P_0} = \frac{(1-\Phi)}{1} + \frac{\Phi\alpha}{2}\frac{2}{3}\left(S + \frac{1}{2}\right), \tag{8.3}$$

where P, P_0, Φ, and α retain the previous definitions, and S is the order parameter given by Eq. (8.4),

$$S = \frac{1}{2}(3\cos 2\theta - 1), \tag{8.4}$$

where θ is the angle between the direction of preferred orientation and the sheet normal unit vectors. The brackets represent an average over the entire set of particles within the system. The order parameter ranges in value from $-\frac{1}{2}$ to 1. A value of $\frac{1}{2}$ represents an orthogonal orientation for the particles in the composite. A value of 1 indicates a perfect alignment of the particles perpendicular to the gas flow. This value of S causes the model to collapse to the Nielsen model. A value of 0 for the order parameter indicates a random orientation [42]. A diagram of the meaning of the orientation factor is given in Figure 8.3.

8.5.3
Fredrickson and Bicerano Model

In this model, the filler particles are disk shaped, whereas in the previous two models the particles are assumed to be ribbon-like. These plate-like particles are impermeable with net orientation of the plates, but there is no positional order for the plates, which creates a nematic phase. This model focuses on dilute and semidilute regimes (i.e., the volume fraction of particles is small). It is assumed that the permeability of the polymer is not influenced by the presence of particles in the matrix. The final equation given by Fredrickson and Bicerano is Eq. (8.5),

$$\frac{P}{P_0} = \frac{1}{4}\left[\frac{1}{1+\alpha_1\kappa\alpha\varphi} + \frac{1}{1+\alpha_2\kappa\alpha\varphi}\right]^2, \tag{8.5}$$

where P, P_0, Φ, and α retain their previous definitions, and κ is a geometric factor. In this case, the aspect ratio is the ratio of radial dimension of the disk to the thickness. The geometric factor, κ, for this model is given by Eq. (8.6) [43]

$$\kappa = \frac{\Pi}{\ln \alpha}. \tag{8.6}$$

8.5.4
Cussler Model

All of the assumptions from the Nielsen model remain in the Cussler model except for the regularity of the array. The Cussler model for relative permeability of a composite with monodisperse particles in a regular array is given by Eq. (8.7)

$$\frac{P}{P_0} = \frac{1-\Phi}{(1-\Phi)} + \alpha^2\Phi^2, \tag{8.7}$$

where α is the aspect ratio of the particle given by Eq. (8.8),

$$\alpha = \frac{R}{t} \tag{8.8}$$

and R is $\frac{1}{2}$ the intermediate dimension of the filler particle and t is the smallest dimension of the filler particle. The Cussler model for relative permeability of a composite with monodisperse particles in a random array is given in Eq. (8.9) [44]

$$\frac{P}{P_0} = \frac{1-\Phi}{(1+(2/3)\Phi\alpha)^2}. \tag{8.9}$$

8.5.5
Gusev and Lusti Model

The Gusev and Lusti model is derived from a computer simulation. This allows more variables to be taken into account than the previous models. This model accounts for the geometric factors associated with the increased tortuosity as well as the changes in the permeability of the polymer matrix on the molecular level. The Gusev and Lusti model for the relative permeability of a composite is given in Eq. (8.10),

$$\frac{P}{P_0} = \exp\left[-(\alpha\Phi/x_0)^\beta\right], \tag{8.10}$$

where x_0 and β are constants determined by a regression on computer-generated data. The values given by Gusev and Lusti for the constants are $\beta = 0.71$ and $x_0 = 3.47$ [44].

The simple solution–diffusion description of the steady state transport of a penetrant in a homogeneous polymer matrix indicates that the permeability coefficient, P, is the product of solubility, S, and diffusivity, D, coefficients, that is, a similar form has been assumed to apply for composites comprised of particles,

which do not sorb or conduct the penetrant, dispersed in a matrix whose local characteristics are assumed to be unaffected by the presence of the particles. The latter assertion is an assumption of "composite theory" and its validity should be tested when the particles are very small or have a high surface-to-volume ratio as is the case for so-called "nanocomposites." Simple composite theory for the type of systems mentioned earlier, in the absence of adsorption by the filler or effects of the filler on the surrounding polymer matrix, would predict the penetrant solubility in the composite to be

$$S = S_0(1 - \Phi), \tag{8.11}$$

where S_0 is the penetrant solubility coefficient in the pure polymer matrix and f is the volume fraction of particles dispersed in the matrix. In this approximation, the solubility does not depend on the morphological features of the phases. However, the diffusion process is more complex. The particles act as impenetrable barriers so that the penetrant must follow an elongated, or tortuous, path in order to diffuse through the composite. This can be accounted for by a tortuosity factor, f,

$$\mathrm{D} = D_0 f. \tag{8.12}$$

According to simple composite theory, this tortuosity factor depends on the content of particles, f; the particle shape, for example, an aspect ratio, a; and the location and orientation of the particles in space; however, it should not depend on absolute particle size or what the penetrant is. Combining the above equations gives

$$P = DS = S_0(1 - \Phi)D_0 f = (1 - \Phi)P_0 f \tag{8.13}$$

or

$$f = \frac{P}{P_0(1 - \Phi)}, \tag{8.14}$$

where P_0 is the penetrant permeability coefficient in the pure polymer matrix. In principle, this impedance or tortuosity factor, f, can be calculated by an appropriate solution to Fick's law if a complete description of the two-phase morphology is known. There is an extensive literature devoted to this problem using varying approaches and levels of sophistication or approximation [46,47]. The following are the three main influence factors (a) the influence of the extent of exfoliation or intercalation can be simply represented by the aspect ratio L/W. As the extent of intercalation increases, the thickness W of exfoliated platelets increases and the aspect ratio L/W decreases. (b) The influence of the orientation of the silicate platelets in a polymer matrix can be represented by an orientation parameter S, which is defined by $S = (3\cos 2\theta - 1)/2$. When all platelets are parallel to the direction of diffusion ($\theta = 0$), then the order parameter is $S = -1/2$. When $\theta = \Pi/2$, the orientation of the platelets is perpendicular to the diffusion direction and $S = 1$ ($\theta = 0$) indicates perfect alignment, and $S = 0$ ($\theta = 54.74$) indicates random distribution [48]. Thus, the effective aspect ratio with perfect alignment becomes $L/W\cos 2\theta$. (c) The influence of the dispersion distance ∫ between two silicate platelets can be considered by the volume fraction φ. In exfoliated PCNs, $\varphi = W/$∫ since the silicate platelets are randomly dispersed in the polymer matrix.

8.6 Techniques Used to Study the Permeability of Polymers and Nanocomposites

Free volume present in nanocomposite systems plays a major role in determining the overall performance of the membranes. Positron annihilation lifetime spectroscopy (PALS) is an efficient technique used for the analysis of free volume. The diffusion of permeant through polymeric membranes can be described by two theories, namely, molecular and free-volume theories. According to the free-volume theory, the diffusion is not a thermally activated process as in the molecular model, but it is assumed to be the result of random redistributions of free-volume voids within a polymer matrix. Cohen and Turnbull developed the free-volume models that describe the diffusion process when a molecule moves into a void larger than a critical size, V_c. Voids are formed during the statistical redistribution of free volume within the polymer. It is found that the relative fractional free volume of unfilled polymer decreases on the addition of layered silicates. The decrease is attributed to the interaction between layered silicate and polymer because of the platelet structure and high aspect ratio of layered silicates. The decrease is explained to the restricted mobility of the chain segments in the presence of layered silicates. This results in reduced free-volume concentration or relative fractional free volume [49].

The molecular transport through a polymer membrane depends also on the amount of the existing free volume. The free volume is created by the inefficient chain packing of the polymer generated by chain segment rearrangement. The increase of the free volume facilitates the diffusion process because of the creation of easier pathways for the solutes. In polymer-nanocomposite membranes the presence of the inorganic phase can influence the size and the number of the free volume holes, especially at the interfaces. Consequently, the change in the permeability of such systems is a balance between the barrier properties of the impermeable nanoplatelets and the possible increase of the free volume of the matrix. Therefore, the nanoplatelets may not always promote efficiently the final barrier properties of the material.

PALS is a nondestructive technique that provides an effective approach for the study of the free volume in the solid state. It is based on the localization of the positronium (Ps) in the free volume holes because of their repulsion by the surrounding atoms. Generally, the annihilation spectra in polymers consist of three exponentially decaying components that correspond to the three main processes of their annihilation [50]. Each of these processes is characterized by the mean lifetime and the probability of annihilation (intensity). The longest lifetime corresponds to the annihilation process of o-Ps in the free volume holes. This is the process that is used to estimate the free volume in the amorphous polymers. The size of the free volume holes, R, in the polymer can be determined from the measured lifetime, so Ps, using the semiempirical equation

$$\tau_{\text{o-Ps}} = \frac{1}{2}\left[1 - \frac{R}{R_0} + \frac{1}{2\pi}\sin\left(\frac{2\pi R}{R_0}\right)\right]^{-1}. \tag{8.15}$$

The relative intensity gives the probability for the formation of o-Ps, which is proportional to the number of holes, that is, the overall free volume [51,52]. Plotting the measured lifetime of the o-Ps and the intensity as a function of clay particles loading, one can estimate any variation in the polymer free volume that may be caused by the presence of the nanoclay particles [51].

8.7 Calculation of Breakthrough Time

The permeation process is described as a process in which chemicals move through a material at a molecular level, which is caused by the concentration difference in permeating chemicals between the outer and the inner sides of the material. Material permeation resistance is generally characterized using breakthrough times and permeation rates. Breakthrough time is defined as the length of time it takes for a chemical to pass or permeate through a barrier membrane until the chemical is first detected on the opposite side, following the initial contact of a chemical with the protective clothing. Breakthrough time measures how quickly a chemical moves through a barrier film and represents the maximum length of time during which the protective clothing could be worn without losing adequate protection. As discussed later, the determination of breakthrough time is strongly dependent on the detection limit of the test method and system. Permeation rate is a measurement of the mass flux through a unit area of material for a unit time, which is commonly expressed in units of micrograms per square centimeter per minute. The working time of a clothing material based on an ordinary film t_{active} is given by Cussler [53]

$$t_{\text{active}} = \frac{d_{\text{film}}^2}{D_{\text{film}}}, \tag{8.16}$$

where d_{film} is the thickness of the film and D_{film} its diffusion coefficient. If the latter is reduced, according to any of the models described in this review, then the working time of the film will increase accordingly, for example, [54]

$$t_{\text{active}} = \frac{d_{\text{film}}^2}{D_0}\left(1 + \frac{\alpha^2\phi^2}{1-\phi} + \frac{\alpha\phi}{\sigma} + \frac{4\chi\phi}{\pi(1-\phi)}\right)\ln\left[\frac{\pi\alpha^2\phi}{\sigma(1-\phi)}\right]. \tag{8.17}$$

If, further, use is made of reactive additives, then the working time of the composite film becomes

$$t_{\text{active}} = \frac{3c_{2,0}}{\nu H c_{1,0}} \times \frac{d_{\text{film}}^2}{D_0}\left(1 + \frac{\alpha^2\phi^2}{1-\phi} + \frac{\alpha\phi}{\sigma} + \frac{4\alpha\phi}{\pi(1-\phi)}\ln\left[\frac{\pi\alpha^2\phi}{\sigma(1-\phi)}\right]\right). \tag{8.18}$$

Chlorobutyl rubber is known for its exceptional gas barrier performance. Chlorobutyl rubber nanocomposites were prepared and permeability studies were carried out using various gases such as nitrogen, oxygen, and carbon dioxide

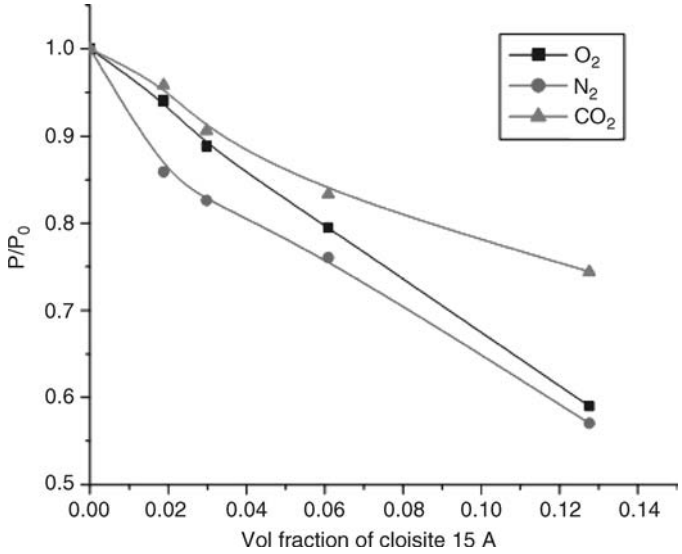

Figure 8.4 Relative permeability of chlorobutyl nanocomposites in different gases [55].

[55,56]. Figure 8.4 clearly shows the effectiveness of chlorobutyl nanoclay composites as barrier materials and films.

The breakthrough times of chlorobutyl rubber nanocomposites have been calculated using the aspect ratios and diffusion coefficients obtained from swelling experiments, and the plot of the breakthrough times against the clay loading using toluene as solvent shows the effectiveness of these materials to be used as potential volatile organic compound (VOC) barrier membranes [55].

8.8 Applications

Low permeability nanocomposite materials can be used in a variety of applications especially in packaging. Polyethylene (PE), polypropylene (PP), and poly(ethylene terephthalate) (PET) are widely used in bottles and containers. Nanocomposite route offers unique possibilities to enhance the properties of these materials, provided that adequate thermally resistant and legislation complying nanoadditives are used. However, their limited barrier properties to oxygen make them inappropriate for products requiring long self-life. Polyester nanocomposites offer superior barrier properties to oxygen and high transparency and are suitable for use in the manufacture of closed containers [57]. A material for hydrogen storage tanks is another area of applications for organoclay compositions [58].

Another area of research on this subject is the development of coatings incorporating nanoplatelets [59–61]. Polymeric nanocomposite coatings are an alternative inexpensive oxygen barrier material [62]. Such anticorrosive coatings can be used on zinc-steel plates

for automobiles [63]. Asphalt-nanocomposite-based coatings can be useful for materials for building components such as shingles [64]. Low permeability nanocomposite materials can be used in a variety of applications especially in liquid and food packaging.

8.9 Conclusions

There is a need for more systematic measurements to clarify the effects of the inorganic particles on the permeation process. PALS measurements may also be useful to reveal the influences of the nanoplatelets on the free volume and the interfacial regions. A lot of future work is needed to obtain optimal parameters (or percolation threshold) of the clay fillers and to improve their barrier and mechanical properties. Future prospects lie in the development of coatings incorporating nanoplatelets.

References

1 Liang, X., King, D.M., Groner, M.D., Blackson, J.H., Harris, J.D., George, S.M., and Weimer, A.W. (2008) *Journal of Membrane Science*, **322**, 105–112.
2 Sharma, A., Tripathi, B., and Vijay, Y.K. (2010) *Journal of Membrane Science*, **361** (1–2), 89–95.
3 Giannelis, E.P. (1996) *Advanced Materials*, **8**, 29–35.
4 Usuki, A., Koiwai, A., Kojima, Y., Kawasumi, M., Okada, A., Kurauchi, T. *et al.* (1995) *Journal of Applied Polymer Science*, **55**, 119–123.
5 Dennis, H.R., Hunter, D.L., Chang, D., Kim, S., Ehite, J.L., Cho, J.W. *et al.* (2001) *Polymer*, **42**, 9513–9522.
6 Kojima, Y., Usuki, A., Kawasumi, M., Okada, A., Fukushima, Y., and Kurauchi, T. (1993) *Journal of Materials Research*, **8**, 1185–1189.
7 Sur, G.S., Sun, H.L., Lyu, S.G., and Mark, J.E. (2001) *Polymer*, **42**, 9783–9789.
8 Liu, L., Qi, Z., and Zhu, X. (1999) *Journal of Applied Polymer Science*, **71**, 1133–1138.
9 Du, X., Xiao, M., Meng, Y., and Hay, A.S. (2004) *Polymer International*, **53**, 789–793.
10 Tjong, S.C., Meng, Y.Z., and Xu, Y. (2002) *Journal of Applied Polymer Science*, **86**, 2330–2337.
11 Tjong, S.C. and Meng, Y.Z. (2003) *Journal of Polymer Science Part B Polymer Physics*, **41**, 1476–1484.
12 Yano, K., Usuki, A., and Okada, A. (1997) *Journal of Polymer Science Part A Polymer Chemistry*, **35**, 2289–2294.
13 Takahashi, S., Goldberg, H.A., Feeney, C.A., Karim, D.P., Farrel, M., O'Leary, K., and Paul, D.R. (2006) *Polymer*, **47**, 3083–3093.
14 Lape, N.K., Nuxoll, E.E., and Cussler, E.L. (2004) *Journal of Membrane Science*, **236**, 29–37.
15 Perry, D., Ward, W.J., and Cussler, E.L. (1989) *Journal of Membrane Science*, **44**, 305–311.
16 Lape, N.K., Yang, C., and Cussler, E.L. (2002) *Journal of Membrane Science*, **209**, 271–282.
17 Yang, C., Smyrl, W.H., and Cussler, E.L. (2004) *Journal of Membrane Science*, **231**, 1–12.
18 Falla, W.R., Mulski, M., and Cussler, E.L. (1996) *Journal of Membrane Science*, **119**, 129–138.
19 Bharadwaj, R.K. (2001) *Macromolecules*, **34**, 9189–9192.
20 Gusev, A.A. and Lusti, H.R. (2001) *Advanced Materials*, **13**, 1641–1643.
21 Fredrickson, G.H. and Bicerano, J. (1999) *Journal of Chemical Physics*, **110**, 2181–2188.
22 Sinha Ray, S., Yamada, K., Okamoto, M., Ogami, A., and Ueda, K. (2003) *Chemistry of Materials*, **15**, 1456–1465.

23 Sinha Ray, S., Okamoto, K., and Okamoto, M. (2003) *Macromolecules*, **36**, 2355–2367.

24 Fornes, T.D., Yoon, P.J., Hunter, D.L., Keskkula, H., and Paul, D.R. (2002) *Polymer*, **43**, 5915–5933.

25 Krishnamoorti, R. and Giannelis, E.P. (1997) *Macromolecules*, **30**, 4097–4102.

26 Goldberg, H.A., Feeney, C.A., Karim, D.P., and Farrell, M. (2002) *Rubber World*, **226**, 15–17.

27 Feeney, C.A., Farrell, M., Tannert, K., Goldberg, H.A., Lu, M., and Grah, M.D. (2000) US Patent No. 6,087,016. Assigned to InMat LLC and Michelin.

28 Feeney, C.A., Farrell, M., Tannert, K., Goldberg, H.A., Lu, M., Grah, M.D. *et al.* (2001) US Patent No. 6,232,389. Assigned to InMat LLC and Michelin Recherche et technique SA.

29 O'Leary, K., Paul, D.R., (2004) *Polymer*, **45**, 6575–85.

30 Mogri, Z. and Paul, D.R. (2001) *Polymer*, **42**, 2531–2542; O'Leary, K. and Paul, D.R. (2004) *Polymer*, **45**, 6575–6585.

31 Nielsen, L.E. (1967) *Journal of Macromolecular Science-Chemistry*, **A1** (5), 929–942

32 Guadagno, L., Vertuccio, L., Sorrentino, A., Raimondo, M., Naddeo, C., Vittoria, V., Iannuzzo, G., Calvi, E., and Russo, S. (2007) *European Polymer Journal*, **43** (4), 1097–1104.

33 Xu, B., Zheng, Q., Song, Y., and Shangguan, Y. (2006) *Polymer*, **47** (8), 5 l, 2904–2910.

34 Herrera-Alonso, J.M., Marand, E., Little, J.C., and Cox, S.S. (2009) *Journal of Membrane Science*, **15**, 208–214.

35 Tsai, T.-Y., Lina, W.-H., Lina, Y.-Y., Hsua, Y.-C., and Raya, U. (2008) *Desalination*, **233**, 183–190.

36 Wang, Y., Zhang, H., Wu, Y., Yang, J., and Zhang, L. (2005) *European Polymer Journal*, **41** (11), 2776–2783.

37 Bhole, Y.S., Wanjale, S.D., Kharul, U.K., and Jog, J.P. (2007) *Journal of Membrane Science*, **306** (1–2), 277–286.

38 Herrera-Alonso, J.M., Sedlakova, Z., and Marand, E. (2010) *Journal of Membrane Science*, **349** (1–2), 251–257.

39 Herrera-Alonso, J.M., Sedláková, Z., and Marand, E. (2010) *Journal of Membrane Science*, **363** (1–2), 48–56.

40 Cui, L., Yeh, J.-T., Wang, K., Tsai, F.-C., and Fu, Q. (2009) *Journal of Membrane Science*, **327** (1–2), 226–233.

41 Nielsen, L.E. (1992) *Journal of Macromolecular Science-Chemistry*, **1**, 929–942.

42 Yang, C., Smyrl, W.H., and Cussler, E.J. (2004) *Membrane Science*, **231**, 1–12.

43 Lape, N.K., Nuxoll, E.E., and Cussler, E.L. (2004) *Journal of Membrane Science*, **236**, 29–37.

44 Gusev, A.A. and Lusti, H.R. (2001) *Advanced Materials*, **13**, 1641–1643.

45 Bharadwaj, R.K. (2001) *Macromolecules*, **34**, 9189–9192.

46 Takahashi, S., Goldberg, H.A., Feeney, C.A., Karim, D.P., Farrell, M., O'Leary, K., and Paul, D.R. (2006) *Polymer*, **47**, 3083–3093.

47 Herrera-Alonso, J.M., Sedlakova, Z., and Marand, E. (2010) *Journal of Membrane Science*, **349** (1–2), 251–257.

48 Liang, Y., Wang, Y., Wu, Y., Lu, Y., Zhang, H., and Zhang, L. (2005) *Polymer Testing*, **24**, 12.

49 Pethrick, R. (1997) *Progress in Polymer Science*, **22**, 1–47.

50 Eastmond, G.C., Daly, J.H., McKinnon, A. S., and Pethrick, R.A. (1999) *Polymer*, **40**, 3605–3610.

51 Choudalakis, G. and Gotsis, A.D. (2009) *European Polymer Journal*, **45** (4), 967–984.

52 Wang, S.J., Liu, L.M., Fang, P.F., Chen, Z., Wang, H.M., and Zhang, S.P. (2007) *Radiation Physics and Chemistry*, **76**, 106–111.

53 Cussler, E.L. (1984) *Mass Transfer in Fluid Systems*, Cambridge University Press, Cambridge.

54 Falla, W.R., Mulski, M., and Cussler, E.L. (1996) *Journal of Membrane Science*, **119**, 129–133.

55 Saritha, A., Kuruvilla, J., Sabu, T., and Muraleekrishnan, R. (2012) *Composites Part A*, **43**, 864–870.

56 Saritha, A., Kuruvilla, J., Sabu, T., and Muraleekrishnan, R. (2012) *Journal of Applied Polymer Science*, **124** (I6), s4590–s4597.

57 Barbee, R. and Matayabas, C. (2000) US Patent WO0078855 December 28, 2000, European Patent EP 0 670 058 B1, July 8, 1998, Canadian Patent CA 2,149,891, February 15, 2000, Finnish Patent FI 952480, December 13, 2002.

58 Jang Bor, Z. (2006) US Patent US2006030483, February 9, 2006.
59 Nobel, M.L., Mendes, E., and Picken, S.J. (2007) *Journal of Applied Polymer Science*, **104** (4), 2146–2156.
60 Nobel, M.L., Picken, S.J., and Mendes, E. (2007) *Progress in Organic Coatings*, **58** (2–3), 96–104.
61 Nobel, M.L., Mendes, E., and Picken, S.J. (2007) *Journal of Applied Polymer Science*, **103** (2), 687–697.
62 Raju, K.V. and Suresh, K. (2005) US Patent US2005145138, July 7, 2005.
63 Lee, Y.C. and Kim, M.J. (2007) WO2007055498, May 18, 2007.
64 Mehta, V. and Kanze, B. (2007) WO2007109314, September 27, 2007.

9
Polymer Nanocomposites Characterized by Thermal Analysis Techniques

Carola Esposito Corcione, Antonio Greco, Mariaenrica Frigione, and Alfonso Maffezzoli

9.1
Introduction

Polymer composites reinforced with inorganic fillers of dimensions in the nanometer range, known as nanocomposites, have attracted great attention of researchers due to unexpected synergistic properties derived from two components. The most studied polymer nanocomposites (PNs) are composed of thermoplastic or thermosetting matrix and organically modified montmorillonite (OMMT) [1–4] or carbon nanotubes (CNTs) [5–7].

Polymer–clay nanocomposites are characterized by improved thermal, mechanical, barrier, fire retardant, and optical properties compared to the matrix of conventional composites, commonly called "particulate microcomposites," because of their unique phase morphology deriving from layer intercalation or exfoliation that maximizes interfacial contact between the organic and inorganic phases and enhances bulk properties [8].

Since their discovery in 1991 by Iijima [9], CNTs have been extensively studied by researchers in various fields such as chemistry, physics, materials science, and electrical engineering. CNTs possess high flexibility, low mass density, and large aspect ratio (typically about 300–1000). They have a unique combination of mechanical, electrical, and thermal properties that make them excellent candidates to substitute or complement the conventional nanofillers in the fabrication of multifunctional PNs [5].

The rich bibliography on polymer–clay nanocomposites shows that the effect of montmorillonite on thermal properties of matrix is complex and many factors contribute to the enhancement of the glass transition, such as the OMMT dispersion, interfacial strength, type of polymer matrix, preparation method, possible catalytic effects induced by organomodifier and/or montmorillonite itself, and so on [10]. Also, in the case of CNTs, many studies report the importance of thermal properties of nanocomposites containing CNTs, particularly with thermogravimetric analysis (TGA), since a significant enhancement in thermal stability of the

Polymer Composites: Volume 2, First Edition. Edited by Sabu Thomas, Kuruvilla Joseph, Sant Kumar Malhotra, Koichi Goda, and Meyyarappallil Sadasivan Sreekala.

polymeric matrices filled with the nanotubes was observed compared to the unfilled ones [4].

In PN, the efficiency of intercalation of the polymer in the lamellar galleries is usually measured by means of X-ray diffraction (XRD) and/or transmission electronic microscopy (TEM). Although the wide-angle XRD offers a convenient method to determine the interlayer spacing of the silicate layers in the intercalated nanocomposites, little can be said about the spatial distribution of the silicate layers or on the structural nonhomogeneities in nanocomposites. On the other hand, TEM is very time intensive, and only gives qualitative information on the sample as a whole, due to the small investigable area [11]. Differential scanning calorimeter (DSC) has been widely applied to the study of many phenomena occurring during the thermal scan of nanofillers and PN, such as melting, crystallization, cure kinetics, and glass transition. These properties present peculiar change when dispersion at nanoscale is achieved. Dynamic mechanical thermal analysis (DMTA) was frequently used in nanocomposites characterization since it allows measurement of the stiffness and energy losses as a function of temperature. DMTA data are strongly affected by the degree and the scale of dispersion of nanofillers. Thermal mechanical analysis (TMA) was mainly used to measure the coefficient of thermal expansion (CTE) of nanocomposite materials in comparison with those of the matrix. TGA has been used to analyze the effect of the introduction of nanofillers into polymer matrix and on the thermal stability of the polymer. The literature concerning the analysis of thermal stability and degradation of PN by TGA covers numerous original papers as well as comprehensive review articles. Polymer decomposition, in the presence of either oxidative or nonoxidative gas, significantly depends on the presence of fillers and on their dispersion scale.

Most reviews deal with the effects of different nanofillers on the properties of polymer matrices. However, this work does not intend to be a comprehensive review on the thermal properties of polymeric nanocomposites, but rather aims to illustrate the versatile applications of thermal analysis (TA) in the emerging field of polymer nanomaterial research. Although analyzing bulk samples of several milligrams size, TA is also capable to provide information on the average structure of the nanocomposite even at the nanoscale. Therefore, this chapter will address the most relevant results obtained by TA that can be used to obtain indirect evidence of nanodispersion, highlighting the strong potential of such instruments, as low-cost techniques frequently available in most industrial and research laboratories.

9.2
Thermal Analysis Methods

9.2.1
Differential Scanning Calorimetry

Differential scanning calorimetry has been widely applied in the investigation of numerous phenomena occurring during the thermal heating of organoclays and

polymer–clay nanocomposites or nanotubes, involving glass transition temperature (T_g), melting, crystallization, and curing.

The DSC method is commonly applied to investigate the α-transition in polymers and their composites. The α-transition is related to the Brownian motion of the main chains at the transition from the glassy to the rubbery state and the relaxation of dipoles associated with it.

Referring to clay nanocomposites, the DSC technique is able to highlight appreciable enhancements in T_g brought about by the presence of nanosized montmorillonite in many polymers. This effect was typically ascribed to the confinement of intercalated polymer within the silicate galleries that prevents the segmental motions of the polymer chains. In the case of polyurethane (PU)–urea nanocomposites, the changes in T_g were also interpreted as a result of effective links between the polymeric chains and the silicate surface [12]. It was pointed out that these anchored polymer chains could form an interphase region, where the segment relaxation was slower than in the bulk. The restricted relaxation behavior for the PNs with intercalated and exfoliated silicates primarily depended on the exfoliation extent of the layered silicates and on the interaction strength between the silicate surfaces and the PU macromolecules.

Nanocomposite adhesives obtained using a montmorillonite, modified with organic cations (OMMT), in a PU matrix were synthesized and characterized by Esposito Corcione and Maffezzoli [13]. A mix of exfoliated and intercalated layers was obtained, as ascertained by the measurements of structural and macroscopic properties of the nanocomposites. A significant increase of T_g of the nanocomposites as a function of OMMT content was also observed by calorimetric analysis, confirming the mentioned limitations to chain segment mobility induced by OMMT. The intercalation of polyester polyol between OMMT lamellae was easily achieved by mixing. The presence of a significant fraction of rigid amorphous phase (x_{ra}) was also revealed by calorimetric analysis. The rigid amorphous fraction of the PU nanocomposites increased with increasing volume fraction (Φ) of OMMT, as reported in Figure 9.1.

The segmental mobility significantly reduced as OMMT content increased, indicating that PU chains immobilization occurs when they are intercalated between OMMT lamellae. In analogy with the interpretation of rigid amorphous fraction used for semicrystalline polymers, the heterogeneous stack model was considered closer to the behavior of these nanocomposites. Furthermore, a substantial constant value of the characteristic size of the cooperatively rearranging region (ζ_a) at T_g was calculated.

In a different work, the data obtained by temperature-modulated differential scanning calorimetry (TMDSC) showed the relationship between the interlayer distance (Δd) and the increase of heat capacity (ΔC_p) for PU–clay intercalated nanocomposites [14]. The ΔC_p values of nanocomposites with interlayer distances smaller than the characteristic length ζ_a of bulk PU (1.45 nm) were reduced. However, for nanocomposites with interlayer spacing larger than 2 nm, cooperatively rearranging of PU was substantially unmodified by the presence of the nanofiller, and ΔC_p values remained the same as that of bulk PU.

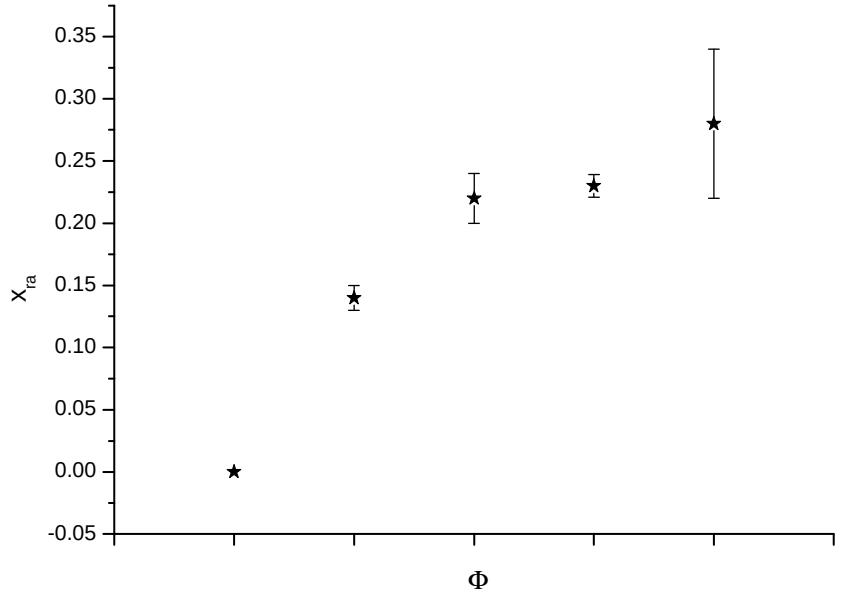

Figure 9.1 Rigid amorphous fraction of the PU nanocomposite.

Other nanocomposites, however, showed a lower T_g, or were characterized by no change in T_g, compared to the neat polymer [15]. T_g of nanocomposites based on amorphous poly(ethylene terephthalate) (PETg) and OMMTs, obtained by melt intercalation, was also found to slightly decrease [16], as proved by using the DSC technique. The neat PETg was completely amorphous, with T_g of about 68.1 °C. After the addition of the nanofiller, T_g decreased to 67.1 and 66.0 °C for the samples with 10 and 20 wt% of OMMT respectively, as shown in Figure 9.2.

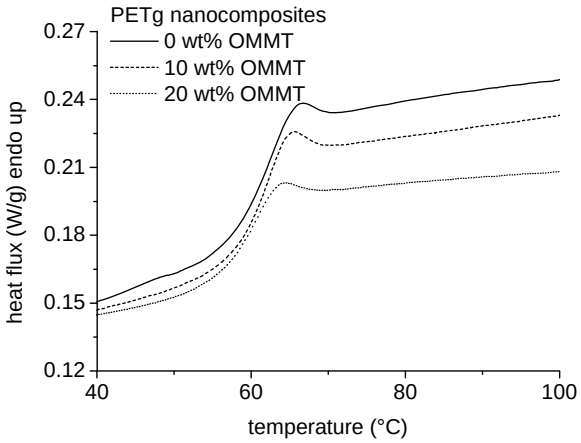

Figure 9.2 Glass transition temperature of nanocomposites based on amorphous poly(ethylene terephthalate) (PETg) and organically modified montmorillonites.

The absence of any other exothermal or endothermal signal confirmed that the nanocomposite was also amorphous. This is in agreement with the results reported by Kattan *et al.* [17] that the PETg keeps its amorphous state in most practical experimental conditions. The decrease of T_g can be attributed to the plasticization effect of the organic modifier of the OMMT, characterized by a very low T_g.

Reference. [18] showed the strong influence of preparation route on the thermal properties of polystyrene (PS) nanocomposites. An appreciable reduction in T_g was observed only for composites obtained from solution, whereas the composites obtained by melt intercalation showed T_g values approximately equal to that of neat polymer. Some difficulties in detecting changes in T_g for polymer–clay nanocomposites occurring with the conventional DSC [19] method could be overcome using the TMDSC method.

DSC analysis was also used to measure T_g of the CNT nanocomposites, such as in the case of coiled carbon nanotubes (CCNT) dispersed in an epoxy matrix [20]. Compared to the neat epoxy, a shift of T_g to higher temperatures is observed in the composites with single-walled carbon nanotubes (SWCNTs) and multiwalled carbon nanotubes (MWCNTs), while there is a decrease in T_g in the CCNT–epoxy composites. The ΔH of polymerization of the single-walled nanotube (SWNT)–epoxy composites was higher than that of the unfilled epoxy, while the ΔH values calculated for both the multiwalled nanotube (MWNT)–epoxy and CCNT–epoxy composites were lower than that of the neat epoxy. In particular, the ΔH of MWNT is slightly lower than that of neat resin, whereas for CCNT the ΔH is significantly lower than that of the neat epoxy. It was inferred that during the glass transition process, SWNTs act as a heat sink to accelerate the heat absorption of the epoxy, while CCNTs act as heat-shielding filler and prevent the epoxy from exchanging energy. The observed changes revealed that the tube surface configuration plays an important role in the glass transition behavior of epoxy matrices. It has been demonstrated that the incorporation of carbon fillers can affect the structure of the cured epoxy by restricting the nucleophile–electrophile interaction during the cure reaction by a steric hindrance effect. Accordingly, nanotubes with different shapes would have different steric hindrance effects on the cure reaction occurring in the epoxy in the presence of the hardener. The particular helical shape of CCNTs should have a more steric hindrance effect than the straight nanotubes, such as SWNTs and MWNTs. As a result, the cure reaction of the epoxy would be influenced more by CCNTs than by the SWNTs and MWNTs.

Differential scanning calorimetry was also used by Greco *et al.* [21] to study the thermal characteristics of the species produced during the ring-opening polymerization of cyclic butylene terephthalate (CBT). The effects of the addition of small amounts of sodium and organomodified montmorillonite on a tin-catalyzed polymerization was analyzed. It was found that the addition of the nanofiller significantly affected the polymerization of CBT, shifting the onset of the polymerization reactions to higher temperatures. This is evident by comparing DSC curves of the CBT01 (unfilled) and CBT13MMT (filled with OMMT) systems heated up to different temperatures in a first heating scan, reported in Figures 9.3 and 9.4, respectively.

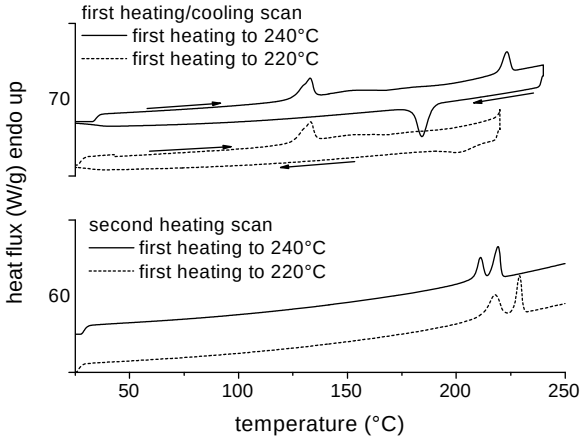

Figure 9.3 DSC curves of the CBT01(unfilled) and CBT13MMT (filled with OMMT) systems.

This behavior was attributed to the tin catalyst being adsorbed in the lamellar galleries of the filler, thus reducing its activity for the polymerization reactions. As a consequence, CBT was formed at higher temperatures, preventing it from crystallizing during the heating scan. However, the nanofiller acts as efficient nucleating agent for crystallization during the cooling cycle. When long isothermal holding times are used at temperatures lower than the equilibrium melting point of PBT, the resulting polymer can crystallize to some extent and the crystal so produced has a nucleating effect on the crystallization taking place during the subsequent cooling cycle.

The DSC study of the curing process and its kinetics can give insight into the actual mechanism of cure reaction and its effect on degree of cross-linking and, as a

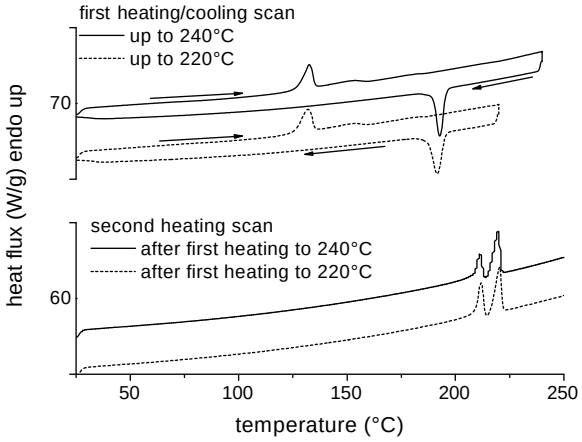

Figure 9.4 DSC curves of the CBT01(unfilled) and CBT13MMT (filled with OMMT) systems.

consequence, on mechanical properties. A proper DSC, modified for irradiation of the sample using a UV light source (p-DSC), was used by Esposito Corcione *et al.* [22] to study the kinetic behavior of novel nanocomposite coatings based on a cycloaliphatic epoxy resin (CE) with two different o-boehmites (OS1 and OS2), prepared by photochemically initiated cationic polymerization. The reactivity of the nanocomposites matrix was found lower than that of the neat resin, as shown in Figure 9.5a and b in the case of the nanofiller OS2. This behavior was attributed to the light shielding of the boehmites as a consequence of scattering due to the presence of clusters in the micrometer size range.

On the other hand, the results of a DSC analysis performed to investigate the curing process of nitrile rubber (NBR)–layered clay nanocomposites showed a

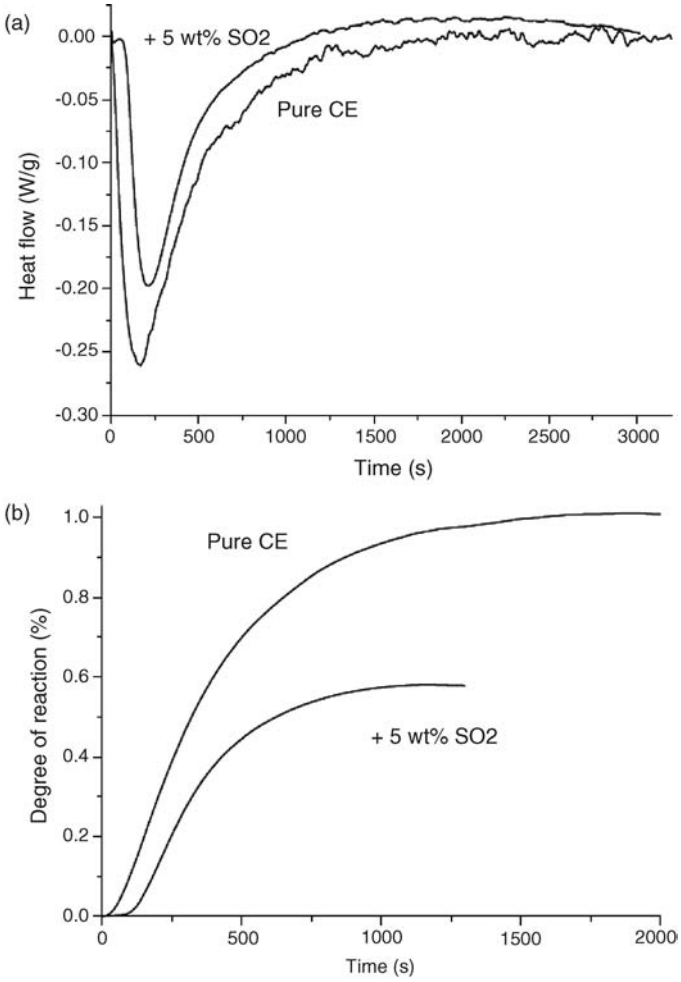

Figure 9.5 Kinetic behavior of novel nanocomposite coatings based on a cycloaliphatic epoxy resin (CE) with two different o-Boehmites (OS1 and OS2).

reduction in curing time and an increase in enthalpy of curing in the systems with organoclay; autocatalytic model showed the best fit in kinetic modeling [23]. However, a little change in the cure behavior of the NBR–unmodified clay system compared to (NBR)–layered clay nanocomposites was observed, suggesting that the accelerating effect was due to introduction of ammonium modifier to OMMT. Furthermore, the cure kinetics studies on natural rubber–organoclay [24] and fluoroelastomer–organoclay [25] nanocomposites showed the suitability of the autocatalytic model for analyzing the cure parameters of rubber–clay nanocomposites. DSC analysis of cure kinetics of fluoroelastomer nanocomposites confirmed the catalytic role of organic modifiers in vulcanization process, whereas the opposite effect, consisting in slowing down the curing reaction, was observed in systems based on unmodified clay. Moreover, in the DSC experiments, a catalytic effect of ammonium compounds on homopolymerization of epoxy resin was observed [26,27]. In Ref. [28], an increase in curing rate with the increasing clay content was considered to be due to the presence of OH groups of the organic modifier of the clay, which could accelerate the epoxy curing reactions.

In Ref. [29], the DSC technique was used to investigate the influence of preparation route for nanocomposite materials based on poly(lactic acid) on the polymer morphology. It was found that the melting enthalpy of poly(lactic acid)–montmorillonite (PLA–MMT) nanocomposites changed with an increase of nano-additive content, depending on the method of nanocomposite preparation. The change in melting enthalpy, ΔH, of the PLA–MMT system prepared by melt extrusion was considerably higher than that measured on systems produced by solvent dissolution method. It was suggested that the binding force between the PLA and the inorganic compound in the composite prepared by melt extrusion method was higher than that relative to the system prepared by solvent dissolution method.

The value of melting enthalpy, measured by the DSC method, is commonly used to calculate the degree of crystallinity. In poly(ethylene oxide) (PEO)–OMMT nanocomposites, the degree of crystallinity continuously decreased with the increasing clay content [30]. A decrease in the degree of crystallinity has also been reported to occur in polyethylene [31], low-density polyethylene (LDPE) [32], poly(vinylidene fluoride) [33], and polyamide 6 [34] nanocomposites reinforced with OMM or with bentonite clays.

Kinetic analysis of the polymer crystallization by the DSC method in isothermal conditions can provide information about the effect of nanoparticles on the mechanism of nucleation and crystals growth. The reduction of the half-crystallization time ($t_{1/2}$) was considered an evidence of the crystallization rate of polypropylene (PP) at low OMMT contents [35]. $t_{1/2}$ was lower than that of neat polymers for the crystallization process of many polymer matrices modified with OMMT [36,37].

The kinetic analysis of isothermal crystallization of PP grafted with maleic anhydride copolymer (PP-*g*-HMA)-based nanocomposites showed significant changes of Avrami exponent n, suggesting the change of the crystal growth process from a three-dimensional crystal growth characteristic of the pristine polymer to a two-dimensional spherulitic growth for the nanocomposites [35].

In another paper, the Avrami plots showed that the crystal growth of PE in the intercalated sample is two dimensional, while it is three dimensional in the exfoliated sample. The activation energy for the crystallization of the intercalated sample is slightly lower than that of the exfoliated sample [38].

The DSC method was also applied to study the influence of nanoparticles on the polymer matrix morphology formation. For example, the polymorphic behavior of polyamide 6 (PA 6) upon the addition of OMMT was studied using this technique [39–41]. During the DSC heating scan, neat PA 6 is likely to show only one endothermic peak at a temperature around 225 °C, which was associated with the melting of α-form crystals ($T_{m,\alpha}$) [42]. When the same polymer was modified with OMMT, an additional endothermic peak was observed at about 215 °C, corresponding to the temperature of melting of the less stable γ-form crystals ($T_{m,\gamma}$). OMMT was in fact able to enhance the formation of γ-form crystals in PA 6 matrix, especially when crystallization took place in a lower temperature range. The origin of the new peak was explained in terms of the melting of a specific fraction of lamellae formed under stress in the volume of intercalated nanoclay sheets and tethered on the host layers by strong (interfacial) ionic interaction. The calorimetric results also indicated that hybrids with small amounts of clay presented lower activation energy than the PA 6 matrix, whereas those with higher clay loadings showed a greater activation energy than the PA 6 matrix.

DSCs have been finally used to measure the thermal conductivity of graphite-intercalated compounds (GICs), together with other techniques [43]. The DSC method gave good results for thermal conductivities lower than 1.5 W/(m K), but diverged from other more reliable techniques at higher values, which suggests that the DSC method is suitable to measure conductivity of materials having thermal conductivities less than about 1 W/(m K).

9.2.2
Thermogravimetric Analysis

TGA performed on numerous PN showed that many polymers filled with montmorillonite and CNTs exhibited improved thermal stability, such as in the case of poly(methyl methacrylate) (PMMA) [44], poly(dimethylsiloxane) (PDMS) [45], PA [46,47], and PP systems [48].

It is usually well accepted that in the case of polymer–clay nanocomposites, the improved thermal stability of the PN is mainly due to the formation of a char that hinders out-diffusion of the volatile decomposition products, as a direct result of the decrease in permeability, usually observed in exfoliated nanocomposites [49]. Despite this, the exact degradation mechanism is currently not clear; such a behavior is probably associated with the morphological changes in proportion to exfoliated and intercalated species with the clay loading. At low clay loading (about 1 wt%), exfoliation dominates, but the amount of exfoliated nanoclay is not enough to enhance the thermal stability through char formation [50]. When increasing the clay concentration (2–4 wt%), much more exfoliated clay is formed; char forms more easily and effectively and, consequently, promotes the thermal stability of the

nanocomposites. At even higher clay loading level (up to 10 wt%), the intercalated structure is the dominant population and, even if char is formed in high quantity, the different morphology of the nanocomposite probably does not allow maintaining a high thermal stability. However, it is known that the chemical nature of the polymers, the type of clays, and their modification route play an important role in the degradation behavior of PN. TGA measurement could also give an indirect information about the amount of exfoliated nanoclay in the PN.

Two important works review the thermal properties and degradation processes of nanocomposites based on different polymer matrices [49,51]. They discuss the basic changes in the thermal behavior of different polymeric matrices – polyolefins, PA, styrene-containing polymers, PMMA, poly(vinyl chloride) (PVC), polyesters, polyimides (PIs), epoxy resins, PUs), ethylene–propylene–diene terpolymer (EPDM), poly(vinyl alcohol) (PVA), and polylactide (PLA) – upon addition of montmorillonite, with special focus on the influence of montmorillonite on kinetics of degradation process and formation of condensed–volatile products in oxidative and pyrolytic conditions. The results of research reported in the mentioned reviews [49,51] indicate that the introduction of layered silicates into polymer matrix causes an increase in thermal stability. Due to the characteristic structure of layers in polymer matrix and their shape and dimensions close to molecular level, several effects have been observed that can explain the changes in thermal properties. Experimental results have shown that layers of MMT are impermeable to gases, meaning that both intercalated and exfoliated structures can create a labyrinth for gas penetrating the polymer bulk. Thus, this effect of "labyrinth" limits the oxygen diffusion inside the nanocomposite during thermal degradation. Similarly, in the samples exposed to high temperatures, the MMT layers restrain the diffusion of gases evolved during degradation, contributing to keep the neat polymer in contact with a nonoxidizing environment. Moreover, MMT layers are thought to reduce heat conduction. In the presence of MMT layers, strongly interacting with polymer matrix, the motions of polymer chains are limited, as explained in the former section dealing with T_g changes induced by OMMT. This effect brings additional stabilization in the case of polymer–MMT nanocomposites. The heat barrier effect could also provide superheated conditions inside the polymer melt leading to extensive random scission of polymer chain and evolution of numerous chemical species, which, trapped between clay layers, have more opportunity to undergo secondary reactions. As a result, some degradation pathways could be promoted leading to enhanced charring. It is also suggested that the effect of more effective char production during the thermal decomposition of polymer–clay nanocomposites may be derived from a chemical interaction between the polymer matrix and the clay layer surface during thermal degradation. Some authors indicated that catalytic effect of nanodispersed clay is effective in promoting char-forming reactions. Nanodispersed MMT layers were also found to interact with polymer chains in a way that forces the arrangement of macrochains and restricts the thermal motions of polymer domains [50,51]. Generally, the thermal stability of polymeric nanocomposites containing MMT is related to the organoclay content and dispersion. The synthesis methods influence the thermal stability of polymer–MMT nanocomposites as long as they are

governing the dispersion degree of clay layers. Currently, extensive research is devoted to the synthesis of novel thermally stable modifiers (including oligomeric compounds) that can ensure good compatibility and improve the nanocomposite thermal stability due to low migration characteristics [50,51].

Using TGA, several groups have also reported improved thermal stability in nanotube–polymer composites compared to neat polymers [5–7]. Specifically, the onset decomposition temperature T_{onset} and the temperature of maximum weight loss rate T_{peak} are higher in nanocomposites. For example, Ge *et al.* [52] found that 5 wt% MWNT addition caused a 24 °C shift in T_{onset} compared to that of the neat PAN. A number of mechanisms have been suggested. Dispersed nanotubes might hinder the flux of degradation products and thereby delay the onset of degradation. Polymers near the nanotubes might degrade more slowly, which would shift T_{peak} to higher temperatures. Another possible mechanism attributes the improved thermal stability to the effect of higher thermal conductivity in the nanotube–polymer composites that facilitates heat dissipation within the composite [53]. The observed improvement in thermal stability hints that nanotubes could be efficient as fire-retardant additives in polymer matrices.

A significant enhancement in thermal stability has also been recorded for poly (ethylene–vinyl acetate) (EVA) filled with MWNT compared to unfilled EVA: The two degradation steps of the EVA matrix (first the deacetylation and then the volatilization of resulting unsaturated chains) are shifted to higher temperatures with a decrease of volatilization rate of the acetic acid and the formation of a stable char, which is further stabilized through $\pi-\pi$ electronic interactions with the nanotubes [54].

9.3
Dynamic Mechanical Thermal Analysis

DMTA was frequently used in nanocomposites characterization since it allows measurement of the two different moduli of the nanocomposites: the storage modulus (E'), which is related to the ability of the material to return or store mechanical energy, and the loss modulus (E''), which is related to the ability of the material to dissipate energy as a function of temperature. DMTA data generally showed significant improvements in the storage modulus over a wide temperature range for a large number of PNs with MMT, such as PVDF [55], PP [56], and PMMA [57].

In nanocomposites based on PA 6, a linear increase in storage modulus with the increasing clay content was observed with a simultaneous decrease in intensity of the main relaxation peak [58]. The linear change in modulus in a range of temperature below T_g was in accordance with the coupling model, since in the glassy state both the amorphous and the crystal phases of PA 6 have similar mechanical properties. Above T_g, the amorphous phase becomes rubbery and the storage modulus changes from about 1 GPa to 1 MPa. The improvement of dynamic mechanical properties of nanocomposites may be explained in terms of restricted

thermal motions of polymer enveloped by clay nanoplates. The orientation of nanoparticles and higher order structures of polymer also influences the dynamic mechanical properties. Apart from polymer morphology, the strength of interphase interactions was shown to be an important factor [59]. For this reason, DMTA technique could be used as an indirect method to have useful information about orientation, exfoliation, and interphase interactions of nanoclay.

The introduction of a macromolecular compatibilizer, able to improve the interphase properties and facilitate the exfoliation of OMMT, was beneficial also in terms of dynamic mechanical properties.

The DMTA analysis is also commonly used to determine T_g of polymeric materials from the peak of loss angle tangent ($t_g\delta$) or from the maximum of loss modulus (E'').

T_g values of the pure UV-cured epoxy resin (CE) and its o-boehmite (OS1) nanocomposites were measured by means of DMTA technique on samples previously exposed to a dynamic UV lamp, allowing a very high radiation intensity on the surface of the sample (1200 mW/cm^2) [22]. A typical DMTA spectrum related to a UV-cured CE–OS1 (5 wt%) sample is reported in Figure 9.6. The high T_g values obtained clearly indicate that the high intensity of the UV radiation can promote local overheating, determining a well-advanced state of curing. A similar behavior was found in a previous work [60]. For all the products containing up to 5 wt% of the nanofiller, T_g was found very close to that of the pure UV-cured CE resin. By increasing the amount of the nanofiller in the UV-cured dispersion, a slight decrease of T_g is evident, thus indicating a slight lowering of the cross-linking density of the polymer network. Since the slight decrease of T_g was observed also for the nanocomposite based on unmodified boehmite, this phenomenon cannot be only related to the presence of the sulfonic acids used for modifying the boehmite nanoparticles

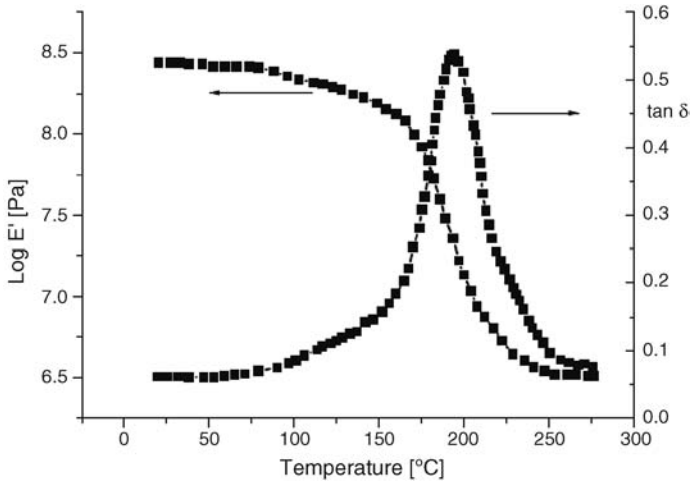

Figure 9.6 Typical DMTA spectrum of an UV-cured CE–OS1 (5 wt%) nanocomposite.

in OS1 and OS2 (such modifying agents could in fact interfere with the photoinitiator in view of the high dissociation constant of the acid, which would produce large amounts of protons). Therefore, this behavior was mainly attributed to a scattering effect of the UV light due to the presence of the nanofillers in the polymer matrix [22].

A different trend was observed in the case of an epoxy matrix filled with the same boehmite nanoparticles (OS1 and OS2) and thermally cured [61]. T_g of the epoxy matrix nanocomposites was measured using dynamic mechanical analysis, corresponding to the maximum of the loss modulus E''. The loss modulus of nanocomposites with different concentrations of boehmite (0–15 wt%) was found to be significantly higher than that of the neat epoxy. An increase of about 50% of the loss modulus in the glassy state was achieved as a result of incorporation of 10 wt% of the nanofiller into the epoxy resin. These losses are accompanied by an increase of T_g up to 9 °C for 10% of boehmite content. On the other hand, E'' was unaffected by the presence of the nanofiller in the rubbery state. Any further increase of nanoparticles concentration was associated with a lower increase of T_g, which can be detected using DMTA analysis. Another relevant feature of PNs is given by the decrease of the intensity and the broadening of the tan δ peak corresponding to T_g [62–64].

DMTA technique was also used to characterize CNT nanocomposites [65,66]. As an example, Gou [65] developed a new processing method for the fabrication of SWNT-reinforced nanocomposites: The nanocomposites were fabricated by infiltration of diluted epoxy resin through a buckypaper followed by hot pressing. The wetting of the nanocomposites was examined using scanning electron microscopy and atomic force microscopy. The results showed that the epoxy resin completely penetrated the buckypaper through the nanoporous structures. The thermomechanical behavior of the nanocomposites was assessed using DMTA by monitoring the storage modulus against temperature. The modulus of the neat epoxy resin was increased by the stiffening effect of the nanotubes. The weight fraction of the nanotubes in the nanocomposites induced a stiffening effect. A slight reduction in T_g values of the nanocomposites containing nanotubes with various compositions was observed. Compared to the neat epoxy resin, there is no apparent T_g peak on the tan δ curves of the nanocomposites. Above T_g, the tan δ curve continuously increases rather than returning to the baseline. For neat epoxy resin, the chain segments cannot completely move below its T_g. The very low value of tan δ for neat resin means that there is no significant energy loss. During the glass transition, the molecule segment absorbs enough energy and begins to move; however, the free space in the polymer is too small, so more energy is required for the resin molecules to move. At a temperature higher than T_g, a larger free volume is available in the polymer, allowing the molecule segments to move freely, leading to a decrease in the tan δ curve. The nanotubes have a large surface area and they are at the same scale as the resin molecules in SWNT buckypaper-reinforced nanocomposites. Therefore, the resin chain segments strongly interact with nanotubes. These strong interactions between the nanotubes and chain segments could be responsible for the high values of tan δ above T_g observed in CNT nanocomposites.

9.4 Thermal Mechanical Analysis

TMA is a highly sensitive technique for the measurement of expansion and contraction of cross-linked or filled materials, including nanocomposites [67]. TMA was used to measure the CTE of nanocomposite materials based on PA 6 [68,69], PP [70], PA [71], and PS [72]. It has been generally found that CTE is lower in nanomaterials in comparison to unmodified polymer, especially for low contents of OMMT. In general, the extent of CTE reduction depends on the particle rigidity, dispersion of the clay platelets in the matrix, and efficient stress transfer to clay layers. It is believed that the retardation of chain segmental movement through incorporation of organically modified clays also leads to decrease in the CTE [73].

In order to investigate, for example, the anisotropy of thermal expansion of PA 6–montmorillonite nanocomposites, TMA measurements were performed on the injection-molded samples in three orthogonal directions, that is, flow direction (FD), transverse direction (TD), and normal direction (ND). PA 6 modified with OMMT was found to exhibit lower values of CTE than the pure polymer in the direction parallel to the melt flow during injection molding [68], while increased values of CTE were measured in the direction normal to the melt flow. The latter result suggested a nonuniform orientation of exfoliated platelets about FD, since perfect alignment of disk-like platelets in an isotropic matrix must yield identical expansion coefficients for both FD and TD. Chains may have more orientation along FD than TD, thus leading to lower thermal expansion. Of course, disparity between the two directions may also reflect differences in the orientation of polymer crystallites. This trend may be explained by platelet orientation and anisotropy effects.

TMA results may indirectly provide information about the spatial orientation of MMT layers in nanocomposite materials.

A trend of CTE similar to the latter results was obtained by TMA measurements performed on the MWCNTs infused through and between glass fiber tows along the through-thickness direction [74]. Both pristine and functionalized MWNTs were used in fabricating multiscale glass fiber-reinforced epoxy composites. The CTEs of the resin and the resin–fiber system were tested by TMA with a ramp rate of 5 °C/min.

It was supposed that the CTE of MWNTs is negative. Thus, the addition of MWNTs, especially the well-dispersed and functionalized MWNTs, may reduce the CTEs of the nanocomposites [75]. The thermal expansion curves demonstrated that the CTE at temperatures above T_g was much higher than the corresponding CTE at temperatures below T_g. At temperatures below T_g, the CTE values of CNT-reinforced epoxy–glass fiber samples were lower than that of epoxy–glass fiber sample with only 1 wt% of MWNTs, since the CTE of MWNTs is negative. Moreover, a lower CTE was obtained in functionalized MWNT–epoxy–glass fiber nanocomposites at temperatures below T_g, which suggested that smaller CNT bundles produced smaller CTE values below T_g.

TMA can also be used to measure T_g, in terms of change in the CTEs, as the polymer turns from glass to rubber state with a dramatic change in free molecular

volume. Thus, T_g can be determined from the thermal expansion curve. The reduction of T_g, in the presence of nanofiller, indicated that the cross-linking density of functionalized MWNT–epoxy–glass fiber nanocomposite is obviously decreased because of the interference of functionalized groups on the MWNTs. However, T_g of the MWNT–epoxy–glass fiber nanocomposite was almost the same as that of pure epoxy, which suggested that the pristine MWNTs did not participate in the epoxy curing reaction and were not fully integrated into the epoxy cross-linked network [74].

9.5 Conclusions

PNs, that is, polymer composites reinforced with inorganic fillers of dimensions in the nanometer range, have attracted great attention of researchers, due to unexpected synergistic properties derived from the two components.

In PN, the efficiency of intercalation of the polymer in the lamellar galleries is usually measured by means of XRD and/or TEM. Although the wide-angle XRD offers a convenient method to determine the interlayer spacing of the silicate layers in the intercalated nanocomposites, little can be said about the spatial distribution of the silicate layers or on structural nonhomogeneities in nanocomposites. On the other hand, TEM is very time intensive, and only gives qualitative information on the sample as a whole, due to the small investigable area.

On the other hand, TA is a useful tool to investigate a wide variety of properties of polymers and it can also be applied to PN in order to gain a further insight into their structure. This chapter presents some useful examples of applications of differential scanning calorimetry, TGA, DMTA, and TMA for the characterization of nanocomposite materials.

References

1 Komarneni, S.J. (1992) *Materials Chemistry*, **2**, 1219.
2 Gleiter, H. (1992) *Advanced Materials*, **4**, 474.
3 Ziolo, R.F., Giannelis, E.P., Weinstein, B. A., O'Horo, M.P., Granguly, B.N., Mehrota, V., Russel, M.W., and Huffman, D.R. (1992) *Science*, **257**, 219.
4 Bauera, F., Glasela, H.-J., Hartmanna, E., Langgutha, H., and Hinterwaldner, R. (2004) *International Journal of Adhesion and Adhesives*, **24**, 519.
5 Moniruzzaman, M. and Winey, K.I. (2006) *Macromolecules*, **39**, 5194–5205.
6 Bredeau, S., Peeterbroeck, S., Bonduel, D., Alexandre, M., and Dubois, P. (2008) *Polymer International*, **57**, 547–553.
7 Breuer, O. and Sundararaj, U. (2004) *Polymer Composites*, **25** (6), 641.
8 Esposito Corcione, C., Prinari, P., Cannoletta, D., Mensitieri, G., and Maffezzoli, A. (2008) *International Journal of Adhesion and Adhesives*, **28**, 91–100.
9 Iijima, S. (1991) *Nature*, **354**, 56.
10 Leszczynska, A. and Pielichowski, K. (2008) *Journal of Thermal Analysis and Calorimetry*, **93** (3), 677–687.
11 Ray, S.S. and Okamoto, M. (2003) *Progress in Polymer Science*, **28**, 1539–1641.

12 Sreedhar, B., Chattopadhyay, D.K., and Swapna, V. (2006) *Journal of Applied Polymer Science*, **100**, 2393.
13 Esposito Corcione, C. and Maffezzoli, A. (2009) *Thermochimica Acta*, **485**, 43–48.
14 Xia, H. and Song, M. (2005) *Thermochim Acta*, **429**, 1.
15 Tian, H. and Tagaya, H. (2007) *Journal of Materials Science*, **42**, 3244.
16 Greco, A., Esposito Corcione, C., Strafella, A., and Maffezzoli, A. (2010) *Journal of Applied Polymer Science*, **118** (6), 3666–3672.
17 Kattan, M., Dargent, E., Ledru, J., and Grenet, J. (2001) *Journal of Applied Polymer Science*, **81**, 3405–3412.
18 Torre, L., Lelli, G., and Kenny, J.M. (2006) *Journal of Applied Polymer Science*, **100**, 4957.
19 Verdonck, E., Schaap, K., and Thomas, L.C. (1999) *International Journal of Pharmaceutics*, **192**, 3.
20 Lu, M., Lau, K.-T., Xu, J.-C., and Li, H.-L. (2005) *Colloids and Surfaces A: Physicochemical and Engineering Aspects*, **257–258**, 339–343.
21 Lanciano, G., Greco, A., Maffezzoli, A., and Mascia, L. (2009) *Thermochimica Acta*, **493**, 61–67.
22 Esposito Corcione, C., Frigione, M., Maffezzoli, A., and Malucelli, G. (2008) *European Polymer Journal*, **44**, 2010–2023.
23 Choi, D., Kader, M.A., Cho, B.-H., Huh, Y., and Nah, C. (2005) *Journal of Applied Polymer Science*, **98**, 1688.
24 López-Manchado, M.A., Arroyo, M., Herrero, B., and Biagiotti, J. (2003) *Journal of Applied Polymer Science*, **89**, 1.
25 Kader, M.A. and Nah, C. (2004) *Polymer*, **45**, 2237.
26 Lan, T., Kaviratna, P.D., and Pinnavaia, T.J. (1996) *Journal of Physics and Chemistry of Solids*, **57**, 1005.
27 Ton-That, M.-T., Ngo, T.-D., Ding, P., Fang, G., Coleand, K.C., and Hoa, S.V. (2004) *Polymer Engineering and Science*, **44**, 1132.
28 Seo, K.S. and Dae, S.K. (2006) *Polymer Engineering and Science*, **46**, 1318.
29 Tian, H. and Tagaya, H. (2007) *Journal of Materials Science*, **42**, 3244.
30 Hikosaka, M.Y., Pulcinelli, S.H., Santilli, C. V., Dahmouche, K., and Craievich, A.F. (2006) *Journal of Non-Crystalline Solids*, **352**, 3705.
31 Gopakumar, T.G., Lee, J.A., Kontopoulou, M., and Parent, J.S. (2002) *Polymer*, **43**, 5483.
32 Morawiec, J., Pawlak, A., Slouf, M., Galeski, A., Piorkowska, E., and Krasnikowa, N. (2005) *European Polymer Journal*, **41**, 1115.
33 Priya, L. and Jog, J.P. (2002) *Journal of Polymer Science Part B: Polymer Physics*, **40**, 1682.
34 Tjong, S.C. and Bao, S.P. (2004) *Journal of Polymer Science Part B: Polymer Physics*, **42**, 2878.
35 Wu, J.-Y., Wu, T.-M., Chen, W.-Y., Tsai, S.-J., Kuo, W.-F., and Chang, G.-Y. (2005) *Journal of Polymer Science Part B: Polymer Physics*, **43**, 3242.
36 Xu, W.B., Zhai, H.B., Guo, H.Y., Zhou, Z. F., Whitely, N., and Pan, W.-P. (2004) *Journal of Thermal Analysis and Calorimetry*, **78**, 101.
37 Wang, Y., Shen, C., Li, H., Li, Q., and Chen, J. (2004) *Journal of Applied Polymer Science*, **91**, 308.
38 Xu, J.-T., Wang, Q., and Fan, Z.-Q. (2005) *European Polymer Journal*, **41**, 3011.
39 Chiu, F.-C., Lai, S.-M., Chen, Y.-L., and Lee, T.-H. (2005) *Polymer*, **46**, 11600.
40 Wu, T.M., Chen, E.C., and Liao, C.S. (2002) *Polymer Engineering and Science*, **42**, 1141.
41 González, I., Eguiazábal, J.I., and Nazábal, J. (2006) *Composites Science and Technology*, **66**, 1833.
42 Li, T.-C., Ma, J., Wang, M., Tjiu, W.C., Liu, T., and Huang, W. (2007) *Journal of Applied Polymer Science*, **103**, 1191.
43 Fukushima, H., Drzal, L.T., Rook, B.P., and Rich, M.J. (2006) *Journal of Thermal Analysis and Calorimetry*, **85** (1), 235–238.
44 Blumstein, A. (1965) *Journal of Polymer Science Part A-I*, **3**, 2665.
45 Burnside, S.D. and Giannelis, E.P. (1995) *Chemistry of Materials*, **7**, 1597.
46 Qin, H., Su, Q., Zhang, S., Zhao, B., and Yang, M. (2003) *Polymer*, **18**, 7533.
47 Ide, F. and Hasegawa, A. (1974) *Journal of Applied Polymer Science*, **18**, 963.
48 Zanetti, M., Camino, G., Peichert, P., and Mülhaupt, R. (2001) *Macromolecular Rapid Communications*, **22**, 176.
49 Leszczynska, A., Njuguna, J., Pielichowski, K., and Banerjee, J.R. (2007) *Thermochimica Acta*, **453**, 75–96.

50 Alexandre, M. and Dubois, P. (2000) *Materials Science and Engineering*, **28**, 1–63.

51 Leszczy′nska, A., Njuguna, J., Pielichowski, K., and Banerjee, J.R. (2007) *Thermochimica Acta*, **454**, 1–22.

52 Ge Jason, J., Hou, H., Li, Q., Graham Matthew, J., Greiner, A., Reneker Darrell, H., Harris Frank, W., and Cheng Stephen, Z.D. (2004) *Journal of the American Chemical Society*, **126**, 15754–15761.

53 Huxtable, S.T., Cahill, D.G., Shenogin, S., Xue, L., Ozisik, R., Barone, P., Usrey, M., Strano, M.S., Siddons, G., Shim, M., and Keblinski, P. (2003) *Nature Materials*, **2**, 731–734.

54 Peeterbroeck, S., Laoutid, F., Taulemesse, J.M., Monteverde, F., Lopez-Cuesta, J.M., Nagy, J.B. *et al.* (2012) *Advanced Functional Materials*. doi: 10.1002/adfu.200600936

55 Priya, L. and Jog, J.P. (2003) *Journal of Polymer Science Part B: Polymer Physics*, **41**, 31.

56 Lei, S.G., Hoa, S.V., and Ton-That, M.-T. (2006) *Composites Science and Technology*, **66**, 1274.

57 Meneghetti, P. and Qutubuddin, S. (2006) *Thermochim Acta*, **442**, 74.

58 Masenelli-Varlot, K., Reynaud, E., Vigier, G., and Varlet, J. (2002) *Journal of Polymer Science Part B: Polymer Physics*, **40**, 272.

59 Liu, X., Wu, Q., Berglund, L.A., Lindberg, H., Fan, J., and Qi, Z. (2003) *Journal of Applied Polymer Science*, **88**, 953.

60 Malucelli, G., Bongiovanni, R., Sangermano, M., Ronchetti, S., and Priola, A. (2007) *Polymer*, **48**, 7000–7007.

61 Esposito Corcione1, C., Fasiello, A., and Maffezzoli1, A. (2007) *Journal of Nanostructured Polymers and Nanocomposites*, **3**, 82–89.

62 Al Arbash, A., Ahmad, Z., Al Sagheer, F., and Ali, A.A.M. (2006) *Journal of Nanomaterials*, **43**, 1–9.

63 Huang, J., Lim, P.C., Shen, L., Pallathadka, P.K., Zeng, K., and He, C. (2005) *Acta Materialia*, **53**, 2395–2404.

64 Bandyopadhyay, J., Ray, SS., and Bousmina, M. (2007) *Journal of Industrial and Engineering Chemistry*, **13** (4), 614–623.

65 Gou, J. (2006) *Polymer International*, **55**, 1283–1288.

66 Jin, Z., Pramoda, K.P., Xu, G., and Goh, S. H. (2001) *Chemical Physics Letters*, **337**, 43–47.

67 Krump, H., Luyt, A.S., and Hudec, I. (2006) *Materials Letters*, **60**, 2877.

68 Yoon, P.J., Fornes, T.D., and Paul, D.R. (2002) *Polymer*, **43**, 6727.

69 Shen, L., Lin, Y., Du, Q., and Zhnog, W. (2006) *Composites Science and Technology*, **66**, 2242–2248.

70 Krump, H., Luyt, A.S., and Hudec, I. (2006) *Materials Letters*, **60**, 2877.

71 Liang, Z.-M., Yin, J., Wu, J.-H., Qiu, Z.-X., and He, F.-F. (2004) *European Polymer Journal*, **40**, 307.

72 Fu, H.K., Kuo, S.W., Yeh, D.R., and Chang, F.C. (2008) *Journal of Nanomaterials*, **24**, 1–7.

73 Asif, A., Rao, V.L., Saseendran, V., and Ninan, K.N. (2009) *Polymer Engineering and Science*, **49**, 756–767.

74 Qiu, J., Zhang, C., Wang, B., and Liang, R. (2007) *Nanotechnology*, **18**, 275708–275719.

75 Liang, G.D. and Tjong, S.C. (2006) *Materials Chemistry and Physics*, **100**, 132–137.

10
Carbon Nanotube-Filled Polymer Composites

Dimitrios Tasis and Kostas Papagelis

10.1
Introduction

A nanocomposite is defined as a composite material, where at least one of the dimensions of one of its components is on the nanometer size scale. The challenge and interest in developing nanocomposites is to find ways to create functional materials that benefit from the unique physicochemical properties of nanosized structures within them. Natural materials such as bone, teeth, and so on are very good examples of successful incorporation of inorganic nanostructures within various organic matrices [1]. Such composites exhibit perfectly organized levels of hierarchical structure, offering excellent mechanical enhancement compared to constituent components. The idea of creating multifunctional composite materials with improved performance using a wide variety of matrices is currently under development, although the focus is mainly on polymeric systems. Similarly, the filler particles can be organic or inorganic with a wide range of compositions and sizes. Carbon nanotubes (CNTs) have attracted great attention of researchers due to their exotic physical and structural properties. The combination of these properties suggests that CNTs can act as potential fillers in high-performance polymer composites. During the last decade or so, there has been tremendous progress in the scientific area of CNT–polymer composites, which enabled potential advancements in various sectors of nanotechnology, ranging from ultrastrong materials for bulletproof vests to flexible displays and sports equipment [2]. With CNTs becoming easier to produce and cheaper to buy, the CNT industry would potentially take over the carbon fiber industry and become one of the major additives for polymer composite fabrication.

In this chapter, the development of functional CNT–polymer composites in recent years will be addressed in detail. The focus will be on processing methods for fabricating the superstrong and/or conductive composite materials. In addition, important aspects of the mechanical and electrical behavior of CNT–polymer composites as well as their potential applications will be analyzed.

Polymer Composites: Volume 2, First Edition. Edited by Sabu Thomas, Kuruvilla Joseph, Sant Kumar Malhotra, Koichi Goda, and Meyyarappallil Sadasivan Sreekala.

10.2
Processing Methods

Many research efforts have been directed toward producing CNT–polymer composites for functional and structural applications. However, even after a decade of research, the full potential of employing CNTs as reinforcements has been severely limited due to difficulties associated with dispersion of entangled CNTs during processing and poor interfacial interaction between CNTs and polymer matrix. The nature of dispersion problem for CNTs is rather different from other conventional fillers such as spherical particles and carbon fibers, because CNTs have high aspect ratio (>1000) and thus extremely large surface area. In addition, the commercialized CNTs are supplied in the form of heavily entangled bundles, resulting in inherent dispersion difficulties.

In order to maximize the potential of CNTs as effective filler in polymer composites, the graphitic nanostructures should be homogeneously dispersed within the matrix. Common processing methods for the fabrication of CNT–polymer composites include solution mixing, *in situ* polymerization, melt mixing, and melt spinning. These methods have been comprehensively discussed in recent review articles [3–6]; therefore, we are going to present an overview of the most important accomplishments. In addition, some recent nontraditional processing techniques will be documented. All the aforementioned methods try to address issues that affect the composite properties such as exfoliation of CNT bundles, homogeneous dispersion of individual tubes in the matrix, CNT alignment, and interfacial interaction between the filler and the matrix.

10.2.1
Common Approaches

The method of solution mixing–casting is one of the most used approaches for preparing CNT–polymer composites on a laboratory scale [7–10]. The nanotubes and polymer are mixed in a suitable medium, followed by evaporation of the solvent to result in a composite film. Generally, dispersion of the nanotubes is done separately from dissolution of the polymer because the high shear processes typically involved in dispersion would likely cause molecular weight degradation of the polymer. During the first stage of a typical protocol, the most efficient method for the dispersion of CNT materials in a specific solvent can be achieved by bath or tip ultrasonication. This involves the application of ultrasound energy for the agitation of particles in a solution. It is the most frequently used method for nanoparticle dispersion. The principle of this technique is that when ultrasound propagates in a liquid solvent, attenuated waves are induced in the molecules of the medium through which it passes. The production of these shock waves promotes the "peeling off" of individual nanoparticles located at the outer part of the nanoparticle bundles and thus results in their partial or full exfoliation.

In addition, chemical functionalization of the CNT sidewalls and tips has been used to assist dispersion and enhance chemical affinity with the polymer

matrix [11–14]. For the last step (solvent evaporation), the casting technique has been mainly utilized. Since the casting–evaporation process is a relatively slow procedure resulting in the reagglomeration of carbon nanostructures within the composite, researchers have alternatively used the spin coating technique in order to obtain rapid evaporation of the solvent medium [15,16]. In their seminal work, Safadi *et al.* [15] have elucidated the basic relationships between simple casting and spin casting conditions, concluding that the processing method employed had no effect on the mechanical–electrical properties of the CNT-based composite.

In a very interesting work, Winey and coworkers [17] have established the coagulation method in which a CNT–polymer stable suspension was poured dropwise into a large excess of bad solvent, resulting in the instantaneous precipitation of the polymer chains and trapping of the isolated carbon nanostructures. After isolation of the final composite, it was concluded that CNTs were homogeneously distributed in the thermoplastic matrix [poly(methyl methacrylate) (PMMA)].

One of the advantages of the "solution mixing" method is the possibility to achieve debundling and good-quality dispersion of the CNT material in an appropriate medium. However, solution processing techniques cannot be utilized for insoluble polymers. One additional problem with the solution mixing method is the fact that no environment-friendly medium exists that is able to both dissolve most polymers and disperse CNT material efficiently. One recent development is the use of supercritical fluids to assist in this process. Evaporation can be very quick by simply releasing the pressure. Using a mixture of acrylic monomer and supercritical carbon dioxide, interesting CNT–polymer composite structures have been produced [18].

Using alternative approaches, researchers have used the roll casting technique [19]. The roll casting system comprises two opposing parallel rollers with a gap distance that can be adjusted. A suspension of a CNT–polymer mixture can be slowly dropped onto one roller when rotating, while a solid film is formed after evaporation of the solvent. In an analogous strategy, the groups of Schulte [20] and Chou [21] studied the dispersion of CNTs into viscous epoxy monomers via a common shear mixing technique, that is, calendering (Figure 10.1). The calendering machine, or commonly known as three roll mill, is a machine tool that employs the shear force created by rollers to mix, disperse, or homogenize viscous materials. The general configuration of a calendering machine consists of three adjacent cylindrical rollers each of which runs at a different velocity. The first and third rollers, called the feeding and apron rollers, rotate in the same direction, while the center roller rotates in the opposite direction. The material to be mixed is fed into the hopper, where it is drawn between the feed and center rollers. When predispersed, the material sticks to the bottom of the center roller, which transports it into the second gap. In this gap, the material that remains on the center roller is subjected to even higher shear force due to higher speed of the apron roller. This milling cycle can be repeated several times to maximize dispersion. The narrow gaps (mechanically or hydraulically adjusted from 500 to $\sim$5 μm) between the rollers, combined with the mismatch in angular velocity of the adjacent rollers, result in locally high shear forces with a short residence time. By using this processing method, formation of a conductive

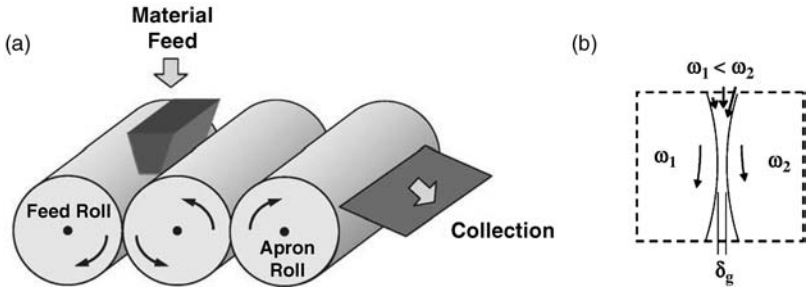

Figure 10.1 (a) Schematic diagram showing the general configuration of a three roll mill. (b) Region of high shear mixing between the feed and center rolls. Reprinted from Ref. [21] with permission from Elsevier, Copyright 2006.

percolating network at CNT concentrations below 0.1 wt% was enabled in the as-prepared polymer composites. The thermal conductivity increased linearly with nanotube concentration to a maximum increase of 60% at 5 wt% CNTs [20,21].

When dealing with thermoplastic matrices, which are insoluble in aqueous or organic media, melt processing is the preferable technique for fabricating CNT-based composites [22–24]. The major advantage of this method is that no solvent is employed to disperse CNTs. In addition, melt mixing is the most promising approach for the fabrication of CNT–polymer composites on industrial scale. In general, melt processing involves the mixing of polymer melt with CNTs by application of intense shear forces. Depending on the final morphology/shape of the composites, the bulk samples can then be processed by several techniques such as extrusion, injection molding, and compression molding [25].

Except the case of bulk composites, melt processing can also be utilized for the fabrication of composite fibers through the melt spinning–drawing technique [22,26]. Melt spinning is the preferred method of manufacturing polymeric fibers. The polymer is melted and pumped through a spinneret (die) with numerous holes (one to thousands). The molten fibers are cooled, solidified, and collected on a take-up wheel. Stretching of the fibers in both the molten and solid states provides orientation of the polymer chains along the fiber axis. Polymers such as poly(ethylene terephthalate) and nylon 6,6 are melt spun in high volumes. One of the main drawbacks of the melt processing method is the potential of thermal degradation and/or oxidation of the polymeric matrix during the heating period.

As a versatile alternative approach, *in situ* polymerization of vinyl monomers in the presence of CNTs has been extensively studied in the last decade [27–30]. The main advantage of this method is that it produces chemically modified tubes with grafted polymer chains, mixed with free polymer chains. Moreover, due to the small size of monomers, the homogeneity of the resulting composite adducts is much higher than the mixing of CNTs and long polymer chains in solution. In this sense, the method allows preparation of the composites with high CNT weight fraction.

Concerning the preparation of anisotropic CNT–polymer composites by *in situ* polymerization process, Kimura *et al.* [31] have mixed styrene monomer with nanotubes and subjected the suspension to a constant magnetic field of 10 T. By polymerizing the mixture, the nanotubes were found to be kept aligned within the polymer matrix. Analogous experiments with an epoxy thermoset as a matrix showed that the thermal and electrical properties of the composites were significantly enhanced by magnetic alignment during processing [32]. In an analogous work, Bauhofer and coworkers [33] dispersed multiwalled carbon nanotubes (MWCNTs) in an epoxy system based on a bisphenol-A resin and an amine-curing agent. The application of both AC and DC electric fields during nanocomposite curing induced the formation of aligned conductive nanotube networks between the electrodes. The network structure formed in AC fields was found to be more uniform and more aligned compared to that in DC fields.

10.3
Novel Approaches

10.3.1
CNT-Based Membranes and Networks

A very versatile approach, the layer-by-layer (LBL) approach involves building up a composite film by alternate dipping of a glass substrate into a dispersion of CNTs and a polymer solution. This protocol results in the adsorption of CNT and polymer monolayers onto the glass surface and the formation of a composite film with thickness on the micrometer scale [34,35]. In order to improve the structural integrity of the film, chemical cross-linking can be induced by heating at 120 °C and/or using bifunctional reagents such as glutaraldehyde [36]. This approach provides multifunctional composites with layered structure. This method has significant advantages as thickness and nanotube–polymer ratio can easily be controlled and very high nanotube loading levels can be obtained (about 50 wt%). The only drawback is that it is relatively a slow process. Such LBL-assembled composites have shown potential applications such as transparent and flexible conductors [37], sensors [38], and neural interface electrodes [39].

In order to prepare CNT–polymer composites with a high CNT loading, independent groups have studied the impregnation of organic thermosetting prepolymers [40] and thermoplastic polymers [41] into the porous macroscopic sheets of randomly entangled CNTs, called buckypapers. The latter can be prepared by filtration of either surfactant-stabilized CNT suspensions or oxidized CNT material in water [42]. The thickness of these CNT preforms ranges between 50 and 200 μm, whereas the porosity is about 75%. The intercalation process could be obtained by simply soaking the nanotube sheets in polymer [41] or in epoxy-based prepolymer solutions [40]. The resulting polymer-intercalated sheets displayed improvements in both the Young's modulus and the tensile strength, compared to pristine CNT sheets as well as the neat matrix.

A similar impregnation technique was demonstrated by Wang *et al.* [43]. They also prepared buckypapers, but impregnated an epoxy-hardener blend into their free pores by a filtration process along the thickness direction. To reduce the viscosity, the blend was slightly diluted with acetone (ratio of epoxy prepolymer to acetone ~70 : 30). A hot press molding process was used for curing the final nanocomposites having high CNT loading (up to 40 wt%). The research results showed that the proposed buckypaper–resin infiltration approach is quite suitable for the fabrication of nanocomposites with controllable nanostructure and high CNT loading, which are important for the development of high-performance nanotube-based composites.

In all the aforementioned cases, the orientation of the carbon nanostructures within the composites is random. To maximize the translation of individual nanotube mechanical and physical properties to the macroscopic film level, it is attractive to align the CNTs in an in-plane direction. The groups of Colbert and Wang, independently, reported the fabrication of such CNT sheets, which were produced by filtrating single-walled carbon nanotube (SWCNT) suspensions in a 17.3 T magnetic field [42,44]. In addition, they studied the electrical, thermal, and mechanical properties of the neat buckypapers as well as of their polymer composites. In the nanocomposites, the CNT volume loading was about 50% for aligned composites and 25–30% for random composites. It has to be stated that the magnetic alignment method cannot be widely applied since the high magnetic field makes the broad application of this process inconvenient and the problems of nanotube waviness and agglomeration are not easily resolved.

In an alternative approach, Liang and coworkers [45] fabricated CNT sheet-reinforced bismaleimide (BMI) resin nanocomposites with high concentrations (60 wt%) of aligned tubes. Applying simple mechanical stretching and prepregging (preresin impregnation) processes on commercially available sheets of randomly dispersed millimeter-long MWCNTs led to substantial alignment enhancement of the carbon nanostructures as well as high packing density of nanotubes in the resultant nanocomposites. In the first stage, the authors used a simple mechanical stretch method to align the carbon nanostructures in the buckypaper sheets. For example, for a 40% stretched CNT sheet (i.e., the poststretch sheet was 40% longer than the prestretch sheet), the degree of alignment of the CNT sheet was shown to be dramatically improved.

Load carrying along the alignment direction showed improvements from the poststretching samples. The mechanical properties of the neat MWCNT sheets of different stretch ratios were measured. The tensile strength at break and Young's modulus of a randomly dispersed CNT sheet (the control sample) were approximately 205 MPa and 1.10 GPa, respectively. During the stretching, MWCNTs self-assembled and aligned themselves along the load direction. The MWCNT rope sizes increased and the packing density became higher compared to prestretched MWCNT sheets. Along the alignment direction, the mechanical properties were significantly improved. The tensile strengths increased to 390, 508, and 668 MPa for the 30, 35, and 40% stretched samples corresponding to 90, 148, and 226%

improvements, respectively. The poststretch Young's modulus measurements along the alignment direction showed even more dramatic improvements, from 1.10 GPa for the randomly dispersed sheet (prestretch) to 11.93, 18.21, and 25.45 GPa, respectively. In a subsequent step, the CNT dry preform was impregnated into a BMI resin solution in acetone, under pressure conditions. Curing of the resulting prepreg resulted in superstrong as well as conductive composite films.

Concerning the mechanical properties of the composites, the tensile strength of the randomly dispersed MWCNT–BMI composite (the control sample) was approximately 620 MPa and Young's modulus was 47 GPa. After stretching to improve alignment and nanotube packing, the tensile strength and Young's modulus of the 30% stretched CNT–BMI composite were 1600 MPa and 122 GPa, respectively. When the stretch ratio increased to 35%, the tensile strength and Young's modulus increased respectively to 1800 MPa and 150 GPa. The tensile strength and Young's modulus of the 40% stretched MWCNT–BMI composite were as high as 2088 MPa and 169 GPa, respectively.

Unprecedentedly, high electrical conductivity was also realized in the stretched MWCNT–BMI composites. The electrical conductivity along the alignment direction of the CNTs was significantly higher than that of prestretched control samples (915 S/cm). An increasing degree of alignment raised the electrical conductivity: 1800 S/cm for the 30% stretched specimen, 3000 S/cm for the 35% stretched specimen, and 5500 S/cm for the 40% stretched specimen. These high conductivity measurements were attributed to (i) high concentrations of MWCNTs in the composite samples (60 wt%), (ii) millimeter-long MWCNTs without functionalization that preserved intrinsic electrical conductivity, and (iii) dense packing of MWCNTs leading to better contacts among nanotubes.

Recently, the same group reported that chemical functionalization of the CNT sheets by epoxidation reaction (Figure 10.2) – prior to the impregnation step – improved further the mechanical properties of the CNT–resin composite membranes [46]. The tensile strength and Young's modulus of the functionalized random CNT sheet–BMI nanocomposites reached 1437 MPa and 124 GPa, respectively, which are about two times greater than those of pristine random CNT sheet–BMI nanocomposites previously reported [45]. For functionalized 40% stretched aligned CNT sheet–BMI nanocomposites, the tensile strength and Young's modulus reached 3081 MPa and 350 GPa, respectively. These values are 48 and 107% higher over those of pristine 40% stretched CNT sheet–BMI nanocomposites. Such CNT-based polymer composites have exhibited the highest values of tensile strength and elastic modulus, among the reported data of literature.

Alternatively, for producing buckypapers with long and aligned CNTs, independent groups [47,48] developed a sophisticated method, called the "domino pushing process," starting with a carpet of aligned arrays of CNTs (forest). The aligned MWCNT arrays were fabricated by a chemical vapor deposition (CVD) method. All CNTs in the aligned CNT arrays are considered to be long, extending from the bottom to the top, forming a thick CNT forest standing on the silicon substrate. The "domino pushing" (Figure 10.3) method comprises the following three steps:

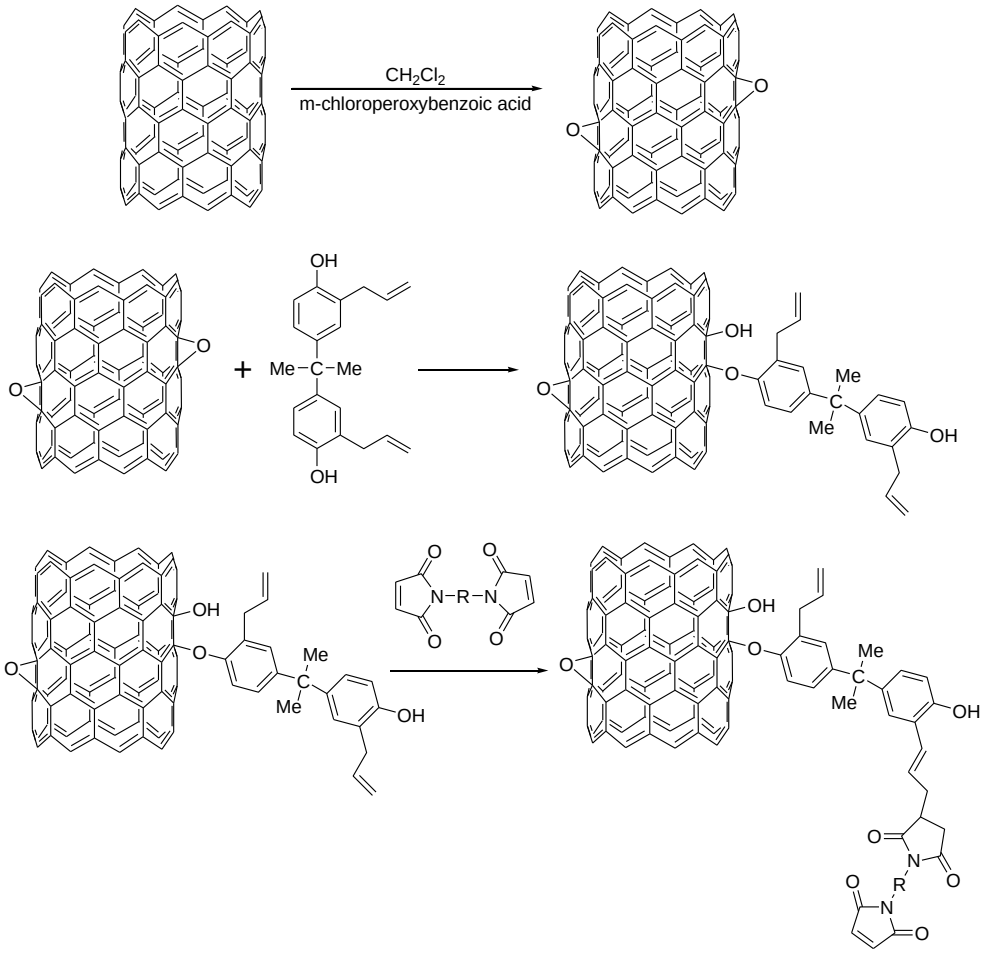

Figure 10.2 Proposed reaction mechanism of functionalized CNTs and BMI 5250-4 resin.

a) The CNT array is covered with a piece of microporous membrane and all the CNTs of the CNT array are forced toward one direction by pushing a cylinder that is placed upon the CNT array with constant pressure. Thus, all CNTs in the CNT array form an aligned buckypaper.
b) The aligned buckypaper is peeled off the silicon substrate with the membrane.
c) Liquid solvent is spread on the microporous membrane, so the aligned buckypaper can be peeled off the membrane easily.

These aligned CNT buckypapers with controllable structure exhibit many potential applications such as supercapacitor electrodes [47] as well as dry preforms for polymer impregnation [48]. Due to the alignment of carbon nanostructures, the

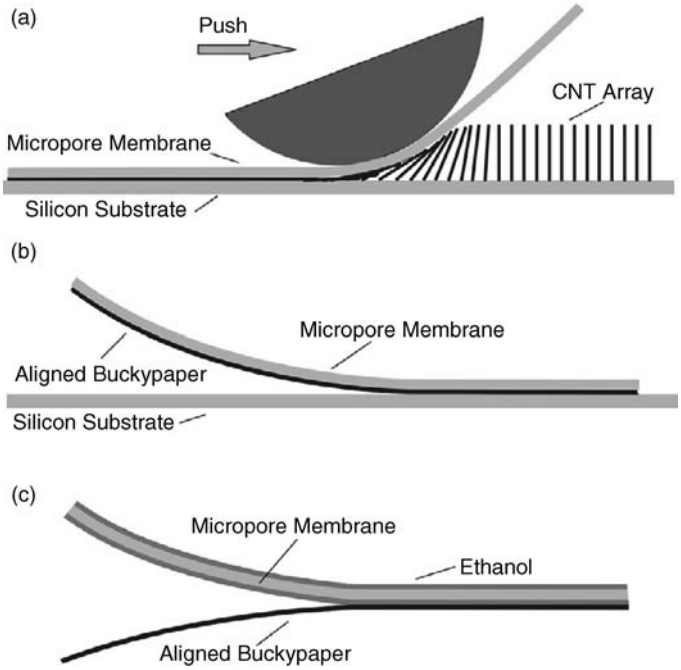

Figure 10.3 Schematics of the domino pushing method. (a) Form aligned buckypaper. (b) Peel the buckypaper off the silicon substrate. (c) Peel the buckypaper off the microporous membrane. Reprinted from Ref. [47] with permission from IOP Publishing, Copyright 2008.

"domino pushing" approach has shown great potential in producing CNT composites with strength and stiffness superior to current commercial composites.

By using a sophisticated process, Fan and coworkers [49] developed a method to form continuous CNT sheets by directly drawing CNTs from superaligned CNT arrays (Figure 10.4). In this manner, the carbon nanostructures can be joined end-to-end by van der Waals interactions to form a continuous and aligned CNT sheet. Many of these continuous and aligned CNT sheets can be stacked together to make a CNT preform with thickness on a centimeter scale. In a subsequent study of the same group, such CNT preforms have been used as structural reinforcements for fabricating CNT–epoxy composite films by vacuum-assisted resin infiltration (VARI) method [50]. Composite films with CNT weight fraction ~8% exhibited a Young's modulus value of about 11 GPa (347% improvement), whereas the corresponding value for tensile strength was about 130 MPa (50% enhancement).

Analogous experiments have been recently performed by using resin transfer molding (RTM) technique [51]. RTM involves placing a textile preform into a mold, injecting the mold with a liquid resin at low injection pressure, and curing the resin to form a solid composite (Figure 10.4). RTM is a simple process that can make composites with large sizes and complex shapes within short cycle time and at low

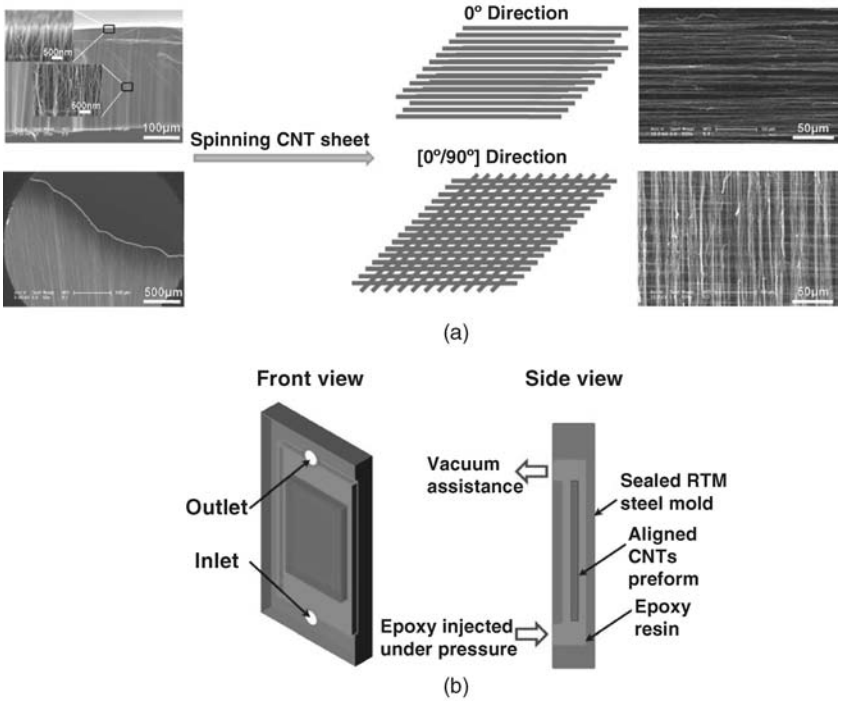

Figure 10.4 (a) Schematic and SEM images of CNT preforms with [0] and [0/90] alignment of CNT sheets. (b) Schematic of the RTM process for fabricating CNT–epoxy composites. Reprinted from Ref. [51] with permission from Elsevier, Copyright 2010.

cost and can be applied to many kinds of low-viscosity thermosetting polymers. These CNT–epoxy composites showed significantly improved mechanical and electrical properties with Young's modulus up to 20.4 GPa, tensile strength up to 231.5 MPa, and electrical conductivity up to 13 000 S/m.

A controlled, efficient, and cost-effective method to produce CNT–polymer composites, in which the density and position of the tubes within the composite can be controlled, was developed by independent groups. In the first step, CNTs were grown by chemical vapor deposition on prepatterned templates in the form of aligned dense arrays (forests) [52,53], periodic arrays [54], or sponges [55]. These CNT networks were then incorporated into a polymer matrix by spin coating a curable prepolymer film on the as-grown tubes. Such polymer composites showed electrical resistivity comparable to pure CNT scaffolds. This controlled method of producing freestanding nanotube–polymer composite films represents an efficient method of combining these materials for potential flexible electronic applications in an inexpensive and scalable manner. In an analogous processing strategy, Valentini *et al.* [56] used electrodeposited CNTs as templates for the preparation of semi-transparent conductive films by infiltration of methyl methacrylate and subsequent polymerization into the free pores of the CNT film.

10.3.2
CNT-Based Fibers

In a different approach for preparing CNT–polymer composites, researchers have focused their efforts on the fabrication of composite micro- or nanofibers. Fiber production techniques are best suited for obtaining aligned tubes within the polymer matrix, thus providing superstrong composite materials.

Apart from the traditional melt spinning method discussed above, composite fibers can also be produced by solution-based processing such as the coagulation–spinning method. In Ref. [57], SWCNTs were dispersed homogeneously in a surfactant solution. Nanotube aggregation was obtained by injecting the CNT dispersion into a rotating aqueous bath of poly(vinyl alcohol) (PVA), such that the nanotube and PVA dispersions flowed in the same direction at the point of injection. Due to the tendency of the polymer chains to replace surfactant molecules on the graphitic surface, the nanotube dispersion was destabilized and collapsed to form a fiber. These wet fibers could then be retrieved from the bath, rinsed, and dried. Significant rinsing was used to remove both surfactant and PVA. Shear forces during the flow led to nanotube alignment. These fibers displayed tensile moduli and strength of 9–15 GPa and ∼150 MPa, respectively.

Two years later, the same group developed a modified protocol in order to enhance further the tensile behavior of the CNT fibers containing small amounts of polymer [58]. The authors observed that the mechanical properties of these fibers could be significantly improved by stretching when wet. This tended to align the nanotubes further, resulting in moduli of ∼40 GPa and strengths of up to 220 MPa. Using solvents that possess lower chemical affinity with the polymer appeared to yield better SWNTs alignments. The authors hypothesized that in a poorer solvent, there are less sliding effects and that the cohesion of the nanotubes–polymer network is better within the fibrillar structure.

Utilization of denaturated single-stranded DNA as a surfactant for the preparation of the CNT dispersion gave poorer mechanical results. For stretched CNT–DNA–PVA fibers, the tensile moduli and strength were ∼19 GPa and ∼125 MPa, respectively [59]. In the meantime, the coagulation–spinning method was further optimized by Baughman and coworkers [60]. They injected the SWCNT dispersion into the center of a coflowing PVA–water stream in a closed pipe. The wet fiber was then allowed to flow through the pipe before being wound on a rotating mandrel. Flow in a more controllable and more uniform conditions in the pipe resulted in more stable fibers. Crucially, wet fibers were not rinsed to remove most of PVA (final SWCNT weight fraction ∼60%). This resulted in large increases in Young's modulus and strength to 80 and 1.8 GPa, respectively.

By adopting the protocol of Vigolo *et al.* [57], Poulin and coworkers [61] used a hot drawing treatment, a concept inspired from textile technologies, to improve the properties of CNT–PVA fibers. The authors have shown that SWCNT- and MWCNT-based fibers (containing equal amount of CNTs and PVA polymer) could be drawn at temperatures above the PVA glass transition temperature (∼180 °C), resulting in improved nanotube alignment and polymer crystallinity. The latter has been shown to

be critical to enhancing stress transfer between nanotubes and polymer in composite materials. These so-called hot-stretched fibers exhibited values of elastic moduli between 35 and 45 GPa and tensile strengths between 1.4 and 1.8 GPa, respectively. The higher strain-to-failure value was estimated about 11%, whereas the toughness was about 55 J/g, which is significantly higher than the toughness of Kevlar.

A sophisticated method for obtaining high-strength polymer fibers is gel spinning. Some high-strength polyethylene and aramid fibers are produced by gel spinning. The technique depends on isolating individual chain macromolecules in the solvent so that intermolecular entanglements are minimal. Entanglements make chain orientation more difficult and also lower the strength of the final product. Not completely separated, as they would be in a true solution, the polymer chains are bound together at various points in liquid crystal form. This produces strong interchain forces in the resulting filaments that can significantly increase the tensile strength of the fibers. In their seminal studies, the groups of Kumar [62] and Wang [63] studied independently the fabrication of CNT–polymer fibers by gel spinning technique. The CNT–polymer blend was not in a true liquid state. In the form of a precisely heated gel, it is processed by an extruder through a spinneret. The extrudate was drawn through the air and then cooled in a bath of bad solvent. The end result is a fiber with a high degree of molecular orientation, and therefore with exceptional tensile strength. In addition, the liquid crystals are aligned along the fiber axis by the shear forces during the extrusion. The modulus and the tensile strength of the PVA–CNT (3 wt%) composite fiber was 40 and 20% higher than that of the control PVA gel spun fiber, respectively [62].

Using a similar protocol, CNT–polymer solutions have been spun into fibers using a dry-jet wet spinning technique [64–66]. This was achieved by extruding a hot CNT–polymer solution through a cylindrical die. The extrusion jet was placed at a small distance above the coagulation bath, which is maintained at room temperature. The nascent fibers descend into the liquid, pass under a guide, and move into the bath while undergoing stretch. Then, they are withdrawn from the bath and wound up. Significant mechanical property increases were recorded for the composite fibers compared with the control samples with no CNT reinforcement. The tensile modulus and the tensile strength of the CNT–polyacrylonitrile composite fiber (10% CNT weight fraction) were higher than the values for the neat polymer fiber by approximately 100 and 45%, respectively [66].

Another method used to form composite-based fibers from solution is electrospinning. This technique involves electrostatically driving a jet of polymer solution out of a nozzle onto a metallic counterelectrode. In 2003, two groups independently described electrospinning as a method to fabricate CNT–polymer composite fibers [67,68]. Composite dispersions of CNTs in either PAN or PEO in DMF and ethanol–water, respectively, were initially produced. Electrospinning was carried out using air pressure of 0.1–0.3 kg/cm^2 to force the solution out of a syringe 0.5 mm in diameter at a voltage difference of 15–25 kV with respect to the collector. Charging the solvent caused rapid evaporation resulting in the coalescence of the composite into a fiber, which could be collected from the steel plate. Fibers with diameters between 10 nm and 1 μm could be produced in this fashion.

In an alternative approach, CNT fibers were prepared by the "direct spinning" method from a CVD reaction zone [69]. Such CNT fibers exhibited diameters of about 10 μm and density values between 0.3 and 1.1 g/cm^3. The tensile strength of the resulting CNT fibers was estimated about 9 GPa [70]. Such aligned fibers of CNTs have been impregnated with epoxy [71] in order to improve the load-bearing capability of CNTs inside fibers. In Ref. [71], CNT fibers having tensile strength ~0.55 GPa and modulus ~22 GPa were infiltrated with an epoxy monomer–curing agent mixture within a special mold. Tensile and compression tests showed that the composite stiffness and fiber volume fraction are fully related parameters. Moreover, with the assumption that the specimens are unidirectional composites, the ultimate tensile strength of CNT–fiber composites was found to be 90% of the value predicted by the simple rule of mixtures. Composites with CNT volume fraction of about 27% exhibited stiffness and tensile strength values of 18.8 GPa and 253 MPa, respectively.

In a similar approach, Xie and coworkers [72] have synthesized CNT films by CVD method. The reticulate architecture of the nanotube bundles showed enhanced potential for fabricating superstrong polymer composites due to its advantage of evenly delivering load over a large interfacial area (Figure 10.5). In a recent study, the

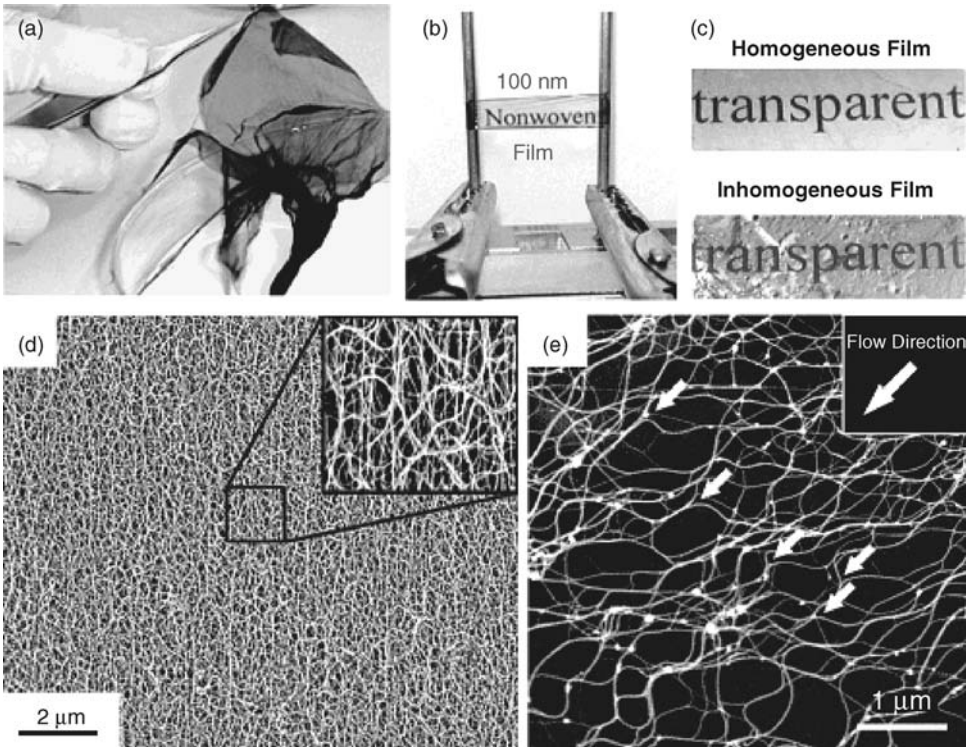

Figure 10.5 Photo images (a–c) of as-grown CNT films with thickness in the range of 100–250 nm. SEM images of a 250 nm thick film (d) and a single layer of bundles peeled off from a 100 nm thick film (e). Reprinted from Ref. [72] with permission from American Chemical Society, Copyright 2007.

same group fabricated composite fibers with enhanced tensile strength and modulus [73]. The CVD-grown CNT films were first split into narrow strips. After the intercalation of either epoxy prepolymer or PVA by solution infiltration process, they were fabricated into fibers through a twisting process. Finally, the polymer-intercalated fibers were cured or dehydrated in an oven at elevated temperatures. The strength values of epoxy- and PVA-infiltrated fibers ranged from 0.9 to 1.6 GPa and 0.7 to 1.3 GPa, respectively. Concerning the elastic modulus values of the epoxy- and PVA-infiltrated fibers, these ranged from 30 to 50 GPa and 20 to 35 GPa, respectively.

10.4
Mechanical Properties of Composite Materials

Experimental studies on CNTs have shown that longitudinal elastic moduli on the order of 1 TPa and the tensile strength in excess of 160 GPa can be achieved for individual SWCNTs [74–76]. As a result, many research groups have been directed toward producing CNT–polymer composites for functional and structural applications. Therefore, there has been an immense effort to establish the most suitable conditions for the transfer of mechanical load to individual nanotubes in a polymer composite material. A prerequisite for such an endeavor is the efficient dispersion of individual CNTs and the establishment of a strong chemical affinity (covalent or noncovalent) with the surrounding polymer molecules. As it is well known, any aggregation of CNTs in polymer composites results in inferior properties as it prevents efficient stress transfer to individual nanotubes [77]. So far, the majority of the processing methods lead to materials that contain low-volume fractions of CNTs that, at least in absolute mechanical property values, cannot seriously compete with commercial polymer composites.

10.5
Basic Theory of Fiber-Reinforced Composite Materials

Let us consider a composite material as an isotropic, elastic matrix filled with perfectly bonded, aligned, elastic fibers cover the full length of the specimen. Then, on application of a stress in the fiber alignment direction, the matrix and fibers will be equally strained. Under these circumstances, a composite property such as modulus of elasticity, shear modulus, Poisson's ratio, or tensile strength is the volume-weighted average of the constituting phases (matrix and dispersed phase) properties. This is the well-known rule of mixtures. In the case of tensile modulus E_c and strength σ_c, the alignment directions are given by

$$E_c = (E_f - E_m)V_f + E_m, \tag{10.1}$$

$$\sigma_c = (\sigma_f - \sigma_m)V_f + \sigma_m, \tag{10.2}$$

where $E_f(\sigma_f)$ is the fiber modulus (strength), $E_m(\sigma_m)$ is the matrix modulus (strength), and V_f is the fiber volume fraction. Taking into account the influence of fiber length and orientation, Eq. (10.1) can be transformed to

$$E_c = (\eta_o \eta_1 E_f - E_m) V_f + E_m, \tag{10.3}$$

where η_o is the orientation efficiency factor, with $\eta_o = 1$ for aligned fibers, $\eta_o = 3/8$ for in-plane aligned fibers, and $\eta_o = 1/5$ for randomly aligned fibers. Also, η_1 is the length efficiency factor, which is given by

$$\eta_1 = 1 - \frac{\tanh(a \cdot l/D)}{a \cdot l/D}, \tag{10.4}$$

where

$$a = \sqrt{\frac{-3E_m}{2E_f \ln V_f}}. \tag{10.5}$$

It should be stressed that an increase of Young's modulus can be achieved by increasing the nanotube content and using high aspect ratio fillers, namely, longer and thinner nanotubes (for $l/D > 15$, $\eta_1 \approx 1$).

It is well documented [78] that there is a critical length l_c that the fibers must have to strengthen a material to their maximum potential. The stress transferred to the fiber reaches the maximum value (σ_f) at a length l_c from the end of the fiber. This means that short fibers can carry stresses less effectively than the long ones and they seem to have a smaller effective modulus for reinforcement purposes. The critical length l_c is given in Eq. (10.6):

$$l_c = \frac{\sigma_f d}{2\tau}, \tag{10.6}$$

where d is the diameter of the fiber and τ is the interfacial stress transfer that describes the maximum stress transferred to the reinforcement when the matrix is under stress. In the case of a hollow cylinder such as CNTs, a more general relation for the critical length l_c is applicable:

$$l_c = \frac{\sigma_f d}{2\tau}\left[1 - \frac{d_i^2}{d^2}\right], \tag{10.7}$$

where d and d_i are the external and internal nanotube diameters, respectively [79].

Concerning the composite strength σ_c, Eq. (10.2) holds for quite long aligned fibers. For midlength fibers, Eq. (10.2) is modified to the following:

$$\sigma_c = (\eta_s \sigma_f - \sigma_m) V_f + \sigma_m, \tag{10.8}$$

where $\eta_s = 1 - (l_c/2l)$ is the strength efficiency factor. For fibers having $l < l_c$, $\eta_s = l/2l_c$ and Eq. (10.8) becomes

$$\sigma_c = \left(\frac{\tau l}{d} - \sigma_m\right) V_f + \sigma_m. \tag{10.9}$$

Equation (10.9) shows that the composite strength depends on the strength of matrix–fiber interface, τ, and not on the fiber's strength. The above-mentioned relations should be used as a benchmark to calculate the composite strength and modulus. Modulus can be determined if the external and inner diameters of CNTs

are known by electron microscopy. Also, to calculate the composite strength, the critical length l_c or, equivalently, the shear strength τ must be known. For example, "pull-out" experiments give a good estimation for τ [80].

10.6
Stress Transfer Efficiency in Composites

As already mentioned, CNT dispersion and stress transfer must all be optimized to reach maximum mechanical properties. One of the most challenging issues in polymer nanocomposites is the determination of the stress transfer efficiency through the interface between CNTs and polymer matrix. This is a prerequisite to take advantage of the extremely high modulus and strength of CNTs. In addition, the high aspect ratio of CNTs necessitates huge interfacial areas available for stress transfer compared to traditional micrometer-size fiber composites.

Raman spectroscopy has been extensively used to assess the degree of stress–strain transfer in a variety of composites reinforced with carbon-based materials such as carbon fibers, various types of CNTs [81,82], and, very recently, graphene [83]. Figure 10.6 shows the main spectral features of a SWCNT, with 514.5 nm excitation. Briefly, Raman spectrum consists of the radial breathing mode (RBM) region, where all the carbon atoms are moving in-phase in the radial direction. Also, at about 1580 cm^{-1} appears the G band in which neighboring atoms move in opposite directions along the surface of the tube as in the 2D graphite. This doubly degenerate band exhibits two different components, the lower frequency component associated with vibrations along the circumferential direction (G^-) and the higher frequency component (G^+) attributed to vibrations along the nanotube axis

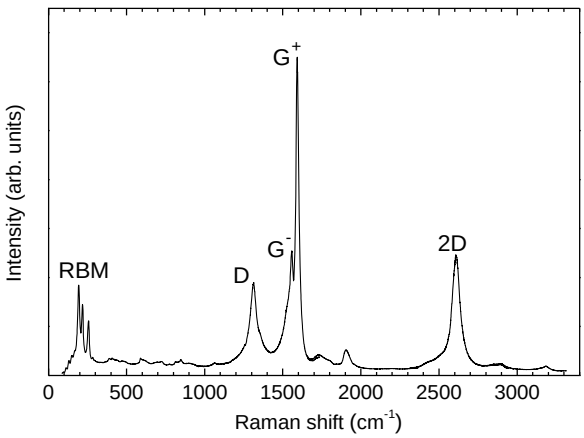

Figure 10.6 Typical Raman spectrum of SWCNT with 514.5 nm excitation. The more intense Raman features are assigned.

direction. The weak feature at around 1340 cm^{-1} is the energy-dispersive disorder-induced D band. The 2D band is its second-order harmonic mode.

The interfacial shear strength is a substantial parameter for any fiber-reinforced composite. The first thing to determine is whether any stress is transferred to the nanotubes at all. It turns out that this is reasonably straightforward to ascertain by Raman spectroscopy. The carbon reinforcements exhibit relatively strong Raman signal; the G and 2D peaks have been found to shift considerably under stress, enabling stress transfer to be monitored through optically transparent matrices. Although the 2D peak exhibits a much broader linewidth compared to the G band, its noticeable high-frequency shift allows small stress–strain variations to be easily detected, making this mode highly sensitive upon application of tensile or compressive stress–strain [81].

Several nanotube–polymer composite systems have been extensively studied by means of Raman spectroscopy under strain ranging from −1 to 4%. For more detailed study on this topic, refer to Ref. [81]. It is important to stress that in these measurements, a large number of nanotubes are measured simultaneously resulting in a Raman response that is an ensemble average of many different nanotube diameters and chiralities. Figure 10.7 shows the strain-induced shift of −15 cm^{-1}/%

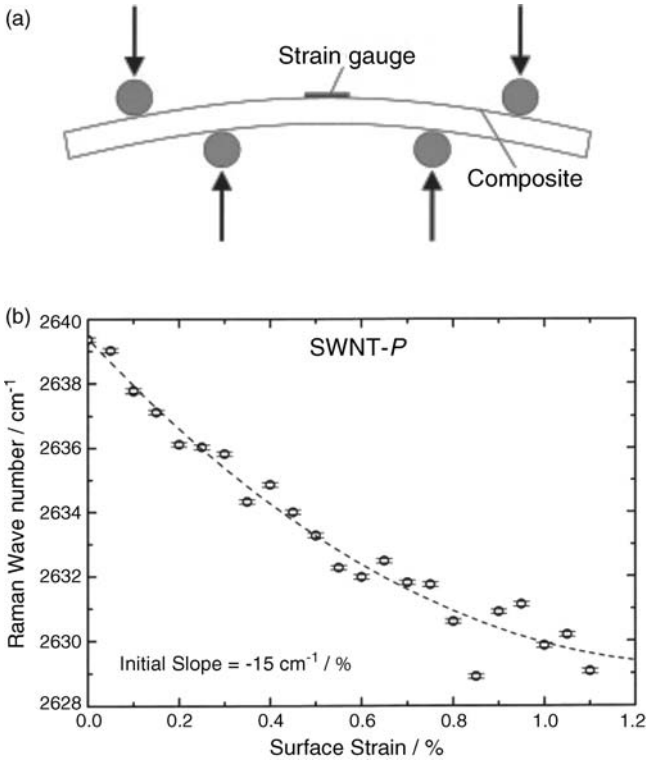

Figure 10.7 Composite specimen under four-point bending. Variation of the 2D Raman peak position with tensile strain for SWCNTs dispersed in epoxy resin. Reprinted with permission from Ref. [84].

for the 2D peak of SWCNTs dispersed in epoxy resin [84]. Also, concerning the G band, a wide spread of values have been reported ranging from -0.17 to $-36\,cm^{-1}/\%$ (see Ref. [81] and references therein).

According to Cui *et al.* [82], the stress transfer in double-walled CNTs from the outer to the inner walls within polymer composites is poor, such that the inner walls are virtually unstressed during the tensile and compressive deformation. The implication of this finding is that a significant reduction in the effective modulus of the reinforcement in MWCNTs composites is expected.

10.7
Mechanical Properties: Selected Literature Data

CNTs exhibit excellent mechanical properties with Young's modulus as high as 1000 GPa and tensile strength of 50–200 GPa. The combination of these exceptional mechanical properties along with the low density, high aspect ratio, and high surface area makes CNTs an ideal candidate for reinforcement in composite materials. Both SWCNTs and MWCNTs have been utilized for reinforcing thermosetting as well as thermoplastic polymers. The mechanical properties of such nanocomposites depend strongly on the dispersion state of nanofillers within the polymer matrix. In addition to dispersion, there are other major requirements that need to be satisfied for effective reinforcement of CNTs in composites. They include a high CNT aspect ratio, alignment, and chemical affinity between the carbon nanostructures and polymer matrix.

In order to compare the mechanical parameters of the CNT–polymer composites, such as their tensile strength and elastic modulus, the absolute values of the parameters as well as the percent increase of these values compared with those of the neat matrix will be documented. It is quite clear that a certain percentage of reinforcement of a polymer matrix with, for example, a 1 wt% CNT material is more efficient than with a higher CNT weight fraction. In Table 10.1, the most important research studies concerning the reinforcement of CNT–polymer composites have been illustrated and some general conclusions are given. We will focus on the main factors that influence the mechanical properties of the composites: the composite processing methods, the chemical modification of the CNT sidewalls and tips, and the polymer matrix itself.

10.8
Electrical Properties of Composite Materials

CNTs could have either metallic or semiconducting properties, depending on their diameters and chiralities. Due to their exceptional electrical properties, CNTs have become one of the most attractive materials to be used as conductive fillers in polymer composites. Electrical conductivity in insulating polymer composites is well described by means of the percolation threshold. The percolation threshold is the filler concentration at which the electrical conductivity increases sharply by orders of magnitude, indicating that conductive paths span the macroscopic sample [87].

Table 10.1 Mechanical properties of the composites.

Matrix	CNT type	CNT weight fraction (wt%)	Processing method	Composite tensile strength in MPa (% increase)	Composite Young's modulus in GPa (% increase)	Composite storage modulus in GPa at room temperature (% increase)	Mechanical testing	Reference
PMMA	PMMA-grafted MWCNTs	20.00	Solution mixing–casting			31 (1100)	DMA	[85]
PVA	Purified SWCNTs	60.00	Coagulation–spinning method	1800 (–)	80 (–)		Tensile	[60]
PVA	Pristine SWCNTs	50.00	Coagulation–spinning–hot drawing	1800 (–)	45 (–)		Tensile	[61]
	Pristine MWCNTs			1400 (–)	35 (–)			
PVA	Oxidized SWCNTs	60.00	Layer-by-layer deposition–cross-linking	505 (1200)	15.6 (800)		Tensile	[86]
PEI	Oxidized SWCNTs	50.00	Layer-by-layer deposition–cross-linking	325 (2700)	11 (>3000)		Tensile	[34]
PEI	Bamboo MWCNTs	50.00	Layer-by-layer deposition–cross-linking	150 (1500)	4.5 (1500)		Tensile	[35]
Epoxy	Pristine SWCNTs	31.30	Random buckypaper solution impregnation			15 (492)	DMA	[43]

(*continued*)

Table 10.1 (*Continued*)

Matrix	CNT type	CNT weight fraction (wt%)	Processing method	Composite tensile strength in MPa (% increase)	Composite Young's modulus in GPa (% increase)	Composite storage modulus in GPa at room temperature (% increase)	Mechanical testing	Reference
Epoxy	Thin MWCNT array – domino pushing process	32.00	Resin impregnation in acetone–prestretching–curing	400 (500)	22.3 (800)		Tensile	[48]
Epoxy	Stacks of aligned MWCNT thin sheets	8.00	Vacuum-assisted resin infiltration	130 (50)	11 (347)		Tensile	[50]
Epoxy	Stacks of aligned MWCNT thin sheets	15.00	Resin transfer molding	231 (160)	20.4 (716)		Tensile	[51]
Epoxy	DWCNT fiber	22.00	Resin impregnation	253 (500)	18.8 (1400)		Tensile	[71]
Epoxy	CVD-grown CNT films		Resin impregnation–twisting–curing	1250 (2000)	40 (1200)		Tensile	[73]
Bismaleimide	Stretched MWCNT buckypaper	60.00	Resin impregnation	2088 (–)	169 (–)		Tensile	[45]
Bismaleimide	Stretched epoxide-modified MWCNT buckypaper	60.00	Resin impregnation	3081 (–)	359 (–)		Tensile	[46]

For composites with discrete fillers, the DC conductivity obeys a percolation-like power law:

$$\sigma_c = \sigma_o(v - v_c)^t, \tag{10.10}$$

where σ_c is the conductivity of the composite material, σ_o is the conductivity of the conductive reinforcement (nanotubes), v is the volume fraction of the reinforcement, v_c is the percolation threshold, and t is the conductivity critical exponent. It is important to stress that Eq. (10.10) is valid for concentrations above the percolation threshold ($v > v_c$) and solely in the vicinity of v_c. Also, since the mass densities of polymers and SWCNTs are similar, the mass fraction m and the volume fraction v are also same [088].

Homogeneous CNT–polymer composites show dramatic improvements in electrical conductivity at low percolation threshold ~0.005–0.1 wt% for SWCNTs loading. In all cases, the desired properties of host polymers such as lightweight, optical clarity, and low melt viscosities are retained. For example, Figure 10.8 shows the

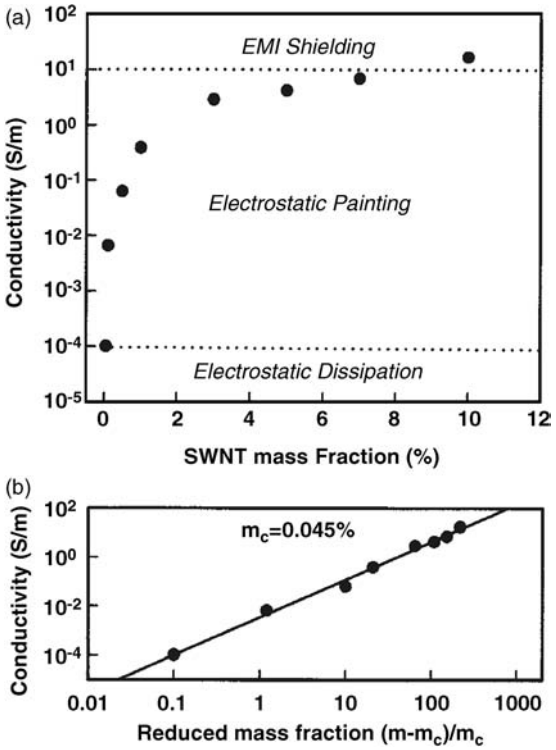

Figure 10.8 (a) Electrical conductivity of PPE-functionalized SWNT polycarbonate composite as a function of SWCNT weight loading, at room temperature. Dashed lines represent the approximate conductivity lower bound required for several electrical applications. (b) Variation of DC conductivity of PPE–SWNTs–polycarbonate composite with the reduced mass fraction of SWNTs. Reprinted with permission from Ref. [88].

electrical conductivity of polystyrene composites fabricated using noncovalently functionalized, soluble SWCNTs [88]. The conductivity of pure polystyrene is 10^{-14} S/m, while the conductivity of pristine HiPco SWCNTs is 5×10^4 S/m. As seen in Figure 10.8, the conductivity of the nanocomposite increases sharply between 0.02 and 0.05 wt% SWCNT loading, indicating the formation of a percolation network. Fitting the data to Eq. (10.10), an extremely low concentration threshold is derived ($m_c = 0.045$ wt%).

The percolation concentration threshold depends sensitively on nanotube dispersion, aspect ratio, degree of alignment, and functionalization. Nanotube dispersion affects considerably the spatial distribution of CNTs. Bad dispersion leads to aggregation of nanotubes, reduces their aspect ratio, decreases the number of discrete fillers in a composite, and consequently increases the percolation threshold. The improvement of dispersion has become a challenge to maximize the properties of CNT–polymer composites. In order to overcome self-aggregation as well as to improve wettability of and adhesion to host matrix, many approaches were employed to introduce functional groups covalently or noncovalently onto the surface of CNTs [89]. In general, higher aspect ratio CNTs give better values for the electrical conductivity. However, in this case, a competitive effect arises since higher aspect ratio nanotubes are more difficult to disperse.

Finally, SWCNT concentrations higher than 0.3 and 3 wt%, respectively are sufficient for applications in electrostatic painting and electromagnetic interference shielding, respectively (Figure 10.8). Other applications of electrically conductive CNT–polymer composites are in printable circuit wiring and as transparent conductive coatings.

10.9
Electrical Properties: Selected Literature Data

Electrical conductivity in nanotube–polymer composites exhibits percolation-type behavior, where the presence of interconnected nanotube network results in a dramatic increase of the electrical conductivity. Physical parameters of composite materials such as electrical conductivity, percolation threshold (v_c), and critical exponent (t) have been intensively studied to achieve polymer–CNT conductive composites at low filler concentrations. However, as already mentioned, numerous studies show that the percolation threshold and conductivity depend strongly on the polymer type and synthesis method, aspect ratio of CNTs, disentanglement of CNT agglomerates, uniform spatial distribution of individual CNTs, and degree of alignment.

A wide range of values for conductivity and percolation thresholds of CNT composites has been reported in the literature during the last decade, depending on the processing method, polymer matrix, and nanotube type. Recent review articles can be found in Refs [6,87,90]. In Table 10.2, selected research studies concerning the DC electrical properties of CNT–polymer composites are presented. Also, a comparison between the different types of polymeric matrices, CNTs type

Table 10.2 Electrical properties of the composites.

Matrix	CNT type	CNT weight fraction (wt%)	Processing method	Composite electrical conductivity (S/m)	v_c (wt%) t	Reference
PS	PPE-functionalized SWCNTs	0.01–10	Solution mixing	6.89 (7 wt%)	0.045 3.3	[91]
UHMWPE	SWCNTs	$\leq$3	Dry mixing–sintering	$\approx10^{-2}$ (2 wt%)	0.09 2.25	[92]
HDPE	SWCNTs	$\leq$8	Fast crystallization from dilute solution	$\approx$70 (8 wt%)	0.13 3.54	[93]
PVC	MWCNTs	$\leq$1.26	Mechanical mixing and hot compaction	$\approx10^{-2}$ (1.26 wt%)	0.000846 3.3	[94]
PMMA	SWCNTs	$\leq$8	Solution mixing	$\approx$70 (8 wt%)	0.33 2.1	[95]
PMMA	SWCNTs	10.4	Solution mixing–casting	$\approx$50 (10.4 wt%)	0.429 2.1	[96]
PVA	MWCNTs	$\leq$22.5	Solution mixing	0.27 (22.5 wt%)	0.72 2.7	[97]
P3HT	MWCNTs	$\leq$30	Solution mixing	$\approx5\times10^{-1}$ (30 wt%)	0.1 1.68	[98]
PCL	Purified SWCNTs	$\leq$3	Solution mixing	$\approx2\times10^{-3}$ (3 wt%)	0.09 1.5	[99]
PI	SWCNTs	$\leq$1.3	*In situ* polymerization	$\sim10^{-4}$ (1.3 wt%)	0.0065 1.5	[100]
PI	Purified SWCNTs	$\leq$1.3	*In situ* polymerization	3×10^{-5} (0.65 wt%)	0.065 1.5	[101]

(*continued*)

Table 10.2 (*Continued*)

Matrix	CNT type	CNT weight fraction (wt%)	Processing method	Composite electrical conductivity (S/m)	v_c (wt%) t	Reference
PI	Purified SWCNTs	≤6.5	*In situ* polymerization	$\approx 5 \times 10^{-3}$ (6.5 wt%)	0.00065 2.77	[102]
Epoxy	Aligned MWCNTs	≤1	Shear mixing	≈2 (0.01 wt%)	0.0025 1.2	[103]
Epoxy	CNTs	≤2.5	Solution mixing	1.3×10^{-2} (2.5 wt%)	0.3 1.44	[104]
Epoxy	SWCNTs	≤15	Solution mixing	≈10 (15 wt%)	0.062 2.68	[105]
PmPV	MWCNTs	35	Solution mixing	10^{-2} (0.35 wt%)	—	[106]
PmPV	CNTs	≤36	Solution mixing	3 (36 wt%)	8.4	[107]
PVDF	Trifluorophenyl-functionalized MWCNTs	<0.36	Solution mixing	$\approx 10^{-2}$ (0.324 wt%)	0.144 1.54	[108]
PPS	MWCNTs	≤5.4	Powder mixing and compression	$\approx 10^{3}$ (5.4 wt%)	0.396 3.55	[109]

and additional treatment (purification–functionalization), processing method, and electrical characteristics such as room temperature maximum conductivity, percolation threshold v_c, and critical exponent t are illustrated. Filler weight fraction range, room temperature maximum conductivity of neat polymer matrix, and pristine CNTs are also included in Table 10.2.

10.10 CNT–Polymer Composite Applications

As already described, CNTs are among the strongest and stiffest fibers ever known. These excellent mechanical properties combined with other physical properties of CNTs exemplify huge potential applications of CNT–polymer nanocomposites. Ongoing experimental works in this area have shown some exciting results, although the much-anticipated commercial success has yet to be realized in the years ahead. Following the first report on the preparation of a CNT–polymer nanocomposite in 1994 [7], many research efforts have been made to understand their structure–property relationship and find useful applications in different fields. Concerning the structural composites, the unique mechanical properties of CNTs such as high modulus, tensile strength, and strain to fracture are explored to obtain structural materials with much improved mechanical properties. As for CNT–polymer functional composites, many other unique properties of CNTs such as electrical, thermal, and optical properties are utilized to develop multifunctional composites for applications in the fields of heat resistance, chemical sensing, electrical and thermal management, photoemission, electromagnetic absorbing and energy storage performances, and so on.

Nanometer-size catalyst supports have recently attracted great attention because of their high surface area and outstanding stability and activity in the liquid phase. In particular, CNT-supported catalysts have been selected for highly efficient catalysis because they provide different contact areas that can be functionalized in various ways. Several routes have been developed to link the catalytic metal nanoparticles to the CNT surface [89]. Examples include chemical deposition with and without the aid of reducing agents, electrochemical deposition, and direct assembly of metal nanoparticles onto pristine and/or modified CNT sidewalls.

By selecting Pt and PtRu nanoparticles as the model because of their wide use in fuel cells, Chen and coworkers [110] reported a sophisticated strategy to disperse metal nanoparticles on CNTs. Their approach was based on the thermal-initiation free radical polymerization of the monomer 3-ethyl-1-vinylimidazolium tetrafluoroborate ([VEIM]BF4) to form an ionic liquid polymer (PIL) on the CNT surface, which introduced a large number of surface functional groups on the CNTs with uniform distribution to anchor and grow metal nanoparticles. The PIL film on the CNTs created a distribution of ionic species with positive charge that prevented aggregation of the CNTs and induced stable nanotube suspensions in water, which served as the medium to stabilize and anchor metal nanoparticles. The PtRu–CNTs–PIL (or Pt–CNTs–PIL) electrocatalyst showed better performance in the direct

electrooxidation of methanol than the PtRu–CNTs (or Pt–CNTs) electrocatalyst. Such CNT–PIL hybrids exhibited enhanced perspectives as promising catalyst supports in fuel cells.

Alternatively, CNT–polymer composites have been utilized as polymer electrolyte membranes in fuel cell devices (PEMFCs) [111]. Sulfonic acid-functionalized CNTs were blended with Nafion polymer so that the proton transport capability of the polymer matrix could be enhanced appreciably. Ionic conductivity measurements of Nafion and CNT–Nafion membranes revealed almost one order of magnitude higher conductivity for the composite than that for neat matrix.

Although not highlighted in this chapter, other promising research fields in which CNT–polymer assemblies have been recently integrated, include thermoelectric power devices that convert thermal energy into electricity [112], planar nanoheterojunction photovoltaic systems [113], electrode materials for thin film microbatteries [114], light-emitting field-effect transistors [115], wastewater purification agents [116], stretchable light-emitting devices [117], osteoblast outgrowth agents in bone tissue engineering applications [118], and electromechanical actuators [119].

References

1 Zapanta LeGeros, R. (2008) *Chemical Reviews*, **108**, 4742.
2 Breuer, O. and Sundararaj, U. (2004) *Polymer Composites*, **25**, 630.
3 Grady, B.P. (2010) *Macromolecular Rapid Communications*, **31**, 247.
4 Byrne, M.T. and Gunko, Y.K. (2010) *Advanced Materials*, **22**, 1672.
5 Chou, T.-W., Gao, L., Thostenson, E.T., Zhang, Z., and Byun, J.-H. (2010) *Composites Science and Technology*, **70**, 1.
6 Spitalsky, Z., Tasis, D., Papagelis, K., and Galiotis, C. (2010) *Progress in Polymer Science*, **35**, 357.
7 Ajayan, P.M., Stephan, O., Colliex, C., and Trauth, D. (1994) *Science*, **265**, 1212.
8 Jin, L., Bower, C., and Zhou, O. (1998) *Applied Physics Letters*, **73**, 1197.
9 Shaffer, M.S.P. and Windle, A.H. (1999) *Advanced Materials*, **11**, 937.
10 Qu, L., Lin, Y., Hill, D.E., Zhou, B., Wang, W., Sun, X., Kitaygorodskiy, A., Suarez, M., Connell, J.W., Allard, L.F., and Sun, Y.-P. (2004) *Macromolecules*, **37**, 6055.
11 Hill, D.E., Lin, Y., Rao, A.M., Allard, L.F., and Sun, Y.-P. (2002) *Macromolecules*, **35**, 9466.
12 Tseng, C.-H., Wang, C.-C., and Chen, C.-Y. (2007) *Chemistry of Materials*, **19**, 308.
13 Chatterjee, T., Mitchell, C.A., Hadjiev, R.A., and Krishnamoorti, V.G. (2007) *Advanced Materials*, **19**, 3850.
14 Simmons, T.J., Bult, J., Hashim, D.P., Linhardt, R.J., and Ajayan, P.M. (2009) *ACS Nano*, **3**, 865.
15 Safadi, B., Andrews, R., and Grulke, E.A. (2002) *Journal of Applied Polymer Science*, **84**, 2660.
16 Schmidt, R.H., Kinloch, I.A., Burgess, A. N., and Windle, A.H. (2007) *Langmuir*, **23**, 5707.
17 Du, F., Fischer, J.E., and Winey, K.I. (2003) *Journal of Applied Polymer Science B*, **41**, 3333.
18 Yue, B., Wang, Y., Huang, C.Y., Pfeffer, R., and Iqbal, Z. (2007) *Journal of Nanoscience and Nanotechnology*, **7**, 994.
19 Geng, H., Rosen, R., Zheng, B., Shimoda, H., Fleming, L., Liu, J., and Zhou, O. (2002) *Advanced Materials*, **14**, 1387.
20 Gojny, F.H., Wichmann, M.H.G., Köpke, U., Fiedler, B., and Schulte, K. (2004) *Composites Science and Technology*, **64**, 2363.
21 Thostenson, E.T. and Chou, T.W. (2006) *Carbon*, **44**, 3022.
22 Haggenmueller, R., Gommans, H.H., Rinzler, A.G., Fischer, J.E., and Winey, K.I. (2000) *Chemical Physics Letters*, **330**, 219.

23 Jin, Z., Pramoda, K.P., Xu, G., and Goh, S.H. (2001) *Chemical Physics Letters*, **337**, 43.

24 Potschke, P., Fornes, T.D., and Paul, D.R. (2002) *Polymer*, **43**, 3247.

25 Mago, G., Fisher, F.T., and Kalyon, D.M. (2008) *Macromolecules*, **41**, 8103.

26 Chen, X., Burger, C., Fang, D., Sics, I., Wang, X., He, W., Somani, R.H., Yoon, K., Hsiao, B.S., and Chu, B. (2006) *Macromolecules*, **39**, 5427.

27 Jia, Z., Wang, Z., Xu, C., Liang, J., Wei, B., Wu, D., and Zhu, S. (1999) *Materials Science and Engineering A*, **271**, 395.

28 Chen, G.Z., Shaffer, M.S.P., Coleby, D., Dixon, G., Zhou, W., Fray, D.J., and Windle, A.H. (2000) *Advanced Materials*, **12**, 522.

29 Velasco-Santos, C., Martinez-Hernandez, A.L., Fisher, F.T., Ruoff, R., and Castano, V.M. (2003) *Chemistry of Materials*, **15**, 4470.

30 Yao, Q., Chen, L., Zhang, W., Liufu, S., and Chen, X. (2010) *ACS Nano*, **4**, 2445.

31 Kimura, T., Ago, H., Tobita, M., Ohshima, S., Kyotani, M., and Yumura, M. (2002) *Advanced Materials*, **14**, 1380.

32 Choi, E.S., Brooks, J.S., Eaton, D.L., Al-Haik, M.S., Hussaini, M.Y., Garmestani, H., Li, D., and Dahmen, K. (2003) *Journal of Applied Physics*, **94**, 6034.

33 Martin, C.A., Sandler, J., Windle, A.H., Schwarz, M., Bauhofer, W., Schulte, K., and Shaffer, M.S.P. (2005) *Polymer*, **46**, 877.

34 Mamedov, A., Kotov, N., Prato, M., Guldi, D.M., Wicksted, J.P., and Hirsch, A. (2002) *Nature Materials*, **1**, 190.

35 Olek, M., Ostrander, J., Jurga, S., Möhwald, H., Kotov, N., Kempa, K., and Giersig, M. (2004) *Nano Letters*, **4**, 1889.

36 Shim, B.S., Zhu, J., Jan, E., Critchley, K., Ho, S., Podsiadlo, P., Sun, K., and Kotov, N. (2009) *ACS Nano*, **3**, 1711.

37 Shim, B.S., Zhu, J., Jan, E., Critchley, K., and Kotov, N. (2010) *ACS Nano*, **4**, 3725.

38 Wang, L., Chen, W., Xu, D., Shim, B.S., Zhu, Y., Sun, F., Liu, L., Peng, C., Jin, Z., Xu, C., and Kotov, N. (2009) *Nano Letters*, **9**, 4147.

39 Jan, E., Hendricks, J.L., Husaini, V., Richardson-Burns, S.M., Sereno, A., Martin, D.C., and Kotov, N. (2009) *Nano Letters*, **9**, 4012.

40 Spitalsky, Z., Tsoukleri, G., Tasis, D., Krontiras, C., Georga, S., and Galiotis, C. (2009) *Nanotechnology*, **20**, 405702.

41 Coleman, J.N., Blau, W.J., Dalton, A.B., Munoz, E., Collins, S., Kim, B.G., Razal, J., Selvidge, M., Vieiro, G., and Baughman, R.H. (2003) *Applied Physics Letters*, **82**, 1682.

42 Walters, D.A., Casavant, M.J., Qin, X.C., Huffman, C.B., Boul, P.J., Ericson, L.M., Haroz, E.H., O'Connell, M.J., Smith, K., Colbert, D.T., and Smalley, R.E. (2001) *Chemical Physics Letters*, **338**, 14.

43 Wang, Z., Liang, Z., Wang, B., Zhang, C., and Kramer, L. (2004) *Composites Part A*, **35**, 1225.

44 Gonnet, P., Liang, Z.Y., Choi, E.S., Kadambala, R.S., Zhang, C., Brooks, J.S., Wang, B., and Kramer, L. (2006) *Current Applied Physics*, **6**, 119.

45 Cheng, Q., Bao, J., Park, J., Liang, Z., Zhang, C., and Wang, B. (2009) *Advanced Functional Materials*, **19**, 3219.

46 Cheng, Q., Wang, B., Zhang, C., and Liang, Z. (2010) *Small*, **6**, 763.

47 Wang, D., Song, P., Liu, C., Wu, W., and Fan, S. (2008) *Nanotechnology*, **19**, 075609.

48 Bradford, P.D., Wang, X., Zhao, H., Maria, J.-P., Jia, Q., and Zhu, Y.T. (2010) *Composites Science and Technology*, **70**, 1980.

49 Liu, K., Sun, Y., Chen, L., Feng, C., Feng, X., Jiang, K., Zhao, Y., and Fan, S. (2008) *Nano Letters*, **8**, 700.

50 Cheng, Q., Wang, J., Jiang, K., Li, Q., and Fan, S. (2008) *Journal of Materials Research*, **23**, 2975.

51 Cheng, Q., Wang, J., Wen, J.J., Liu, C.H., Jiang, K., and Fan, S. (2010) *Carbon*, **48**, 260.

52 Raravikar, N.R., Schadler, L.S., Vijayaraghavan, A., Zhao, Y., Wei, B., and Ajayan, P.M. (2005) *Chemistry of Materials*, **17**, 974.

53 Wardle, B.L., Saito, D.S., Garcia, E.J., Hart, A.J., de Villoria, R.G., and Verploegen, E.A. (2008) *Advanced Materials*, **20**, 2707.

54 Lahiff, E., Ryu, C.Y., Curran, S., Minett, A.I., Blau, W.J., and Ajayan, P.M. (2003) *Nano Letters*, **3**, 1333.

55 Gui, X., Cao, A., Wei, J., Li, H., Jia, Y., Li, Z., Fan, L., Wang, K., Zhu, H., and Wu, D. (2010) *ACS Nano*, **4**, 2320.

56 Valentini, L., Bon, S.B., and Kenny, J.M. (2007) *Carbon*, **45**, 2685.

57 Vigolo, B., Penicaud, A., Coulon, C., Sauder, C., Pailler, R., Journet, C., Bernier, P., and Poulin, P. (2000) *Science*, **290**, 1331.

58 Vigolo, B., Poulin, P., Lucas, M., Launois, P., and Bernier, P. (2002) *Applied Physics Letters*, **81**, 1210.

59 Barisci, J.N., Tahhan, M., Wallace, G.G., Badaire, S., Vaugien, T., Maugey, M., and Poulin, P. (2004) *Advanced Functional Materials*, **14**, 133.

60 Dalton, A.B., Collins, S., Munoz, E., Razal, J., Ebron, V., Ferraris, J., Coleman, J.N., Kim, B.G., and Baughman, R.H. (2003) *Nature*, **423**, 703.

61 Miaudet, P., Badaire, S., Maugey, M., Derre, A., Pichot, V., Launois, P., Poulin, P., and Zakri, C. (2005) *Nano Letters*, **5**, 2212.

62 Zhang, X., Liu, T., Sreekumar, T.V., Kumar, S., Hu, X., and Smith, K. (2004) *Polymer*, **45**, 8801.

63 Wang, Y., Cheng, R., Liang, L., and Wang, Y. (2005) *Composites Science and Technology*, **65**, 793.

64 Kumar, S., Dang, T.D., Arnold, F.E., Bhattacharyya, A.R., Min, B.G., Zhang, X., Vaia, R.A., Park, C., Wade Adams, W., Hauge, R.H., Smalley, R.E., Ramesh, S., and Willis, P.A. (2002) *Macromolecules*, **35**, 9039.

65 Weisenberger, M.C., Grulke, E.A., Jacques, D., Rantell, T., and Andrews, R. (2003) *Journal of Nanoscience and Nanotechnology*, **3**, 535.

66 Sreekumar, T.V., Liu, T., Min, B.G., Guo, H., Kumar, S., Hauge, R.H., and Smalley, R.E. (2004) *Advanced Materials*, **16**, 58.

67 Ko, F., Gogotsi, Y., Ali, A., Naguib, N., Ye, H., Yang, G.L., Li, C., and Willis, P. (2003) *Advanced Materials*, **15**, 1161.

68 Dror, Y., Salalha, W., Khalfin, R.L., Cohen, Y., Yarin, A.L., and Zussman, E. (2003) *Langmuir*, **19**, 7012.

69 Li, Y.-L., Kinloch, L.A., and Windle, A.H. (2004) *Science*, **304**, 276.

70 Koziol, K., Vilatela, J., Moisala, A., Motta, M., Cunniff, P., Sennett, M., and Windle, A.H. (2007) *Science*, **318**, 1892.

71 Mora, R.J., Vilatela, J.J., and Windle, A.H. (2009) *Composites Science and Technology*, **69**, 1558.

72 Ma, W., Song, L., Yang, R., Zhang, T., Zhao, Y., Sun, L., Ren, Y., Liu, D., Liu, L., Shen, J., Zhang, Z., Xiang, Y., Zhou, W., and Xie, S. (2007) *Nano Letters*, **7**, 2307.

73 Ma, W., Liu, L.Q., Zhang, Z., Yang, R., Liu, G., Zhang, T.H., An, X., Yi, X., Ren, Y., Niu, Z., Li, J., Dong, H., Zhou, W., Ajayan, P.M., and Xie, S. (2009) *Nano Letters*, **9**, 2855.

74 Treacy, M.M.J., Ebbesen, T.W., and Gibson, J.M. (1996) *Nature*, **381**, 678.

75 Yu, M.-F., Lourie, O., Dyer, M.J., Moloni, K., Kelly, T.F., and Ruoff, R.S. (2000) *Science*, **287**, 637.

76 Yu, M.-F., Files, B.S., Arepalli, S., and Ruoff, R.S. (2000) *Physical Review Letters*, **84**, 5552.

77 Andrews, R. and Weisenberger, M.C. (2004) *Current Opinion in Solid State & Materials Science*, **8**, 31.

78 Hull, D. and Clyne, T.W. (1996) *An Introduction to Composite Materials, Cambridge Solid State Science Series*, Cambridge University Press.

79 Kelly, A. and Tyson, W.R. (1965) *Journal of the Mechanics and Physics of Solids*, **13**, 329.

80 Manoharan, M.P., Sharma, A., Desai, A. V., Haque, M.A., Bakis, C.E., and Wang, K.W. (2009) *Nanotechnology*, **20**, 295701.

81 Kumar, R. and Cronin, S.B. (2008) *Journal of Nanoscience and Nanotechnology*, **8**, 122.

82 Cui, S., Kinloch, I.A., Young, R.J., Noe, L., and Monthioux, M. (2009) *Advanced Materials*, **21**, 3591.

83 Gong, L., Kinloch, I.A., Young, R.J., Riaz, I., Jalil, R., and Novoselov, K.S. (2010) *Advanced Materials*, **22**, 2694.

84 Cooper, C.A., Young, R.J., and Halsall, M. (2001) *Composites Part A*, **32**, 401.

85 Huang, G.L., Shieh, Y.T., and Hwang, K. C. (2004) *Advanced Functional Materials*, **14**, 487.

86 Shim, B.S., Zhu, J., Jan, E., Critchley, K., Ho, S., Podsiadlo, P., Sun, K., and Kotov, N.A. (2009) *ACS Nano*, **3**, 1711.

87 Winey, K.I., Kashiwagi, T., and Mu, M. (2007) *MRS Bulletin*, **32**, 348.

88 Ramasubramaniam, R., Chen, J., and Liu, H. (2003) *Applied Physics Letters*, **83**, 2928.

89 Karousis, N., Tagmatarchis, N., and Tasis, D. (2010) *Chemical Reviews*, **110**, 5366.

90 Bauhofer, W. and Kovacs, J.Z. (2009) *Composites Science and Technology*, **69**, 1486.

91 Ramasubramaniam, R., Chen, J., and Liu, H. (2003) *Applied Physics Letters*, **83**, 2928.

92 Mierczynska, A., Mayne-L'Hermite, M., Boiteux, G., and Jeszka, J.K. (2007) *Journal of Applied Polymer Science*, **105**, 158.

93 Jeon, K., Lumata, L., Tokumoto, T., Steven, E., Brooks, J., and Alamo, R.G. (2007) *Polymer*, **48**, 4751.

94 Mamunya, Y., Boudenne, A., Lebovka, N., Ibos, L., Candau, Y., and Lisunova, M. (2008) *Composites Science and Technology*, **68**, 1981.

95 Benoit, J.M., Corraze, B., Lefrant, S., Blau, W.J., Bernier, P., and Chauvet, O. (2001) *Synthetic Metals*, **121**, 1215.

96 Chauvet, O., Benoit, J.M., and Corraze, B. (2004) *Carbon*, **42**, 949.

97 Hernandez, Y.R., Gryson, A., Blighe, F.M., Cadek, M., Nicolosi, V., Blau, W.J., Gun'ko, Y.K., and Coleman, J.N. (2008) *Scripta Materialia*, **58**, 69.

98 Musumeci, A.W., Silva, G.G., Liu, J.W., Martens, W.N., and Waclawik, E.R. (2007) *Polymer*, **48**, 1667.

99 Mitchell, C.A. and Krishnamoorti, R. (2007) *Macromolecules*, **40**, 1538.

100 Park, C., Ounaies, Z., Watson, K.A., Crooks, R.E., Smith, J., Lowther, S.E., Connell, J.W., Siochi, E.J., Harrison, J.S., and St Clair, T.L. (2002) *Chemical Physics Letters*, **364**, 303.

101 Ounaies, Z., Park, C., Wise, K.E., Siochi, E.J., and Harrison, J.S. (2003) *Composites Science and Technology*, **63**, 1637.

102 Mclachlan, D.S., Chiteme, C., Park, C., Wise, K.E., Lowther, S.E., Lillehei, P.T., Siochi, E.J., and Harrison, J.S. (2005) *Journal of Polymer Science Part B: Polymer Physics*, **43**, 273.

103 Sandler, J.K.W., Kirk, J.E., Kinloch, I.A., Shaffer, M.S.P., and Windle, A.H. (2003) *Polymer*, **44**, 5893.

104 Brau, S., Demont, P., Peigney, A., Laurent, C., and Lacabanne, C. (2003) *Macromolecules*, **36**, 5187.

105 Li, N., Huang, Y., Du, F., He, X., Lin, X., Gao, H., Yanfeng Ma, Y., Li, F., Chen, Y., and Eklund, P.C. (2006) *Nano Letters*, **6**, 1141.

106 Curran, S.A., Ajayan, P.M., Blau, W.J., Carroll, D.L., Coleman, J.N., Dalton, A.B., Davey, A.P., Drury, A., McCarthy, B., Maier, S., and Strevens, A.A. (1998) *Advanced Materials*, **10**, 1091.

107 Coleman, J.N., Curran, S., Dalton, A.B., Davey, A.P., McCarthy, B., Blau, W., and Barklie, R.C. (1998) *Physical Review B: Condensed Matter*, **58**, 7492.

108 Dang, Z.M., Wang, L., Yin, Y., Zhang, Q., and Lei, Q.Q. (2007) *Advanced Materials*, **19**, 852.

109 Yang, J., Xu, T., Lu, A., Zhang, Q., and Fu, Q. (2008) *Journal of Applied Polymer Science*, **109**, 720.

110 Wu, B., Hu, D., Kuang, Y., Liu, B., Zhang, X., and Chen, J. (2009) *Angewandte Chemie International Edition*, **48**, 4751.

111 Kannan, R., Kakade, B.A., and Pillai, V.K. (2008) *Angewandte Chemie International Edition*, **47**, 2653.

112 Hewitt, C.A., Kaiser, A.B., Roth, S., Craps, M., Czerw, R., and Carroll, D.L. (2012) *Nano Letters*, **12**, 1307.

113 Ham, M.-H., Paulus, G., Lee, C.Y., Song, C., Kalantar-Zadeh, K., Choi, W., Han, J.-H., and Strano, M.S. (2010) *ACS Nano*, **4**, 6251.

114 Hyder, M., Lee, S.W., Cebeci, F., Schmidt, D., Shao-Horn, Y., and Hammond, P.T. (2011) *ACS Nano*, 5, 8552.

115 Gwinner, M.C., Jakubka, F., Gannott, F., Sirringhaus, H., and Zaumseil, J. (2012) *ACS Nano*, **6**, 539.

116 Maggini, L., Raquez, J.-M., Marega, R., Ahrens, J., Pineux, F., Meyer, F., Dubois, P., and Bonifazi, D. (2013) *ChemSusChem*, **6**, 367.

117 Yu, Z., Niu, X., Liu, Z., and Pei, Q. (2011) *Advanced Materials*, **23**, 3989.

118 Shao, S., Zhou, S., Li, L., Li, J., Luo, C., Wang, J., Li, X., and Weng, J. (2011) *Biomaterials*, **32**, 2821.

119 Terasawa, N., Ono, N., Mukai, K., Koga, T., Higashi, N., and Asaka, K. (2012) *Carbon*, **50**, 311.

11
Applications of Polymer-Based Nanocomposites

Thien Phap Nguyen

11.1
Introduction

A composite material is made by using two or more different materials to form a unique one having, expectedly, the best properties of one or all the components. Depending on the materials used, several results can be obtained. The first possibility is the case of composites possessing the expected properties of one component but none from the others. In this case, it will be used for the properties of that component, and the other component(s) will serve as a support, which may be useful for putting the composite material in shape. The second possibility concerns composites having the expected properties of all the components and therefore can be used for obtaining the combined properties. Of course, the structure of the composites has a strong impact on their properties [1], and the preparation technique of composites is highly important for controlling the structural characteristics and hence their properties that could then be used for practical applications.

In this chapter, we focus on polymer (organic material)-based composites, which are made by using a polymer (or an organic material) and an inorganic material together in a matrix. These composites present a wide range of applications based on the attractive properties of the polymers (lightweight, large surface, ease to put in shape, and low cost). They are generally used as a matrix and inorganic materials are incorporated into this matrix as fillers. In most cases, the size of the fillers is in the nanometer range, and such a composite is called a nanocomposite. Both the matrix and the fillers can play a prime role in the determination of the physical properties of the composites, and the potential applications will depend on the choice of the properties of the component to be used.

The chapter is organized as follows. First, the different preparation techniques and their consequences on the structure of the composites are shortly recalled. Applications in the most important and representative fields including mechanical, thermal, optical, electrical and energy, and biomedical are given. Finally, the issues and the future of the composite use are discussed.

Polymer Composites: Volume 2, First Edition. Edited by Sabu Thomas, Kuruvilla Joseph, Sant Kumar Malhotra, Koichi Goda, and Meyyarappallil Sadasivan Sreekala.

11.2
Preparation of Polymer-Based Nanocomposites

Polymers used as a matrix in composites can be nonconjugated (such as poly(methyl methacrylate) (PMMA)) or conjugated (such as poly(phenylene vinylene) (PPV)). While the former is usually electrically insulating, the latter is semiconducting. Both have interesting optical properties but poor mechanical behavior. For obtaining a polymer film, the common technique uses an adapted solvent to dissolve the polymer material and the film is deposited by spin coating or casting of the solution in a controlled manner on a substrate.

The fillers are generally inorganic materials, but in some cases they can have an organic structure. They can be classified into particles (oxides and quantum dots (QDs)), one-dimensional (1D) elements (sheets), two-dimensional (2D) elements (nanotubes and whiskers), and three-dimensional (3D) elements (core–shell quantum dots). The geometrical shape of the fillers affects their dispersion in the polymer matrix. It is usually necessary to obtain a uniform distribution of the fillers inside the volume of the polymer host in order to avoid filler aggregation, which can modify the characteristics of the composites. Indeed, the organization of the fillers in the matrix influences their properties by two effects. The first effect is the formation of filler aggregates or small clusters due to the fact that the interaction between the fillers and the polymer is weak, and their dispersion in the matrix is poor. These formations can drastically change the electrical transport through the composite films, as well as their mechanical properties. The second effect concerns the bridging between polymer chains, by changing their natural cross-links, which in turn leads to a modification of the thermal behavior of the polymer. Therefore, after incorporation of the fillers into the polymer solution, mechanical mixing (stirring or sonication) is necessary and the homogeneity of the composites will then depend on the medium viscosity and the reactivity. Another way to prevent the fillers from aggregating is to coat them by a polymer shell to reduce their surface energy, thus reducing their interaction. The technique consists of dispersing the fillers in a polymer solution, which will be precipitated in a nonsolvating phase. It can also be realized by *in situ* polymerization of monomers, which are previously deposited on the surface of the fillers. In the latter process, a nanocomposite is formed (fillers coated by a polymeric shell).

The various ways of dispersion of the fillers in the composite can be best illustrated by layered clay and polymer mixing (Figure 11.1). The fillers are in the form of sheets that are a few nanometer thick and a few hundred nanometer

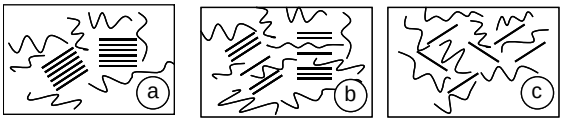

Figure 11.1 Different possibilities of layered clay dispersion in a polymer matrix: (a) phase separation; (b) intercalated structure; (c) exfoliated (delaminated) structure.

long. If they are spatially close enough to prevent the polymer chains to be inserted between the sheets, there will be a *phase separation* of the materials. When one or a few chains can intercalate between the clay layers, which preserves their ordered spatial arrangement, the structure is called *intercalated*. If all the sheets are uniformly distributed in the polymer matrix with random orientation, the composite is *exfoliated* or *delaminated*. To check the structure of such composites, X-ray diffraction is an efficient technique. In the exfoliated structure, no clay diffraction peaks will be found, and in phase-separated and intercalated structures, these peaks are apparent but shifted because of the change in the spacing between diffraction planes.

The preparation techniques of composites have a great influence on the properties of the materials and their use in applications.

11.3
Applications of Nanocomposites

11.3.1
Mechanical Properties and Applications

Polymers have very low mechanical characteristics but are useful because of their flexibility in applications requiring such a property. They are usually deformed at high strain under loading. It is possible to make strong and flexible materials by using a polymer matrix and nanosized hard fillers. Several particulate fillers are used for improving mechanical properties and decreasing weight, such as carbon black, silica, clay, and oxide. The incorporation of fillers in the polymer reinforces its strength and stiffness and also favors heat conduction. It is well known that carbon black is added to rubber in tires to reduce the thermal damage and improve their lifetime. More recently, new fillers with high mechanical properties have been considered for polymer–composite fabrication. Among these new materials, carbon nanotubes (CNTs) have remarkable mechanical characteristics making them ideal candidates to be used in applications.

CNTs are an allotropic form of carbon. They have two different forms: (i) single-walled CNTs (SWCNTs), which are formed by a single layer of graphene sheet and rolled into a cylindrical tube, and (ii) multiwalled CNTs (MWCNTs), which are composed of several concentric tubes. These materials are hollow and have a large contact surface, which favors bondings with polymer chains. Furthermore, they are chemically inert and support high oxidation stability. From the mechanical viewpoint, CNTs have high Young's moduli ($\sim$1 TPa) and strength ($\sim$100 GPa) [2], which enable their use in sports equipment such as tennis rackets or golf clubs. One of the drawbacks of the materials is their tendency to form bundles due to van der Waals interactions, which prevent the uniform dispersion of the tubes in the host matrix. Therefore, it is necessary to functionalize the nanotubes [3] in order improve the interaction with the polymer. The process consists of grafting functional groups on the sidewalls of the tubes. For instance, carboxylic (COOH) groups grafted on the

CNT surface have been proven to reinforce the CNT–polymer interaction leading to improved Young's modulus and strength of the composites [4,5]. A large number of CNT-based composites have been realized to reinforce the mechanical behavior of polymers such as polyurethane [6] and polyimide [7]. A very high improvement in the mechanical characteristics of the polymer has been obtained for a low CNT content (0.5 wt%) in polyimide composites [7]. In general, the CNT content does not exceed 5 wt% and produces a large increase in Young's modulus and strength in most cases. A well-documented report of CNT-based polymer composites with their mechanical properties has been recently published by Spitalsky *et al.* [8].

Another material family that is particularly interesting for the fabrication of composites with enhanced mechanical performance consists of polymer–clay and layered silicate [9]. These materials can be found in the nature and their cost is low compared to that of nanotubes. The most commonly used materials are montmorillonite, hectorite, and saponite. As previously mentioned, the preparation of composites needs special care for obtaining well-dispersed clay sheets in the polymer matrix (exfoliated composites) since their properties strongly depend on the uniform distribution of the fillers. When this condition is fulfilled, a large increase in moduli of the nanocomposites could be obtained with less than 1% clay content. The most known example of clay–polymer composites is that using polyamide or nylon 6 [10,11]. This polymer possesses high tensile strength and is chemically stable and therefore has a wide field of application in thread and string production. A significant increase in the Young's modulus and the strength of the polymer was observed when incorporating less than 5% of clay. However, the organoclay structure strongly affects the morphology of the composites and a very careful choice of the modifier to improve the interaction between the clay and the polymer is particularly important for obtaining reliable results [11].

Another application domain of nanocomposites in the mechanical field is their use as solid lubricants. Indeed, polymers are known to have high friction and wear coefficient. Friction is defined as a force existing between two surfaces or a force of a medium acting on a moving object. The friction coefficient is then the ratio of the force resisting sliding to the normal force. Wear is an erosion of a surface by the action of another surface or solid. The wear rate is the volume of material removed per unit of normal load per unit distance of sliding (units: $mm^3/(N\ m)$). Adding fillers, especially nanoparticles, to a polymer matrix may improve both friction and wear coefficient. The mechanism can be explained by the fact that a better adhesion between the polymer and the particles is due to the large contact surface. This adhesion prevents the particles to be pulled out, and thus improves the wear. However, the choice of the filler size is necessary because these fillers can also abrade the counterface. Ideally, the fillers should present the same size scale as the counterface asperities in order to fill them when putting the surfaces into contact. Polytetrafluoroethylene (PTFE) is a popular material for tribological applications in space technology because it has low friction, can stand high temperatures, and is chemically inert. Loading oxide nanoparticles onto PTFE allows a significant reduction in the wear of the polymer while the friction slightly increases [11–13]. When using alumina particles of 40 nm size and at a concentration of 20 wt%, the

PTFE composites exhibit an improved wear resistance by more than two orders of magnitude [13]. Recently, more applications using new fillers such as clay or CNTs have been realized. For instance, kaolin particles of formula $(OH)_8Si_4Al_4O_{10}$ and of 100 nm size added to PFTE drastically improve the wear loss from ~715 to 8 mm^3. The use of SWCNTs shows a limited improvement in wear resistance because the nanotubes do not have strong interactions with the polymer [14].

Potential applications of nanocomposites in automotives include strengthened lightweight components such as exterior parts of cars and window glasses coated with composite thin films.

11.3.2
Thermal Properties and Applications

Two interesting aspects of polymer nanocomposites are considered for applications exploiting the thermal properties of these materials.

The first aspect concerns the improvement in the thermal conductivity κ of polymers, which usually have a low heat conduction and high thermal expansion coefficient (CTE). Efficient heat transfer by conduction requires materials of high thermal conductivity, acting as a heat sink [15]. These parameters are of prime importance in electronic packaging because of the increase in dissipated heat power density of integrated circuits. The traditional nanocomposites using epoxy resins ($\kappa \sim 0.2$ W/(m K), CTE $\sim 90\,^{\circ}C^{-1}$) with ceramic fillers such as silica, alumina, and aluminum nitride (AlN) have been studied for electronic device encapsulation [16]. However, the thermal conductivity and the CTE improvements in these composites were modest. More materials have been proposed to improve the heat dissipation and the CTE including silicon [17], AlN, silicon carbide (SiC), or boron nitride (BN) [18] used as fillers in polymer matrices. The chosen fillers have high thermal conductivities and low CTE. The most promising materials are CNT-based nanocomposites because of their very high value of thermal conductivity ($\kappa \sim 3000$–6000 W/(m K)) [19], and the CNTs can form thermal conducting paths throughout the film surface. Both SWCNTs and MWCNTs have been used in polymer composites and show effective improvements in the thermal conductivity by more than 150% with, however, a relatively high CNT content (~20 wt%) [20]. This value does not correspond to the percolation threshold found in electrical characteristics of CNT-based composites, which is usually smaller than 0.5% [21]. A possible cause of the low thermal conduction can be the high thermal resistance between the overlaps of the tubes inside the polymer matrix. Therefore, some new techniques have been proposed to reduce the thermal loss. For instance, aligned MWCNTs embedded in silicone elastomer [22] greatly enhanced the thermal conductivity (0.65 W/(m K)) with low CNT loading (~0.3 wt%) compared to dispersed CNT composites (~0.03 W/(m K) with the same loading). A new architecture of nanocomposites using both MWCNTs and Al_2O_3 microparticles has been proposed recently to disperse the CNT network within the polymer matrix [23]. The idea is based on the fact that the conductivity of the composite should depend on that of the CNTs and not on the thermal contacts between them. Therefore, if the dispersion of

nanotubes is optimized, a percolation threshold should be observed. A drastic increase in the thermal conductivity was obtained, reaching 0.4 W/(m K) in this system for 0.15 wt% of CNTs, which is obviously the percolation threshold. These experiments tend to prove that the dispersion of fillers remains the principal issue for obtaining high-quality nanocomposites. Such a process can be simplified by using 2D carbon nanosheets incorporated into an epoxy polymer [24]. The heat transport would occur along the carbon planes, avoiding thermal loss at polymer–filler interfaces. The measured thermal conductivity in these materials is close to 80 W/(m K) for 33 vol% carbon nanosheets, which is very high compared to CNT-based composites. Applications of high thermal conductivity composites can also be found in thermal pastes for providing high thermal contact conductance across mating surfaces. The advantage of these pastes over conventional pastes using metal or ceramic particles is the nanosize of the materials, allowing a high compressibility and a larger contact area between the surfaces. SWCNTs added to polyethylene glycol-based dispersion at 0.6 vol% provide a thermal contact conductance of 20×10^4 W/(m^2 K), which is better than that of commercial products using silver or ceramic pastes [25].

The second aspect of nanocomposite use for their thermal properties concerns their stability and flammability [26]. By their nature, polymers are flammable materials and their ignition temperature is generally low as compared to metals or inorganic compounds. When exposed to high heat, their surface is decomposed, producing a mixture of combustible gases (usually toxic), solid residue, and liquid products, which react with oxygen in air resulting in an additional heat production and an acceleration of the combustion. The degradation of a decomposed polymer can be characterized by parameters such as the onset temperature (T_{osX} is the temperature that records X% weight loss of material) and the temperature of maximum weight loss rate (T_{peak} is the temperature representing the maximum in the rate of mass change or the rate of degradation). It can be determined from thermal gravimetric experiments by plotting the mass change as a function of the temperature (dm/dT). To reduce the flammability of polymers, fire retardants are added to the polymer matrix to interrupt the combustion process, forming polymer composites. The fillers include halogenated organics (vapor release), inorganic hydroxide (water release), and inorganic particles. Despite their efficiency, the halogenated fire retardants are toxic and unfriendly for environment while the efficiency of hydroxide retardants is at the expense of its mechanical properties. Nanoparticle fillers are highly attractive for this purpose, because they can improve both the physical and flammability properties of the polymer nanocomposite. New nanomaterials have been prepared for flame retardant polymers such as CNTs [27], clay [28], or polyhedral oligomeric silsesquioxane (POSS) [29]. In both CNTs and clay composites, it was found that the onset temperature and the temperature of maximum weight loss rate are higher than those in the pure polymer. The flame retardancy can be explained either by the improvement in the thermal conductivity of composites, which facilitates the heat release and delays the degradation, or by the slower degradation rate of polymer chains in contact with the fillers. In most cases, it was observed that a network of fillers was formed on the residue surface after

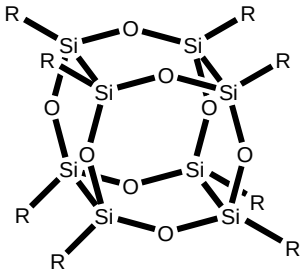

Figure 11.2 Structure of polyhedral oligomeric silsesquioxane. R represents organic substitution groups.

combustion [30]. This network may hinder the ejection of decomposed products by creating a protective layer during the combustion and then delay the onset of degradation. In POSS composites, the polymer chains are attached to an inorganic core structure (silicon and oxygen) by the organic units (also called functional groups), which provide compatibility or reactivity to the polymer matrix. The structure of POSS is given in Figure 11.2. The inorganic part of POSS provides thermal stability and fire resistance to the composites and the organic part in fire retardant systems, a reinforcement of the polymer chains, by changing the viscosity and the mechanical properties, contributes to the improvement in the heat resistance of the composites. It has been demonstrated in POSS–epoxy nanocomposites that the nature of the nonreactive ligands to the POSS core has a strong effect on the flammability of the composites (phenyl ligands are more efficient than isobutyl ligands). A reduction of 40% in heat release rate was obtained for 3.7 wt% POSS incorporation. Some improvements in the thermal stability and the fire retardancy of polypropylene-based composites have been observed by adding metal atoms (aluminum) to the corner of the POSS core [31] as compared to bare POSS. However, substituting aluminum by zinc atoms, there are no significant changes in the polymer combustion behavior.

11.3.3
Electrical Properties and Applications

Conductive polymer composites have been realized for improving the electrical properties of the polymer by the incorporation of conductive particles into the matrix, which is generally insulating. In this way, the electrical characteristics of such composites will be close to those of the conductive particles whereas the mechanical characteristics and the processing techniques are typical for polymers. These materials are intended to replace as far as possible nonconducting polymer matrix in applications. Using a similar technique to fabricate cermets, metal particles have been incorporated into polymers [32] to increase their conductivity. However, these fillers are heavy and expensive. Therefore, modern nanocomposites are made with highly conducting particles, in particular with CNTs.

The composites become electrically conductive when the filler content reaches a limit value, known as the percolation threshold. Starting from this value, the conductivity of the composite increases sharply by the gradual formation of a conductive pathway through the polymer matrix and then tends to that of the fillers. The dependence of the conductivity on the filler concentration is given by a scaling law of the form

$$\sigma = \sigma_0(\Phi - \Phi_C)^t, \tag{11.1}$$

where σ is the composite conductivity, Φ is the filler concentration, Φ_C is the percolation threshold, and t is the critical exponent.

The electrical conductivity of polymer/CNTs has been extensively studied. Recent databases for these composites have been established for comparison with the values of percolation threshold and critical exponent [8,33]. It can be seen that there is a large discrepancy between these values. The percolation threshold has been reported to range from 0.0025 to several wt%, and many parameters such as dispersion [34], alignment [35], polymer type [36], and processing methods [37] seem to have a strong effect on Φ_C. The maximum value of the conductivity for nanocomposites also seems to be dependent on the polymer and the CNT type. A composite conductivity of ~3000 S/m has been reported for MWCNT/PMMA composites with a low percolation threshold (~0.003 wt%) [38], while it is only 0.1 S/m for polyvinyl chloride (PVC)/ultrahigh molecular weight polyethylene (UHMWPE) but with very much lower percolation threshold (~0.0004 wt%) [39].

The use of conductive polymer composites in electrical applications is multifold. By adjusting the filler concentration in the polymer matrix to control the conductivity of the materials, it is possible to provide a range of electrical resistivity for electrical and electronic components to control, in turn, the electrical conduction, static charge dissipation, and lightning protection. On the other hand, the dielectric constant of the composites can also be controlled by modifying the filler amount [40,41]. Polymers have low dielectric constant and fillers usually have high dielectric constant. At concentrations close to the percolation threshold, the dielectric loss usually increases dramatically as the resistivity decreases suddenly. Therefore, a controlled combination of electrical resistivity and dielectric constant through the filler can provide nanocomposites that are suitable for cable accessories, for instance. In this field, as carbon provides a good reflection of electromagnetic radiation, polymer composites are efficient for electromagnetic interference (EMI) shielding and also for waveguiding. EMI shielding consists of reflecting the electromagnetic radiation by a material, which must have highly mobile carriers to interact with the electromagnetic field. These materials should be conductive like metals, in which electrons are free. Conventional metals for EMI shielding can be made by bulky pieces, by coated thin films, and by fibers, and new conductive composites are attractive for replacing them due to their good mechanical properties as well as their easy processability. The efficiency of EMI shielding is expressed by the shielding effectiveness (SE), which is defined by

$$\mathrm{SE} = 10\log\frac{P_{\mathrm{in}}}{P_{\mathrm{out}}}, \tag{11.2}$$

where P_{in} and P_{out}, respectively, are the power of incident and transmitted waves through the shield.

For commercial or military applications, a high value of SE in the range of 40–80 dB is needed. In PMMA/SWCNT composites [42], the SE values are found to be dependent on the nanotube content over the X band (8–12 GHz) and the microwave (200–2000 MHz) frequency range. For 15 wt% SWCNTs, the measured SE varies from 26 to 35 dB. For MWCT/PMMA composites, a SE value of 27 dB was reported, which is still to be improved. The improvement can be achieved by using conducting polymers (such as polyaniline (PANI) and polypyrrole (PPy)) mixed with metal fillers to increase the electrical conductivity. The SE measured for PANI/Ag composites in the frequency range from 10 MHz to 1 GHz is ~50 dB [43], which is acceptable for commercialization. Another approach using buckypaper (BP), which is a thin film of entangled CNTs, has shown that the EMI shielding could be greatly improved by the high concentration of CNTs in this structure and thus their high electrical conductivity [44]. A single layer of BP shows a maximum SE value of 60 dB and using BP multilayer this value is close to 100 dB, with an additional advantage, which is the possibility to fabricate large panel surface. Another possibility to produce more convenient and practical supports for composite materials concerns the deposition of thin films by spray directly onto fabric [45], a cheap and simple process for obtaining highly conductive composites.

Several other applications of the conductive polymer composites can also be found in heaters [46], thermistors [47], and strain sensing devices [48], among others, and this list is not exhaustive, considering the very quick developments of nanotechnology.

11.3.4
Optical Properties and Applications

Most of the important applications of polymer-based nanocomposites have been realized in the optical area by the interesting association of the organic and inorganic components. Usually, optical composites are seen to be mixtures of a functional material and a processable matrix [49]. Optically functional parts include quantum-confined semiconductors, inorganic oxides, organic materials (small molecules), and polymers. The processable matrix materials are usually polymers but can also be copolymers, polymer blends, glass, or ceramics.

Depending on the optical function of the materials, two application fields can be distinguished. The first applications concern the transmission of light and the second ones concern the optical energy transformation by the composites.

11.3.4.1 Transmission of Light

In the first category of composites, the properties of the functional part are combined with the polymer matrix to provide stable structures such as waveguides, thick coatings, and UV absorbing layers while maintaining high transparency. Passive films used for optical devices need high transparency, which is usually altered by addition of nanofillers. These are inorganic nanoparticles of metals or

semiconductors, which are optical additives for polymers. Introduction of nanoparticles, even transparent ones, leads to translucent or opaque materials because of light scattering by the particles. In order to minimize this effect, the particles should have small sizes and should be well dispersed in the polymer matrix. Indeed, the intensity loss of transmitting light by scattering varies with particle size, and can be taken into account for particles of diameters above 100 nm [50]. Using nanosized particles (<10 nm), composite films are practically transparent if no significant aggregations occur. Highly transparent films could be realized using silica or titania particles in different polymer matrices [51,52]. Particle agglomeration probability increases when their size decreases, leading to strong scattering of incident light. Therefore, a method for preventing aggregation of particles is required for obtaining transparent composites. This can be realized by hydrophobization of inorganic nanoparticles (SiO_2) before incorporating them into a polymer matrix [53]. Another technique using core–shell structured nanoparticles with controlled refractive index (RI) by varying the shell content added to an epoxy matrix exhibits an 87% transmittance at 800 nm [54]. On the other hand, quantum size effects have to be considered. They include the color emission dependence on the (small) particle size, which can affect the expected optical properties of the films.

For applications that need high RI composites, it is necessary to use metal oxide of high RI as fillers. As conventional polymers have RI in the range from 1.4 to 1.6, and the RI of multicomponent materials can be calculated by [55]

$$n_C^2 = \sum_i n_i^2 V_i, \tag{11.3}$$

where n_i and V_i are the RI and volume fraction of the individual component, respectively, the incorporation of inorganic particles can provide RI value in the range from 1.5 to 1.9 [56]. Lead sulfide (PbS) [57] having high RI (>4) is promising for the fabrication of high RI composite materials. In a similar way, low-index composite materials can also be prepared using metal fillers in polymer matrices. Composites with RI close to 1 could be obtained by using gold in gelatin with metal content up to 90 wt%. Applications of these materials include antireflection films, lenses, waveguides, and so on. Antireflection coatings are used to favor the light transmittance at the surface of the optical devices, and thus decrease the reflection loss. To cover the visible range, it is usual to use multilayer structures, which combine alternate layers of high and low RI. The RI of each layer can be controlled by adjusting the relative inorganic/organic content [58] and reflectance as low as 1% could be obtained in the visible range (at 550 nm). Other applications of high RI composites concern photonic bandgap materials, which allow the control of the light flow through them by the difference in the RI values in different parts. These composites will allow the confinement of light within some parts of the materials and since the wavelengths of photons are inversely proportional to their energy, light of certain wavelengths will pass through these parts and light of other wavelengths will be blocked [59]. 3D waveguides and microlenses using inorganic–organic hybrid polymer networks have been prepared with low optical loss [60].

Several composite materials have been used for optical limiting owing to their interesting nonlinear scattering properties. These materials exhibit nonlinear extinction of a strong intensity radiation, while transmitting it normally at low intensity. The transmitted fluence tends to be constant and independent of the input fluence, whatever its intensity. Such behavior is exploited to control and prevent damage risk of laser beams, for instance. The nanocomposites should have large nonlinear refractive index and fast response time. Polyaniline with silver nanoparticles is a good material [61] for optical limiting, as well as CNT-based composites [62].

11.3.4.2 **Energy Conversion**

In the second category of nanocomposites, the functional part is combined with the polymer matrix to enhance the energy conversion of the polymer. These materials are particularly interesting for practical applications, and we shall focus on two types of devices, which will have a strong impact on the everyday life in the near future. These are organic light emitting diodes (OLEDs) and organic photovoltaic cells (OPVs).

OLEDs Since the first commercial product, a screen for car stereo, launched by Pioneer in 1997, OLED technology has been widely developed. Applications of display screens can be found in mp3 players, cameras, cell phones, and 11.7 inch TV produced by Sony in 2010 with high brightness (600 cd/m^2) and expected long lifetime (10 years).

An organic light emitting diode is composed of an active layer, which is an organic material (small molecules or conjugated polymer) sandwiched between two electrodes. The positively biased electrode or anode is a transparent conductive material (usually indium tin oxide (ITO)) and the negatively biased electrode is a low-work function metal (usually calcium or barium). The thickness of each layer is a few hundred nm (usually 100 nm for the active layer). The working principle of OLEDs is shown in Figure 11.3. Electrons from the cathode and holes from the anode are injected into the active layer over potential barriers at the contacts upon application of a voltage to the diode. In a basic device, the electrodes are in direct contact with the active layer but such a structure is not efficient because the amount of injected charge carriers is low. Indeed, additional layers are intercalated between the active layer and the electrodes to improve the charge injection and thus the efficiency of light emission. These layers are called transport layers: hole transport layer (HTL) at the anode side and electron transport layer (ETL) at the cathode side. Inside the active layer, electrons and holes are transported to recombination centers, where they form excitons. Only the radiative decay of excitons provides photons whose energy corresponds to the wavelength of the emitted radiation that will propagate out of the diode, giving rise to the emitted light. The color of the emitted light depends on the optical gap of the active material. To date, all colors in the visible spectrum can be obtained with the use of available conjugated polymers and small molecules. Therefore, there is a real interest for producing OLEDs for displays because of many advantages that they can offer to these devices, such as lightweight,

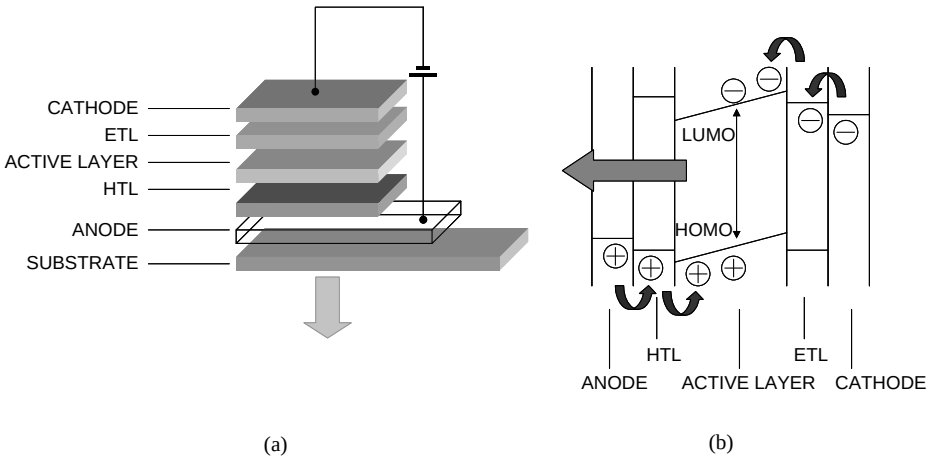

Figure 11.3 Working principle of OLEDs: (a) structure of OLEDs; (b) schematic energy band diagram and light emitting process.

large emitting surface, low cost (small amount of material used), and large panel of colors [63].

To describe and compare the performance of OLEDs, several parameters are defined. The first parameter is the external quantum efficiency η_e, which is defined as the ratio between the number of emitted photons and the number of injected charges. It expresses the ability of the material to convert electrical energy to luminous energy and can be written as

$$\eta_e = \frac{h\nu}{eV}, \tag{11.4}$$

where h is the Planck constant, ν is the frequency, e is the electronic charge, and V is the applied voltage. The second parameter is the total power efficiency η_T, defined as the ratio between the number of collected photons in the external medium and the number of injected charges. Indeed, not all the emitted photons in the active region are emitted into the external medium because of reabsorption or internal reflections. The η_T efficiency expresses the conversion ability of the whole device, and can be written as

$$\eta_T = \eta_e \eta_O, \tag{11.5}$$

where η_O is the optical efficiency, defined as the ratio between the number of the collected photons outside the diode and the number of the emitted photons inside the diode.

It can be seen from Eq. (11.5) that the efficiency of OLEDs depends on the number of created photons in the active material, which is a function of the number of transported carriers and the charge balance. As a matter of fact, the motilities of holes and electrons are different in organic materials, holes being more mobile than

electrons in general. As a consequence, there will be locally an unbalanced charge state inside the organic material and the carrier recombination can occur at the border of the active layer (either at the anode or at the cathode contact), leading to a low recombination rate and a high loss of photons due to quenching resulting from the carrier accumulation. On the other hand, the device efficiency also depends on the optical outcoupling, that is, the extraction of photons out of the devices.

In practice, the performance of OLEDs is also evaluated by their lifetime, which should address industrially applicable levels (~10 000 h). The short lifetime of devices results from degradations occurring in different parts of the diode during operation. Several degradation processes have been identified such as thermal instabilities, chemical and photooxidation of the active layer, and diffusion of metal from electrodes [64].

Nanocomposite materials are used in OLEDs for improving their performance in different ways. The principal use concerns incorporation of nanoparticles into an emitting polymer matrix. These particles are usually oxide or semiconductor materials but CNTs and clay are also used for many applications.

Oxide nanoparticles such as TiO_2 or SiO_2 are added to luminescent conjugated polymers for obtaining a high current intensity, and thus, expectedly, an increase in efficiency [65]. Although they are insulating, their organization inside the polymer films can enhance the electrical field and then can favor the current flow. With a small content of oxide particles (<5%), light scattering effect is negligible and the optical properties of polymer are not affected by the transparent particles.

Semiconductor nanoparticles or nanocrystals (NCs) in composites are usually emitting materials, such as cadmium selenide (CdSe) [66], zinc sulfide (ZnS) [67], and other compounds containing sulfur [68]. When a nonluminescent polymer matrix is used, the emitted light will be that of the semiconductor material [69]. If the polymer matrix is luminescent, then color emission can be from both materials. For instance, in the case of CdSe/PPV composites, the red light of particles was observed at low current intensity and then progressively it changed to green light of the polymer at high intensity [66]. One interesting optical property of the NCs is the confinement effect when the size of the particles becomes small enough (quantum dots). The bandgap of QDs increases when their size decreases, and the emitted light can be modulated by changing the particle size. For CdSe, when the size of the particles varies from 2 to 6 nm, the corresponding light covers a wide range of colors from blue to red [70]. This property is exploited for obtaining white light OLEDs by incorporating core–shell QDs of CdSe/ZnS having three different sizes (corresponding to red, green, and blue emission) into a diphenylcarbazole matrix [71].

As for CNTs used in polymer composites, their role is to enhance the injection of both electrons and holes into the polymer because of the absence of potential barrier between CNTs and the electrodes [72]. A maximum electroluminescence (EL) efficiency is obtained in poly(methoxy(ethylhexyloxy)–*p*-phenylene vinylene) (MEHPPV)/SWCNTs with 0.02 wt% CNT concentration, and higher CNT content leads to a decrease in the EL response [73].

The modifications in the device emission properties produced by the composites as compared to pure organic material can be explained as follows.

First, the deposition of the composite layer is carried out by spin coating of the particle containing polymer solution on the substrate covered by an HTL. For some materials, during the drying phase, nanoparticles tend to accumulate at the bottom of the deposited film by gravitation [74], enhancing the surface contact between the active layer and the HTL. Consequently, the injection current increases and, in turn, improves the device efficiency. As an example, devices using MEHPPV with TiO_2 or SiO_2 nanoparticles show an increase in performance, in both current density and external quantum efficiency, by a factor of 10 as compared to that of pure polymer-based devices [75]. On the other hand, in some cases, the incorporated particles can form a conducting pathway through the active layer when the concentration is sufficiently high, thus improving the carrier mobility [76]. It should be noted that although oxide particles are insulating, their surface conductivity is sufficient to favor the formation of a conducting pathway. It is also possible that aggregation of particles, which occurs when the concentration of particles becomes important, could improve the charge balance by blocking selectively one type of carriers and therefore enable their recombination with counterparts [70]. In this case, the carrier transport would not be improved and can even be reduced because of the formation of insulating aggregates in the active film. The light emission is instead enhanced due to the charge balance improvement.

Second, incorporation of inorganic particles improves the physical properties of the polymer matrix, especially their thermal and chemical resistance. Degradation experiments clearly show that composite films are much more stable than the pristine-conjugated polymer when exposed to light and air [77]. The presence of inorganic particles in diodes may also prevent electrical shorts by creating a long and tortuous pathway for charge carriers [75], increasing the stability during the diode operation. It is also shown that the particles of very small size could stabilize the polymer structure by neutralizing defects [78] that are sources of chemical degradation reactions in the material. Therefore, OLEDs using composite materials usually exhibit longer lifetime than those having a pristine polymer as an active layer.

In addition, polymer composites are also used as transparent anode in OLEDs to replace ITO. As a matter of fact, although widely used, ITO is suspected to be one of the possible causes for premature degradation of organic devices by the decomposition of its surface upon contact with the polymer film. Diffusion of metal atoms into the polymer film has been observed even when protected with a poly(3,4-ethylenedioxythiophene):poly(styrene sulfonate) (PEDOT:PSS) layer [79]. In addition, thin films are deposited at high temperature and their rigidity is an issue for applications requiring flexibility. Highly transparent and conductive films can be fabricated using the PEDOT:PSS matrix with less than 3 wt% SWCNTs [80]. The resistivity of composite films (3 Ω cm at 3 wt%) is much lower than that of pristine PEDOT:PSS (1000 Ω cm), making it suitable for the transparent electrode. Similar composites using PANI matrix with CNTs have been adapted for inkjet printing with low resistivity [81], although the performance of these materials is lower than that of PEDOT:PSS-based composites. Another composite material using ITO nanoparticles embedded in a PEDOT:PSS matrix with graded work function shows an

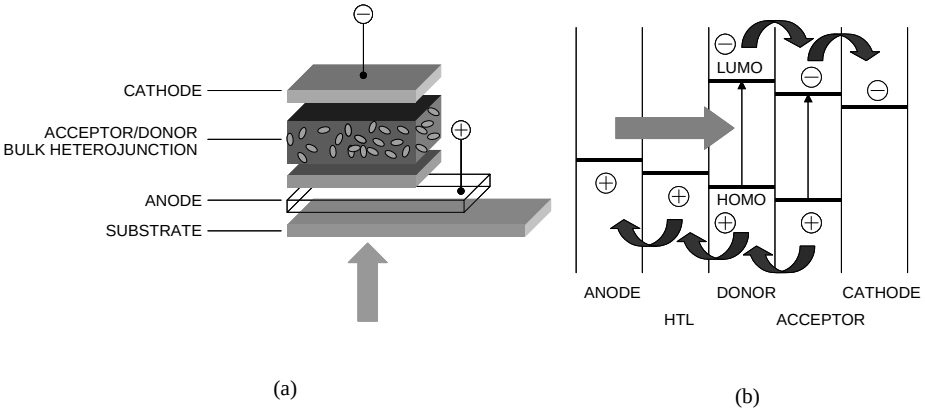

Figure 11.4 Working principle of OPVs: (a) structure of bulk heterojunction OPVs; (b) schematic energy band diagram and energy conversion process.

improved turn-on voltage (67% reduction) as compared to devices using the standard PEDOT:PSS layer [82].

OPVs The development of organic solar cells was initiated by the success of OLED technology when commercial products started to become available on the market. With the energy crisis, OPVs have become a research goal to provide cheap and eco-friendly energy to replace silicon solar cells, which are expensive due to the production cost.

The working principle of an OPV is shown in Figure 11.4. The active material is composed of two components: electron-donor and electron-acceptor materials. Under illumination of the photoactive layer, photons with energy equal to or greater than the bandgap are absorbed and bound electron–hole pairs or excitons are created. These excitons diffuse into the material over a distance called diffusion length, ranging from 5 to 15 nm before dissociation into electrons and holes. If the dissociation occurs in the vicinity of the donor–acceptor interface, the charges will be collected by the components and then transported through them and collected by corresponding electrodes. If it is not the case, they will be lost either by trapping or by recombination.

To define the efficiency of solar cells, the following main parameters are used. First, the external quantum efficiency η_{EQE} (also called the input photon conversion efficiency η_{IPCE}) is defined as the number of generated electrons per incident photon. For a given wavelength λ (nm), it is expressed by

$$\eta_{EQE} = \frac{J_{sc}hc}{P_0\lambda e} = \frac{1240J_{sc}}{P_0\lambda}, \tag{11.6}$$

where J_{sc} is the short-circuit current density (A/cm^2), P_0 is the light incident power (W/cm^2), h is the Planck constant, c is the speed of light in vacuum, and e is the electronic charge. Second, the energy (or power) conversion efficiency η is defined as

the ratio between the maximum power output P_{max} and the power of incident light P_0. It is given by

$$\eta = \frac{P_{max}}{P_0}. \tag{11.7}$$

The standard conditions for efficiency measurements are labeled AM1.5, which correspond to a temperature of 25 °C, an irradiance of 100 mW/cm^2, and an air mass 1.5 spectrum. To optimize the performance of OPVs, it is necessary to maximize the light absorption by using a low-bandgap polymer, which allows harvesting of photons available in the visible spectrum. In addition, the exciton dissociation should be efficient; that is, the collection of the separated charge should be in operation for almost all of them. This can be carried out by using dispersed or bulk heterojunction, where donors and acceptors are mixed in such a way that the contact size between the two components is comparable to the exciton diffusion length in the material. That is why nanocomposites are well adapted for obtaining high-efficiency OPV materials. Further required properties of materials concern the highest occupied molecular orbital (HOMO) and the lowest unoccupied molecular orbital (LUMO) of the two components. They should provide a sufficient offset for charge separation to increase the amount of collected charges. To date, the highest power conversion efficiency obtained in bulk heterojunction polymer is 7.4% [83] and theoretical calculation predicts a possible value of 15% [84].

From the material point view, there are two types of nanocomposites for OPVs: organic particles (especially derivatives of fullerene C_{60}) in a polymer matrix and inorganic particles (semiconductors) in a polymer matrix. The host polymer for both groups is a hole conductor and plays the role of an electron donor. To contribute efficiently to the energy conversion, it should have a strong absorbance and a good electrical conductivity. Polymers such as MEHPPV and poly(3-hexylthiophene) (P3HT) are well adapted for composites.

For the first group of composites, the most used organic particles, which are electron conductors and electron acceptors, are poly(9,9′-dioctylfluorene-*co*-bis-*N*,*N*′-(4-butylphenyl)-bis-*N*,*N*′-phenyl-1,4-phenylenediamine) (F8TB) and fullerene derivatives, especially 6,6-phenyl-C_{61}-butyric acid methyl ester (PCBM). The best performance is usually obtained in devices using the P3HT–PCBM combination ($\eta \sim 5\%$ under AM1.5) [85], although several investigations of new devices based on thieno[3,4-*b*]thiophene and benzodithiophene polymers (PTBs) have recently showed higher efficiency [83].

For the second group of composites, nanoparticles of metal oxides such as TiO_2 [86] and ZnO [87] or semiconductors such as CdSe [88] and ZnSe [89] are incorporated into the polymer to form a blend. These systems have an advantage from the semiconductor particles, which have a high conductivity and high electron mobility. However, the low mobility of polymer holes is inefficient for charge removal at the polymer–particle interfaces. The best efficiency reported in cadmium sulfide (CdS):poly(3-octylthiophene) (P3OT)-based solar cells [90] reached ~2.8%, which is much lower than that of P3HT–PCBM cells. Devices using vertically

ordered inorganic arrays of rods of diameter less than the exciton diffusion length exhibit higher efficiency than dispersed nanoparticles [91].

The performance of both types of composites in OPVs is still modest as compared to semiconductor-based solar cells. Improvement in the layer morphology and development of low-bandgap organic materials can lead to higher power conversion efficiencies. An estimation of the maximum expectable efficiency of bulk heterojunction cells predicts that 10% for solar cells will be reached in the next few years, while practical values of 20–25% would be the limits of the best devices, still to be realized [92]. However, even with low but acceptable $\eta \sim 5\%$, mass production of low-cost cells will be a nice solution for renewable energy sources. The main and difficult to solve issue is the stability of the devices, which should attain industrial commercialization requirements. Stable operation for more than 4000 h has been reported for P3HT:PCBM bilayer structure cells and can be further improved [93].

11.4
Energy Conversion and Storage Capacity and Applications

In the field of energy conversion and storage, polymer nanocomposites are well adapted for electrode materials in lithium ion batteries (LIBs) and superconductors. Generally speaking, conducting polymers such as PANI, PPy, or polythiophene (PT) are used in composites because they can be positively or negatively charged with the Li ions to compensate the injected charges.

For energy conversion, LIBs are lightweight and rechargeable power sources for laptop computers, cameras, cell phones, and in the near future for electric vehicles. A LIB is composed of an anode (such as carbon or metal oxides), an electrolyte (lithium salt in liquid or solid form [94]), and a cathode (metal oxides or lithium transition metal oxides). In order to provide a high energy and a high current density, the electrode materials should have a high charge density (number of available charge carriers per unit of volume), a high voltage (difference between the redox potentials between cathode and anode), and a high reversibility of electrochemical reactions [95]. On the cathode side, nanocomposites of conducting polymer and oxide are used for improving the performance of the electrode. Indeed, the polymer can enhance the conductivity of metal oxide and the rate of Li ion migration from the electrode. For instance, nanostructured vanadium oxide (V_2O_5) has high energy and high power densities and can be used in batteries for electric vehicles. Combined with PANI, the nanohybrid containing 30 mol% polyaniline exhibits a stable capacity of ~300 mAh/g, with significantly enhanced stability [96]. For transition metal oxides, olivine $LiFePO_4$ is a popular material for cathode in LIB because of its stability and high capacity, but it has a low conductivity and ion diffusivity. In order to increase its conductivity, a thin conducting layer of a few nanometer thickness is deposited on its surface. Using composites of $LiFePO_4$/PPy as a cathode in batteries with $LiNO_3$ aqueous electrolyte, the discharge capacity significantly increases as compared to bare $LiFePO_4$ (~49 and ~12 mAh/g, respectively, at 0.1 C) by an improved conductivity of the electrode [97]. Another composite

structure used for cathode is polymer–carbon such as PANI–CNTs. These composites show a high discharge capacity (~139 mAh/g) as well as a good cyclability in lithium metal–polymer cells with ionic liquid electrolyte [98].

For energy storage, supercapacitors are used because of their high capacity and their high charging–discharging rate. A supercapacitor has two electrodes immersed in an electrolyte. The stored energy depends on the electrode surface, so materials used for electrode should have a large surface area. On the other hand, the charge transport in the electrode and at the electrolyte–electrode interface should be high. Therefore, a porous material having a good electrical conductivity is expected for electrodes in supercapacitors. Composites of MWCNTs and PPy have been used as an active electrode with an aqueous electrolyte in supercapacitors, and have shown significantly higher values for capacitance as compared to structures with bare MWCNT electrodes (123 and 5 F/g, respectively, for the CNTs showing the largest difference). More recently, graphene of high electrical conductivity (~7200 S/m) has also been used for flexible electrodes in capacitors with aniline–H_2SO_4 electrolyte. The capacitance of the obtained structures is very high (147 F/g) due probably to the high conductivity of graphene. It could be further improved by replacing the electrode material by a graphene–PANI composite ($C \sim 233$ F/g) since the polymer has lower conductivity. Another approach to enhance the capacitance is to modify the surface structure of the electrode for increasing the electrolyte–electrode contact surface. This has been realized by growing PANI onto the surface of porous carbon [99]. The average diameter of the carbon channels is ~4 nm and their length is ~1 μm. They limit the size of the diffusion length and allow the formation of ordered whisker-like PANI needles of ~10–20 nm diameter and ~80–100 nm length. These needles have V-like shape and when put into contact with the electrolyte, a fast penetration of electrolyte into the pores occurs and the diffused ions can be almost utilized. Capacitance as high as ~1220 F/g has been obtained with this nanocomposite used as electrodes in supercapacitors.

11.5 Biodegradability and Applications

Biodegradation is a process by which a material is naturally decomposed and converted into simple compounds by living organisms. Biodegradable polymers can be natural or synthetic materials. Natural polymers include starch, chitosan, proteins, and derivatives, while synthetic polymers comprise polylactic acid (PLA), polyglycolic acid (PGA), and polyhydroxybutyrate (PHB). When used in nanocomposites, these polymers are useful for applications in medicine, drug release, and food packaging.

11.5.1 Nanocomposites for Medical Applications

The polymers should be biocompatible; that is, in intimate contact with living tissue, they should not produce any undesirable effects in the host system.

In tissue engineering, nanocomposites are designed to develop biological substitutes in order to restore, maintain, or improve tissue function. The most known applications in the field of tissue engineering are bone regeneration and repair [100]. Natural bone is formed of a hydroxyapatite (HA, $Ca_{10}(PO_4)_6(OH)_2$) matrix and a protein-based hydrogel template. Nanocomposites for bone tissue engineering are fabricated by using calcium phosphate nanofillers with a biocompatible polymer, which gives a soft structure adapted to the fixation of the composite on the surface of the broken bones. The calcium phosphate plays the role of a precursor and facilitates the bone apatite formation, whereas the polymer provides a good mechanical behavior to the composites. Several polymers can be used for such composites: cellulosic ether [101], chitosan [102], and PLA [103]. These materials are well adapted for bone repair but it is difficult to control the structure of the composite. Another approach for tissue engineering is the fabrication of 3D porous scaffolds serving as a template for new tissue growth, where the cells can stay and develop. A scaffold should have appropriate pore size in order to allow the supply of nutrients and the evacuation of waste for cells. It should also have a sufficient surface, an adequate porosity, and a good mechanical structure. On the other hand, it should be eliminated after the tissue formation. MWCNTs have been used with chitosan to form a scaffold of nanocomposite, which was tested with success *in vitro* and *in vivo* [104]. Ultrashort SWCNTs used with poly(propylene fumarate) and dodecylated US-tube to form a scaffold for marrow cells have shown good cell attachment and proliferation [105]. However, after elimination the CNTs have been found in blood and the biocompatibility and cytotoxicity of CNTs are still to be investigated to make sure that the use of these materials is safe for health [106]. Therefore, standard polymer–bioceramic composites for scaffolds are still used for bone regeneration. Besides HA, bioactive glasses have excellent biocompatibility and ability for bone bonding. These materials are composed of SiO_2, Na_2O, CaO, and P_2O_5 and their surface can release Ca, P, Na, and Si ions upon reactions with the biological fluid [107], and thus produce a bioactive HA layer that can bond to tissue. Polymers such as PLA [108] and polyurethane [109] have been successfully used with bioglass to form composite scaffold for bone tissue engineering.

The biomaterials for bone tissue are also available for dental applications. However, there are additional requirements on the properties of materials used for dental restorations. Indeed, the composites should have good mechanical (high hardness, wear resistance, adhesion) and thermal (low conductivity, polymerization shrinkage) properties and at the same time should be as esthetic as natural tooth [110]. Usually, polymers for dental composites are based on methacrylate chemistry, for instance, 2,2-bis-[4-(2-hydroxy-3-methacryloyloxypropyl)phenyl]propane (Bis-GMA) is a popular polymer for dental resin [111]. Materials for inorganic fillers are comprised of silica, alumina, or barium glass particles. For improving the physical properties of composites, new materials using nanostructures such as nanoclays [112] or nanorods [113] to increase the mechanical property of the adhesive layer or POSS [114] to increase the thermal stability and to reduce polymerization shrinkage are used.

11.5.2
Nanocomposites for Drug Release Applications

The nanocomposites are formed by adding the drug to a polymer matrix; the latter may itself be a composite material. A drug delivery substance is designed to carry a drug into a targeted site, and to release it progressively at a predetermined rate, in the surrounding tissues. The mechanisms of loading and release of drug from the systems depend on their nature.

For polymer composites, several materials are potentially important for the development of new drug delivery systems. In polymeric nanoparticles, the drug is incorporated inside a surrounding polymer membrane (nanocapsules) or uniformly distributed in the polymer matrix (nanoparticles). The drug loading is achieved either by direct incorporation during the fabrication of the nanoparticles or by absorption of the drug after their formation. The drug release occurs by diffusion through the polymer matrix and also by the biodegradation of the polymer [115]. Biodegradable polymers such as chitosan and PLA are widely used for these systems. In order to control the drug release rate, clay has been added to the polymer, which sustains release of drug by electrostatic interaction [116].

Hydrogels are other efficient drug delivery systems. These are cross-linked polymer networks containing hydrophilic groups but are not water soluble. Because of the water penetration, hydrogels are swollen and are deformable to be confined in places where they are located. For drug loading, the drug is added to the matrix during the cross-linking of the polymer chains or by diffusion after the formation of the network. The drug will be released by diffusion through the pores of hydrogel, whose size is controlled by the swollen state of the material. Chitosan-based hydrogels have been investigated for drug delivery, mainly hydrophilic and small molecules, in different configurations [117,118]. To expand the range of drugs such as large molecular or hydrophobic drugs to be delivered, new strategies have been proposed, for instance, to form a solid molecular dispersion of a poorly soluble drug by using an appropriate solvent to bind the drug to the polymer chains via hydrogen bonding [119].

Dendrimers are a new concept of polymers that has been recently introduced to fabricate drug delivery systems. These materials are composed of two different parts: the inner part is a spherical core made of a polymer or an organic molecule, surrounded by a surface group, which is designed to possess specific functions. In drug delivery use, the core is usually hydrophobic and the drug is covalently attached to the periphery of the dendrimer or is coordinated to the outer functional groups via ionic interactions. The composites are used for antiviral or antibacterial treatment but also as antitumor agents [120].

11.5.3
Nanocomposites for Food Packaging

Food packaging polymers should fulfill several requirements for practical usage and safe preservation of food. First, they should have good mechanical properties but

should be biodegradable and of low cost. Second, they should have antibacterial activity and at the same time have gas barrier properties for preventing water and oxygen diffusion inside the package [121]. Today, most of the polymers used for food packaging fulfill these requirements except that they are not biodegraded. Conversely, biodegradable polymers present poor mechanical behavior and poor barrier quality, and are not adapted for food packaging. Nanocomposites are interesting for replacing industrial plastics and contribute to the preservation of the ecosystem. Biodegradable materials such as starch, polyesters, and PLA-based polymers are used as the host matrix and nanofillers having specific functions are incorporated into them. For instance, particles of clay contribute to enhancing the barrier property and the mechanical strength of the polymer (starch [122] and PLA [123]). Silver nanoparticles have antibacterial activity and can be associated with TiO_2 to enhance the photocatalytic bacterial inactivation [124]. TiO_2 nanoparticles play also the role of oxygen scavengers when added to polymers to sustain the deterioration of foods [125]. CNTs also have antibacterial properties [126] but may present risks for human health and should be carefully tested before incorporation into food packaging materials. Several polymer nanoparticles exhibit particular behavior and are incorporated into the polymer matrix to improve their property for food packaging. For example, chitin [127] or starch [128] nanoparticles have been used to increase tensile strength of polymer films. They further improve the water vapor barrier properties of these films. Chitosan has antibacterial activity and its particles can be loaded in films for food packaging [129]. Antimicrobial and water-resistant papers that have been fabricated for food packaging using chitosan with hydrophobic compounds [130] may be a future material for packaging applications.

11.6 Conclusion and Outlook

Within more than a decade, nanoscience and nanotechnology have been greatly developed, resulting in a wide range of techniques, processes, devices, and applications covering various fields such as mechanical, thermal, electrical, optical, energy, medical, and food, as discussed in this chapter from the aspect of polymer nanocomposites. The supplied list is not exhaustive and the treated topics could be considered as representative in this field.

Despite important progress in understanding the structure–property relationship and in successful experimentation of composite materials and devices, commercial products using polymer composites are still scarce on the market. A number of available commercial utilities taken from company and industry information are recently reviewed [131]. Among these, one can find items such as tennis balls, tennis rackets, tires, automotives, bandage, beverage containers, and so on. Various applications such as OLEDs, dental composites, batteries, and so on can also be added to this list. To explain the limited number of industrial commercialized applications, two facts can be evoked. First, economic competition requires products to be profitable, that is, there should be a high demand for them, and this will

depend on the involved economic sectors. For instance, sports equipment, electronic devices, automotives, and plastics for food packaging may expect a high commercial impact because consumers would be more interested in these products. Second, the fabrication of some composite products requires a high-level control of materials and processes that results in a high cost of production and commercially unfavorable operation.

From the scientific viewpoint, a number of issues are yet to be solved for improving the quality of the material as well as the fabrication process. An important factor to warrant the properties of composites is the quality of the fillers. They should have a well-defined distribution and will therefore need a precise control over the fabrication process. The dispersion of fillers in the polymer matrix should also be carefully performed and controlled for obtaining reliable expected properties. Future developments of nanotechnology should take into account this aspect to simplify the fabrication process by keeping the same material quality. The concept of nanocomposites may be oriented toward a better organization of the structure with ordered or aligned nanofillers, to allow production of high-quality materials at low cost.

Special attention is paid to CNTs, which are the most promising fillers for applications. Although the fabrication techniques have been greatly improved, high-quality CNTs are still expensive, and it is expected that the production cost could be reduced in the future to allow a wider range of commercialized products. The effects of CNTs in particular and other inorganic nanoparticles in general on human health are still not well known and efforts should be spent to overcome the problems before using them in everyday consumer goods.

References

1 Jancar, J., Douglas, J.F., Starr, F.W., Kumar, S.K., Cassagnau, P., Lesser, A.J., Sternstein, S.S., and Buehler, M.J. (2010) Current issues in research on structure–property relationships in polymer nanocomposites. *Polymer*, **51**, 3321–3343.

2 Eder, D. (2010) Carbon nanotube–inorganic hybrids. *Chemical Reviews*, **110**, 1348–1385.

3 Sahoo, N.G., Rana, S., Cho, J.W., Lin, L., and Chan, S.H. (2010) Polymer nanocomposites based on functionalized carbon nanotubes. *Progress in Polymer Science*, **35**, 837–867.

4 Singh, P., Campidelli, S., Giordani, S., Bonifazi, D., Bianco, A., and Prato, M. (2009) Organic functionalisation and characterisation of single-walled carbon nanotubes. *Chemical Society Reviews*, **38**, 2214–2230.

5 Byrne, M.T. and Gun'ko, Y.K. (2010) Recent advances in research on carbon nanotube–polymer composites. *Advanced Materials*, **22**, 1672–1688.

6 Kuan, H.C., Ma, C.C.M., Chang, W.P., Yuen, S.M., Wu, H.H., and Lee, T.M. (2005) Synthesis, thermal, mechanical, and rheological properties of multiwalled carbon nanotubes/waterborne polyurethane nanocomposite. *Composites Science and Technology*, **65**, 1703–1710.

7 Chou, W.J., Wang, C.C., and Chen, C.Y. (2008) Characteristics of polyimide-based nanocomposites containing plasma modified multi-walled carbon nanotubes. *Composites Science and Technology*, **68**, 2208–2213.

8 Spitalsky, Z., Tasis, D., Papagelis, K., and Galiotis, C. (2010) Carbon nanotube–polymer composites: chemistry,

processing, mechanical and electrical properties. *Progress in Polymer Science*, **35**, 357–401.
9 Alexandre, M. and Dubois, P. (2000) Polymer-layered silicate nanocomposites: preparation, properties and uses of a new class of materials. *Materials Science Engineering and Technology*, **R28**, 1–63.
10 Fedullo, N., Sorlier, E., Sclavons, M., Bailly, C., Lefebvre, J.M., and Devaux, J. (2007) Polymer-based nanocomposites: overview, applications and perspectives. *Progress in Organic Coatings*, **58**, 87–95.
11 Fornes, T.D., Hunter, D.L., and Paul, D.R. (2004) Nylon-6 nanocomposites from alkylammonium-modified clay: the role of alkyl tails on exfoliation. *Macromolecules*, **37**, 1793–1798.
12 Li, F., Hu, K.A., Li, J.L., and Zhao, B.Y. (2001) The friction and wear characteristics of nanometer ZnO filled polytetrafluoroethylene. *Wear*, **249**, 877–882.
13 Sawyer, W.G., Freudenberg, K.D., Bhimaraj, P., and Schadler, L.S. (2003) A study on the friction and wear behavior of PTFE filled with alumina nanoparticles. *Wear*, **254**, 391–588.
14 Vail, J.R., Burris, D.L., and Sawyer, W.G. (2009) Multifunctionality of single-walled carbon nanotube–polytetrafluoroethylene nanocomposites. *Wear*, **267**, 619–624.
15 Chung, D.D.L. (2001) Materials for thermal conduction. *Applied Thermal Engineering*, **21**, 1593–1605.
16 Wong, C.P. and Bollampally, R.S. (1999) Thermal conductivity, elastic modulus, and coefficient of thermal expansion of polymer composites filled with ceramic particles for electronic packaging. *Journal of Applied Polymer Science*, **74**, 3396–3403.
17 Dey, T.K. and Tripathi, M. (2010) Thermal properties of silicon powder filled high-density polyethylene composites. *Thermochimica Acta*, **502**, 35–42.
18 Lee, G.W., Park, M., Kim, J., Lee, J.I., and Yoon, H.G. (2006) Enhanced thermal conductivity of polymer composites filled with hybrid filler. *Composites A*, **37**, 727–734.
19 Schelling, P.K., Shi, L., and Goodson, K.E. (2005) Managing heat for electronics. *Materials Today*, **8**, 30–35.
20 Yu, C., Kim, Y.S., Kim, D., and Grunlan, J.C. (2008) Thermoelectric behavior of segregated-network polymer nanocomposites. *Nano Letters*, **8**, 4428–4432.
21 Stéphan, C., Nguyen, T.P., Lahr, B., Blau, W., Lefrant, S., and Chauvet, O. (2002) Raman spectroscopy and conductivity measurements on polymer–multiwalled carbon nanotubes composites. *Journal of Materials Research*, **17**, 396–400.
22 Huang, H., Liu, C.H., Wu, Y., and Fan, S. (2005) Aligned carbon nanotube composite films for thermal management. *Advanced Materials*, **17**, 1652–1656.
23 Bozlar, M., He, D., Bai, J., Chalopin, Y., Mingo, N., and Volz, S. (2010) Carbon nanotube microarchitectures for enhanced thermal conduction at ultralow mass fraction in polymer composites. *Advanced Materials*, **22**, 1654–1658.
24 Veca, L.M., Meziani, M.J., Wang, W., Wang, X., Lu, F., Zhang, P., Lin, Y., Fee, R., Connell, J.W., and Sun, Y.P. (2009) Carbon nanosheets for polymeric nanocomposites with high thermal conductivity. *Advanced Materials*, **21**, 2088–2092.
25 Xu, Y., Leong, C.K., and Chung, D.D.L. (2007) Carbon nanotube thermal pastes for improving thermal contacts. *Journal of Electronic Materials*, **36**, 1181–1187.
26 Laoutid, F., Bonnaud, L., Alexandre, M., Lopez-Cuesta, J.M., and Dubois, Ph. (2009) New prospects in flame retardant polymer materials: from fundamentals to nanocomposite. *Materials Science and Engineering*, **R50**, 100–125.
27 Beyer, G. (2002) Carbon nanotubes as flame retardants for polymers. *Fire and Materials*, **26**, 291–293.
28 Kashiwagi, T., Harris, R.H.Jr., Zhang, X., Briber, R.M., Cipriano, B.H., Raghavan, S. R., Awad, W.H., and Shields, J.R. (2004) Flame retardant mechanism of polyamide 6–clay nanocomposites. *Polymer*, **45**, 881–891.
29 Glodek, T.E., Boyd, S.E., McAninch, I.M., and LaScala, J.J. (2008) Properties and performance of fire resistant eco-composites using polyhedral oligomeric silsesquioxane (POSS) fire retardants.

Composites Science and Technology, **68**, 2994–3001.

30 Rahatekar, S.S., Zammarano, M., Matko, S., Koziol, K.K., Windle, A.H., Nyden, M., Kashiwagi, T., and Gilman, J.W. (2010) Effect of carbon nanotubes and montmorillonite on the flammability of epoxy nanocomposites. *Polymer Degradation and Stability*, **95**, 870–879.

31 Fina, A., Abbenhuis, H.C.L., Tabuan, D., and Camino, G. (2006) Metal functionalized POSS as fire retardants in polypropylene. *Polymer Degradation and Stability*, **91**, 2275–2281.

32 Jana, S., Salehi-Khojin, A., Zhong, W.H., Chen, H., Liu, X., and Huo, O. (2007) Effects of gold nanoparticles and lithium hexafluorophosphate on the electrical conductivity of PMMA. *Solid State Ionics*, **178**, 1180–1186.

33 Bauhofer, W. and Kovacs, J.Z. (2009) A review and analysis of electrical percolation in carbon nanotube polymer composites. *Composites Science and Technology*, **69**, 1486–1498.

34 Xie, N., Jiao, O.J., Zang, C.G., Wang, C.L., and Liu, Y.Y. (2010) Study on dispersion and electrical property of multi-walled carbon nanotubes/low-density polyethylene nanocomposites. *Materials & Design*, **31**, 1676–1683.

35 Wang, Q., Dai, J., Li, W., Wei, Z., and Jiang, J. (2008) The effects of CNT alignment on electrical conductivity and mechanical properties of SWNT/epoxy nanocomposites. *Composites Science and Technology*, **68**, 1644–1648.

36 Kovacs, J.Z., Velagala, B.S., Schulte, K., and Bauhofer, W. (2007) Two percolation thresholds in carbon nanotube epoxy composites. *Composites Science and Technology*, **67**, 922–928.

37 Li, J., Ma, P.C., Chow, W.S., To, C.K., Tang, B.Z., and Kim, J.K. (2007) Correlations between percolation threshold, dispersion state, and aspect ratio of carbon nanotubes. *Advanced Functional Materials*, **17**, 3207–3215.

38 Kim, H.M., Kim, K., Lee, S.J., Joo, J., Yoon, H.S., Cho, S.J., Lyu, S.C., and Lee, C.J. (2004) Charge transport properties of composites of multiwalled carbon nanotube with metal catalyst and polymer: application to electromagnetic interference shielding. *Current Applied Physics*, **4**, 577–580.

39 Lisunova, M.O., Mamunya, Y.P., Lebovka, N.I., and Melezhyk, A.V. (2007) Percolation behaviour of ultrahigh molecular weight polyethylene/multi-walled carbon nanotubes composites. *European Polymer Journal*, **43**, 949–958.

40 Dang, Z.M., Xia, B., Yao, S.H., Jiang, M.J., Song, H.T., Zhang, L.O., and Xie, D. (2008) High-dielectric-permittivity high-elasticity three-component nanocomposites with low percolation threshold and low dielectric loss. *Applied Physics Letters*, **94**, 0429021–0429023.

41 Sengwa, R.J., Choudhary, S., and Sankhla, S. (2010) Dielectric properties of montmorillonite clay filled poly(vinyl alcohol)/poly(ethylene oxide) blend nanocomposites. *Composites Science and Technology*, **70**, 1621–1627.

42 Das, N.C., Liu, Y., Yang, K., Peng, W., Maiti, S., and Wang, H. (2009) Single-walled carbon nanotube/poly(methyl methacrylate) composites for electromagnetic interference shielding. *Polymer Engineering and Science*, **49**, 1627–1634.

43 Joo, J. and Lee, C.Y. (2000) High frequency electromagnetic interference shielding response of mixtures and multilayer films based on conducting polymers. *Journal of Applied Physics*, **88**, 513–518.

44 Park, J.G., Louis, J., Cheng, Q., Bao, J., Smithyman, J., Liang, R., Wang, B., Zhang, C., Brooks, J.S., Kramer, L., Fanchasis, P., and Dorough, D. (2009) Electromagnetic interference shielding properties of carbon nanotube buckypaper composites. *Nanotechnology*, **20**, 4157021–4157027.

45 Hecht, D.S., Hu, L., and Grüner, G. (2007) Electronic properties of carbon nanotube/fabric composites. *Current Applied Physics*, **7**, 60–63.

46 El-Tantawy, F., Kamada, K., and Ohnabe, H. (2002) *In situ* network structure, electrical and thermal properties of conductive epoxy resin–carbon black composites for electrical heater

applications. *Materials Letters*, **56**, 112–126.
47 Wang, S. and Chung, D.D.L. (1999) Temperature/light sensing using carbon fiber polymer–matrix composite. *Composites Part B: Engineering*, **30**, 591–601.
48 Wang, S. and Chung, D.D.L. (2006) Self-sensing of flexural strain and damage in carbon fiber polymer–matrix composite by electrical resistance measurement. *Carbon*, **44**, 2739–2751.
49 Beecroft, L.L. and Ober, C.K. (1997) Nanocomposite materials for optical applications. *Chemistry of Materials*, **9**, 1302–1317.
50 Caseri, W. (2000) Nanocomposites of polymers and metals or semiconductors: historical background and optical properties. *Macromolecular Rapid Communications*, **21**, 705–722.
51 Yu, Y.Y. and Chen, W.C. (2003) Transparent organic–inorganic hybrid thin films prepared from acrylic polymer and aqueous monodispersed colloidal silica. *Materials Chemistry and Physics*, **82**, 388–395.
52 Khanna, P.K., Singh, N., and Charan, S. (2007) Synthesis of nano-particles of anatase–TiO_2 and preparation of its optically transparent film in PVA. *Materials Letters*, **61**, 4725–4730.
53 Stelzig, S., Klapper, M., and Müllen, K. (2008) A simple and efficient route to transparent nanocomposites. *Advanced Materials*, **20**, 929–932.
54 Li, Y.Q., Fu, S.Y., Yang, Y., and Mai, Y.W. (2008) Facile synthesis of highly transparent polymer nanocomposites by introduction of core–shell structured nanoparticles. *Chemistry of Materials*, **20**, 2637–2643.
55 Yamasaki, T. and Tsutsui, T. (1998) Spontaneous emission from fluorescent molecules embedded in photonic crystals consisting of polystyrene microspheres. *Applied Physics Letters*, **72**, 1957–1959.
56 Guan, C., Lü, C.L., Liu, Y.B., and Bai, Y. (2006) Preparation and characterization of high refractive index thin films of TiO_2/epoxy resin nanocomposites. *Journal of Applied Polymer Science*, **102**, 1631–1636.
57 Lü, C., Guan, C., Liu, Y., Cheng, Y., and Bai, Y. (2006) PbS/polymer nanocomposite optical materials with high refractive index. *Chemistry of Materials*, **17**, 2448–2454.
58 Chen, C.C., Lin, D.J., Don, T.M., Huang, F.H., and Cheng, L.P. (2008) Preparation of organic–inorganic nano-composites for antireflection coatings. *Journal of Non-Crystalline Solids*, **354**, 3828–3835.
59 Texter, J. (2003) Polymer colloids in photonic materials. *Comptes Rendus Chimie*, **6**, 1425–1433.
60 Houbertz, R., Fröhlich, L., Popall, M., Streppel, U., Dannberg, P., Bräuer, A., Serbin, J., and Chichkov, B.N. (2003) Inorganic–organic hybrid polymers for information technology: from planar technology to 3D nanostructures. *Advanced Engineering Materials*, **5**, 551–555.
61 Sezer, A., Gurudas, U., Collins, B., Mckinlay, A., and Bubb, D.M. (2009) Nonlinear optical properties of conducting polyaniline and polyaniline–Ag composite thin films. *Chemical Physics Letters*, **477**, 164–168.
62 O'Flaherty, S.M., Hold, S.V., Brennan, M. E., Cadek, M., Drury, A., Coleman, J.N., and Blau, W.J. (2003) Nonlinear optical response of multiwalled carbon-nanotube dispersions. *Journal of the Optical Society of America*, **20**, 49–58.
63 Nguyen, T.P. and Jolinat, P. (2008) Physics and technology of organic light emitting diodes, in *Handbook of Organic Electronics and Photonics* (ed. H.S. Nalwa), American Scientific Publishers, pp. 245–311.
64 Gardonio, S., Gregoratti, L., Melpignano, P., Aballe, L., Biondo, V., Zamboni, R., Murgia, M., Caria, S., and Kiskinova, M. (2007) Degradation of organic light-emitting diodes under different environment at high drive conditions. *Organic Electronics*, **8**, 37–43.
65 Blom, P.W.M., Schoo, H.F.M., and Matters, M. (1998) Electrical characterization of electroluminescent polymer/nanoparticle composite devices. *Applied Physics Letters*, **73**, 3914–3916.
66 Colvin, V.L., Schlamp, M.C., and Alivisatos, A.P. (1994) Light-emitting

diodes made from cadmium selenide nanocrystals and a semiconducting polymer. *Nature*, **370**, 354–357.
67 Yang, Y., Huang, J., Liu, S., and Shen, J. (1997) Preparation, characterization and electroluminescence of ZnS nanocrystals in a polymer matrix. *Journal of Materials Chemistry*, **7**, 131–133.
68 Gaponik, N., Hickey, S.G., Dorfs, D., Rogach, A.L., and Eychmüller, A. (2010) Progress in the light emission of colloidal semiconductor nanocrystals. *Small*, **6**, 1364–1378.
69 Althues, H., Palkovits, R., Rumplecker, A., Simon, P., Sigle, W., Bredol, M., Kynast, U., and Kaskel, S. (2006) Synthesis and characterization of transparent luminescent ZnS:Mn/PMMA nanocomposites. *Chemistry of Materials*, **18**, 1068–1072.
70 Lee, C.W., Chou, C.H., Huang, J.H., Hsu, C.S., and Nguyen, T.P. (2008) Investigations of organic light emitting diodes with CdSe(ZnS) quantum dots. *Materials Science and Engineering*, **B147**, 307–311.
71 Li, Y.Q., Rizzo, A., Cingolani, R., and Gigli, G. (2006) Bright white-light-emitting device from ternary nanocrystal composites. *Advanced Materials*, **19**, 2545–2548.
72 Fournet, P., Coleman, J.N., Lahr, B., Drury, A., Blau, W.J., O'Brien, D.F., and Hörhold, H.H. (2001) Enhanced brightness in organic light-emitting diodes using a carbon nanotube composite as an electron-transport layer. *Journal of Applied Physics*, **90**, 969–975.
73 Xu, Z., Wu, Y., Hu, B., Ivanov, I.N., and Geohegan, D.B. (2005) Carbon nanotube effects on electroluminescence and photovoltaic response in conjugated polymers. *Applied Physics Letters*, **87**, 263118-1–263118-3.
74 Yang, S.H., Nguyen, T.P., Le Rendu, P., and Hsu, C.S. (2005) Optical and electrical investigations of poly(*p*-phenylene vinylene)/silicon oxide and poly(*p*-phenylene vinylene)/titanium oxide nanocomposites. *Thin Solid Films*, **471**, 230–235.
75 Carter, S.A., Scott, J.C., and Brock, P.J. (1997) Enhanced luminance in polymer composite light emitting diodes. *Applied Physics Letters*, **71**, 1145–1147.
76 Nguyen, T.P., Le Rendu, P., Lakehal, M., Joubert, P., and Destruel, P. (2000) Poly(*p*-phenylene vinylene)/porous silicon composites. *Materials Science Technology B*, **69–70**, 177–181.
77 Yang, S.H., Le Rendu, P., Nguyen, T.P., and Hsu, C.S. (2007) Fabrication of MEH-PPV/SiO_2 and MEH-PPV/TiO_2 nanocomposites with enhanced luminescent stabilities. *Reviews on Advanced Materials Science*, **14**, 14–34.
78 Lee, C.W., Renaud, C., Hsu, C.S., and Nguyen, T.P. (2008) Traps and performance of MEH-PPV/CdSe(ZnS) nanocomposite-based organic light-emitting diodes. *Nanotechnology*, **19**, 4552021–4552027.
79 Nguyen, T.P. and de Vos, S.A. (2004) An investigation into the effect of chemical and thermal treatments on the structural changes of poly(3,4-ethylenedioxythiophene)/polystyrenesulfonate and consequences on its use on indium tin oxide substrates. *Applied Surface Science*, **221**, 330–339.
80 Carroll, D.L., Czerw, R., and Webster, S. (2005) Polymer–nanotube composites for transparent, conducting thin films. *Synthetic Metals*, **155**, 694–697.
81 Denneulin, A., Bras, J., Blayo, A., Khelifi, B., Roussel-Dherbey, F., and Neuman, C. (2009) The influence of carbon nanotubes in inkjet printing of conductive polymer suspensions. *Nanotechnology*, **20**, 3857011–38570110.
82 Yilmar, O.F., Chaudhary, S., and Ozkan, M. (2006) A hybrid organic–inorganic electrode for enhanced charge injection or collection in organic optoelectronic devices. *Nanotechnology*, **17**, 3662–3667.
83 Liang, Y., Xu, Z., Xia, J., Tsai, S.T., Wu, Y., Li, G., Ray, C., and Yu, L. (2010) For the bright future-bulk heterojunction polymer solar cells with power conversion efficiency of 7.4%. *Advanced Materials*, **22**, E135–E138.
84 Riede, M., Mueller, T., Tress, W., Schueppel, R., and Leo, K. (2008) Small-molecule solar cells: status and perspectives. *Nanotechnology*, **19**, 424001-1–424001-12.

85 Ma, W., Yang, C., Gong, X., Lee, K., and Heeger, A.J. (2005) Thermally stable, efficient polymer solar cells with nanoscale control of the interpenetrating network morphology. *Advanced Functional Materials*, **15**, 1617–1622.

86 Zeng, T.W., Lin, Y.Y., Lo, H.H., Chen, C. W., Chen, C.H., Liou, S.C., Huang, H.Y., and Su, W.F. (2006) A large interconnecting network within hybrid MEH-PPV/TiO_2 nanorod photovoltaic devices. *Nanotechnology*, **17**, 5387–5392.

87 Beek, W.J.E., Wienk, M.M., and Janssen, R.A.J. (2006) Hybrid solar cells from regioregular polythiophene and ZnO nanoparticles. *Advanced Functional Materials*, **16**, 1112–1116.

88 Greenham, N.C., Peng, X., and Alivisatos, A.P. (1996) Charge separation and transport in conjugated-polymer/semiconductor-nanocrystal composites studied by photoluminescence quenching and photoconductivity. *Physical Review B: Condensed Matter*, **54**, 17628–17637.

89 Yun, D., Feng, W., Wu, H., and Yoshino, K. (2009) Efficient conjugated polymer–ZnSe and –PbSe nanocrystals hybrid photovoltaic cells through full solar spectrum utilization. *Solar Energy Materials and Solar Cells*, **93**, 1208–1213.

90 Salinas, O.H., Lopez-Mata, C., Hu, H., and Nicho, M.E. (2006) Analysis of electrical parameters in heterojunctions based on poly(3-octylthiophene) and cadmium sulfide thin films. *Solar Energy Materials and Solar Cells*, **90**, 2421–2428.

91 Lee, J.C., Lee, W., Han, S.H., Kim, T.G., and Sung, Y.M. (2009) Synthesis of hybrid solar cells using CdS nanowire array grown on conductive glass substrates. *Electrochemistry Communications*, **11**, 231–234.

92 Dennler, G., Scharber, M.C., and Brabec, C.J. (2009) Polymer–fullerene bulk-heterojunction solar cells. *Advanced Materials*, **21**, 1323–1338.

93 Krebs, F.C. and Norman, K. (2007) Analysis of the failure mechanism for a stable organic photovoltaic during 10000h of testing. *Progress in Photovoltaics: Research and Applications*, **15**, 697–712.

94 Fergus, J.W. (2010) Ceramic and polymeric solid electrolytes for lithium-ion batteries. *Journal of Power Sources*, **195**, 4554–4569.

95 Wang, Y. and Cao, G. (2008) Developments in nanostructured cathode materials for high-performance lithium-ion batteries. *Advanced Materials*, **20**, 2251–2269.

96 Ponzio, E.A., Benedetti, T.M., and Torresi, R.M. (2007) Electrochemical and morphological stabilization of V_2O_5 nanofibers by the addition of polyaniline. *Electrochimica Acta*, **52**, 4419–4427.

97 Chen, S.Y., Gao, B., Su, L.H., Mi, C.H., and Zhang, X.G. (2009) Electrochemical properties of $LiFePO_4$/C synthesized using polypyrrole as carbon source. *Journal of Solid State Electrochemistry*, **13**, 1361–1366.

98 Sivakkumar, S.R., MacFarlane, D.R., Forsyth, M., and Kim, D.W. (2007) Ionic liquid-based rechargeable lithium metal–polymer cells assembled with polyaniline/carbon nanotube composite cathode. *Journal of the Electrochemical Society*, **154**, A834–A838.

99 Wang, Y.G., Li, H.Q., and Xia, Y.Y. (2006) Ordered whiskerlike polyaniline grown on the surface of mesoporous carbon and its electrochemical capacitance performance. *Advanced Materials*, **18**, 2619–2623.

100 Murugan, R. and Ramakrishna, S. (2005) Development of nanocomposites for bone grafting. *Composites Science and Technology*, **65**, 2385–2406.

101 Dupraz, A., Nguyen, T.P., Richard, M., Daculsi, G., and Passuti, N. (1999) Influence of a cellulosic ether carrier on the structure of biphasic calcium phosphate ceramic particles in an injectable composite material. *Biomaterials*, **20**, 663–673.

102 Zhang, Y., Reddy Venugopal, J.R., El-Turki, A., Ramakrishna, S., Su, B., and Lim, C.T. (2008) Electrospun biomimetic nanocomposite nanofibers of hydroxyapatite/chitosan for bone tissue engineering. *Biomaterials*, **29**, 4314–4322.

103 Deng, X., Hao, J., and Wang, C. (2001) Preparation and mechanical properties of nanocomposites of poly(D,L-lactide) with

Ca-deficient hydroxyapatite nanocrystals. *Biomaterials*, **22**, 2867–2873.

104 Abarrategi, A., Gutiérrez, M.C., Moreno-Vicente, C., Hortigüela, M.J., Ramos, V., López-Lacomba, J.L., Ferrer, M.L., and del Monte, F. (2008) Multiwall carbon nanotube scaffolds for tissue engineering purposes. *Biomaterials*, **29**, 94–102.

105 Shi, X., Sitharaman, B., Pham, Q.P., Liang, F., Wu, K., Billups, W.E., Wilson, L. J., and Mikos, A.G. (2007) Fabrication of porous ultra-short single-walled carbon nanotube nanocomposite scaffolds for bone tissue engineering. *Biomaterials*, **28**, 4078–4090.

106 Smart, S.K., Cassady, A.I., Lu, G.Q., and Martin, D.J. (2006) The biocompatibility of carbon nanotubes. *Carbon*, **44**, 1034–1047.

107 Yunos, D.M., Bretcanu, O., and Boccaccini, A.R. (2000) Polymer–bioceramic composites for tissue engineering scaffolds. *Journal of Materials Science*, **43**, 4433–4442.

108 Zhang, K., Wang, Y., Hillmyer, M.A., and Francis, L.F. (2004) Processing and properties of porous poly(L-lactide)/bioactive glass composites. *Biomaterials*, **25**, 2489–2500.

109 Ryszkowska, J.L., Auguścik, M., Sheikh, A., and Boccaccini, A.R. (2010) Biodegradable polyurethane composite scaffolds containing Bioglass® for bone tissue engineering. *Composites Science and Technology*, **70**, 1894–1908.

110 Nguyen, P. (2006) *Les polymères utilisés dans les composites dentaires: concept, développement et prospectives*. Dissertation, University of Nantes.

111 Moszner, N. and Salz, U. (2001) New developments of polymeric dental composites. *Progress in Polymer Science*, **26**, 535–576.

112 Atai, M., Solhi, L., Nodehi, A., Mirabedini, S.M., Kasraei, S., Akbari, K., and Babanzadeh, S. (2009) PMMA-grafted nanoclay as novel filler for dental adhesives. *Dental Materials*, **25**, 339–347.

113 Sadat-Shojai, M., Atai, M., Nodeh, A., and Khanlar, L.N. (2010) Hydroxyapatite nanorods as novel fillers for improving the properties of dental adhesives: synthesis and application. *Dental Materials*, **26**, 471–482.

114 Soh, M.S., Yap, A.U.J., and Sellinger, A. (2007) Methacrylate and epoxy functionalized nanocomposites based on silsesquioxane cores for use in dental applications. *European Polymer Journal*, **43**, 315–327.

115 Soppimath, K.S., Aminabhavi, T.M., Kulkarni, A.R., and Rudzinski, W.E. (2001) Biodegradable polymeric nanoparticles as drug delivery devices. *Journal of Controlled Release*, **70**, 1–20.

116 Yuan, Q., Shah, J., Hein, S., and Misra, R. D.K. (2010) Controlled and extended drug release behavior of chitosan-based nanoparticle carrier. *Acta Biomaterialia*, **6**, 1140–1148.

117 Hamidi, M., Azadi, A., and Rafiei, P. (2008) Hydrogel nanoparticles in drug delivery. *Advanced Drug Delivery Reviews*, **60**, 1638–1649.

118 Narayan Bhattarai, N., Gunn, J., and Zhang, M. (2010) Chitosan-based hydrogels for controlled, localized drug delivery. *Advanced Drug Delivery Reviews*, **62**, 83–99.

119 Hoare, T.R. and Kohane, D.S. (2008) Hydrogels in drug delivery: progress and challenges. *Polymer*, **49**, 1993–2007.

120 Boas, U. and Heegaard, P.M.H. (2004) Dendrimers in drug research. *Chemical Society Reviews*, **33**, 43–63.

121 Arora, A. and Padua, G.W. (2009) Review: Nanocomposites in food packaging. *Journal of Food Science*, **75**, R43–R49.

122 Avella, M., De Vlieger, J.J., Errico, M.E., Fischer, S., Vacca, P., and Volpe, M.G. (2005) Biodegradable starch/clay nanocomposite films for food packaging applications. *Food Chemistry*, **93**, 467–474.

123 Cabedo, L., Feijoo, J.L., Villanueva, M.P., Lagarón, J.M., and Giménez, E. (2006) Optimization of biodegradable nanocomposites based on aPLA/PCL blends for food packaging applications. *Macromolecular Symposia*, **233**, 191–197.

124 Page, K., Palgrave, R.G., Parkin, I.P., Wilson, M., Savin, S.L.P., and Chadwick, A.V. (2007) Titania and silver–titania composite films on glass: potent antimicrobial coatings. *Journal of Materials Chemistry*, **17**, 95–104.

125 Mills, A., Doyle, G., Peiro, A.M., and Durrant, J. (2006) Demonstration of a

novel, flexible, photocatalytic oxygen-scavenging polymer film. *Journal of Photochemistry and Photobiology A: Chemistry*, **177**, 328–331.

126 Kang, S., Pinault, M., Pfefferle, L.D., and Elimelech, M. (2007) Single-walled carbon nanotubes exhibit strong antimicrobial activity. *Langmuir*, **23**, 8651–8673.

127 Chang, P.R., Jian, R., Yu, J., and Ma, X. (2010) Starch-based composites reinforced with novel chitin nanoparticles. *Carbohydrate Polymers*, **80**, 420–425.

128 Kristo, E. and Biliaderis, C.G. (2007) Physical properties of starch nanocrystal-reinforced pullulan films. *Carbohydrate Polymers*, **68**, 146–158.

129 Qi, L., Xu, Z., Jiang, X., Hu, C., and Zou, X. (2004) Preparation and antibacterial activity of chitosan nanoparticles. *Carbohydrate Research*, **339**, 2693–2700.

130 Bordenave, N., Grelier, S., and Coma, V. (2010) Hydrophobization and antimicrobial activity of chitosan and paper-based packaging material. *Biomacromolecules*, **11**, 88–96.

131 Paul, D.R. and Robeson, L.M. (2008) Polymer nanotechnology: nanocomposites. *Polymer*, **49**, 3187–3204.

12
Health Hazards and Recycling and Life Cycle Assessment of Nanomaterials and Their Composites

Lucas Reijnders

12.1
Introduction

The emergence of nanotechnology has led to an increased interest in new applications of engineered inorganic nanoparticles, including C-based nanoparticles such as carbon black, fullerenes, carbon nanotubes, and carbon nanofibers. Engineered nanoparticles are defined here as particles that are <100 nm in at least one dimension. The interest in applications of engineered inorganic nanoparticles extends to their use in composites with organic polymers (nanocomposites). The use of combinations of organic polymers and engineered inorganic nanoparticles has already a substantial tradition, because rubber tires traditionally contain carbon black that is at least partly nanoparticulate [1]. Current interest in engineered inorganic nanoparticles for commercial application in polymers includes, apart from carbon-based nanoparticles, nanoclay (montmorillonite, hydrotalcite, pyrophyllite, halloysite, fluorohectorite, bentonite, beidellite, kaolinite, and sepiolite), silica (SiO_2), Ag, ZnO, CeO_2, and titania (TiO_2). Applications of these engineered inorganic nanoparticles that are studied include coatings, elastomers, resins, and plastics and focus on the improvement by nanoparticles of characteristics such as tensile strength, abrasion resistance, degradability, cleanability, hygienic properties and antimicrobial activity, sensing properties, hardness and scratch resistance, flame retardancy, cell density and size, permeability control, tear strength, weatherability, electrical conduction, hardness, stiffness, crack growth resistance, and stability [2–12].

However, the use of nanoparticles in nanocomposites may also have less desirable side effects. For instance, thermo-oxidative stability may be reduced, which may have negative consequences for performance and service time [13,14]. Furthermore, polymer degradation under solar irradiation may be increased, and hazardous nanoparticles may be released during their life cycle (which starts with resource extraction and ends with final disposal) [15,16]. The release of engineered nanoparticles from nanocomposites and the scope for reduction of hazard and risk to health during the nanocomposite life cycle are considered in this chapter. This chapter also deals with other environmental aspects of

Polymer Composites: Volume 2, First Edition. Edited by Sabu Thomas, Kuruvilla Joseph, Sant Kumar Malhotra, Koichi Goda, and Meyyarappallil Sadasivan Sreekala.

nanocomposites: environmental life cycle assessment or analysis and life cycle management, especially recycling that may reduce the life cycle environmental impact of nanocomposites.

12.2 Health Hazards of Inorganic Nanoparticles

Engineered nanoparticles may be released during the nanocomposite life cycle [16]. From the studies done so far, it is often far from clear whether the engineered particles are released as such or as part of a larger particle [16]. One would expect that hazard and risk associated with such releases are strongly dependent on the nature (e.g., size and composition) of the particles that are released in practice [16–18]. Health hazards of engineered inorganic nanoparticles have been studied to a limited extent [17–30]. To the extent that they have been studied, most studies have regarded engineered nanoparticles as such. Little attention has been given to functionalized, compatibilized, organomodified, and coated nanoparticles. Inorganic nanoparticles treated with functionalizing, organomodifying, and compatibilizing substances are often used in polymeric nanocomposites to promote dispersion of nanoparticles in polymeric matrices. Coatings on inorganic nanoparticles and functionalization can be used to suppress unwanted characteristics. A case in point is the coating of TiO_2 nanoparticles with silica or alumina to suppress the photocatalytic activity of TiO_2 nanoparticles [16]. The nanoparticles whose hazards will be discussed here are SiO_2 nanoparticles, fullerenes, carbon nanofibers and nanotubes, nanoclay, nanosilver, and ZnO and TiO_2 nanoparticles. Regarding the latter, SiO_2-coated TiO_2 nanoparticles will also be considered. This selection is made on the basis of the relative abundance of hazard-oriented studies about engineered inorganic nanoparticles that are relatively often considered for commercial application.

There is evidence that the inorganic nanoparticles considered here are hazardous to lung tissue when inhaled and may, depending on size, also be a cardiovascular hazard [17,19]. The actual hazard to the lungs following inhalation depends on diameter, surface area, structure, surface energy, surface charge, agglomeration, shape and number, and, in some cases, the toxicity of soluble compounds released from the nanoparticles [17–26]. All other things being equal, anatase TiO_2 nanoparticles seem, for instance, to be more hazardous to lung tissue than rutile TiO_2 nanoparticles. A SiO_2 coating on TiO_2 nanoparticles seems to increase hazard to lung tissue [21]. Carbon nanofibers and nanotubes that are longer than 10 μm seem to be more hazardous than carbon black or C_{60} fullerenes. This may be so because macrophages have more difficulty in clearing from the lungs such fibers and tubes than spherical fullerenes or amorphous carbon black nanoparticles and because inhaled carbon nanotubes can reach the outer lining of the lungs and cause scarring [24,25].

Suggestive evidence exists that some inorganic nanoparticles can be translocated from the nasal area via the olfactory nerve to the central nervous system [26]. There, they might induce enhanced inflammation [26]. There is also some evidence that

after ingestion TiO_2 and SiO_2 nanoparticles may be hazardous to the intestines [26]. Following eventual translocation from the digestive tract to other organs, for instance in the case of Ag nanoparticles [28], nanoparticles may contribute to inflammation of such organs [26,28]. Carbon nanotubes may be a health hazard on dermal exposure, especially when catalyst-derived metal residues are present [25]. The same holds for uncoated TiO_2 nanoparticles and may also hold, to a lesser extent, for commercially available coated TiO_2 nanoparticles [26,29]. Uncoated TiO_2 nanoparticles and carbon nanotubes have been found to exhibit immunotoxicity [26,27]. Large-scale use of nanosilver might give rise to increased silver resistance of pathogens, which might be detrimental to the medical use of silver against pathogens [23]. A main molecular mechanism underlying the health hazards of nanoparticles may be the formation of reactive oxygen species, which cause oxidative damage to tissues [17–22,25,26]. This in turn may induce effects such as inflammation, (lung) fibrosis, and DNA damage, possibly leading to cancer. However, the generation of reactive oxygen species is probably not the only mechanism underlying hazards. For instance, SiO_2-coated TiO_2 nanoparticles lead to a relatively high hazard of lung inflammation, which is unexpected in view of the relatively low generation of reactive oxygen species by nanoparticles with a SiO_2 surface [21]. Also, the necrotic effect of anatase TiO_2 nanoparticles is unlikely to be explained on the basis of oxidation reactions only [19]. The role of soluble substances released by nanoparticles as a determinant of hazard has already been mentioned. Physical interactions between inorganic nanoparticles and components of living cells may also be a determinant of hazards. Such physical interactions include physical damage to membranes by carbon nanotubes [27] and changes in protein folding, aggregation, and gene expression by nanosized silica [30,31].

12.3
Nanocomposite Life Cycles and Life Cycle Assessment

Nanocomposites have a “cradle” (resource extraction) and a “grave” (final disposal). Between the two is the life cycle. A life cycle may include one product, but may also extend to a series of products. For instance, nanocomposite rubber tires may be subject to recycling, and thus the nanocomposite rubber material may end up in new rubber products or asphalt.

The environmental impact of product life cycles may be evaluated by (environmental) life cycle assessment, also called life cycle analysis. Life cycle assessment is generally divided into four stages [32]:

- goal and scope definition,
- inventory analysis,
- impact assessment, and
- interpretation.

Life cycle assessment has been developed for analyzing current products from resource extraction to final waste disposal, or from cradle to grave. Apart

from analyzing the status quo, life cycle assessments may also deal with changes in demand for, or supply of, products and with novel products. The latter type of assessment has been called *consequential*, as distinguished from the analysis of status quo products, which has been called *attributional*. The life cycle assessment of current nanocomposite tires is in the category attributional, whereas the life cycle assessment of nanocomposite products in the development stage would be consequential.

Different data may be needed in attributional and consequential life cycle assessments. Whereas in attributional life cycle assessment one, for example, uses electricity data reflecting current power production, in consequential life cycle assessment one needs data regarding changes in electricity supply. For the shorter term, assessing a marginal change in capacity of current electricity supply may suffice to deal with changes in electricity supply. When the longer term is at stake, major changes in energy supply, including complex sets of energy supply technologies, should be assessed.

When novel products go beyond existing components, materials, and processes, knowledge often partly or fully relates to the research and development stage or to the limited production stage. These stages reflect immature technologies. Comparing these with products of much more mature technologies may be unfair, as maturing technologies are optimized and tend to allow for better resource efficiency and a lower environmental impact.

It should be realized that the assumptions involved lead to considerable uncertainty regarding the outcomes of consequential life cycle assessments, as these assumptions may be at variance with "real life" in the future.

In the goal and scope definition stage, the aim and the subject of the life cycle assessment are determined. This implies the establishment of "system boundaries" and often the definition of a "functional unit." System boundaries refer to what is included and excluded in life cycle assessment. Thus, boundaries between technological systems and significant and insignificant processes are drawn. For instance, the nanocomposite life cycle will usually include transport, but the system boundaries may be drawn in such a way that making and maintaining means of transport and infrastructure for transport are excluded from life cycle analysis. When biopolymers are used in nanocomposites, one should consider the options of drawing the boundary in such a way to include or exclude indirect effects thereof on land use for food production.

A functional unit is a quantitative description of the service performance of a product. Examples are a 1 l bottle that can make 25 return trips or a coating for 1 m^2 soft wood that will meet specified criteria for protection, color, and gloss over a 5-year period, when exposed outdoors to temperate climatic conditions. Using functional units as an object for life cycle assessment facilitates between-product comparisons.

The inventory analysis gathers the necessary data regarding the extraction of resources and emissions for all processes involved in the product life cycle. For this purpose, databases have been developed, such as Ecoinvent, the Chinese National Database, Spine (www.globalspine.com), JEMAI, and the European Reference Life Cycle Data System, which give estimates about resource extraction and emissions

Box 12.1 Aspects of environmental impact that can be considered in life cycle assessment [32].

Resource depletion (abiotic, biotic)
Desiccation
Effects of land use on ecosystems and landscape
Greenhouse gas emissions, changes in albedo
Impact on the ozone layer
Acidification
Photo-oxidant formation
Eutrophication or nitrification
Human toxicity
Ecotoxicity
Nuisance (odor, noise)
Radiation
Casualties
Waste heat

that are common in Europe, China, the United States, and Japan for specified processes.

In full life cycle assessments, the inventories cover emissions and resource extractions, which may lead to a wide range of impacts (see Box 12.1).

In life cycle assessments, the problem arises that production systems may have more than one output. For instance, mineral oil refinery processes may generate not only feedstock for polymer production but also gasoline, kerosene, heavy fuel oil, and bitumen. In the case of multi-output processes, extractions of resources and emissions have to be allocated to the different outputs. There are several ways to do so [31]. Major ways to allocate are based on physical units (in the case of refineries, for example, energy content, hydrogen content, or weight of outputs) or on monetary value (price). There may also be allocation on the basis of substitution. In the latter case, the environmental burden of a coproduct is established on the basis of another similar product. Different kinds of allocation may lead to different outcomes of life cycle inventories. The outcome of the inventory stage is a list with all extractions of resources and emissions of substances causally linked to the functional unit considered.

The next stage in the life cycle assessment is impact assessment. This implies characterization. Characterization serves to aggregate the impacts of extractions of resources and emissions in the categories outlined in Box 12.1. For instance, emissions of greenhouse gases may be aggregated as emissions of CO_2 equivalents, while assuming a specific time horizon, for example, 100 years. In estimating human toxicity, quantitative estimates of toxicological impacts per unit of emission

via specified pathways to humans are used as characterization factors. In traditional life cycle assessment, the environmental impact was determined without being specific as to place and time of resource extractions and emissions. Increasingly, however, adaptations of life cycle assessment become available that are place and time specific.

The interpretation stage connects the outcome of the impact assessment to the real world. In this stage, the uncertainties involved should be addressed. These have a variety of origins including uncertainties about the correspondence of models and the data used to the real world, and assumptions made, for example, emissions being indeterminate regarding time and place, which are at variance with the real world. Sensitivity analysis may be a part of the interpretation stage and, for instance, consider the dependence on assumptions. Similarly, uncertainty analysis may also be a part of the interpretation stage. Several approaches to uncertainty analysis have been proposed. These include the use of Monte Carlo techniques, matrix perturbation, or Taylor series expansion. In practice, both uncertainty and sensitivity analyses have been applied in a limited way. Finally, in the interpretation stage conclusions may be drawn. For instance, one may conclude that in specified respects and under specified assumptions product A has a lower environmental impact than product B or that most of the environmental burden of a product is associated with a specific stage in the nanocomposite life cycle, which would be a preferable target for environmental improvement [32].

It may be expected that cumulative fossil fuel demand linked to a nanocomposite life cycle will be a major determinant of the environmental impact [33] of nanocomposite life cycle. Apart from the case that crops are used as feedstock for polymer production, cumulative fossil fuel demand may even be the main determinant of the overall environmental burden [33].

A problem with life cycle assessment of nanocomposites is that so far no generally agreed upon way has been found to deal with the health hazard and risk associated with nanoparticles [34]. An important reason for this is that human toxicity and ecotoxicity are normally linked to the emitted mass of substances, whereas the determinants of nanoparticle hazards are, as pointed out in the previous section, factors such as number of particles and surface characteristics. An additional problem is that there may be size-dependent nonlinearities in the relation between surface and hazard to human health [26]. The same may hold for ecotoxicity [26]. However, the other aspects indicated in Box 12.1 pose no insurmountable problem to nanocomposite life cycle assessment.

12.4 Life Cycle Assessment of Nanoparticles and Nanocomposites in Practice

So far, there has been limited life cycle assessment of nanoparticles. Examples include carbonaceous nanoparticles and TiO_2 nanoparticles. These assessments show that production of such particles requires relatively large inputs of energy and materials, if compared with larger sized particles [35–39]. For instance, 1 kg TiO_2

nanoparticles may require a three to four times larger input of energy than 1 kg conventional, larger sized, TiO_2 particles [35,36]. An estimated 385 kg of benzene has been suggested to be needed for the production of 1 kg of C_{60} (fullerene) by combustion [37]. And the energy input linked to the production of 1 kg of carbon nanoparticles has been found equivalent to the energy needed for the production of up to 100 kg of aluminum [38,39].

So far, very few peer-reviewed applications of cycle assessment methodology to nanocomposites consisting of inorganic nanoparticles and organic polymers are available. Lloyd and Lave [40] have studied life cycle impacts of using nanoclay–polymer composites in automobiles, considering toxics, energy use, and emissions linked to the latter and comparing nanocomposites with steel and aluminum. The toxicity of nanoclay was presumed to be zero by Lloyd and Lave [40]. Khanna and Bakshi [41] studied carbon nanofiber–polymer composites in comparison with steel, focusing on energy use. In both cases [40,41], a potential environmental benefit of nanocomposites, if compared with the competing metal(s), was suggested by the authors. There is one study dealing with a specific stage of the product life cycle, drawing on the methodology for life cycle assessment that has been discussed in the previous section. Corti and Lombardi [42] have looked at final disposal processes of end-of-life tires with a life cycle assessment methodology.

It should be noted that the limitations of the studies of Lloyd and Lave [40] and Khanna and Bakshi [41] are important to their conclusions. A sensitivity analysis regarding the impact of assumptions on the outcomes of the studies by Lloyd and Lave [40] and Khanna and Bakshi [41] shows that reuse of car components and recycling of materials were neglected in both cases. At present, including recycling would favor the life cycle environmental performance of steel and aluminum over the performance of a nanocomposite as the former are recycled, and can in principle be recycled indefinitely, whereas, apart from tires, there does not seem to be substantial materials recycling of nanocomposites. Provided that transport distances and inputs in recycling processes remain limited, recycling generally has an environmental benefit over the use of virgin resources [40,43,44]. When recycling implies many use cycles, the benefit may become large. This stresses the importance of nanocomposite recycling to environmental performance.

12.5
Nanocomposite Life Cycle Management, Including Recycling

Recycling is a loosely used concept. As such, it covers a range of activities varying from product reuse to incineration combined with energy recovery. The latter has been called energetic or thermal recycling.

Recyclability may vary strongly between nanocomposite applications. Coatings like paints would seem to have very limited recyclability, apart from incineration with energy recovery (energetic recycling). The only meaningful option for materials recycling would seem to be the grinding of paint residues (e.g., leftovers in containers and production wastes) to produce fillers. Nanocomposite tires on the

Box 12.2 Social and economic arrangements conducive to recycling of nanocomposite products and materials [45–52].

- High prices of virgin nanocomposites
- A tradition of design for recycling or ecodesign
- Policies conducive to design for recycling or ecodesign
- Policies favoring materials recycling (e.g., demanding recycling targets, as established in the European Union for end-of-life cars in 2015 [52])
- Labeling to identify the chemical nature of the nanocomposite
- Extended producer responsibility of nanocomposites
- Bans on incineration and landfilling
- Well-organized recycling centers
- Separate collection of end-of-life products or "wastes"
- Well-developed "reverse logistics" for end-of-life products

other hand may be retreaded, ground to rubber powder for a wide variety of applications, and pyrolyzed.

Recycling may also vary widely depending on socioeconomic arrangements [45–52]. Factors favoring product and materials recycling are summarized in Box 12.2.

Recycling is an important determinant of environmental performance [40–46,53]. To the extent that nanocomposites can be recycled a number of times as product, material, or constituent substances, with limited inputs into the recycling process, the environmental performance per cycle of usage might improve. Also, incineration of nanocomposites with energy recovery may be expected to do better environmentally than landfilling [42].

The environmental benefit of many use cycles for nanocomposite materials and constituent substances, or conversion products thereof, is at variance with a strategy aiming at biodegradable nanocomposites, which are characterized by degradation after one cycle of usage [54–57]. From the environmental point of view, biodegradable nanocomposites would only seem worth considering when inputs in the recycling process are very high and when the hazard of substances released by degradation, which would probably include nanoparticles, is low. It would seem hard to come up with a case in which such conditions would be met by nanocomposites. A possible exception might be nanocomposite products (e.g., packaging) that contain, and are soiled by, highly greasy material and are composted in a highly contained way.

The best strategy for recycling has been the subject of much discussion. An interesting proposal for such a strategy aims at resource cascading: the maximum exploitation of the quality (as well as value and performance) and service time of resources [58,59]. This strategy will be used as a backdrop for what probably currently is the best example of discarded nanocomposite product recycling: the

Box 12.3 Descending steps in the current resource cascade for end-of-life tires [60,62–64].

1. Retreading
2. Use of rubber powder (also called crumb rubber or rubber granulate), to a large extent in products with a lower standard regarding rubber quality
3. Pyrolysis
4. Combustion with energy recovery

recycling of rubber tires. Estimates suggest that worldwide 35% of rubber tires are subject to some form of recycling, whereas the average recycling rate for plastics worldwide is probably well below 10% [51,60]. The apparent scope for recycling of rubber tires is also interesting because the rubber polymers in tires are in the category of thermoset polymers. This category is often thought to have less potential for recycling than thermoplastic polymers [51,61]. Box 12.3 summarizes the descending steps in the resource cascade as applied to end-of-life tires. Thereafter, the scope for resource cascading of nanocomposite polymers will be discussed more generally.

Important to resource cascading is the performance or quality of the materials over time. Quality should preferentially be preserved. In the case of nanocomposites consisting of organic polymers and inorganic nanoparticles, this means primarily that degradation should be prevented. When oxygen is available, inorganic nanoparticles may generate reactive oxygen species, which may cause scission of polymer chains [13,14,26,28,65]. Scission may be increased at elevated temperatures and in the presence of compatibilizers such as long-chain amines, quaternary ammonium salts, and maleated compounds. Polymer scission may be suppressed by the addition of, preferentially immobile, antioxidants and by the use of compatibilizers that have improved thermal stability, such as imidazolium derivatives and crown ethers [13,14,65]. In the presence of solar irradiation, scission of polymers may increase when nanoparticles turn out to be photocatalytically active. The latter applies to both uncoated TiO_2 nanoparticles and montmorillonite nanoclay and may be furthered by the presence of organomodifiers and polymer polarity [15,16,66,67]. Polymer scission by photocatalytic activity may be suppressed by coating of TiO_2 nanoparticles (e.g., by silica or alumina) and by, preferentially immobile, UV absorbents, hindered amine light stabilizers (HALS), metal deactivators, and antioxidants [15,16,66,67].

To the extent that degradation of the material occurs, the introduction of self-healing properties may also be considered. These have as yet no commercial application, but self-healing properties have been experimentally demonstrated in the case of polydimethylsiloxanes and Diels–Alder elastomers [68]. From the point of view of resource cascading, it is important that the inclusion of substances conferring self-healing properties does not interfere with later stages in the resource cascade.

Recycling options in the case of nanocomposite polymers are theoretically many. The resource cascade, as will be proposed below, will reflect studies done on neat polymers, composites, and nanocomposites [69–96]. It should be noted that resource cascading of nanocomposites might be more difficult than resource cascading of neat polymers. This is illustrated by the reprocessing with screw extruders of nylon 6–nanoclay composites [70]. Reprocessing of these composites into products with the same quality is relatively difficult, as nanoclay layers may reagglomerate and chain scission may be increased, if compared to the neat nylon 6 polymer [70]. The increased occurrence of chain scission may be counterbalanced by increased use of chain extenders during materials recycling [88].

In the following, the options for resource cascading will be considered descending along the resource cascade [51,69,79,90].

The best option for resource cascading of nanocomposites would be reuse of the same product and recycling of production scrap into high-quality products.

The second best option would be remanufacturing [97]. Retreading of tires comes in this category, as would, more in general, the provision of a nanocomposite product that has been subject to wear and tear with a new surface layer.

Third, one can consider materials recycling. For this purpose, discarded nanocomposites are converted into granulates or powder. This is followed by reprocessing of nanocomposite polymer granulates, preferentially into products with a composition and quality similar to the original product. Thus, virgin components of nanocomposites can be replaced. The extent of the potential for replacement of virgin components of the nanocomposite, without loss of product performance, may in practice be limited. In the case of powders made from used thermoset composite resins, usage as substitute fillers without intolerable loss of performance may be below a loading level of 10% [61]. In the case of recycling styrene–butadiene rubber (SBR), tolerable usage may be substantially higher. It has been suggested that up to 50% granulates from end-of-life SBR products may be used without loss of performance [98].

In materials recycling, the use of inputs for cleaning of "wastes" should preferentially be minimized [94]. Well-controlled life cycles of products, with source separation of wastes, are conducive to such minimization. Also preferable are low additional inputs such as energy, restabilizers, antioxidants, metal deactivators, chain extenders, and compatibilizers. Such low inputs are conducive to limiting resource use and emissions [86,89]. A low input of energy is also helpful in limiting polymer chain scission as the latter may increase at elevated temperatures [65]. Product and material design for recycling or ecodesign can help in minimizing inputs in reprocessing nanocomposites into high-quality products [52].

It will probably not always be possible to achieve conservation of quality during reprocessing at low inputs. So, an optimization problem may arise, in which quality requirements may be lowered to achieve environmentally acceptable input levels.

An alternative possibility is to include nanocomposite granulates in a polymeric matrix of a different composition, using compatibilizer to achieve acceptable properties. It should, however, be noted that nanocomposites with more than one type of polymer present may be more difficult to recycle, while maintaining high quality levels, than when one type of polymer is present [51,84].

Fourth, one may think of chemical recycling: recycling constituents or conversion products of the nanocomposite. In the case of condensation polymers with ether, ester, or amide linkages, depolymerization is an option that can give rise to relatively high yields of the original constituents of the polymer [69,71–73,99]. The constituents obtained by depolymerization in turn can be used for repolymerization [69]. This type of chemical recycling has an environmental impact that may be substantially better than the next option in the resource cascade: incineration with energy recovery [69].

Also, the nanoparticles used may be very valuable and may be preferentially recovered, as is the case with larger sized carbon fibers, which can in principle be recovered by recycling processes with limited loss of performance [61,95,96]. In such cases, care should be taken to limit inputs in chemical recycling [99] and maximize good-quality product and coproduct yields, otherwise the environmental burden thereof may be such that chemical recycling may be doing worse environmentally than incineration with energy recovery. Another option is chemical recycling that makes use of pyrolysis, cracking, or gasification, including the catalytic varieties thereof. In this way, valuable small molecules may be obtained [61,77,100–103]. In fact, there is some overlap with the first type of chemical recycling mentioned here, as for some polymers (polyamide 6, polystyrene) some types of pyrolysis may generate >70% yields of constituent monomers [74,77,87]. In the case of other polymers, pyrolysis often tends to generate complex mixtures that may only allow for very limited yields of molecules that are fit for chemical recycling [61].

In the context of this type of chemical recycling by pyrolysis, it may also be noted that the presence of nanoparticles may considerably change the degradation characteristics of polymers on pyrolysis and thereby the conversion products that are generated [100–103].

The lowest recycling-type step of the resource cascade for nanocomposites is usually incineration with energy recovery [69,79]. To the extent that nanocomposites are incinerated that contain nanoparticles serving as fire retardants, it is to be expected that the calorific value of the nanocomposite will turn out to be lower than the corresponding value of the neat polymer [61].

12.6
Reducing Nanoparticle-Based Health Hazards and Risks Associated with Nanocomposite Life Cycles

On the basis of available research, there are leads to the reduction of nanocomposite life cycle hazards and risks.

In the production stage of nanocomposites, the release of hazardous particles may be reduced by *in situ* generation of nanoparticles in the polymers used, as described for nanosilica [104]. When *in situ* production of nanoparticles is not possible, reducing the nonproduct output of nanoparticle production is an important way to reduce hazard [104]. Flow focusing, to better control the size distribution of

nanoparticles, and catalytic chemical vapor deposition techniques for the control of nanofiber growth are examples of production technologies that may reduce non-product outputs.

In the usage stage, robustness of the nanocomposite against degradation and wear and tear might reduce the release of nanoparticles [16]. Robustness against degradation can be improved by minimizing the generation of reactive oxygen species by nanoparticles by judicious choice of, where appropriate, size, crystal structure, and coating of nanoparticles to be included in polymeric nanocomposites [16,104–106]. Also, to reduce hazard and risk from release during usage, materials may be designed in such a way that only relatively large particles are released [16,104]. The design should be such that this property also applies to recycled nanocomposites. It may be noted that design for the release of large particles may be at variance with tribomechanical product specifications that might require the release of nanoparticles [16].

In recycling, low temperatures may limit nanocomposite degradation, which may be conducive to lowering future releases of nanoparticulate materials. Also, contained processing might reduce the release of nanoparticles, and thereby reduce risk [77].

To the extent that nanoparticles are released during the life cycle of nanocomposites, there may be scope for reduction of hazard by appropriate coatings for, and functionalization and purification of, nanoparticles [104]. For instance, it has been argued that the dermal hazard of TiO_2 nanoparticles can be reduced by persistent coatings of, for example, alumina or silica [26]. The human health hazard of amorphous SiO_2 nanoparticles may be reduced by functionalization with amidosilanes [26]. The hazard of carbon nanotubes can probably be reduced by purification, which leads to the elimination of metal catalyst residues [25], or by the development and application of catalyst-free synthesis processes [104]. The hazard of carbon nanotubes can be modulated by introducing functional groups (functionalization) [25]. For instance, modifications that lead to increased solubility in water may be expected to reduce hazard [27,104,107]. Functionalized hydrophilic carbon nanotubes may reduce complement activation (a response of the immune system), cytotoxicity, and inflammation hazard [104,107]. Also, designing carbon nanotubes in a way conducive to degradability by neutrophil myeloperoxidase might reduce inflammation hazard to the lungs [108].

Hazard reduction may furthermore be possible by judicious choice of nanoparticle size or crystal structure. When the hazard of nanoparticles is strongly influenced by the solubility of constituents, as seems likely in the case of ZnO and Ag nanoparticles, this type of hazard may be reduced by applying relatively large nanoparticles [105,109]. In the case of TiO_2 particles, there is evidence that there is a nonlinear relation between size and the photocatalytic generation of reactive oxygen species (ROS), with a maximum around 33 nm [106]. Applying either larger or smaller nanoparticles might reduce hazard linked to the photocatalytic generation of ROS. When given a specific size, functionality of TiO_2 nanoparticles is independent of crystal structure, and the rutile variety may be preferred as it generates less reactive oxygen species than anatase [29,104].

12.7 Conclusion

Resource cascading may reduce the environmental burden of nanocomposite polymers. Such cascades may include reuse of products, self-healing, remanufacturing, materials recycling, chemical recycling, and incineration with energy recovery. Design for recycling and suitable socioeconomic arrangements regarding the disposal stage of products can be conducive to furthering recycling.

Life cycles of nanocomposites can give rise to the release of inorganic nanoparticles. These may be hazardous, depending on characteristics such as size, shape, and surface. There are options to reduce the release of nanoparticles and the hazards and risks thereof during the nanocomposite life cycle. These include judicious choices regarding production processes, materials design, containment, particle size and crystal structure, coating, and functionalization.

References

1 Kohjia, S., Katoh, A., Shimanuki, J., Hasegawa, T., and Ikeda, Y. (2005) *Journal of Materials Science*, **40**, 2553–2555.
2 Kumar, R. and Münstedt, H. (2005) *Biomaterials*, **26**, 2081–2088.
3 Kelarakis, A., Yoon, K., Sics, I., Somani, R. H., Hsiao, B.S., and Chu, B. (2005) *Polymer*, **46**, 5103–5117.
4 Hanu, L.G., Simon, G.P., and Cheng, Y. (2006) *Polymer Degradation and Stability*, **91**, 1373–1379.
5 Zhu, L. and Wool, R.P. (2006) *Polymer*, **47**, 8106–8115.
6 Wang, T., Dalton, A.B., and Keddie, J. L. (2008) *Macromolecules*, **41**, 7656–7661.
7 Lee, J.L., Zeng, C., Cao, X., Han, X., Shen, J., and Xu, G. (2005) *Composites Science and Technology*, **65**, 2344–2363.
8 Pavlidou, S. and Papespyrides, C.D. (2008) *Progress in Polymer Science*, **33**, 1119–1198.
9 Paul, D.R. and Robeson, L.M. (2012) *Polymer*, **49**, 3187–3204.
10 Hamdani, S., Longuet, C., Perrin, D., Lopez-Cuesta, D., and Ganachaud, F. (2009) *Polymer Degradation and Stability*, **94**, 465–495.
11 Camargo, P.H.C., Satyanarayana, K.G., and Wypych, F. (2009) *Materials Research*, **12**, 1–39.
12 Pal, K., Rajasekar, R., Kang, D.J., Zhang, Z.X., Pal, S.K., Kim, J.K., and Das, C.K. (2010) *Materials and Design*, **21**, 23–34.
13 Zhou, Q. and Xanthos, M. (2009) *Polymer Degradation and Stability*, **94**, 327–338.
14 Pfaendner, R. (2010) *Polymer Degradation and Stability*, **95**, 369–373.
15 Bottino, D.A., Di Pasquale, G., Fabbri, E., Orestano, A., and Pollicino, A. (2009) *Polymer Degradation and Stability*, **94**, 369–374.
16 Reijnders, L. (2009) *Polymer Degradation and Stability*, **94**, 873–876.
17 Oberdöster, G., Stone, V., and Donaldson, K. (2007) *Nanotoxicology*, **1**, 2–25.
18 Oberdörster, G. (2010) *Journal of Internal Medicine*, **267**, 89–105.
19 Braydich-Stolle, L.K., Schaeublin, N.M., Murdock, R.C., Jiang, J., Biswas, P., Schlager, J.J., and Hussain, S.M. (2009) *Journal of Nanoparticle Research*, **11**, 1361–1374.
20 Fadeel, B. and Garcia-Bennet, A.E. (2010) *Advanced Drug Delivery Reviews*, **62**, 362–374.
21 Rossi, E.M., Pylkänen, L., Koivisto, A.J., Vippola, M., Jensen, K.A., Mettinen, M., Sirola, K., Nykäsenoja, H., Karisola, F., Sternvall, T., Kiilunen, M., Passanen, P., Mäkinen, M., Hämeri, K., Joutsenari, F., Jokiniemi, J., Wolff, H., Savolainen, S.,

and Alenius, H. (2010) *Toxicological Sciences*, **113**, 422–433.
22 Wijnhoven, S.W.P., Peijnenburg, W.J.G. M., Herberts, C.A., Hagens, W.I., Oomen, A.G., Heugens, E.H.W., Roszek, B., Bisschops, J., Gosens, I., van de Meent, D., Dekkers, S., de Jong, W.H., van Zijverden, M., van Sips, A.J.A.M., and Geertsma, R.E. (2009) *Nanotoxicology*, **3**, 109–138.
23 Silver, S. (2003) *FEMS Microbiology Reviews*, **27**, 341–354.
24 Donalson, K. and Poland, C.A. (2009) *Nature Nanotechnology*, **4**, 708–710.
25 Shvedova, A.A. and Kagan, V.F. (2010) *Journal of Internal Medicine*, **267**, 106–118.
26 Reijnders, L. (2010) Hazards of TiO_2 and amorphous SiO_2 nanoparticles, in *Toxic Effects of Nanomaterials* (ed. H. Khan), Bentham Science Publishers.
27 Kunzman, A., Andersson, B., Thurnherr, T., Krug, H., Scheynius, A., and Fadeel, B. (2010) *Biochimica and Biophysica Acta*, **1810** (3), 361–373.
28 Park, E., Bae, E., Yi, J., Kim, Y., Choi, K., Lee, S.H., Yoon, J., Lee, B., and Park, K. (2010) *Environmental Toxicology and Pharmacology*, **30** (2), 162–168.
29 Tiano, L., Armeni, T., Venditti, E., Barucca, G., Mincarelli, L., and Damiani, E. (2010) *Free Radical Biology & Medicine*, **49** (3), 408–415.
30 Xu, Z., Wang, S., and Gao, H. (2010) *Journal of Hazardous Materials*, **180** (1–3), 375–383.
31 Gong, C., Tao, G., Yang, L., Liu, J., Liu, Q., and Zhuang, Z. (2010) *Biochemical and Biophysical Research Communications*, **397** (3), 397–400.
32 Rebitzer, G., Ekball, T., Frischknecht, R., Hunkeler, D., Norris, G., Rydberg, T., Schmidt, W., Suh, S., Weidema, B., and Penningtton, D.W. (2004) *Environment International*, **30**, 701–720.
33 Huijbregts, M.A.J., Rombouts, L.J.A., Hellweg, S., Frischknecht, R., Hendriks, J., van de Meent, D., Ragas, A.J.M., Reijnders, L., and Struijs, J. (2006) *Environmental Science & Technology*, **40**, 641–648.
34 Bauer, C., Buchgeister, J., Hischier, R., Poganietz, W.R., Schebek, L., and Warsen, J. (2008) *Journal of Cleaner Production*, **16**, 910–926.
35 Meyer, D.E., Curran, M.A., and Gonzalez, M.A. (2009) *Environmental Science & Technology*, **43**, 1256–1263.
36 Osterwalder, N., Capello, C., Hungerbuhler, K., and Stark, W.J. (2006) *Journal of Nanoparticle Research*, **8**, 1–9.
37 Roes, A.L., Alsema, E.A., Blok, K., and Patel, M.K. (2009) *Progress in Photovoltaics: Research and Applications*, **17**, 372–393.
38 Khanna, V., Bakshi, B.R., and Lee, L.J. (2008) *Journal of Industrial Ecology*, **12**, 394–410.
39 Kushnir, D. and Sanden, B. (2008) *Journal of Industrial Ecology*, **12**, 360–375.
40 Lloyd, S.M. and Lave, L.B. (2003) *Environmental Science & Technology*, **37**, 3458–3466.
41 Khanna, V. and Bakshi, B.R. (2009) *Environmental Science & Technology*, **43**, 2978–2084.
42 Corti, A. and Lombardi, L. (2004) *Energy*, **29**, 2089–2108.
43 Björklund, A. and Finnveden, G. (2005) *Resources, Conservation and Recycling*, **44**, 309–317.
44 Huang, Y., Brird, R., and Heidrich, O. (2009) *Journal of Cleaner Production*, **17**, 283–296.
45 Krozer, J. and Doelman, P. (2003) *Journal of Sustainable Product Design*, **3**, 3–17.
46 Krook, J. and Eklund, M. (2010) *Applied Ergonomics*, **41**, 362–367.
47 Binder, C.R., Quirici, R., Domnitcheva, S., and Stäubli, B. (2008) *Journal of Industrial Ecology*, **12**, 207–228.
48 Luttropp, C. and Johanson, J. (2010) *Journal of Cleaner Production*, **18**, 346–354.
49 Beukering, B.J.H. and van Jansen, M.A. (2001) *Resources, Conservation and Recycling*, **33**, 253–265.
50 Milanez, B. and Bührs, T. (2009) *Journal of Cleaner Production*, **17**, 608–615.
51 Reijnders, L. (2007) Improving resource cascading, in *Trends in Conservation and Recycling of Resources* (ed. C.V. Loeffe), Nova Science Publishers, New York.
52 Santini, A., Herman, C., Passarini, F., Vassura, I., Luger, T., and Morselli, L. (2010) *Resources, Conservation and Recycling*, **54** (12), 1128–1134.
53 Vogtländer, J.C., Brezet, H.C., and Hendriks, C.F. (2001) *International*

Journal of Life Cycle Assessment, **5**, 344–355.
54 Liao, H. and Wu, C. (2005) *Journal of Applied Polymer Sciences*, **97**, 397–404.
55 Zhao, R., Torley, P., and Halley, P.J. (2008) *Journal of Materials Science*, **43**, 3058–3971.
56 El Fray, M. (2009) *Advanced Engineering Materials*, **11**, B35–B39.
57 Singh, N.K., Purkyashta, B.D., Roy, J.K., Banik, J.M., Yashpal, M., Singh, G., Malik, S., and Maiti, P. (2010) *Applied Materials and Interfaces*, **2**, 69–81.
58 Sirkin, T. and ten Houten, M. (1994) *Resources, Conservation and recycling*, **11**, 215–277.
59 Reijnders, L. (2000) *Resources, Conservation and Recycling*, **28**, 121–133.
60 Al-Salem, S.M., Lettieri, P., and Baeyens, J. (2009) *Journal of Hazardous Materials*, **172**, 103–129.
61 Pickering, S.J. (2006) *Composites Part A*, **37**, 1206–1215.
62 Perugini, F., Mastellone, M.L., and Arena, U. (2005) *Environmental Progress*, **24**, 137–154.
63 Zhang, S.L., Xin, Z.X., Zhang, Z.X., and Kim, J.K. (2009) *Waste Management*, **29**, 1480–1485.
64 Xin, Z.X., Zhang, Z.X., Pal, K., Byeon, J. U., Lee, S.H., and Kim, J.K. (2010) *Materials and Design*, **31**, 589–593.
65 Thompson, M.R. and Yeung, K.K. (2006) *Polymer Degradation and Stability*, **91**, 2396–2407.
66 Morlat Therias, S., Mailhot, B., Gonzalez, D., and Gardette, J. (2005) *Chemistry of Materials*, **17**, 1072–1078.
67 Morlat Therias, S., Fanton, E., Tomer, N. S., Rana, S., Singh, R.P., and Gardette, J. (2006) *Polymer Degradation and Stability*, **91**, 3033–3039.
68 Murphy, E.B. and Wudl, F. (2010) *Progress in Polymer Science*, **35**, 223–251.
69 Nakatani, J., Fuji, M., Moriguchi, Y., and Hirao, M. (2010) *International Journal of Life Cycle Assessment*, **15** (6), 590–597.
70 Russo, G.M., Nicolais, V., Di Mano, L., Montesano, S., and Incarnato, L. (2007) *Polymer Degradation and Stability*, **92**, 1925–1933.
71 Chen, J., Liu, G., Jin, L., Ni, P., Li, Z., He, H., Xu, Y., Zhang, J., and Dong, J. (2010) *Journal of Analytical and Applied Pyrolysis*, **87**, 50–55.
72 Goto, M. (2009) *Journal of Supercritical Fluids*, **47**, 500–507.
73 Zia, K.M., Bhatti, H.N., and Bhatti, I.A. (2007) *Reactive and Functional Polymers*, **67**, 675–692.
74 Czernik, S., Elam, C.C., Evans, R.J., Meglen, R.R., Moens, L., and Tatsumoto, K. (1998) *Journal of Analytical and Applied Pyrolysis*, **46**, 51–64.
75 Achilias, D.S., Roupakias, C., Megalokonomos, P., Lappas, A.A., and Antonakou, E.V. (2007) *Journal of Hazardous Materials*, **149**, 536–542.
76 Garforth, A.A., Ali, S., Hernandez-Marines, J., and Akah, A. (2004) *Current Opinion in Solid State and Materials Science*, **8**, 419–425.
77 Hong, J.H., Choi, C.W., Ramasundaram, S., Prabu, A.A., Lee, J.S., Kim, K.J., Yang, J.H., and Lee, D.J. (2008) *Polymer Degradation and Stability*, **93**, 392–400.
78 Huang, K., Tang, L.-H., Zhu, Z.-B., and Zhang, C.-F. (2005) *Polymer Degradation and Stability*, **89**, 312–316.
79 Chilton, T., Burnley, S., and Nesaratnam, S. (2010) *Resources, Conservation and Recycling*, **54** (12), 1241–1249.
80 Braun, D. (2002) *Progress in Polymer Science*, **27**, 2171–2195.
81 Awaja, F. and Pavel, D. (2005) *European Polymer Journal*, **41**, 1453–1477.
82 Perez, J.M., Vilas, J.L., Laza, J.M., Arnaiz, S., Mijangos, F., Bilbao, E., Rodriguez, M., and Leon, L.M. (2020) *Journal of Materials and Processing Technology*, **210**, 727–733.
83 Villalobos, M., Awojulu, A., Greley, T., Turco, G., and Deeter, G. (2006) *Energy*, **31**, 3227–3234.
84 Vilaplana, F., Ribes-Greus, A., and Karlsson, S. (2006) *Polymer Degradation and Stability*, **91**, 2163–2170.
85 Botta, L., Dintcheva, N.T., and La Mantia, F.P. (2009) *Polymer Degradation and Stability*, **94**, 712–718.
86 Cheng, X., Shi, H., Adams, C.D., and Ma, Y. (2010) *Environmental Science and Pollution Research*, **17** (7), 1323–1330.
87 Cho, K., Jang, B., Kim, K., and Park, D. (2006) *Reaction Kinetics and Catalysis Letters*, **88**, 43–50.

88 Xu, X., Ding, Y., Qian, Z., Wang, F., Wen, B., Zhou, H., Zhang, S., and Yang, M. (2009) *Polymer Degradation and Stability*, **94**, 113–123.

89 Coulier, L., Orbons, H.G.M., and Rijk, R. (2007) *Polymer Degradation and Stability*, **92**, 2016–2015.

90 Le Borgne, R. and Feillard, P. (2001) *International Journal of Life Cycle Assessment*, **6**, 167–176.

91 Ragosta, G., Musto, P., Martuscelli, E., and Russo, P. (2000) *Journal of Materials Science*, **35**, 3741–3751.

92 Stevenson, W. and White, J.R. (2002) *Journal of Materials Science*, **37**, 1091–1100.

93 Goto, M., Sasaki, M., and Hirose, T. (2006) *Journal of Material Science*, **41**, 1509–1513.

94 Santos, A.S.F., Texeira, B.A.N., Agnelli, J. A.M., and Manrich, S. (2005) *Resources, Conservation and Recycling*, **45**, 159–171.

95 Pinero-Hernanz, R., Garcia-Serna, J., Dodds, C., Hyde, J., Poliakoff, M., Cocero, M.J., Kingman, S., Pickering, S., and Lester, E. (2008) *Journal of Supercritical Fluids*, **46**, 83–92.

96 Yuyan, L., Guohua, S., and Linghui, M. (2009) *Material Science and Engineering A*, **520**, 179–183.

97 Parkinson, H.J. and Thompson, G. (2003) *Proceedings of the Institute of Mechanical Engineers*, **218**, 1–13.

98 Carli, L.N., Boniatti, R., Texeira, C.E., Nunes, R.C.R., and Crespo, J.S. (2009) *Materials Science and Engineering C*, **29**, 383–386.

99 Hashimoto, T., Mori, H., and Urushisaki, M. (2008) *Journal of Polymer Science Part A*, **46**, 1893–1901.

100 Keane, M.A. (2009) *ChemSusChem*, **2**, 207–214.

101 Zhang, J., Cui, P., Tian, X., and Zheng, K. (2007) *Journal of Applied Polymer Science*, **104**, 9–14.

102 Lewicki, J.P., Liggat, J.J., Hayward, D., Pethrick, R.A., and Patel, M. (2009) Degradative thermal analysis and dielectric spectroscopy studies of aging in polysiloxane nanocomposites, in *Polymer Degradation and Performance* (ed. M. Celina), American Chemical Society, Washington, DC.

103 Cheul-Kyu, L., Yong-Ki, K., Phirada, P., Jung-Suk, K., Kun-Mo, L., and Chang-Sik, J. (2010) *Transportation Research Part D*, **15**, 197–203.

104 Reijnders, L. (2008) *Journal of Industrial Ecology*, **12**, 297–306.

105 Auffan, M., Rose, J., Bottero, J., Lowry, G. V., Joliver, J., and Wiesner, M.K. (2009) *Nature Nanotechnology*, **4**, 634–641.

106 Bernard, A.S. (2010) *Nature Nanotechnology*, **5**, 271–274.

107 Kostarelos, A., Bianco, A., and Prato, A. (2009) *Nature Nanotechnology*, **4**, 672–633.

108 Kagan, V.E., Konduru, N.V., Feng, W., Allen, B.L., Conroy, J., Volkov, J., Vlasova, I.I., Belikova, N.A., Yanamala, N., Kapralov, A., Tyurina, Y.Y., Shi, J., Kisin, E.R., Murray, A.R., Franks, J., Stilz, D., Gou, P., Klein-Seetharaman, J., Fadeel, B., Star, A., and Shvedova, A.A. (2010) *Nature Nanotechnology*, **5**, 354–359.

109 Sotiriou, G.A. and Pratsinis, S.E. (2010) *Environmental Science & Technology*, **44** (14), 5649–5654.

Index

Polymer Composites: Volume 2, First Edition. Edited by Sabu Thomas, Kuruvilla Joseph, Sant Kumar Malhotra, Koichi Goda, and Meyyarappallil Sadasivan Sreekala.

d